2013

Assessment of post-compaction characteristics of an unsaturated silty sand

Ana Paula Ribeiro Heitor
University of Wollongong

UNIVERSITY OF WOLLONGONG

Department of Engineering,

School of Civil, Mining and Environmental Engineering

Assessment of Post-compaction Characteristics of an Unsaturated Silty Sand

Ana Paula Ribeiro Heitor

(LicEng, MEng)

This thesis is presented as part of the requirements for the

award of the Degree of Doctor of Philosophy

of the

University of Wollongong

January 2013

“the habit of active utilisation of well-understood principles is the final possession of wisdom”

Alfred North Whitehead

CERTIFICATION

I, Ana Paula Ribeiro Heitor, declare that this thesis, submitted in fulfilment of the requirements for the award of Doctor of Philosophy, in the Department of Civil Engineering, University of Wollongong, is wholly my own work unless otherwise referenced or acknowledged. The results, ideas and convictions presented are those of the author, except when stated otherwise, and only she is accountable for them. The document has not been submitted for qualification at any other academic institution.

Ana Heitor

January 2013

ABSTRACT

Conventional field compaction control methods including nuclear gauge, sand cone and rubber balloon, are effective at the time of placement. However, their measurements are discrete and have a limited depth of investigation, which may not be suitable for post-construction compaction quality assessments of deeper fills or larger surface areas. In this situation, classical destructive geotechnical surveys (i.e. boreholes, cone penetration tests) are sought to evaluate the current fill conditions. Nevertheless, these methods often do not provide the level of required information because only certain locations are tested and furthermore they have tremendous implications in terms of cost. The use of available non-destructive cost and time effective methodologies, such as shear wave velocity surveys (i.e. SASW, spectral analysis of surface waves or HVSR, horizontal-to-vertical spectral ratio), offers a valuable alternative to efficiently control compaction over large areas during post-construction stages, and locate areas within the existing formations where the soil was not sufficiently compacted. In fact, shear wave velocity (V_s) has been used in the past to evaluate the quality of compaction or the *in-situ* void ratio, but in most of these studies the effect of partial saturation has been neglected. While this may not be a major concern for natural ground profiles where the ground water level (GWL) is close to the surface, for reclaimed fill areas it is a significant problem where the GWL is usually located deeper. This is particularly noteworthy, because, high *in situ* V_s may not truly represent a higher degree of densification. Furthermore, compacted soil is under unsaturated condition, which means that in-situ suction has an important role in controlling the shear strength.

This doctoral thesis addresses the effects of partial saturation in the implementation of a field methodology based on the propagation of shear wave velocity and suction for evaluating the compaction quality. It encompasses the use of both small and large strain range in relation to laboratory and field approaches to characterise the behaviour of materials under different compaction conditions, as well macrostructure characterization using X-ray CT-scan techniques. The small strain behaviour was characterized using Bender elements for both as compacted and post-compaction conditions. Specimens representative of different compaction conditions, that is water content and energy levels, were tested straight after compaction and subjected to isotropic confining pressures while maintaining constant water content conditions

to evaluate the effect of in-situ overburden stress. Moreover, cycles of wetting and drying were also imposed to the compacted specimens in an effort to understand the effect of climatic variations on the measured V_s and its relative importance for the field site in Penrith. During these tests the suction was controlled and measured using an array of different techniques including axis translation technique, filter paper method and a small tip tensiometer.

The mechanical behaviour of the silty sand soil was investigated through constant water content direct shear (CWDS) tests, given that in-service strain is likely to exceed the small strain domain in which V_s is measured. While suction during the test was not measured, a simple formulation based on the pore air pressure associated with the volumetric changes of the specimen undergoing undrained shearing was proposed. Specimens were tested for different compaction conditions (i.e water content and energy levels) in both as compacted and post compacted states.

A new empirical formulation for evaluating the current void ratio or degree of compaction based on shear wave propagation and suction or water content is proposed in this thesis. The performance of the methodology developed was first calibrated for site-specific silty sand soil in laboratory and then assessed for field site located in Penrith, in which the evaluation of the current compaction degree is of paramount importance for the future redevelopment of the site. The thesis also addresses numerous practical guidelines and recommendations for the future.

ACKNOWLEDGEMENTS

I wish to express my heartfelt thanks to all that contributed to the successful completion of this work. First and foremost, I thank my supervisors Prof. Buddhima Indraratna and Dr. Cholachat Rujiakiamjorn for their patient guidance, valuable discussions, proofreading and advice with all the questions that arose from the elaboration of this dissertation, and especially for their extended friendship.

To the technical staff at UOW for the well appreciated help in equipment fabrication and troubleshooting, in particular Mr. Alan Grant, Mr. Ian Laird, Mr. Frank Crabee and Mr. Douglas Henness. To all of the students that have passed in Centre for Geomechanics and Railway Engineering in these three years, particularly Mrs. Nayoma Tennakoon, Mr. Kourosh Kianfar, Mr. Wuditha Premadasa, Mrs. Rasika Athukorala, Mr. Kumara Chandrasiri, Mrs. Maria Rashidi for all the fruitful discussions and good friendship. To Mr. Roseller Oblimar for all the well-appreciated help while performing some of the laboratory experiments.

To the Australian Research Council (ARC), Penrith Lakes Development Corporation (PLDC) and Coffey Geotechnics for the financial support provided and assistance by Mr. Robert Golaszewski (PLDC), Mr. Michael Hudges (Coffey Geotechnics), Mr. Pavlick Harutoonian (UWS) and Dr. Chin Leo (UWS).

During the period of my candidature I was always very fortunate to find help outside of UOW whenever I desperately needed it, particularly with aspects related with unsaturated soil testing. A sincere vote of thanks goes to Dr. Sergio Lourenco (Cardiff University), Prof. Peter Robertson (Gregg Drilling and Testing), Prof. Harianto Rahardjo (Nayang Technical University), Prof. Leong (Nayang Technical University) and Prof. Alessandro Tarantino (Strathclyde University) that kindly dedicated their time to answer my questions via email.

To Ms. Laia Ledo, Ms. Xanna Janssen, the Martins and the Yakan family and particularly to Mr. Eren Uz for their constant friendship that helped me through critical moments. A big thank you also goes to Dr. Wojciech Solowski for his patience and much helpful advice during the write-up period. Extended thanks are also due to Bill Clayton for editing and proofreading. To A/Prof. Arul Arulrajah and Dr. Adrian Russell for their careful and thorough review, must helpful comments and suggestions in the revision of the thesis.

Finally, to my parents and my sister that have unwavering encouraged me through every step of this journey and supported me through the most difficult moments.

LIST OF PUBLICATIONS

The following awards and publications are related with this PhD thesis.

a. Awards

AGS Young Professional Night Competition (2010) First Prize for Geotechnical Research Contributions at the Young Geotechnical Engineers presentations held at Australian Geomechanics Society - *Sydney Chapter, the Institution of Engineers Australia*, Sydney (8th September 2010)

AGS NSW Research Award (2012) First Prize for Geotechnical Research Contributions at the Research Award presentations held at Australian Geomechanics Society (Shared) - *Sydney and Newcastle Chapters, the Institution of Engineers Australia*, Sydney and Newcastle (9th and 15th of May 2012)

b. Refereed scholarly journal papers

Heitor, A., Indraratna, B. and Rujikiamjorn, C. (2012). Characterization of compacted using shear wave velocity and matric suction. *Australian Geomechanics Journal*, 47 (2), 79-86.

Heitor, A., Indraratna, B. and Rujikiamjorn, C. (2012). Laboratory study of small strain behavior of a compacted silty sand. *Canadian Geotechnical Journal* (Accepted)

c. Refereed scholarly journal papers in preparation

Heitor, A., Indraratna, B. and Rujikiamjorn, C. (2013). Evaluating the compaction degree based on in situ V_s and water content.

Heitor, A., Indraratna, B. and Rujikiamjorn, C. (2013). Elastic properties of a compacted silty sand soil during cycles of wetting and drying.

d. Refereed conference papers

Indraratna, B., Heitor, A. and Rujikiamjorn, C. (2011). Effect of compaction energy on shear wave velocity of dynamically compacted silty sand soil., *Proceedings of the 5th Asia-Pacific Conference on Unsaturated Soils (AP-UNSAT 2011)*, A. Jotisankasa, A. Sawangsuriya, S. Soralump & W. Mairaing (Eds.) Kasetsart University, Pattaya, Thailand, 635-640.

Heitor, A., Indraratna, B., Rujikiatkamjorn, C., and Golaszewski, R. (2012). Characterising compacted fills at Penrith Lakes development site using shear wave velocity and matric suction. *Proceedings 11th Australia - New Zealand Conference on Geomechanics: Ground Engineering in a Changing World*, 15 – 18 July 2012, Melbourne, Australia, Narsilio, G. A., Arulrajah, A., and Kodikara, J. (Eds.), 1262-1267.

Rujikiamjorn, C., Heitor, A., Indraratna, B. and (2012). The effect of dry unit weight, suction, and imparted energy on the modulus of a compacted mixture of sand and kaolin, *Proceedings of the 2nd International Conference on Transportation Geotechnics* (in press)

Heitor, A., Indraratna, B. and Rujikiamjorn, C. (2012). Use of the soil modulus for compaction control of compacted soils. *Proceedings of the International Conference on Ground Improvement and Ground Control* (in press)

LIST OF SYMBOLS

Letters

a	parameters that control the rate of increase of V_s
a_s	empirical parameter of the $A(S_r)$
A	parameter associated with the soil structure
$A(S_r)$	degree of saturation function
b_{ij}	empirical exponent of suction
b	empirical exponent of suction
b_s	empirical parameter of the $A(S_r)$
B	width of the footing
c'	effective cohesion at zero suction
C_{ij}	empirical constant
C	empirical constant
e	void ratio
e_{max}	maximum void ratio
e^*_{min}	minimum void ratio
e_w	water ratio
e_{wm}	microstructural water ratio
E	compaction energy
E_{unsat}	unsaturated elastic modulus
$f(e)$	void ratio function
$f(s)$	suction function
g	gravity acceleration
G_s	specific gravity
G_0	small strain shear modulus
G_r	reference small strain shear modulus
G_{unsat}	unsaturated small strain shear modulus
h	solubility constant
H_s	depth of moisture change
I_w	influence factor
K_0	earth pressure coefficient at rest
$k_{is(unsat)}$	unsaturated modulus of sub-grade reaction
L	thickness of the shear band
L_f	length of the footing
L_{tt}	tip to tip distance
$L_{tt\text{-}i}$	initial tip to tip distance or wave path length
l_b	bender elements cantilevered length
n	fitting parameter associated with the state of stress
n_s	porosity
n_0	initial porosity
N_c , N_γ, N_q	bearing capacity factor
p_a	atmospheric pressure
p_r	reference pressure
p'	mean effective stress
$q_{ult(unsat)}$	unsaturated ultimate bearing capacity
S_{max}	maximum degree of saturation

S_r	degree of saturation
S_0	the initial degree of saturation
S_{rm}	degree of saturation of the macropores
s	suction or also represented (u_a-u_w)
s_i	initial (as compacted) suction
u_a	pore air pressure
u_{ao}	initial absolute pore air pressure
u_{af}	final absolute pore air pressure
u_w	pore water pressure
$(u_a-u_w)_{AVR}$	average value of measured suction
V_a	volume of the air
V_{ao}	initial volume of the air
V_{af}	final volume of the air
V_s	shear wave velocity
$V_{s,\max}$	maximum shear wave velocity
$V_{s,sat}$	saturated shear wave velocity
$V_{s,n}$	normalised shear wave velocity
V	volume of an unsaturated soil unit
V_0	initial volume
V_s	volume of solids (volume of soil grains)
V_v	volume of voids
V_w	volume of the pore fluid
w	water content
w_i	initial (as compacted) water content
Δx	horizontal shear displacement
Δy	vertical displacement
z	depth

Greek letters

α	constant of proportionality
β	empirical parameter that reflects the nature of the grain contacts
ε_1 , ε_3	principal strains
ε_v	volumetric strain
ε_y	vertical strain
ϕ	empirical parameter that controls the rate of increase of V_s
ϕ'	effective friction angle at zero suction
ϕ^b	friction angle that reflects the increase in strength caused by an increase in suction
ϕ^a	friction angle that reflects the increase in strength caused by an increase in vertical stress
ϕ_{ds}	direct shear stress ratio
$(\phi_{ds})_r$	stress ratio at a residual state
γ_b	bulk unit weight
γ_d	dry unit weight
$\gamma_{d,field}$	dry unit weight measured in the field
$\gamma_{d,lab}$	maximum dry unit weight for standard compaction energy
γ_w	water unit weight

γ_{yx}	shear strain
χ	effective stress parameter
κ	parameter related to the plasticity index
λ	wave length
ρ	total density
ρ_a	density of the gas (air)
ρ_s	density of the solid grains
ρ_w	density of the fluid (water)
σ_m	mean confining pressure
σ_r	reference stress of 1kPa
σ_{mid}	field mean effective stress at the mid layer
σ_v	vertical stress ($= \gamma_b z$)
σ'_v	average skeleton stress
$(\sigma\text{-}u_a)$	net stress used in axis translation technique
θ_w	volumetric water content
θ	empirical parameter
φ	empirical parameter that controls the rate of increase of V_s
δ	angle of dilation
δ_f	angle of dilatancy at peak failure
τ	shear strength
τ_{sat}	shear strength of saturated state
ξ_c, ξ_γ	shape factors

Abbreviations

AC	As compacted
BE	Bender Elements
CPT	Cone Penetration Test
CWDS	Constant Water content Direct Shear
DC	Dynamic compaction
DHGD	Downhole Gamma Density
DMT	Flat plate dilatometer
GWL	Ground Water Level
HCT	High Capacity Tensiometer
HVSR	Horizontal-to-vertical spectral ratio
OMC	Optimum water content
PLDC	Penrith Lakes Development Corporation
PC	Post compacted
SASW	Spectral analysis of surface waves
TMI	Thornthwaite Moisture Index

TABLE OF CONTENTS

LIST OF FIGURES

LIST OF TABLES

CHAPTER ONE

1 INTRODUCTION

1.1 BACKGROUND

Compaction has been widely used in civil works to improve the geotechnical and geomechanical characteristics of soil. The inauspicious circumstances of some accidents, whether they were related to poor compaction or a lack of understanding of the compaction process, have resulted in an intensive study of compacted materials. Proctor (1933) was the first to develop and describe the behaviour of compacted soil and introduced the concept of a compaction curve, including a definition of the optimum moisture content. Since then, several researchers (i.e. Seed and Chan, 1959, Lambe, 1958, Turnbull and Foster, 1956, Casagrande and Hirschfeld, 1960, Olson and Langfelder, 1965 Olson, 1963) have successfully identified the structure, stress-deformation characteristics, shear strength, development of pore pressure, and the effective strength characteristics of compacted soil along the compaction curve. Despite these major achievements, the effect that changes in the structure of soil caused by compaction have on the mechanical and hydraulic behaviour, especially under unsaturated conditions, is still not well understood. In fact, soils compacted with different moisture contents or energies are often treated as essentially different soils. This aspect is of particular importance in terms of quality control because the common end product specifications (AS 3798 - 2007) do not stipulate the compaction paths, only the final target conditions in relation to water content and dry unit weight.

Conventional methods for controlling compaction in the field, including nuclear gauge, and sand cone and rubber balloon, are adequate for the control the compacted soil at the time of placement, yet because of their localised nature, these techniques may not be suitable for deeper fills or for assessing larger areas. This is particularly important in the detection of soft spots that may lead to problems related to insufficient bearing capacity during the service life of the fill, so under these conditions, alternative non-destructive methods based on the shear wave velocity propagation should be considered. Shear wave velocity surveys, have been used extensively in many geotechnical applications to evaluate the dynamic properties of ground

subjected to cyclic loads (i.e. vibrations caused by the traffic of heavy, fast moving vehicles, and earthquakes). The shear wave, which propagates through the soil skeleton, is an adequate variable to verify the quality of compaction during construction (Waddel et al, 2010). However, its direct application for assessing the current state of compacted fills (post-construction stages) is not straightforward because compacted soil is under unsaturated condition and the in-situ suction plays an important role in controlling the shear strength. Indeed, recent studies on the propagation of shear waves in unsaturated soils showed that an increase in suction increases the stiffness of the soil skeleton, which in turn increases the shear wave velocity or small strain shear modulus (Wu et al., 1984; Cho and Santamarina, 2001; Ng and Menzies, 2007; Mancuso et al., 2002). While the theoretical concepts and fundamental basis of the propagation of shear wave and suction have been well established individually and separately, only a limited number of studies have focussed on the propagation of shear waves in soils compacted under different conditions (water content and energy).

In this thesis, a new methodology is proposed to assess the quality of compaction in post-construction stages and older compacted embankments where few or no records of the method of control at the time of construction are available. This methodology is based on propagation of the shear wave while considering unsaturated conditions.

1.2 RESEARCH MOTIVATION

The principal motivation behind the study presented herein is related to the field estimation of compaction degree of a field site in Penrith (Australia) comprising of compacted soil to a depth of approximately 15-20m, which extends over a surface area of 2000 hectares. The ground water level on site is located at approximately 12-15m depth, which means that the fills are essentially under unsaturated conditions.

The beginning of the Penrith lakes scheme in the early 80's involved removing sand and gravel and subsequent rehabilitation by backfilling the quarried areas. In general, the filling work was achieved according to the specifications on the Deed of Agreement (DOA), with placement and compaction using scrapers and compaction control based on certain relative dry unit weight specifications. However, before the DOA a significant portion of the landform was already constructed without any historical records of the placement methodology. Due to insufficient compaction records, these particular fill areas can be deemed as an uncontrolled

fill. As a consequence, the scope for future land use is restricted to parkland without suitable verification methods to confirm the level of compaction. Thus, the assessment of the current conditions in terms of strength, that is, sufficient bearing capacity is of paramount importance.

1.3 OBJECTIVES AND SCOPE

The ultimate study goal is to develop and validate a new methodology for assessing the degree and depth of compaction of large areas during post-construction stages. This joint project combines different specialities and brings together partners from research and practitioners' engineering teams,

- University of Wollongong, UOW (for laboratory validation),
- University of Western Sydney, UWS (for field validation),
- Penrith Lakes Development Corporation, PLDC (for assistance in site validation),
- Coffey Geotechnics (for assistance in the analysis of in situ destructive testing).

This research project has been conducted in two companion PhD dissertations: the present PhD thesis at UOW and the PhD thesis of Harutoonian (2012) at UWS. The work carried out at UWS focussed on a field implementation of the new methodology for assessing the shear wave velocity based on ambient noise techniques (horizontal-to-vertical spectral ratio, HVSR). It proposed field implementation guidelines and inversion algorithms to determine the *in situ* shear wave velocity.

The present study focuses on the experimental validation of a methodology that enables the fundamental properties of soil to be calibrated with the shear wave velocity. The aim is to study the small strain and large strain response of compacted soil, and to propose a novel empirical formulation for shear wave velocity coupled with the effects of water retention and degree of compaction.

The specific objectives are as follows:

i) The development of a soil model to evaluate the degree of compaction based on the propagation shear wave velocity (V_s) and the compaction induced suction for as compacted and post compacted (in service) states,

ii) To quantify the essential laboratory and field parameters, with special reference to the behaviour of soil at Penrith Lakes Development Corporation (PLDC), i.e. the shear

strength based on the as compacted suction and any variation of the deformation modulus with field density and degree of saturation.

iii) To calibrate the properties of soil at Penrith Lakes assessed in both field and laboratory, including several profiles of the shear wave velocity (V_s), in order to establish comprehensive guidelines and reference charts for practicing engineers to determine the location(s) of insufficient compaction, and predict associated behaviour in terms of bearing capacity through empirical relations and shear strength parameters for future infrastructure development.

1.4 ORGANIZATION OF THE THESIS

This dissertation is divided into 8 chapters. Chapter one introduces the background and motivation for the thesis. It also outlines the structure and organisation of this thesis.

Chapter 2 provides a review of the current state of research on the behaviour of compacted soil, including the fundamentals and currently available literature on unsaturated compacted soil, with respect to the shear strength, water retention characteristics, small strain stiffness, and shear wave velocity. It also gives some insights into the available constitutive models for unsaturated compacted soil. The models discussed include those predicting deformation under loading at constant suction as well as those for water retention behaviour and the compaction process itself.

Chapter 3 introduces the site at Penrith Lakes in terms of background, and provides some results of the characterisation of the materials used in this work. It also outlines the main results obtained by destructive geotechnical investigations conducted in the field benchmark areas prior to this study.

Chapter 4 outlines the apparatus available for measuring the shear wave velocity and suction, highlighting the advantages and limitations of the types most commonly used. The results from Computed Tomography scans (X-ray CT) performed on selected compacted specimens are shown and discussed in terms of the soil macrostructure.

Chapter 5 describes the experimental results of small strain behaviour in as compacted and post compacted conditions. The specimens were tested with Bender elements straight after

compaction and under isotropic confining pressures. In addition, the specimens compacted at different energy levels were also subjected to post-compaction wetting and drying cycles. The results of selected specimens tested in full saturation conditions are also shown. The results were presented in terms of shear wave velocity and small strain modulus.

Chapter 6 describes the theoretical formulation for evaluating the degree of compaction based on shear wave propagation and suction. A simple formulation for evaluating the small strain stiffness of compacted soil prepared with different water contents and compaction efforts using a single set of parameters is also developed.

Chapter 7 provides a thorough investigation of the stress-strain behaviour of the reference soil at strain ranges expected during in the service life of fills. A novel formulation for estimating suction during a direct shear test, based on volumetric changes, is also introduced, as are the details of its implementation in the analysis of a constant water content direct shear test (CWDST). The shear strength is evaluated in an as compacted and post compacted state through CWDST.

Chapter 8 describes some examples of these applications in practice. It includes a step by step example for evaluating the degree of compaction on the field benchmark areas at Penrith Lakes. The results from the small strain and larger strain conditions are compared and estimations of the bearing capacity are given. The practical implications of the small strain stiffness in relation to the common of end product specifications are also discussed.

Chapter 9 presents a final summary of the main findings from the thesis and offers some recommendations for future work.

CHAPTER TWO

2 . LITERATURE REVIEW

2.1 GENERAL

The aim of this chapter is to analyse the current state of research related to the behaviour and constitutive modelling of compacted soils in regards their shear strength and small strain stiffness, water retention characteristics, and structure. It begins by introducing the fundamental studies of soil compaction theory and engineering behaviour and thereafter important aspects of unsaturated soil in terms of water retention, microstructure, shear strength and small strain stiffness, are discussed and explained. Subsequently, a review of the constitutive models available to describe macroscopic stress-strain behaviour and the small strain stiffness of compacted soil is presented. Finally, on the basis of the literature review, the current knowledge is summarised and the anticipated contribution of this present study is outlined.

2.2 FUNDAMENTALS OF COMPACTED SOIL

2.2.1 Soil Compaction Theory

Compaction is one of the most common procedures used throughout the world to improve the geomechanical properties of soil, and yet few theories have been brought forward to adequately explain the characteristic behaviour of soil under compaction. These characteristics have long been identified in the progressive works by Proctor (1933), but since then, qualitative theories such as Proctor's theory (1933), Hogentogler's theory (1936), Lambe's theory (1958) and Olson's theory (1963), have been developed to explain the compaction procedure.

In Proctor's theory (1933) "soils are thought to be compacted by forcing the smaller particles to move into spaces between larger ones, thus increasing soil density and decreasing voids". The higher strength on the dry side can be accounted for by the capillary effect and as the water content increases, it acts as lubricating agent contributing to a reduction of inter-particle friction (reducing the shear strength). Moreover at higher water contents, the voids

equal the volume of the contained water which results in a soil with less density, and increased plasticity.

Hogentogtler (1936) proposed that water is adsorbed onto the surface of soil particles forming layers around each particle. At lower moisture contents, the high viscosity of water between the contact points of the particles would give the soil a high shearing strength. The addition of water would help lubricate the particles and lead to higher dry densities.

Lambe's theory (1958) investigated the compaction process from the physico-chemical point of view. At lower water contents the high concentration of electrolytes reduces the osmotic repulsion between the soil particles and allows for flocculation to occur. This flocculation of the particles induces low dry densities on the dry side of the compaction curve. The addition of water decreases the concentration of electrolytes and allows double layers to form, which results in a more dispersive soil structure (Figure 2.1). Seed and Chan (1959) extended Lambe's concept and demonstrated that clayey soils compacted on the dry of optimum develop a flocculated structure with randomly oriented particles, whereas on the wet side of an optimum moisture content, the soil develops a more dispersed structure where the particles are parallel. Soils with a flocculated structure are stiffer, develop higher shear strength in undrained loading and exhibit lower compressibility, higher permeability, and a higher collapse or swelling potential than dispersed structured ones.

Olson (1963) developed a theory based on the concepts of effective stress, by considering Bishop (1959) relationship for unsaturated soil and changes in pore water pressure during compaction, through Skempton's A and B parameters When compaction is first applied, shearing stresses develop between particles and upon reaching the shearing strength of the contact surfaces, the contacts yield and the particles slide over each other, and the density of the soil increases. Increasing moisture contents (or degree of saturation) can lead to increasing B-values and the generation of higher pore water pressures as subsequent blows are applied (Figure 2.2).

This progressive increase in dry density with increasing water content in the soil is mainly due to changes in total lateral stresses, residual negative pore water, and pore pressures during the application of stress which results in changes in confining stresses (B-values) and shearing stresses (A-values). When the air phase in the soil becomes discontinuous and air is trapped, its permeability drops to zero and no further densification is possible, so the soil

reaches its optimum moisture content (OMC). Beyond the OMC the pore-water pressures increase slightly as the blow is applied and then decreases again, becoming sufficiently negative at large strains to allow the soil to resist the applied stress.

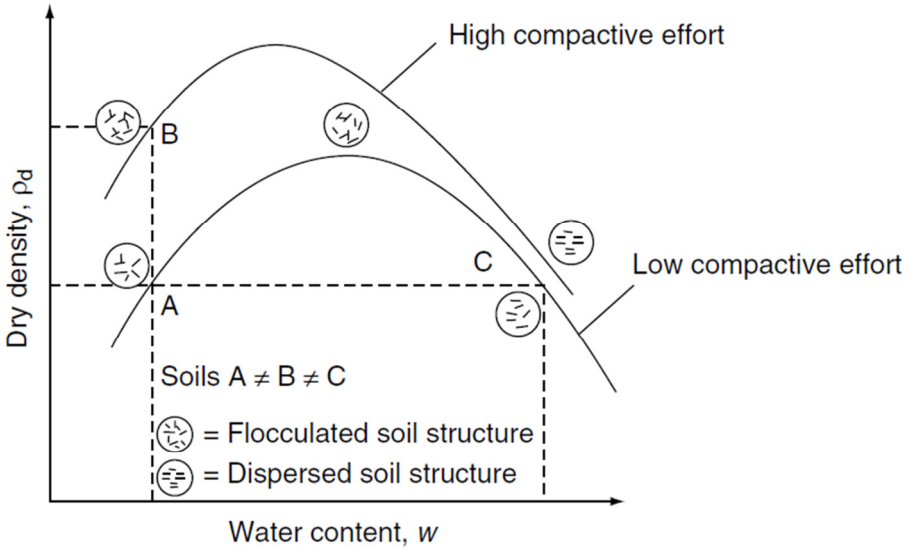

Figure 2.1 Soil structure varying along the compaction curve for clay specimens (Lambe, 1958).

In common engineering practice, both Proctor and Lambe's theories are accepted, whereas Hogentogler's and Olson's are less well known. Nevertheless, Olson's approach is interesting because it already incorporates the concept of unsaturated soil and may be the most adequate way of describing the compaction curve quantitatively, although the physico-chemical properties surely control the shape of the compaction curve to some extent, as they control the electrical forces of interaction between soil particles.

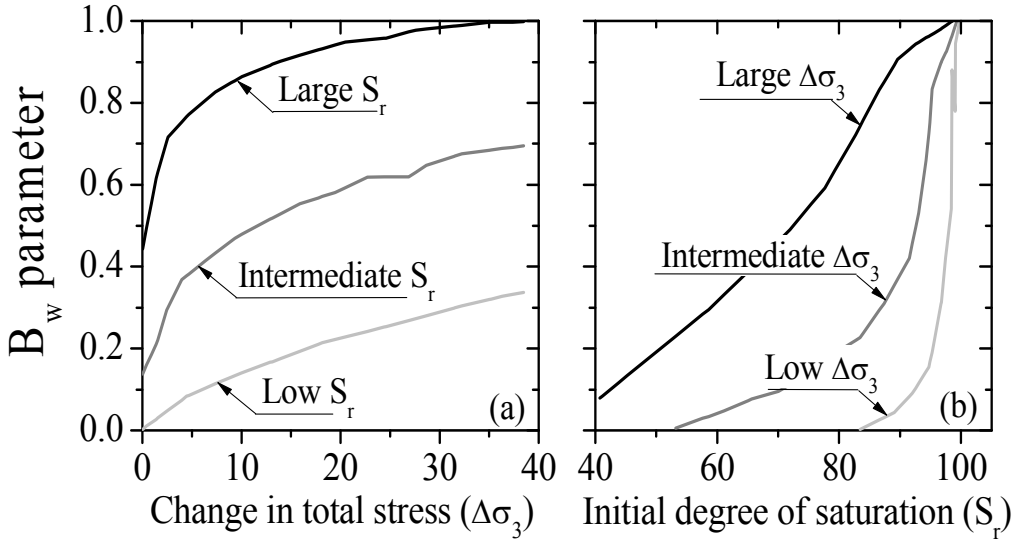

Figure 2.2 B value with the degree of saturation (after Olson, 1963).

2.2.2 Engineering behaviour

The initial moisture is the main parameter responsible for the difference in engineering behaviour of compacted soil because it strongly influences the microstructure developed through compaction. Given the paramount importance of compacted fills in many civil construction works such as dams, and road and rail infrastructures, a great deal of research effort has been put into characterising these materials according to their geomechanical performance. Table 2.1 lists a summary of the main research findings associated with different aspects of engineering behaviour of compacted soils.

2.3 BEHAVIOUR OF UNSATURATED COMPACTED SOIL

2.3.1 Overview of unsaturated soil

Unsaturated soils are present in most geotechnical engineering structures, including earth dams, river levees, road and rail embankments. While in saturated soils the mechanical behaviour can be described by Terzaghi's law of effective stress, the mechanical behaviour of unsaturated soils is more complex because the voids are filled with air and water. In fact, while this topic has witnessed a widespread research effort over the last decades in scholarly academia, the transfer of technology to practicing engineers has been rather slow. For this reason, unsaturated soil is still often treated as in fully saturated condition in engineering practice.

Table 2.1: Summary of the main research findings related to compacted materials

Investigator	Variable investigated	Significance of findings
Lambe (1958)	Shear Strength	1) Result of the combination between granular type strength plus a colloidal type strength 2) Influenced by particle spacing, particle orientation, applied stress and soil-water system characteristics 3) Increased strength for increased compactive effort and reduced strength for progressive added water
Casagrande and Hirschfeld (1960)	Shear strength	1) For specimens prepared at the same dry unit weight the shear strength decreases as the degree of saturation increases (for Sr=100% the failure envelope becomes horizontal)
Lambe (1958)	Compressibility	1) The application of progressive compressive load seems to change the particle's orientation: aline the particles in a parallel array 2) Large enough pressure would cause the particle orientation from both wet and dry side to be the identical 3) There is a pressure required to start significant changes in the orientation (equivalent to the preconsolidation pressure, or compactive effort) depending as well on the pore fluid and period of load application.
Lambe (1958)	Permeability	4) Depends of soil composition, particle size curve, void ratio, degree of saturation and structure. 5) Random orientation of particles on dry side leads to larger pores (larger permeability), whereas on the wet side the nearly parallel arrangement lead to smaller pores yielding lower permeability values
Seed and Chan (1959)	Undrained Compressive Strength	1) Samples compacted on the dry side have higher compressive strengths and the material appears to be brittle whereas in the wet side the material appears to be more plastic 2) In the small strain domain the soil structure has a tremendous importance in the strength performance of the soil 3) At larger strains, i.e. at 20% of the peak stress, the influence is less evident and stress values are nearly the same value for both cases.
Ajaz and Parry (1975) & Indraratna et al. (1990)	Tensile Strength	1) The maximum tensile strains at failure increase with moulding moisture content regardless of the type of test or the optimum moisture content (OMC). 2) At comparable moisture contents the ability of compacted soils to sustain tensile strain decreases with the increasing compaction effort
Seed and Chan (1959) & Kenai et al. (2006)	Influence of compaction method in the compacted soil strength	1) The differences in stress-strain response caused by difference in the method of compaction are larger on the wet side of the compaction curve 2) In the domain of higher strains the influence of the method of compaction in the shear strength of soil is minimum. 3) Subjecting the sample to vibratory motion prior to static compaction leads to changes both in the compaction curve as well as in the compressive strength.

2.3.2 Soil-Water retention behaviour

2.3.2.1 Suction Potential

Suction potential is the potential energy of water relative to pure water in a reference state. It quantifies the tendency of water to move from one area to another due to osmosis, gravity, mechanical pressure, or capillary action. Commonly referred as the free energy state of soil-water, the suction potential can be measured in terms of its partial vapour pressure (Fredlund and Rahardjo, 1993). From a thermodynamic standpoint, total suction can be quantitatively described by Kelvin's equation Eq. (2.1) as follows (Ng and Menzies, 2007),

$$s = -\frac{RT}{v_{v0}\omega_v}\ln\left(\frac{u_v}{u_{v0}}\right) \tag{2.1}$$

where s is the total suction (kPa), R is the universal gas constant (J/(mol.K)), T is the absolute temperature (K), v_{w0} is the specific volume of water (m^3/kg), ω_v is the molecular mass of water vapour (g/mol), u_v is the partial pore-water vapour (kPa), and u_{v0} is the saturated pressure of water vapour over a flat surface of pure water at the same temperature (kPa). The term (u_v/u_{v0}) is called relative humidity, or RH (%).Two different potentials affect the total suction potential and these effects are additive. The two components are the pressure or capillary potential (u_a-u_w) and the osmotic potential (π), in Eq.(2.2).

$$s = \left(u_a - u_w\right) + \pi \tag{2.2}$$

Capillary potential or matric suction

The capillary potential corresponds to the intrinsic pressure of water which could be evaluated with respect to the atmospheric reference pressure. While the water pressure in saturated soil (i.e. below the water table) is positive and the liquid phase is in compression, in unsaturated soil, (i.e. above the water table) the hydrostatic water pressure is negative and therefore the liquid phase is in tension. This tension, designated as matric suction, is a result of the interaction of three phases (i.e. soil, water, and air) and it represents the difference in pressure between the soil water and the air, as in Eq. (2.3).

$$s = \left(u_a - u_w\right) \tag{2.3}$$

In the above relationship, s represents the matric suction, and u_a and u_w are the air and water pressure, respectively. In most cases the air pressure is the atmospheric pressure and hence, the suction is equal to the negative water pressure. The matric suction represents the combined effect of adsorption between the soil and water molecules, and capillary action within the soil matrix. While the adsorbed water is tightly bonded to the soil particles and could be considered

as a part of a solid skeleton, capillary action is a result of liquid surface tension. Surface tension pulls the liquid column up until there is a sufficient weight of liquid for gravitational forces to overcome the intermolecular forces. The difference between water and air pressures is related to the curvature of the interface of air and water phases (radii r_1 and r_2), and the surface tension (T_s) (Figure 2.3), or,

$$s = \left(u_a - u_w\right) = T_s \left(\frac{1}{r_1} + \frac{1}{r_2}\right) \tag{2.4}$$

The force derived by the capillary action acting on the grain contacts, can easily be quantified using a simple two spheres model (Mancuso et al., 2002), and its increase with increasing matric suction can be inferred by considering Fisher (1926) solution (Figure 2.4).

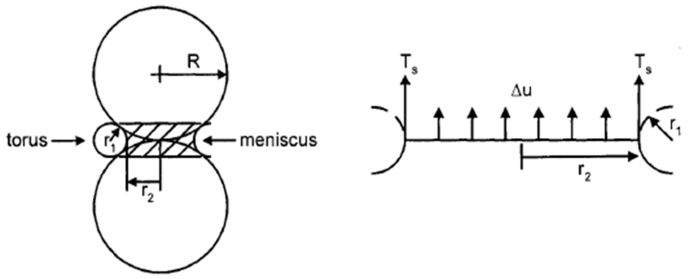

Figure 2.3 Schematic illustration of micro-scale models for unsaturated (a) spherical particles and (b) platy particles(Cho and Santamarina, 2001).

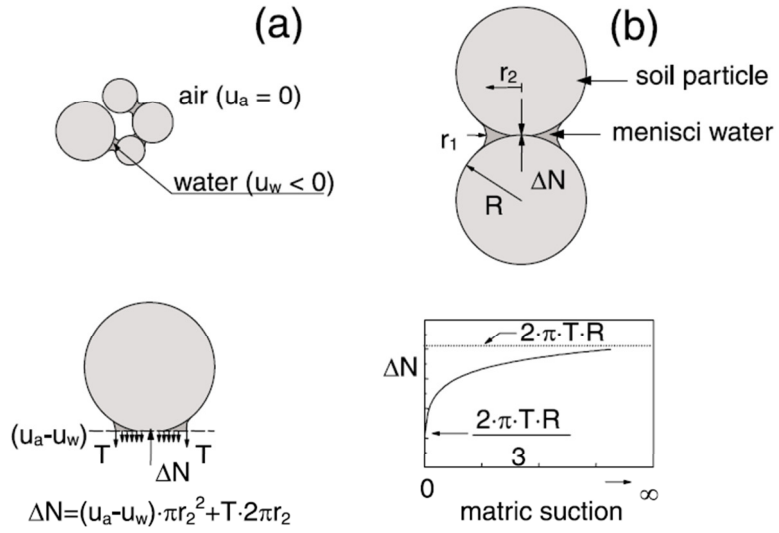

Figure 2.4 Schematic illustration of micro-scale models for unsaturated spherical particles (Mancuso et al., 2002).

Osmotic potential or osmotic suction

The osmotic potential of water is linked to the dissolved solutes (i.e. salts) in soil water. Pure water is usually defined as having a solute potential of zero that increases in a negative order for increasingly higher concentrations of solute in the pore fluid. Because osmotic suction can only be observed if the soil water comes in contact with pure water through a perfect semi-permeable membrane that should only allow water to pass through and not the solutes, it is not usually measured in soils. However, the concept of osmotic pressure has been used to design new testing equipment for testing of unsaturated clayey soils (i.e. Boso et al., 2005; Blatz et al., 2008; among others).

The matric suction is widely accepted to be the governing component of suction in describing the mechanical behaviour of unsaturated soils, and it has been used to formulate the mechanical constitutive models for these materials (see for example Alonso et al., 1990; Gallipoli et al., 2003;Cui and Delage, 1996; D'Onza et al., 2011). Therefore, from this point onwards in this work, the term suction refers to matric suction, unless stated otherwise.

2.3.2.2 Soil water retention curve

To adequately describe the hydraulic properties and understand the volumetric behaviour of unsaturated soil, it is necessary to establish a relationship between suction and the amount of water in the soil, which can be expressed either in terms of water content (mass), volumetric water content, or degree of saturation (volume). This relationship is often referred to as the soil-water retention curve or SWRC. The desaturation process expressed by the SWRC can divided into three main ranges, that is, the boundary effect zone, the transition zone, and the residual zone (Figure 2.5). The first transition point represents the air-entry value (AEV) which corresponds to the suction value that must be exceeded before air recedes into the soil pores. Before AEV has been exceeded the soil remains fully saturated and suction acts as an additional pressure. The second transition point represents the residual suction, upon which an increase in suction no longer produces significant change in the amount of water in the soil.

The shape and location of transition points is strongly dependent on the type of soil, particle size distribution (Fredlund et al., 2002), and its structure (Vanapalli et al., 1996). For instance, the SWRC curves of soils that are composed predominantly of sand show smaller

AEV values (in the order of 10 kPa), sharper slope curves with limited transition zones, whereas soils composed of clay show larger AEV and smoother curves with larger transition ranges. Note also that the shape and location of the transitions points in the SWRC is also affected if a different scale, i.e. double logarithm representation, is adopted instead. For instance, in the double logarithm representation of the SWRC, the transition to the residual zone is omitted and the AEV, which is extrapolated by the linear sections of the curve when degree of saturation is approaching unity, may differ (Figure 2.6).

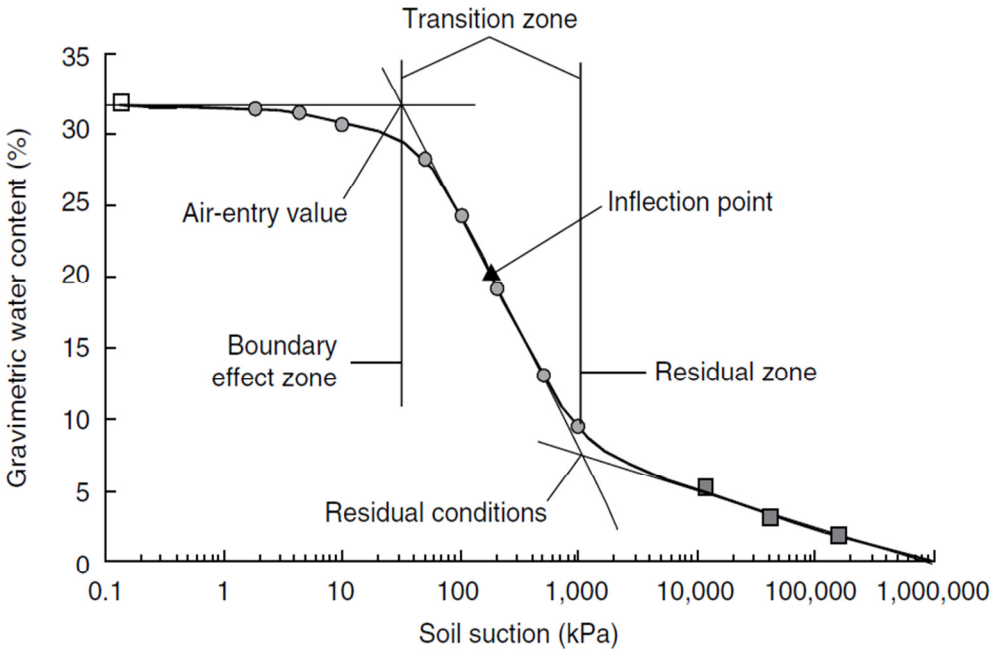

Figure 2.5 SWRC for a sandy soil (Fredlund, 2006).

SWRC for different compaction states

Vanapalli et al. (1996) compared the soil water retention curves of samples of glacial till that were statically compacted on the dry and wet side of the optimum moisture content. Although the difference in the SWRC that were obtained from specimens compacted on the dry side and at optimum moisture content could be explained by invoking the void ratio dependency (Gallipoli et al., 2003 model discussed later), the same cannot be said for the curves representing the wet side of the optimum specimens, which seem to be related more towards a difference in structure. The same experimental evidence is given for dynamically compacted residual soil tested with different compaction efforts (Marinho and Stuermer, 2000). This highlights that the differences in the water retention behaviour observed at different compaction induced states are likely to be independent of the different compaction procedures.

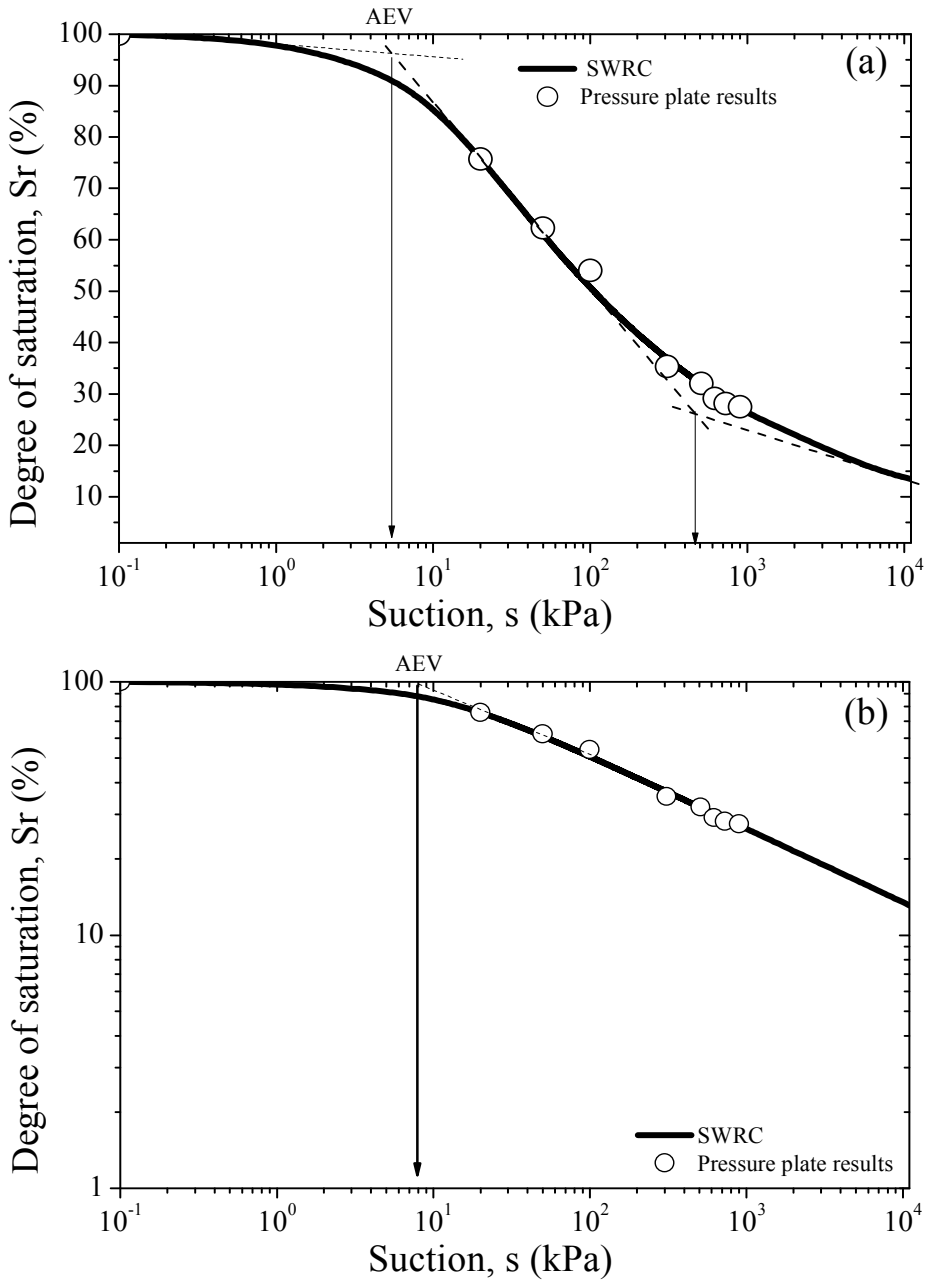

Figure 2.6 Conceptual representation of the SWRC using (a) semi-logarithm scale and (b) double logarithm scale.

Miller et al. (2002) compacted samples using three different compaction efforts and studied the soil water retention curves of the specimens compacted at optimum moisture content for each energy level, having approximately the same degree of saturation. As with the soil water retention behaviour on the dry side of optimum, these curves can be explained in terms of the initial compaction induced void ratio caused by increasing the compaction effort. In this case, although the specimens were compacted at different moisture contents and void ratios, the degree of saturation remained the same.

Another aspect associated with the desaturation process is the reduction in volume by shrinkage (volumetric changes) which at earlier stages can be directly related to the amount of water lost by the soil through evaporation (Marinho, 1994). In the large suction range, however, volumetric changes are more complex and directly associated with the changes in soil structure. The effect of suction on the soil structure will be discussed further in the following section.

Hysteresis

The water retention behaviour depends on whether the soil is being dried or wetted. Typically, the SWRC wetting curve plots below the drying curve in the suction-water content space (Figure 2.7). This difference has often been explained by the 'ink-bottle' effect (i.e Pham et al., 2005) which is related to the existence of large pores connected through smaller pores. To extract water from these smaller pores, higher values of suction must be exceeded and therefore at any given suction stage during drying, some water may be trapped in the larger pores. While this effect is significant during drying, it is less important during wetting. Any differences between the drying and wetting curves at zero suction can be attributed to air being entrapped during the wetting process. Other explanations of the hysteresis phenomena include the effects of different contact angles obtained when the meniscus is advancing or retreating, and the effect of chemical swelling/shrinking of soil minerals due to the presence of water.

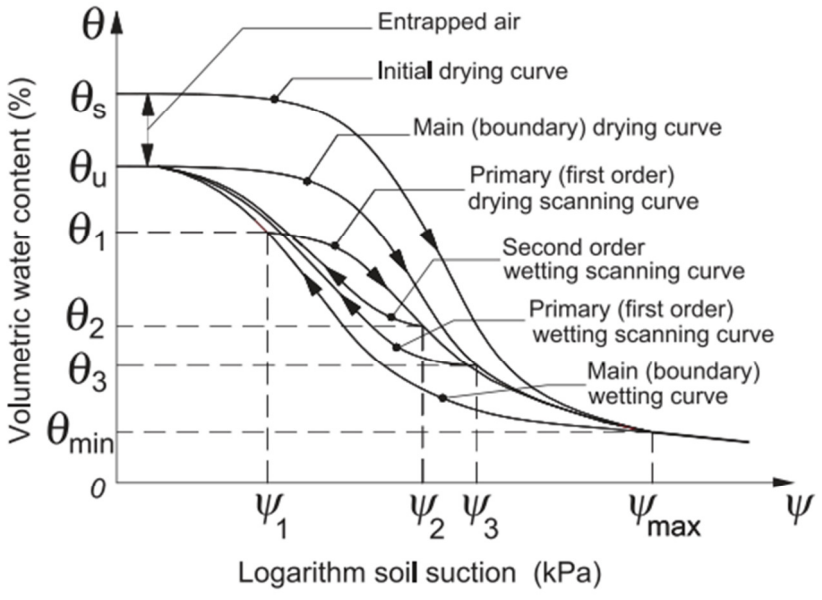

Figure 2.7 SWCC hysteresis (Pham et al., 2005)

In practice, the soil may not always follow a continuous path from a totally dried or wetted state. In most cases, the soil is likely to be at an intermediate stage described by the scanning curves. In Figure 2.7, one can observe that an infinite number of drying and wetting curves can be defined for subsequent cycles of wetting and drying. Note that the hysteresis amplitude is progressively decreasing for an increasing number of drying and wetting cycles. In addition, while the 'ink-bottle' effect is still present, its importance has been reduced, which may indicate that the soil is experiencing irrecoverable structural changes and the pore size distribution is becoming more uniform. This experimental data is also in accordance with the findings by Colmenares (2002) for bentonite soils. Further details about the effect of the increase in suction on soil structure are given in the following section.

Influence of Bimodal porosity

Compacted soils, particularly those compacted at the dry side of optimum moisture content, often exhibit different pore sizes sets (described in more detail in the following section). This is usually referred as double or bimodal porosity. The SWRC of soils that show bimodal porosity features are notorious because they show two different air entry values, associated to the macropore and micropore ranges (Figure 2.8). While in the low suction range the hydraulic behaviour is mainly controlled by the macroporosity (inter-aggregates porosity), for suction values exceeding the micropore air entry ($S_{m(ae)}$) the microporosity (intra-aggregate porosity) governs. In a bimodal water retention curve, an inflection point corresponding to the point where the macroporosity appears to have completely desaturated and the microporosity begins to desaturate may also be defined (Figure 2.8). According to Burger and Shackelford (2001) the water retention data for soil suctions smaller and greater than the suction corresponding to this point could be evaluated separately according to the physical properties macro- and micropores, respectively.

The importance of bimodal porosity on the hydraulic behaviour has also been reported for compacted sand and diatomaceous earth mixtures (Coppola, 2000; Burger and Shackelford, 2001; Zhang and Chen, 2005), kaolin (Bagherieh et al., 2009), gneissic residual soils and bentonite (Russell, 2010) and silty clay (Casini et al., 2012).

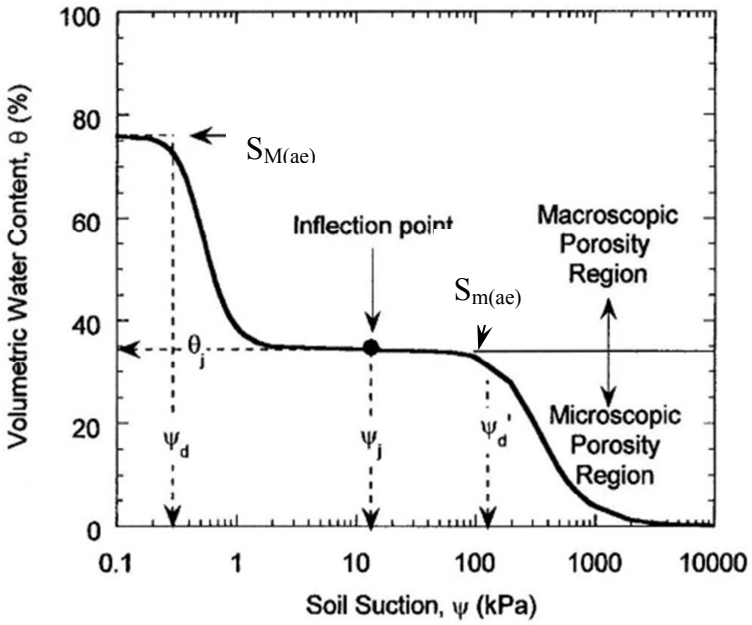

Figure 2.8 Conceptual respresentation of a bimodal SWRC (modified after Koliji et al., 2006).

Models

There have been different empirical models proposed to model the behaviour of SWRC. Leong and Rahardjo (1997) critically compared the available models and reported that the van Genutchen (1980) and Fredlund and Xing (1994) models performed best in capturing the unimodal SWRC over the entire range of suction. Although the Fredlund and Xing model, as expressed in Eq. (2.5), has more capability in the high suction range, it requires more parameters, which may offer some difficulties in the fitting process. Conversely, the van Genutchen model given in Eq. (2.6) and Eq. (2.7) gives a good approximation and is much simpler to apply.

$$\theta_v = C(\psi)\frac{\theta_s}{\left\{\ln\left[e+(\alpha s)^n\right]\right\}^m} \text{ with } C(\psi)=1-\frac{\ln\left(1+\frac{s}{\psi_r}\right)}{\ln\left(1+\frac{1.000.000}{\psi_r}\right)} \tag{2.5}$$

$$S_{re}=\frac{1}{\left[1+(\alpha s)^n\right]^m} \text{ with } m=1-\frac{1}{n} \tag{2.6}$$

$$S_{re}=\frac{\theta-\theta_r}{\theta_s-\theta_r}=\frac{nS_r-\theta_r}{\theta_s-\theta_r} \tag{2.7}$$

where S_{re} represents the effective degree of saturation that can be expressed in terms of porosity (n), residual volumetric water content (θ_r) and saturation volumetric water content(θ_s); α, n and

m are fitting parameters, ψ_r corresponds to suction value at residual water content, and s is the suction.

To describe the shape of a bimodal SWRC, the unimodal models may be extended to include the macroporosity (fitting parameters α_M, n_M and m_M) and microporosity (fitting parameters α_m, n_m and m_m) ranges as represented in Eq. (2.8), using for instance the van Genutchen (1980) model. The parameters p_M and p_m represent the relative percentage of the components with the large-pore series and the small-pore series in the soil mass.

$$S_{re} = p_M \frac{1}{\left[1+\left(\alpha_M s\right)^{n_M}\right]^{m_M}} + p_m \frac{1}{\left[1+\left(\alpha_m s\right)^{n_m}\right]^{m_m}} \tag{2.8}$$

In the above relationships, the SWRC equation does not take into account any changes in the volume of the soil, so Gallipoli et al., 2003 proposed an extension for the van Genutchen (1980) model and included the void ratio as function of α, and Eq. (2.6) was modified as follows

$$S_{re} = \frac{1}{\left[1+\left(\phi e^{\psi} s\right)^{n}\right]^{m}} \tag{2.9}$$

where e represents the void ratio and ϕ, ψ, m, n are material parameters obtained using best-fit methods such as the least-squares method.

While the models shown above are fitted with SWRC experimental data, more recently, many authors have proposed other methods to establish the drying and wetting branches of the SWRC for a wide range of different soils based on particle size distribution (PSD). These models stem from the consideration of the PSD density functions (i.e. Fredlund et al., 2002; Zhang and Chen, 2005) and from pore-solid fractal analysis (i.e. Huang and Zhang, 2005; Russell and Buzzi, 2012). The use of these models may prove very advantageous; however, caution must be exercised particularly for predicting hydraulic behaviour of soils reflecting different compaction states, when the soil structure plays an important role. Worth noting are also the SWRC models that incorporate the effect of the change in the microstructure during desaturation (i.e. Romero et al., 1999; Romero et al., 2011 and Zhou et al., 2012).

2.3.3 Soil structure

Differences in compaction are usually thought to produce essentially different soils. In fact, the change of soil structure caused by variations of the compaction-induced states, such as the water content and compaction effort, often results in distinct mechanical and hydraulic behaviour (Vanapalli et al., 1996; Wheeler and Sivakumar, 2000). Many research studies focused on investigating the different types of fabric developed when soil is compacted and how it affects the overall stress-strain behaviour (Seed and Chan, 1959; Barden and Sides, 1970), particularly the difference in structure derived from specimens being compacted on the dry and wet side of the compaction curve and subjected to different levels of compaction energy or pressure (mechanical wetting). Recently, it has also been shown that post-compaction changes in suction also have a strong influence on the fabric of the soil.

2.3.3.1 Influence of initial water content

Microscopic observations on compacted silts compacted to different initial water contents (Delage et al., 1996) using Scanning Electron Microscopy (SEM) techniques, showed that specimens on the dry side developed an open pore structure with large inter-aggregate pore spaces. On the other hand, the structure of soil at the optimum moisture content (OMC) is more constricted where the inter-aggregate pore spaces are reduced and the fines matrix begins to dominate. This matrix prevails on the wet side where porosity consists of significantly smaller intra-aggregate pores.

Evaluations of the soil structure based on mercury intrusion porisometry (MIP) conducted by Delage et al., 1996 in silts and Tarantino and De Col, 2008 in clay, also confirmed that there are smaller entrance pore values in specimens compacted on the wet side of the optimum moisture content (OMC). Moreover, it was observed that in both soils, a bimodal pore size distribution develops on the dry side of OMC. A bimodal pore size distribution is mainly caused by particle aggregation, that in turn leads to a microstructure that consists of relatively small intra-aggregate voids (microporosity) and larger inter-aggregate voids (macroporosity) between the aggregates (Figure 2.9 and Figure 2.10). In contrast, when the initial water content is increased and the soil moves towards OMC and the wet side of OMC, the microstructure consists of a matrix which is composed of smaller intra-aggregate pores and exhibits a typically unimodal pore size distribution. The role of inter-aggregate and

intra-aggregate porosity in the soil-water retention curves and associated soil permeability has also been identified by Romero et al., 1999 (see also section 2.3.2.2).

2.3.3.2 Mechanical wetting

While the change in the microstructure of compacted soil subjected to hydraulic wetting has been well documented, there have been fewer studies that investigated the effect of mechanical wetting (compaction energy or forming pressure). Early MIP studies conducted on specimens of kaolin produced by dynamic compaction at different energies (Diamond, 1970) showed that an increase in compaction energy mainly influences the macroporosity range. In fact, while the microporosity range (pore diameter < 0.1μm) seems relatively unaffected (Figure 2.11), the bimodal pore size distribution obtained for the lowest compaction energy becomes progressively unimodal for the higher compaction energies. Recent studies conducted by Tarantino and De Col, 2008 on statically compacted kaolin showed a similar tendency (Figure 2.12). While changes in macroporosity (0.8μm <pore diameter < 10μm) as the forming pressures increased are evident, the differences for micropores were smaller. This seems to indicate that regardless of the method of compaction adopted, a decrease in the void ratio caused by compaction at constant water content is only reflected on the macropores of the soil. Further evidence has also been given by the MIP studies conducted by Cuisinier and Laloui (2004) and Koliji et al. (2010) on specimens of silt subjected to post-compaction mechanical loading.

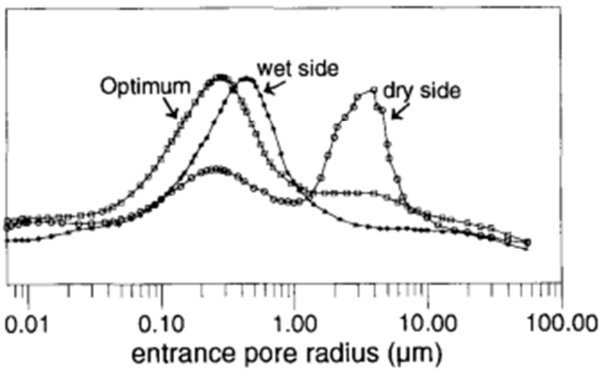

Figure 2.9 MIP pore size distribution curves for compacted silt in terms of (a) volume frequency and (b) cumulative intrusion volume (Delage et al., 1996).

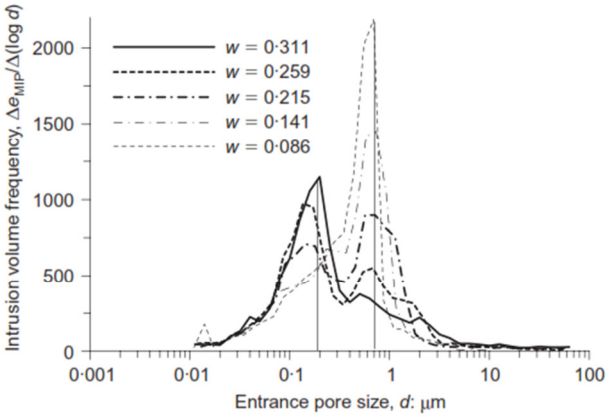

Figure 2.10 MIP pore size distribution curves in terms of intrusion volume frequency for compacted kaolin with different moisture contents (w) (Tarantino and De Col, 2008).

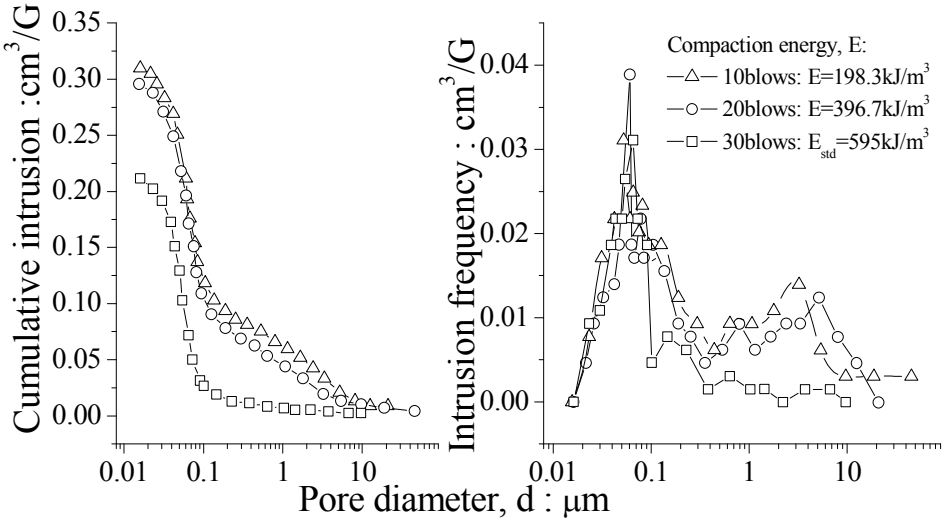

Figure 2.11 Fabric evolution in kaolin by MIP (a) cumulative intrusion and (b) intrusion frequency for specimens compacted at the water content of 26% and different compaction energies (cumulative intrusion data from Diamond, 1970).

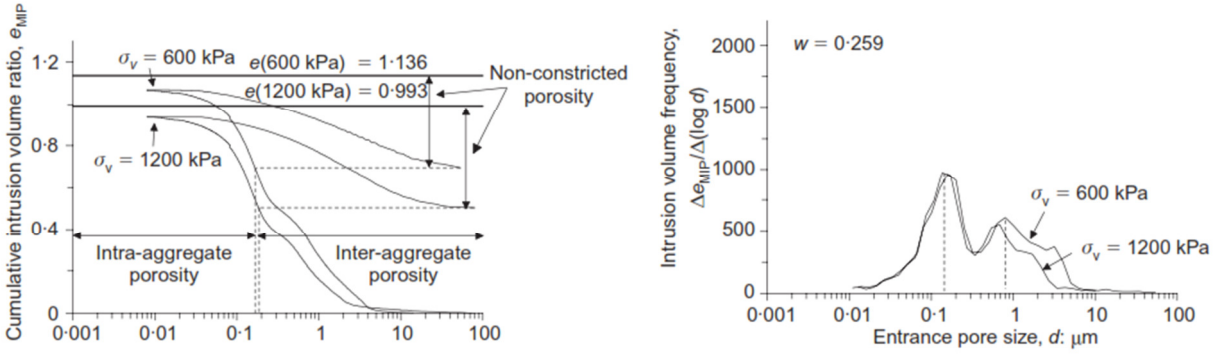

Figure 2.12 Fabric evolution in kaolin specimens during static compaction with different forming pressures (Tarantino and De Col, 2008).

2.3.3.3 Effects of changes in suction on the microstructure of soil

As outlined before, wetting and drying of soil leads to structural changes which are associated with the complex interaction between the micro and macropores of the soil. MIP studies on London clay performed by Monroy (2005) show that when soil is wetted, the bimodal structure (predominantly composed of micro and macropores) derived from compaction progressively changes into a more unimodal structure, largely concentrated in the mesopores range but still showing smaller peaks in the macro and micropore ranges (Figure 2.13). It was also reported that the structure that resulted from a wetting process was influenced by whether volumetric changes were allowed to take place. For a wetting process at a constant volume, the peak in mesopores is less pronounced and the volume of meso and macro pores is reduced.

Cuisinier and Laloui (2004), and more recently, Koliji (2006), reported that the bimodal porosity is recovered when a silty soil is subjected to drying from a saturated state (Figure 2.14). Indeed, while the volume of mesopores decreases, the volume of micro and macropores rises, which suggests that as particles of soil move along the drying path, they become aggregated (Figure 2.15). Note however that the ranges in pore sizes in which significant changes take place may not be the same for every soil type, in fact, it is likely that the zone limits and width of the four different domains of pore classes in Figure 2.15 differ for different soils. Adding to the experimental evidence from the previous studies, Ferber et al (2006) found that upon cyclic drying and wetting, the inter-aggregate volume seems to systematically decrease. This could be explained by the clay platelets inside the aggregates rearranging (optimising) their position during each cycle of wetting and drying..

Recently, the more widespread application of Environmental Scanning Electron Microscopy (ESEM) for soils has enabled the observation of specimens with minimal disturbance, unlike its predecessor technique SEM (Romero and Simms, 2008). Lourenco et al. (2012) conducted ESEM observations on sand and clay specimens at different relative states of humidity that simulate wetting and drying cycles. While during wetting the menisci in the specimen of sand increased in a dome shape until it collapsed to form a continuous liquid phase, menisci in clay are less evident and wetting takes place by the continuous growth of a film of water. The importance of the contact angles, that is, the change in the menisci's curvature in subsequent cycles of wetting, was also outlined.

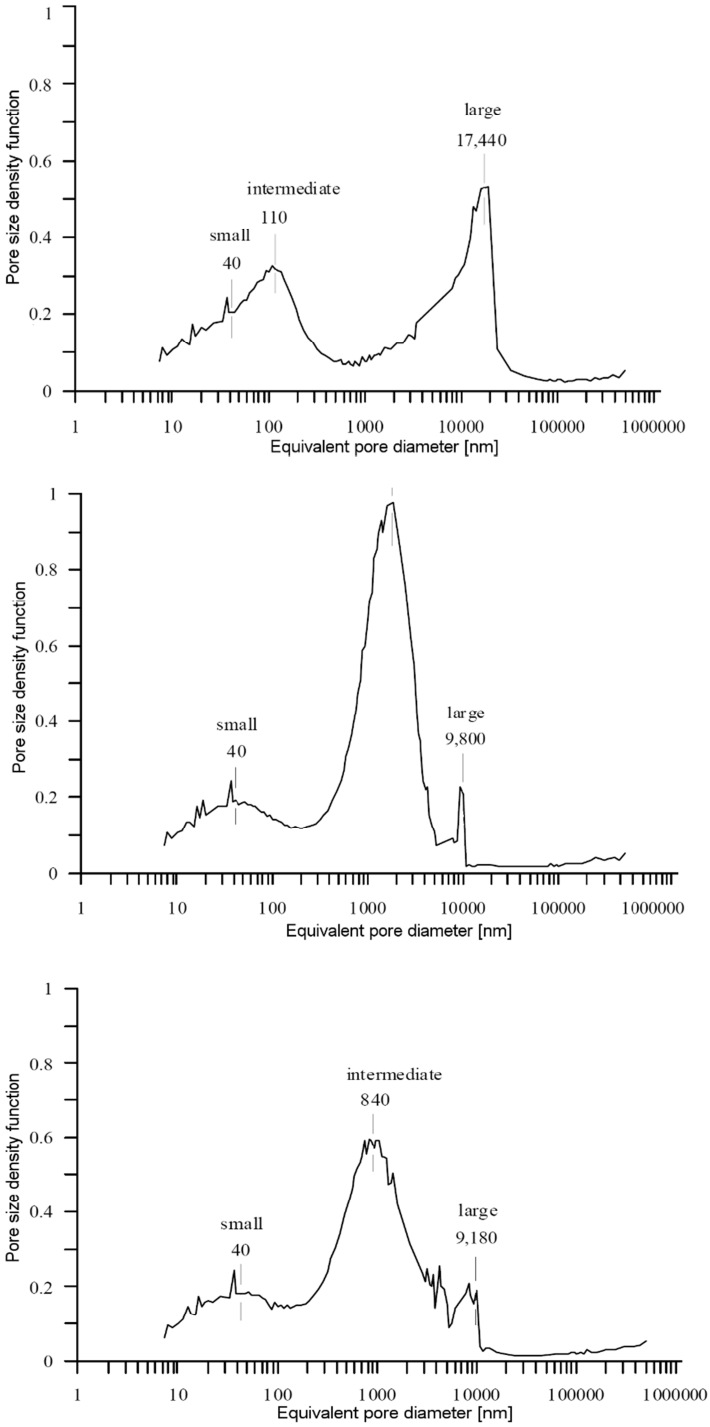

Figure 2.13 Fabric evolution during wetting (a) pore structure after compaction, (b) after free swelling and (c) after swelling at constant volume (Monroy, 2005).

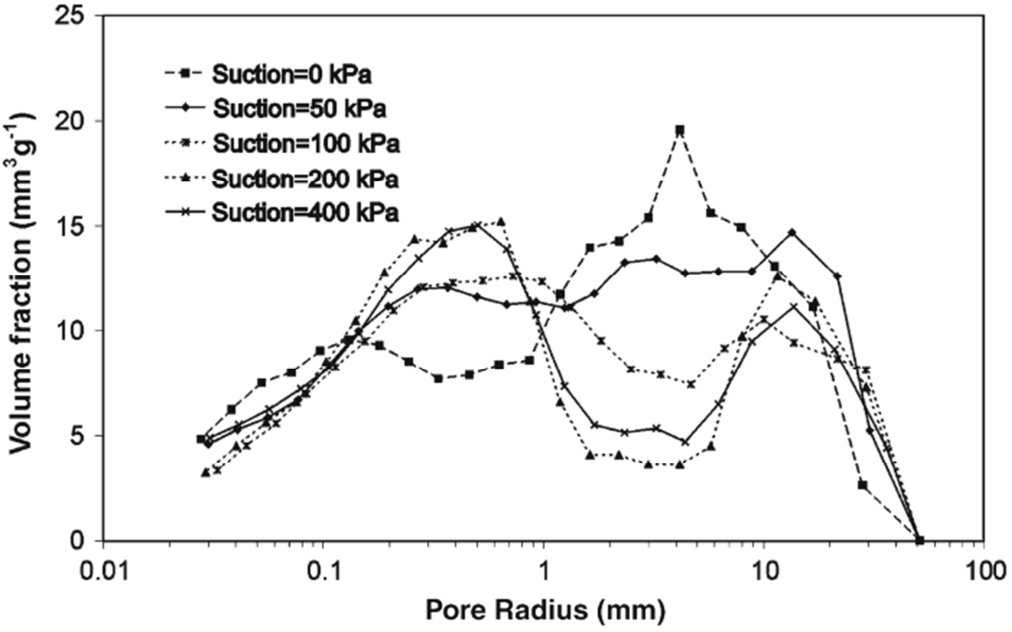

Figure 2.14 Fabric evolution during drying with suction increas from 0 up to 400 kPa (Cuisinier and Laloui, 2004 reported in Koliji et al., 2006)

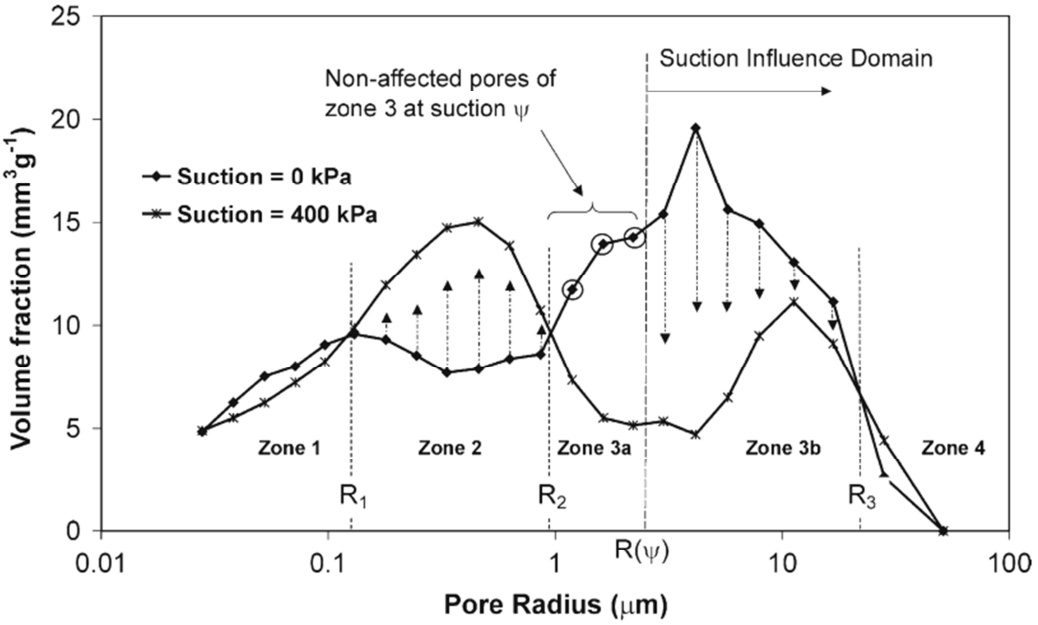

Figure 2.15 Fabric evolution during drying (Koliji et al., 2006)

Other experimental techniques are the X-ray CT-scan tomography or neutron tomography. Koliji et al. (2010) conducted neutron tomography observations of the structure of soil at the inter-aggregate pore scale during wetting and drying cycles in a suction controlled oedometer. An increase in suction was accompanied by a decrease in the volume of aggregates whereas a decrease in suction resulted in an increase in the volume of aggregates (Figure 2.16). While these changes in volume in the high range of suction (500-3000kPa) were reversible, in

the low range the aggregated volume in the wetting path was slightly smaller than in the drying path. These results may offer some confirmation of the irreversible structural changes inferred from the water retention behaviour of soil during cycles of drying and wetting.

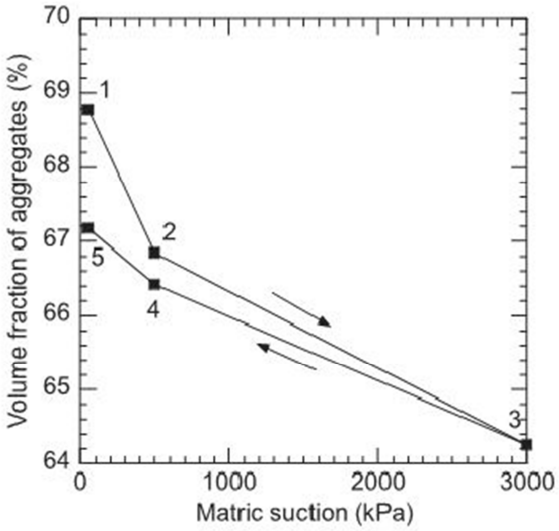

Figure 2.16 Variation of the aggregate volume of the Bioley silt during a drying-wetting cycle (Koliji et al., 2010)

2.3.4 Shear strength

Changes in suction can substantially influence the shear strength of soil. There is a general agreement that an increase of suction under post compaction conditions results in an increase in the shear strength (i.e. Ng and Zhan, 2006; Vaunat et al., 2007). Furthermore, Vanapalli et al. (1996) suggested that the magnitude of this increase in shear strength was associated with different ranges of the soil water retention curve (Figure 2.17).

In general, unsaturated shear strength is expressed using the criterion that is often referred as the "extended Mohr-Coulomb failure envelope" (Figure 2.18). By considering the independent stress variables approach, the shear strength equation for unsaturated soil can be formulated as a linear combination of the two independent stress state variables (Fredlund and Rahardjo, 1993) shown in Eq. (2.10) and illustrated in Figure 2.18.

$$\tau = c' + (\sigma_f - u_a)\tan\phi' + s\tan\phi^b \qquad (2.10)$$

where c' and ϕ' are the cohesion and friction angle for the soil in a saturated state and ϕ^b is the friction angle that reflects the increase in strength caused by an increase in suction.

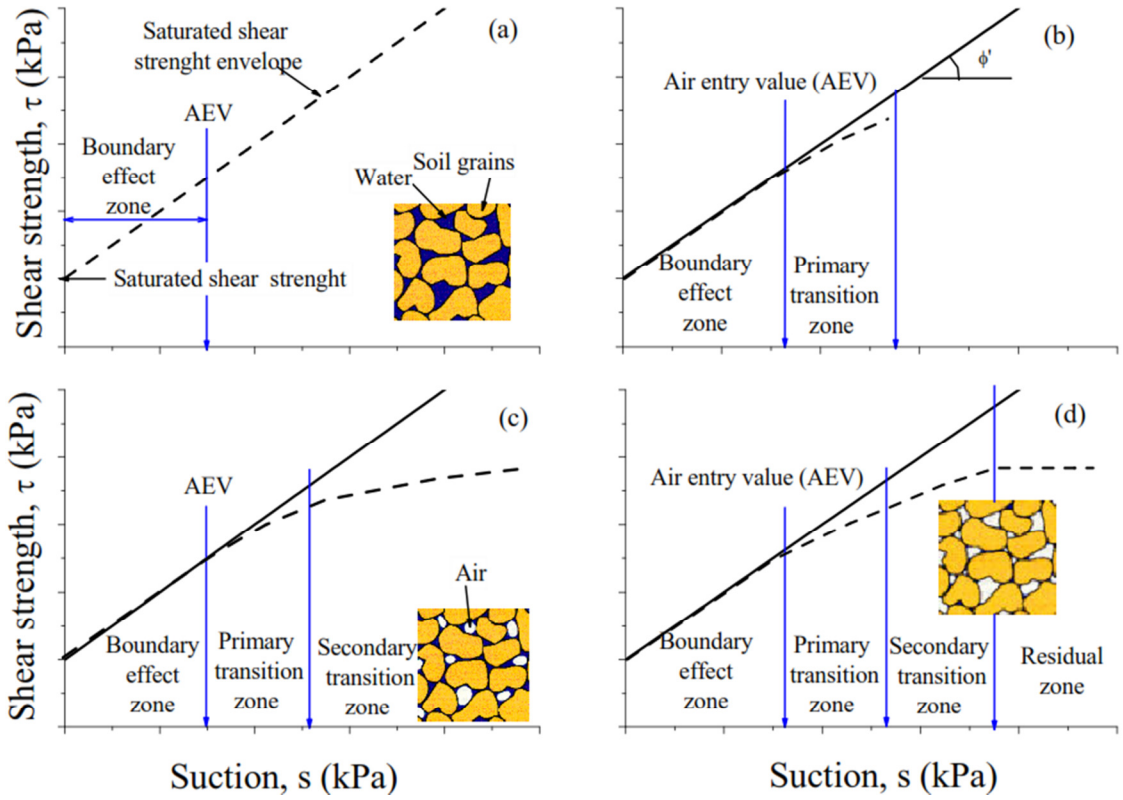

Figure 2.17 Variation of shear strength with suction (a) boundary stage, (b) primary transition stage, (c) secondary transition stage and (d) residual stage of desaturation (modified after Vanapalli et al., 1996)

Subsequent studies (i.e. Escario and Saez, 1986; Fredlund, 1987 and Gan et al., 1988) demonstrated that ϕ^b was not constant, as initially anticipated. Indeed, ϕ^b was found to be equivalent to ϕ' before AEV, and beyond that it decreased with increasing suction. The term $\tan\phi^b$ in Eq. (2.10) was modified to incorporate this change as follows, (Eq.(2.11) proposed by Vanapalli et al., 1996 and Eq. (2.12) proposed by Fredlund et al., 1996 and Vanapalli et al., 1996):

$$tan\phi^b = \frac{\theta - \theta_r}{\theta_s - \theta_r} tan\phi' \tag{2.11}$$

$$\tan\phi^b = \Theta^k \tan\phi' \tag{2.12}$$

where θ_s, θ_r, and θ_w are the saturated, residual, and current volumetric water content, respectively, and Θ^k is the normalised volumetric water content. Eq. (2.10) implicitly assumes that the friction angle ϕ' (commonly taken as the saturated friction angle) is independent of

suction. Past experimental data reported by Delage and Graham (1995) demonstrated that this assumption was not entirely correct, i.e. cohesion and friction angle increased with suction. On the other hand, considering Bishop's effective stress concept for unsaturated soil (Bishop, 1959), the shear stress criterion expressed in Eq. (2.10) can be rewritten as follows,

$$\tau = c' + \left[\left(\sigma_f - u_a \right) + \frac{\tan \phi^b}{\tan \phi'} s \right] \tan \phi' \tag{2.13}$$

where the original Bishop's parameter χ is now given by $tan\phi^b / tan\phi'$.

With regards to the shear strength in compacted soils, Vanapalli et al. (1996) investigated the relationship between the SWCC and the unsaturated shear strength of a compacted glacial till. The shear strength and behaviour was found to be depend on the structure of the soil (or aggregation causing double porosity structure), derived from compacting the soil at different initial water contents. Moreover, the variation in shear strength with respect to the suction was reported to be nonlinear, whereas the rate of increase in the shear strength due to suction was found to be related to the rate at which the soil became desaturated (Figure 2.19).

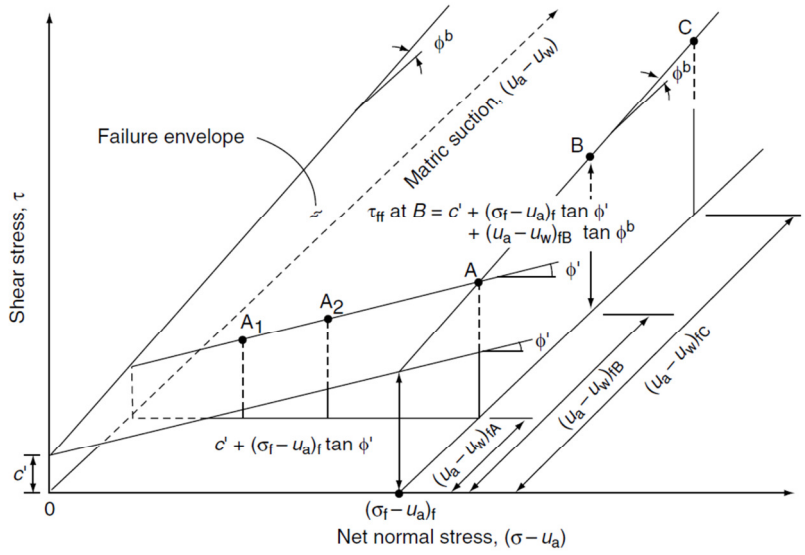

Figure 2.18 Extended Mohr-Coulomb failure envelope for unsaturated soils established for direct shear tests (Fredlund and Rahardjo, 1993).

The shear strength envelopes with respect to suction were developed for specimens compacted at dry of OMC, OMC, and wet of OMC. At a particular level of net normal stress and suction, the specimens compacted at wet of OMC developed a higher shear strength than

the specimens compacted at dry of OMC (Figure 2.19). This result, which might not be considered intuitive at first sight, can be explained if the difference in the initial fabric of the soil is taken into account, that is, the specimen compacted wet of the optimum water content the rate of desaturation is smaller which means that at any given suction level, the water availability at the inter-aggregate contacts is larger and so to its ability to communicate suction.

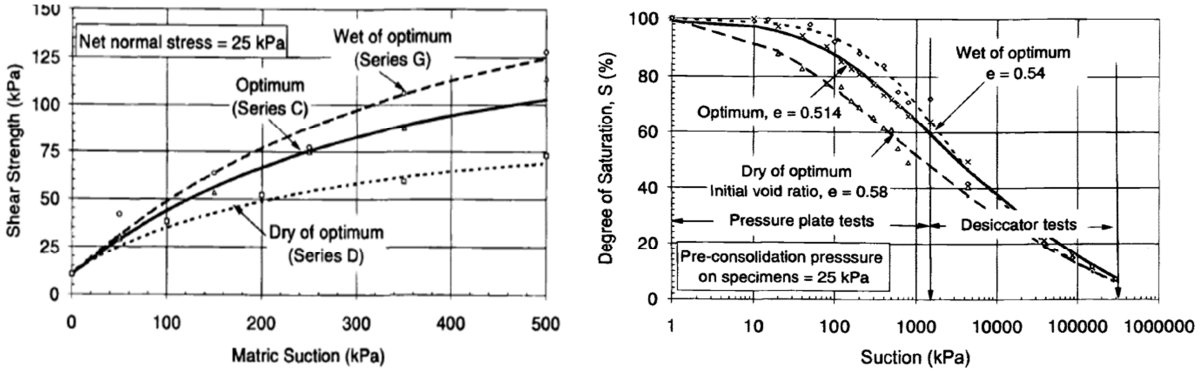

Figure 2.19 Unsaturated shear strength and suction (left) and SWCC (right) for net normal stress=25kPa (Vanapalli et al., 1996).

More recently, Koligi (2006) and Bagherieh et al. (2009) investigated the one-dimensional compression response of statically compacted soils with double porosity structure. The most notable features reported are an increase in compressibility index and yielding increase with suction and the dependency of the compression behaviour on the porosity changes during mechanical loading, that is, the aggregated soils, exhibited greater compressibility than the non-aggregated soils in both the normal compression and unloading–reloading zones.

2.3.5 Small strain stiffness

The stiffness of soil in the small strain range is an important and fundamental property in describing its engineering behaviour under cyclic loading when applied to a wide range of geotechnical problems, for instance in relation to vibrations caused by heavy and fast moving vehicles, heavy earthworks, machinery, and earthquakes, among others. In general, the small strain range lies in the elastic threshold of strain, typically below 10^{-3}% (Atkinson, 2007) where deformations are purely elastic and recoverable, and the materials exhibit linear-elastic behaviour. The propagation of small-strain elastic waves (i.e. body waves) causes very small perturbations in a granular medium, such as soil, thus enabling the assessment of on-going

internal changes in the medium without causing any disturbance to the structure, fabric, or permanent deformation (Santamarina et al., 2001).

2.3.5.1 Waves in a unsaturated particulate media

Soils are particulate materials that can be found in three different states, dry, saturated, and partially saturated. The wave velocities and attenuation characteristics are very different for each of those states. For example, in a dry medium (solid and gas phases), the elastic wave velocities are intrinsically associated with the stiffness of the skeleton, whereas for a saturated medium (solid and fluid phases), the wave velocities depend on the characteristics of the mixture (i.e. bulk modulus, shear modulus and mass density). In this domain, the wave velocity is strongly correlated with the testing frequency (Youn et al., 2008), that is, if the frequencies are low, the solid and fluid phases move together due to the viscosity of the pore fluid, whereas for high frequencies, the relative motion between the phases occurs as the effect of viscosity is relatively small compared to the effect of inertia. The boundary between the two ranges is defined by a characteristic frequency or f_c.

In a partially saturated medium (solid, fluid, and gas phases) the capillary forces or suction add to the skeletal contact forces that in turn contribute to an increase in the stiffness of contacts and the skeleton. The waves (P and S waves) propagating through a partially saturated media are affected differently by increasing degrees of saturation. The P-waves apply volumetric strains to the soil, causing the velocity to be controlled mainly by the bulk modulus of the ground where the saturation of material can substantially influence the velocity of waves travelling through the material. In some cases the skeletal velocity of the material may even be masked (i.e. the bulk modulus of water is higher than the value in the soil skeleton). On the other hand, shear waves (S waves) propagate perpendicularly to the direction of motion, and shear distortion is applied, which is why S waves can only be transmitted through solids, as fluids (liquid and gas) do not support shear stresses. Consequently, shear waves are almost completely unaffected by the presence of water in the material, and while for saturated and dry conditions the shear wave velocity (V_s) may be approximately the same in some cases, for intermediate states of saturation where capillary forces are present, the V_s changes quite considerably (i.e. Wu et al., 1984; Qian et al., 1993) (Figure 2.20).

Much like the shear strength, small strain stiffness was also found to be associated with the retention of soil water characteristics. Indeed, an increase in the shear wave velocity or

small strain shear modulus (see Appendix A) is directly related to the different ranges observed in the SWRC (i.e. Cho and Santamarina, 2001 and Mancuso et al. 2002). Cho and Santamarina (2001) reported an increase in the V_s in the transition from funicular to pendular states, where the development of water menisci at the particle contacts would contribute to a considerable increase in the stiffness of the soil skeleton (Figure 2.21).

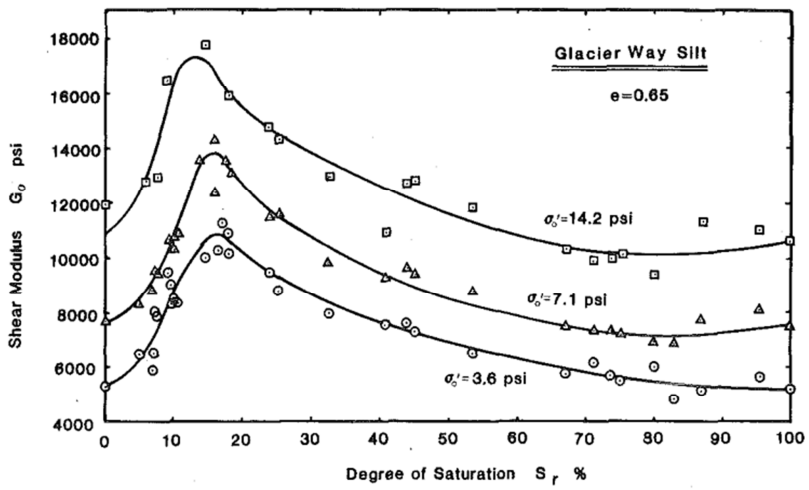

Figure 2.20 Variation of the measured low amplitude shear modulus with degree of saturation for Glacier Way silt (Wu et al., 1984).

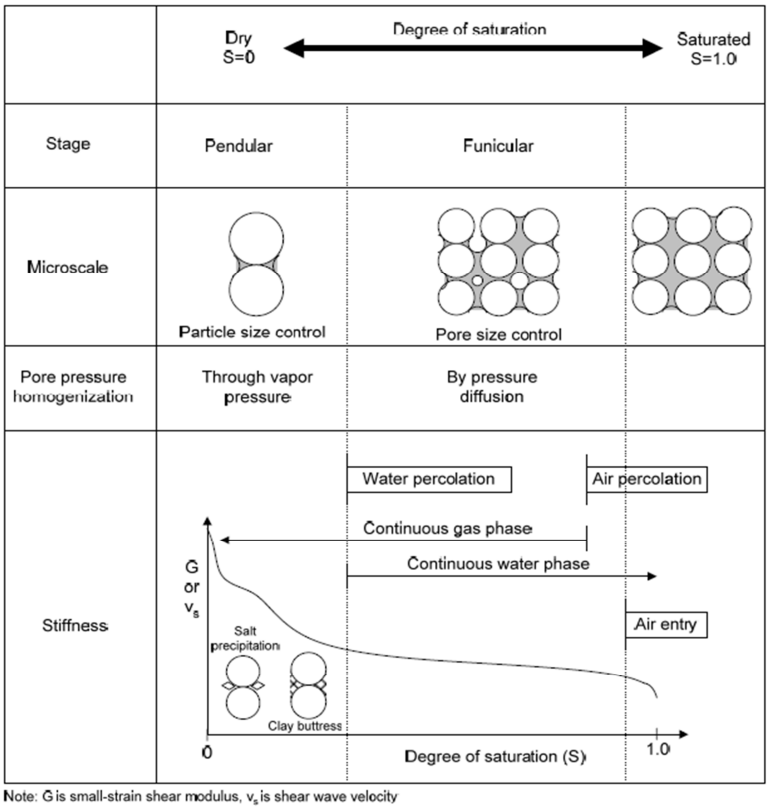

Figure 2.21 Measured variation of shear wave velocity and small strain shear modulus with increasing saturation or decreasing of suction stresses (Cho and Santamarina, 2001).

Mancuso et al. (2002) investigated the effect of suction on the small strain shear modulus in the low suction range and found that the shear modulus increased with suction, however, a noted inflexion was seen at AEV and two distinct ranges were defined, a bulk water regulated zone and a menisci water regulated zone. Before AEV the shear modulus increases linearly with suction, thereafter its increase is predominantly non-linear. Similar observations were also reported for a range of different soils by Marinho et al. (1996); Alonso et al. (1998); Vinale et al. (2001), Inci et al. (2003), and Sawangsuriya et al. (2009). Mancuso et al. (2002) also revealed that the small strain shear modulus is affected by the soil fabric derived from the compaction process. In this study an increase in the shear modulus was observed on two specimens compacted at different initial water contents, that is, at OMC and wet of OMC. It is interesting to note that although the tendency is similar, the transition points (or AEV) are consistent with the behaviour that might be expected from the SWRC of specimens prepared in such conditions (i.e. Vanapalli, 1996, Marinho and Stuermer, 2000). Furthermore, these observations are also consistent with effect of inherent double porosity differences associated to compacted soils prepared at OMC and wet of OMC, particularly evident in the small strain shear modulus rate of increase with suction. Also, the data presented in Figure 2.22 seems to suggest that the small strain shear modulus is more sensitive to changes in suction when the SWRC is within the macroporosity range, remaining nearly constant in once the residual water content is exceed (also interpreted as the beginning of microporosity range, see i.e. Romero et al. 1999). Moreover, the small strain shear modulus exhibit a strong dependency on the net confining stress for both specimens, that is, specimens subjected to higher net confining stress showed the largest small strain shear modulus (Figure 2.22).

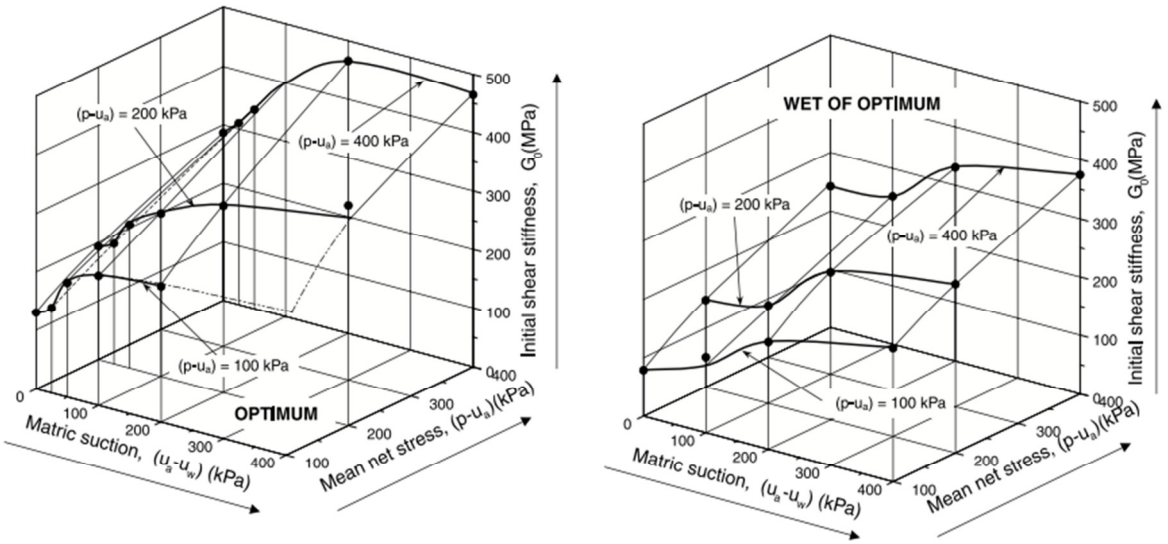

Figure 2.22 Variation of small strain shear modulus with increasing suction and mean net stress for specimens compacted (left) at OMC and (right) wet of OMC (Mancuso et al., 2002)

The effect of hydraulic hysteresis and suction history has recently been investigated by Ng et al. (2009), and Ng and Xu (2012). Figure 2.23 shows the variation of shear modulus for a drying-wetting cycle at a constant mean net stress. The most striking aspect is the hysteresis between the drying and wetting curves, although the size of the loop is small. This means that at any given suction, the shear modulus of the wetting path has a higher value than the drying path. Furthermore, the effect of suction in the degree of anisotropic stiffness during drying and wetting tests is small when the specimens are subjected to isotropic stress states. Figure 2.23 also represents the shear modulus data for different current suction ratio ($CSR=s_{max}/s_{current}$), where the shear modulus typically increases by about 20% when the CSR increases from 1 to 2.

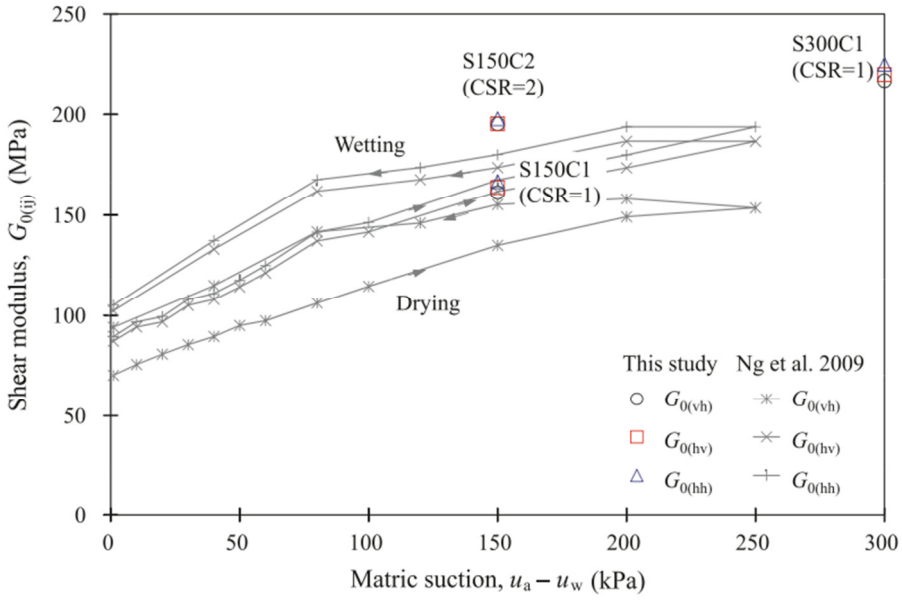

Figure 2.23 Variation of Small strain shear modulus with suction during drying-wetting cycles (Ng and Xu, 2012)

2.4 CONSTITUTIVE MODELS

2.4.1 General

Since the earlier work by Alonso et al. (1990), often referred to as the Barcelona Basic Model (BBM), there have been numerous models proposed for unsaturated soil, including those of Bolzon et al (1996), Cui and Delage (1996), Wheeler and Sivakumar (2000), Sivakumar and Doran (2000); Blatz and Graham (2003), Loret and Khalili (2002), Gallipoli et al (2003), Wheeler et al. (2003), Sun et al (2007), Thu et al (2007), Sheng et al (2008), Kohler and Hofstetter (2008). In a cooperative research effort seven universities recently came together to benchmark different approaches to modelling the mechanical and water retention behaviour of

unsaturated soils (D'Onza et al., 2011). While the various models appear to produce coherent qualitative predictions, there were small quantitative discrepancies usually related to the specific approach to calibration. This benchmark exercise also exposed the "*dangers of formulating ever more sophisticated constitutive models without dedicating the necessary attention to the development of robust procedures for selecting parameter values*" (D' Onza et al., 2011); particularly while modelling shearing under content water content conditions. In summary, the choice of one given model over another greatly depends on the purpose and the testing conditions adopted. While some models perform extremely well in certain conditions, the number of parameters and the testing program necessary to evaluate them, may render the application of a particular model cost prohibitive.

2.4.2 Hydromechanical coupled models

There seems to be a general agreement among the several authors that the compacted soil should be modelled using an elasto-plastic framework (i.e. Alonso et al., 1990; Cui and Delage, 1996;Wheeler and Sivakumar, 2000; Sivakumar and Doran, 2000; Sun et al., 2007). Although these models vary in detail, all are based on the common principle that mechanical behaviour can be separated into recoverable (elastic) and non-recoverable (plastic) components defined by a state boundary surface or yield surface (Blatz and Graham, 2003). Another important feature of modelling the behaviour of unsaturated soil is related with the water retention curve. These aspects are usually modelled separately, but recent models by Wheeler and Sivakumar(2000), Wheeler et al. (2003), Gallipoli et al. (2003), Sheng et al. (2008) and Tarantino and De Col (2009) showed that the model performance benefits from mechanical and hydraulic coupling, particularly in terms of the irreversible changes of void ratio during wetting-drying cycles.

2.4.3 Compacted soil using a single framework

The vast majority of constitutive models for compacted unsaturated soils outlined in the previous sub-sections treat specimens compacted with different initial water content or compaction efforts or pressures as essentially different soils. This means that the behaviour, for instance of dry, optimum water content (OMC), and wet of OMC, is modelled and calibrated using completely different sets of parameters. In practice it is common sense to recognise that field compaction is not 'spot on' in terms of the optimum values defined in the laboratory, and yet current models do not have the flexibility to account for that. In reality, single framework models where compacted soil is tackled as the "same" soil may be more suitable to evaluate

ranges of soil performance, without requiring an excessive amount of laboratory tests. Despite its importance, less research focused on evaluating the behaviour of compacted soil under a single framework, albeit there have been few contributions.

The model by Toll (1990) where the influence of fabric produced by compaction is included under a critical state framework is worth noting. More recently, Tarantino (2007) presented a possible critical state framework for unsaturated compacted soils with an aggregated structure based on the results of Tarantino and Tombolato (2005). Tarantino and De Col (2009) proposed a single framework model for compacted states where the mechanical and hydraulic paths were coupled. Finally, Koliji's (2010) model incorporates inter-particle bonding, fabric and partially saturated effects in a single framework, and is capable of modelling the degradation of structure that occurs during mechanical loading, while coupling those with water retention. In the following sub-sections these selected models are introduced and their key features are briefly described.

2.4.3.1 Toll (1990) model

This model was originally developed based on a critical state model for saturated soils with total stresses and suction considered separately to describe unsaturated conditions (Toll, 1990; Toll, 2000). Its most interesting feature is that fabric is taken into account by including two individual stress ratios, in which the change is governed by the degree of saturation (Figure 2.24). The degree of saturation is thought to represent changes in the degree of aggregation where soils at low degrees of saturation would represent fully aggregated soil in which the aggregates play an important role in the behaviour of the soil. In contrast, at high degrees of saturation, during compaction, the aggregates become instable and the degree of aggregation decreases. The complete critical state framework includes Eq. (2.14) and Eq. (2.15).

$$q = M_a\left(\sigma - u_a\right) + M_w(u_a - u_w) \tag{2.14}$$

$$v = \Gamma_{aw} - \lambda_a \ln\left(\sigma - u_a\right) - \lambda_w \ln(u_a - u_w) \tag{2.15}$$

where M_a, M_w, Γ_{aw}, λ_a, λ_w are the function of the degree of saturation and fabric of the soil. Toll and Ong (2003) also applied this framework to a residual sandy clay soil and found that the normalised functions of degree of saturation M_a, and M_w were similar to Kiunyu lateritic gravel.

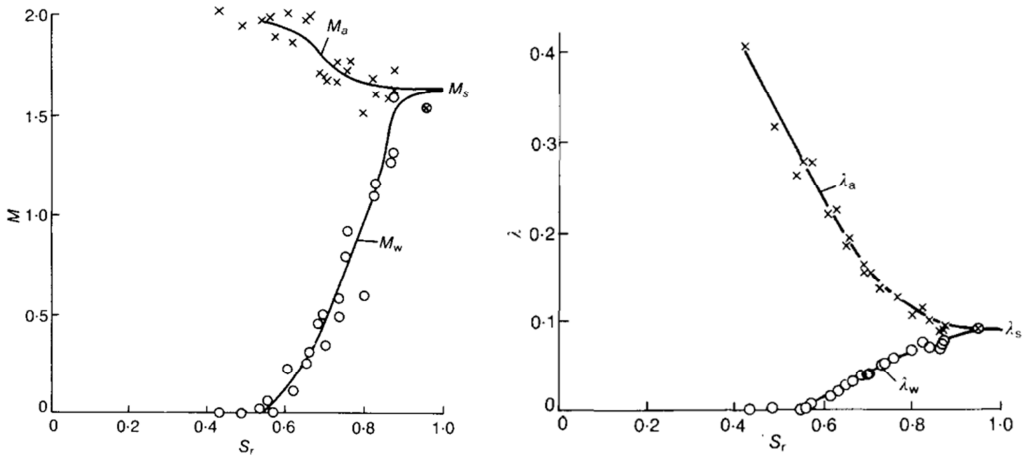

Figure 2.24 Variation of (left) critical state stress ratios, Eq. (2.14) and of (right) slope of the critical state surface, Eq. (2.15) with degree of saturation (Toll, 1990)

2.4.3.2 Tarantino (2007) model

This model was developed based on the experimental direct shear data from Tarantino and Tombolato (2005). It is based on the assumption that water menisci have a negligible effect on the ultimate shear strength. They suggested that the ultimate shear strength can be modelled in terms of average skeleton stress with the degree of saturation of the macropores (S_{rM}) in terms of the total degree of saturation (S_r), as in Eq.(2.16). The complete formulation involves five state variables, the mean net stress, the suction, the deviator stress, the void ratio and water ratio, and three critical state equations, to predict the deviator stress in Eq. (2.16), the degree of saturation in Eq. (2.17), and the void ratio in Eq. (2.18).

$$q = M\left(\sigma + sS_{rM}\right) = M\left(\sigma + s\frac{e_w - e_{wm}}{e - e_{wm}}\right) \tag{2.16}$$

$$S_r = \frac{e_w}{e} = \left[\frac{1}{1+\left(\phi e^{\psi} s\right)^n}\right]^m \tag{2.17}$$

$$e = \left[\Gamma - \lambda \ln(\sigma + sS_r)\right] \cdot \left\{1 - a\left[1 - \exp(b\xi)\right]\right\} \tag{2.18}$$

where M is the saturated critical state parameter, e_{wm} is the 'microstructural' water ratio, which separates the region of inter-aggregate porosity from the region of intra-aggregate porosity; ϕ, ψ, n, m are soil parameters; Γ and λ are the saturated critical state parameters, and a and b are two additional parameters which can be determined from isotropic compression tests. The

major advantage of this model is that it couples shear strength with water retention behaviour through the term S_{rM} and requires only one additional parameter, e_{wm}.

2.4.3.3 Tarantino and De Col (2008) model

This model is based on the experimental investigation of statically compacted kaolin. The main features being that the mechanical and water retention behaviour of unsaturated soil is coupled, suction varies during static compaction loading with loading cycles causing a decrease in suction whereas unloading cycles are associated with an increase in suction. In the initial stages of compaction the vertical load increment is carried out by inter-particle contacts acting on the menisci, this suggests that each meniscus has a bonding effect with the soil skeleton (Figure 2.25).

The post compaction state suction defined three distinct regions on the compaction plane (Figure 2.26), that is,

I. Equal suction contours have positive slope

II. Equal suction contours have a negative slope

III. Equal suction contours have no slope

The complete formulation for the one dimensional coupled mechanical water retention model is given in Eq. (2.19) to Eq. (2.21). While Eq. (2.17) and (2.19) are used to model the irreversible paths, Eq. (2.20) and Eq. (2.21) are used to model the reversible paths by assuming constant water content conditions and a single set of parameters.

$$e = e_s \left[1 + a \left(\frac{s^*}{\sigma_v^{''}} \right)^b \right] \tag{2.19}$$

$$S_r = S_{r0} - k_s (s - s_0) \tag{2.20}$$

$$de = -kd(\ln \sigma_v^{''}) \tag{2.21}$$

where a and b are material parameters, e_s represents the void ratio under saturated conditions, s_0 and S_{r0} represent the point on the main wetting surface from which the scanning curve detaches, and k_s is the slope of the scanning curve. The coupled model correctly reproduces the positive slope in the post compaction equal suction lines and its progressive decrease as the

water content decreases. The model allows for both mechanical and hydraulic paths to be modelled, contrary to some of the earlier models proposed for unsaturated soils.

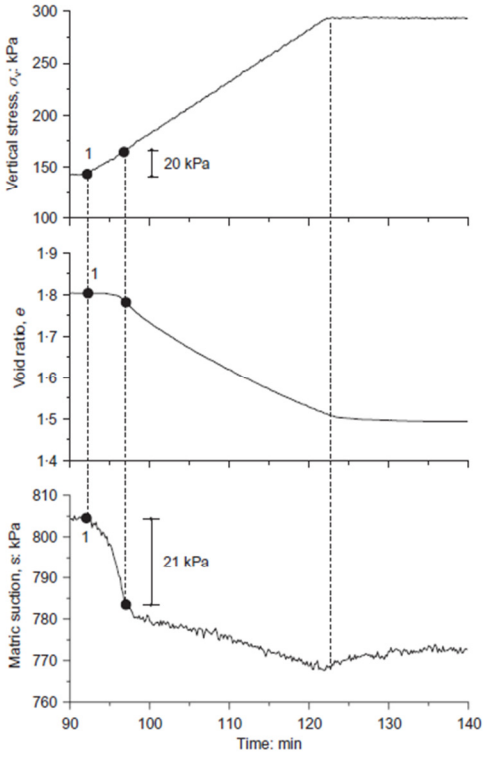

Figure 2.25 Contribution of the water menisci in the inter-contact particles on the support the initial stages of loading (Tarantino and De Col, 2008)

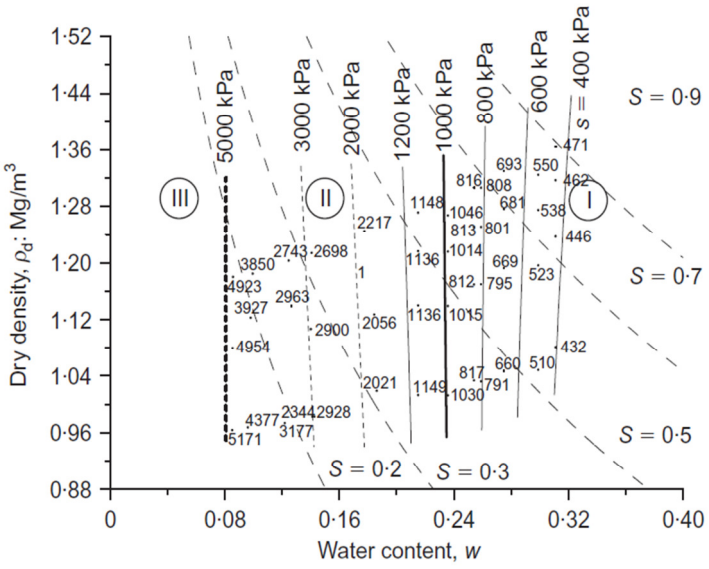

Figure 2.26 Post-compaction suction data and contours of equal suction values (Tarantino and De Col, 2008)

2.4.3.4 Koliji et al. (2010) model

The Koliji et al. (2010) model uses a single framework for modelling the degradation of structure that occurs during mechanical loading, while coupling inter-particle bonding, and fabric with the water retention characteristics. The key features proposed by Koliji's et al (2010) model are related to an evaluation of partial saturation, which is considered to have a double effect in aggregated soils. A new parameter that links the evolution of the macropore volume fraction (internal structure of the soil) to plastic strains (macroscopic behaviour) described by an experimentally based relationship is introduced.

The above model was validated by predictions of the experimental data of oedometer tests on unsaturated aggregated soil. The model also addressed additional features including the non-linear stress–stress relationship during virgin compression, and an increase in the degree of saturation during compression at a constant suction. This model represents great step forward into an explicit consideration of the influence of fabric on constitutive relationships. This is unprecedented as far as this author knows, but its application is extremely limited because the experimental program required for evaluating the model parameters ranges from mechanical tests to pore size evaluation techniques using more sophisticated apparatus such as MIP or Neutron tomography. All of which renders it cost and time prohibitive.

2.4.4 Small strain stiffness empirical models

A number of empirical relationships have been proposed to predict the behaviour of shear wave velocity or small strain shear modulus in compacted soil (Table 2.2). In these relationships the small strain shear stiffness depends mainly on the initial void ratio, external confinement or mean effective stress, and the degree of saturation and suction. There are two main families of empirical models that are used to evaluate shear wave velocity or small strain shear modulus: micro-mechanical and macro-mechanical models (Table 2.2).

In the micro-mechanical approach, based on the Hertz-Mindlin contact theory, the shear wave velocity is modelled by incorporating the equivalent stress developed at the water menisci of spherical and platy shaped particles. The water in the menisci is considered to be in a pendular range while the equivalent stress is calculated in a manner similar to that developed on the capillary forces with increased suction, as proposed by Fisher (1926). Models such as those proposed by Cho and Santamarina (2001), and thereafter Santamarina et al. (2005);

Alramahi et al. (2007) and Claria and Rinaldi (2007) are of this type. These models combine the effect of the equivalent effective stresses due to suction and applied external stresses.

In contrast, the macro-mechanical approach, typically developed for small strain shear modulus models, is based on the empirical relationships first proposed for saturated conditions (Stokoe et al., 1991; Rampello et al., 1995) and later extended to account for a dependent suction. The model developed by Mancuso et al. (2002), whereby the shear modulus in compacted soil was structurally dependent and established the existence of two ranges where the soil modulus was influenced by bulk water and menisci water is noteworthy because the shear modulus was modelled using two different relationships for two different ranges, and are therefore discontinuous. The remaining models referred to are of this type. Both types of models require fitting parameters that usually depend on the structure or stress state of the soil.

2.4.4.1 Claria and Rinaldi (2007) model

Claria and Rinaldi (2007) investigated the propagation of shear wave velocity in specimens of loess soil prepared by dynamic compaction over a wide range of moisture contents. As compacted suction was also monitored. The specimens were then subjected to isotropic confinement under constant water content conditions, and the shear wave velocity was monitored at every loading stage. To investigate the effect of post-compaction suction on shear wave propagation, selected specimens were subjected to wetting or drying and subsequently tested in isotropic triaxial tests.

The water content increases compressibility and favours the development of a more dense structure at any given confining pressure. Suction stiffens the structure of the soil by increasing the inter-particle contact stresses, even in the absence of external applied pressures. Thus, at an applied confining pressure of zero, the wave velocity has non-zero values and depends mainly on the moisture content (Figure 2.27). Claria and Rinaldi (2007) data for shear wave velocity on compacted samples under unconfined condition reveal that V_s remains approximately constant for moisture contents under the optimum, possibly due to the combined effect of a decrease in suction stresses (increasing moisture content), and an increase in the dry unit weight of the soil as it moves closer to optimum (Figure 2.27).

Table 2.2. Empirical relationships for V_s and G_0 of compacted soils

Type	General form of the relationship	Soil type	Testing method	Reference
Micromechanical approach				
Shear wave velocity	$V_s = V_{sat}\left[1+\frac{2\sigma'_{eq}}{(1+K_0)\sigma'_v}\right]^{\beta}\sqrt{\frac{e+G_s}{eS_r+G_s}}$	Various sands	Bender elements	Cho and Santamarina, 2001
Shear wave velocity	$V_s \approx V_s^{S_{r=1}}\left(1+S_r\frac{s}{0.75\sigma'}\right)^{\beta}$	Not specified	Bender elements	Santamarina et al., 2005
Shear wave velocity	$V_s = \alpha\left(\frac{\sigma-u_a}{\sigma_{ref}}\right)^{\beta}\left(1+S_r\frac{s}{\sigma-u_a}\right)^{\beta_{unsat}}$	River silt and Ottawa sand mixes		Alramahi et al., 2007
Shear wave velocity	$V_s = ks + B\left(\frac{\sigma_m}{\sigma_r}\right)^{\beta}$	Loess	Bender elements	Claria Jr and Rinaldi, 2007
Macromechanical approach				
Small strain shear modulus	$G_{\max} = \left[1+H(S_r)\right]G_{\max}^{dry}$	Fine grained sands	Resonant column	Wu et al., 1984
	$G_{\max} = G_{\max}^{Sr=1} * f(s)$	Metrano silty sand	Torsional tests	Alonso, 1998; Vinale et al., 1999
Small strain shear modulus	$\frac{G_0}{p_a} = A\left[\frac{(\sigma-u_a)+s}{p_a}\right]^{n} OCR^{m}$ (before AEV) $G_0 = (G_0)_s\left\{(1-r)e^{-\beta(s-s^*)}+r\right\}$ (after AEV)	Metrano Silty sand	Resonant column Torsional tests	Mancuso et al., 2002
Small strain shear modulus	$G_{\max} = G_{\max}^{Sr=1} + f(s)$	Metrano silty sand		Leroueil and Hight, 2003
Small strain shear modulus	$G_0 = Af(e)\left[\frac{\sigma-u_a}{p_r}\right]^{n}\left[1+\frac{s}{p_r}\right]^{2b}$	Clayey silt	Bender elements	Ng and Menzies, 2007
Small strain shear modulus	$G_{\max} = \left(w\frac{E}{E_{std}}\frac{w_{opt}}{w_{opt,std}}\right)\{\alpha\log(s)-\beta\}$	Subgrade soils	Bender elements	Sawangsuriya et al., 2008
Small strain shear modulus	$G_{\max} = Af(e)(\sigma_m-u_a)^{n}+C\Theta^{k}(s)$ (1) $G_{\max} = Af(e)\left[(\sigma_m-u_a)+\Theta^{k}(s)\right]^{n}$ (2)	Subgrade soils	Bender elements	Sawangsuriya, 2009

The shear wave propagation as postulated by Claria and Rinaldi (2007) was modelled as a sum of the contribution of effective stresses due to suction and applied external stress. To avoid using the equivalent contact stress approach (Cho and Santamarina, 2001), due to the complexity of its evaluation in real particulate systems, the authors developed an alternative expression where the shear wave velocity, that resulted from the contribution of suction, was evaluated with respect to the soil state parameters such as the moisture content or suction (Eq. (2.22)).

$$V_{s0} = k(u_a - u_w) = ks \tag{2.22}$$

where V_{s0} represents the shear wave velocity at zero confining pressure and the slope k can be interpreted as a result of the void ratio and soil structure influence on shear wave velocity (Figure 2.27b). It is observed that the higher the void ratio, the lower the slope k. The complete framework also takes into consideration the effect of confining stress (Figure 2.28) as follows,

$$V_s = V_{s0} + B\left(\frac{\sigma_m}{\sigma_r}\right)^{\beta} \tag{2.23}$$

where σ_m represents the mean effective stress, σ_r is a reference stress, B and β are materials parameters that depend on the initial stiffness of the soil skeleton, and are thus related to the water content and compressibility. The equation performs well over the range of tested water contents and confining pressures, albeit having two main shortcomings. The first aspect is related to the fact that the shear wave velocity at zero confining pressure, as expressed in Eq. (2.22), becomes zero for fully saturated conditions, which is not necessarily the case in most soils (Richart et al., 1970). The second aspect is related to the fact that there is not a single set of parameters.

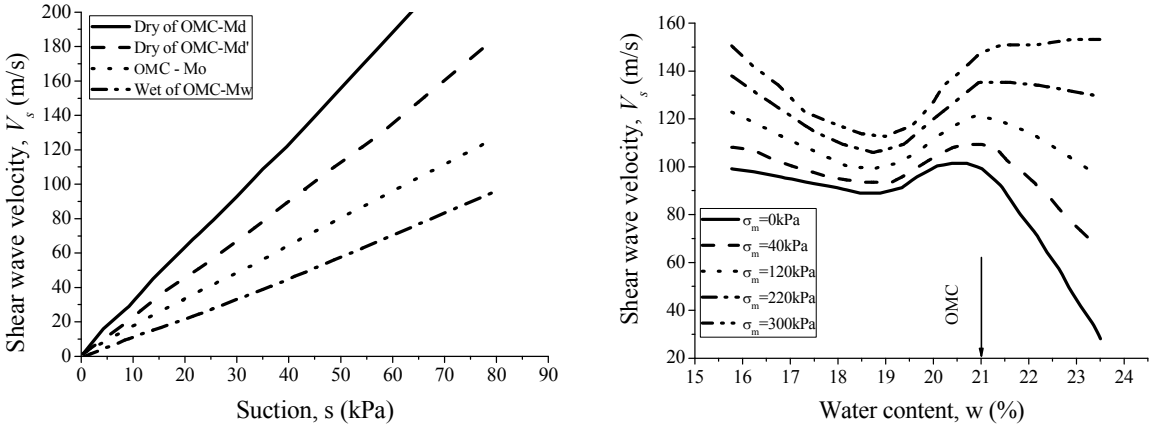

Figure 2.27 Variation of shear wave velocity with suction (left) with increasing confining pressure and (right) unconfined conditions with the slope k defined as in Eq. (2.22) (modified after Claria and Rinaldi, 2007).

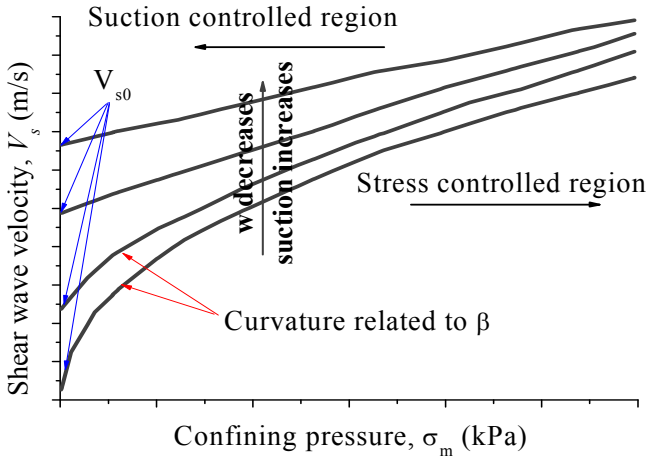

Figure 2.28 Interpretation of Eq.(2.23) in the shear wave velocity confining pressure plane (modified after Claria and Rinaldi, 2007)

2.4.4.2 Sawangsuriya et al. (2008) model

The influence of compaction energy on the propagation of the shear wave was studied by Sawangsuriya et al. (2008) while investigating the shear modulus for three compacted subgrade soils under the compaction conditions expressed in Eq. (2.24).

$$G_0 = \left(w \frac{E}{E_{std}} \frac{w_{opt}}{w_{opt,std}} \right) (\alpha \log \psi - \beta) \tag{2.24}$$

where G_0 corresponds to the small strain shear modulus, w moisture content, w_{opt} the optimum moisture content obtained for a given energy E, $w_{opt\text{-}std}$ is the optimum moisture content under standard compaction energy E_{std}, α and β are fitting parameters dependent on the composition of the soil, and ψ is the suction.

In Eq. (2.24), the influence of dry unit weight is excluded, as Sawangsuriya et al. (2008) assumed that once the soil is compacted, the effects of the dry unit weight variations on the shear modulus are relatively small, which is expected given that the shear modulus is directly related to bulk density (see Appendix A). Nevertheless when plotting the normalised small strain shear modulus divided by the normalised dry unit weight and normalised water content against suction, the obtained linear relationship was somehow found to be more dispersive in the higher suction domain (Figure 2.29). The main advantage of this relationship is that for the first time the as compacted small strain shear modulus has been

obtained using a single set of parameters. The performance of the relationship is remarkable considering that different soil fabric derived from compacting soil at different water contents and imparted energies are all predicted within the same empirical relationship. This is probably owing to the fact that the water retention characteristics are explicitly included in the expression (water content and suction), which suggests that they may control the modulus to higher extent compared to the dry unit weight, or even differences in the fabric. In fact, the only shortcoming is related to the fact that the energy applied must be known.

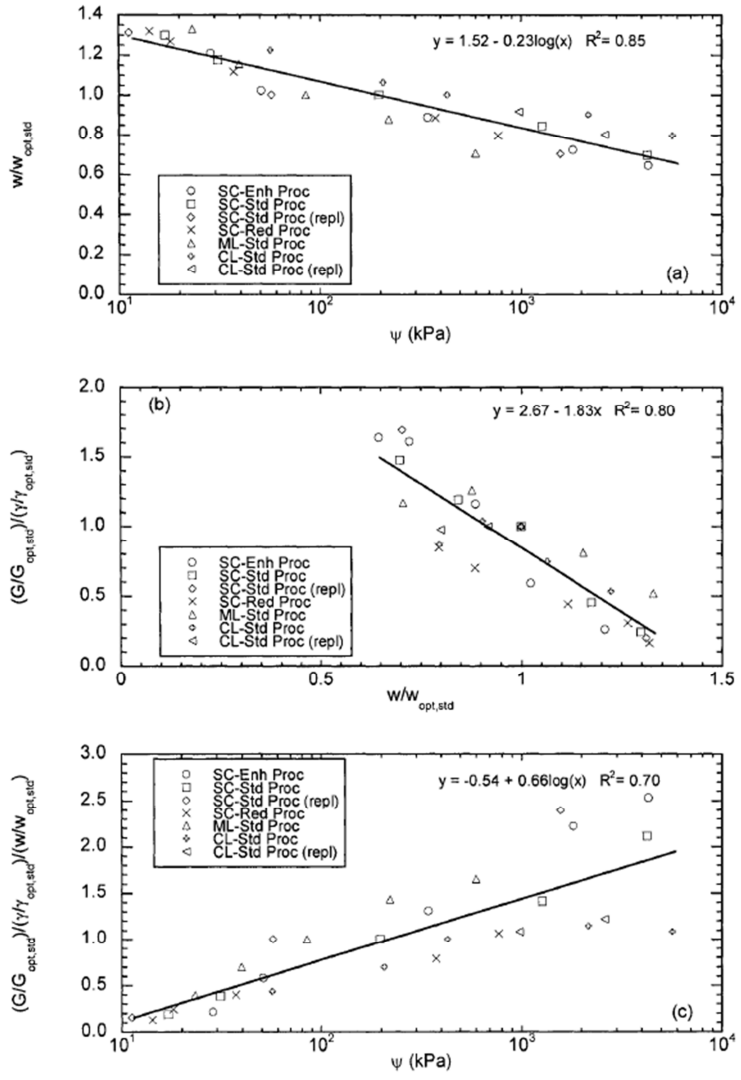

Figure 2.29 Relationship between the small strain shear modulus, normalised dry unit weight, normalised water content and suction (Sawangsuriya et al. 2008).

2.5 SHEAR WAVE VELOCITY FOR FIELD COMPACTION EVALUATION

The use of shear wave propagation to evaluate the quality of compaction, in terms of dry unit weight is not completely unprecedented. Indeed, Kim and Park (1999) evaluated ground densification using a spectral analysis of surfaces waves (SASW) and calibrated an empirical relationship for dry unit weight (γ_d), and the shear wave velocity (V_s), using resonant column (RC) tests. The methodology was mainly developed to access the quality and depth of ground densification due to dynamic compaction induced by the drop of a pounder. The V_s - γ_d relationship was established considering the effect of confinement (in the lab or at depth in the field) by using the normalised shear wave velocity, $V_{s,n}$ expressed as follows,

$$V_{s,n} = V_s \left(\frac{P_a}{\bar{\sigma}_m} \right)^n \tag{2.25}$$

$$\bar{\sigma}_m = \frac{(1+2k_0)\sigma'_v}{3} \tag{2.26}$$

where P_a is the reference stress (typically atmospheric pressure), $\bar{\sigma}_m$ is mean effective stress computed based on the vertical effective stress and σ'_v, and the earth pressure coefficient at rest (k_0). The results showing how V_s - γ_d is established are shown in Figure 2.30.

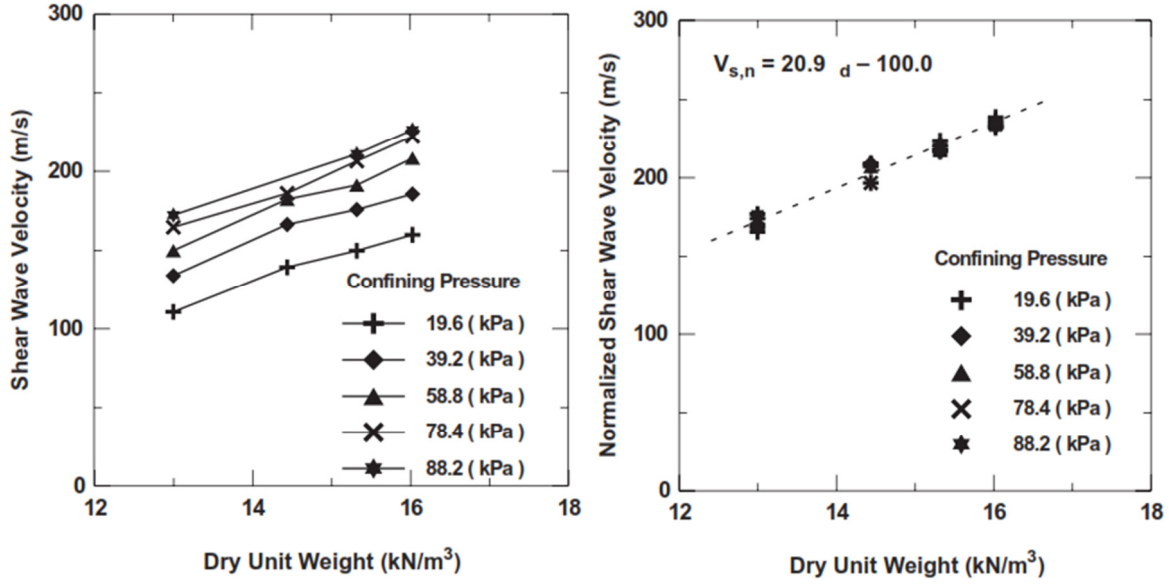

Figure 2.30 Variation of (left) V_s-d relationship and (right) $V_{s,n}$-d with increasing confining pressure (Kim and Park, 1999).

The proposed relationship was evaluated for two field sites where the estimations of dry unit weight were compared to those obtained using sand cone tests. The results matched

well, despite the fact that a relationship was developed for typically dry or saturated conditions, and did not take into account the effect of partial saturation that bears significant importance in the shear wave propagation, as outlined in the previous sections. This surprisingly good prediction may be related to two different aspects. On one hand the type of soil material used, i.e. in granular materials the suction would have a lesser influence and on the other hand with the thickness of ground profile fraction that was under unsaturated conditions. In this particular case the ground water level (GWL) was extremely close to the surface (i.e. GWL=2m depth) which might suggest that a good part of the profile was still within the capillary fringe and hence close to fully saturated conditions.

Recently, Cha and Cho (2007) attempted to relate the field shear wave velocity-void ratio-shear strength of sandy soils through experimental evaluation. Natural sands taken from various reclaimed or recently deposited sites were used for reconstituting specimens at different void ratios using an oedometer cell. The shear wave velocity was monitored using bender elements while changing the applied stress in the cell for each specimen. To correlate V_s with the shear strength properties, that is, the friction angle, direct shear tests were conducted in specimens prepared in the same manner. A relationship between the field V_s and shear strength was developed for different void ratios, thus, the relationship between V_s and the void ratio (Eq. (2.27), and the void ratio and friction angle (Figure 2.31) were also established. The interesting feature of this expression is that V_s was assumed to vary linearly between the upper and lower bounds of the void ratio e_{min} and e_{max} respectively.

$$e_{field} = e_{\max} - (e_{\max} - e_{\min}) \frac{V_{s-field} - V_{s-e\max}}{V_{s-e\min} - V_{s-e\max}} \tag{2.27}$$

where $V_{s\text{-}field}$ represents the field value of V_s , $V_{s\text{-}max}$ is the shear wave velocity at e_{max} and $V_{s\text{-}min}$ is the shear wave velocity at e_{min}. The proposed relationships were evaluated for three different sites. The predicted peak internal friction angles agreed well with those in the field based on SPT tests. This approach enables the friction angle to be predicted using the void ratio and V_s, provided that the values in the field stay within the established upper and lower bounds of the void ratio. However, the influence of partial saturation was not included because the study was carried out for fully saturated conditions.

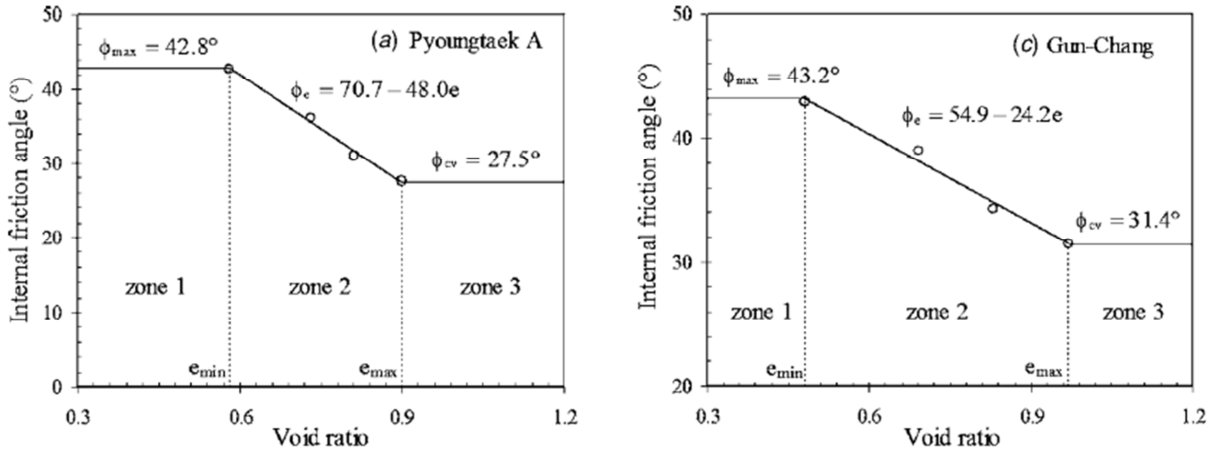

Figure 2.31 Variation of the internal friction angle with the void ratio (Cha and Cho, 2007).

2.6 SUMMARY AND CONTRIBUTION

The literature review presented in this chapter focused on topics that are relevant for the subsequent work presented in the following chapters. The topics include: understanding the behaviour of compacted soil under unsaturated conditions in terms of its hydraulic properties and mechanical response, particularly at small strain, and some of the available frameworks for analysing and explaining such behaviour, and the methodologies available to evaluate the quality of compaction using shear wave velocity.

Despite the fact that methodologies based on the shear wave velocity to evaluate the quality of compaction or in situ void ratio were proposed, all the methodologies ignored the effect of partial saturation. While this may not be an issue for natural ground profiles where GWL is close to the surface, it is certainly a problem where the GWL is located at higher depths, which is the case in most man made fills. Under those circumstances, one cannot afford to neglect its effect in a field evaluation of the quality of compaction because a high shear wave velocity may not truly represent higher densification, as highlighted in the previous sections.

In contrast, since conventional compaction of fine grained soils involves an in situ control of the moisture content, the density obtained is not only due to the physical rearrangement of the particles, but also a change in the structure of the soil itself. This aspect adds further difficulty in analysing current soil conditions. The available models that predict the behaviour of compacted soil either lack the flexibility or simplicity to address the change

in behaviour under a single framework that is necessary to adequately evaluate compaction quality.

The main contribution of this work is to address the effects of partial saturation in the implementation of a field methodology based on the propagation of shear wave velocity for evaluating compaction quality. It uses both small and large strain range experimental approaches to characterise the behaviour of materials under different compaction conditions.

CHAPTER THREE

3 THE PENRITH LAKES SITE

3.1 INTRODUCTION

The Penrith Lakes scheme is situated just north of Penrith, NSW (see Appendix B), and covers an area of over 2000 hectares. Penrith Lakes has been a major source of fine to coarse grained sand and gravel for the Sydney construction industry since the 1950's. Today, it is the largest sand and gravel quarry in Australia, and supplies over 50% of the Sydney market with sand and aggregate. Sizes vary from fine grained sands to coarse sands (75 microns to 5mm) and gravel (5mm to 300mm), both round and crushed. The site has been operating as a quarry over many decades. The quarry operations has involved the removal of overburden sand and gravel to depths of 20m, and subsequent rehabilitation by back filling the quarried areas.

In general, the landfill work was achieved according to the specifications on the Deed of Agreement (DOA), with scrapers used for placement and compaction, and compaction control based on certain relative maximum dry unit weight (MDUW) specifications. However, before the DOA, a significant portion of the land was already filled, but without any historical records of the placement methodology. For this reason, these particular areas can be deemed as uncontrolled fill. The scope for future land use is restricted to parkland, without suitable verification methods to confirm the level of compaction. Thus, an assessment of its current conditions in terms of its bearing capacity is of paramount importance.

3.2 SITE LOCATION

The Penrith Lakes scheme (Penrith, NSW) is located on the Hawkesbury-Nepean river floodplain at the foot of the Blue Mountains (Figure 3.1). In the geological context, this region consists of quaternary alluvium, gravel, sand, silt and clay, and the bedrock substrate in this region consists of shale and sandstone, all of which are part of the Wianamatta group (i.e. Bringelly shale, Minchinbury sandstone and Ashfield shale).

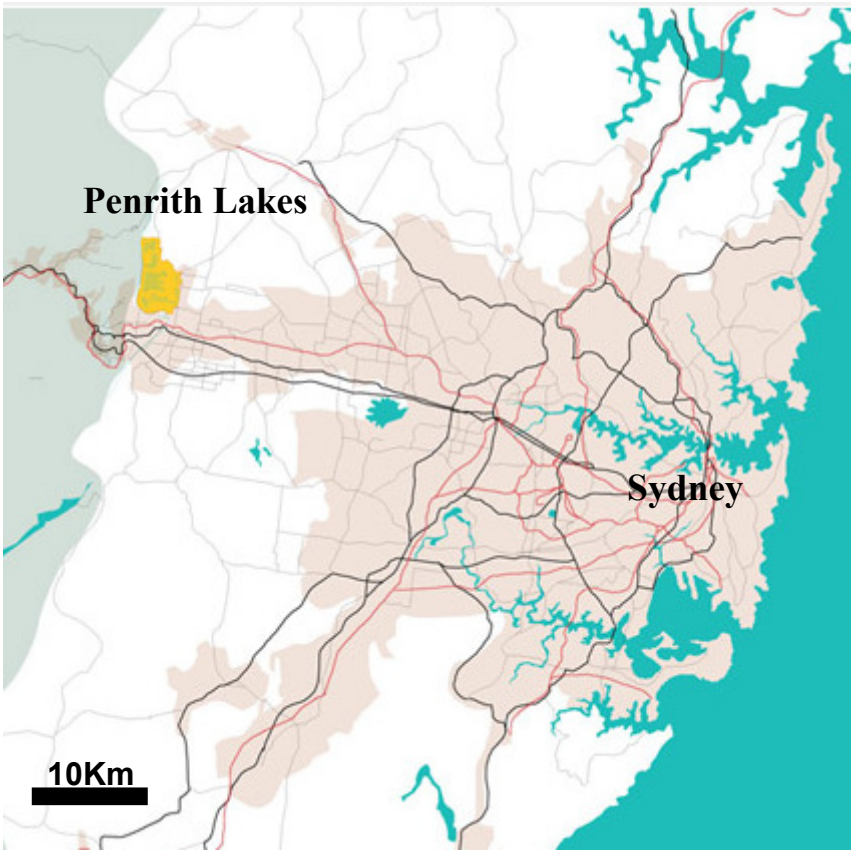

Figure 3.1 General site location (courtesy of Penrith Lakes, 2007).

3.3 MATERIALS

The material used for backfilling was composed of a variety of different materials typically ranging from low plasticity (plasticity index varying between 10-15%) silty sands, sandy clays and silty clays. The material variability on site was quite significant given the large period of time in which the quarry and backfilling operations have been taking place. For the purpose of evaluating the performance and suitability of the proposed field methodology two benchmark areas were selected. At the time of the testing, the access to the compacted fills was carried out by means of boreholes. Unfortunately, the amount of sample that was collected enabled only the classification of the different materials encountered in the borehole by visual inspection. Nevertheless, to gauge the material variability on site, different locations were visited and samples were collected at surface for characterization in terms of the index properties. A summary of the Particle size distribution results is shown in Figure 3.2. According to the Unified Soil Classification System (USCS), the particles size

distributions presented in Figure 3.2 show that the materials range from CL, SM, SP-SM and SC.

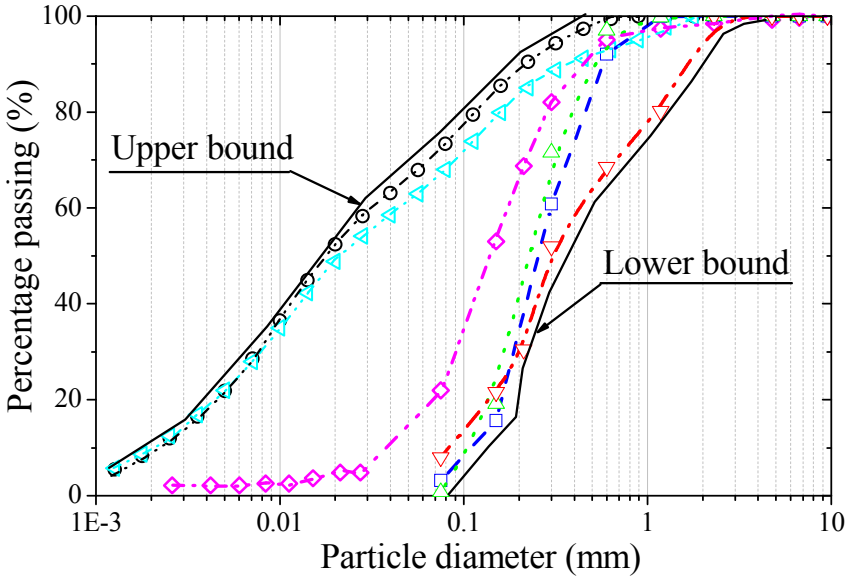

Figure 3.2 Summary of the (a) particle size distributions and (b) optimum moisture content and maximum dry unit weight of different soils encountered on site.

Furthermore, given the importance of the compaction behaviour, the optimum moisture content (OMC) and maximum dry unit weight (MDUW) data for a variety of soils encountered on site currently being used in the filling operations is represented in Figure 3.3. For ease of visualisation only the MDUW and OMC obtained for the soils compacted at an energy level corresponding to standard compaction effort (AS 1289.5.1.1 - 2003) are represented. Typically the MDUW varies between 17.46 and 19.42 kN/m^3 for a variation of OMC between 11.5 to 17%. Notice that clay soils generally have a lower MDUW and higher OMC whereas silty sand soils have a higher MDUW and lower OMC. The compaction curve of the soil selected for the subsequent study described in the proceeding chapters is also represented for reference.

The material variability on site imposed the greatest challenge in the steps of devising a feasible testing program for investigating the compaction behaviour and associated shear wave velocity (V_s). The greatest problem arises from the consideration of seemingly different clayey and sandy type of soils within the same framework because the compaction behaviour is quite different (see i.e. MDUW and OMC in Figure 3.3) and hence associated shear wave velocity. If the criteria for compaction acceptance relies on the dry unit weight measurement,

which is usually the case (AS 3798 - 2007), then the selection of soil with higher MDUW would result in considering a higher MDUW and V_s baseline for comparison, which means that clayey soils would then be considered as under compacted. While this is a very conservative approach, leading to any clay soils present to be deemed as under compacted, it is necessary to tackle the variability of the materials on site and satisfy the minimum performance criteria established for the site (i.e. residential housing). So in this way, performance of the material can be directly associated with measured shear wave velocity and hence small strain shear modulus.

Thus, instead of dealing with different soils, that would lead to the consideration of different model parameters and require the execution of destructive testing such as boreholes to evaluate the site conditions, in this study more emphasis was placed on the type of soil that appeared to be more representative on site (represented in the diamond series in Figure 3.2) albeit it is acknowledged that using only one type of material is a simplification.

Note that, for field dry unit weight compaction evaluations performed in Chapter 8, the compaction behaviour of the selected soil was taken as a reference and the 95% MDUW baseline was used only as a comparison indicator.

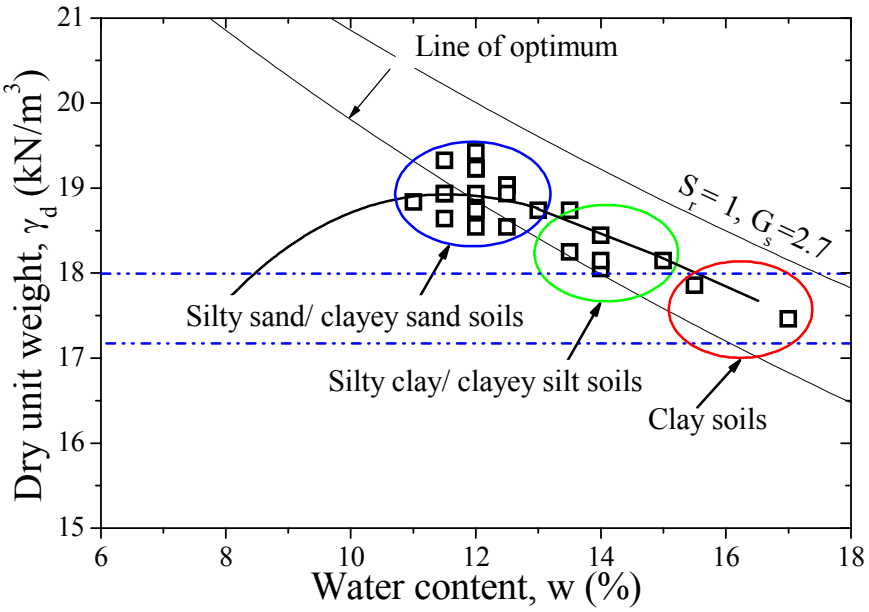

Figure 3.3 Summary of the optimum moisture content and maximum dry unit weight loci for a variety of different soils on site (compaction data is courtesy of Coffey Geotechnics).

3.3.1 Reference silty sand soil

The selected soil is a silty sand soil, poorly graded, and corresponds to relatively homogeneous alluvium sediments of river origin. The soil consisted of particles ranging in size from cobbles to silt/clay, and can be classified as SP-SC (Unified Soil Classification System, USCS) and as A-2-4 (AASHTO method M145). For the laboratory tests, the larger size particles (d>2mm) were removed and the material was dried in air and then desegregated using a mortar and pestle so that the particles could meet a nominal size of 2.36mm. The particles size distribution or PSD (Figure 3.4) shows that the soil consists of 89% sand and 11% fines, of which 7% is silt and the remaining 4% is clay size particles. The effective size d_{10} (10% of material passed) was smaller than 0.08mm, d_{30} (30% of the material passed) is 0.11 and d_{60} (60% of the material passed) is 0.18mm, resulting in an estimated uniformity coefficient (c_u) of 2.5 and curvature coefficient (c_c) of 0.9. This classifies the material as uniformly graded.

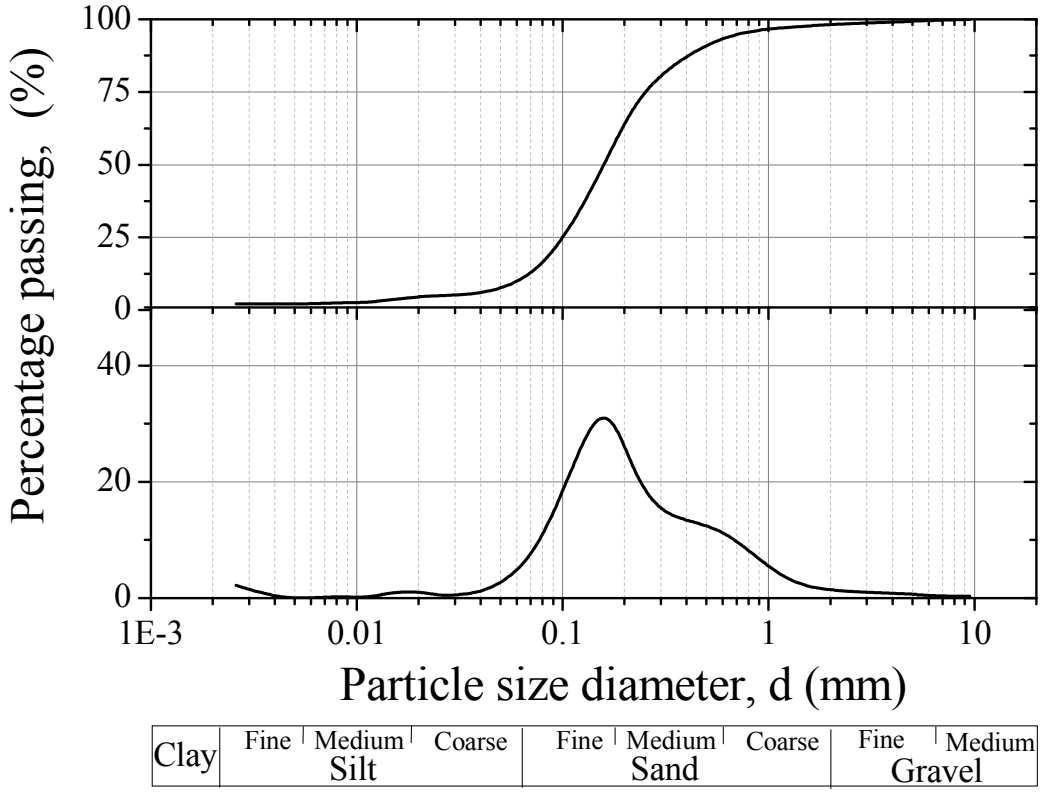

Figure 3.4 Particle size distribution of the silty sand material.

The particle size distribution, shown in Figure 3.4, is represented terms of its cumulative and individual percentages. It shows that the soil is mainly dominated by one

characteristic population of sizes of 0.15mm. The Atterberg limits obtained by the cone penetrometer test for the Liquid Limit (LL) (AS 1289.3.9.1 - 2002), and the rolled thread for the Plastic Limit (PL) (AS 1289.2.1 - 2009) are shown in Table 3.1., which classifies the fill material as low plasticity, according to the Casagrande plasticity chart (AS 1289.3.9.1 - 2002). The activity of clay minerals of fill material can be determined by dividing the PI by the percentage of clay material. In this case the clay minerals of the fill material are considered to be active with swelling properties according to Skempton (1953) classification, since an activity value of 2.5 is obtained.

Compaction curves were obtained for different levels of compaction energy by using the 2.7 kg hammer (Proctor) compaction test with 15, 25, and 35 blows per layer, and by using the 4.9 kg hammer (Modified Proctor) compaction test (AS 1289.5.1.1 - 2003 and AS 1289.5.2.1 - 2003 respectively).

Table 3.1. Atterberg limits of the backfilling silty sand soil

Natural moisture content (%)	Liquid limit , LL (%)	Plastic limit , LP (%)	Plasticity index, PI (%)
12	25.5	15.5	10

The different energy levels selected aided in determination of the maximum dry unit weight for the material, and hence, the corresponding optimum moisture content, or OMC. As per end-product specifications (i.e. AS 3798 - 2007) the compaction of earth structures should be performed with moisture control preferably at a water content close to OMC, given that at these values the material exhibits its best performance, as was highlighted in the previous chapter. In the case of the fill material at Penrith Lakes, as presented in Figure 3.5, it was determined that for the standard Proctor test, the maximum dry unit weight or MDUW of 19.02kJ/m^3 was achieved at an OMC of 12.0%. 19 tests were performed to obtain the water content-dry unit weight relationships for the additional energies. The summary of MDUW and OMC are shown in Table 3.2. The OMC points at each energy level i.e., the line of optima, were approximated to a line of equal degree of saturation where $S_r = 0.79$. The lines that represent full saturation ($S_r = 1$) is also represented.

For each compaction energy, the dry unit weight increases as the moisture content increased to the OMC. Beyond this point (i.e. the wet side of the compaction plane), the dry unit weight decreases as the water content increases. This tendency can be explained from a microscopic perspective by considering the interaction between water, air, and solid grains on

the menisci. On the dry side of the compaction plane (i.e. points located below the line of optima), the suction that acts on the particle contacts to oppose slippage is high, and the compaction process yields low dry unit weights and an aggregated soil structure (Delage et al., 1996). The progressive addition of moisture reduces suction and facilitates particle slippage, so the soil experiences higher dry unit weights until it reaches its maximum at OMC, as represented by the line of optima in Figure 3.5. Beyond the OMC, the air phase becomes discontinuous i.e., the air is occluded in bubbles (Barden and Sides, 1970; Barden and Pavlakis, 1971). In this condition, any applied external compaction energy is likely to be supported by the water phase in the soil, since compaction occurs over a relatively short period and the system is water undrained.

Table 3.2. Compaction maximum dry unit weight and OMC for different energy levels.

Energy level KJ/m^3	Maximum dry unit weight, γ_{dmax} : kN/m^3	Optimum moisture content, w : %
358	18.3	13.5
596	18.98	12
834	19.4	10.5
2703	20.4	8.5

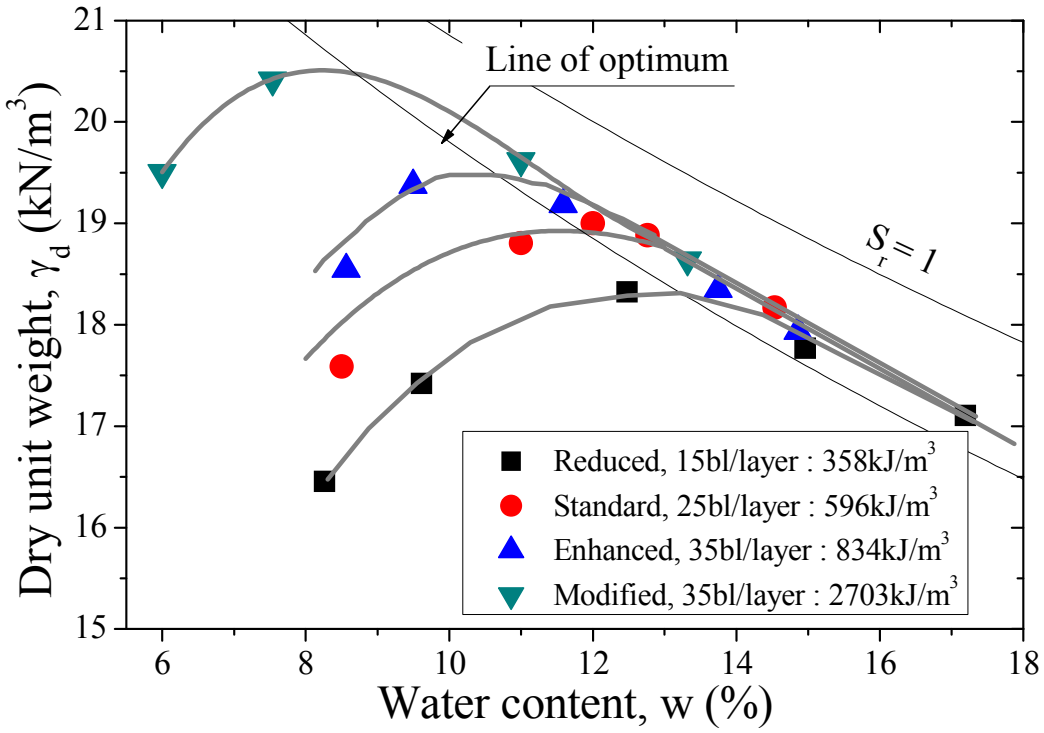

Figure 3.5 Compaction curves for different energy levels.

3.4 BENCHMARK FIELD TESTING AREAS

An important step in validating the methodology proposed in this thesis is its validation with field measurements. Two adjacent areas (designated Areas 7 and 9), that were improved by dynamic compaction (DC) to ensure that the deep fill materials were adequately compacted, were selected for this purpose (Figure 3.6). These areas were initially backfilled in two different stages, the first from 1975-1976 using scrappers, and later from 1993-1997 by scrapper and truck dumping and spreading (Moyle, 2007). Therefore, the characteristics in terms of dry unit weight initially anticipated for the fill materials of these areas were expected to be largely below the common end-product specifications (i.e. AS 3798 - 2007) mainly due to the manner in which the soil had been compacted and the lack of any reliable historical records. The main reason these areas were selected was because, in spite of being initially anticipated as areas of poor compaction, they were assessed as satisfactory in terms of bearing capacity needed to support the design requirements after DC.

The DC improvement design parameters for this site were set in terms of the height of the drop, the falling weight of the pounder, the number of drops, and the drop spacing. A pounder of 20t (octagonally shaped) attached to a crane was dropped from approximately 23 m above the ground, and three passes were used to provide a grid pattern spacing of 4.2m for Area 9 and 6m for Area 7 (Moyle, 2007).

Figure 3.6 Location of benchmark areas 9 and 7 (modified after Moyle, 2007).

During the DC, the penetration, heave, and changes in the topography were monitored. After the DC the area was surveyed for quality assessment purposes. The post DC investigation included an electric friction cone penetrometer test (or CPT), augered boreholes, flat plate dilatometer (or DMT) in the borehole, *in situ* tube sampling in the borehole, and down-hole Gamma density (DHGD) tests.

The CPT tests were conducted at four different locations and both the cone resistance (q_c), sleeve friction (f_s) and friction ratio (F_r) were monitored. The boreholes were drilled to depths that varied between 13m and 14.2m. The flat dilatometer tests conducted in the boreholes and had readings spaced about 0.3m within the layers of weak soil. The results of the flat dilatometer tests enabled the evaluation of the vertical drained constraint modulus; however the calculations involved in its determination did not consider unsaturated conditions. For this reason the results shown in Figures 3.9-3.12 are only meant to be taken as a comparison measure to confirm the obtained the q_c and f_s from CPT tests. Further corrections in relation to the measurement of either in situ suction or water content would be required to analyse the results more conclusively. For further details on the corrections necessary for the analysis of in situ boreholes flat dilatometers tests and CPT tests in unsaturated conditions, the reader is referred to Russel and Khalili (2006) or Pournaghiazar et al. (2011). In order to verify the density results obtained with the DHGD, in situ tube sampling was also carried at selected boreholes depths. The calliper width measured during DHGD, which corresponds to the measured borehole diameter when the natural gamma detector probe is pushed to the sidewall of the borehole, is also represented. The calliper width of its own has very little relevance to the engineering behaviour of soils, however it is a good indicator to gauge the amount of deformation occurring in the borehole after drilling process is completed.

3.4.1 Designated Area 7

The location of the augered boreholes and CPT tests conducted in area 7 are shown in Figure 3.7. To evaluate the performance of the proposed relationship under field conditions, only two of the four boreholes will be analysed. A summary of the CPT, in situ wet density, width of calliper and results of the DMT are shown for the boreholes located at CS7.2 and CS7.3 (Figure 3.9 and 3.10).

The borehole log indicates there is some variability of materials with depth, ranging from material classified as silty clay at ground level to sandy clay towards the end of the borehole. The ground water level (GWL) was found to be at a depth of 11m. The in-situ wet density (or bulk density) varies with depth, having a minimum value of 1.9t/m^3 or 18.63kN/m^3 and an average of approximately 2.1t/m^3 or 20.58kN/m^3 overall. The calliper width is consistent with the depth and remained above 100mm. The values of the DMT ranged from 40-60MPa but were smaller at a depth of 11m, which may be related to the proximity of the GWL. Note that the distribution of wet density with depth is more heterogeneous in CS 7.3, which curiously, is also reflected in the cone resistance (q_c) CPT results.

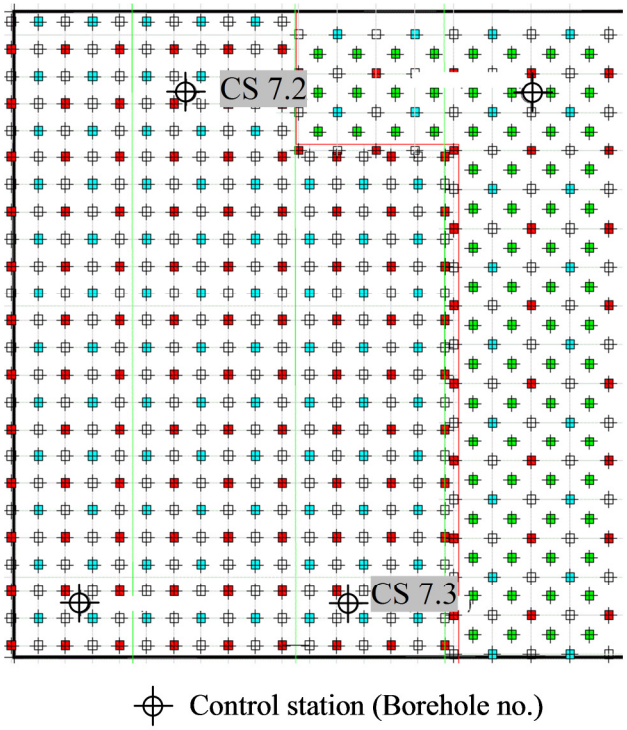

Figure 3.7 Location of the augered boreholes and CPT tests overlayed by DC soil improvement grid in Area 7 (modified after Moyle, 2007).

3.4.2 Designated Area 9

The location of the augered boreholes and CPT tests conducted in area 9 are shown in Figure 3.8. To evaluate the performance of the proposed relationship for field conditions, only two of the four boreholes will be analysed. The summary of the CPT, in situ wet density, width of

the calliper, DMT, and results of the extensometer are shown for the boreholes located at CS9.2 and CS9.3 (Figure 3.11 and Figure 3.12).

The borehole logging indicates that the type of materials varies with the depth; from material classified as silty sand and clayed sand, to sandy clay towards the end of the borehole. Although it was not represented, the ground water level (GWL) was found at a depth of 10.5m, which confirmed that a substantial portion of the ground is under unsaturated conditions. The in situ wet density (or simply bulk density) varies with depth, having a minimum value of 1.9t/m^3 or 18.63kN/m^3 and an average of approximately 2.1t/m^3 or 20.58kN/m^3 overall. The width of the calliper is consistent with the depth and stays above 100mm. The DMT values range from 40-60MPa, but were smaller at depths of 9m and 12m, which may be related to the proximity of the GWL.

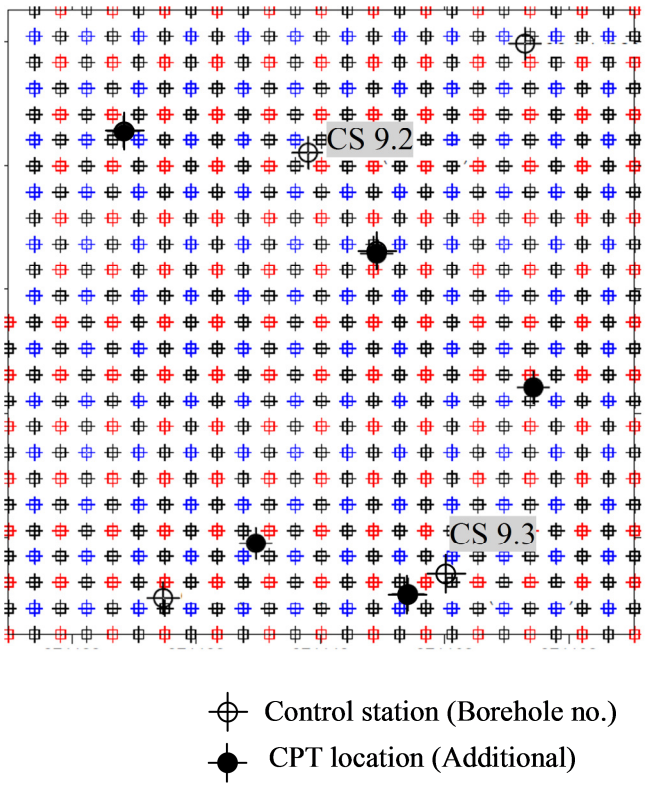

Figure 3.8 Location of the augered boreholes and CPT tests overlayed by DC soil improvement grid in Area 9 (modified after Moyle, 2007).

3.5 SUMMARY

The Penrith Lakes site was introduced in this chapter. First, the aspects related to the background and location of the site were introduced, followed by a general classification of

the materials representative of the site, together with the compaction curves developed for different levels of compaction energy. A site validation of the methodology would consist of comparisons with the measurements of the in-situ shear wave and predicted degree of compaction, against the density obtained via classical destructive geotechnical investigations such as boreholes, CPT, GHGD, DMT, and the width of the calliper. The general characteristics and site location of the two different areas selected for that purpose were outlined, and the results of the geotechnical investigation of selected boreholes were presented.

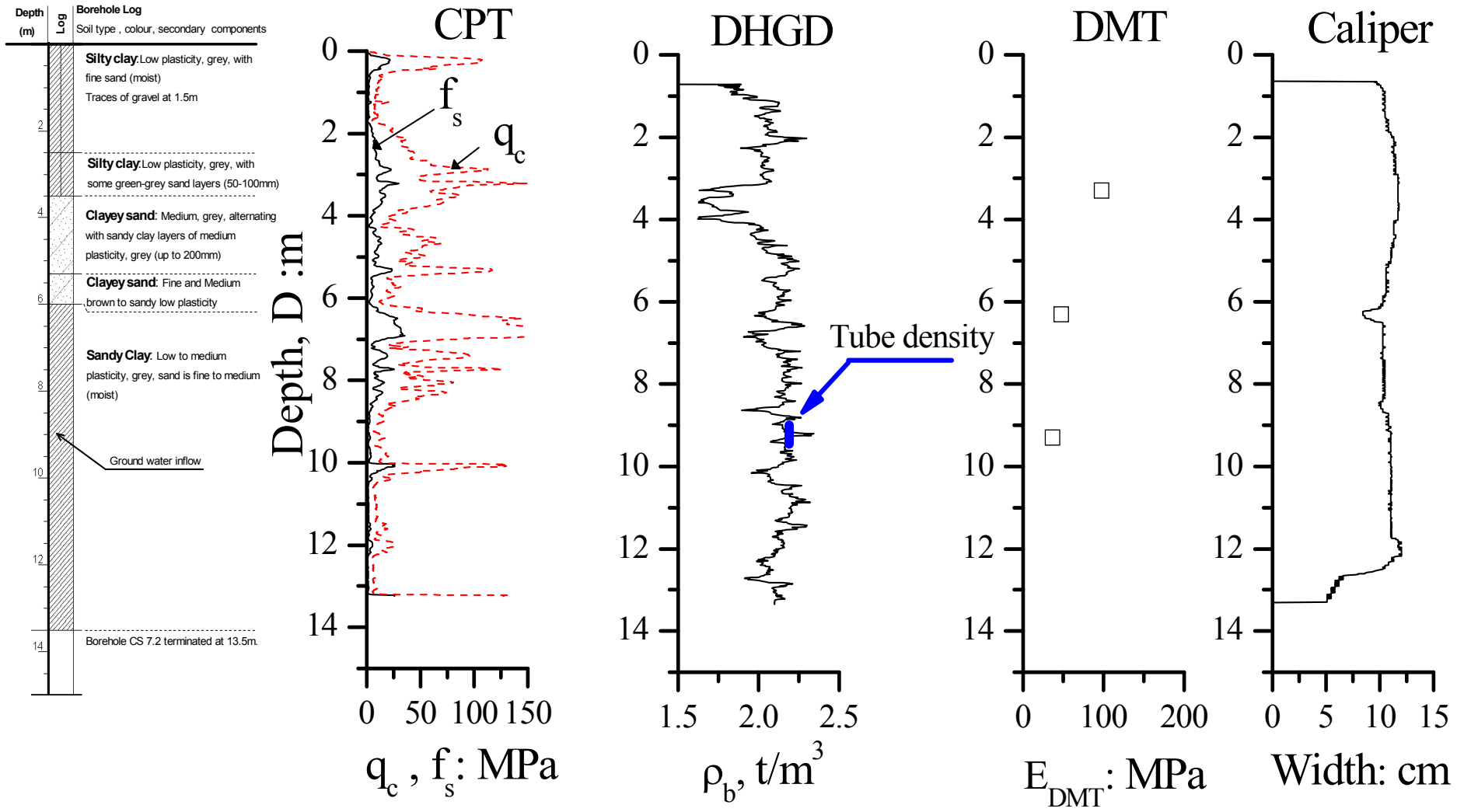

Figure 3.9 Summary of the test results from CS 7.2 (modified after Moyle, 2007)

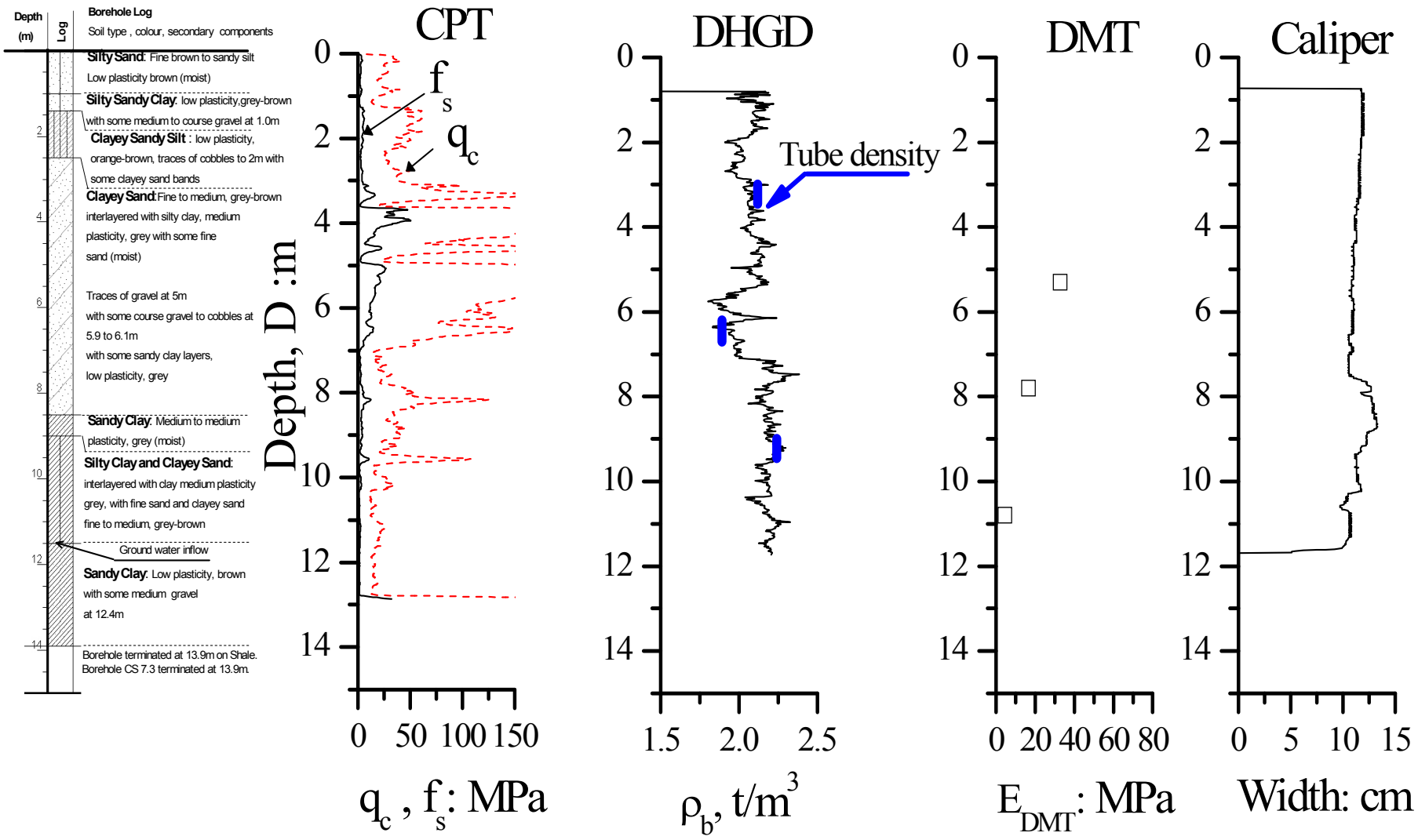

Figure 3.10 Summary of the test results from CS 7.3 (modified after Moyle, 2007)

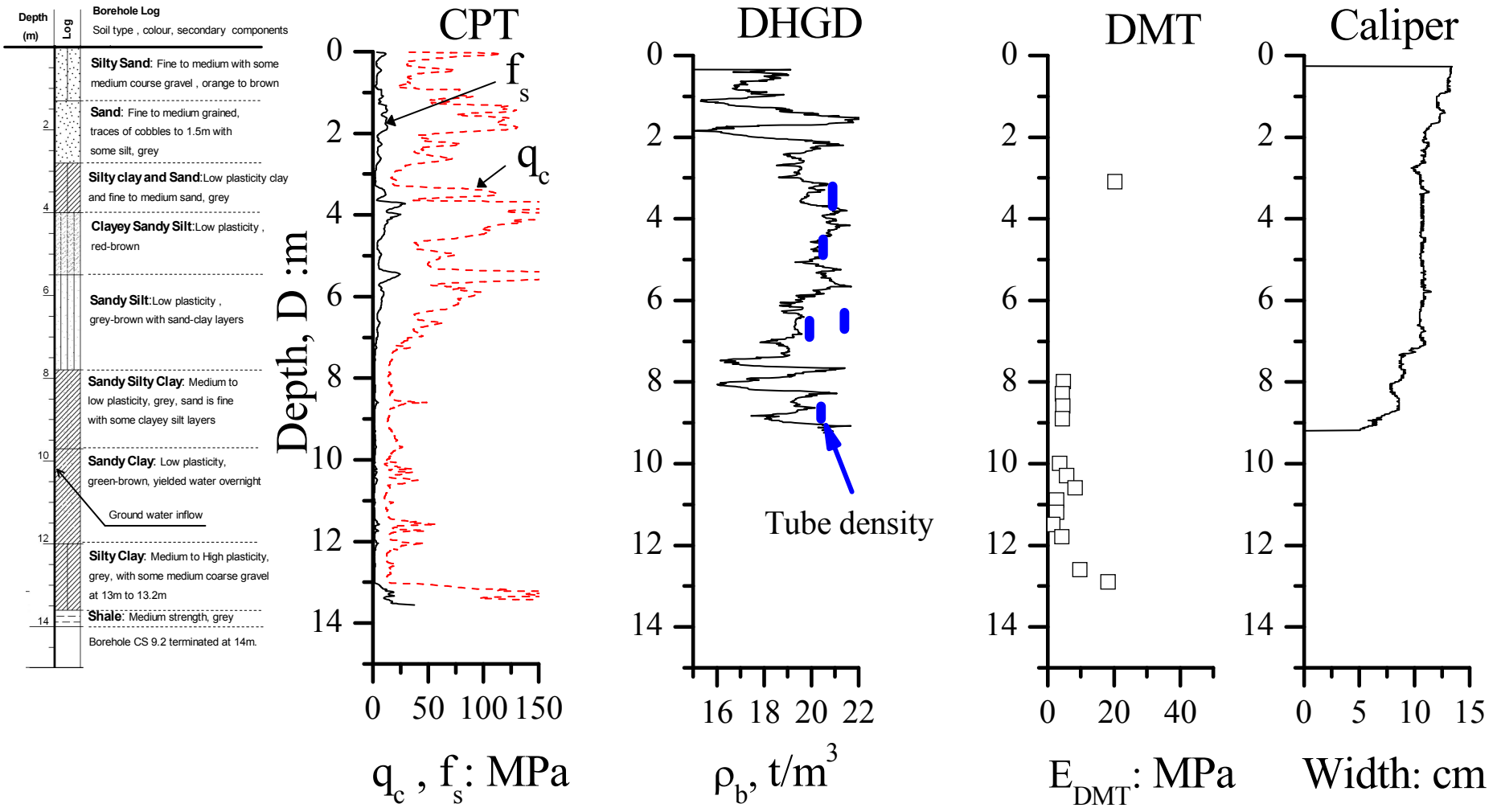

Figure 3.11 Summary of the test results from CS 9.2 (modified after Moyle, 2007)

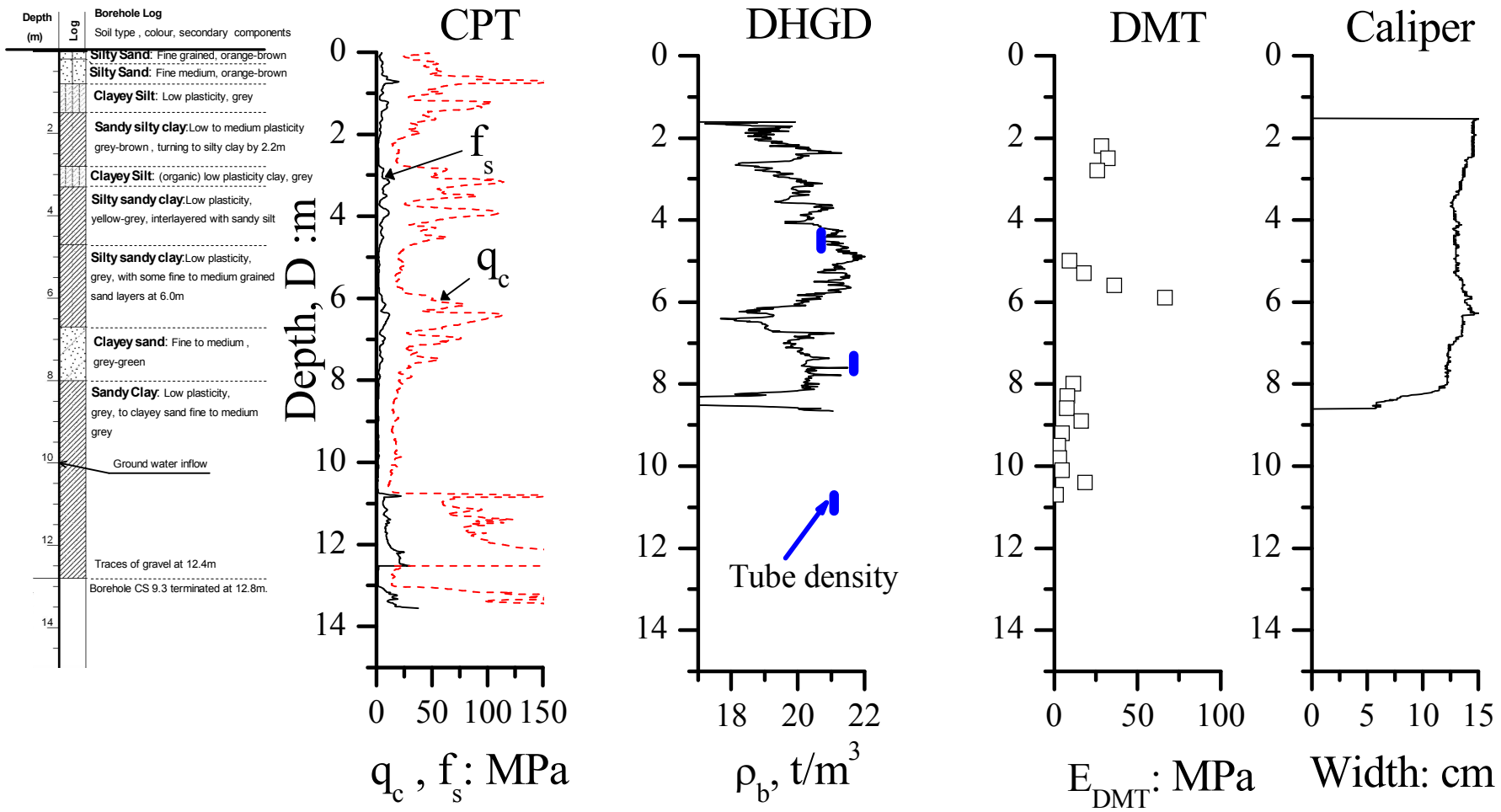

Figure 3.12 Summary of the test results from CS 9.3 (modified after Moyle, 2007)

CHAPTER FOUR

4 . LABORATORY AND FIELD TESTING PROGRAM

4.1 GENERAL

In this thesis, the technique proposed to verify the characteristics of compaction, including the field and laboratory tests, involves a low cost and time effective non-destructive test, i.e., the shear wave velocity or V_s. However, to establish an empirical relationship the fundamental properties of the soil based on different compaction states, as defined by different water contents and levels of energy, must be calibrated against an equivalent V_s and suction. Although the V_s and suction for a wide range of different states of compaction has been investigated separately and independently in previous studies, the combined effect on V_s and suction induced by different compacted states has yet to be addressed. Understanding how these variables interact along the compaction plane derived from an insight provided by laboratory tests, is an essential tool to characterise the behaviour of soil though empirical relations.

This chapter describes the methodologies and apparatus used in laboratory and field measurements (Figure 4.1). The laboratory testing program carried out to investigate the small strain stiffness or shear wave velocity in unsaturated compacted specimens, included the extensive use of bender elements encompassing as compacted and post compacted states. The methodology and apparatus are discussed first, and some of the results are shown to illustrate particular aspects related to their analysis.

Suction is an important variable that characterises the state of stress of unsaturated soils, which means that it is imperative to evaluate its relative influence on the measured V_s for different states of compaction. The two methodologies adopted are described in this chapter, and the effect of post compaction change of water content on the hydraulic behaviour of soil using the Soil Water Retention Curve (SWRC) is also discussed. To understand to what extent the difference in compaction affects the hydraulic behaviour, the SWRC was determined from a series of specimens compacted at different moisture contents.

An important aspect related to the geomechanical performance of fills is the proper characterisation of the stress-strain characteristics of soil compacted under different water contents and levels of energy. There are a number of different types of apparatus that can be used to achieve this. For this particular study, a series of constant water content direct shear tests (CWDST) were performed under unsaturated conditions in order to describe the mechanical behaviour of PLDC soil. This meant modifying a conventional shear box apparatus for testing under CW conditions. A description of these modifications and the procedure adopted are outlined later in the chapter.

Different states of compaction alter the inherent fabric of the specimens. As outlined previously in Chapter 2, understanding these changes in the soil fabric is fundamental, because, they affect the mechanical behaviour of the soil, especially in the small strain stiffness range. Although there are limited number of research studies focussed on the soil microstructure available, most were conducted on clayey soils using techniques such as SEM and MIP that are likely to induce some degree of disturbance in the specimens. To avoid this problem the details entailing the use of a medical grade X-ray CT scanner to evaluate the macrostructure of soil are described and the tests results shown thereafter. Furthermore, while MIP or SEM methods enable the fine details to be observed in small samples (typically few grams of soil), CT methods can provide morphological information of larger samples but at lower resolution.

Finally, the procedures used to prepare the specimens and the methodology adopted for the field tests are also described and the results shown.

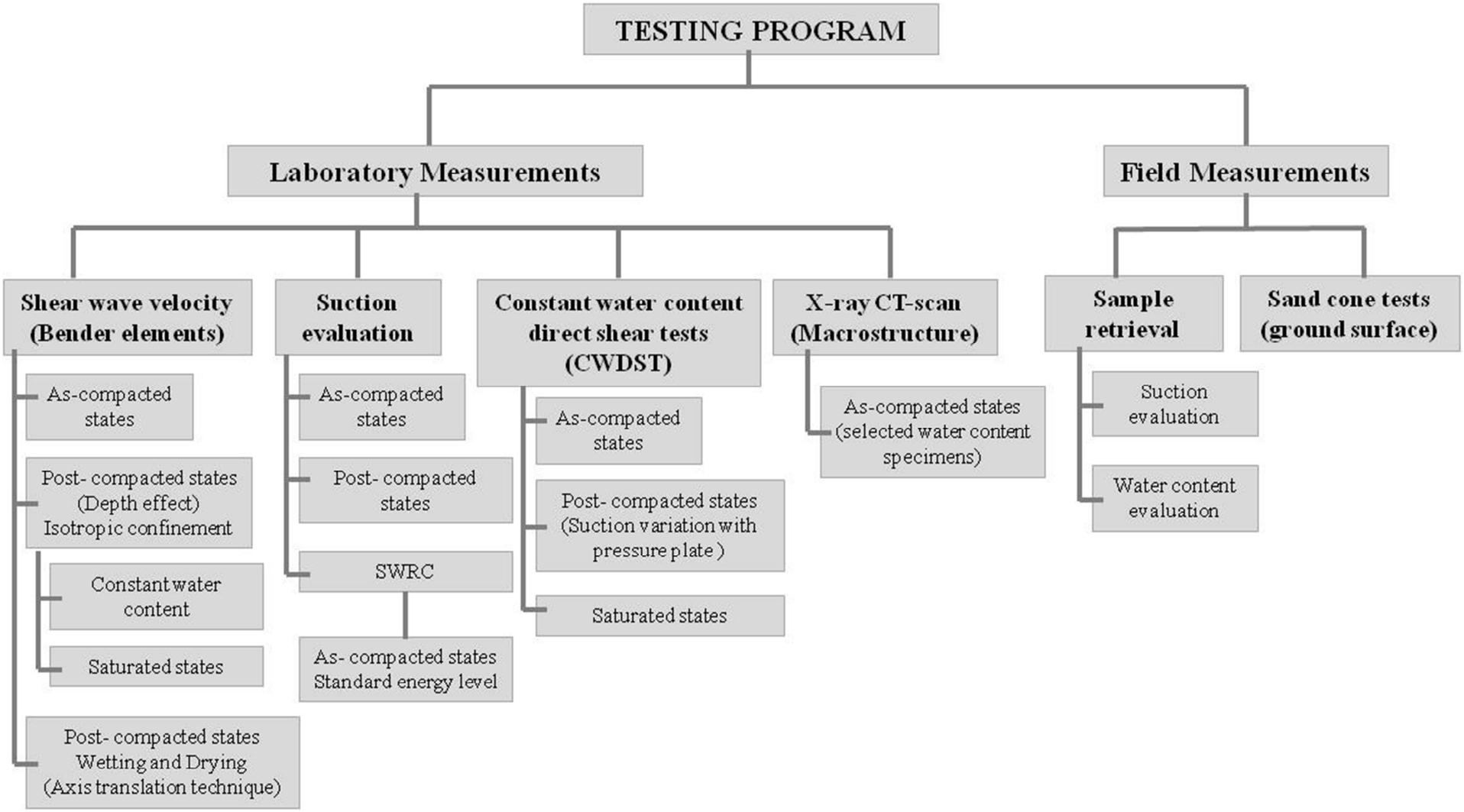

Figure 4.1. Summary of the testing program carried out in the compacted specimens

4.2 LABORATORY MEASUREMENTS

In the next sub-sections, details of the apparatus used in the laboratory to measure the shear wave velocity and suction, and the X-ray CT scan tests conducted on the specimens prepared by compaction with different moisture contents and energy levels, are given.

4.2.1 Shear wave velocity

Despite the increasing accuracy and resolution of static and quasi-static equipment such as local transducers (i.e. LVDT or Linear Variable Differential transducer), dynamic methods are still the best option for testing small and very small strains (i.e. Atkinson, 2007). Indeed, laboratory dynamic testing, based on the velocity of body waves, is one of the simplest ways of determining the small strain stiffness of soils. For instance, very small strain shear modulus, usually designated as simply small strain shear modulus or G_0 is given by

$$G_0 = \frac{\gamma}{g} V_s^2 \tag{4.1}$$

where γ is the bulk unit weight (kN/m^3), g is the gravity acceleration (m/s^2), and V_s is the shear wave velocity (m/s). Of the dynamic testing apparatus available to study small strain behaviour, the two worth noting are bender elements (BE), and the resonant column apparatus (RCA). The primary difference between them is the type of input signals and modes of excitation. While the RCA allows the vibration of soil in torsion or flexure using frequency sweeps to establish the resonance frequency, in the BE a small flexure generated by an applied voltage generates an input wave transmitted through the specimens. The main advantage that BE has over RCA for estimating the shear wave velocity relates to its versatile and simple construction, the actual test procedure itself as well as the ease in which it can be integrated into a wide range of cells and loading conditions (triaxial and oedometers cells, direct simple shear i.e. Dyvik and Madshus, 1985 and Arroyo et al., 2003). Nevertheless, there are some disadvantages, that is, the installation of BE causes local disturbance to the sample in the area they are embedded, and when it is used in very slender samples the derived flexural modes of propagation may hinder it detecting the shear waves (Rio, 2006). In addition, since the procedure for selecting an appropriate set of testing variables and determining the time the waves travel has been not standardised, interpreting the results may prove difficult at times. In fact, despite its growth in popularity over the last decades thanks to its perceived simplicity, "*it would seem sensible to (...) regard the bender element test as*

semi-empirical, requiring validation in each new material and test arrangement, through comparison with results from other types of test (e.g. resonant column and field geophysical tests (...) other laboratories' determinations on the same material, and in-laboratory comparisons with previous tests on similar materials" (Clayton, 2011)

4.2.1.1 Overview of the Bender elements

Bender elements, or bimorphs, consist of two piezoelectric ceramic elements joined to each side of an intermediate conduction shim (Santamarina et al.,2001). When a voltage differential is applied, one of the elements elongates and the other shortens, which in turn causes the bimorph to bend, hence the name (Figure 4.2). BE transducers are usually used in pairs, which means that one acts as a transmitter and the other as a receiver. The tip of the transmitting bender element is embedded in one end of a specimen of soil while the receiving tip is aligned with the transmitter and embedded at the other end. The element acting as a transmitter converts the input electric signal in terms of voltage, into a mechanical energy that generates waves. Some of the components of these waves travel through the specimens and reach the other end where the element is acting as a receiver. Wave components travelling to the tip of the receiving transducer force it to bend, and as a consequence, generating an electric signal. An example of a pair of bender elements assembled in a triaxial cell is shown in Figure 4.3. Apart from the BE, control systems such as a digital control box and a personal laptop with a data acquisition card, as shown in Figure 4.3, are also required to condition the electrical signals. In this study the signal generation was controlled by GDSBES v2.0 (GDS Instruments) software (Figure 4.4) while the data acquisition system had 2 input channels with 16 bit resolution each.

Another important aspect when dealing with digital signal processing is the selection of the correct sampling frequency because it determines the accuracy of the results. The best results are obtained by using the highest sampling frequency because the wave can be synthesised to the highest accuracy. According to the Nyquist-Shannon theorem, the sampling frequency should be set larger than at least twice the frequency of the wave (i.e. for a 10 kHz signal the sampling frequency should be at least 20 kHz), but in practice a sampling rate of 3-5 times the signal frequency is usually adopted. Furthermore, Clayton (2011) suggested that the sampling rate should be less than $1/100^{th}$ the travel time of the transmitter and receiver (typically 10 ms). In this study a somewhat more conservative sampling rate of

300 kHz was used to test frequencies from 0.5 to 15 kHz to ensure there would be an adequate resolution of the time and voltage for the input and output signals.

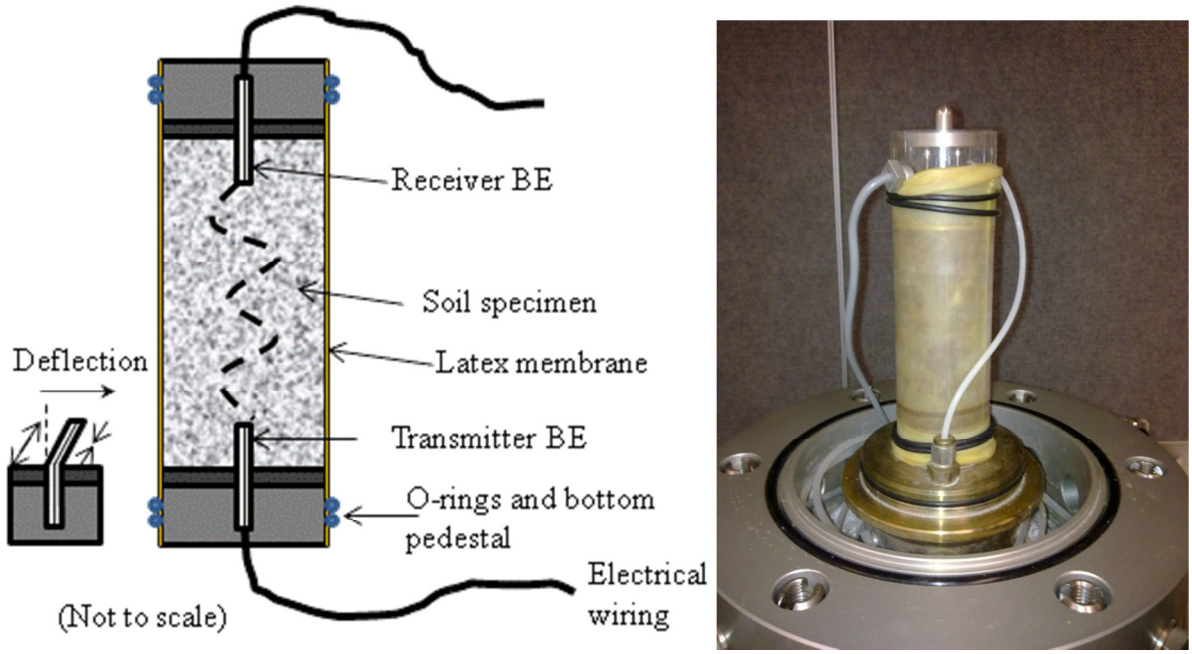

Figure 4.2 Illustration of a pair of BE mounted on a triaxial cell pedestal.

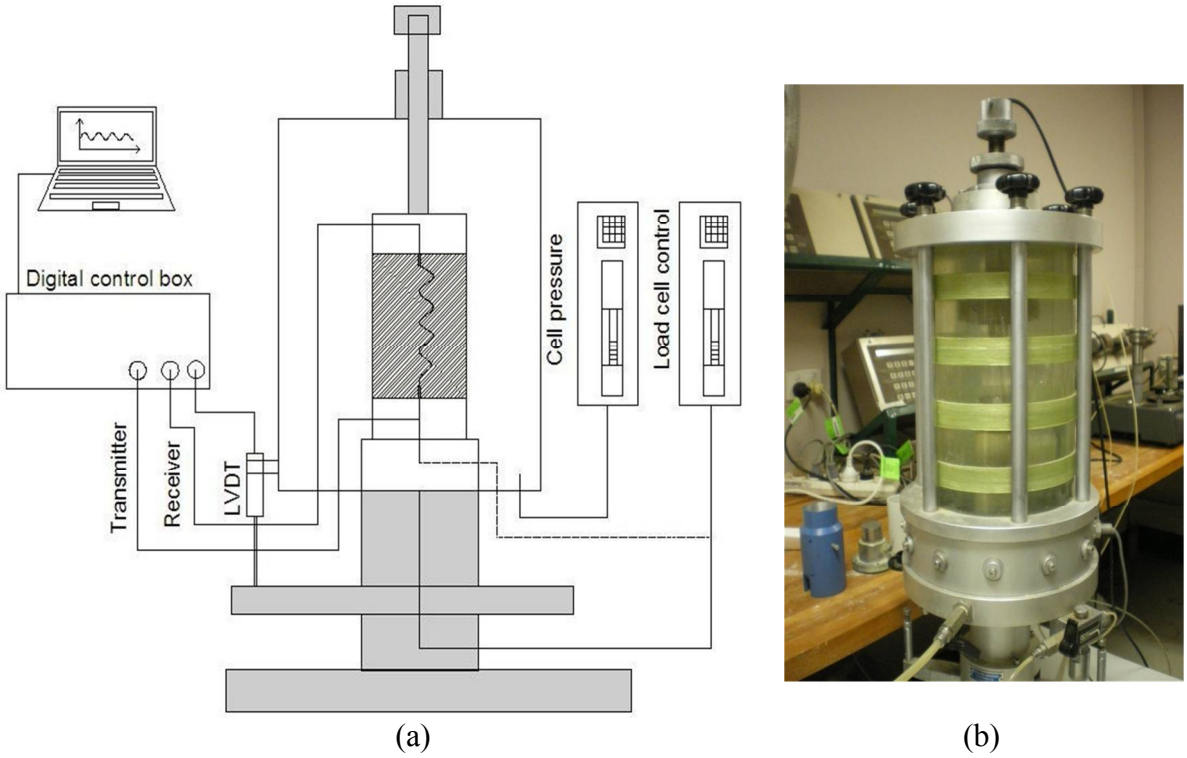

Figure 4.3 Bishop-Wesley type triaxial apparatus with BE (a) diagram and (b) photographic illustration.

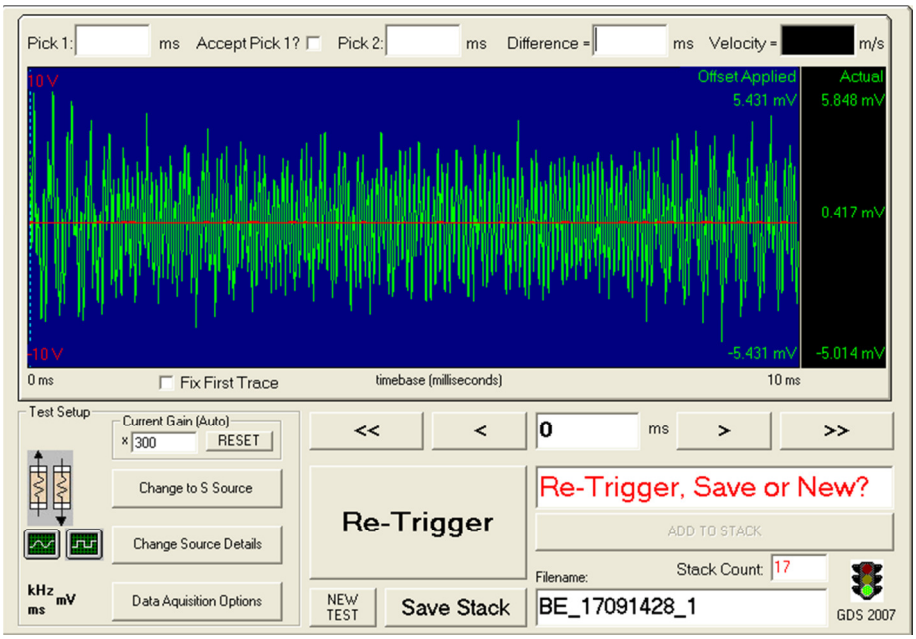

Figure 4.4 Screen shot of the GDSBES v2.0 (GDS Instruments) software.

The BE used in this thesis were fabricated commercially by GDS Instruments and cantilevered in a 50mm diameter triaxial pedestal and top cap. The BE are 11.15mm long by 1.7mm wide, and has a protruding thickness or l_b of 1.5mm. The transmitter was wired in series whereas the receiver was wired in parallel. Although they are polarised in the same direction, in some tests the polarisation was inverted to enable the received signal to be interpreted clearer, particularly when the time domain methods were being used.

4.2.1.2 Waveform: Pulse signal

The most common waveform used for testing with BE is the impulse or pulse signal (Shirley, 1978), because the signal in the time and frequency domain are easy to interpret. Of the different waveform pulse signals available, the sinusoidal and square signals shown in Figure 4.5 (Dyvik and Madshus, 1985) are the two types generally adopted for BE testing. The square signal (Figure 4.5a) has a very well defined start, which is typically the point from when the wave travel time is measured. While this signal was one of the first used in BE testing, inherited from the cross-hole impact signals, issues relating to its sharp initial rise and very broad frequency have gradually resulted in it being used less often. The sharp initial rise may prove be difficult for mechanical devices to reproduce whereas its broad frequency may cause problems in the interpretation the output signals because the near field effects (dispersion phenomena) and modal wave propagation cannot be avoided (Jovicic et al., 1996). In contrast, sinusoidal signals (Figure 4.5b) overcome those difficulties and provide a

clear and well defined signal, although near field components may still be detected (Jovicic et al., 1996). For these reasons, a sinusoidal type of input wave was selected and henceforth the term input signal refers to a sinusoidal signal.

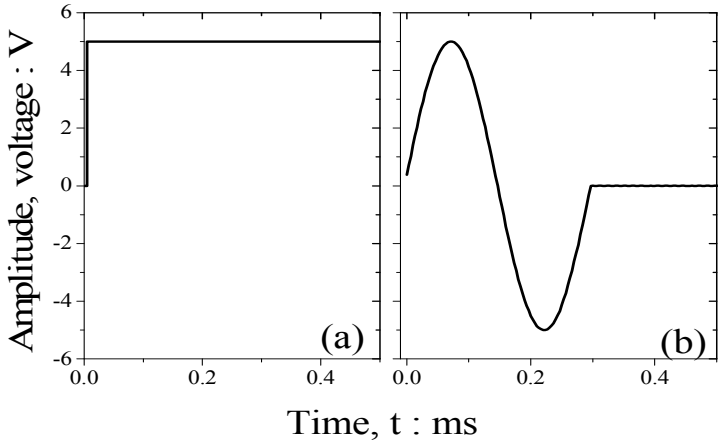

Figure 4.5 Representation of a (a) sinusoidal and (b) square input waves with a frequency of 3 kHz.

The relative importance of other types of waveforms such as continuous wave signals and sweep signals in BE response was not examined in the thesis. For further details, please refer to Rio(2006), Da Fonseca (2009) and Bonal et al. (2012).

4.2.1.3 Testing Frequency

One of the difficulties involved with measuring the shear wave velocity using BE is selection of adequate testing variables, including the frequency (Viggiani and Atkinson, 1995, Brignoli et al., 1996; Jovicic et al., 1996; Leong et al., 2005). Figure 4.6 shows the traces of the shear wave velocity obtained in a specimen compacted on the dry side of OMC (energy, E = 529.5 kN.m/m^3) tested with different excitation frequencies. Excitation frequencies above 3.3 kHz yielded approximately the same travel time (i.e. time to the first bump maximum), whereas lower values of 1.5 kHz, 1 kHz, and 0.5 kHz led to much larger values and a consequent underestimation of the shear wave velocity. It is noted that as the frequency of the waveform increases beyond 3.3 kHz, the strength of the signal reduced significantly. This is consistent with the findings by Arulnathan et al. (1998), who demonstrated that a decrease in wavelength to the length of the bender element (λ/L_b) ratio leads to a deterioration of the received signals. The ratio between the length of the wave path and length of the wave (L_{tt}/λ) also indicates that the chosen testing frequency is adequate. The wave length L_{tt}/λ can be obtained from the tests as follows,

$$L_{tt} / \lambda = \left(L_{tt} / V_s \right) = f \Delta t \tag{4.2}$$

where, f represents the frequency and Δt the wave travel time. By considering the traces of the shear wave in Figure 4.6 we obtain an L_{tt}/λ between 0.4 and 6.8. A sufficient large value is desirable to avoid the influence of the near field effects (i.e. Sanchez-Salinero et al., 1986 with $L_{tt}/\lambda>2$, Pennington et al., 2001 with $2<L_{tr}/\lambda<10$, Arroyo et al., 2003 $L_{tt}/\lambda>2$). In this study it was found that a testing frequency of 3.3 kHz and a L_{tt}/λ that exceeds 1.5 (across specimens compacted with various water contents, see Figure 4.7), could minimise the effect of the near field component and warrant the strength of the received signal. Although a minimum L_{tt}/λ of 1.5 is slightly below 2, this value was selected because it has no effect on the time domain estimations of wave travel time, in fact for frequencies higher than 3.3 kHz; the received signals seem to be independent on their respective testing frequency. Furthermore, although the near field effects strongly influence the estimated travel times in time domain methods, the frequency domain methods are relatively unaffected (Lee and Santamarina, 2005). Worth noting that the strongest output in terms of double sinusoidal amplitude is detected when the input wave is 1 kHz (Figure 4.6), which indicates that this may be the approximate resonant frequency of the soil and BE system. The amplitude of the received signal decreases for higher input frequencies.

4.2.1.4 Signal to noise ratio and wave amplitude

Testing with BE deals with electrical signals and thus the system is potentially capable of picking up noisy electrical sources and other sorts of residual vibration other than the vibration intended by the excitation of the BE transmitter. This means that different sources of noise can be present during laboratory BE testing, such as background emissions from electro-magnetic noise in the electrical systems and residual vibrations from nearby roads, railways or any other sounds, such as people walking nearby, etc.. These sources of noise are random in nature and its influence can be minimised or even eliminated by sampling a larger number of signals and consistently averaging the results.

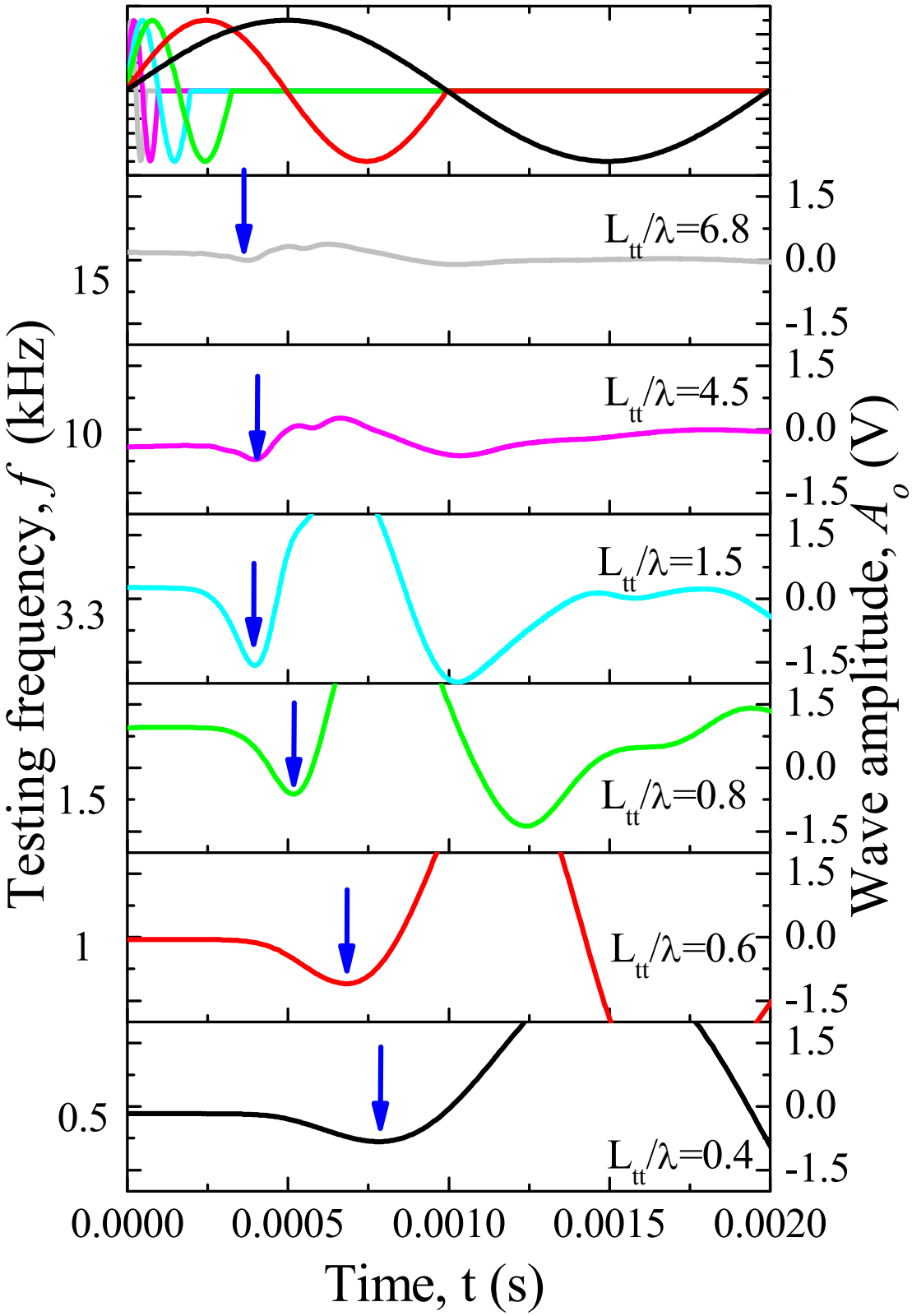

Figure 4.6 Variation of the time domain shear wave velocity traces for input wave frequencies ranging from 0.5kHz to 15kHz for a specimen compacted at a water content of 0.91 and an equivalent standard compaction energy.

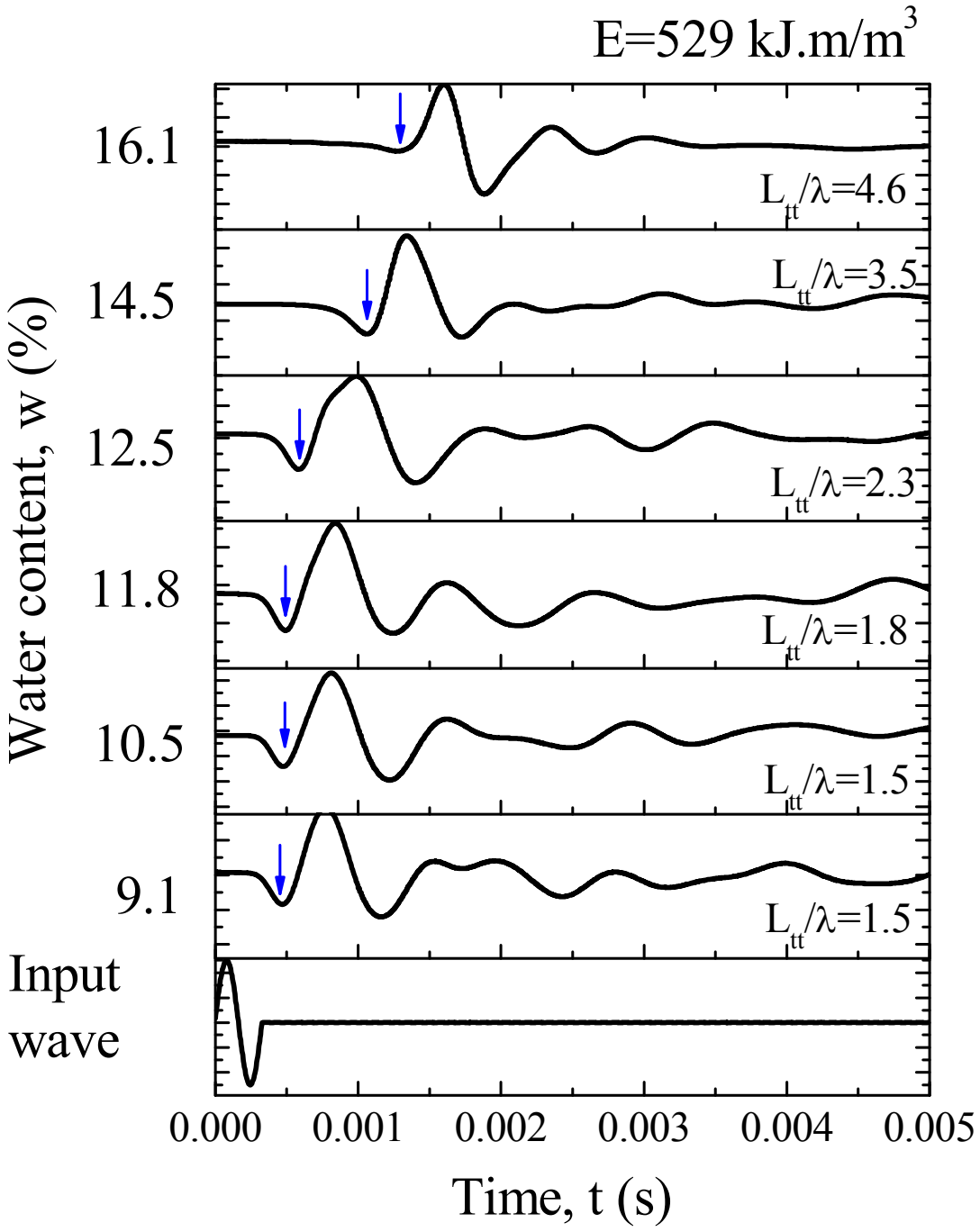

Figure 4.7 Traces of shear waves for specimens compacted under different moisture contents at a compaction energy of 529kJ/m3 (arrows indicate the travel time to the first maximum bump on the received signals).

The desired portion of the signal repeats systematically and its amplitude increases in direct proportion to the number of signals that are averaged. This procedure is also known as

staking. Figure 4.8 shows an example of traces of time domain shear waves for an increasing number of staked signals. For a low number of staked signals (i.e. up to 10) the presence of noise is clear, but its influence subsides when a larger number of sampled signals are staked (i.e. larger than 20).

The signal-to-noise ratio (SNR), as expressed in Eq. (4.3) can also be enhanced by maximising the amplitude of the input signal. A sinusoidal double amplitude wave of 10V in conjunction with systematic staking of 20 sampled signals was enough to reproduce signals that are relatively free of noise.

$$SNR = \frac{P_{signal}}{P_{noise}} \tag{4.3}$$

where the P_{signal} and P_{noise} represents the power of the signal and noise respectively.

4.2.1.5 Travel Time of Wave

There are a number of different methods for estimating the travel time of a shear wave. A clear distinction between the two main different methods can be placed in the domain where the results are analysed; i.e. either using the time domain or frequency domain. While time domain methods are the most common approach, the early arrivals of near field components and wave reflections from the sample boundaries, may result in a significant error in an estimation of the travel time. In such conditions the frequency domain methods may prove more advantageous.

Time Domain Analysis

In this method the time histories of the transmitted and received signals are used to obtain the travel time of the wave by visual picking. An example of a transmitted and received pulse signals is given in Figure 4.9. The travel time can be measured along the horizontal time axis between two characteristic points of the input and output curves. There are a number of subsidiary procedures based on the time domain analysis: the first deflection with time to A-D (Dyvik and Madshus, 1985), characteristic peaks with time between A-A' or B-B'(Viggiani and Atkinson, 1995; Arulnathan et al., 1998), first reversal point with time to A-F (Pennington, 2001), first bump maximum with time to A-E (Leong et al., 2009), and the second arrival or multiple reflections (Arulnathan et al., 1998; Lee and Santamarina, 2005).

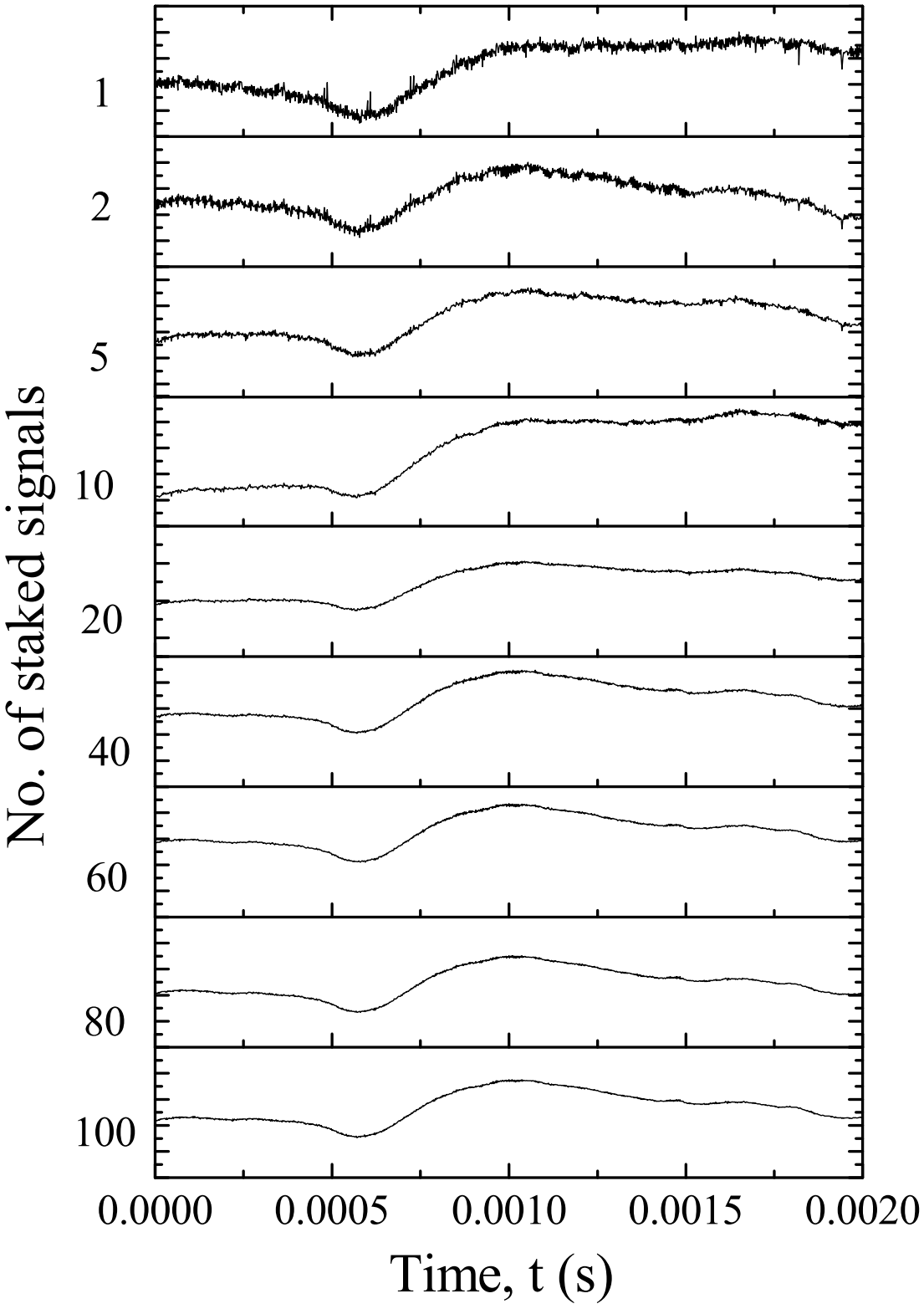

Figure 4.8 Wave time domain traces for increasing number of staked signals of a specimen prepared at water content of 0.125 with compaction energy of 529kJ/m^3.

While multiple reflections detected by the same bender element provides a simple method to overcome uncertainties over the length of travel and travel time (Lee and Santamarina, 2005), visual picking in the time domain is not always clear because of a rapid attenuation of the wave (refer Figure 4.9). The exercise of applying different procedures for estimating V_s reveals quite a significant variation in the inferred travel times (Table 4.1). For instance, Figure 4.9 shows that the times yielded from the different procedures caused the V_s estimations to reach 100m/s difference. The highest V_s was obtained for the first method of first deflection (V_s=167m/s) and the lowest for the characteristic peaks approach A-A' (V_s=76m/s), which perhaps shows that these procedures tend to overestimate (near field component masks the true V_s arrival) and underestimate V_s, respectively. In this study, the first bump maximum procedure or first crossing when the maximum bump is not visible, as suggested by Leong et al. (2009), was adopted from the time domain analysis

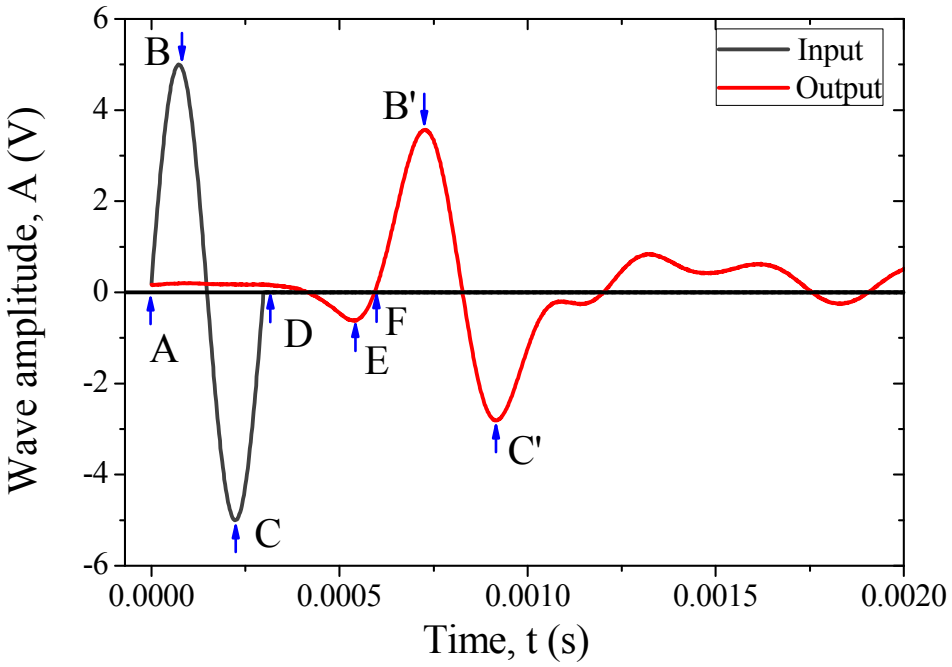

Figure 4.9. Shear wave time domain traces for specimen compacted at *w=12%* and E=529kJ/m^3.

Frequency domain analysis

The signals in the frequency domain procedures are analysed in their frequency content using numerical tools such as Fast Fourier Transforms, or FFT, or more recently wavelets (see Bonal et al, 2012). Fourier transforms provide a global description of the frequency distribution, amplitude, and regularity, whereas the time domain may occasionally be quite subjective and depend on the operator analysing the signals (Clayton, 2011). In contrast, the

frequency domain methods are objective. There are a number of different procedures for analysing the frequency domain, such as cross correlation (Viggiani and Atkinson, 1993), and cross spectral analysis (Viggiani and Atkinson, 1993; Da Fonseca, 2009). Other frequency domain methods such as π-points and phase delay methods are not described any further because they refer to the use of continuous signals and sweep signals. For additional information the reader can refer to studies by Rio (2006) and Da Fonseca (2009).

Table 4.1. Travel times and V_s for different time domain procedures

Time Domain method	Δt (ms)	V_s (m/s)
First deflection A-D	0.37	262.16
Characteristic peaks A-A'	0.662	146.52
Characteristic peaks BB'	0.678	143.06
First reversal point A-F	0.6	161.66
First bump maximum to A-E	0.54	179.62

Note: L_{tt}=97.00 mm

Cross correlation is a mathematical tool that gauges similarities between two different signals such as I(t) and O(t), which refer to input (transmitter) and output (receiver) signals, respectively. The analytical expression for the cross correlation (CC_{io}) function is expressed as follows,

$$CC_{io}(t) = \lim \frac{1}{T} \int_{T} I(t)O(t+\Delta t)dt \tag{4.4}$$

where Δt is the time delay between the two signals, T is the length of time for each signal. The cross correlation function can be obtained using the inverse fast Fourier transform (IFFT) of the cross power spectrum, or $G_{io}(t)$, as expressed in Eq. (4.5) .

$$CC_{io}(t) = IFFT\left[G_{io}(f)\right] \tag{4.5}$$

The cross power spectrum $G_{io}(t)$, that represents the product of the amplitude and phase differences of each signal at a given frequency, is given by:

$$G_{io}(f) = L^*_i(f)L_o(f) \tag{4.6}$$

where $L_i(f)$ and $L_o(f)$ are the linear spectrum of the input and output signals, respectively, and $L^*_i(f)$ represents the complex conjugate of the linear spectrum of I(t). The linear spectrum can in turn be obtained using the FFT tool,

$$L_i(f) = FFT\left[I(t)\right] \tag{4.7}$$

$$L_o(f) = FFT\left[O(t)\right] \tag{4.8}$$

Figure 4.10 shows the linear spectrums, as expressed by Eq. (4.7) and Eq. (4.8), of the input and output signals for the same specimen considered earlier for the time domain analysis (Figure 4.9). The quality of the frequency contents is somewhat poor; this is mainly related to the nature of the Fast Fourier Transform that performs well when handling long continuous signals, but is less capable of processing short signals. Nevertheless, it is clear that more than a single response frequency is being picked up by the BE system. One peak at 1.7 kHz and two other peaks at around 2.1kHz and 3kHz provide the highest responses for excitation pulses.

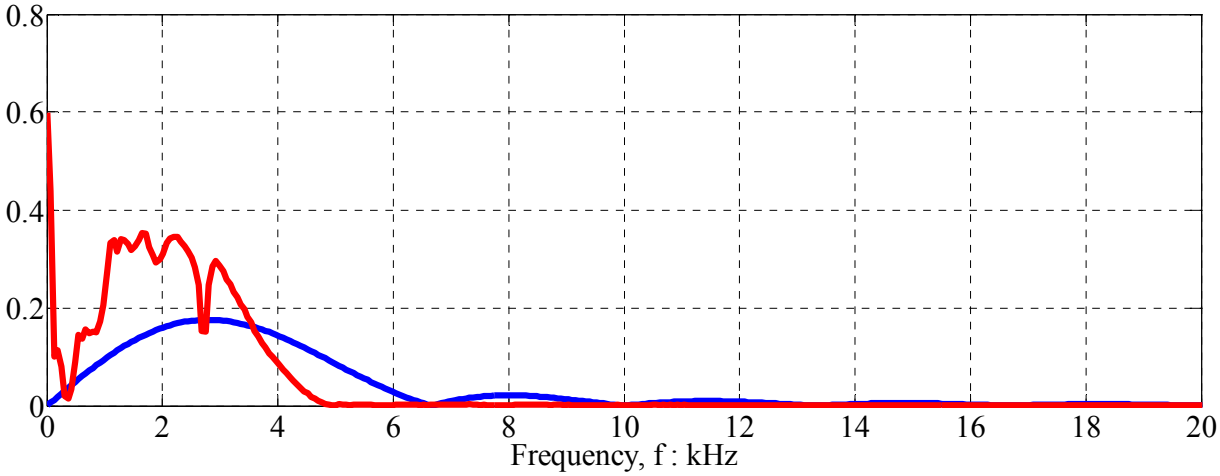

Figure 4.10. Shear wave frequency content of input and output signals specimen compacted at w=12% and E=529kJ/m3.

The cross correlation of the input to output signals, as expressed in Eq. (4.5) and normalised with respect to the maximum absolute value (CCiomax), together with the input and output signal times series, is shown in Figure 4.11. The time shift corresponding to the maximum of the cross correlating function is t_{cc} = 0.73 ms, which yields V_s=132.87m/s. This is a relatively small value compared to those of the time domain methods. This has been pointed out as one of the main drawbacks with considering travel based solely on the maximum correlation peak. The biggest advantage of using the cross correlation of signals is perhaps related with using the multiple reflection method that according to Lee and

Santamarina (2005), "*solves uncertainty not only in travel time but also in travel distance: the travel distance between the first and second event is always twice the plate-to-plate distance*".

While multiple reflections cannot always be easily distinguished in the time domain, by using frequency domain methods such cross correlation it is possible to identify the second arrival of the shear waves (Arulnathan et al., 1998). In Figure 4.11 the first reflection is identified as the time when the signal starts to repeat itself in the cross correlation function at t=1.7ms, whereas the reflection time consists of the travel time between the maximum and first reflection, or t_r=1.05ms, which yields a V_s=187.26m/s (as expressed in Eq. (4.9). Note that wave travel distance is twice the tip to tip distance between the transducer L_{tt} and the protruding distance L_b .

$$V_{s,r} = \frac{2(L_{tt} + 2L_b)}{t_r} \tag{4.9}$$

The closest guess to this value in the time domain corresponds to the first maximum bump (4% difference).

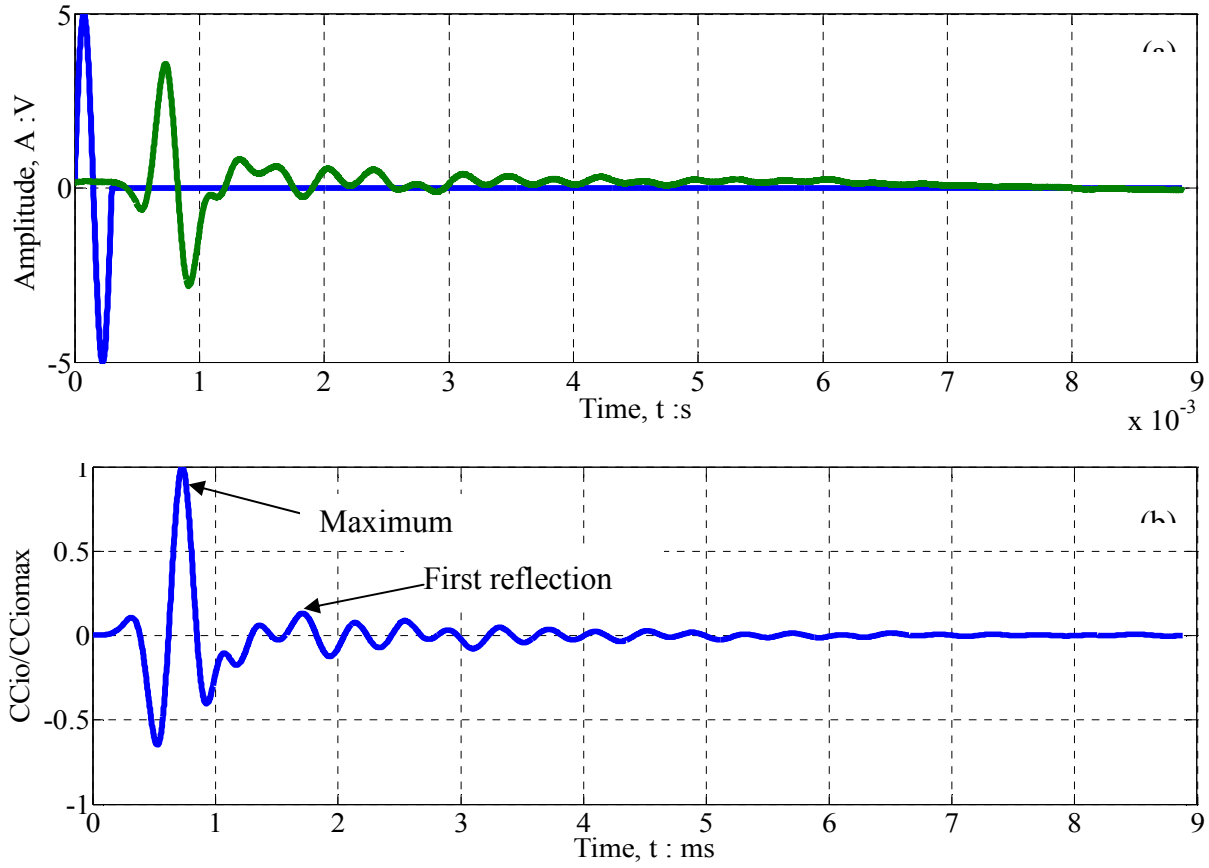

Figure 4.11 Input and output signals (a) time series and (b) cross correlation function.

As a norm, the signals were analysed in the time and frequency domain, as suggested by Jardine and Shibuya (2005), and Da Fonseca et al. (2009). The final estimation of travel time still requires an educated judgment, but for BE testing, information redundancy (time domain and frequency domain) is desirable.

4.2.1.6 Evaluating Vs with BE

The shear wave velocity (V_s) was computed based on the path of the wave length (L_{tt}) that corresponds to the tip to tip distance between the transmitter and receiver, and the travel time (Δt), as follows:

$$V_s = \frac{L_{tt}}{\Delta t} \tag{4.10}$$

The tip to tip distance was measured with a digital calliper, while considering the protruding heights of the bender elements in the specimen (Figure 4.12). The travel time (Δt) was taken as the average time interval to the first bump maximum (time domain) and the multiple reflections (frequency domain). Whenever the first bump was not visible, the time to the first deflection was considered instead.

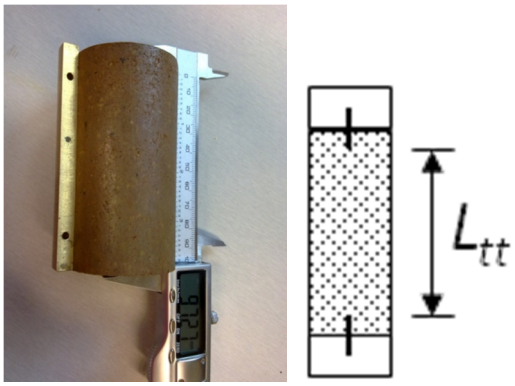

Figure 4.12 Illustration of a compacted specimen with the digital calliper used to measure the total length and diagram.

4.2.1.7 BE measurement repeatability

The shear wave measured by BE was checked for repeatability. The vertical polarised shear wave propagating in the horizontal direction (V_s-vh) was measured across the length of the specimen. Figure 4.13 represents 10 replicated shear waves traces measured in specimens compacted identically with a compaction energy of 529kJ/m^3 (standard Proctor equivalent), but with different water contents, that were tested under unconfined conditions. Furthermore, Figure 4.14 shows the 10 replicated trace shear waves measured in specimens compacted and

prepared identically, with a water content of 14.5%, subjected to different isotropic confinements at intervals of 50kPa, up to 250kPa. Although the trace shear waves were not exactly identical in both instances (attributed to some dissimilarity in the soil fabric), the first arrivals of S-waves measured in both specimens were very comparable.

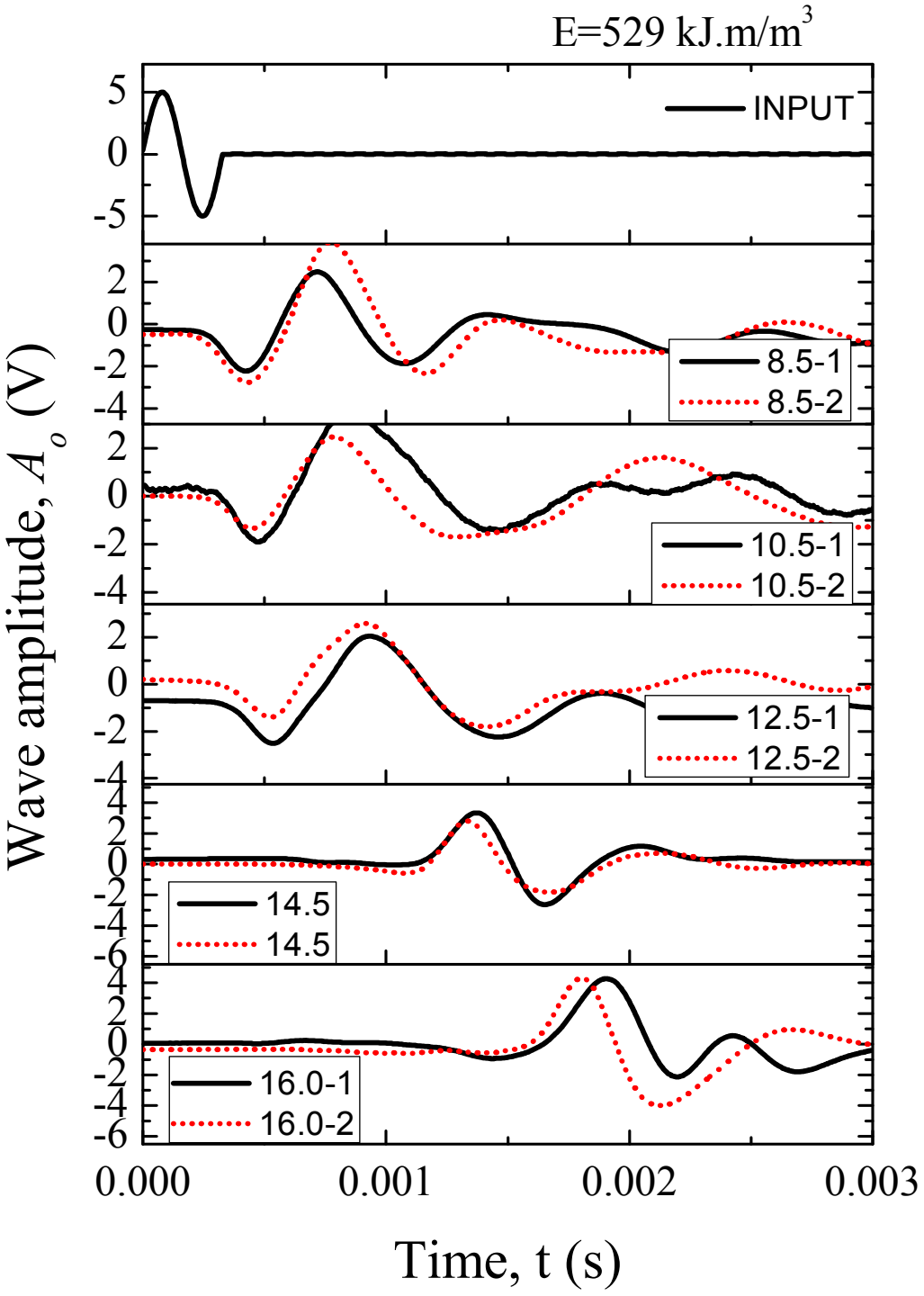

Figure 4.13 Traces of the shear wave measured in identically compacted specimens prepared at different water content and a energy level of 529kJ/m^3.

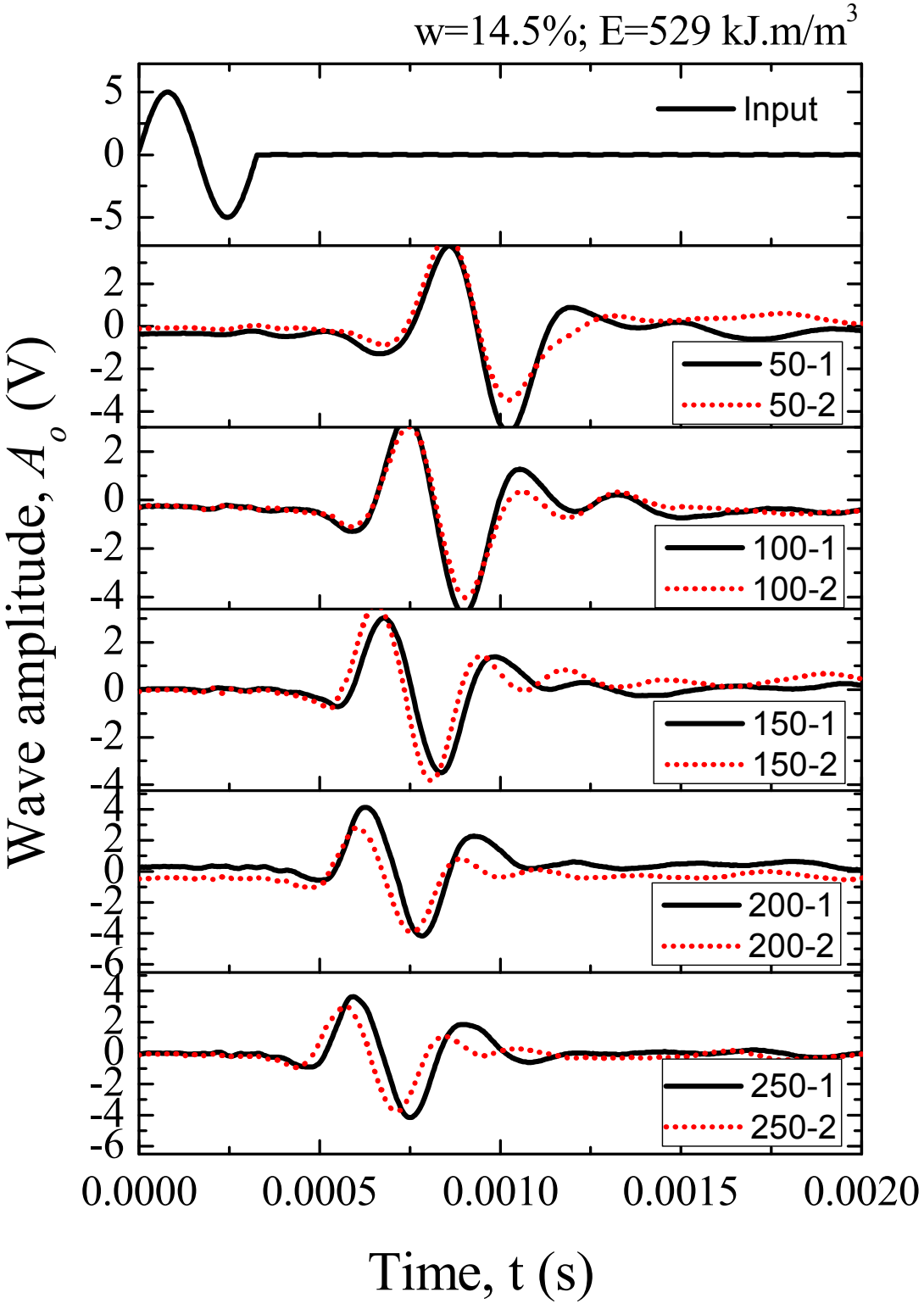

Figure 4.14 Traces of the shear wave with increasing confining pressure measured in two specimens identically prepared at a water content of 14.5% with a compacting energy of 529kJ/m^3.

4.2.2 Suction

Soil suction can be measured by a variety of different methods. The distinction between them can be placed in the range at which they enable suction to be determined (see i.e. Fredlund and Rahardjo, 1993). Although a wide range of systems (Figure 4.15) are commercially available, only those used in this thesis will be described further, namely the filter paper method (contact and non-contact methods), the small tip tensiometer and two axis translation systems, namely, the pressure plate apparatus and an unsaturated triaxial.

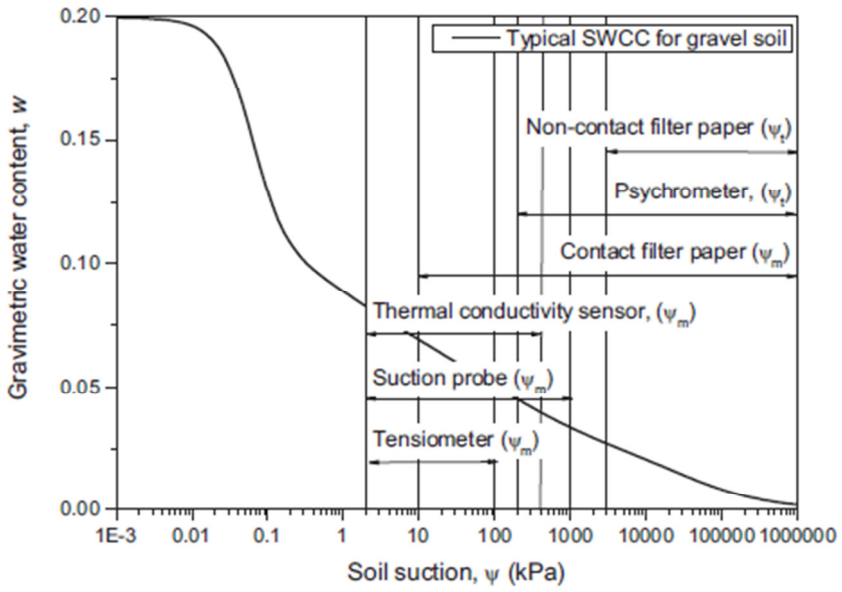

Figure 4.15.Different types of instruments available for a direct measurement of suction (Li et al., 2009)

4.2.2.1 Filter paper method

The filter paper method has been widely used to determine suction, probably because of its simplicity and ability to measure a wide range of suction, as well as being relatively cost effective. This technique was used in accordance with ASTM D5298 (2003) using the Whatman No.42 ashless filter paper. The method has two variations for determining the matric and total suction (see Chapter 2). It consists of placing a stack of three filter papers in contact with the soil specimen (contact method – matric suction) or placing a stack of two filter papers in vapour equilibrium with the specimen (non-contact – total suction, Figure 4.16).

In the contact method the two outer filter papers prevent contamination from the soil, while the middle one is used for the measurement. The outer filter papers were cut slightly larger in diameter compared to the middle paper in order to prevent it from contacting with the soil. To ensure that the central filter paper made good contact, the specimen was wrapped with electrical tape. In the non-contact method a divider is needed to separate the filter paper and the specimens. In this instance a stainless steel divider was used (Figure 4.17). The specimen and filter paper were then kept in a container sealed with electrical tape (Figure 4.16). The sealed container was stored in an insulated cooler to minimise thermal fluctuations. According to ASTM D5298 (2003) the specimen and filter paper should be at an equilibrium with the specimen before the suction is measured; a minimum period of 7 days is required to reach equilibrium. The equilibration time in this study was typically 7 to 10 days. At the end of the equilibration period, the mass of the middle filter paper (contact method) and the two filter papers (non-contact method) were measured with a high precision weight scale (accuracy of 0.0001g) and the filter paper and water content of the specimen were determined. The measurement process consisted of quickly transferring the filter paper from the container holding the specimen to an aluminium cup resting on the high precision weighing scale (accuracy of 0.0001g), to avoid any loss of moisture. Suction can be computed using the bi-linear calibration curves for Whatman No.42. as given by Leong (2002), that is, Eq. (4.11) for matric suction measurements and Eq. (4.12) for total suction measurements. Figure 4.18 shows the graphical solution of Eq. (4.11) and Eq. (4.12). The ASTM calibration curve (ASTM D5298 (2003)) is also represented for comparison.

$$\begin{aligned} \log s &= 2.909 - 0.0229 w_f \quad w_f \geq 47\% \\ \log s &= 4.945 - 0.0673 w_f \quad w_f < 47\% \end{aligned} \tag{4.11}$$

$$\begin{aligned} \log s &= 8.778 - 0.222 w_f \quad w_f \geq 26\% \\ \log s &= 5.31 - 0.0879 w_f \quad w_f < 26\% \end{aligned} \tag{4.12}$$

As an alternative the calibration curve of ASTM D5298 (2003) can also be used, but with the ASTM calibration curve no distinction is made between matric and total suction, which may lead to inaccurate determinations of suction (i.e. Leong et al., 2002; Bulut and Wray, 2005; Power et al., 2008).

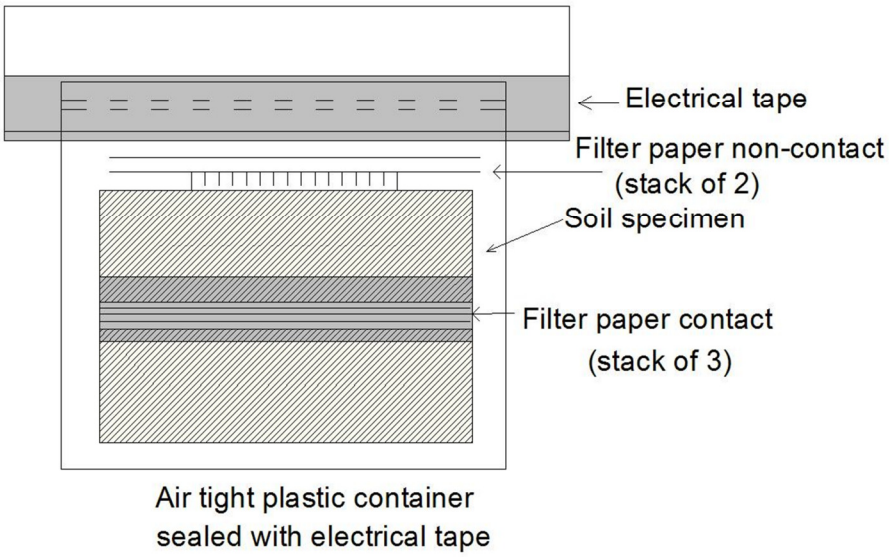

Figure 4.16 Diagram of the filter paper method.

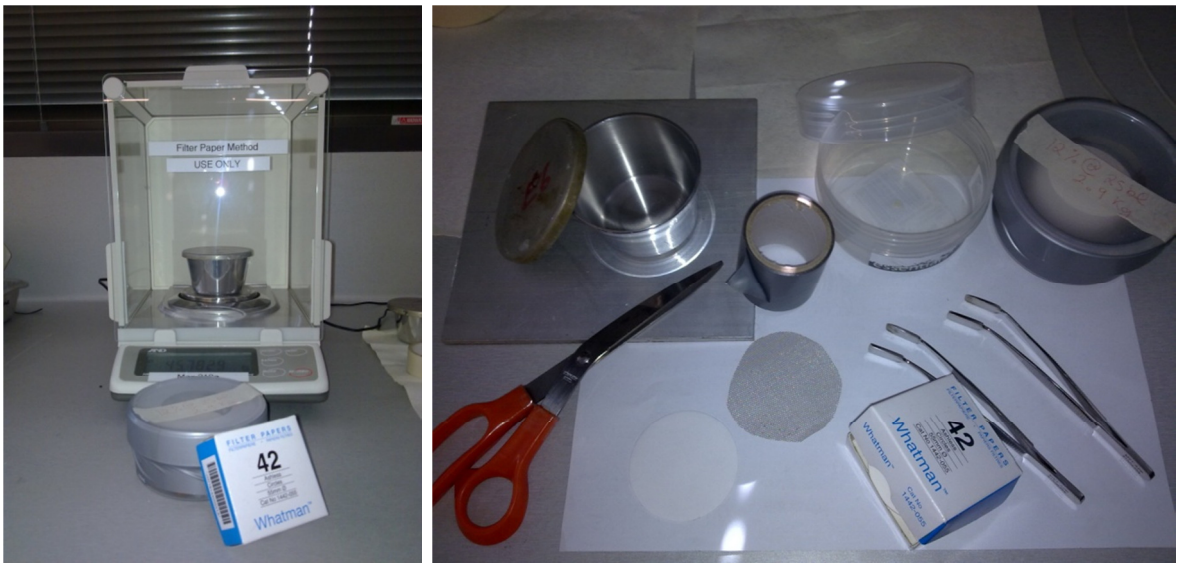

Figure 4.17 Filter paper method using precision weight scale (left) and accessories for contact and non-contact methods (right).

Most specimens were tested using the contact method, but the non-contact method was used for a few specimens compacted on the dry side of OMC because trimming was difficult when the test specimens were being prepared. The influence of osmotic suction on total suction was considered negligible because the amount of salt in the soil was very small. A minimum of two filter paper determinations were performed on each compacted specimen, and the suction was taken as an average of two tests.

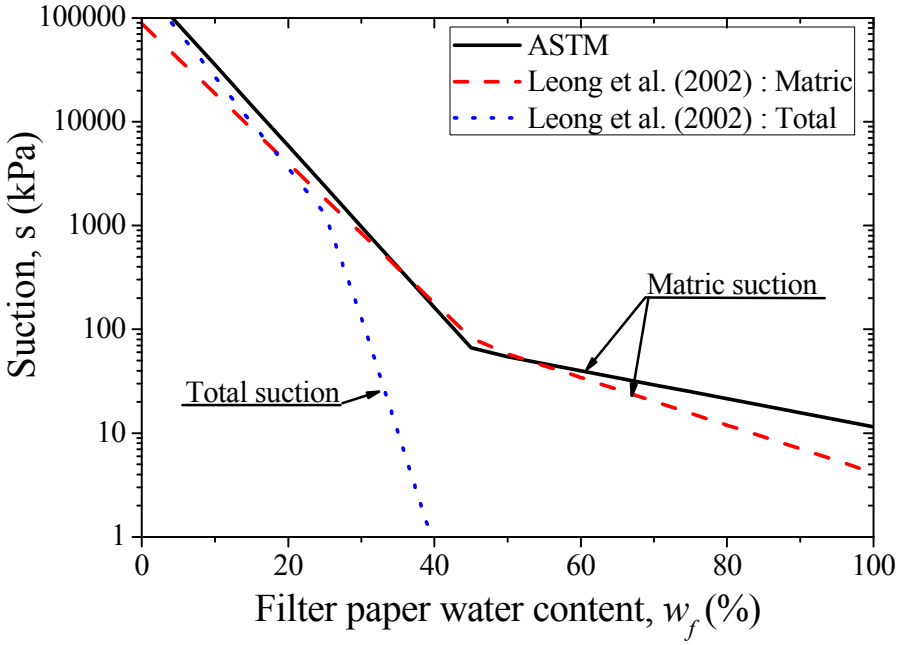

Figure 4.18 Filter paper calibration curves from Leong et al. (2002) and ASTM (2003).

4.2.2.2 Small tip tensiometer

A tensiometer is an alternative method for measuring suction, with the major advantage over the filter paper method being its ability to measure suction rapidly. The periods of equilibration range is in minutes (typically less than an hour) compared to the filter paper method which takes days. However the tensiometer method has one very important limitation, its reading range is usually below the normal cavitation limit of 100kPa. When the ceramic tip and reservoir are fully saturated the pressure gauge reads zero suction, but when the small tip makes contact with a soil specimen with a certain value of suction, water in the tensiometer begins to be drawn through the porous cup ceramic tip toward the soil until equilibrium is reached. This induces a partial vacuum pressure on the tensiometer tube that can be measured by a vacuum gauge. This value represents the suction of the specimen.

The use of de-aired water in the tensiometer aided by the extraction of air bubbles with hand vacuum pumps helps to increase its measuring capability. In this study a maximum suction value of 85kPa could be correlated with the field paper measurements (see sub-section 4.2.2.3), which seems to indicate that a slightly lower limit of 85-90kPa may be more realistic than the more commonly accepted 100kPa. The procedure adopted for the tensiometer saturation consisted of filling the tensiometer body with deaired water, immersing of the ceramic tip in deaired water for a period of 24h and applying of vacuum

cycles with a hand pump (vacuum pressures up to 95kPa) required to remove all air bubbles and guarantee that the response time was kept within a few minutes. This was achieved typically after three or four vacuum cycles, upon which visual inspection of the presence of any air bubbles in the tubing or in the tensiometer body determined it to be free of air bubbles. The tensiometer response was the monitored over time in a specimen with a known suction of 65kPa (Figure 4.19b). The measurements were carried out at the laboratory environment temperature, typically ranging between 20-25^{o}C and the period of time required for suction reading in the vacuum gauge to become constant was allowed to pass. The values of suction were recorded at different time intervals in order to ascertain the tensiometer response time. The suction reading becomes constant after 6 min, however, typically a period of 10min was allowed to pass before taking the suction measurement. Furthermore, to ensure that the response time was kept within a few minutes over extended periods of use, the tensiometer was maintained every week using a procedure similar to the one adopted for the Jet-fill model (Soil Moisture Corp.).

The tensiometer measurements were conducted in accordance with ASTM D3404-91 (2004), and the actual tensiometer used was a Soil Moisture Corp. 2100F series (Figure 4.19). This method was used to measure the suction on the specimens compacted at the OMC and wet side of OMC, in conjunction with the filter paper method. The small tip was inserted into the specimens and the time required for equilibration was allowed to pass. During this time the specimen was wrapped in cling film to minimise any loss of moisture. The measurement was carried out twice and suction was taken as the average of the two values if a variation of less than 2kPa was measured. In those cases a third measurement was conducted.

4.2.2.3 Repeatability of Suction Measurement

The suction measured with the small tip tensiometer and filter paper technique was checked for repeatability in a series of specimens compacted at different energy levels and water contents. The suction on the same specimen was measured using both methods. A comparison of the results are shown in a one to one plot (Figure 4.20), and indicate that the repeatability of these methods for suction ranging typically from 0 to 85 kPa was good; the limiting value is related to the measuring range of the tensiometer.

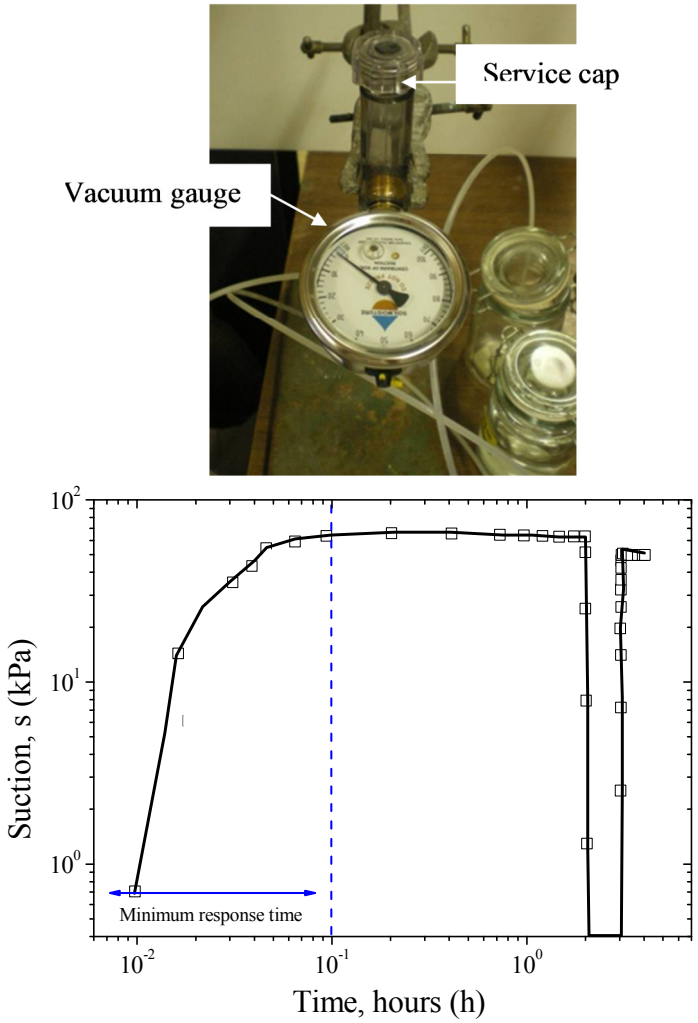

Figure 4.19 Tensiometer (top) set up resting in a retort stand and (bottom) calibration of the measurement response time.

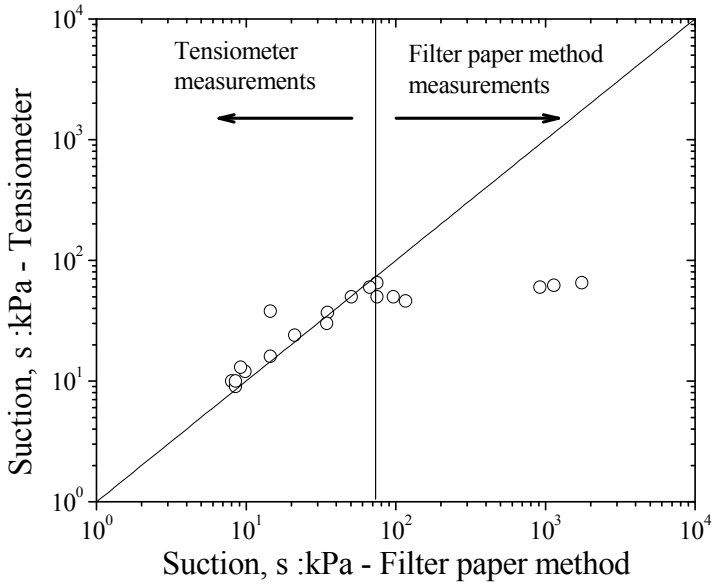

Figure 4.20.Suction measurements by the small tip tensiometer and filter paper method.

4.2.2.4 Axis translation technique

In axis translation systems the suction is not measured directly, it is imposed upon the specimens. These systems are commonly used to determine SWRC and suction control is done by measuring the pressure differential between the air pressure and water pressure. Typically, suction is increased by increasing the air pressure in the system and keeping the water pressure at atmospheric or any predefined pressure. The most common apparatus used to implement this system is the pressure plate apparatus. However, problems with the absence of confinement and its strong SWRC dependency have slowly gained the unsaturated triaxial apparatus some popularity.

Pressure plate apparatus

The pressure plate apparatus consists of a pressure chamber with a saturated high air entry value (HAEV) porous ceramic disc (Figure 4.21) inside. During testing the sample is placed on top of the HAEV, but the maximum differential pressure or suction that can be applied to the specimens depends on the air entry value (AEV) of the HAEV porous ceramic disc inside the chamber. The AEV is the maximum amount of air pressure that can be applied to the chamber before air entry occurs (when air starts to flow through the HAEV porous ceramic disc). The most common ceramic discs have AEV values of 15 bar or 1500 kPa. Once the chamber is sealed, and while the water pressure (u_w) is maintained at atmospheric value, the air pressure (u_a) is increased beyond atmospheric pressure. When the desired pressure differential (i.e u_a-u_w) has been reached the specimens are left to attain equilibrium. The water expelled from them passes through the HAEV porous disc and flows to an outer burette, which is used to observe the amount of water flowing out of the specimen. Regular readings of the water level in the burette are taken and the vertical position of the burette is adjusted so that the water level remains at the same level as the samples inside the chamber to avoid applying any pore water pressure beyond the atmospheric. Since multiple specimens are tested simultaneously the water flowing out cannot be related back to the water content at a particular value of suction. Instead, at the end of the equilibrium period in each suction stage, the weight of the specimen is monitored and the water content can be computed. The system is assumed to reach equilibrium when the volume of water expelled over a 48h period is less than 1ml, which typically takes 7-10days. This process is repeated, imposing different values of air pressure and hence suction, in many stages as necessary to establish the SWRC. At the end of final stage, the final weight and water content of the specimens are determined.

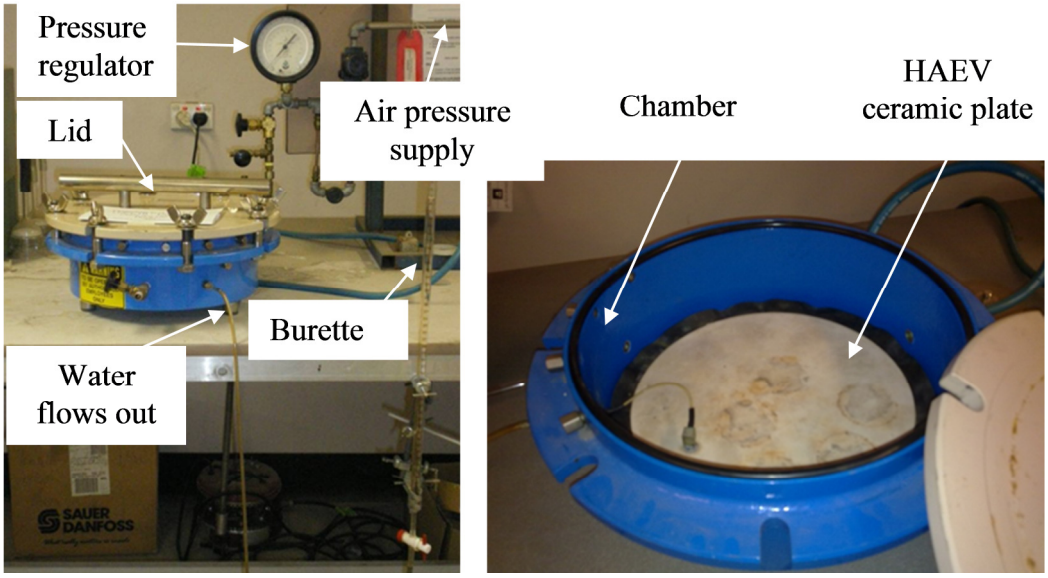

Figure 4.21 Pressure plate apparatus with the lid closed (right) and opened (right).

The tests in this study were conducted using a Soil Moisture Corp. pressure chamber with a ceramic disk with AEV of 15bar. The air supply came from an industrial grade compressed air gas bottle and prior to testing the ceramic disk was saturated by placing it inside the chamber and submerging it in de-aired water. The lid was then fastened and the air pressure was increased until there were no more bubbles of air coming out in the burette. Although ASTM D6836 guidelines are not specific about which size specimen is optimal, Oliveira and Fernando (2006) found that the variations in suction over time are the same for specimens with different volumes and shapes. In this instance, the specimens were 48mm diameter by 20mm (36.19cm^3) high. The samples were compacted and then trimmed to the desirable dimensions using a metallic ring with a sharp bevel. The specimens were saturated using vacuum chamber and then placed inside the chamber. At every stage of suction the weight of the specimen was measured to the nearest 0.01g and then the outside dimensions were measured with callipers with accuracy of 0.01mm. The sample was placed on the plate again and the process was repeated for increasing pressures differentials. The highest suction imposed was 900 kPa and the lowest was 20kPa (value limited by the 10kPa accuracy of the air pressure regulator). At the final stage of suction the sample was dried in an oven to determine the dry mass, after which the water content at different stages was back calculated.

The pressure plate apparatus was used to evaluate the SWRC of five specimens prepared with an equivalent standard compaction level of energy and four different water contents (two specimens each), ranging from the dry to the wet side of OMC. The only

exception was the SWRC represented in Figure 4.23 that belongs to the specimen prepared at a water content of 15.8%. This one was produced by drying in air using the filter paper method rather than the pressure plate apparatus because the specimens were damaged in one of the weigh-ins. The SWRC's (Figure 4.22 and Figure 4.23) were interpolated using the van Genutchen (1980) model extended to accommodate bimodal porosity features and the fitting parameters were found using the least squares method. A summary of the parameters is shown in Table 4.2. Note that the residual degree of saturation values are also represented in Figure 4.22, they were evaluated for the specimens tested for SWRC using the procedure proposed by Miller et al. (2002).

Table 4.2 Summary of the SWCC fitting parameters.

Fitting parameters	Water content , w : %				
	7.21	10.2	12.0	14.2	15.8
α_M	0.07	0.05	0.04	0.05	0.04
m_M	0.13	0.40	0.60	0.60	0.80
n_M	15.00	10.00	3.50	3.50	10.00
α_m	0.0010	0.0009	0.0006	0.0006	0.0012
m_m	0.6	0.7000	0.4	0.4	0.5
n_m	1.2	0.9	1.3	1.3	0.8
$S_{M(ae)}$ (kPa)	1.5	1.5	1.5	1.5	1.5
$S_{m(ae)}$ (kPa)	500	600	700	700	300

Figure 4.22 shows the S_r-s data obtained for all the specimens tested in the pressure plate apparatus. It is interesting to note that the S_r-s points representing the compaction state conditions for all the specimens are deviated slightly from the points defining the SWRC curves, with the exception of specimens prepared at w=14.2%. This is perhaps related to changes in the fabric that soil undergoes when it is first saturated (i.e. wetting), hence the specimen prepared at a higher water content and degree of saturation would be less affected. The results suggest that some of those changes are indeed irrecoverable (see Chapter 2) and hence the points representing the compacted states detach from the main drying curve. The data presented in Figure 4.22 clearly show that the compacted states influence the post compaction hydraulic behaviour of the soil, i.e. specimens compacted at dry of OMC have steeper slopes and air entry values of the macropores ($S_{M(ae)}$) and micropores ($S_{m(ae)}$) located at lower degrees of saturation.

The prime reason for conducting these tests was to evaluate the degree of similarity of the SWRC for different compacted states (i.e. water content). Although there was some degree of similarity yielding almost the same $S_{M(ae)}$ and micropores $S_{m(ae)}$, a strong void ratio and inherent fabric dependency still prevailed and shaped the SWRC response over the mid-suction range. This suggests that without knowing how compaction was carried out in terms of the water content and level of energy applied, evaluating the current condition in terms of the dry unit weight or void ratio of the ground likely to suffer severe changes in the hydraulic regimes caused by climatic fluctuations (i.e. temperature and rainfall) on the basis of its current *Sr-s* conditions, may prove a difficult task.

Unsaturated triaxial apparatus

Much like the pressure plate apparatus, this system consists of imposing a suction by applying a pressure differential to soil specimens and allowing the water to flow in or out. One particular advantage of this system over the pressure plate apparatus is related to the determination of SWRC for a range of loading conditions (confining pressures) and also because it enables the drying and the wetting SWRC branch curves to be determined (Figure 4.24). The motivation for these tests was to gain an insight into the small strain behaviour of specimens subjected to wetting and drying due to climatic conditions.

Particular importance was given to the level of compaction energy, so a series of specimens was prepared with a water content of 12% (equivalent standard energy OMC) with three different energy levels (E = 242.7 kN.m/m^3, E = 529.5 kN.m/m^3 and E = 838.4 kN.m/m^3). The wetting and drying cycles were carried out in the triaxial cell under a confining pressure of 50kPa (equivalent to approximately 2.5m depth). This level of confinement was adopted because it is considered to be a conservative lower bound of the depth where soil is likely to be subjected to wetting and drying cycles from climatic changes considering the recommendation given by distribution of the Thornthwaite moisture index (TMI) (Thornthwaite, 1948) in Australian territories (Austroads, 2004; Fityus and Buzzi, 2008).

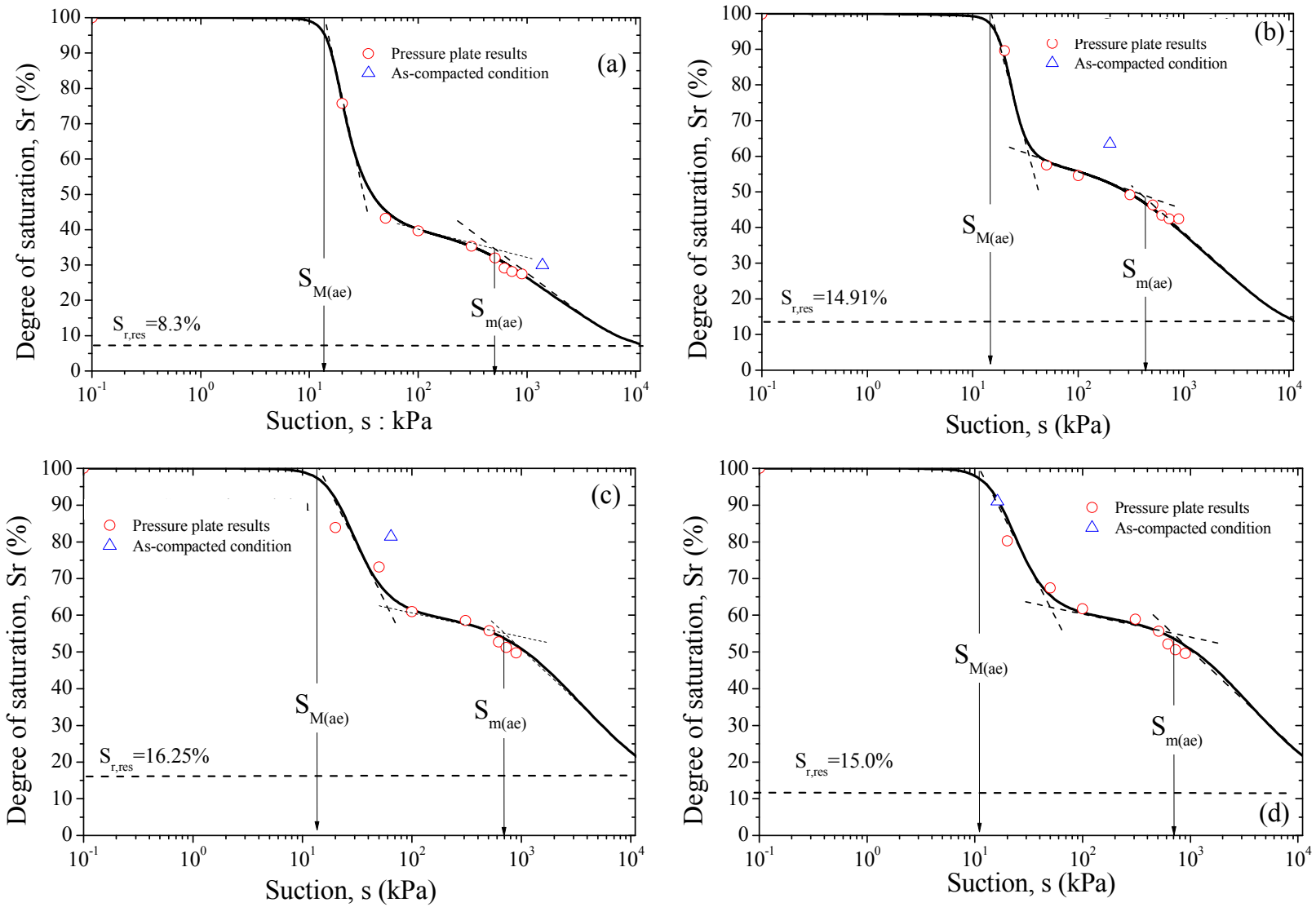

Figure 4.22 SWRC for specimens prepared with an energy level of E = 529.5 kN.m/m^{3}at water content of (a) w=7.21%, (b) w=10.2%, (c) w=12.0% and (d) w=14.2% .

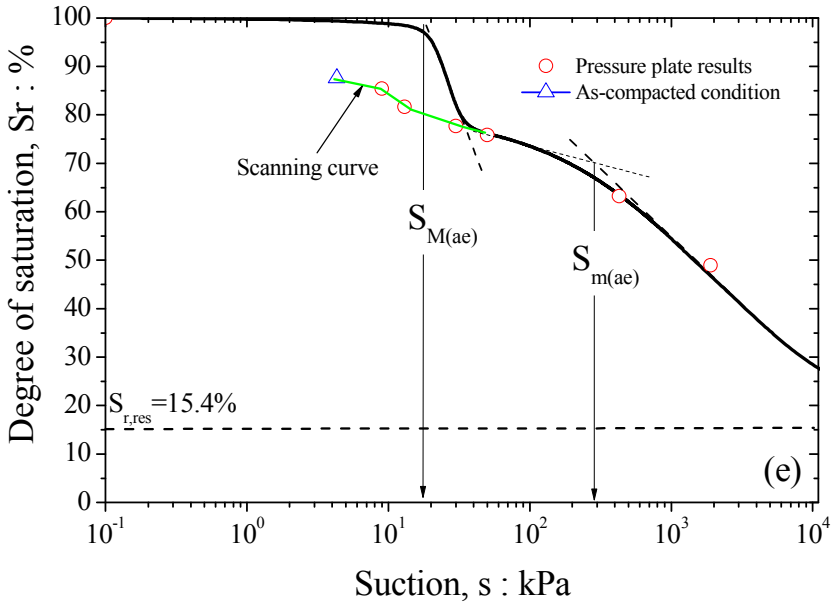

Figure 4.23 SWRC obtained via drying process for a specimen prepared at w=16.3%.

Suction was imposed to the specimens by applying a given air pressure to the top cap of the specimen and a given value of water pressure beneath the HAEV ceramic disk to attain the desired pressure differential. The laboratory air pressure supply (up to 700kPa) was used both for applying air pressure to the top cap and act as confining pressure on the cell. The air pressures applied to the specimen and triaxial cell were controlled with an air pressure controller designed by GDS Instruments (accuracy of $1mm^3$) and the HAEV ceramic disk had an AEV of 15 bar. The water pressure applied beneath the ceramic HAEV disk was controlled by a water pressure controller (GDS instruments, accuracy of $1mm^3$) with a gauge to measure the volume of water flowing in or out of the specimen, as the suction was changed.

The criterion for equilibrium was based on the volumes of water flowing in (wetting) and flowing out (drying), as monitored by the water pressure controller (Figure 4.25). The air pressure was kept constant throughout the test and the desired pressure differential or suction was varied by adjusting the water pressure. In these tests, the increments in each stage were 50kPa and the water pressure was changed at a rate of 0.16kPa/min and kept constant until the end of the equilibration period. Typically, periods of 48h were sufficient for the specimens to reach equilibrium. The axial displacement was also monitored at every stage using an LVDT (Linear Variable Differential Transducer) with an accuracy of 0.001mm. Any changes in the axial strain associated with drying and wetting the specimens were very small, typically less than 0.01%. The change in small strain stiffness was monitored by a pair of bender-extender

elements attached to the bottom pedestal and top cap that enabled both the shear and dilatational waves to be measured (Figure 4.26).

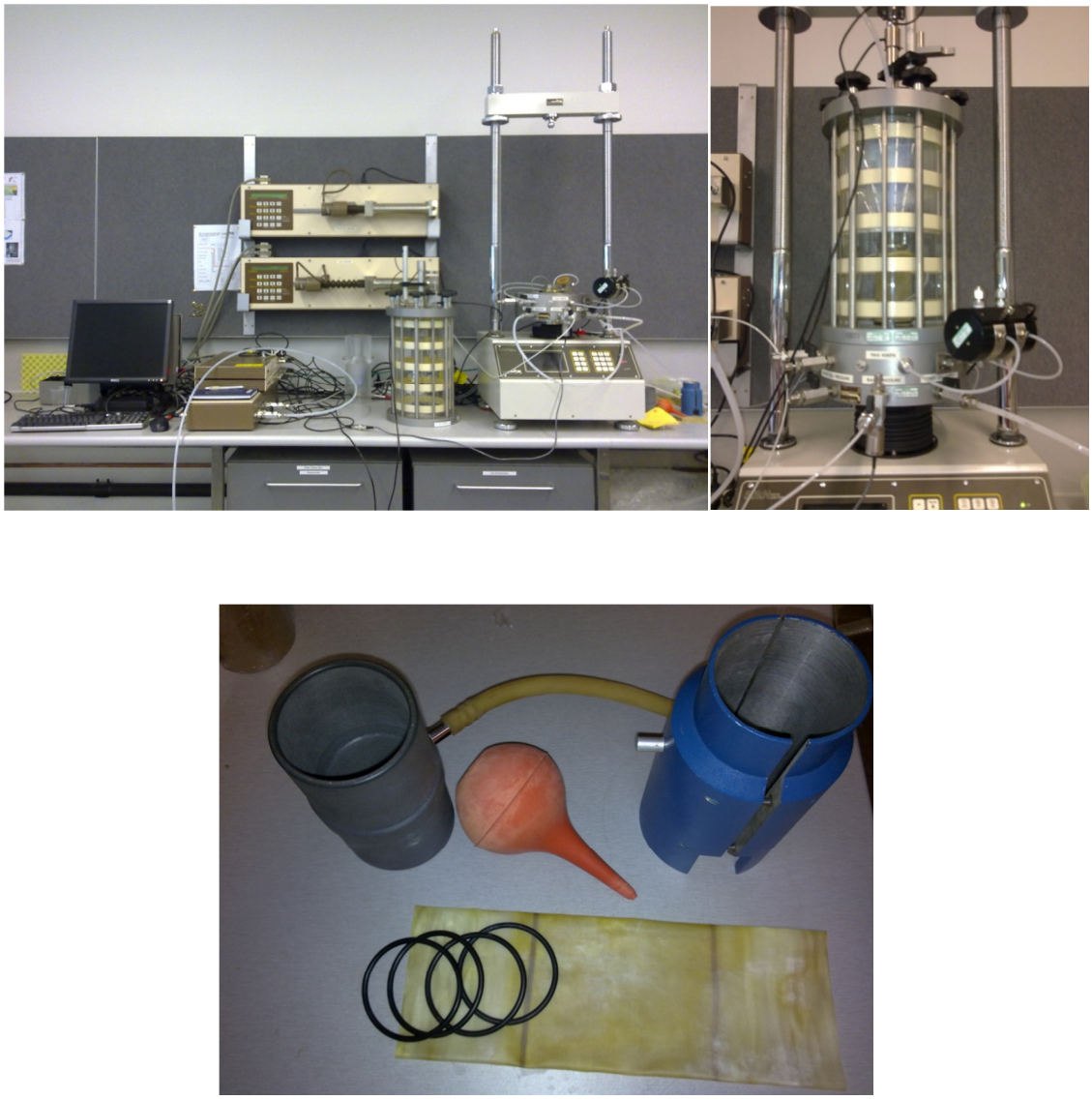

Figure 4.24 Triaxial apparatus for testing unsaturated soil (top) and specimen accessories (bottom).

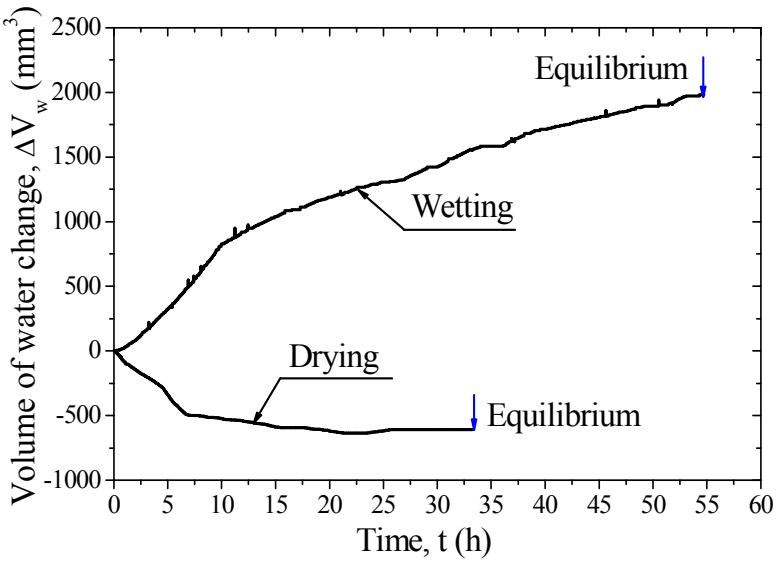

Figure 4.25 Example of a change in the volume of water monitored in the water pressure controller during a drying stage (increment of suction) and a wetting stage (decrement of suction).

As with the pressure plate apparatus, the drying and wetting branches of the SWRC within the range of the suction tested could be determined based of the volume of water change in every step. At the end of the test the moisture content of the specimen was determined by the oven dried method and the differences in the water content monitored by the water pressure controller were verified. The results are shown in the proceeding chapter.

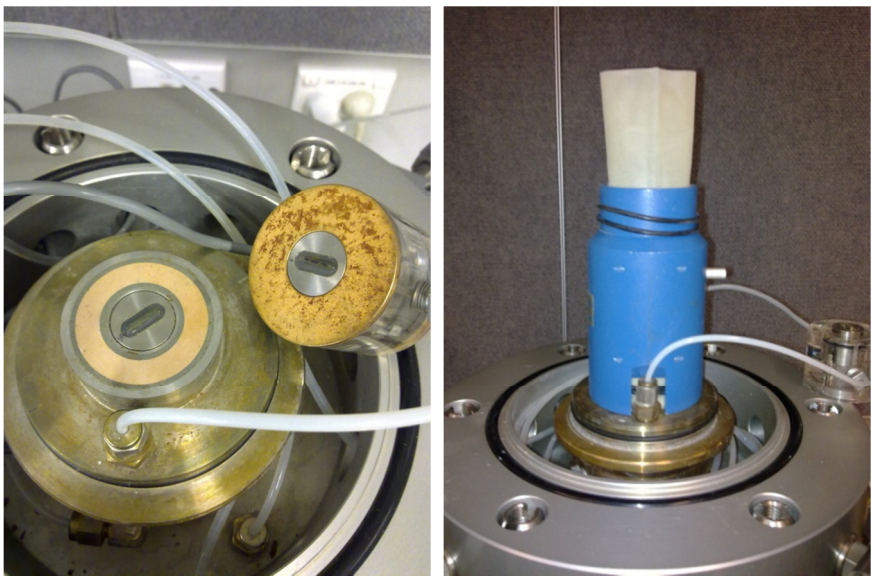

Figure 4.26 Detail of the bender-extender elements cantilevered in the bottom pedestal and top cap, and the specimen being placed for testing.

4.2.3 Constant water content direct shear tests

To establish the mechanical behaviour of the PLDC material a direct shear (DS) testing program was developed and the compacted specimens were tested at constant water content (CW) under unsaturated conditions. A conventional shear box apparatus (AS 1289.6.2.2-1998) with a carriage running on roller bearings and a step motor drive unit capable of applying constant rate horizontal displacements was used. The apparatus was equipped with a load cell to measure the horizontal shear force and two LVDT displacement transducers to measure the horizontal and vertical displacements (accuracy given in Table 4.3). A vertical load was applied with a lever arm loading system with beam ratio of 10:1. Data acquisition was controlled by a LabVIEW program coded "in house" and accompanied with a National Instruments card NI USB-6009 with 8 input channels.

Table 4.3 Accuracy of Transducers

	Unit	Accuracy
5kN load cell	kN	±0.002
Horizontal displacement 25mm LVDT	mm	±0.025
Vertical displacement 10mm LVDT	mm	±0.01

To conduct the tests under CW conditions, an effort was made to prevent any evaporation and ensure undrained conditions as much as possible. This was achieved by running the compression and shearing stage tests in a temperature controlled environment (23 ± 2^{o}C and typically varying less than 1^{o}C during the test), and by enclosing the direct shear box with the assembly in an air tight plastic bag (Figure 4.27 and Figure 4.28). Furthermore, since isolating the air around the sample may not be sufficient, given that pore water can evaporate until the air becomes saturated with water vapour, a 1mm thick film of polyethylene was placed in contact with the specimen and the gaps between the two sliding halves and the bottom half and base were sealed with silicone grease to minimise the volume of air around the specimen (Figure 4.28). Although the proposed system had no independent means of checking whether air tightness was achieved, it shares some similarities with the anti-evaporation system adopted by Caruso and Tarantino (2004) accessed as air tight using a high capacity tensiometer.

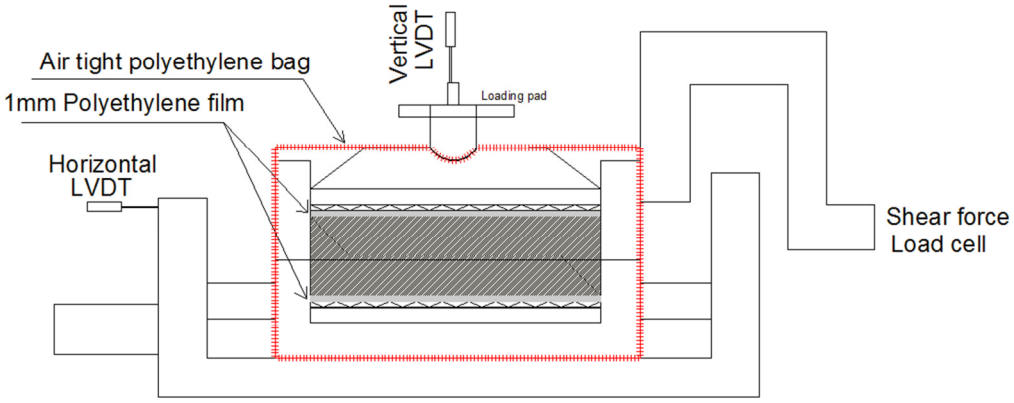

Figure 4.27 Shear box diagram with the system implemented to prevent evaporation.

The procedure used was in accordance with AS 1289.6.2.2 (1998), albeit some small variations. The compacted specimens were extruded into the shear box and then subjected to a compression stage when vertical stresses of 40kPa, 80kPa, and 150kPa were applied and the vertical displacements were monitored. The specimen was kept under compression for overnight periods to ensure that all instantaneous compression occurred before shearing at a constant rate of displacement. At the end of the tests, the specimen was removed to determine its water content and suction using the filter paper method. The displacement rate selected was 0.01mm/min. While a smaller displacement rate may be preferable, the time and expense may render them impractical.

Figure 4.28 Shear box apparatus with the system implemented to prevent evaporation.

To determine the optimum shear rate, various displacement rates were tested using identical specimens to understand what would be the minimum shearing rate that could be used in order to obtain equivalent shear strength behaviour and volumetric changes. The shear

strength and vertical displacement results obtained for displacement rates varying from 1.25 to 0.001mm/min are shown in Figure 4.29. The most striking aspect is that the shear strength seems to be not particularly sensitive to the varying displacement rates, while the vertical displacement shows large differences. This observation is consistent with the study conducted by Ong (1999) cited in Thu et al. (2006). Although the stress–strain curves were found to coincide, the suction at failure increased about 2% when strain rate increased from 0.009 to 0.018 mm/ min and about 10% when strain rate increased from 0.018 to 0.081 mm/ min.

Because suction was not measured, a rationale associated with the hydraulic behaviour regulation caused by volumetric changes in the vicinity of the shear plane is considered to interpret the results of Figure 4.29. In a direct shear test, the shear zone is localised and thin compared to the mass of the specimen (Shibuya et al. 1997). If larger displacement rates are adopted, water content is likely to be uniform in the specimen because the shearing time is small and impedes the water movement. However, volume changes occurring during shearing are likely causing different suctions to occur in the shear band and in the remainder of the specimen because not enough time is allowed for equilibration. Furthermore, if dilation in the shear band occurs, the soil is experiencing a shearing induced drying, which means degree of saturation is decreasing and suction is likely increasing. Thus, higher strength is to be expected (compare the series representing displacement rates of 1.25mm/min and 0.1mm/min). For smaller displacement rates, suction is likely to be constant throughout the specimen due to self-equilibration but water content is likely different across the specimen because the shearing takes place over longer periods of time and water is likely moving in or out of the shear band for shearing in dilation or contraction, respectively. Note that, water is not allowed to flow out and evaporation is minimised, therefore, on average water content would the same during shearing. Worth noticing that series corresponding to displacement rates of 0.01mm/min and 0.001mm/min show some discrepancies in the shear strength in the large displacement range (Figure 4.29). Although a larger strength is obtained for the lowest displacement rate, it is associated with the largest dilation. This discrepancy may be associated with some dissimilarity in the soil fabric. Nevertheless, the shear strength and volumetric behaviour is comparable and thus seems reasonable to assume that a displacement rate of 0.01mm/min may be enough to reproduce the shear strength and volumetric behaviour of those sheared at a 10 times slower rate of 0.001mm/min .

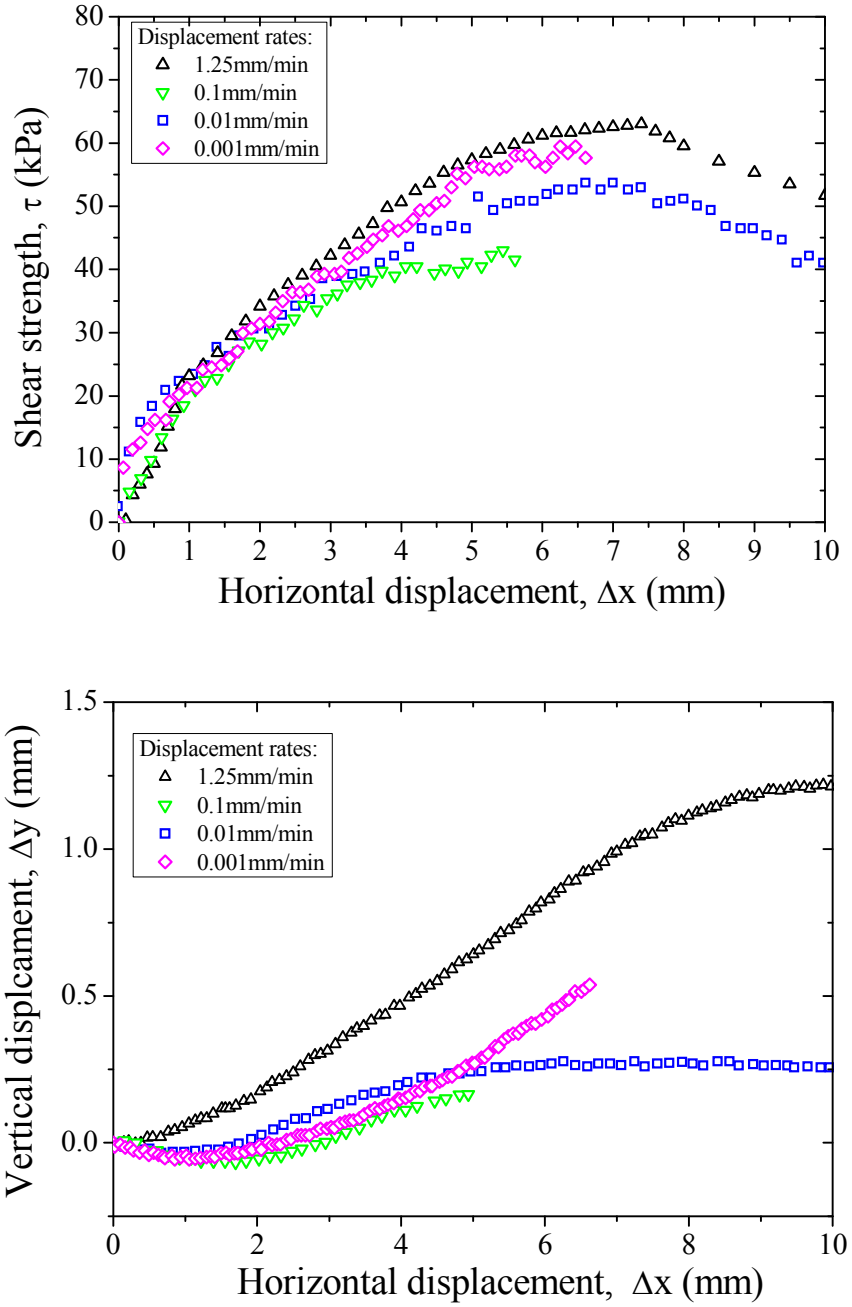

Figure 4.29 Shear test results conducted for the selection of an adequate rate of displacement in terms of (a) shear strength and (b) vertical displacements at a applied vertical stress of 38.5kPa.

An additional test series was conducted under saturated conditions to enable the friction and cohesion parameters under saturated conditions to be determined. The compacted specimens were extruded into the shear box and then flooded with water until they were saturated. After saturation the specimens were allowed to consolidate under three different normal stresses of 40kPa, 80kPa, and 150kPa. Subsequently, the specimens were sheared at a constant displacement rate of 0.01mm/min until reaching peak and residual shear strength.

Although the suction was not measured during the test, it was measured at the initial and final stages, and it was found there was no significant variation (typically <5kPa and <1kPa for specimens prepared at dry and wet of OMC, respectively). Similar findings were obtained for suction controlled constant water content direct shear (CWDS) tests conducted on a speswhite kaolin (Tarantino and Tombolato, 2005). Nevertheless, the suction evaluated during a CWDST was formulated in terms of the development of pore water pressure associated with volumetric changes in undrained direct shear tests, and is given in Chapter 7.

4.2.3.1 Direct shear measurement repeatability

The shear strength behaviour measured by direct shear tests was checked for repeatability. Figure 4.30 represents 6 replicated direct shear results measured in specimens compacted identically, at approximately the same water contents and compaction energy of 529kJ/m^3 (standard Proctor equivalent). Although the obtained shear strength behaviour was not exactly identical in the specimens (attributed to some dissimilarity in the soil fabric), the peak and ultimate states as well as volumetric changes are very comparable.

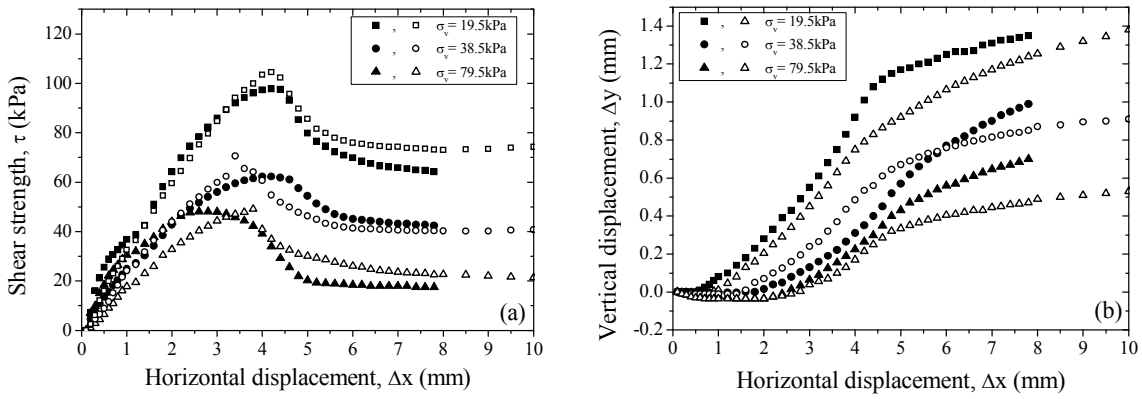

Figure 4.30 Shear tests on specimens prepared at approximately the same water content and energy level (*w=12.8~13%*, E= 596 kJ/m^3) for an applied vertical stress of 19.5kPa, 38.5kPa and 79.5kpa in terms of (a) shear stress and (b) vertical displacement.

4.2.4 X-ray CT scan

CT scanning systems use X-rays to visualise thin, cross sections of the compacted specimens in this work. During this process the X-rays generated from a source located at one side of the gantry, are attenuated through the subject and then captured by a series of detectors placed in the opposite direction. The X-ray source and detectors move in synchrony around the subject

to ensure that every angle of measurement is covered (Figure 4.31). As the X-rays penetrate through the test specimen, some of them are absorbed. The different rates of absorption reflect changes in the density of the specimen (Alshibli et al., 2006).

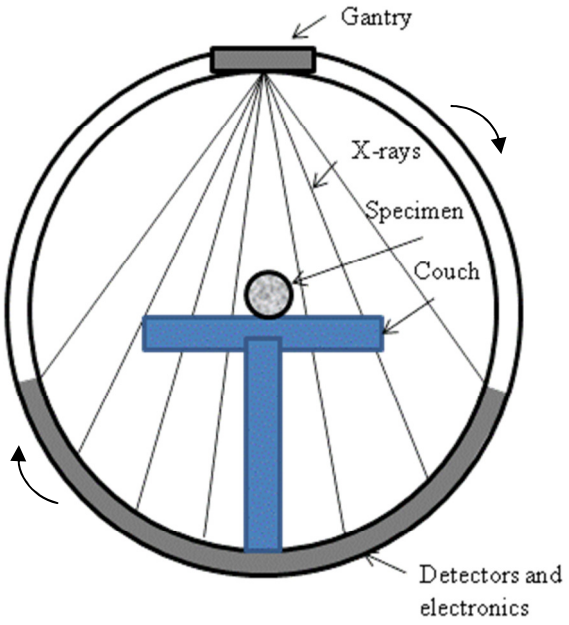

Figure 4.31. Illustration of the fan beam geometry utilised by the CT scanner Toshiba Asteion S4.

A CT scanner computes the linear attenuation coefficient μ, between the X-ray source and the detectors. Attenuation is a measure of the proportion of X-rays absorbed within the scanned material and is linearly related to the bulk density of the subject when hard X-rays (100 kV) are used (Kalender, 2005). Any μ value can be normalised with respect to water and air, and is then designated with a CT number (CTN) which is measured in the dimensionless Hounsfield unit (HU):

$$CTN\left(HU\right)=\left[\frac{\left(\mu_{material}-\mu_{water}\right)}{\left(\mu_{water}\right)}\right]*k \qquad (4.13)$$

where k is a constant that is usually equal to 1000 (Kalender, 2005). There is a direct relationship between each shade of grey in the CT images and CTN, which can be related to the density of the material. The advantage of using CT scanning technology to characterise compacted soil is that images can be obtained without disturbing the samples, so specimens can be tested in an as compacted state, unlike SEM (Scanning electron microscopy) or MIP

(Mercury intrusion porosimeter) although the resolution and ability to image very fine details (i.e. <200μm) is lower than the two latter ones.

The tests were carried out on an X-ray CT scanner, model Toshiba Asteion S4 (Toshiba Corp., 1994) located at the CT Scanning Laboratory at the Centre for Geotechnical and Railway Research (University of Wollongong). The CT scanner (Figure 4.32) was formerly used for medical purposes and can be classified within the medical CT-scanners as a high resolution type (Ketcham and Carlson, 2001) with a resolution of 18 lp/cm at 0% of MTF (modulation transfer function) which is equivalent to 0.2mm (ToshibaFC40). The compacted specimens were wrapped in cling wrap to minimise any loss of moisture during testing. They were then placed in the CT-scan couch and the first test was conducted to evaluate the optimum scanning parameters and the best reconstructive function (different reconstructive functions are related to different parts of the human body). The reconstructive function used to determine the distribution of CTN of the imagined samples was the function originally designed for CT scanning of the head (i.e. ToshibaFC40). This reconstructive function possesses beam hardening that corrects the image artefacts which could result from the absence of lower energy x-rays. For this study the scanning parameters were set at 135kV X-ray tube voltage and 200mA for the X-ray tube current. The X-ray beam was 3mm wide (i.e. slice thickness), the exposure time was 1second, and the field of view (FOV) was 21cm with with a zooming factor of four. Although high energy X-rays (≥150kV) penetrate the objects more effectively than lower energy X-rays, the latter shows any changes in density more distinctively (Ketcham and Carlson, 2001).

4.2.4.1 Some aspects related to CT scan testing

Although the output of CT scans is visual and the interpretation relatively straightforward, slight difficulties can occur during scanning that may render the data more problematic for quantitative use. Difficulties related to scanning artefacts that can obscure details of interest, or cause the CT value of a single material to change in different parts of an image are the most common problems (Ketcham and Carlson, 2001). The two scanning artefacts that are frequently encountered while testing are beam hardening and the ring artefacts.

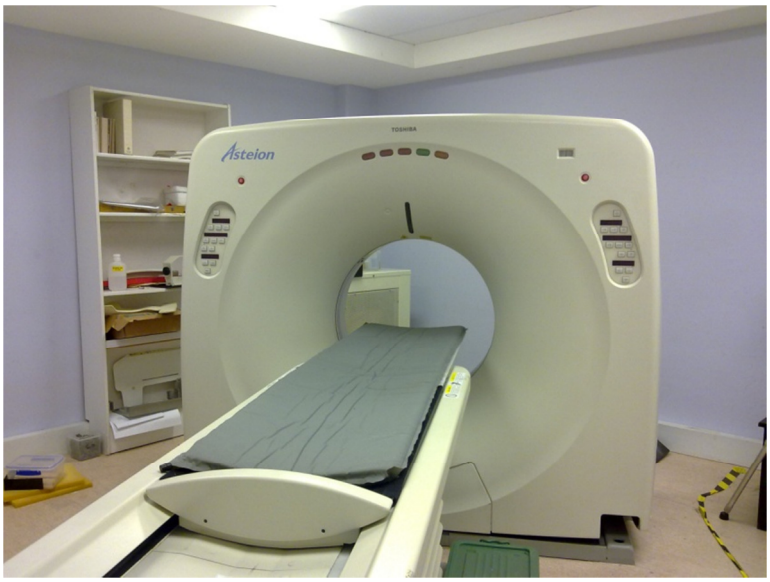

Figure 4.32. CT scanner Toshiba Asteion S4 located at the CT Scanning Laboratory.

Beam hardening causes the edges of an object to appear brighter than the centre, even if the material is the same throughout. This artefact is mainly associated with the "hardening" of the X-ray beam as it passes through the scanned object. The use of a high enough X-ray energy and small samples seems to favour scanning with no beam hardening effect present. However, there are some materials, including soil, that attenuate the X-rays, so beam hardening may be noticeable. Furthermore, the use of higher energy beams to detect attenuation contrasts in materials (i.e. differences in density) is problematic.

Ring artefacts appear as full circles centred on the rotational axis in the scanned images (Figure 4.33). They are caused by shifts in output from detectors, which are the source of the anomalous values in corresponding ray or rays in each view; the position of a ring corresponds to the area of greatest overlap of these rays during reconstruction (Ketcham and Carlson, 2001). The main cause is perhaps related to the detectors responding differently to changes in scanning conditions. These two artefacts are linked with one another and its relative importance in the scanned images should be explored at the scanning stage, rather than trying to remediate the quality of the images via post processing.

The experience of this study showed that while scanning using a wide range of combinations of both X-ray voltage and amplitude, ring artefacts and beam hardening can be

substantially reduced when higher intensities are used in combination with voltages that are high enough. For instance, a specimen compacted at a water content of 0.105 and an energy level of 529kJ/m^3 was imaged at seven different pairs of voltage and intensity values (Table 4.4). The respective raw scanned images resulting from the change in the scanning conditions summarised in Table 4.4, is shown in Figure 4.34. An inspection of Figure 4.34 suggests that the pairs 1, 5, and 6 of the scanning conditions favour an imagining of the details of interest in the specimen. On this basis pair no.1 was adopted for all subsequent CT scan testing.

Table 4.4 Pairs of voltage and intensity utilised to image a compacted specimen.

Pair	Voltage, KV	Intensity, Ma
1	135	200
2	135	150
3	135	100
4	135	50
5	120	200
6	100	200
7	80	300

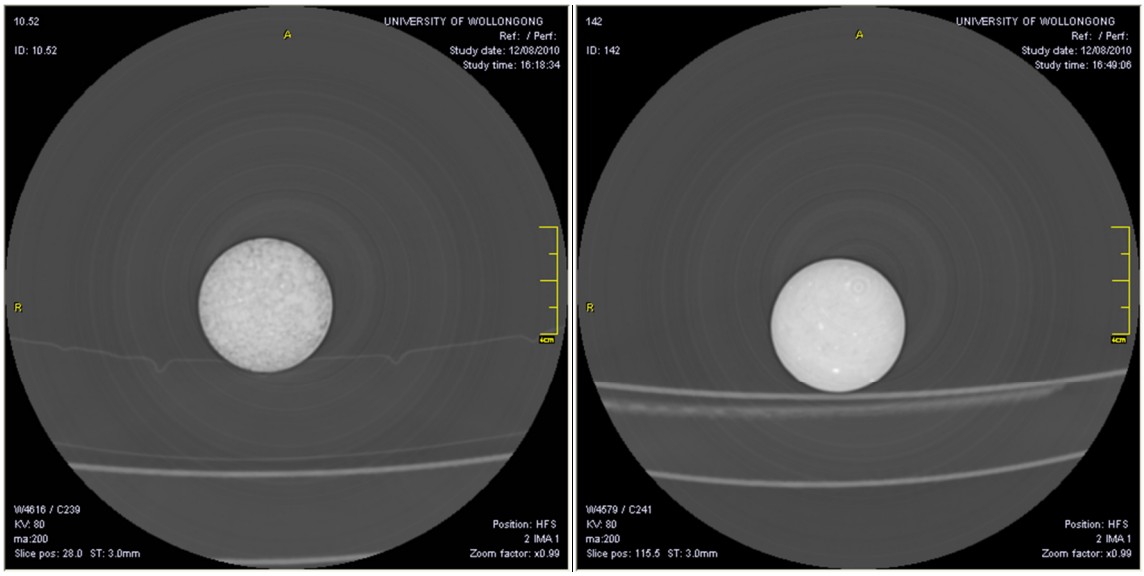

Figure 4.33 CT images of two specimens compacted at water content of 0.105 (left) and 0.142 (right) (E=529kJ/m^3) with ring artifacts and slight beam hardening.

4.2.4.2 Some aspects related with post processing CT scan images

The CT-scan images were analysed using medical radiology software DicomWorks v. 1.3.5. (Puech et al., 2007), including post process filtering (i.e. sharpness and inversion filters).

Window range

The CT values that range from -1024Hu to +3071Hu, that is 4096 grey levels, cannot be viewed on a single view (Kalender, 2005). For that purpose the complete grey scale is usually assigned a given interval of interest or window. Grey levels above the window are displayed in white whereas values below are displayed in black. The selection of an adequate window range is fundamental for isolating particular aspects the object imaged, particularly the width and centre of the window. The centre (C) represents the mean CT value of the interesting structures, while the window width (W) determines the contrast in which the image is viewed. Narrow windows are better for displaying small differences in attenuation whereas wider windows are better for large differences. The choice of C and W depends largely on the range of densities that the object is expected to exhibit. For instance, if we consider the reference CT values of water (0Hu) and air (-1000Hu), the optimal values of the window can be selected by comparing the expected density values with water and air. Figure 4.35 shows the effect of the centre of the window (C) and the width (W) on the images obtained for a specimen compacted at a water content of 0.125 and an energy level of 242.7kJ/m^3.

It is interesting to note that unlike medical applications where the windows vary roughly between -1000Hu and 1000Hu (see Kalender, 2005), the specimen benefits from higher CT values, i.e. compare the image of C150W2500 and C1000W2500. Given that the material is composed of sand and silt, it is expected that a larger viewing range would favour a global observation of the specimens. Indeed, narrow windows such as C500W500 and C1500W500 show less detail, and in fact some of the areas in the latter window appear dark, which indicates that the overall density in those locations is lower than the bottom limit of 1250Hu. Using common image processing threshold techniques may be a useful way of locating those areas where the density is higher; if a more quantitative analysis is of interest. In this study a C1000W2000 window was used to view all the images. The reason for selecting these values is because their upper limit of 2000Hu and bottom limit of 0Hu means that the pores, whether occupied by air and water, are viewed in black and can easily be individualised. This way, given the resolution of the scanner, the soil structure of the specimens can be evaluated in terms of macro-porosity (inter-aggregate pores), by examining differences in the grey scale colour of the images.

Filter enhancement

A CT scan is composed of small volume elements or voxels. Each voxel is assigned a CT value and in a way the image can be viewed as a *m* by *n* matrix of the CT values. Filters consist of applying mathematical operations conducted over the voxel matrix of CT values to enhance specific features on the images. Although the filters are a convenient and powerful tool for processing images, some care is required if the density of the object is to be characterised in quantitative terms. This is because filters alter the original CT values and as a result, the perceived changes in density may not represent the real density. There are a number of different filters that can be used, most of which already have inbuilt functions in common image analysis software, e.g., the Matlab image processing toolbox. In this study two types of filters were utilised in post processing the inverse and sharp filters from the scanned images. The inverse filter simply inverses the CT values of an image (Figure 4.36), and the sharp filter enhances the images and reduces the blurring that results from applying zoom factors to the images. The white areas correspond to air filled and water filled pores whereas grey and dark areas correspond to aggregations and sand particles, respectively.

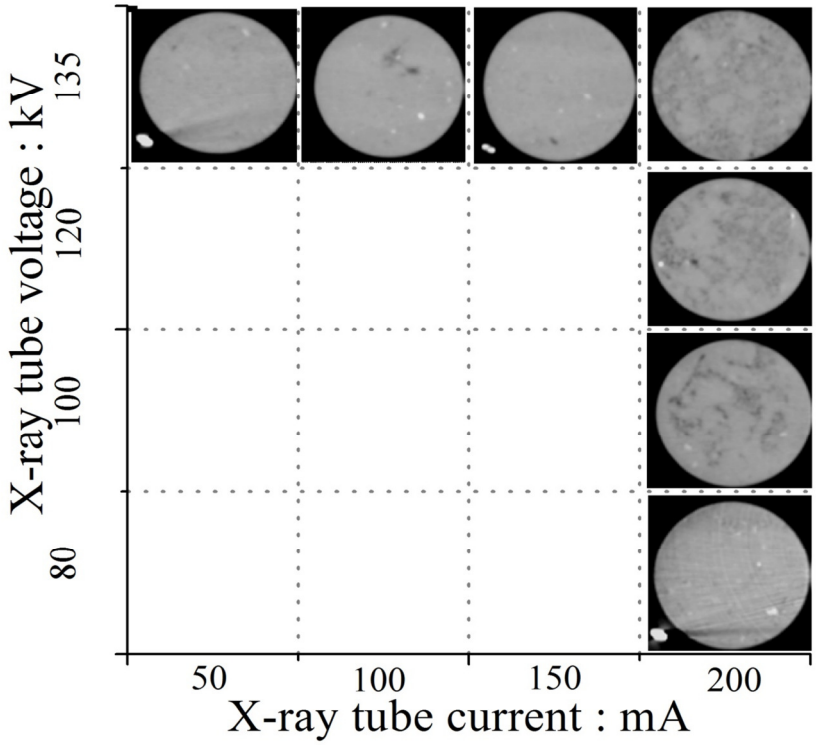

Figure 4.34. Pairs of voltage and intensity utilised to image a specimen compacted at a water content of 0.125 and an energy level of 242.7kJ/m^3 (specimen is 50mm in diameter).

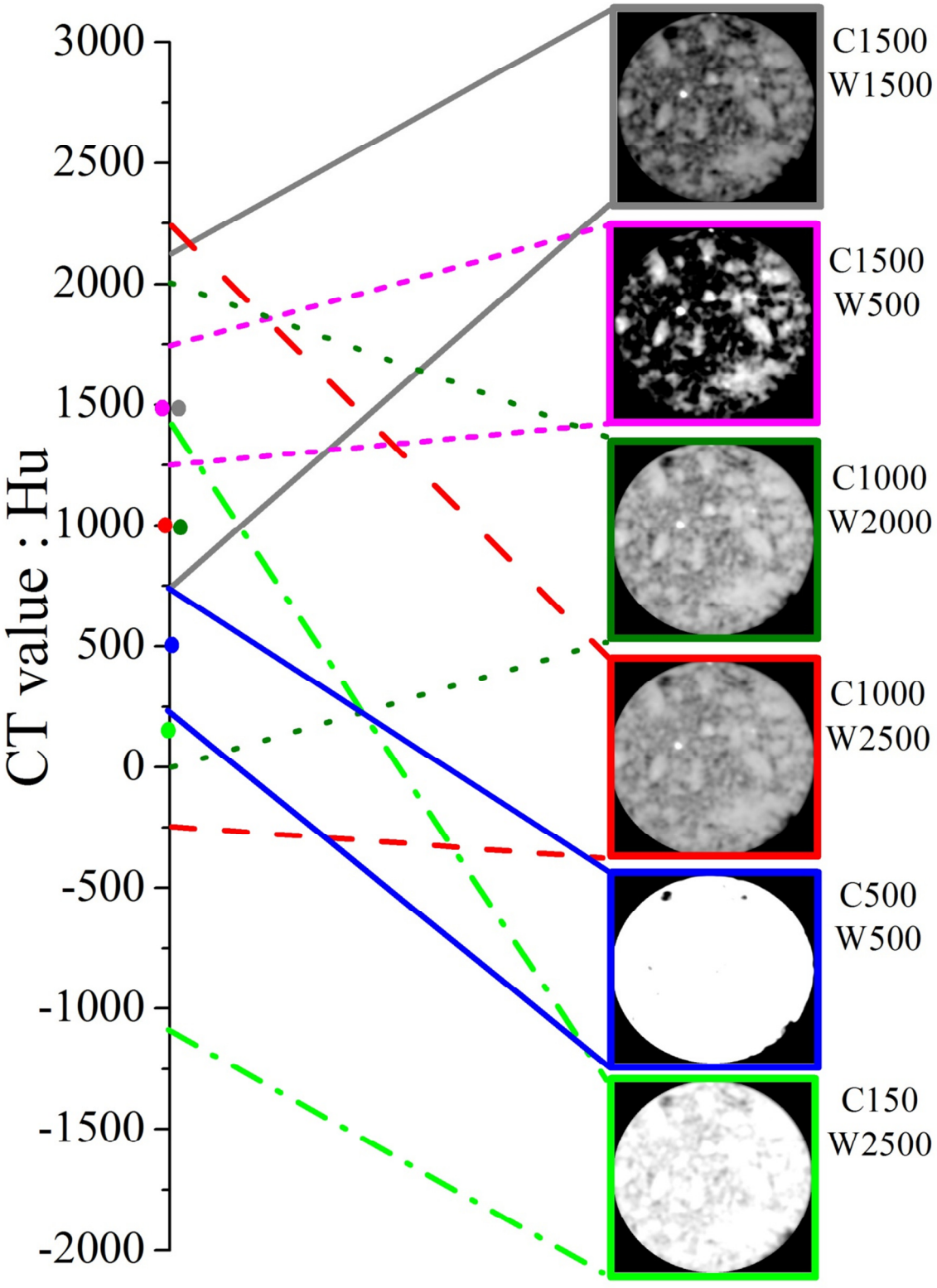

Figure 4.35 Influence of the centre of the selected window (full circles) and the width (represented by the lines) in the CT images of a specimen compacted at a water content of 0.125 and an energy level of 242.7kJ/m^3.

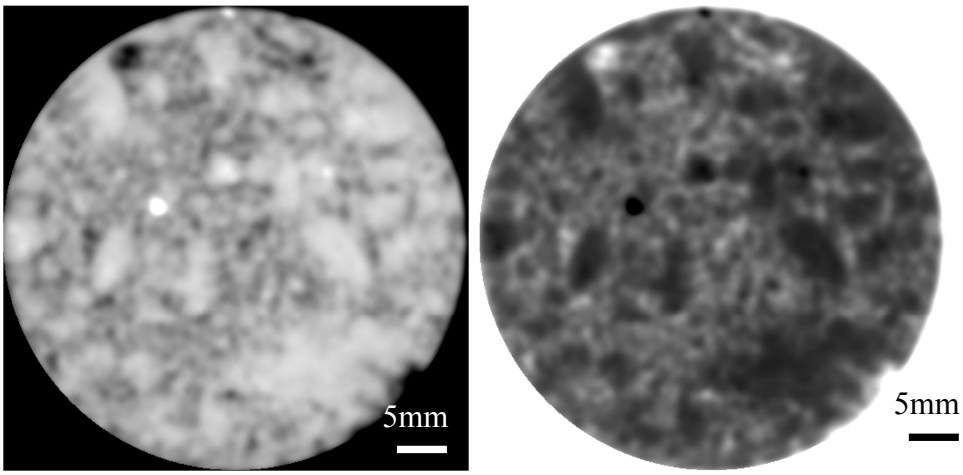

Figure 4.36 Original and post-processed with an inverse filter images on a specimen compacted at a water content of 0.125 and an energy level of 242.7kJ/m^3

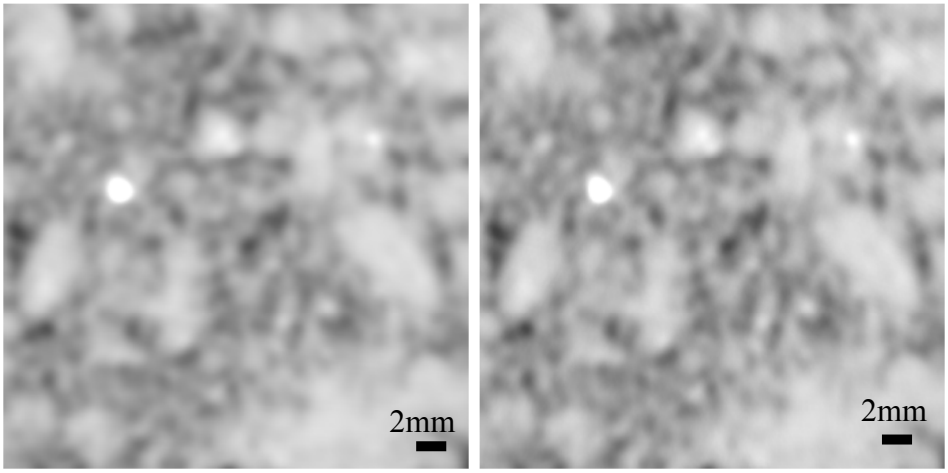

Figure 4.37 Original and post processed with sharp filter images on a specimen compacted at a water content of 0.125 and an energy level of 242.7kJ/m^3, and a zoom factor of 1.5 times.

Binary images

For clarity, the images were further post-processed using segmentation functions in Matlab that allowed for the pores to be individualised in the images. The image processing by segmentation is based on the analysis of grey values in the image pixels. The grey values of each image are best represented by the histogram of grey values (Figure 4.38). While the histogram exhibits a predominantly unimodal distribution, there is a small peak closer to 50 grey level. The first peak corresponds to the voids and the second major one to the soil matrix

within the aggregates. To individualise the pores, the image was segmented and this has been done by finding the minimum point between two peaks in the histogram, also represented in Figure 4.38. This point was selected as the threshold and the pixels to the right side of this limit have been identified as the soil. The spatial resolution of the images (200 μm) does not allow the detection of micropores in the images; therefore, the segmented image contains both solid particles and intra-aggregate pores represented in white (Figure 4.40).

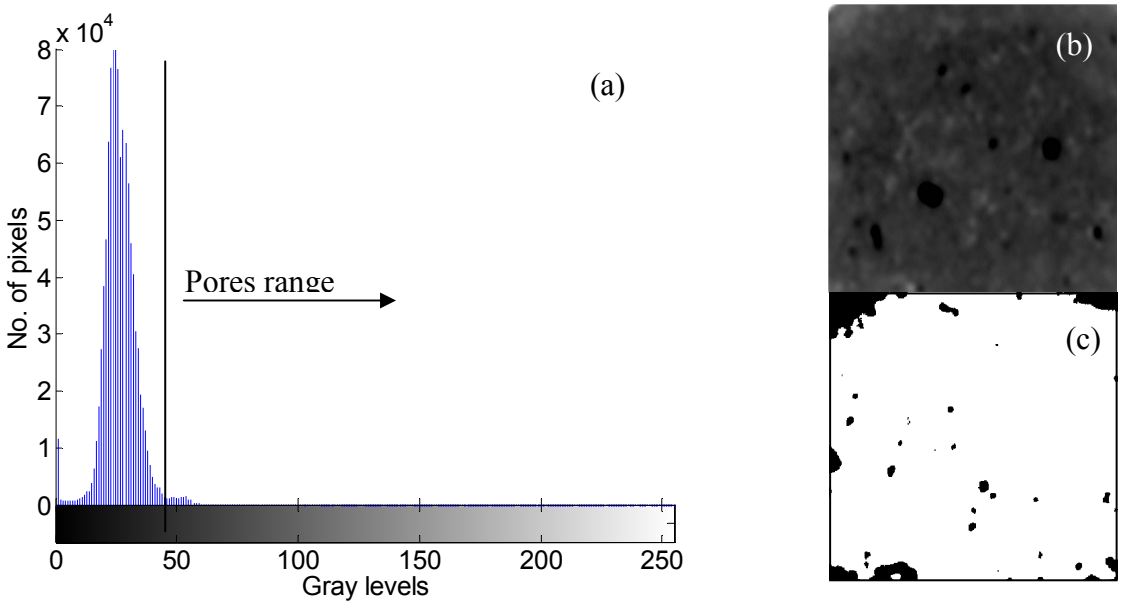

Figure 4.38 Segmentation post-processing, (a) histogram and (b) original image and (c) binary equivalent.

4.2.4.3 CT images in compacted specimens

A total of 6 compacted specimens were tested using the CT scanner. The specimens were prepared so that a range of different compaction states could be attained in terms of water content and energy levels. To investigate the influence of energy level on the compacted soil macrostructure, four specimens were prepared at a water content of 0.125 for different compaction energy levels, namely E_1 = 154.5kN.m/m^3, E_2 = 242.7kN.m/m^3, E_3 = 529.5kN.m/m^3 (standard Proctor equivalent) and E_4 = 838.4kN.m/m^3. To investigate the effect of the water content, two additional specimens were prepared at an energy level of E_1 = 154.5 kN.m/m^3 and a water content of 0.135 and 0.155. The CT scan images and the correspondent binary equivalents of these specimens are shown in Figure 4.39 and 4.40. The change in the structure of the soil was evaluated in terms of its macroporosity (inter-aggregate pores) since the resolution scale of the CT images only enables macroporosity size range features to be

identified. In Figure 4.39 the white areas represent air filled and water filled pores, whereas the grey and dark areas correspond to aggregations and sand particles, respectively.

The reason why evaluating the structure of the soil based on macroporosity is appropriate, relates to the fact that soil produced during compaction is composed of aggregations and is characterised by a bimodal distribution of pore volumes that indicates the existence of macro and microporosity (see Figure 4.22). The total porosity is the result of the sum of the respective terms of macroporosity, corresponding to the pores between the aggregates (inter-aggregate) and microporosity, corresponding to the pores within the aggregates (intra-aggregates). Moreover, in aggregated soils the macropores are retained by the aggregated structure and the aggregates themselves are formed as a result of inter-particle bonding. Due to this interaction between the fabric of the soil and inter-particle bonding (two components of soil structure), the current macroporosity of the sample may be considered as a representative measure of the structure of the soil.

The changes in structure derived from compacting the soil as the moisture content is increased, are shown in Figure 4.39 (a), (e), and (f). The specimens compacted on the dry side of OMC exhibit a soil structure dominated by a large amount of macropores (i.e. the whiter areas). The macropores are moderately lost with an increasing moisture content with the specimen compacted to 0.135 water content in Figure 4.39(e) showing less amount of macropores and they seem to be nearly absent in the specimen compacted to 0.155 water content (wet side of OMC) shown in Figure 4.39 (f). At this point the macrostructure of the soil resembles a matrix where the grains of sand are easily individualised. These results are consistent with the experimental evidence of MIP and SEM testing of silt specimens compacted at dry, OMC, and wet of optimum, as provide by Delage (1996).

The results of four samples compacted to the same moisture content ($w \approx 0.125$) and four different compaction energies are also shown in Figure 4.39(a) - (d). The images confirm that the specimens compacted with a higher compaction effort show fewer macropores. Thus the soil starts with a structure dominated by aggregations with a larger amount of macropores and during compaction at constant water content, as the degree of saturation increases, encompassed by an increase in the dry unit weight, the water available in the pores increases. This process seems to change the soil into a more matrix dominated structure.

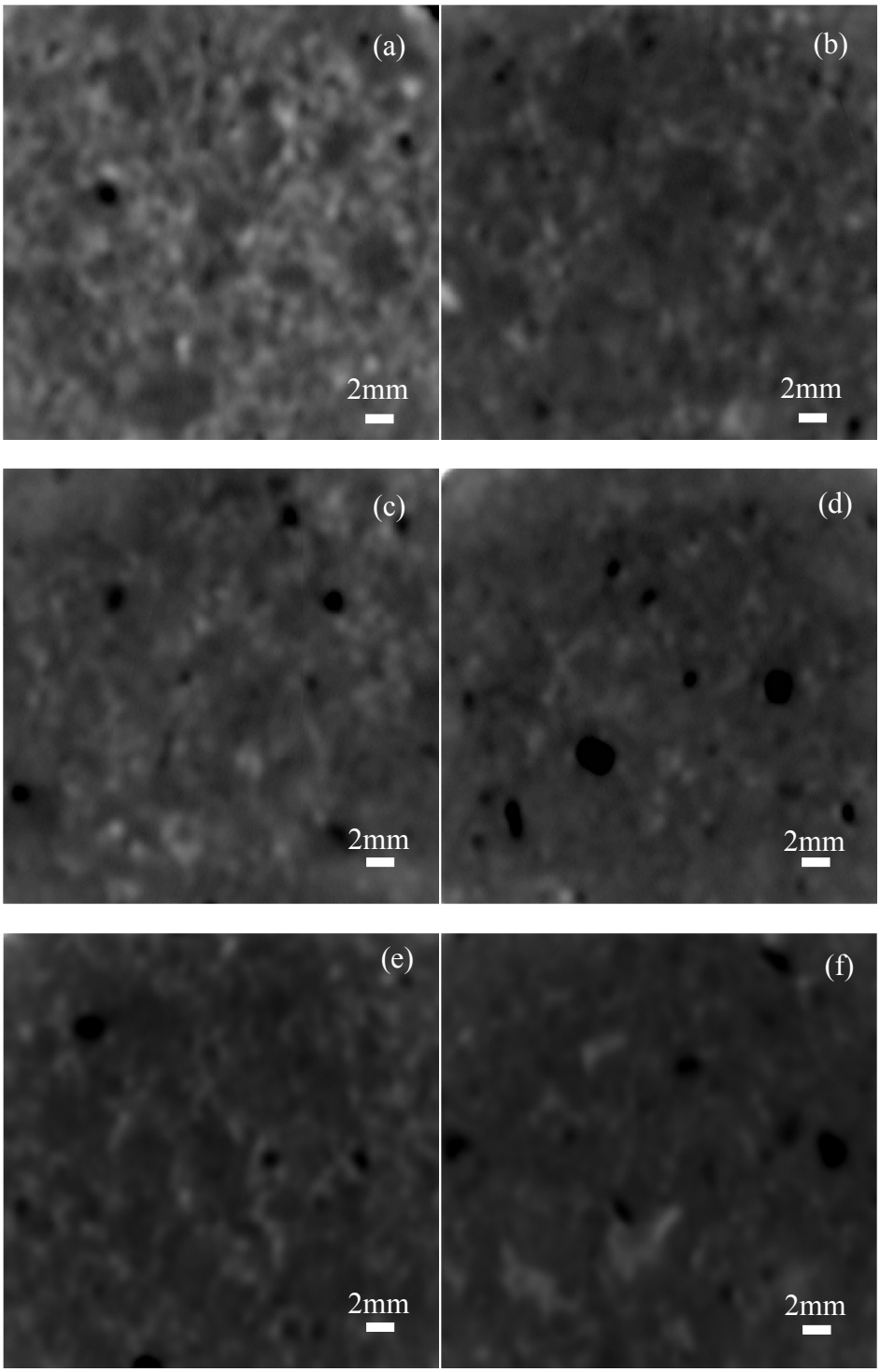

Figure 4.39 Post processed CT scan images of specimens compacted at (a) 0.125 at E_1 = 154.5 kN.m/m^3, (b) 0.125 at E_2 = 242.7 kN.m/m^3, (c) 0.125 at E_3 = 529.5 kN.m/m^3, (d) 0.125 at E_4 = 838.4 kN.m/m^3, (e) 0.135 at E_1 = 154.5 kN.m/m^3 and (f) 0.155 at E_1 = 154.5 kN.m/m^3.

This is particularly evident in Figure 4.39 and 4.40 (a) and (c) which correspond to those specimens compacted at E=154.5 kN.m/m^3 and 529.5 kN.m/m^3, respectively. The differences obtained by those specimens compacted at E=838.4 kJ.m/m^3 were comparatively

smaller because at this point the soil had reached the wet side and increasing the compaction effort did not yield any substantial variation in the dry unit weight.

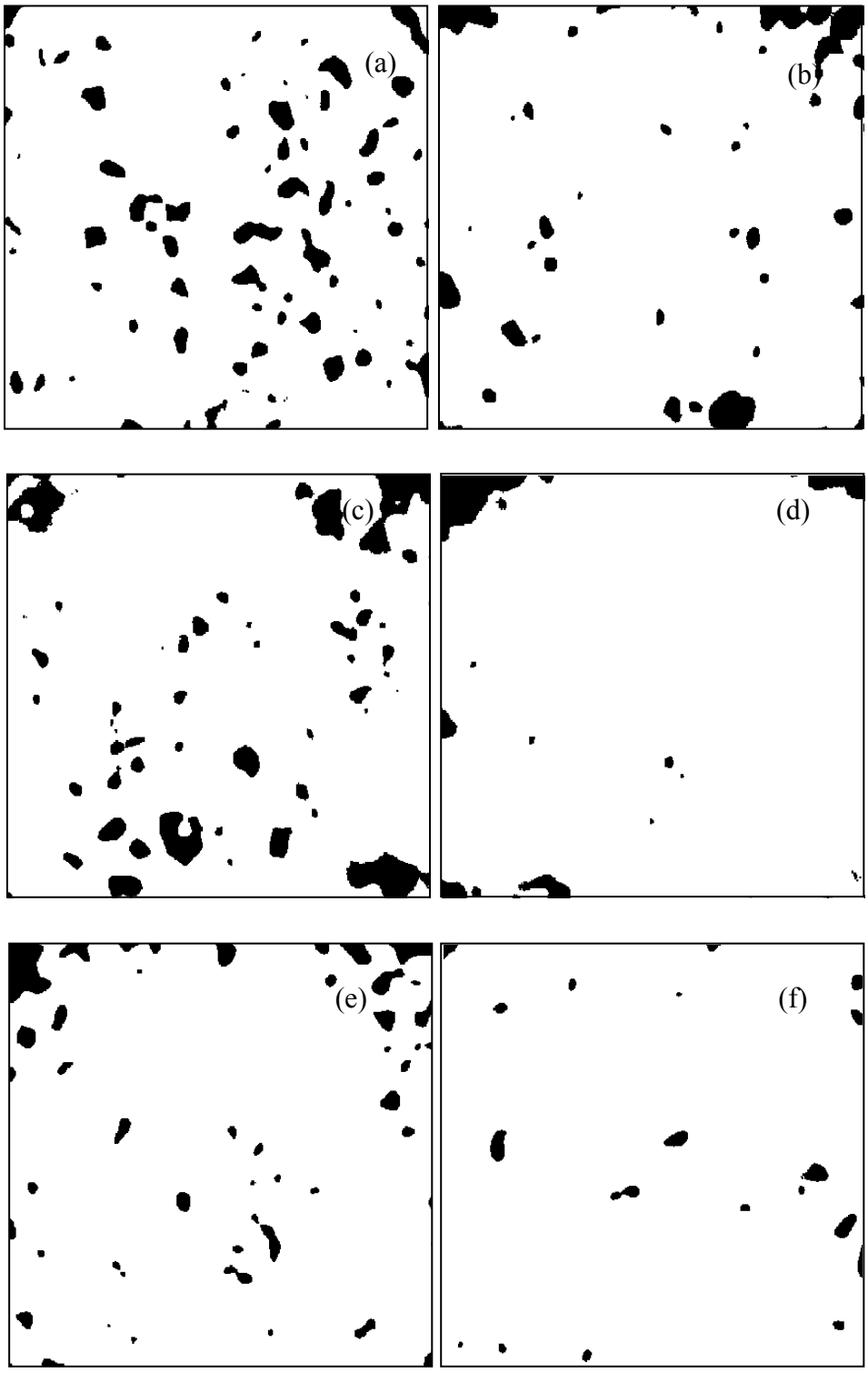

Figure 4.40 Binary post-processed CT scan images of specimens compacted at (a) 0.125 at E_1 = 154.5 kN.m/m^3, (b) 0.125 at E_2 = 242.7 kN.m/m^3, (c) 0.125 at E_3 = 529.5 kN.m/m^3, (d) 0.125 at E_4 = 838.4 kN.m/m^3, (e) 0.135 at E_1 = 154.5 kN.m/m^3 and (f) 0.155 at E_1 = 154.5 kN.m/m^3

Hence, it is likely that the soil is being sheared at nearly a constant volume, which could explain the resemblance in the macrostructure. These results were consistent with the MIP tests conducted by Tarantino and De Col, 2008 on statically compacted kaolin. Larger forming pressures only seemed to affect the macroporosity range, that is, the porosity of the inter-aggregates was reduced while the intra-aggregate porosity did not seem to be affected.

4.3 PREPARING THE SPECIMENS

Before compaction, the soil was dried in air for several days and subsequently disaggregated with a mortar and pestle to meet a nominal size of 2mm. Any larger particles were discarded as their respective percentage in weight was not significant. The required amount of water was sprayed onto the soil and then mixed together with a masonry trowel. Any moist lumps were disaggregated before placing the mixture in a plastic bag, which was kept overnight under controlled temperature and humidity for moisture equilibration. All the specimens were dynamically compacted. A series of compacted specimens were prepared by using a standard Proctor mould for different levels of energy, to evaluate the compaction characteristics of the PLDC soil (see chapter 3).

4.3.1 Bender element and triaxial testing

For bender element and triaxial testing smaller specimens were used, that is, 50.1mm diameter by 101.5 mm high, giving a volume of 200.09cm^3 comparing with a volume of 1000cm^3 for a standard Proctor mould. These dimensions were chosen so that the diameter and height of the specimen would minimise the near field effects (Leong et al., 2005). To prepare the specimens to those dimensions, a custom made mould was designed (Figure 4.41). The standard Proctor conditions were achieved by targeting the same dry unit weights. For each level of energy adopted the number of blows applied by a 1.5kg drop hammer from a height of 100mm, had to be calibrated to meet the dry unit weights of those obtained for the Proctor mould (AS 1289.5.1.1 - 2003). Calibration was conducted by trial and error with various combinations in the number of blows following the procedure described by Sridharan and Sivapullaiah (2005). The soil was compacted in three layers, and to calibrate the standard

Proctor equivalent compaction energy applied to the smaller mould, five different levels of energy corresponding to 15, 18, 22, 24, and 38 blows per layer were applied (Figure 4.42). The energy level closest to the standard Proctor dry unit weights (red squares in Figure 4.42) was 24 blows per layer. This corresponds to 529.5kJ/m^3, which is slightly below the 596kJ/m^3 of the Standard Proctor level.

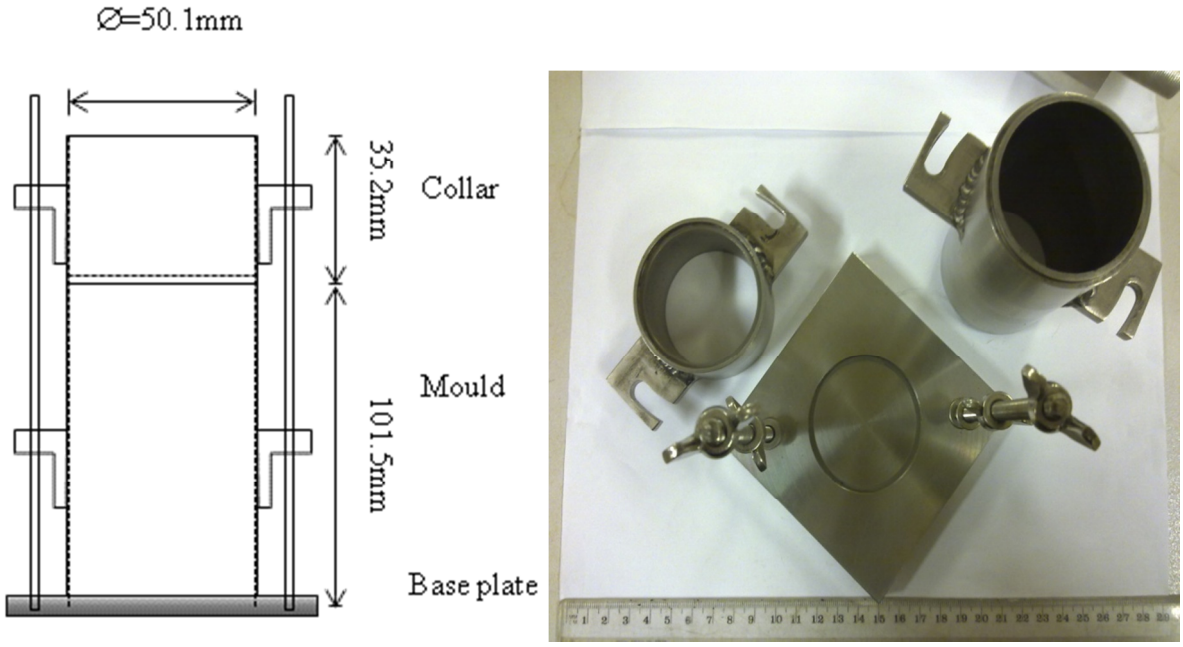

Figure 4.41 Diagram and illustration of the compaction mould

For the other levels of energy a similar procedure was adopted (Figure 4.43). Four different levels of compaction energy (E_1 = 154.5 kN.m/m^3, E_2 = 242.7 kN.m/m^3, E_3 = 529.5 kN.m/m^3, E_4 = 838.4 kN.m/m^3) were then utilised to mould the soil into 50mm diameter by 100 mm high specimens to be utilised to measure the suction and shear wave velocity. Note that the modified Proctor energy was not considered because those high levels of energy were not attained using the drop hammer designed for this mould. Thus, the upper reference bound in terms of energy was taken as the equivalent Enhanced Proctor (40% above standard Proctor, see Chapter 3). This is appropriate within the PLDC context since poor compaction states are likely to have occurred in the field during the filling operations so investigating conditions below standard Proctor should be emphasised rather than above it. This was the driving motivation for considering one additional compaction effort below the Standard (E=154.5kN/m^3) for characterising the as compacted conditions. Moreover, the current specifications for the design requirements at PLDC are based in standard Proctor compaction.

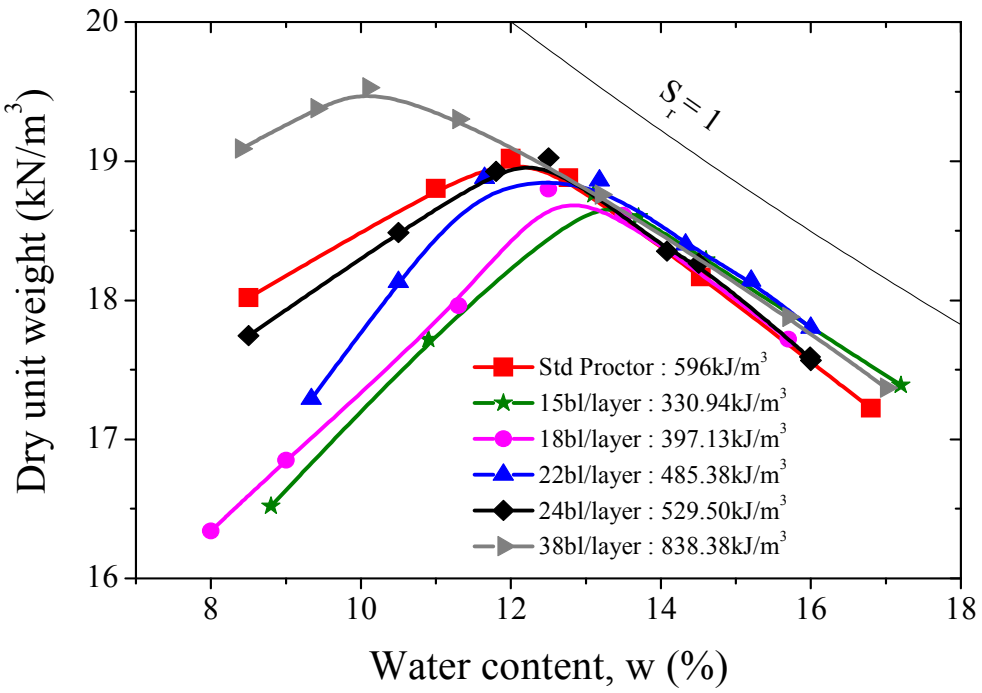

Figure 4.42 Small compaction mould calibration for standard Proctor dry unit weights.

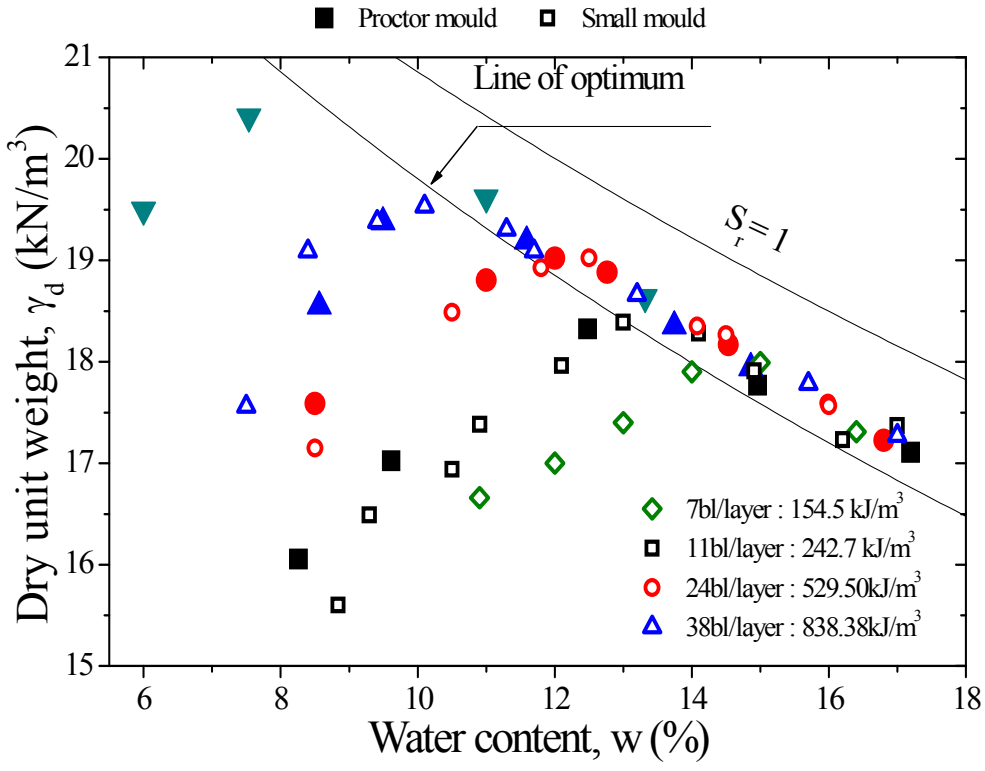

Figure 4.43 Small compaction mould calibration for standard Proctor dry unit weights for all energy levels (close symbols refer to Proctor mould where open symbol refer to the 50mm diameter mould).

4.3.2 Constant Water content direct shear box (CWDST)

The specimens for CWSDT testing were carefully trimmed from the 1L standard mould compacted soil cylinders to minimise disturbance, while the excess of soil was typically used to determine the water content (Figure 4.44). The procedure was completed in a matter of minutes to minimise exposure to air to prevent the loss of any moisture. Thereafter the specimens were wrapped in cling film and stored inside a plastic bag. Typically, the specimens used in the standard direct shear box were trimmed to 60×60×25mm. Those specimens used to study post-compaction states, required an additional preparation stage. To attain the desired level of suction (i.e. 50kPa and 100kPa) the specimens were placed in a pressure plate apparatus where the suction was increased by the axis translation technique and a similar procedure to that used to determine the SWRC (see section 4.2.2.4). The specimens were kept inside the pressure plate apparatus for 7 to 10 days to reach the required equilibrium.

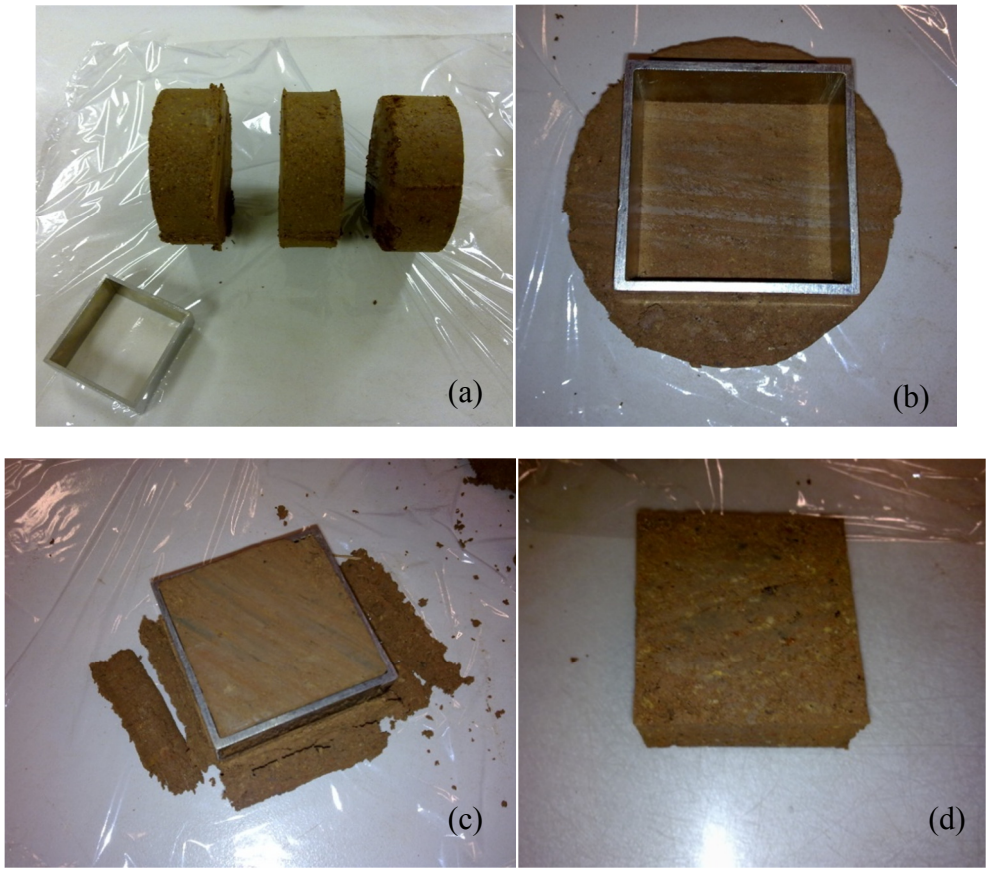

Figure 4.44 Preparing the CWDST specimen: (a) 1L Standard mould, (b) - (c) trimming procedure and (d) specimen ready.

4.4 FIELD MEASUREMENTS

Calibrating the empirical relationships developed for this particular study required calibration in the laboratory and the field. In Chapter 3 the summary results of destructive boreholes conducted in the benchmark areas was shown. Field validation requires an additional set of data related to the retrieval of samples of soil from the site to evaluate their moisture content. Field measurements of suction are also essential, and indeed, all the techniques outlined in section 4.2.2 to measure soil suction, apart from the axis translation technique, have been suggested for use in field conditions. The tensiometer was attempted for surface conditions but for a "spot" measurement in depth, the installation is somewhat difficult so filter paper was used in the disturbed samples using a drilling rig. In addition, sand cone tests were also conducted at the surface of the fill to determine the in situ dry unit weight.

4.4.1.1 Sand cone tests

In benchmark Area 9, sand cone tests were conducted to evaluate the in situ dry unit weight at the surface ground. The test was conducted in accordance with the procedure given in AS12.5.3.1, 2004. The sand used for the test was uniform beach sand that had been dried in an oven for 6 hours to remove any water. After letting the sand cool down for a few minutes it was then placed in the sand bottles. A dry unit weight of 12.06kN/m^3 was obtained for the sand using the volume calibration cylinder in the laboratory (Figure 4.45). The results of the sand cone tests conducted at three different locations in Area 9 are summarised in the Table 4.5. The locations for these measurements are the boreholes described in Chapter 3. One additional measurement was conducted around 20 metres west of the location of CS1 to evaluate the variability of the surface compaction conditions.

According to the standard Proctor curve (see Figure 4.43), the maximum dry unit weight or $\gamma_{d,max}$ is 19.02kN/m^3 for the reference soil tested, which means that 0.95 of $\gamma_{d,max}$ is 18.05kN/m^3 and 0.90 of $\gamma_{d,max}$ is 17.11kN/m^3. The values obtained in the ground surface sand cone test suggest that two of the dry unit weights obtained were below 0.95 of $\gamma_{d,max}$ and one was below 0.90 of $\gamma_{d,max}$ when the baseline maximum dry unit weight of the soil tested is used for comparison. This might be related to the improvement in dynamic compaction conducted at this location. The surface conditions were probably affected by the impact craters and thus

the soil might not have been adequately compacted after DC treatment, hence the lower dry unit weights. The surface water content also showed some variability (within 3% for the different locations). These values were only taken as a reference because they just refer to surface conditions and thus, for validation purposes the dry unit weight obtained using down-hole Gamma density (DHGD) tests are considered instead.

Table 4.5 Summary of the sand cone test results

Location	A6:CS1	A6:CS1 +20m	A6:CS2
Bulk unit weight, γ_b : kN/m^3	21.28	18.93	19.45
Dry unit weight, γ_d kN/m^3	18.78	16.99	17.71
Water content, w :%	13.2	11.4	10.0

Figure 4.45 Sand cone and laboratory calibration for the sand cone test.

4.4.1.2 Retrieval of samples of soil for an evaluation of the water content and suction

The retrieval of samples of soil on site had two main objectives, the collection of a large amount of soil for laboratory testing and checking the water content and suction in the field. The samples used for the laboratory benchmark study, of which the results are reported in the following sections, were collected from a trench in Area 9 that had been opened by an excavator to depths of 2m (Figure 4.46). Approximately 200L of material was collected. One important aspect considered at PLDC, was the matter of material variability (see section 3.3).

On more than one occasion, other areas of the site (see Appendix B) were visited and samples were collected at the ground surface. It was found that there was some variability (see section 3.3, Figure 4.47) with material collected at different locations. As a reference, the materials collected at surface in the location of the control stations analysed and used for field validation are shown in Figure 4.47. Furthermore, observations of the materials collected in the disturbed sampling for water content and evaluation of suction also revealed that with depth, there were some horizons in Areas 7 and 9 where the material was more clayey, but usually not representative (see Appendix E).

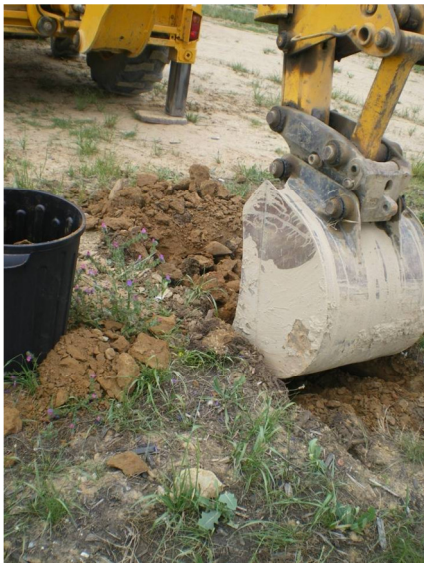

Figure 4.46 Trench for soil identification and sample retrieval

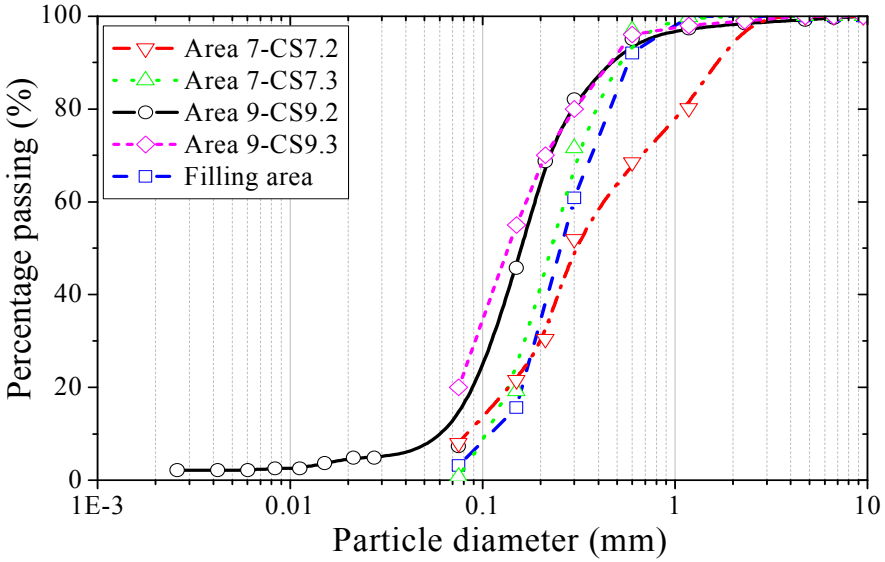

Figure 4.47 Particle size distributions for the PLDC soil collected at different locations.

To evaluate the moisture content and suction at depth, a two-person hydraulic auger drive manufactured by Dormer Engineering was used (Figure 4.48). Initially the aim was to retrieve undisturbed samples, but because there were small pebbles within the fills and it was difficult to extract totally undisturbed samples when driving the sample tube into the soil by dynamic percussion, the disturbed sampling method was adopted instead. The filter paper method was used to measure field suction (non-contact method) because of the tensiometer limited the reading range and difficult field installation for "spot" measurements at various depths. For filter paper measurements, the undisturbed samples retrieved from the site were placed in a small container and the non-contact method was performed following the procedure described in section 4.2.2.1.

Figure 4.48 Hand operated drilling rig for retrieving disturbed samples, and detail of the auger.

Area 7 – Location 1: CS7.2 and Location 2: CS 7.3

A summary of the water content and suction obtained for various depths in Area 7 are shown in Figure 4.49 and Figure 4.50, respectively. Anomalous high water content readings of 0.2-0.23 were measured at depths between 0.25m and 1.7m in location CS7.2. The characterisation of the soil closely matched the boreholes at these locations and a photographic illustration of the samples of soil collected is shown in Appendix E. The larger in situ water content is associated with horizons where clay prevailed (see Appendix E and Chapter 3). Beyond depths of 1.7m the variations were smaller. It is interesting to note that in location CS7.3, where two different sampling stages were carried out because it was difficult

to avoid the pebbles in the fill, the water content closely correlated to those in Area 9, despite its geographical distance (i.e. approximately 250 metres). This seems to suggest that there is some horizontal continuity on site in terms of the water content, albeit more sampling would be required to establish this hypothesis. This is outside the scope of the present work.

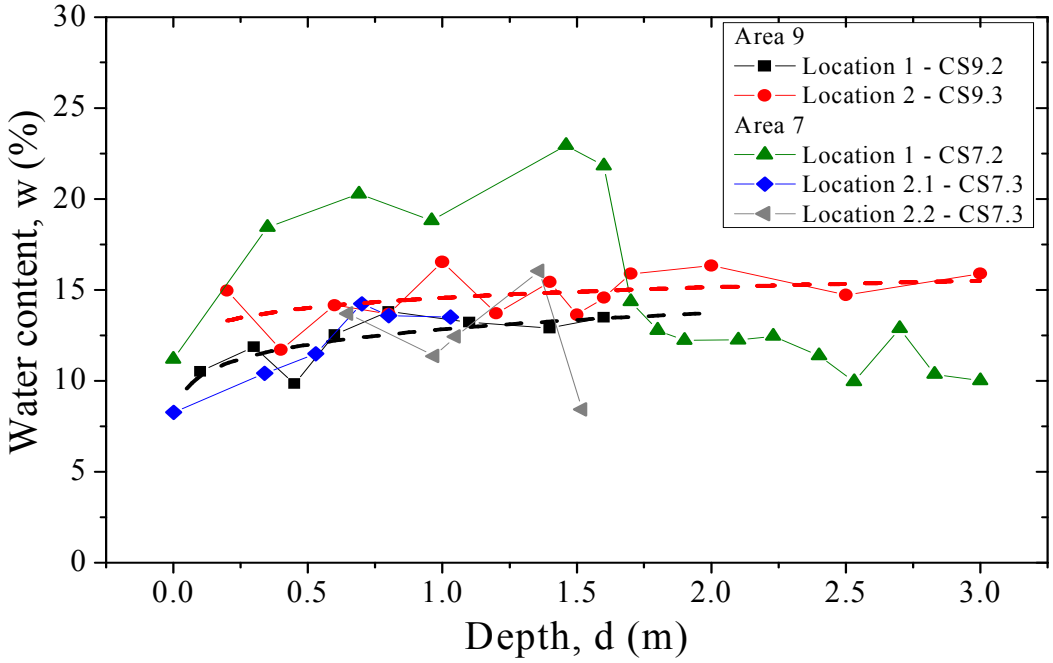

Figure 4.49 Field water content at depth, for Area 7 and 9.

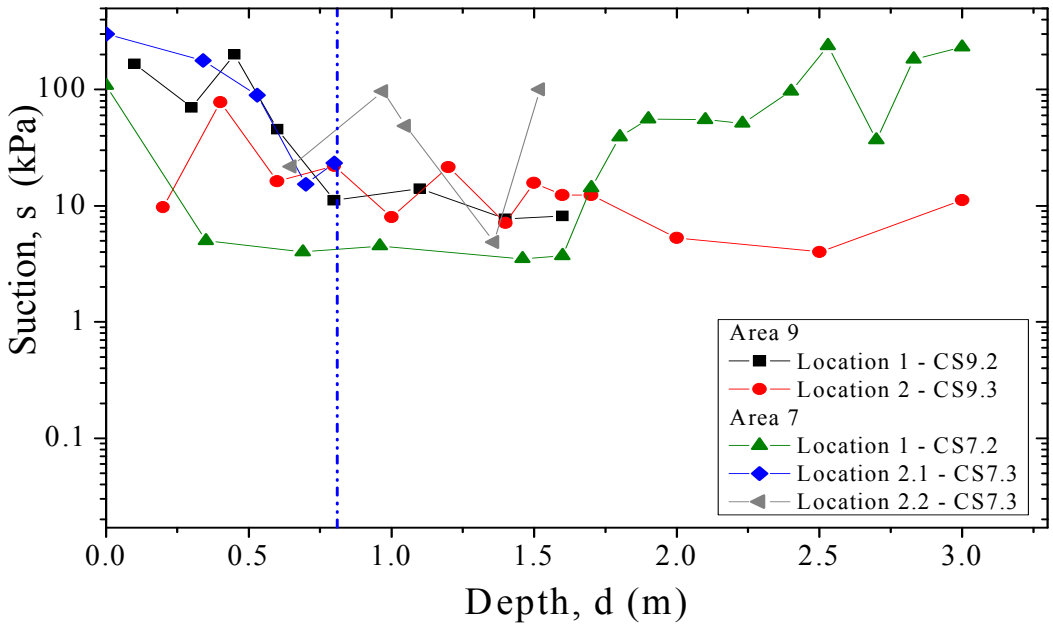

Figure 4.50 Field suction at depth, for Area 7 and 9.

In contrast, larger variations were recorded for in situ suction, owing to a rapid change in the water content from about 0.2-0.23, with suction as low as 3.5kPa to 0.08 to 0.1, and typically above 100kPa. Despite this variation it seems that when depths of 1.75m are exceeded, the suction remains steady at 150kPa.

Area 9 – Location 1 :CS9.2 and location 2 : CS9.3

Similar observations to those made at Area 7 can be made for Area 9. A summary of the water content and suction obtained at various depths in Area 9 are shown in Figure 4.49 and Figure 4.50, respectively. The characterisation of the soil closely matched the boreholes at these locations and a photographic illustration of the samples of soil collected is shown in Appendix E. The ground water content in Area 9 showed some variability in two locations; the maximum water content was 0.165 at depth of 1m in location 1, and a minimum of 0.095 at a depth of 0.5m in location 2. Higher water contents detected for samples collected around 1m deep (CS9.2 and CS9.3), and at 1.7 – 2m (CS9.2) deep, are consistent with the existence of clayey horizons. In contrast, the suction among the two locations show less variations (Figure 4.50). Where the depths exceeded 0.8 m, the suction consistently remained within 5 to 25kPa at both locations.

4.5 SUMMARY

The methodologies and apparatus used in laboratory and field measurements were outlined in this chapter. A dynamic test adopting bender elements was used to evaluate the shear wave velocity in the compacted specimens. The laboratory set-ups and particularly the aspects related to their analysis were discussed. The two different methodologies adopted for measuring suction were described and the effect of post compaction changes in water content on the hydraulic behaviour of soil was investigated using the Soil Water Retention Curve (SWRC). The results showed that the difference in compaction conditions affects the hydraulic behaviour, with the specimens compacted at dry of optimum water content (OMC) having steeper slopes than those on the wet of OMC.

A description of the modifications and the procedure adopted to enable constant water content direct shear tests (CWDST) to be performed under unsaturated conditions was also outlined in the chapter.

The details entailing the use of a medical grade X-ray CT scanner to evaluate the macrostructure of compacted soil were described and the tests results were shown thereafter. The specimens compacted on the dry side of OMC had a soil structure dominated by a large amount of macropores whereas macropores were moderately lost with an increasing moisture content. Furthermore, the specimens compacted with a higher compaction effort show fewer macropores for increasing compaction effort, indicating that the structure dominated by aggregations with larger amount of macropores progresses into a matrix dominated structure during compaction at constant water content.

Finally, the procedures used to prepare the specimens and the methodology adopted for the field tests were also described and their results shown.

CHAPTER FIVE

5 . UNSATURATED SMALL STRAIN BEHAVIOUR FOR AS COMPACTED AND POST COMPACTED STATES

5.1 GENERAL

The method proposed in this thesis to verify the compaction efficiency involves a low cost, and effective non-destructive testing method (shear wave velocity, V_s based) that must be calibrated against a set of field and laboratory test data. To establish empirical relationships, the fundamental soil properties for different compaction states (i.e. defined by different water content and energy levels) must be calibrated against the equivalent V_s and suction. An understanding of how these variables interact along the compaction plane, that derives from laboratory tests, is essential to aid in the characterisation of soil behaviour though empirical relations.

This chapter presents the laboratory data in terms of the small strain stiffness (G_0) or shear wave velocity (V_s) in unsaturated compacted specimens that represents the behaviour of as compacted and post compacted states. Particular features of the relationship between G_0 or V_s, suction, water content, and dry unit weight for different energy levels are outlined. The small strain stiffness behaviour of post compacted states in terms of the effect of confinement and wetting and drying cycles is also examined. Both the shear wave velocity and shear modulus were computed because the small strain shear modulus or G_0 is intrinsically defined on the basis of the bulk unit weight and the shear wave velocity. For that reason the discussion is in some cases addressed separately, albeit some observations may be duplicated.

5.2 AS COMPACTED STATE

A total of 25 compacted specimens prepared at various water contents and energy levels were tested under unconfined conditions using bender elements to evaluate the V_s and the tensiometer and filter paper method to measure the suction (Table 5.1). Additional specimens were prepared to check the BE test repeatability (shear wave series given in section 4.2.1.7)

and for the X-ray CT scan analysis (results are given in section 4.2.4.3). Their compaction characteristics are also shown in Table 5.1. The reader is referred to the previous chapter for the details associated with the tests procedure and apparatus, as well as the methods of analysis.

5.2.1 Compaction characteristics

The soil moisture-dry unit weight curves associated with the four different compaction energies are shown in Figure 5.1. The OMC points of each energy level, i.e. the line of optima, were approximated to a line of equal degree of saturation (S_r) of 0.8. The lines that represent full saturation (S_r = 1) and S_r = 0.67 are shown to delineate the ranges of aggregation or type of fabric likely to occur along the compaction curves. For each compaction energy, the dry unit weight increases as the moisture content increases to the OMC. Beyond this point (i.e. wet side of the compaction plane), the dry unit weight decreases with increasing water content. This tendency can be explained from a microscopic perspective by considering the interaction between water, air, and grains on the menisci. On the dry side of the compaction plane (points located below the line of optima), the suction that acts on the particles to oppose slippage is high, and the compaction process yields low dry unit weights and an aggregated soil structure with large amount of macropores (see CT-scan image of the specimen compacted at 0.125 water content and energy of 154.5 kN.m/m^3, Figure 4.39a and the SWRC of the specimen compacted at 0.721 and energy of 529.5 kN.m/m^3, Figure 4.22a). The progressive addition of water reduces suction and facilitates particle slippage. Thus, the soil experiences higher dry unit weights until it reaches its maximum at OMC, as represented by the line of optima in Figure 5.1a. Beyond the OMC, the air phase becomes discontinuous, i.e. air is occluded in bubbles (Barden and Sides, 1970; Barden and Pavlakis, 1971). In this condition, any external compaction energy that is applied is likely to be supported by the water phase in the soil, since compaction occurs over a relatively short period and the system is water-undrained. Figure 5.1a also shows that the curves representing different energy levels converge to a common asymptote, i.e. under a constant water content condition an increase in compaction energy does not yield a substantially different dry unit weight (w = 12.5% for energy levels of 529.5 kN.m/m^3 and 838.4 kN.m/m^3). This is better illustrated in Figure 5.1b. The equal water content line of w = 11.5% reaches its optimum at a higher compaction energy E_3 (point 3), after which it starts to converge to a nearly constant dry unit weight (point 4).

Table 5.1. Summary of the testing program for the as compacted states test series

Test ID	Energy level, E : kJ/m^3	Water content , w: %	Bulk unit weight, γ_b: kN/m^3	Dry unit weight, γ_d : kN/m^3	Tip to tip distance L_{tt} : mm	Void ratio e	Water ratio e_w	Degree of saturation S_r
7-1	154.4	10.9	18.48	16.66	98.47	0.59	0.29	0.50
7-2	154.4	13	19.66	17.4	96.45	0.52	0.35	0.67
7-3	154.4	15	20.69	17.99	97.66	0.47	0.41	0.86
7-4	154.4	16.4	20.15	17.31	95.74	0.53	0.44	0.84
11-1	242.69	8.84	16.98	15.60	98.96	0.70	0.24	0.34
11-2	242.69	10.50	18.72	16.94	99.28	0.56	0.28	0.50
11-3	242.69	12.10	20.13	17.96	98.57	0.47	0.33	0.69
11-4	242.69	12.20	20.39	18.17	96.5	0.46	0.33	0.72
11-5	242.69	14.10	20.86	18.28	99.39	0.45	0.38	0.85
11-6	242.69	16.20	20.02	17.23	95.87	0.54	0.44	0.81
24-1	529.50	8.50	18.63	17.17	98.94	0.54	0.23	0.42
24-2	529.50	9.13	19.48	17.85	98.55	0.48	0.25	0.51
24-3	529.50	10.20	20.33	18.45	99.00	0.44	0.28	0.63
24-4	529.50	10.54	20.47	18.52	98.72	0.43	0.28	0.66
24-5	529.50	11.34	20.65	18.56	92.00	0.43	0.31	0.72
24-6	529.50	11.80	21.18	18.94	97.96	0.40	0.32	0.80
24-7	529.50	12.50	21.41	19.03	99.24	0.39	0.34	0.86
24-8	529.50	13.00	21.26	18.81	99.22	0.41	0.35	0.86
24-9	529.50	14.50	20.93	18.28	98.90	0.45	0.39	0.87
24-10	529.50	16.10	20.39	17.57	98.93	0.51	0.43	0.86
38-1	838.37	8.12	20.59	19.04	98.36	0.39	0.22	0.56
38-2	838.37	9.41	21.20	19.38	95.69	0.37	0.25	0.69
38-3	838.37	10.11	21.33	19.37	98.71	0.37	0.27	0.74
38-4	838.37	11.30	21.48	19.30	94.78	0.37	0.31	0.82
38-5	838.37	13.20	21.12	18.66	97.77	0.42	0.36	0.85
38-6	838.37	15.70	20.57	17.78	97.6	0.49	0.42	0.87
BE-R1	529.50	8.6	18.70	17.20	98.94	0.54	0.24	0.44
BE-R2	529.50	10.45	20.36	18.43	99.01	0.43	0.28	0.65
BE-R3	529.50	12.48		18.93				
BE-R4	529.50	14.31	20.94	18.31	98.9	0.45	0.39	0.87
BE-R5	529.50	15.99	20.40	17.59	98.73	0.50	0.43	0.86
CT-7-5	154.4	12.65	19.93	17.70	-	0.50	0.36	0.68
CT-7-6	154.4	13.4	20.49	18.06	-	0.47	0.36	0.78
CT-7-7	154.4	15.3	20.62	17.89	-	0.48	0.41	0.86
CT-11-7	242.69	12.6	20.74	18.42	-	0.44	0.34	0.78
CT-24-11	529.50	12.60	21.26	18.88	-	0.40	0.34	0.84
CT-38-7	838.37	12.6	21.37	18.98	-	0.40	0.34	0.86

Note that the water unit weight is γ_w=9.81 kN/m^3 and two times BE protruding distance is 3mm, $e=\gamma_w G_s/\gamma_w - 1$ and $e_w=S_r e$

This indicates that any additional energy applied will cause shear at a constant volume and density, because the soil is incapable of mobilising further strength at that moisture content. This might suggest the existence of a possible compaction ultimate state, which means that once the soil reaches this state, even if additional energy is applied, the dry unit weight remains nearly constant. When the soil is compacted at a higher initial water content of w = 12.5%, the initial S_r is greater and the line of optima is reached at a lower energy. This explains the progressive shift of OMC to the lower water content range observed in Figure 5.1a, i.e. 14.5% for E_1 to 10.5% for E_4 energy levels.

Figure 5.2a shows the compaction data considered in Figure 5.1 but is re-plotted using an alternative compaction representation proposed by Hilf (1956) based on the void ratio (e) and the water ratio (e_w). The vertical scale representing the void ratio is inverted for ease of interpretation. The most striking aspect is that the common asymptote identified in Figure 5.1a is now clearly expressed by a linear relationship defined by a degree of saturation line of 0.865, a so called maximum degree of saturation or S_{max} (Figure 5.2a). To a certain extent this line can be interpreted as an upper bound for the compaction states.

5.2.1.1 Suction of the compacted specimens

Figure 5.3a shows the water retention data for specimens compacted at different energy levels. The suction values varied from 616 kPa on the dry side of the OMC (highest compaction effort) to 5 kPa on the wet side of the OMC (lowest compaction effort). In these tests, the amount of suction developed by compaction was not very high because the clay fraction in the tested soil was very small (< 12%). Overall, the suction decreases with an increasing water content. Although there is no apparent relationship between suction and compaction energy, all data points seem to converge to a logarithmic regression line given by Eq. (5.1) ($R^2 > 0.95$).

$$w(s) = -1.56\ln(s)+18.50 \tag{5.1}$$

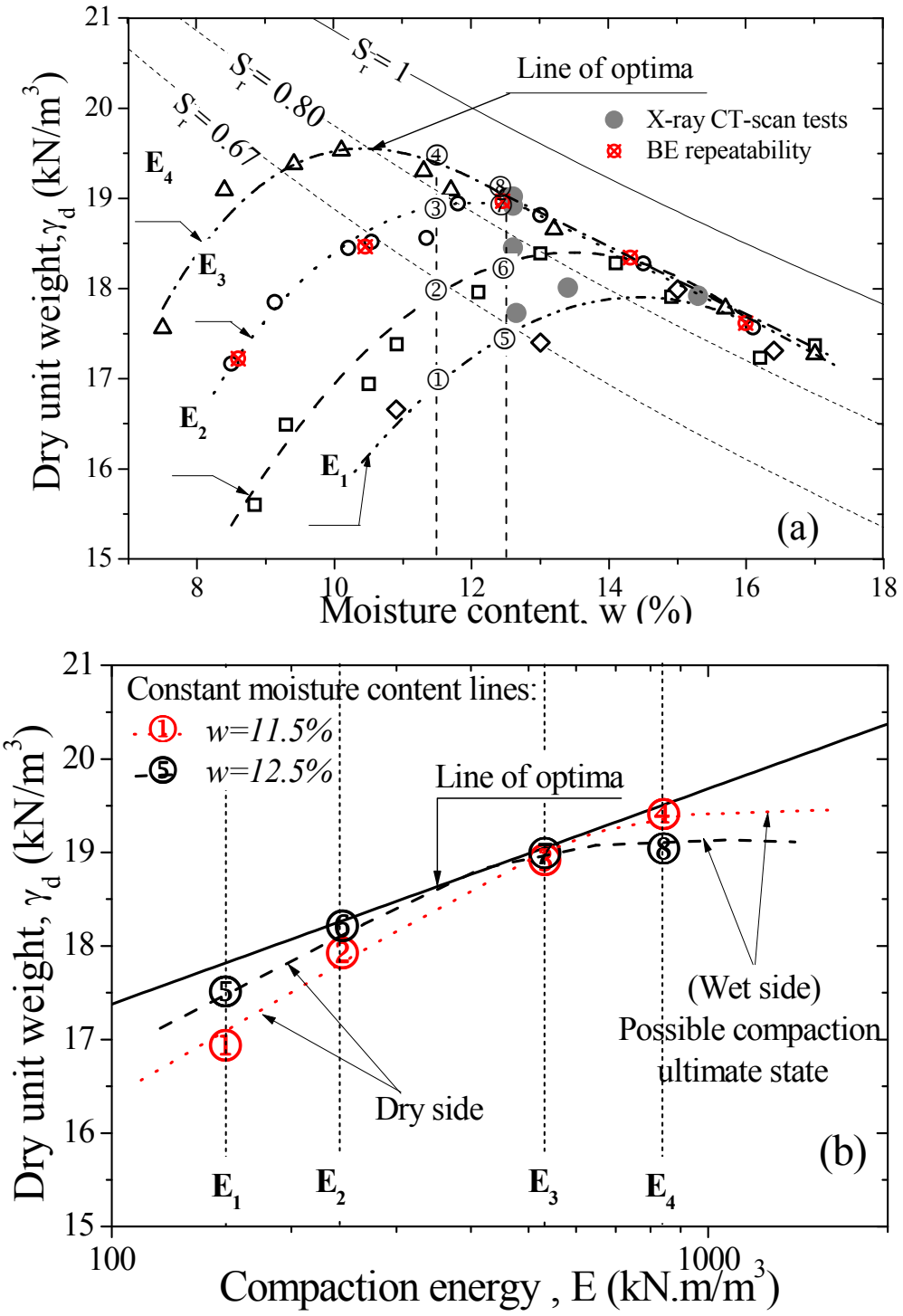

Figure 5.1 (a) Compaction curves obtained for different energy levels: E_1 = 154.5 kN.m/m^3, E_2 = 242.7 kN.m/m^3, E_3 = 529.5 kN.m/m^3 and E_4 = 838.4 kN.m/m^3 and (b) Effect of compaction energy in dry unit weight for constant moisture content lines of w = 11.5% and 12.5%.

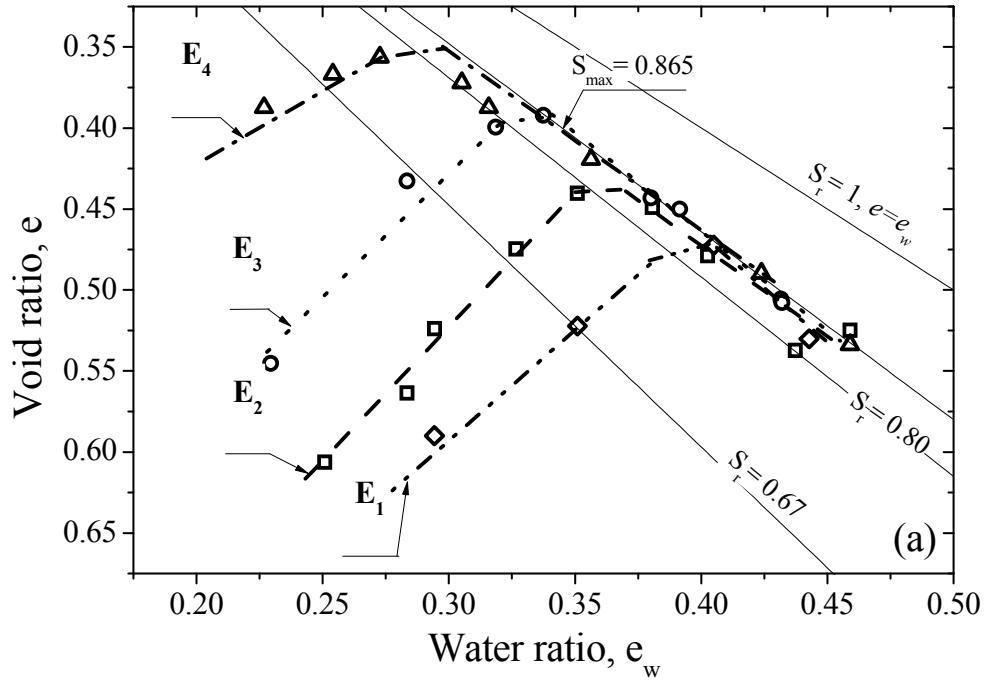

Figure 5.2 (a) Alternative representation of the compaction curves obtained for different energy levels: E_1 = 154.5 kN.m/m^3, E_2 = 242.7 kN.m/m^3, E_3 = 529.5 kN.m/m^3 and E_4 = 838.4 kN.m/m^3.

This indicates that the hydraulic behaviour of the PLDC compacted soil may be independent of the compaction characteristics (i.e. change in the water content and energy level).This relationship may also be associated with the continuously disturbed line as defined by Croney (1977) cited in Brady (1988). Despite the fact that the continuously disturbed line concept is likely to be present for other types of soil, this *w-s* logarithm relationship may not necessarily be associated to all types of soils, particularly those with a higher percentage of clay, or to other compaction methods (i.e. static or kneading). While the use of the relationship expressed in Eq. (5.1) enables a relatively simple and straightforward appraisal of field suction for a range of water contents, some degree of caution must be exercised because the suction values may change with increasing energy (i.e. Region II in Figure 5.3b). Here, the suction contour lines have a positive slope indicating that suction increases with S_r at a constant water content. The existence of distinct regions of equal suction contours has been previously highlighted in the experimental evidence of statically compacted specimens provided by Romero et al. (1999) (Region I) and by Tarantino and De Col (2008) (Region II) in Figure 5.3b.

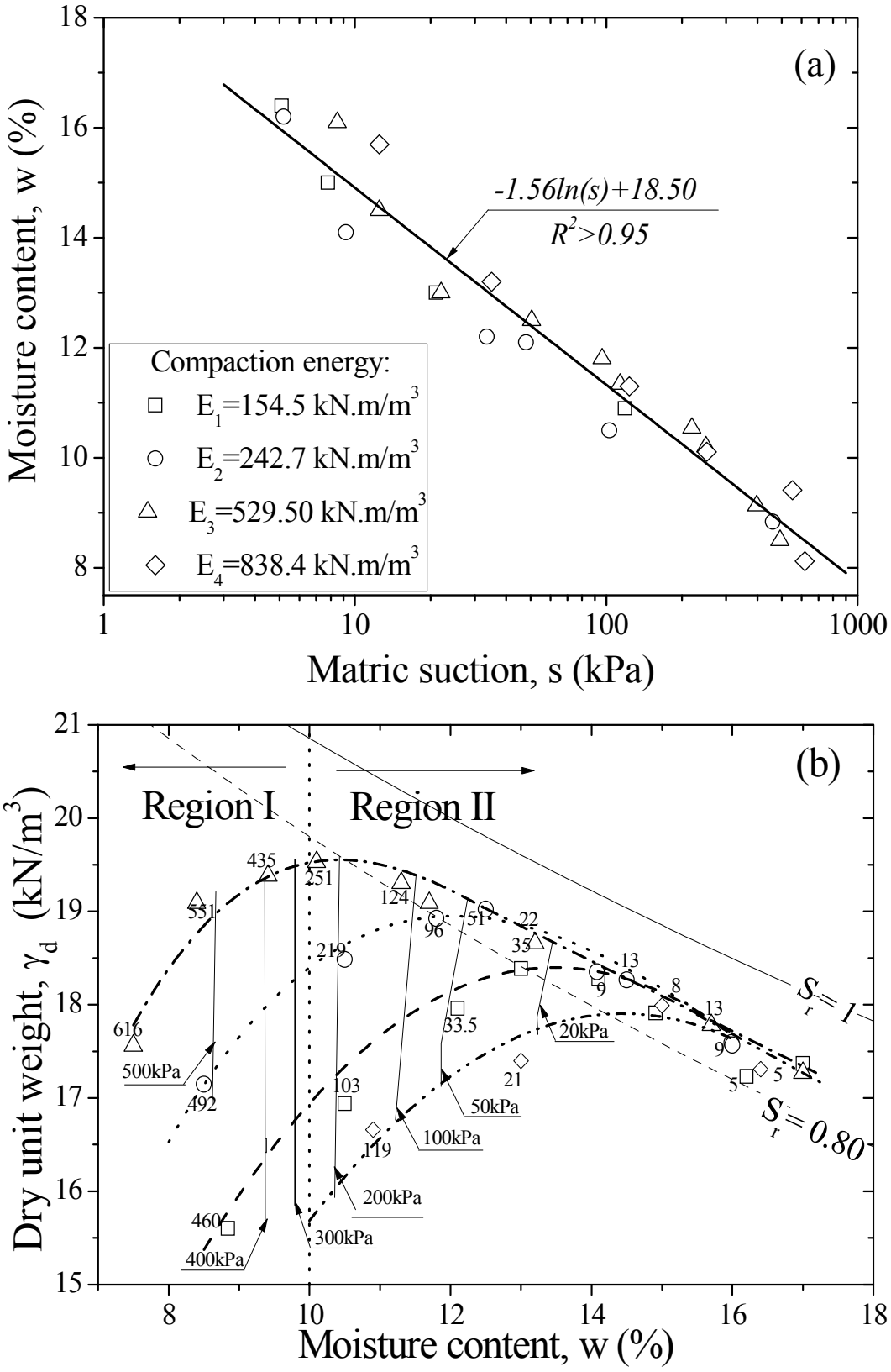

Figure 5.3 Post-compaction matric suction data (a) in terms of moisture content, and (b) contours of constant matric suction represented on the compaction plane (the values refer to suction in kPa).

5.2.1.2 Small strain behaviour: V_s and G_0

To investigate the small strain behaviour of the compacted specimens, a non-destructive technique using a pair of Bender elements was adopted in a standard Bishop-Wesley triaxial apparatus. The system was able to generate and detect shear waves, which enabled the evaluation of V_s and G_0 was computed as follows:

$$G_0 = \frac{\gamma_b}{g} V_s^2 \tag{5.2}$$

where γ_b is the bulk unit weight (kN/m^3) given in Table 5.1, g is the gravity acceleration (m/s^2), and V_s is the shear wave velocity (m/s). The specimens were enclosed beforehand in a silicone membrane to minimise moisture losses while measuring the V_s. The shear wave velocity propagating vertically, with the soil particles vibrating in a horizontal polarization plane, was monitored. In this study, the influence of inherent anisotropy on V_s or G_0 was not addressed (see Appendix C), because every specimen was prepared using the same method, so any induced anisotropy is likely to affect all of them in a similar manner.

An example of the results of the shear wave time domain series is shown earlier in Figure 4.7 for specimens compacted with the same energy level (E3 = 529.5kJ.m/m3) but different water content (w = 9.1, 10.5, 11.8, 12.5, 14.5 and 16.1%). The time domain shear wave traces for all other energy levels are given in Appendix G. The results will be showed in terms of both V_s and G_0 given the dependence of the small strain shear modulus on the bulk unit weight (i.e. Eq.(5.2)), although more emphasis will be placed on the V_s.

Figure 5.4 shows the relationship between V_s, suction and dry unit weight for the specimens compacted with E_3= 529.5 kN.m/m^3. The most striking aspect is that $V_{s,max}$ did not correspond to the maximum dry unit weight. In fact the values of V_s remained in a similar order of values for 8% < w < 10% and decreased sharply when w = 10.5%, just before the OMC was exceeded. This behaviour, which might not be considered intuitive at first sight, can be attributed to the combined effect of interrelated changes in dry unit weight, suction, and soil structure. As the dry unit weight progressively increases, the soil skeleton compresses and V_s is expected to increase (Ng et al., 2009). Concurrently, a decrease in suction weakens the contact stresses acting on the soil skeleton, and thus V_s is expected to decrease (Cho and

Santamarina, 2001). The balance of the changes in dry unit weight and matric suction on the dry side of the OMC causes the shear wave velocity and, hence, the G_0, to remain approximately constant. Furthermore, in this range (dry side of OMC) the microstructure of the compacted soil is similar, i.e. composed of aggregations with a typically bimodal porosity composed of inter-aggregate macropores and intra-aggregate micropores (Delage et al., 1996). As the water content increases, the matric suction stresses decrease even further, and after exceeding the OMC, so too does the dry unit weight, causing the V_s to decrease abruptly. Similar experimental observations were made by Sawangsuriya et al. (2008) in terms of the small strain shear modulus for sandy clays. Note that a similar trend is obtained for the V_s or G_0 variation with suction and dry unit weight (Figure 5.5a-c).

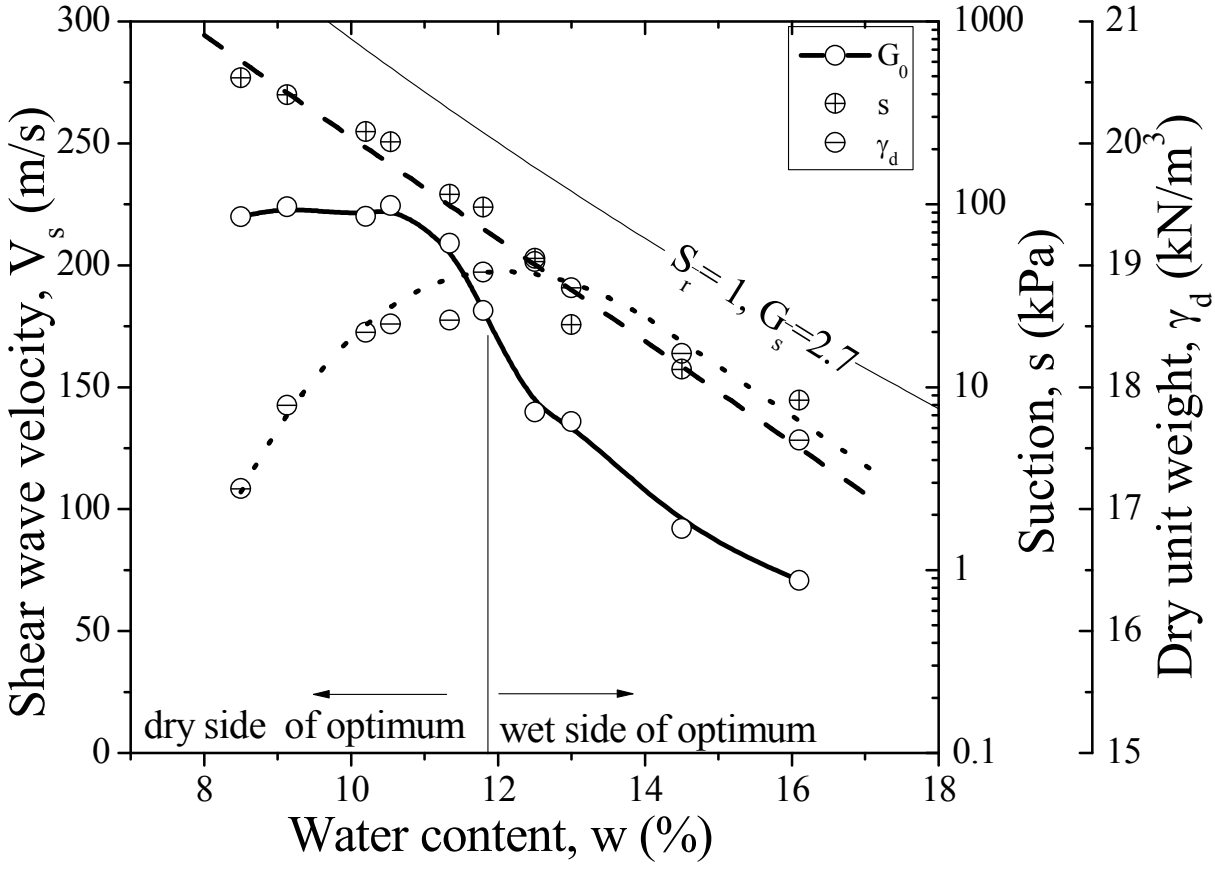

Figure 5.4 V_s, suction and dry unit weight of the specimens compacted at various moisture contents for compaction energy E_3 = 529.50 kN.m/m^3.

The V_s and G_0 values obtained for different compaction energies are depicted in Figure 5.5 and Figure 5.6, respectively. The measured V_s and G_0 values ranged from 273m/s and 153MPa on the dry side of the OMC (E_4 = 838.4 kN.m/m^3) to 70m/s and 13 MPa on the wet

side of the OMC (E_1 = 154.5 kN.m/m^3). Figure 5.5a shows the relationship between V_s and dry unit weight in the specimens compacted with different energy levels. For a given dry unit weight, the shear wave velocity varies from the dry side of the compaction plane to the wet side, and to some extent the V_s - γ_d resembles the compaction curve representation. Higher values are obtained for the higher energy levels (V_s: E1<E2<E3), with maximum values on the compaction plane dry side. The V_s and G_0-water content-suction relationships shown in Figure 5.5b-c and Figure 5.6a-b indicate that on the dry side of the OMC, V_s or G_0 is controlled by the compaction energy, since an increase in energy translates to an increase in V_s or G_0 at nearly constant suction (see Figure 5.5c). At higher water contents $w \geq 13\%$, the effect of suction on V_s or G_0 becomes increasingly pronounced, since an increase in compaction energy does not yield a higher V_s or G_0. It is interesting to note that on the wet side of the OMC, lower V_s or G_0 values were obtained under the highest energy levels (i.e. E = 838.4 kN.m/m^3). Consider in the example the water content paths of 11.5% and 12.5%, the same as those represented in Figure 5.1b. When the soil crosses a degree of saturation line just before line of optima at an energy level of 529.50kN.m/m^3, V_s has its maximum value for *w=11.5%.* Although a further increase in the energy level still produces a marginal increase in the dry unit weight, the corresponding V_s actually drops slightly.

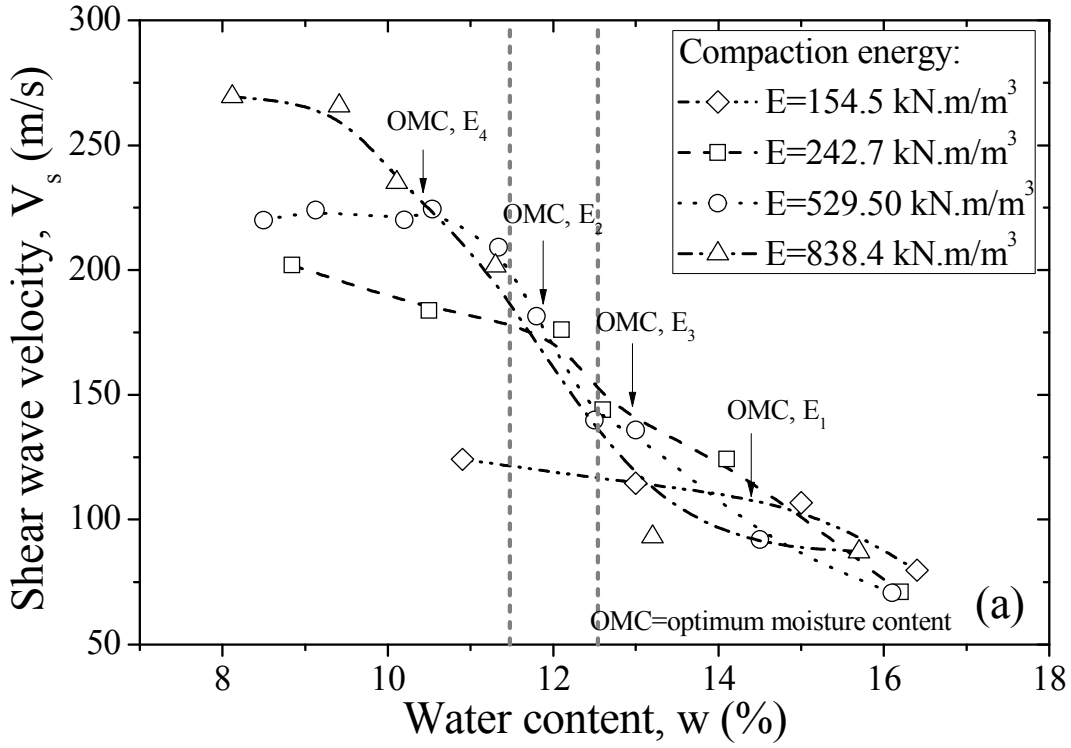

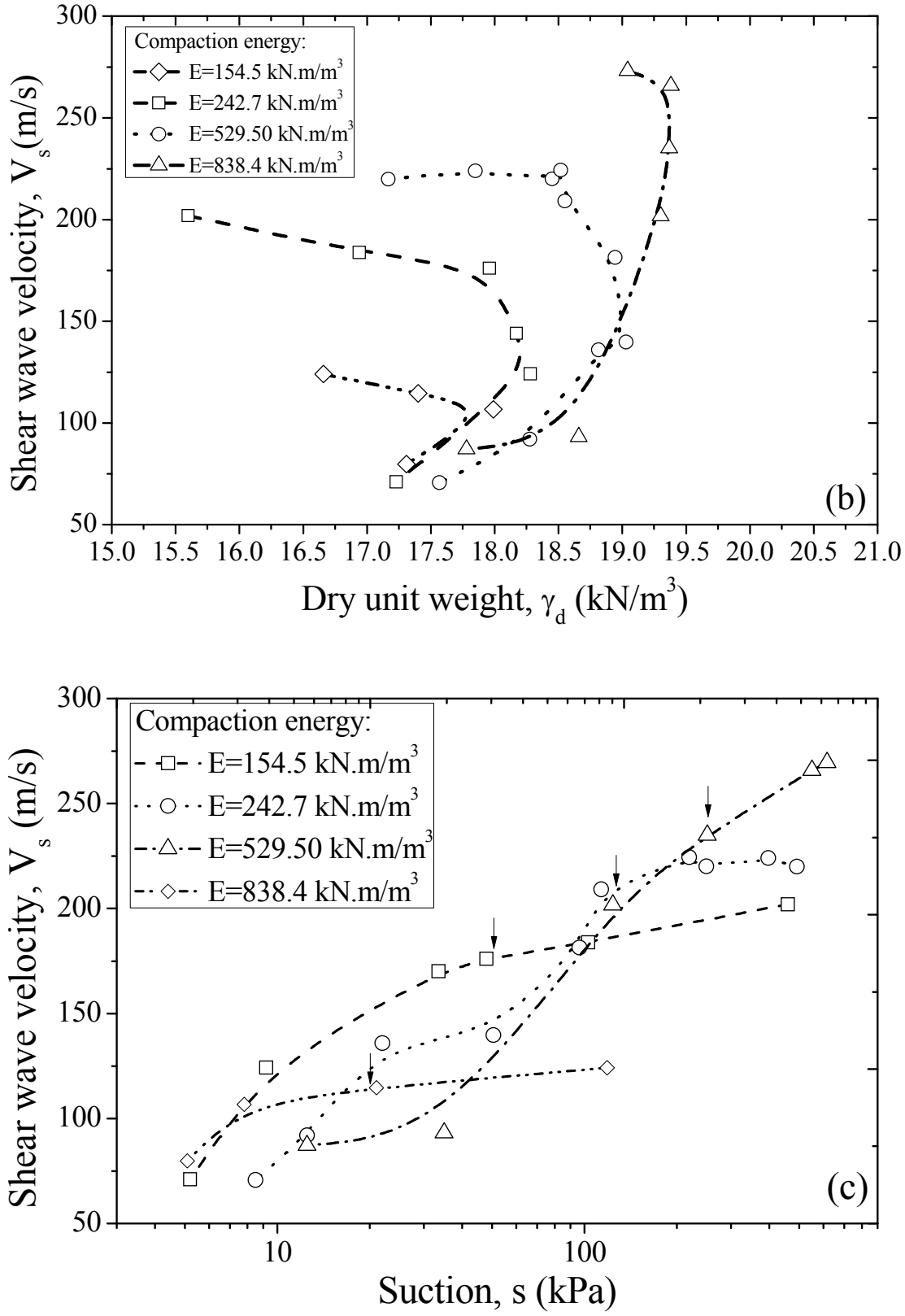

Figure 5.5 Variation of shear wave velocity of specimens compacted with different compaction energy levels in terms of (a) moisture content and (b) dry unit weight (c) suction.

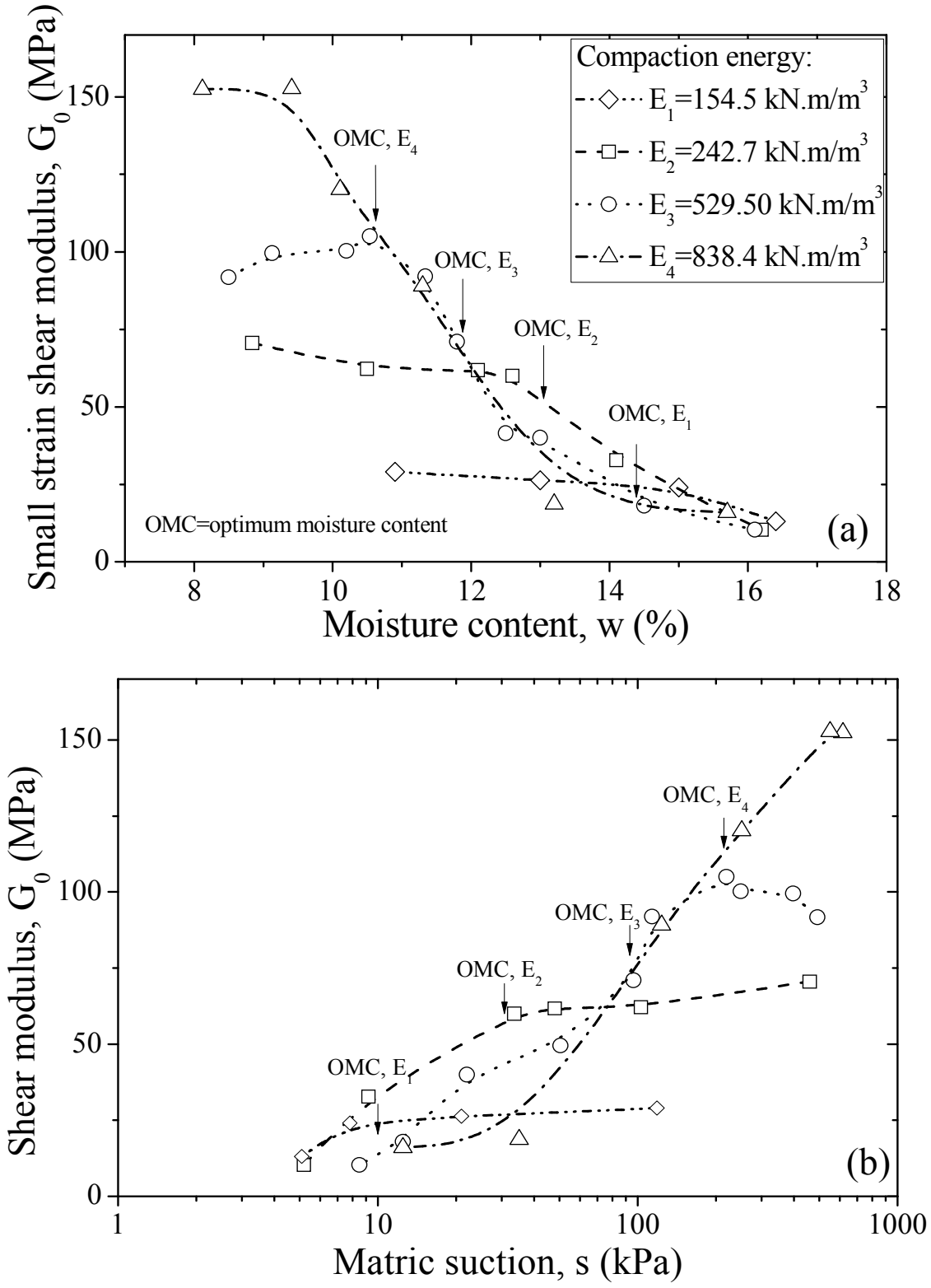

Figure 5.6 Variation of small strain shear modulus of specimens compacted with different compaction energy levels in terms of (a) moisture content and (b) matric suction.

This behaviour is even more evident for *w=12.5%* where V_s is maximum for an even lower energy level of 242.7 kN.m/m^3 while higher energy levels of 529.50kN.m/m^3 and 838.4 kN.m/m^3 exhibit progressively lower V_s values. It seems that during compaction through constant water content paths, once the degree of saturation representing the line of optima is exceeded, V_s starts to decrease with increasing compaction energy. This suggests that imparting higher levels of compaction energy in the field, or over compacting, does not necessarily yield superior shear stiffness. The present results support the premise that it may contribute to the deterioration of the shear strength characteristics, represented here by the small strain stiffness. Similar findings were obtained by Turnbull and Foster (1956) in as compacted CBR field tests on lean clays. Another interesting point revealed by Figure 5.5 and 5.6 is the possible existence of an upper maximum limit for the change of V_s and G_0 with water content across all energy levels.

Figure 5.7 shows the relationship between G_0 and compaction energy along the constant moisture content lines where the energy dependence in the dry side is clearly illustrated, which is similar to Figure 5.1b. In the lower moisture content range ($w \leq 10\%$) G_0 exhibits an almost linear logarithmic increase with increasing compaction energy. As the moisture content increases, G_0 becomes constant (w = 16%) or in some cases (w = 13, 14, 15%) decreases with increasing compaction energy. V_s shows similar trends, and for that reason it is not represented.

Figure 5.8a-b shows the relationship between V_s or G_0 and S_r for various energy levels defining three distinct regions based on the extent of the aggregation that is distinguishable in the CT-scan images (i.e. extensive, moderate, and insignificant). The extent of aggregation distinguishable was defined based on the type of fabric and macroporosity reflected in the CT-scan images shown in Figures 4.39 and 4.40, and the regions boundaries were based on the patterns of the V_s or G_0 variation. At $S_r < 0.67$ (Region ①: extensive aggregation), V_s or G_0 remains approximately constant for each energy level, although accompanied by a decrease in suction and an increase in dry unit weight, as shown earlier (see Figure 5.5 and Figure 5.6). The soil in this region show an aggregated fabric with large amount of macropores and an increase in compaction energy causes G_0 to increase logarithmically (highlighted in Figure 5.7). Figure 4.39a, which belongs to a specimen compacted in Region ①, shows that the

macrostructure is dominated by the presence of aggregations (grey areas) with large inter-pores (white areas), while the sand particles (dark coloured areas) are not easily distinguished.

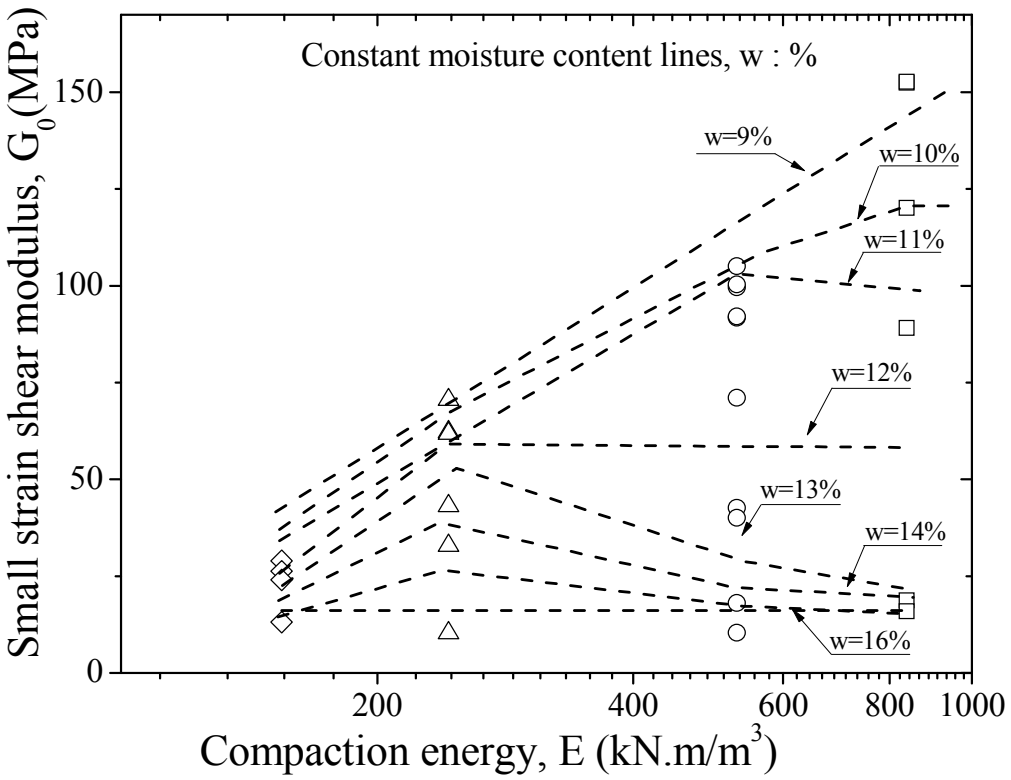

Figure 5.7 Small-strain modulus and compaction energy relationship for constant moisture content lines.

With an increase in S_r in Region ②, V_s or G_0 starts to decrease, where the greater the compaction energy, the greater the rate of decrease in V_s or G_0. For example, for E_4 = 838.4 kN/m^3, V_s and G_0 decreases from from 270m/s to 201m/s and 150 MPa to ~60 MPa, while for E_3 = 529.50 kN/m^3 the corresponding drop is from 225m/s to 181m/s and ~100 MPa to 60 MPa, respectively. With an increase in S_r, the aggregations become deformable and they likely to come together to form a 'matrix dominated' structure during compaction. In this range, the suction is considerably reduced, thus a decrease in V_s or G_0 may be expected. This is supported by Figures 4.39b and 4.40b, which show a decreasing macroporosity, as evidenced by a decrease in the white and grey coloured areas. Note also the similarity in soil macrostructure of two specimens compacted at different energy levels but to the same degree of saturation points (see Figure 4.39 (b) and (e) and Table 5.1). This seems to suggest that when the soil is compacted to the same degree of saturation under different energy levels, it

exhibits a similar macrostructure that in turn lends support to the delineation of the distinguishable aggregation ranges based on the degree of saturation.

At S_r > 0.80 (Region ③: insignificant aggregation), V_s or G_0 converges rapidly to a minimum value of 70m/s and 10 MPa respectively, regardless of the imparted compaction energy. At this point the suction values are very low and the aggregates are almost fused together and the fine fraction includes sand grains with a "matrix" dominated macrostructure. This transition to a "matrix" dominated type of macrostructure, characteristic of OMC conditions and Region ③, is easily observed earlier in Figure 4.39c where the aggregations are difficult to individualise and macroporosity is substantially reduced (Figure 4.40c). The sand grains (black) can be easily individualised from the matrix. These results are also consistent with SEM images of silt compacted on the wet side of the OMC obtained by Delage et al. (1996).

It is interesting to note that changes in the macrostructure that are associated with an increase in compaction energy, as illustrated earlier in Figure 4.39a-c under constant water content conditions (w = 12.5%), are possibly the reason for the decrease in G_0, particularly at higher compaction energies (Figure 5.5). This indicates that G_0 exhibits a strong dependence on the soil structure, as outlined in studies on structured sands by Cuccovillo and Coop (1997).

5.2.1.3 As compacted states key points

The major key points to retain from the behaviour of suction and V_s or G_0 along the different compaction states that the soil might experience if either water content or energy level is varied are the following:

a) there is a clear relationship between the water content and suction which is independent of the imparted compaction energy,
b) V_s or G_0 is sensitive to the suction, water content, dry unit weight, and compaction energy. The level of this sensitivity seems to be related to the final compaction state, i.e. on the dry side of OMC, an increase in the compaction energy or dry unit weight at constant suction translates into an increase in V_s or G_0 whereas in the wet side of OMC it might contribute to a decrease in V_s or G_0,

c) V_s or G_0 exhibits the highest value on the dry side of OMC and starts to decrease when the water content is just below OMC for all energy levels,

d) There is an intimate relationship between the V_s or G_0 and soil macrostructure, which in turn was related to the degree of saturation.

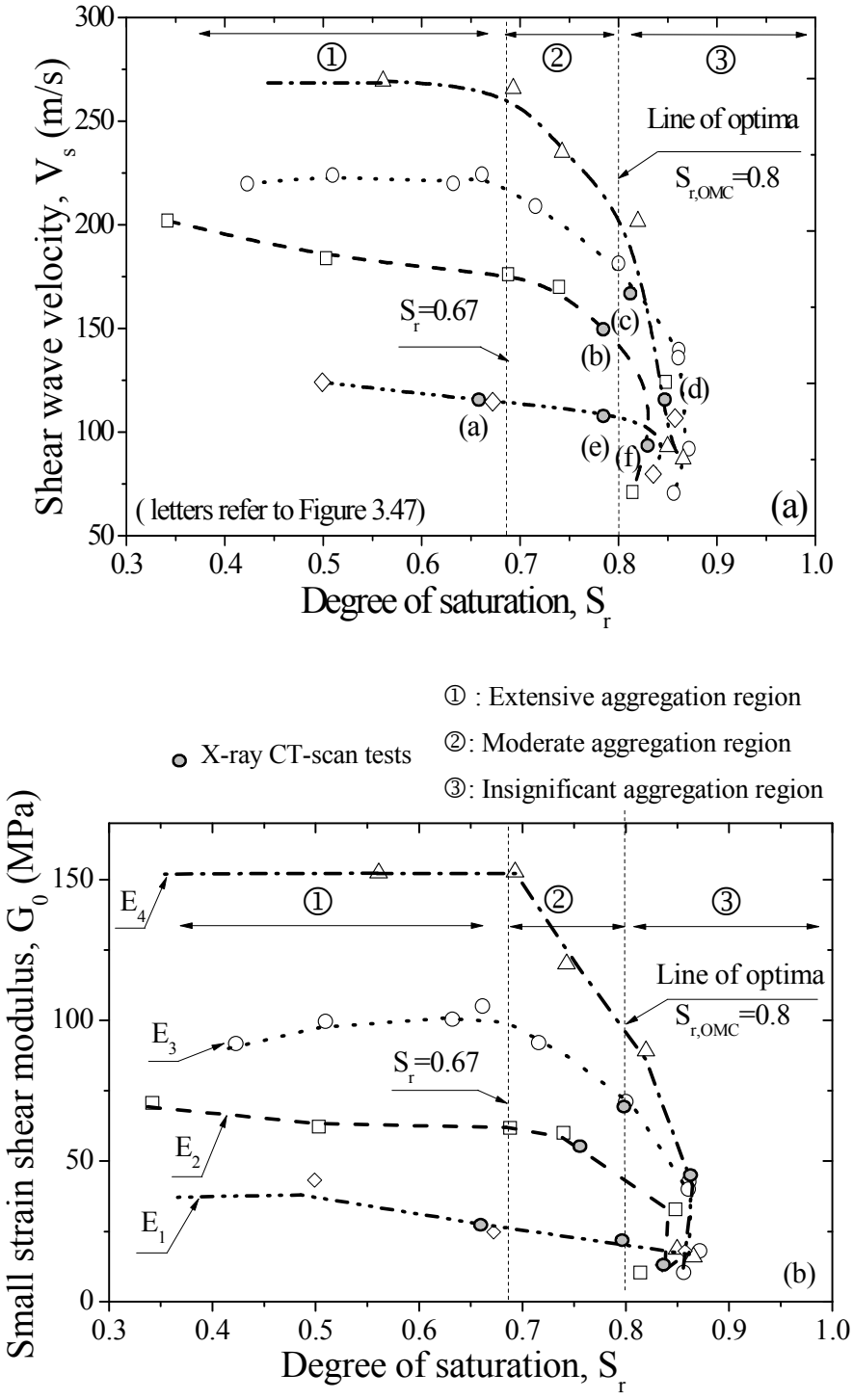

Figure 5.8 Variation of (a) V_s and (b) G_0 with S_r for the various compaction energy levels.

5.2.2 Post-compaction states: Confinement

A total of 15 compacted specimens selected among those used to characterise the as compacted states were tested using bender elements under isotropic confined conditions (Table 5.1). An additional 5 specimens were prepared to check the BE test repeatability (shear wave series given earlier in section 4.2.1.7). Their compaction characteristics and testing conditions are given in Table 5.2. The isotropic confining pressures were applied in a Bishop-Wesley triaxial cell and V_s was monitored using bender elements that were cantilevered in the 50mm diameter top cap and bottom pedestal (see earlier Figure 4.3). The confining pressures were incremented at a rate of 1kPa/min until they reached the desired confinement stress. When a given confining stress was attained it was kept constant while the axial displacements induced by confinement were monitored by an exterior LVDT (Linear variation displacement transducer with accuracy of 0.001mm), and axial strain was computed. Usually a period of 1hour was sufficient to allow for all axial displacements to take place and at the end of this period the V_s was measured. In an attempt to replicate the expected field conditions, the tests were carried out under constant water content conditions. During isotropic compression, suction was not monitored, however Nyunt et al. (2011) observed that the pore pressure differential $(u_a\text{-}u_w)$ or suction changes during undrained shearing of sand specimens are just marginal (i.e. less than 5kPa). Furthermore the isotopic compression tests conducted at constant suction by Biglari et al. (2012) showed that for the range of confining stresses considered in this study, the specific exchange of water volume lead to very small changes in the water content (i.e. 0.4%). Thus, it is expected that the variation in suction during the isotropic compression stages is very small. For specimens prepared at higher moisture contents, the confining stresses applied, particularly those higher than 200kPa, caused the specimens to reach saturated conditions. Details associated with the methods used to analyse the shear wave traces are given in the previous chapter, and the extended shear wave traces are shown in Appendix G.

While using the first bump maximum time domain method to analyse the wave traces for increasing confinement, using an input wave frequency of just 3.3kHz yields increasingly smaller L_{tt}/λ ratios. In some of the specimens, predominantly those of the dry side of optimum water content (OMC), higher input frequencies in the order of 7kHz had to be considered.

Table 5.2. Summary of the initial conditions and testing program for the post compacted states confinement test series

Test ID	Energy level, E : kJ/m^3	Water content , w: %	Bulk unit weight, γ_b: kN/m^3	Dry unit weight, γ_d : kN/m^3	Tip to tip distance $L_{tt\text{-}i}$: mm	Void ratio e	Water ratio e_w	Degree of saturation S_r	Confining pressure, σ_m kPa
11-1-C	242.69	8.84	16.98	15.60	98.96	0.70	0.24	0.34	50-250
11-2-C	242.69	10.50	18.72	16.94	99.28	0.56	0.28	0.50	50-250
11-3-C	242.69	12.10	20.13	17.96	98.57	0.47	0.33	0.69	50-250
11-5-C	242.69	14.10	20.86	18.28	99.39	0.45	0.38	0.85	50-250
11-6-C	242.69	16.20	20.02	17.23	95.87	0.54	0.44	0.81	50-250
24-1-C	529.50	8.50	18.63	17.17	98.94	0.54	0.23	0.42	50-250
24-4-C	529.50	10.54	20.47	18.52	98.72	0.43	0.28	0.66	50-250
24-6-C	529.50	11.80	21.18	18.94	97.96	0.40	0.32	0.80	50-250
24-9-C	529.50	14.50	20.93	18.28	98.90	0.45	0.39	0.87	50-250
24-10-C	529.50	16.10	20.39	17.57	98.93	0.51	0.43	0.86	50-250
38-1-C	838.37	9.41	21.20	19.38	95.69	0.37	0.25	0.69	50-250
38-4-C	838.37	11.30	21.48	19.30	94.78	0.37	0.31	0.82	50-250
38-5-C	838.37	13.20	21.12	18.66	97.77	0.42	0.36	0.85	50-250
38-6-C	838.37	15.70	20.57	17.78	97.6	0.49	0.42	0.87	50-250
BE-R1-C	529.50	8.6	18.70	17.20	98.94	0.54	0.24	0.44	50-250
BE-R2-C	529.50	10.45	20.36	18.43	99.01	0.43	0.28	0.65	50-250
BE-R3-C	529.50	12.48	21.29	18.93	98.87	0.40	0.34	0.84	50-250
BE-R4-C	529.50	14.31	20.94	18.31	98.9	0.45	0.39	0.87	50-250
BE-R5-C	529.50	15.99	20.40	17.59	98.73	0.50	0.43	0.86	50-250

Note that the isotropic confining pressure was applied in 50 kPa increments until reaching 250kPa and $L_{tt\text{-}i}$ refers to initial tip to tip length.

The results are presented only in terms of V_s given the difficulty associated with the inaccuracies in determining the bulk unit weight (i.e. change in volume) with increasing confinement and consequently G_0. The results are grouped by different energy levels, while some comparisons are made for specimens compacted at approximately the same water content and different energy levels. Figure 5.9, 5.10 and 5.11 show the variation of V_s in terms of confining pressure and moisture content for specimens compacted at energy levels of 242.69kN/m^3, 529.50kN/m^3 and 838.37kN/m^3, respectively. In general the V_s witnessed an increase with increasing confining pressure for all energy levels, although the rate of increase showed some differences. Higher V_s rate of increase was observed for specimens compacted

at a higher water content, specifically those prepared at the wet side of OMC, i.e. *w=14.1%* and *w=16.2%* for an energy level of 242.69kN/m^3 (Figure 5.9) which is consistent with the experimental findings obtained for compacted silt by Claria and Rinaldi (2007). The V_s-*w* representation with increasing confining stresses shows that across the different water contents the tendency observed for the as compacted still prevails. This result contrasts somewhat with the data obtained by Claria and Rinaldi (2007), who reported a substantial increase in V_s with increasing confinement on the specimens belonging to the wet side of OMC. This difference may be attributed to the fact that constant water conditions were not assumed.

Figure 5.12 shows the comparison results of specimens prepared at approximately the same water content *w≈8.5%* and *w≈16.1%* but for increasing energy level. The results of the specimens representative of the dry of OMC conditions, confirm the behaviour of the as compacted states, that is, in this range of water content an increase in energy is reflected by an increase in V_s. Note that the lower V_s values obtained for the energy level of 838.37kJ/m^3 by comparison with an energy level of 529.5 kJ/m^3 are easily justified by the slightly higher initial water content.

On the specimens compacted on the wet side of OMC, a higher V_s was obtained for the highest compaction effort. Note however that the specimen corresponding to 838.37kJ/m^3 was prepared at a slightly lower (≈0.3%) water content compared to the other two energy levels, which may have caused the large difference in terms of V_s between the three specimens. This is most likely related to the influence of suction, since the specimens prepared at higher energies levels exhibited the largest suction values. In addition, although this difference is small for the as compacted states (i.e. less than 10m/s for specimens prepared at 242.7 kJ/m^3 and 529.5 kJ/m^3) the increase of confining stress causes differences that can go as high as nearly 50m/s.

During the various stages of confining pressure imposed upon the specimens, the axial strain was also monitored, mainly for correcting the L_{tt} distances used in the V_s evaluation. Figure 5.13 shows the changes in the computed axial strain with isotropic confinement. Larger compressibility values were observed for specimens compacted on the wet side of OMC for all energy levels, except 838.37kJ/m^3. For these particular specimens, saturation

conditions were reached and slight pore water pressure may have developed from an additional increment of confining stress, thus may inducing less compressibility.

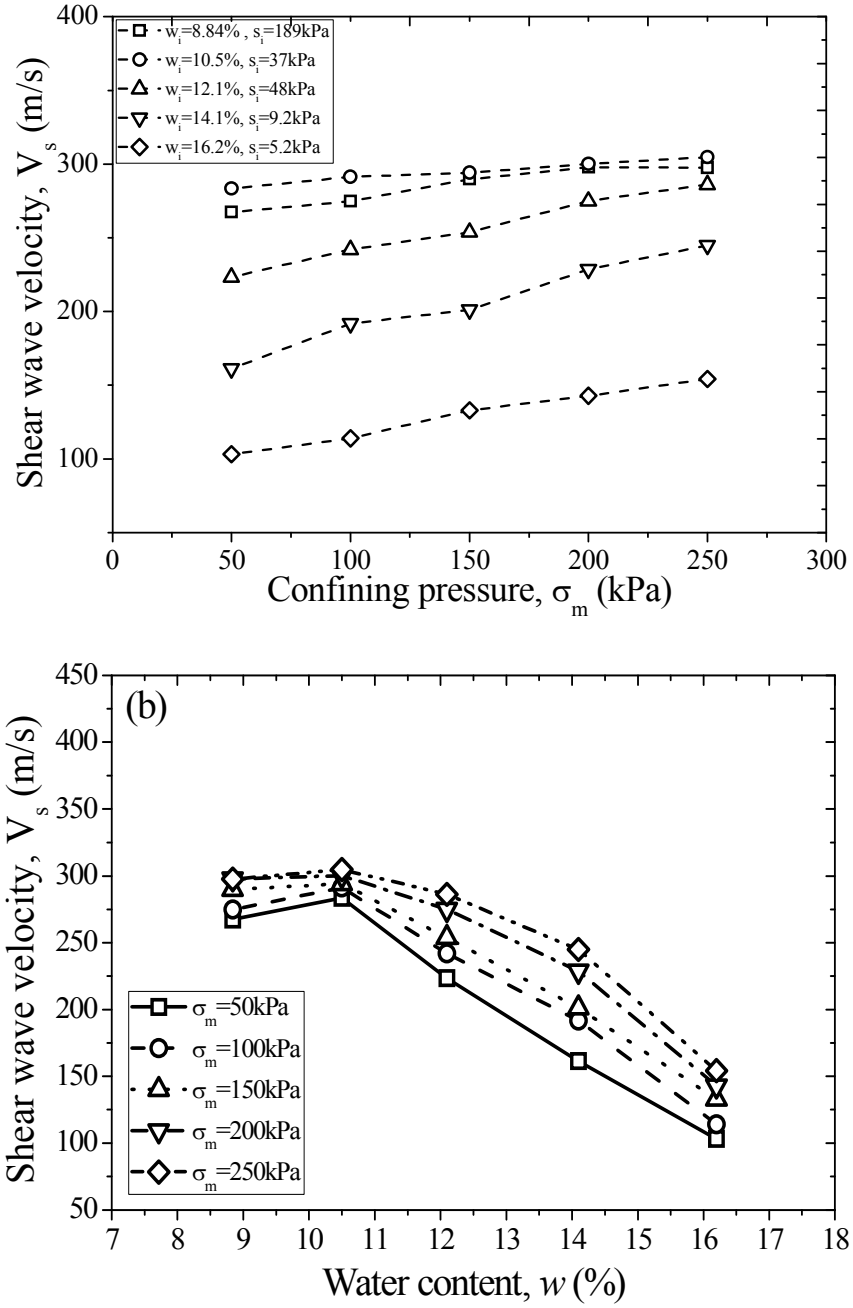

Figure 5.9 Variation of V_s in terms of (a) confining pressure and (b) moisture content for specimens compacted at energy level of 242.69kN/m^3.

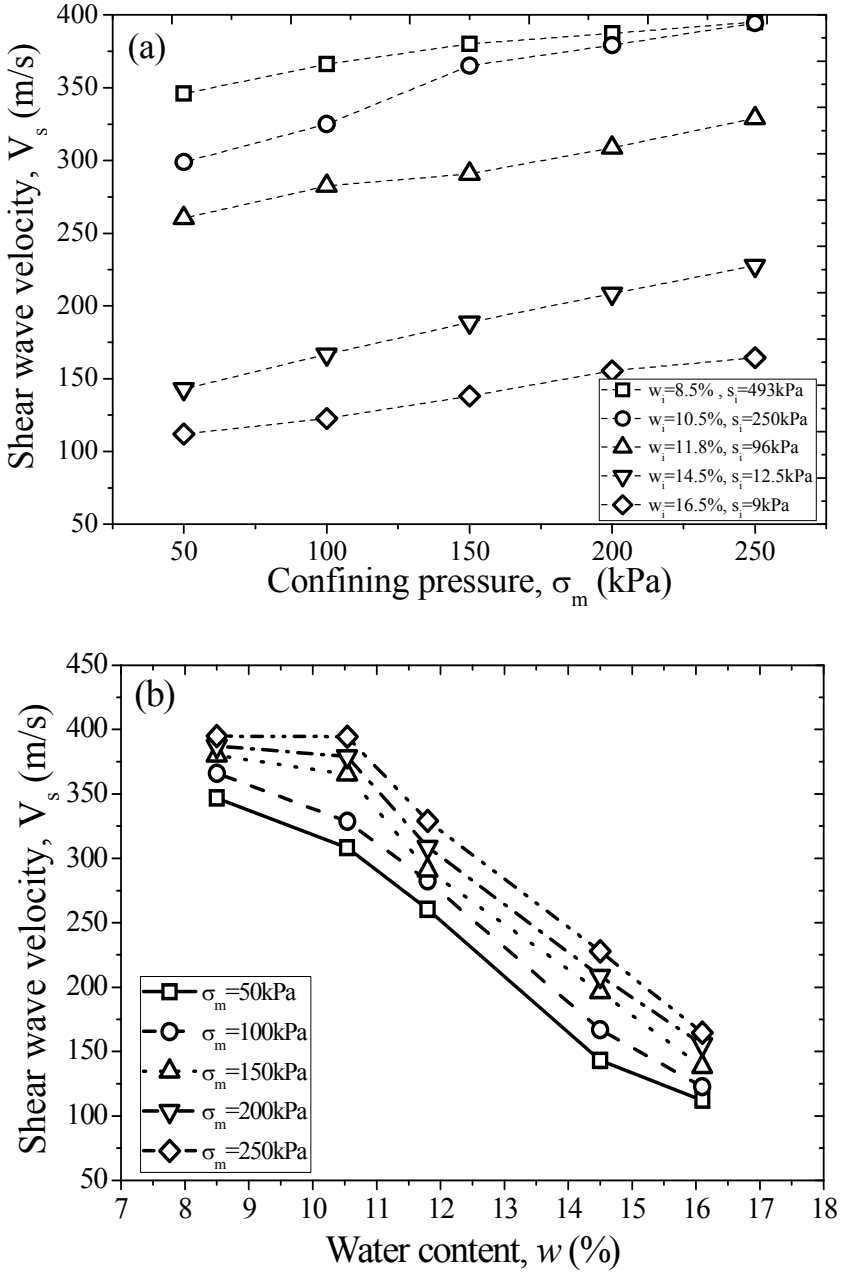

Figure 5.10 Variation of V_s in terms of (a) confining pressure and (b) moisture content for specimens compacted at energy level of 529.50kN/m^3.

The reduction of the wave path length (L_{tt}) on the specimens prepared at wet of OMC, however was not enough to produce significant changes in the wave velocity (Figure 5.9, 5.10 and 5.11). This indicates that in spite of soils being compacted at moisture contents that may exhibit large changes in axial strains, the V_s seems relatively unaffected and shows a steady increase with confining pressure or equivalent depth in field conditions.

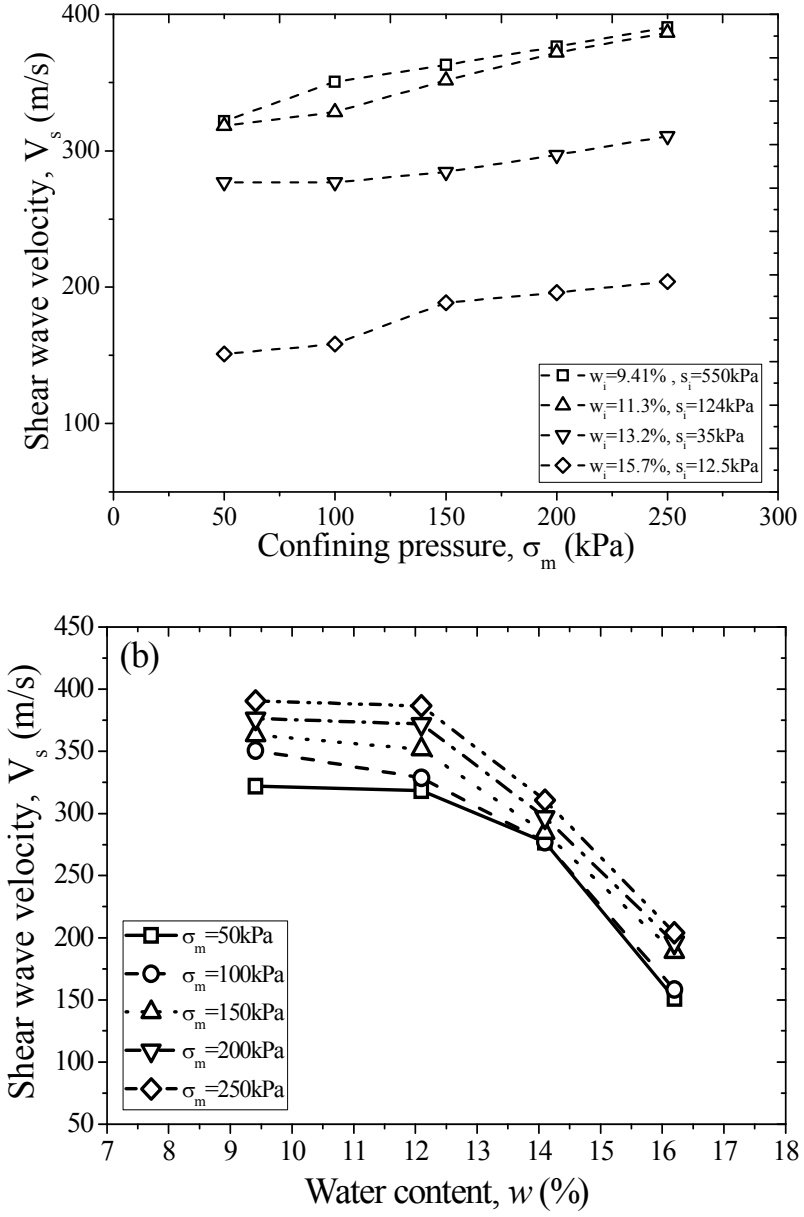

Figure 5.11 Variation of V_s in terms of (a) confining pressure and (b) moisture content for specimens compacted at energy level of 838.37kJ/m^3.

5.2.3 Post-compaction states: Effect of wet-drying cycles

A total of 3 compacted specimens were tested using bender elements under isotropic confined conditions for V_s evaluation under wetting and drying cycles. An emphasis was placed on investigating the effect of compaction energy rather than the moisture content. The three

specimens selected were representative of the reference energy optimum water content (i.e. E= 529.50kN/m^3) and were prepared with increasingly higher energy levels. Their compaction characteristics and testing conditions are given in Table 5.3.

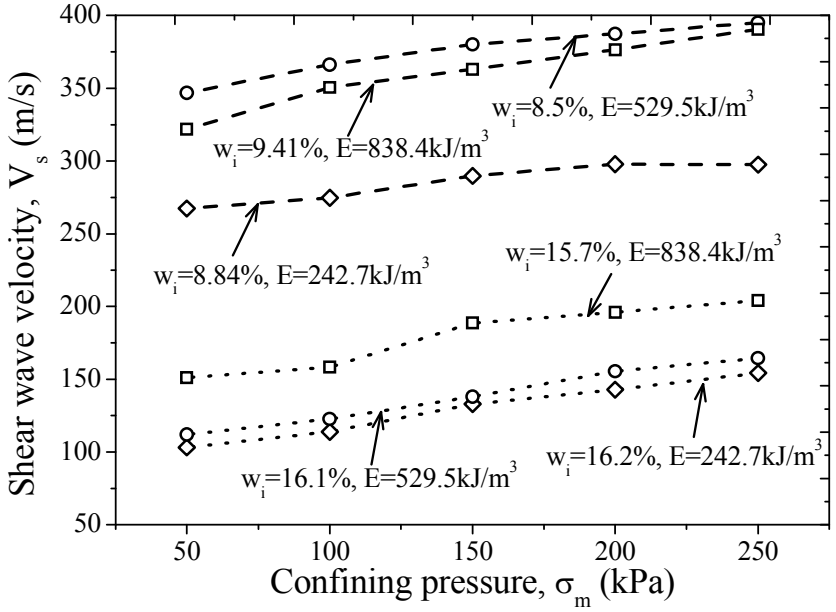

Figure 5.12 Variation of V_s confining pressure for specimens compacted at approximately the same water content and different energy level.

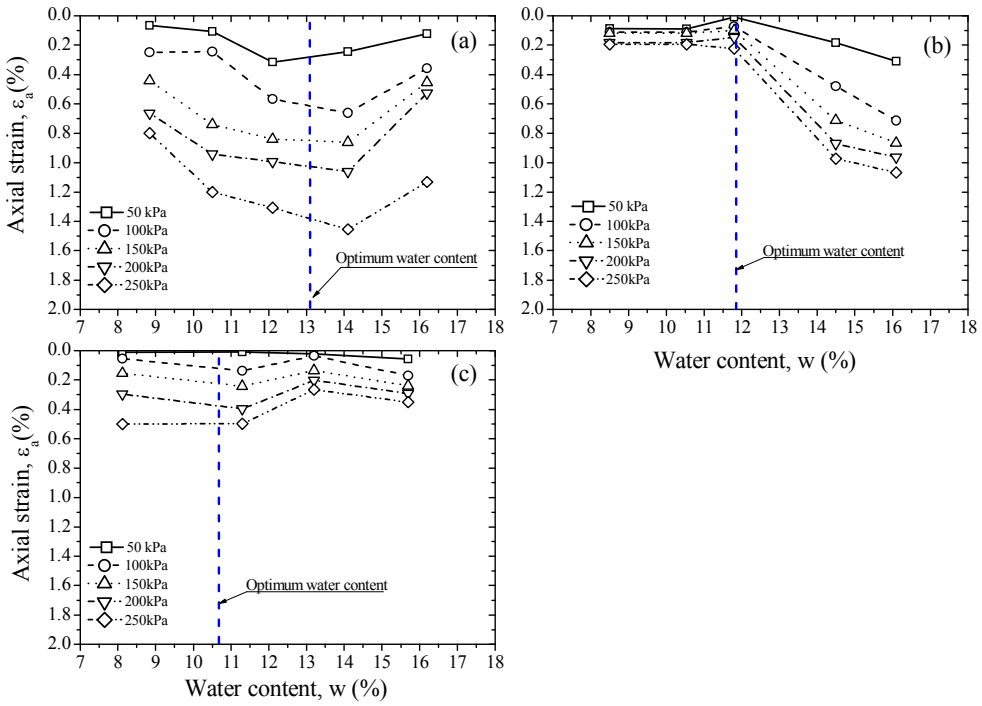

Figure 5.13 Volumetric strain with increasing confining pressure for specimens compacted at energy level of (a) 838.37kN/m^3, (b) 529.5kN/m^3 and (c) 254.5kN/m^3.

The tests were conducted in a load frame based triaxial cell and V_s was monitored using bender-extender elements that were cantilevered in the 50mm diameter top cap and HAEV bottom pedestal (see earlier Figure 4.24 and Figure 4.26). Details of the procedure were given earlier in section 4.2.2.4. Furthermore, the details associated with the methods of analysis of the shear wave traces are given in the previous chapter and the extended shear wave traces are shown in Appendix G. During this test series the bender-extender elements cantilevered in the top cap and bottom pedestal also enabled an evaluation of the velocity of the compressional waves or V_p. Since the prime aim of this study is to address the evaluation of V_s under different conditions, the V_p traces and their results are not reported here.

Table 5.3 Summary of the initial conditions and testing program for the post compacted states wetting-drying series

Test ID	Energy level, E: kJ/m^3	Water content, w: %	Dry unit weight, γ_d : kN/m^3	Tip to tip distance $L_{tt\text{-}i}$: mm	Confining pressure, (σ-u_a): kPa	Wetting (↓) and drying(↑) paths (u_a-u_w) stages: kPa
11-7-WD	242.69	11.8	18.25	98.24	50	74: 50↓ 25↓50↑100↑150↑100↓50↓25↓50↑
24-11-WD	529.50	12.0	19.01	98.37	50	67: 50↓ 25↓ 50↑ 100↑ 150↑ 200↑ 300↑ 250↓ 200↓ 150↓ 100↓ 50↓ 25↓ 50↑ 300↑ 50↓
38-7-WD	838.37	12.1	19.23	99.18	50	65: 50↓ 25↓ 50↑ 100↑ 150↑ 100↓ 50↓ 25↓ 50↑

Note that $L_{tt\text{-}i}$ refers to initial tip to tip length, the isotropic confining pressure represents the difference between the cell pressure and top cap air pressure or (σ-u_a) and suction represents the pressure differential between the top cap air pressure and bottom pedestal water pressure (u_a-u_w).

The variation of V_s with increasing (drying) and decreasing (wetting) suction for all three specimens are depicted in Figure 5.14. The most striking aspect, common for all three specimens is that V_s exhibits higher values when following the wetting paths. This might not correspond to the expected intuitive behaviour at first glance, but it can be associated with the soil-water exchange in soil pores also responsible for the hysteretic response observed in the SWRC represented in Figure 5.15 (i.e. the ink-bottle effect, see section 2.3.2.2.2). In addition,

the soil fabric is also evolving into a more constricted porosity centred at the microporosity range when the soil dries, and partly recovering some of the macroporosity when it is wetted (Cuisinier and Laloui, 2004, Monroy, 2005). The results represented in Figure 5.14 show that V_s not only seems to be sensitive to these fabric changes but also exhibits hysteretic response. These results are also consistent with the studies on decomposed tuff conducted by Ng et al., 2012. Nonetheless, the hysteresis amplitude shows some differences among the three specimens, for instance at a suction of 25kPa the energy level of 254.5kJ/m^3 is about 30m/s, while for energy levels of 529.5kJ/m^3 and 838.7kJ/m^3, and it is around 24m /s and16 m/s, respectively. This difference is likely related to the initial soil macrostructure of the specimens.

Recalling the CT-scan images of specimens prepared for increasing energy levels (Figure 4.37), it was observed that the macropores associated with the an aggregated structure decrease, and eventually the soil structure changes into "matrix". Thus, the amount of hysteresis amplitude seems to be directly related to the extent of macroporosity. Furthermore, these results seem to suggest that the poorer the compaction is, yielding larger percentages of macropores, the larger V_s hysteresis amplitude is in cycles of wetting and drying that the soil is likely to experience due to climatic changes. The extent of these changes of amplitude at higher depths (i.e. higher confining stresses) was not considered. Nevertheless it would seem reasonable to assume that for higher depths, smaller amplitudes would be expected. The relevant depth of climatic influence or H_s is variable for different locations and can be estimated based on Thornthwaite moisture index (see section C.6 in Appendix C).

Further inspection of Figure 5.14b reveals another important point; while the V_s value is recovered when the soil is subjected to a second cycle of drying at a suction of 300kPa, in the subsequent wetting cycle V_s displays again hysteretic behaviour and shows an increase of 17m/s. V_s would be expected that to show slight hysteresis on both paths, similar to the SWRC response (Figure 5.15), but this is not the case. A possible explanation may lie within the changes in the soil structure; Koliji et al., 2010 reported that in a high suction range the volume of aggregations are reversible, whereas in low suction the wetting path shows fewer aggregations. Furthermore, Ng and Xu (2012) referred to the recent suction ratio or CSR, that is, the maximum suction that the soil has experienced over the current suction, in governing the small strain stiffness and mechanical response at small strain. However, the results

presented here suggest that not only is the CSR important, so too are the number of cycles of wetting-drying, since at a suction 50kPa, a CSR of 6 was obtained for both the first and second cycles, and yet V_s differs by 17m/s.

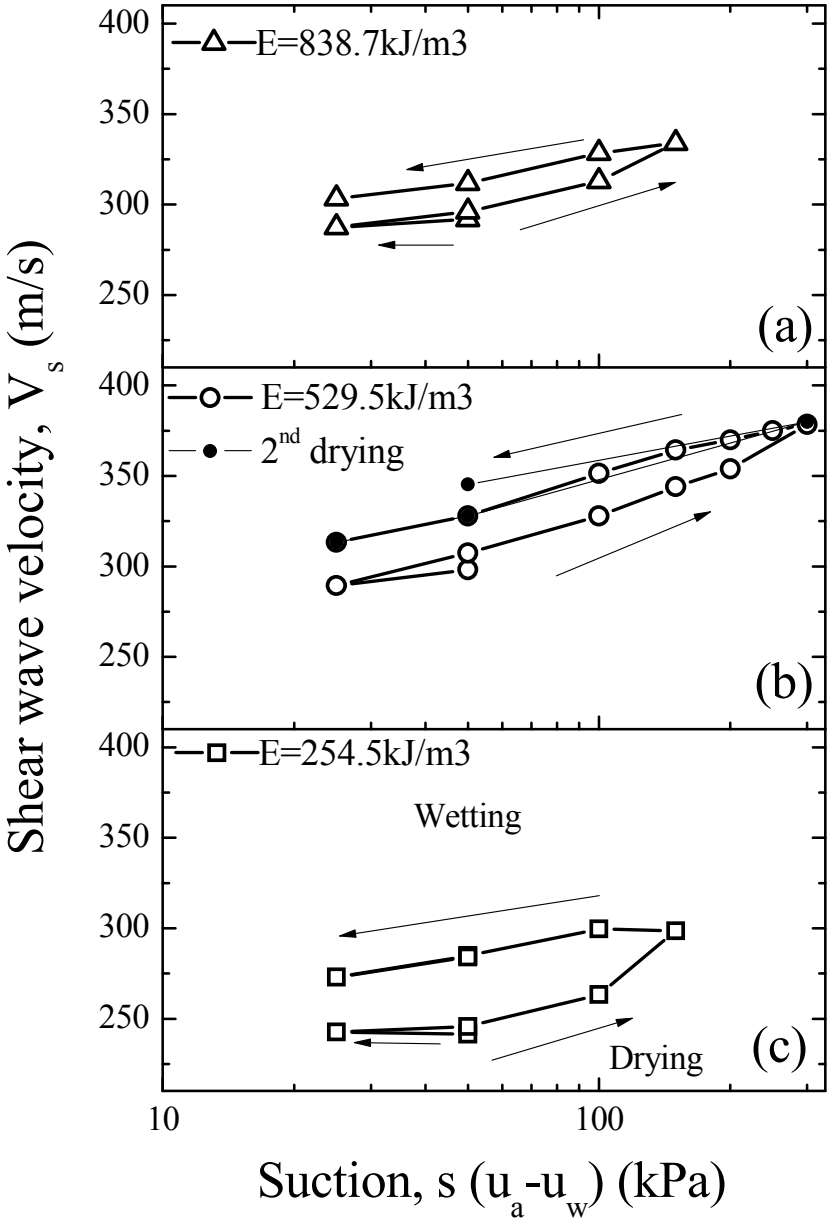

Figure 5.14 Variation of V_s with suction during a drying-wetting cycle of specimens prepared at energy level of (a) 838.37kN/m^3, (b) 529.5kN/m^3 show also a second drying cycle and (c) 254.5kN/m^3.

Figure 5.15a shows the corresponding water retention data computed based on the volume of water at the end of the equilibrium stages and axial strains monitored by the water pressure controller and a LVDT, respectively (Figure 5.16). These points do not represent the

SWRC, and in fact they lie on the scanning curves. The SWRC of a specimen compacted at 12% for an energy level of 529.5kJ/m3 is also given for reference only, since the resulting SWRC for confining stress of 50kPa would likely resemble the additional curve represented.

A marked hysteresis was observed in all three specimens, although the vertical position varied. This difference is related to the initial dry unit weight and soil structure. The water retention data is also replotted in terms of water content (Figure 5.15b). The equivalent changes in suction of 25-300kPa resulted in variations in the water content of about ±1.5%. This indicates that even a small change in water content in the field may lead to considerably different values of V_s. Observing these differences in field surveys conducted in both wet and dry conditions (i.e. winter or summer) may offer some insight into the current condition of the site in terms of the degree of compaction, provided of course that the depth of influence is high enough to overcome the resolution of the field V_s ground profiles. Note that the bimodal character of the SWRC was not observed in these tests. Possible reasons are associated with the fact that the suction testing range represented was lying on the macroporosity branch of the SWRC and some of amount of the macropores may have been closed during isotropic compression. Similar observations have been reported compacted kaolin (Bagherieh el al., 2009)

Figure 5.16 shows the volume of water exchanged during the equilibration periods for every suction stage. Usually, the larger volumes of water associated with the drying paths and curve shapes are consistent. Figure 5.16b shows some oscillations that are related to the air pressure control that at times showed some small variations, and although the suction increment period adopted for every stage was large, the system was still susceptible to the small variations.

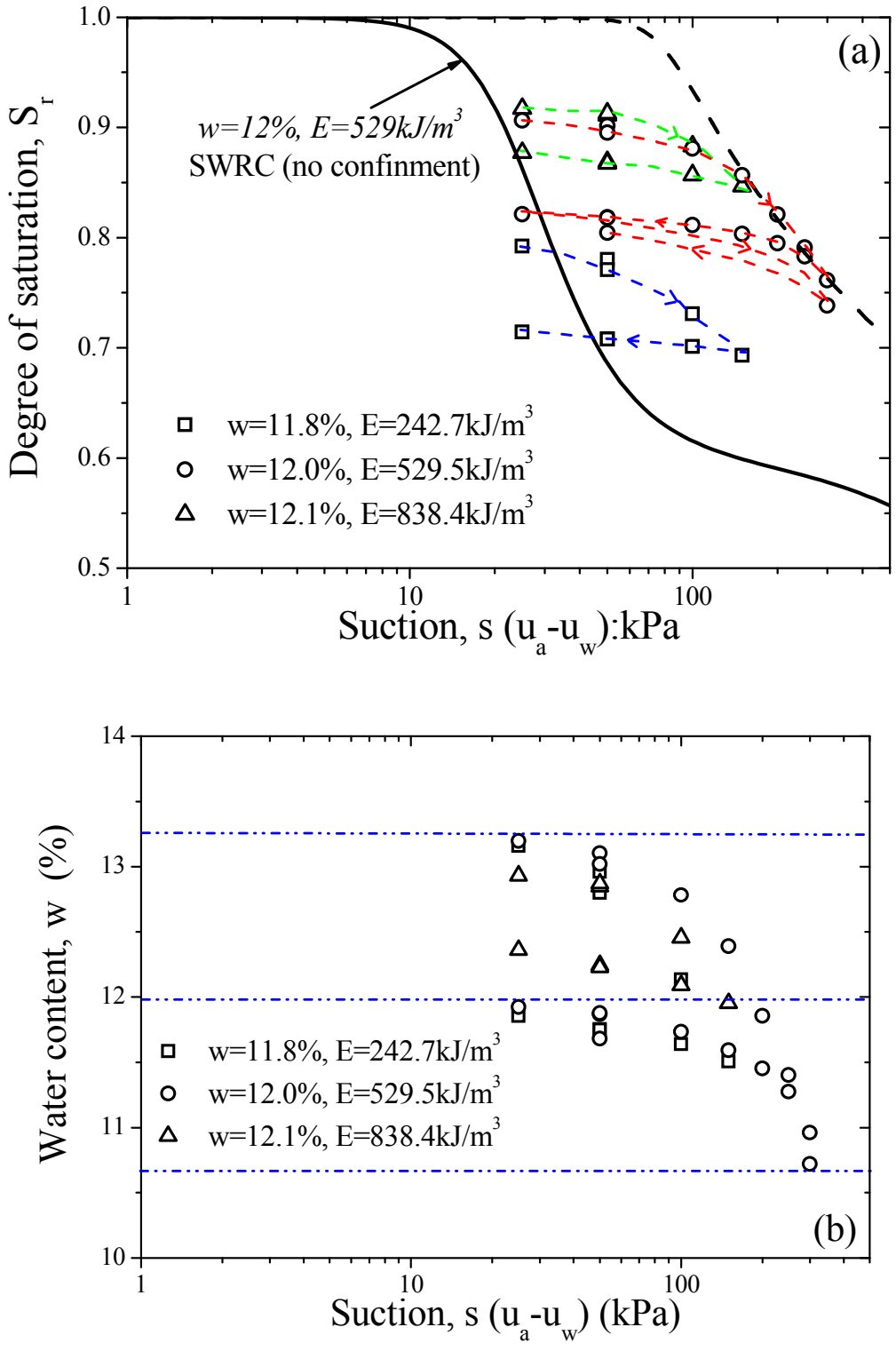

Figure 5.15 Water retention data of the drying-wetting cycles of specimens prepared at different energy levels and approximately same water content (a) in terms of degree of saturation and (b) in terms of water content.

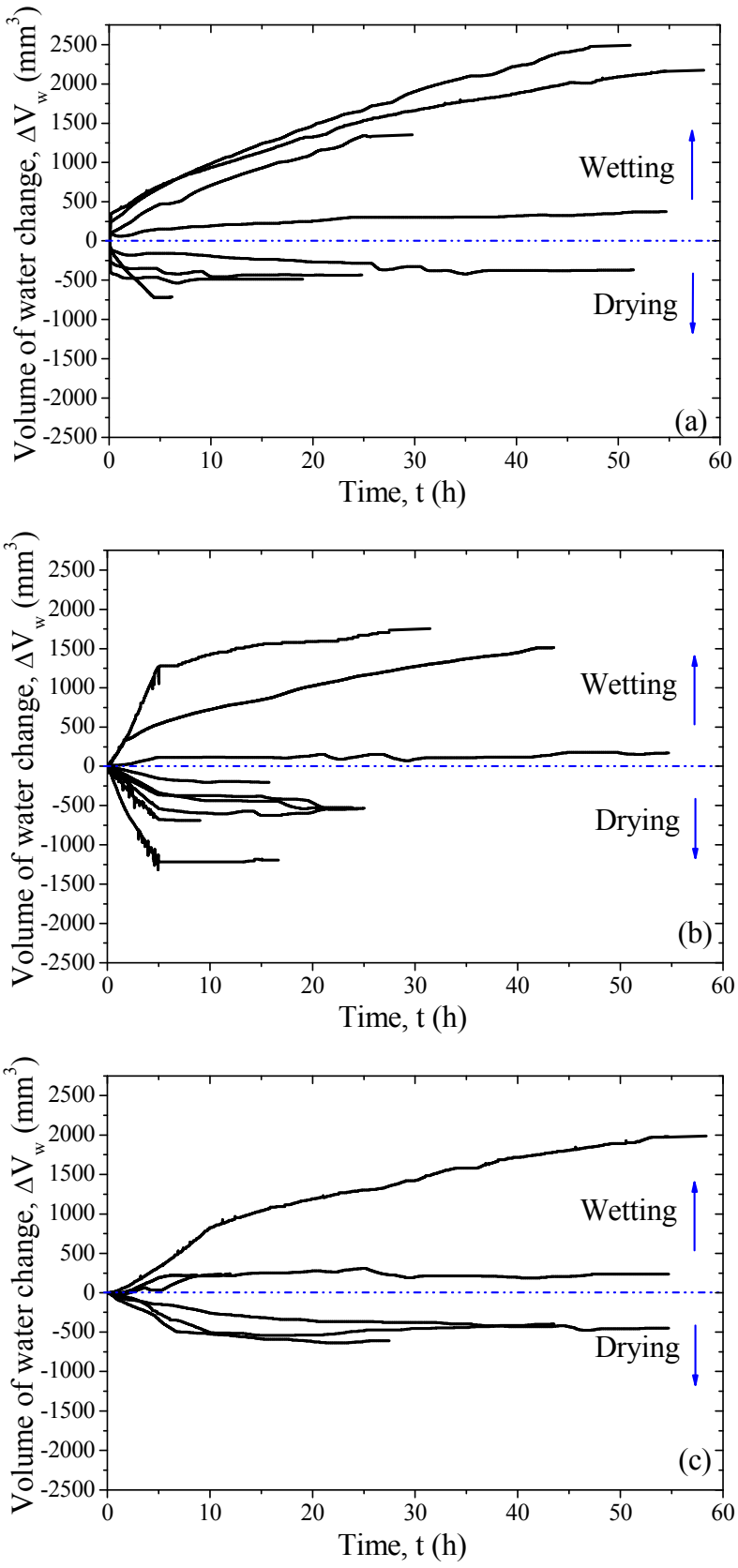

Figure 5.16 Variation of the volume of water during equalization stages (a) 254.5kN/m^3, (b) 529.5kN/m^3 show also a second drying cycle and (c) 838.37kN/m^3 254.5kN/m^3.

5.2.4 Saturated shear wave velocity for selected compaction specimens

A total of 4 compacted specimens were tested using bender elements under isotropic confined conditions for V_s evaluation under saturated conditions. Their compaction characteristics and testing conditions are given in

Table 5.4. The isotropic confining pressures were applied in a Bishop-Wesley triaxial cell and V_s was monitored using bender elements that were cantilevered in the 50mm diameter top cap and bottom pedestal (see earlier Figure 4.3). The confining pressures were incremented at a rate of 1kPa/min until they reached the desired confinement stress. When a given confining stress was attained it was kept constant while the axial displacements induced by confinement were monitored by an exterior LVDT (Linear variation displacement transducer with accuracy of 0.001mm), and axial strain was computed. Usually a period of 1hour was sufficient to allow for all axial displacements to take place and at the end of this period the V_s was measured.

Table 5.4. Summary of the initial conditions and testing program for the saturated states.

Test ID	Energy level, E : kJ/m^3	Water content , w: %	Bulk unit weight, γ_b: kN/m^3	Dry unit weight, γ_d : kN/m^3	Tip to tip distance $L_{tt\text{-}i}$: mm	Void ratio e	Water ratio e_w	Degree of saturation S_r	Confining pressure, σ_m kPa
24-1-S	529.50	8.50	18.63	17.17	98.94	0.54	0.23	0.42	100-250
24-2-S	529.50	10.54	20.47	18.52	98.72	0.43	0.28	0.66	100-250
24-3-S	529.50	11.80	21.18	18.94	97.96	0.40	0.32	0.80	100-250
24-4-S	529.50	14.40	20.94	18.30	97.90	0.45	0.389	0.87	100-250

Note that the isotropic confining pressure was applied in 50 kPa increments until reaching 250kPa and $L_{tt\text{-}i}$ refers to initial tip to tip length.

Figure 5.17 show the variation of the saturated of V_s in terms of confining pressure grouped by the specimen initial moisture content. In general the V_s witnessed an increase with increasing confining pressure for all specimens, although the contrary to the as compacted states the specimens prepared at higher initial void ratio showed the largest V_s (Figure 5.17). This seems to indicate that at saturated state, the initial void ratio a more pronounced effect on

V_s, which is consistent with the experimental findings obtained for a variety of compacted sandy type soils by Cha and Cho (2007).

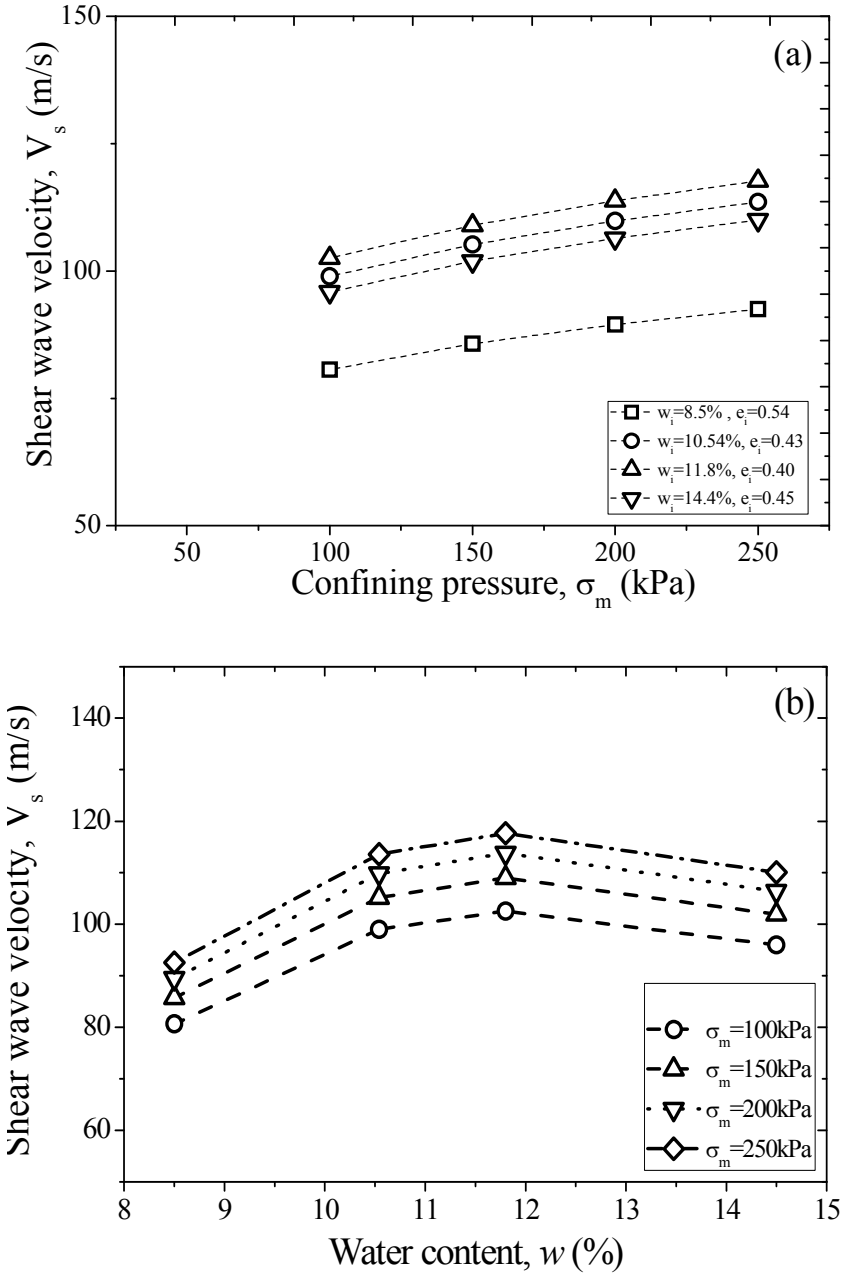

Figure 5.17 Variation of V_s in terms of (a) confining pressure and (b) moisture content for specimens compacted at energy level of 529.50kN/m^3.

5.3 SUMMARY

This chapter presented the results in relation to the characteristic unsaturated small strain behaviour of compacted soil. Both the as compacted states and post compacted states were studied. Salient features were observed for the as compacted behaviour along the four different energy levels considered. The unique water content-suction relationship, the increase of V_s with increase of energy level on the low water content range, and the decrease in mid water content range are worth noting. Furthermore, a close relationship was found between V_s and the degree of saturation, which was in turn related to the degree of aggregation reflected in the soil macrostructure, rather than with dry unit weight or water content, which were the initially anticipated governing variables.

The effect of depth was investigated in a series of tests in which the specimens were subjected to an isotropic compression under constant water content. The V_s was found to increase with confining stress, although the rate of increase was strongly associated with the initial water content.

To evaluate the importance of field variations of water content, a series of specimens were subjected to cycles of wetting and drying. There was a marked hysteresis both on the V_s-suction plane and in the water retention data. The V_s-s hysteresis amplitude differed for specimens compacted under different energy levels; higher amplitudes were found for specimens with lower initial dry unit weight, albeit still small (maximum within 30m/s). It was also noted that subsequent cycles of drying caused reversible V_s values whereas wetting paths still showed hysteresis, contributing to a successive increase in V_s. The results also showed that a great deal of understanding about the current state of compacted fills in post-construction stages can be achieved by simply conducting V_s field surveys in different climatic seasons, i.e. the larger the V_s variations, the poorer the conditions in terms of compaction degree that may be expected.

CHAPTER SIX

6 . EMPIRICAL FORMULATION FOR EVALUATING COMPACTED STATES USING SHEAR WAVE VELOCITY

6.1 GENERAL

This chapter describes the theoretical formulation for evaluating the degree of compaction based on the shear wave velocity and suction. First, general definitions related to terminologies used in this and subsequent chapters are introduced, followed by an explanation of the main aspects related to the propagation of a shear wave in soil. The empirical relationship that enables the degree of compaction to be evaluated based on the shear wave propagation and suction is then derived. The underlying assumptions are also discussed and explained in detail. For predicting the small strain shear modulus in as compacted state materials, a simple formulation for evaluating the modulus of compacted soil prepared with different water contents and compaction efforts is also developed.

6.2 DEFINITIONS

In this section, commonly used terms and sign conventions used in unsaturated soil mechanics that will appear throughout the following sections, are defined with the relevant terminology.

6.2.1 Signal and Axes convention

A Cartesian coordinate system is used, in which the axes denoted by numbers 1, 2, and 3 correspond to the x, y, and z directions. Compression is taken as positive, whereas dilation is considered negative. Suction refers to matric suction and is assumed to be positive (despite it representing negative pore water pressures).

6.2.2 Weight and volume relationships for unsaturated soils

The volume of an unsaturated soil unit V represents the sum of the volume of solids (volume of soil grains) V_s, volume of the pore fluid V_w and volume of the air V_a , or $V = V_s + V_w + V_a$.

The void ratio *e* represents the proportion of the volume of voids V_v ($=V_w+V_a$) to the volume of solids, or $e=\frac{V_v}{V_s}$ whereas the specific volume ν represents the volume of soil divided by the volume of solids, or $v=\frac{V}{V_s}=1+e$. The porosity represents the fraction of the volume of the voids over the total volume, or $n=\frac{V_v}{V}$. The total density ρ of an unsaturated soil unit is expressed as the sum of the contributing solid-water-air phases or $\rho=(1-n)\rho_s+nS_r\rho_w+n(1-S_r)\rho_a$ where S_r represents the degree of saturation.

6.2.3 Quantities describing the water content

The amount of water in soil can be expressed in terms of mass, known as the gravimetric water content, or in terms of volume, known as the volumetric water content. The terminology associated with the gravimetric water content in the thesis is simply water content. The water content is expressed by the mass ratio of water and solid particles in any unit soil volume $w=\frac{m_w}{m_s}$ whereas the volumetric water content is defined by the volume ratio of water and total volume of soil $\theta_w=\frac{V_w}{V}$. Conversely, in unsaturated soil, the amount of water in the soil is often represented by the degree of saturation (S_r), expressed by the ratio of the volume of water and volume of the voids, $S_r=\frac{V_w}{V_v}$. The different quantities can be interrelated by $\theta_w=nS_r=\frac{wG_s}{1+e}$ where *n* represents porosity, G_s is the specific gravity of solids, and *e* is the void ratio. Note that the amount of water stored in the voids can also be represented by the water ratio (e_w), and it is defined as the ratio of the volume of water and volume of the solids, or $e_w=\frac{V_w}{V_s}$.

6.2.4 Terminology associated with the compaction paths

In the following sections, two different terms are used to express the paths that soil experiences during compaction, that is, hydraulic wetting and mechanical wetting. Hydraulic wetting refers to wetting by an increase in the initial moulding water content, whereas

mechanical wetting refers to an increase in the degree of saturation caused by compaction under constant water content, where the equality $eS_r = wG_s$ holds.

6.3 EVALUATING COMPACTION BASED ON V_S AND SUCTION

The most important aspects that influence the shear wave velocity in soils are its current state, anisotropy, ageing, cementation, and temperature (see Appendix C for further details). The particular considerations made for this study related to these aspects are as follows:

a) V_s is assumed to be a function of the confining pressure, particle arrangement, and suction,
b) inherent anisotropy is not addressed because all the specimens were prepared using the same methodology,
c) ageing is not taken into account since its influence is nearly absent from sandy type materials,
d) the influence of cementation on V_s is not considered because a natural bonding agent is absent in the materials used in the fills, and the content of salts is negligible,
e) the effect of temperature on V_s is not considered since only the top part of the fills are likely to be exposed to drastic oscillations in temperature.

Next, the assumptions associated with the model are introduced and an empirical equation for estimating the degree of compaction based on the shear wave velocity and suction is derived.

6.3.1 Assumptions

The empirical relationship that enables the degree of compaction based on the shear wave propagation and suction to be evaluated, was derived from two main assumptions, that are presented here (further details are given in Appendix C).

Assumption 1: *The depth of moisture change or H_s that is affected by climatic fluctuations is limited to the top 1-1.5m depth.* Thus, the hydraulic hysteresis likely to be observed in these materials in cycles of wetting and drying is not accounted for in the formulation mainly because only a small portion of the ground profile is likely to experience these changes

(Figure 6.1). The H_s may be estimated based on the Thornthwaite moisture index (TMI) (Thornthwaite, 1948) distribution for Australian territories given in a report published by Austroads, 2004 , i.e. for Penrith Lakes location the equivalent H_s is 1.5m (AS 2870-1996; Fityus and Buzzi, 2008). This constitutes a relatively small portion of the ground profile at Penrith Lakes where an evaluation of the degree of compaction is sought, as evidenced by the historical data provided by the PLDC outlined in Chapter 3.

Assumption 2: *The field suction or moisture content variation below the depth of the active zone (or depth of moisture change) in time is small. Therefore it is assumed that the moisture content of the fill is likely to be the same as when they were compacted.* This seems reasonable given that Oliveira and Marinho (2007), and Mendes (2011), showed that for columns of soil and full size embankments, the upper layers are more susceptible to changes in moisture throughout the different seasons than those located at higher depths where approximately the same water content and suction is maintained.

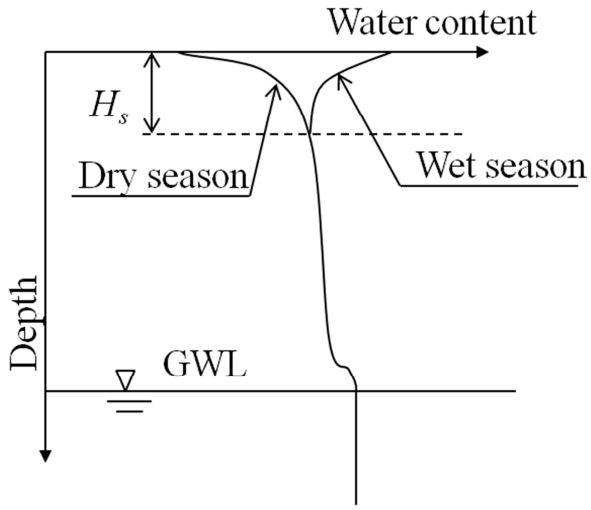

Figure 6.1 A profile of the ground water content exposed to seasonal climatic variations, (Note that the change in moisture in the H_s range is rather exaggerated).

6.3.2 Empirical formulation

The results of this study shown in Chapter 5 generally show that the propagation of the shear wave velocity in compacted soil is governed by a combination of the soil skeleton (particle arrangement or void ratio), applied confining pressure, and suction stresses. However, when

the soil is compacted, both the particle arrangement and change in the suction are derived from differences in the compaction history (i.e. compacted on the dry or wet side of OMC and different level of compaction energy). To better understand the individual effect of these parameters on V_s, additional compacted specimens were prepared at different compaction energies (i.e. an increase in dry unit weight or decrease in the void ratio) and subjected to a drying process (i.e. an increase in the suction).

6.3.2.1 Dry unit weight or void ratio influence

The V_s was monitored in seven different specimens prepared at a compaction water content of 10.5% for different compaction efforts (Table 6.1) applied in three layers, following the procedure given in Chapter 4. A compaction water content of 10.5% was selected because the suction contours in this range were nearly vertical and thus independent of the energy applied (see Figure 5.3 with a suction of 205 kPa). Figure 6.2 shows the relationship between V_s and e (or dry unit weight), showing that the shear wave velocity increases for smaller void ratios, an increase that appears to be linear under approximately constant suction (typically with a variation within 10kPa between specimens). Similar findings reported by Richart et al. (1970) and Cha and Cho (2007) for soils tested under saturated conditions agreed with the present results, which means that provided that the suction remains approximately constant, a change in the void ratio or dry unit weight causes a linear proportional change in V_s. The shear wave time domain traces for these specimens are shown in the Appendix G.

Table 6.1 Summary of the compaction states of the specimens prepared at *w=10.5%*.

Specimen ID	Water content, w (%)	No. Of blows	Compaction energy, E (kJ/m^3)
10.5-e-1	10.5	11	242.69
10.5-e-2	10.5	13	286.81
10.5-e-3	10.5	15	330.94
10.5-e-4	10.5	18	397.13
10.5-e-5	10.5	22	485.38
10.5-e-6	10.5	24	529.5
10.5-e-7	10.5	38	838.38

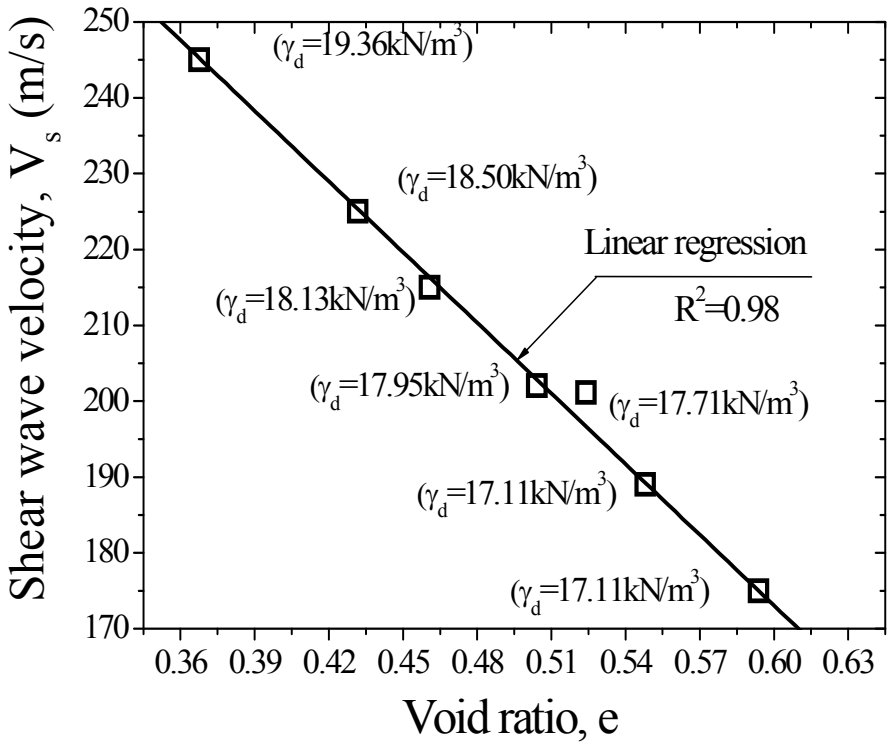

Figure 6.2 Shear wave velocity with increasing void ratio at approximately constant suction.

6.3.2.2 Influence of matric suction – drying process

The shear wave velocity was monitored in three different specimens prepared at a compaction water content of 15.8% with an initial suction of 9kPa. The specimens were left to dry for pre-determined time periods and whenever the difference in weight was significant, the specimens were wrapped in cling film and left for 6 hours in a temperature and moisture controlled room to attain moisture equilibrium. Thereafter, V_s was measured and then part of the specimen was trimmed and placed in an air tight container to determine the suction by the filter paper method. The time intervals selected were 20, 60, 90, 180, and 300 minutes. The volumetric changes caused by shrinkage due to drying were also monitored using a digital calliper; typically, the volumetric changes were under 1%. Figure 6.3, where the relationship between V_s with increasing suction is represented, shows that these parameters are associated, and in fact the shear wave velocity increased almost linearly in the low suction range.

As the soil becomes increasingly unsaturated, the shear wave velocity increased steadily and seemed to converge to a maximum value in the higher suction domain where a logarithmic increase in suction leads to a marginal increase in V_s. This behaviour is consistent

with the theoretical model of the contact force derived from interaction of the water meniscus between two spheres (Fisher, 1926; Figure 6.4), although there is a marked inflection point which likely corresponds to the value of the air entry suction. This inflection point may be interpreted as the result of the presence of bulk water and regulated ranges of the water menisci (Mancuso et al., 2002), which means that in a low range suction, the bulk water effect dominates the V_s behaviour owing to the absence of air, thus increasing nearly linearly with the logarithmic increase in suction. In contrast, for larger values of suction the amount air gradually increases, and the V_s behaviour is in turn governed by the water menisci developed with the particle contacts, while at very large suctions it tends asymptotically towards a maximum value.

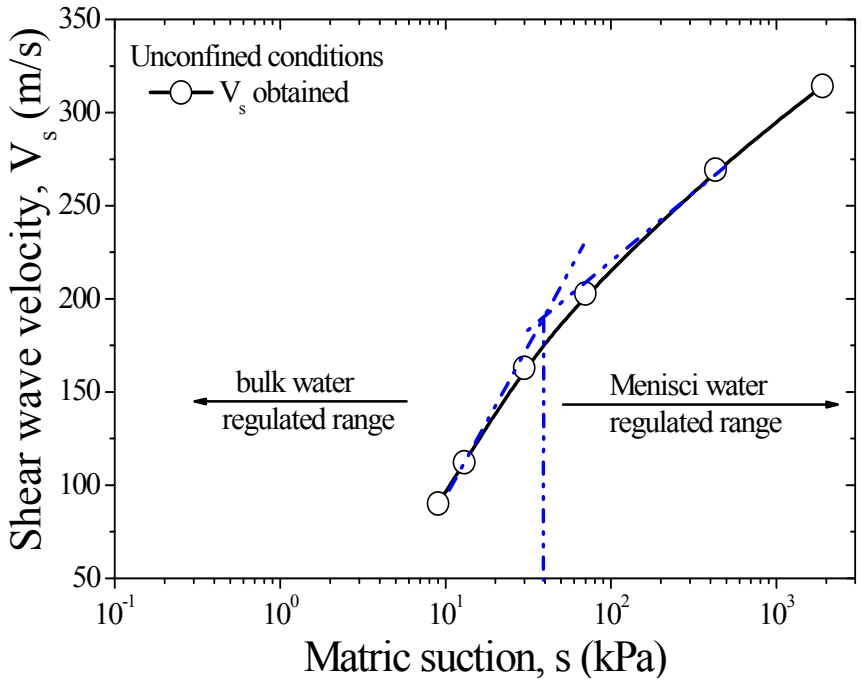

Figure 6.3 Shear wave velocity with suction (drying process) at approximately constant void ratio.

6.3.2.3 Combined effect of dry unit weight and suction

For saturated or dry conditions, the shear wave velocity for particulate materials, or V_{sat} can be given by Hardin and Richart (1963), Stokoe et al. (1991); Santamarina and Cascante (1996),

$$V_{s,sat} = \theta \left(\frac{\sigma'_m}{\sigma_r} \right)^{\beta} \tag{6.1}$$

where θ and β are empirical parameters, σ'_m is the mean effective stress and σ_r is a reference stress of 1kPa used for dimensionality. The empirical parameter β reflects the nature of the grain contacts; for instance β=1/6 for Hertzian contacts, β=1/4 for plastic spherical contact (angular or rough particles), β≈0.2 to 0.25 for sands (the looser the sand the higher the β), and β≈0.27 to 0.3 for kaolin (Cho and Santamarina, 2001).

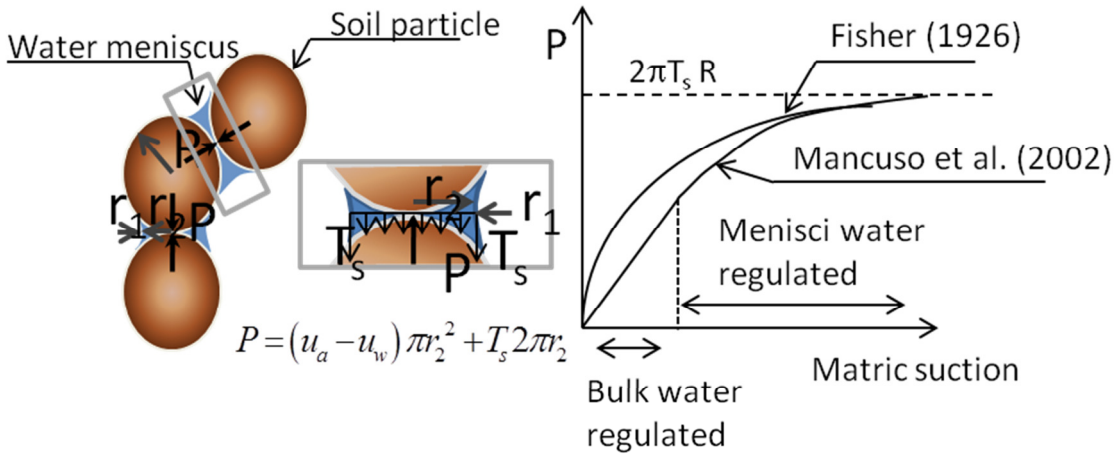

Figure 6.4 Contact force derived from the interaction of water meniscus between two spheres (modified after Mancuso et al., 2002).

Under unsaturated soil conditions, suction plays an important role in describing the current state of stress, and undoubtedly also governs the V_s. As outlined in Chapter 2, a number of empirical models have been proposed for modelling V_s under unsaturated conditions, usually by extending the Eq. (6.1) while considering the independent stress variables. For instance, the relationship proposed by Ng and Yung (2007) represented in Eq. (6.2), in which the unsaturated V_s is expressed by the product between $V_{s,sat}$ represented in the first term of Eq. (6.2), and the suction $s = u_a - u_w$ is represented by the second term.

$$V_{s,ij} = C_{ij} f(e) \left(\frac{\sigma_i - u_a}{\sigma_r} \times \frac{\sigma_j - u_a}{\sigma_r} \right)^{n/2} \left[1 + \frac{u_a - u_w}{\sigma_r} \right]^{bij} \tag{6.2}$$

where C_{ij} is a material constant representing the soil fabric given in m/s, *f(e)* is a void ratio function relating to the V_s dependency on void ratio, b_{ij} is an empirical exponent of suction which reflects the influence of suction on the V_s behaviour and the subscript $_{ij}$ refers to the propagation of the wave and polarisation of the particle motion. Neglecting the anisotropy influence between the different planes of wave propagation (see Appendix C), Eq. (6.2) may be simplified to:

$$V_s = C\, f(e)\left(\frac{\sigma_m}{\sigma_r}\right)^{n/2}\left[1+\frac{f(s)}{\sigma_r}\right]^b \tag{6.3}$$

While adopting *f(s)=s* as a linear function of suction, as shown in Eq. (6.2), may adequately predict the increase in V_s with suction, it provides an unlimited increase in V_s for an increasing *s,* and this is a limitation for the larger suction range. An alternative close form expression, which provides more realistic behaviour of V_s based on Figure 6.3, is described by:

$$f(s) = \left[\frac{\varphi}{\ln\left[\exp(1)+\frac{\phi}{s}\right]^a}\right] \tag{6.4}$$

where the coefficients ϕ, a, and φ are parameters that control the rate of increase of V_s with suction and the maximum V_s values at very high suctions, respectively. It is noted that Eq. (6.4) resembles the inverse of a commonly adopted SWRC function form (i.e. Fredlund and Xing, 1994). The inverse function is used because, contrary to the behaviour of the SWRC, in which the degree of saturation (or water content or volumetric water content) decreases with increasing suction, V_s increases with suction. Although a simpler *f(s)* expression based on a logarithm relationship adopted by Heitor et al. (2012) adequately reproduces V_s-*e* behaviour along the compaction plane, Eq. (6.4) is preferred because it provides a more realistic approach in the high suction range.

In Eq. (6.3), the dependency of V_s on the void ratio is represented by *f(e)*,which is often adopted as an exponential function. This is somewhat contrary to the experimental results represented in Figure 6.2 where there is a linear increase in V_s with the void ratio, at nearly constant suction. Furthermore, Cha and Cho (2007) showed that the saturated V_s for any given void ratio can be expressed by a linear function of the V_s values corresponding to the upper and lower limits of the void ratio, which is more consistent with the results obtained. Thus it seems reasonable to consider an *f(e)* so that the current state of the soil in terms of the void ratio can be obtained in relation to an idealised upper and lower bound, or

$$f(e) = \frac{e_{\max} - e}{e_{\max} - e^*_{\min}} \tag{6.5}$$

where e_{max} is the maximum void ratio and e^*_{min} is the minimum void ratio and both are material parameters. While the maximum void ratio or e_{max} can be determined by AS 1289.5.1-1998 (e_{max}=1.04), e^*_{min} has a slightly different meaning to that of the conventional e_{min} usually determined for non-cohesive materials, and thus e^*_{min} refers the lowest void ratio (i.e. e^*_{min}=0.29) representing OMC conditions for modified compaction effort.

The void ratio, or *e* expressed in Eq. (6.5), can easily be converted to the dry unit weight or γ_d using $\gamma_d = \frac{\gamma_w G_s}{1+e}$ where γ_w represents the unit weight of water and degree of compaction, or relative compaction (*R*) can be obtained by considering $R(\%) = \frac{\gamma_{d,field}}{\gamma_{d,lab}} \times 100$ where $\gamma_{d,lab}$ represents the OMC maximum dry unit weight for standard compaction energy, and $\gamma_{d,field}$ is the dry unit weight measured in the field. In this way the field degree of compaction can be established based on V_s and suction (or water content, see Figure 5.3a).

Considering $V_{s,sat} = C\left(\frac{\sigma_m}{\sigma_r}\right)^{n/2}$, Eq. (6.3) can be rewritten as follows,

$$V_s = V_{s,sat} f(e)\left[1 + \frac{f(s)}{\sigma_r}\right]^b \tag{6.6}$$

with *f(e)* expressed by Eq. (6.5) and *f(s)* expressed by Eq. (6.4). For saturated conditions, when s=0, Eq. (6.6) converges into a similar form of Eq. (6.1), which allows for a smooth transition between saturated and unsaturated states. This implies that V_s has its minimum value at saturated conditions and increases when the soil enters the unsaturated domain. Notice that after air entry value is attained the changes in V_s are minimal. In that sense, when air entry value is reached V_s decreases just marginally with decreasing suction and in a way it can be thought that saturated conditions are recovered at that point.

In the next sub-section the predicting capabilities of the proposed approach will be evaluated.

6.3.3 Verification of the empirical formulation

To verify the empirical formulation, comparisons were made between the predictions of the proposed model, and the test results for as compacted and post compacted states shown earlier in Chapter 5.

6.3.3.1 As compacted states

The parameters of the model, including soil materials parameters are listed in Table 6.2. Note that just one simple set of parameters caters for a range of different compaction states. For as compacted states, confinement is absent and therefore the term of $V_{s,sat}$ Eq. (6.4) is assumed to be a constant. The test data from the specimens represented in Figure 6.2 and Figure 6.3 are replotted, together with the predictions in Figure 6.5. Figure 6.5a shows that the *f(e)* predictions correctly translate the experimental trends whereas Figure 6.5b shows that *f(s)* adopted in Eq. (6.6) provides more accurate predictions than the linear function of suction assumed in Eq. (6.2), particularly in the higher suction range (i.e. s>30kPa). There are however, small discrepancies in the lower suction range (i.e. s<15kPa) that are related to the influence of the bulk water on the behaviour of V_s (Figure 6.4). The relative importance of this range within the compaction states is probably insignificant given that even if the water content is increased, the soil will never reach fully saturated conditions because of the existence of a possible ultimate compaction state outlined in section 5.2.1. Furthermore, this *f(s)* shape is also consistent with the experimental observations of Sawangsuriya et al, 2008 on the small strain shear modulus.

Table 6.2 Summary of the model parameters as compacted states

		Material parameters				Fitting parameters		
		e_{max}	e_{min}	$V_{s,sat}$: m/s	φ	ϕ	a	b
Present study	Silty sand	1.04	0.23	42	102	180	2.3	0.47
Sawangsuriya et al (2008)	Sand clay SC*	0.89	0.21	60	100	711	1.12	0.47

*letter refers to Unified soil classification system (USCS)
Note that: e_{max} and e_{min} for Sawangsuriya et al (2008) are unknown and the values considered were assumed to be reasonable.

The predictions, together with the test data of specimens compacted with different initial water content and energy levels are given in Figure 6.8. There was a good agreement between the predicted results and the actual trends. Similarly, remarkably consistent shapes were obtained for the three different energy levels represented, albeit in the prediction in the high moisture content range lead to small inaccuracies that are mainly associated with the lower V_s values for higher energy levels. This is mainly the result of the over compaction described in the previous chapter (see section 5.2.1.2), and found to be associated with change

of the soil macrostructure, which is not explicitly considered in the model. This constitutes a limitation for the present framework. Nevertheless the approximation may be considered acceptable, usually within a 20m/s interval, which is reflected on the 1:1 plot between the measured and predicted V_s represented in Figure 6.7.

The proposed model was also used to predict the experimental data for specimens of sand clay that were compacted at different energy levels and water contents, and reported in Sawangsuriya et al. (2008). The material and fitting parameters are also given in Table 6.2, and the experimental data and the model predictions are given in Figure 6.8. The predictions agree well with the results of the experiments, despite the fact that both e_{max} , e_{min} were unknown and the values adopted were found to be reasonable. Despite the more pronounced overlapping over compaction in this soil, the Eq. (6.6) still correctly predicts the experimental trends. The predicted and measured values of V_s are also compared for this soil, in Figure 6.7. Likewise the silty sand used in this study, the majority of the predicted and measured values matched well within an interval of 20m/s.

6.3.3.2 Post compacted states: confining pressure

The main difference between the performance of the model in relation to the as compacted states, lies on how we consider the term relating to the saturated shear wave velocity, or $V_{s,sat}$. For as compacted states, given the absence of confinement, $V_{s,sat}$ was taken as an additional constant but in fact Eq. (6.6) implies that $V_{s,sat} = C\left(\frac{\sigma_m}{\sigma_r}\right)^{n/2}$ which is naturally a function of the level of pressure, or confinement. To validate the model and calibrate the parameters to be used for a field comparison and assessments, the V_s results of the confining pressures and the saturation tests, reported earlier in section 5.2.2, were used. The parameters of the model adopted are listed in

Table 6.3. The prediction of the confining pressure, together with the test data of specimens compacted with different initial water content and energy levels are given in Figure 6.10 as well as the prediction of the saturated shear wave velocity obtained for specimens compacted at various water contents and energy level of 529.5kN/m^3. There is a good agreement between the predicted results and the tendencies of the actual test data. As expected, the model correctly predicts the increase of V_s with increasing confinement. The strong non-linear

increase of V_s on the low confining stress range reported by Claria and Rinaldi (2007), particularly on the specimens compacted to higher water contents or close to saturated states, is not observed. This is possibly related to the levels of confining stress adopted, i.e. above 50kPa in this study. In contrast, for higher confining stress levels the predicted behaviour is consistent with the experimental observations of Claria and Rinaldi (2007) that are represented schematically in Figure 6.9.

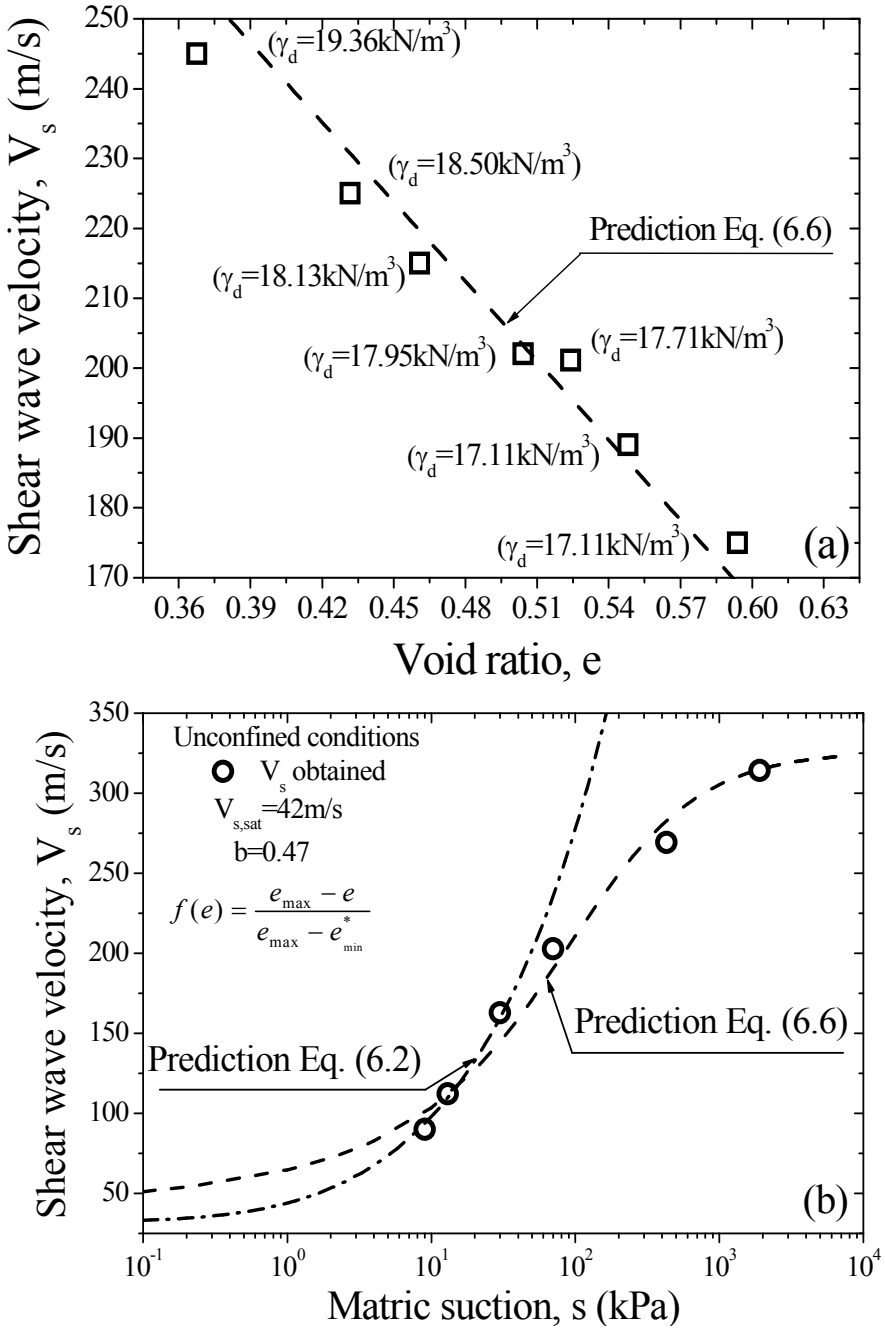

Figure 6.5 Comparison between the test data and model predictions, (a) influence of void ratio and (b) influence of suction.

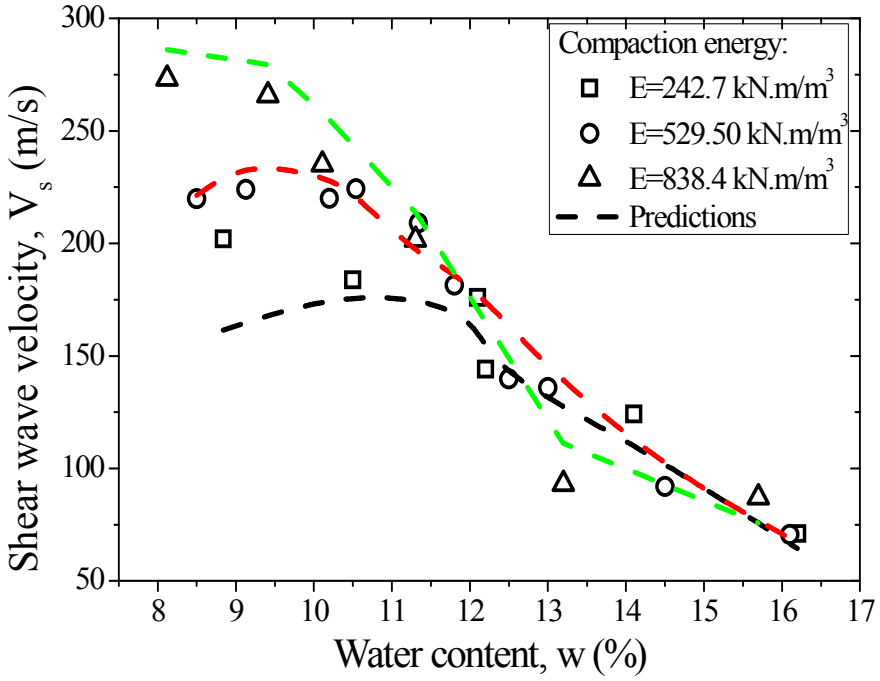

Figure 6.6 Comparison between the test data and model predictions for different water content and energy levels.

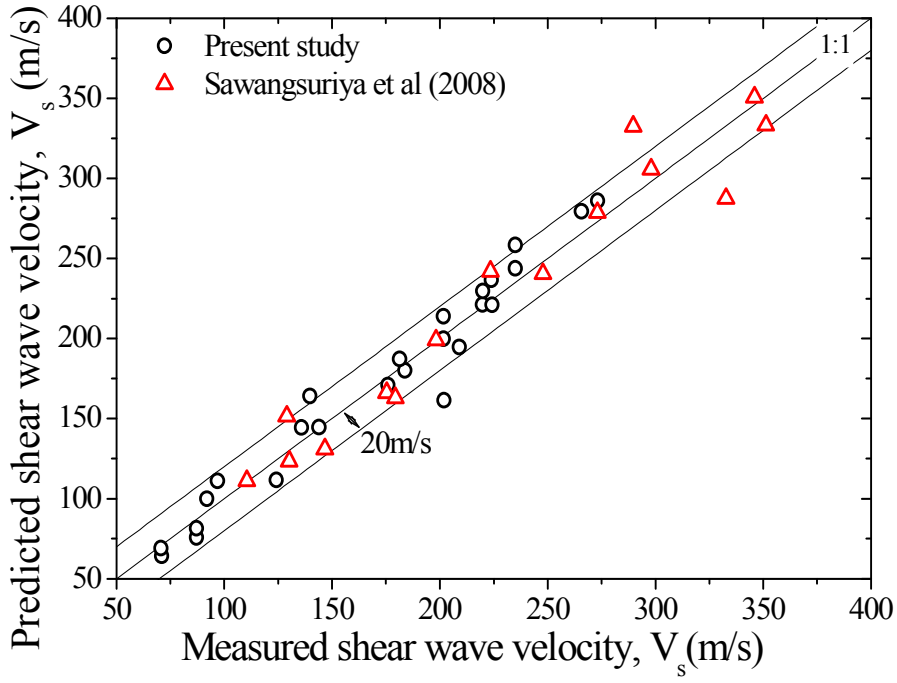

Figure 6.7 Comparison between the test data and model predictions for the present study and data from Sawangsuriya et al. (2008).

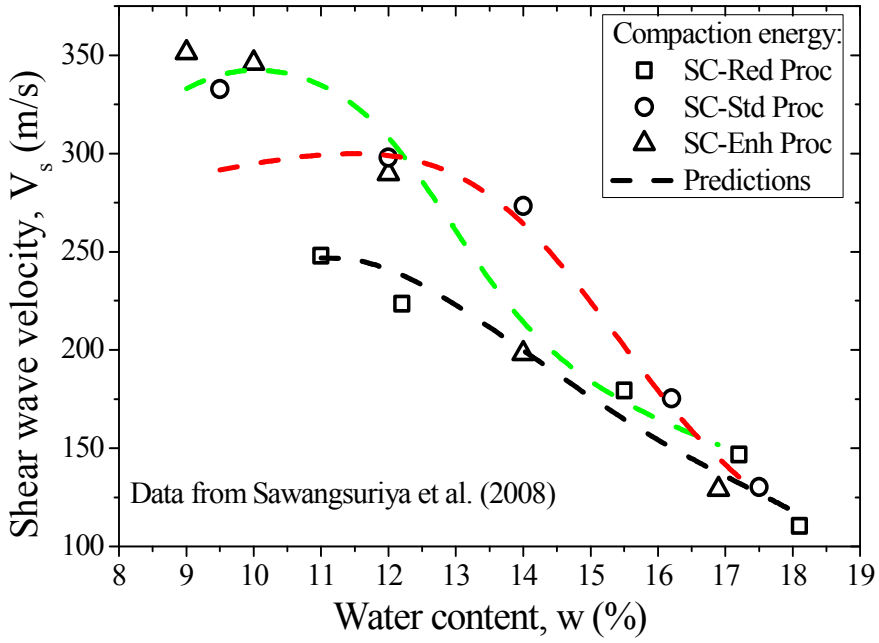

Figure 6.8 Comparison between the test data and model predictions for a sand clay soil for different water content and energy levels, data from Sawangsuriya et al. (2008).

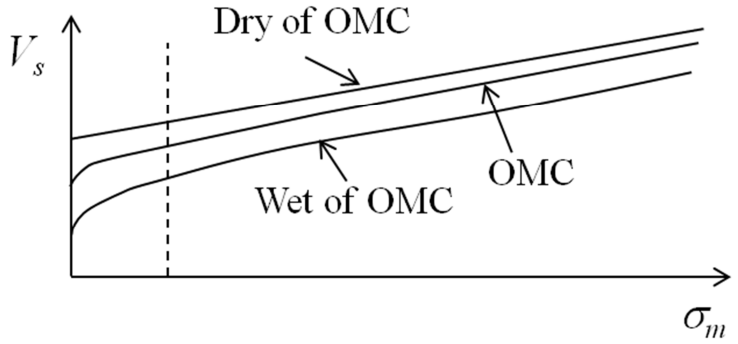

Figure 6.9 Effect of the level of confinement on V_s (modified after Claria and Rinaldi, 2007).

Table 6.3 Summary of the model parameters post compaction states

	Material parameters				Fitting parameters		
n	e_{max}	e_{min}	C	φ	ϕ	a	b
0.3	1.04	0.23	30.5	100	170	2.0	0.49

There are however, some small discrepancies between the predictions and the test data, particularly on the specimens prepared at the dry side of OMC. The model tends to slightly over estimate V_s and while this is not evident for the as compacted states it is certainly worthy of note for increasing confinement. The reason for this difference is likely related to the fact that a common set of parameters, i.e. parameter C and n, are used to model the considerably different soil fabric that occurs along the compaction curve. While the soil compacted to water contents around OMC and wet of OMC share some similarities in terms of the soil macrostructure (see section 4.2.4.3), soil compacted to water contents on the dry of OMC differ. This difference in structure is likely to be the cause of a small degree of scattering in the high V_s range, typically between 325m/s and 400m/s, as observed in the Figure 6.11. Nevertheless, the response of the model throughout a wide range of different water content and energy levels may still be considered acceptable (Figure 6.11).

6.3.4 Analysis of the empirical formulation

In this section, the effect of the void ratio and suction, and the parametric study of the proposed relationship are addressed. While one parameter is changed the others are held constant.

6.3.4.1 Effect of the void ratio and suction

To investigate how the void ratio and suction influence the prediction, the void ratio and suction were checked while the other parameters constant were kept constant (Table 6.3), as represented in Figure 6.12a and Figure 6.12b, respectively. Figure 6.12a shows that the slightly smaller void ratios yielded higher values of V_s, which is consistent with the well reported void ratio dependency on both G_0 and V_s (i.e. Richart et al., 1970). Moreover, the difference observed for the V_s-s curves is rather small in the low suction range, but it becomes noticeable in the medium and high suction domains. This behaviour is in accordance with the SWRC of the compacted specimens shown earlier in section 4.2.2.4 and with the void ratio dependent Gallipoli et al. (2003) hydraulic model. Furthermore, the implicit concept behind these curves is that two specimens compacted to the same void ratio, one at the dry of OMC and the other on the wet of OMC, would lie on the same curve. This is because more emphasis is placed on the void ratio and suction pair effect on V_s, although inevitably the difference in fabric is to some extent taken into account.

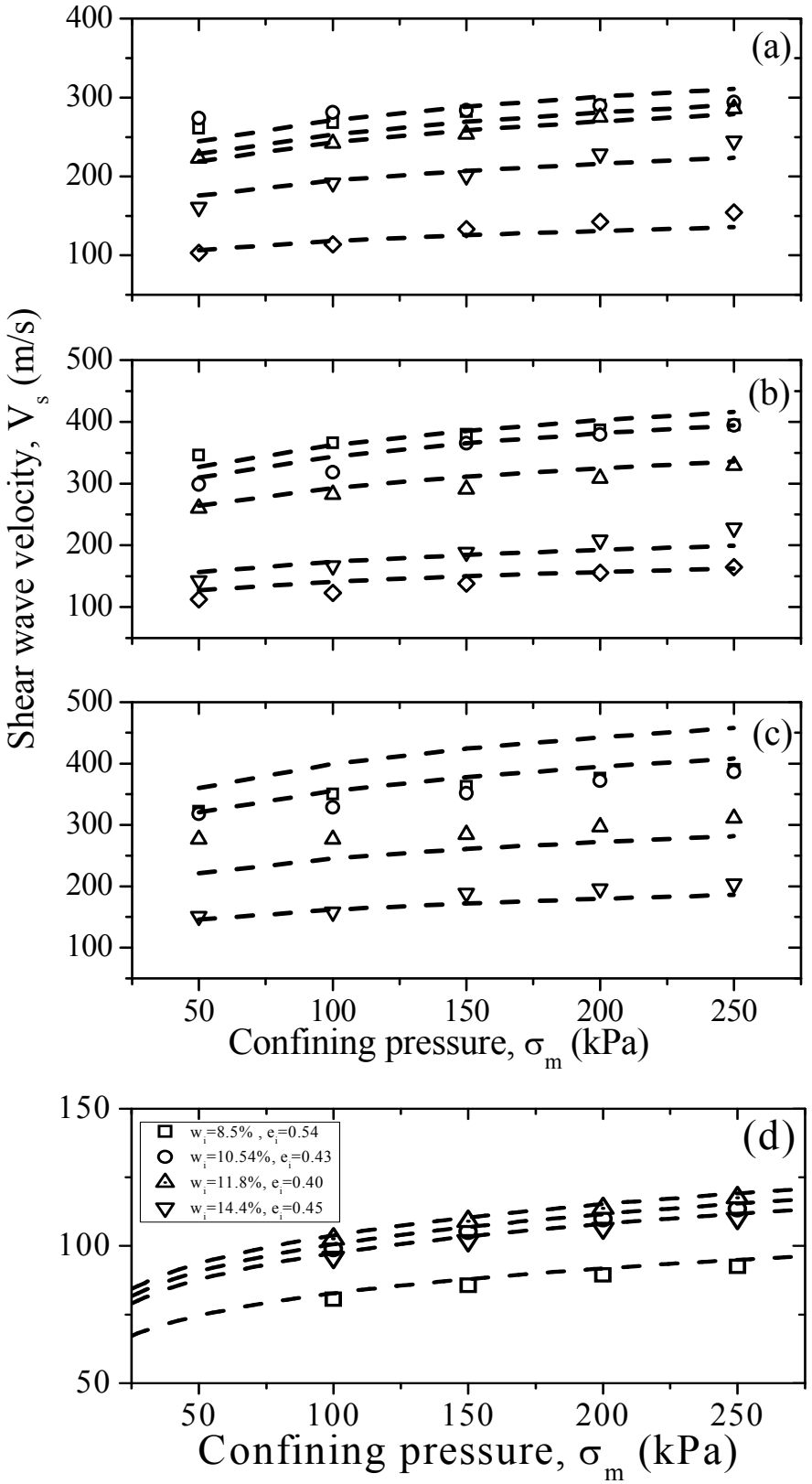

Figure 6.10 Comparison between the test data and model predictions with (a) to (c) increasing confining pressure and (d) for the saturated states.

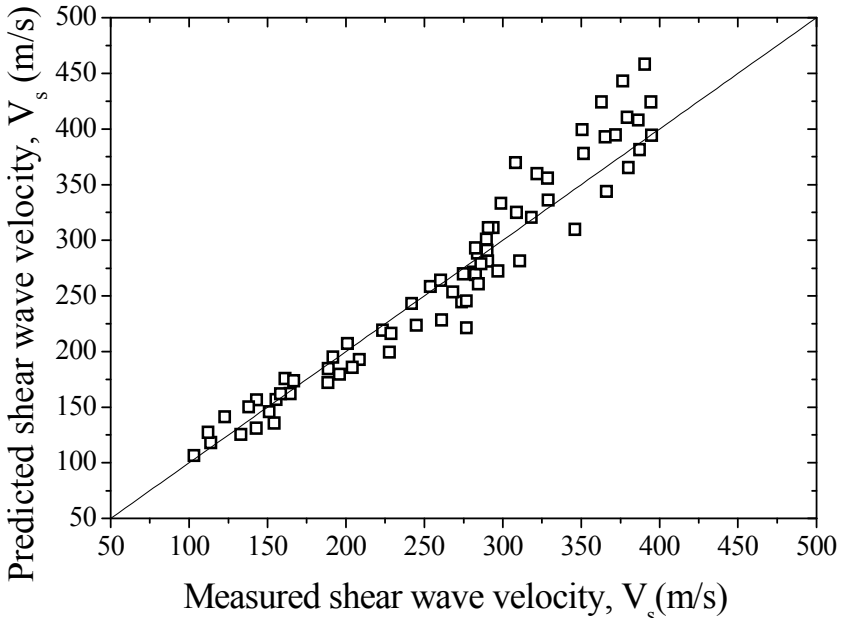

Figure 6.11 Comparison between the test data and model predictions with increasing confining

The higher suction on the dry side of OMC prevents particle slippage and compaction, and yields larger void ratios and more aggregated macrostructure, whereas on the wet side of OMC the aggregated macrostructure changes into a matrix and when void ratio reaches the ultimate state, it remains approximately constant, which means that a decrease in V_s is caused solely by a decrease in suction.

Figure 6.12b shows that for constant suction, V_s increases linearly with a decrease in the void ratio. The slope of the linear relationship gradually becomes larger for larger suction values, which indicates that the prediction is capturing the strengthening of the soil skeleton, caused by an increase in suction, as was also reported by Cho and Santamarina (2001).

6.3.4.2 Parametric study

A parametric study of the proposed *f(s)* shows the behaviour of the V_s-*s* curves under the separate influence of the different parameters. The parameter φ controls the V_s values at very large suctions. Its effect on the predictions can be seen in Figure 6.13a where φ varies between 50 and 200 while the other parameters remain constant. Figure 6.13b shows how parameter ϕ influences the initial break of the curve and represents the inflection point. Parameter ϕ provides an indication of the range where V_s converges to a maximum value, such that larger the value of ϕ is, the larger the suction when V_s start to converge to a

maximum value. The parameter *a* influences the break in the V_s-*s* curve into the bulk water regulated domain. Figure 6.13c, where the effect of *a* is represented shows that for smaller values of *a*, the V_s-*s* curves show smoother transitions between the bulk and menisci water regulated domains.

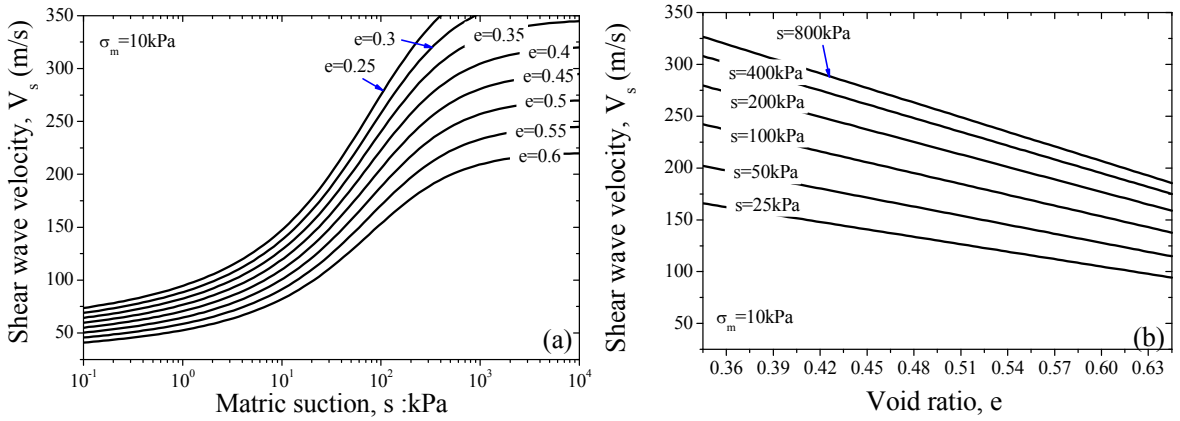

Figure 6.12 Influence of (a) the void ratio, and (b) suction, on the model predictions.

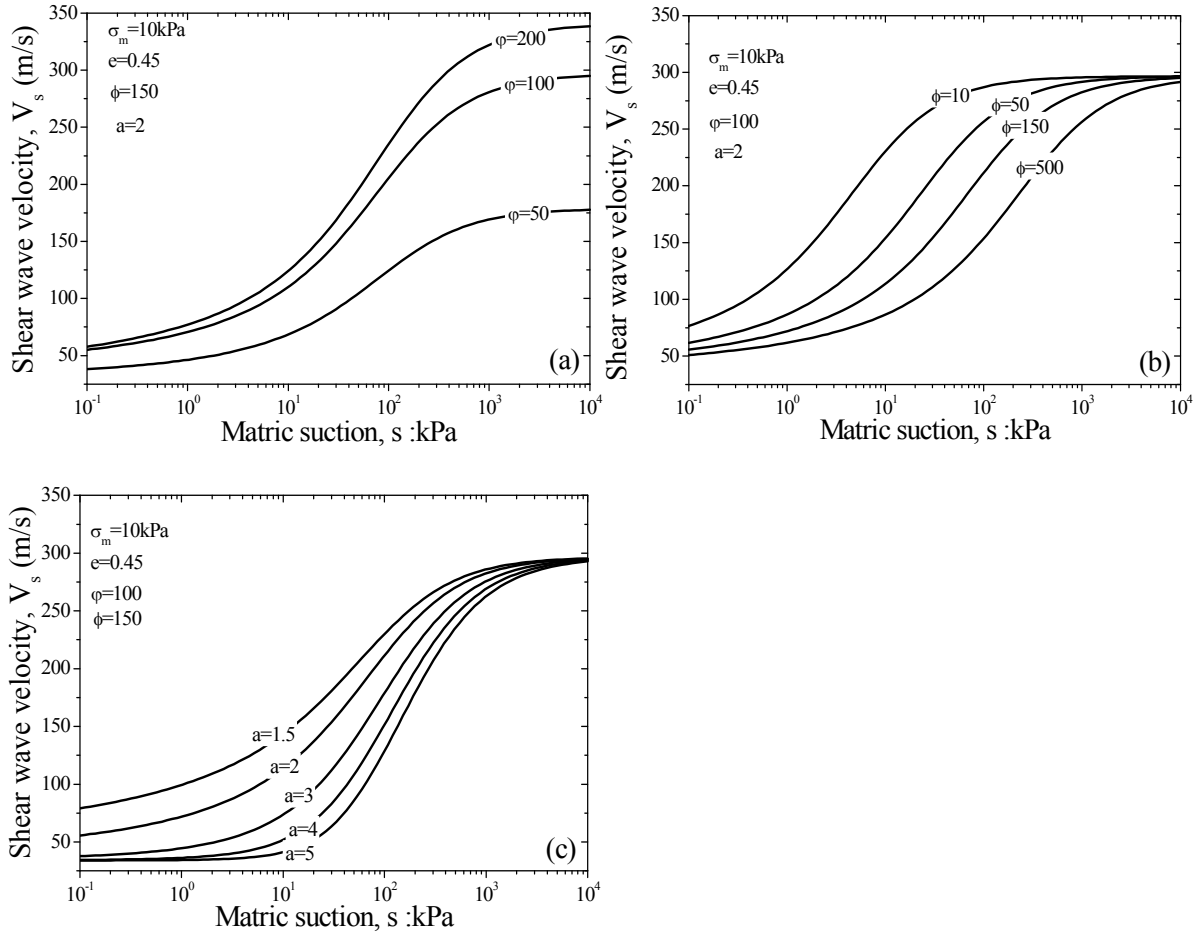

Figure 6.13 Parametric study of the *f(s)* proposed function.

6.4 SMALL STRAIN SHEAR MODULUS FOR AS COMPACTED STATES

To describe G_0 adequately, the void ratio dependency and current mean effective stress should be considered. A general relationship for G_0 in saturated soil proposed by Mitchell and Soga (2005) can be expressed by:

$$G_0 = Af(e)\left(p'\right)^n \tag{6.7}$$

where A is a parameter associated with the soil structure, $f(e)$ is a function of the void ratio, p' is the mean effective stress, and n is a fitting parameter associated with the state of stress. Although the fitting parameters n and A are not dimensionless in Eq. (6.7) and depend on the units chosen, they can be made dimensionless by normalising the mean effective stress term and G_0 by a reference pressure p_r (e.g. atmospheric pressure, p_a = 100 kPa), and by a reference modulus (G_r) taken as the saturated shear modulus of a specimen compacted at OMC with a standard compaction effort, respectively.

Under unsaturated conditions the effect of pore air (u_a) and water pressures (u_w) or suction (u_a - u_w) on the behaviour of G_0 are of key importance. The mean effective term in Eq. (6.7) can be modified to describe the state of stress on unsaturated soil following an expression proposed by Khalili et al. (2004), with the effective stress parameter χ form suggested by Vanapalli and Fredlund (2000) to be $\chi = S_r^{\kappa}$. Thus, Eq. (6.7) can be normalised and extended as follows:

$$\frac{G_0}{G_r} = Af(e)\left[\frac{\left(p-u_a\right)+S_r^{\kappa}\left(u_a-u_w\right)}{p_r}\right]^n \tag{6.8}$$

where κ is a parameter related to the plasticity index and the void ratio function $f(e)$ follows Lo Presti (1995), as suggested for a wide range of soil types, $f(e) = e^{-x}$, where x is the void ratio exponent parameter.

The parameter A in Eq. (6.8) is associated with the soil structure and is usually taken as a constant. However, the structure changes in the compacted specimens such that A should be

defined as a function of an alternative variable related to the compacted condition. Among the variables involved in the compaction process (i.e. moisture content, suction, dry unit weight), the degree of saturation S_r seems to be the most adequate on the basis of the experimental data shown earlier in section 5.2.1.2, and Toll (2000) has also suggested that S_r can be associated with the degree of aggregation. Therefore, A can be defined as $A(S_r)$, where changes in soil structure are assumed to be related to changes in S_r. In practical applications, the $A(S_r)$ relationship is likely to be defined for only one energy level, i.e. typically the standard compaction energy. For this reason, the points belonging to the equivalent standard compaction energy are used to establish the $A(S_r)$ relationship, whereas the data from the additional energies are used to validate it.

The parameter A is calculated using Eq. (6.8) and the parameters adopted are summarised inTable 6.4. Figure 6.14 shows the computed A with respect to the variation of S_r, which can be approximated by Eq. (6.9) based on the maximum saturation value (S_{max}) defined as the asymptotic degree of saturation line shown in the previous chapter.

$$A(S_r) = a_s \left[\frac{S_{max}}{S_r} - 1 \right]^{b_s} \tag{6.9}$$

where a_s and b_s are empirical parameters that can be found using the least square method fitting procedure (i.e. Kemmer and Keller, 2010). Once $A(S_r)$ function is known, G_0 can be predicted for any point located in the compaction plane using Eq. (6.8), and assuming that the net-confining stress term ($p - u_a$) is null for unconfined conditions. G_0 values are compared with the predicted values in Figure 6.15. The predictive procedure may be considered satisfactory (standard error of 3%), considering that the structure derived from different compaction conditions was not directly quantified by the relationship proposed in Eq.(6.8). The results support the argument that S_r can be used to indicate the structure of the compacted soil. However, in view of the fact that S_r is described by changes in the macroporosity, it should not be used as an absolute method to quantify the structure of the compacted soil (Romero et al., 1999).

The constant moisture content contours representing different compaction histories were predicted using Eq. (6.8) and (6.9) and are shown in Figure 6.16. These contours

represent the mechanical wetting paths that the soil experiences when compaction energy is increased, whereby the changes in void ratio and dry unit weight are directly represented by the degree of saturation. In the lower range of saturation (S_r < 0.67), an increase in the dry unit weight is accompanied by an increase in G_0 and a reduction in macroporosity of the soil structure. This is consistent with the CT-scan images of the specimens compacted with increasing compaction energy (see earlier Figure 4.39). Furthermore, MIP studies performed by Tarantino and De Col (2008) in statically compacted kaolin specimens also confirm that while the microporosity range is relatively unaffected by the increase of compaction pressure, the change in dry unit weight is directly associated with the reduction in the macroporosity. Similar findings were also reported by Cuisinier and Laloui (2004) for clay specimens subjected to mechanical loading. A further reduction in macroporosity contributes to an additional increase in G_0 leading to a peak at S_r = 0.77. Thereafter, the soil structure would gradually change from an "aggregated" type to a "matrix" type. This lends support to the assumption that G_0 is sensitive to changes in particle aggregation, as indicated by the three distinct regions in Fig. 6.14. These findings are also consistent with the experimental observations of Marinho et al. (1994) where larger values of G0 were obtained for water contents slightly before attaining OMC.

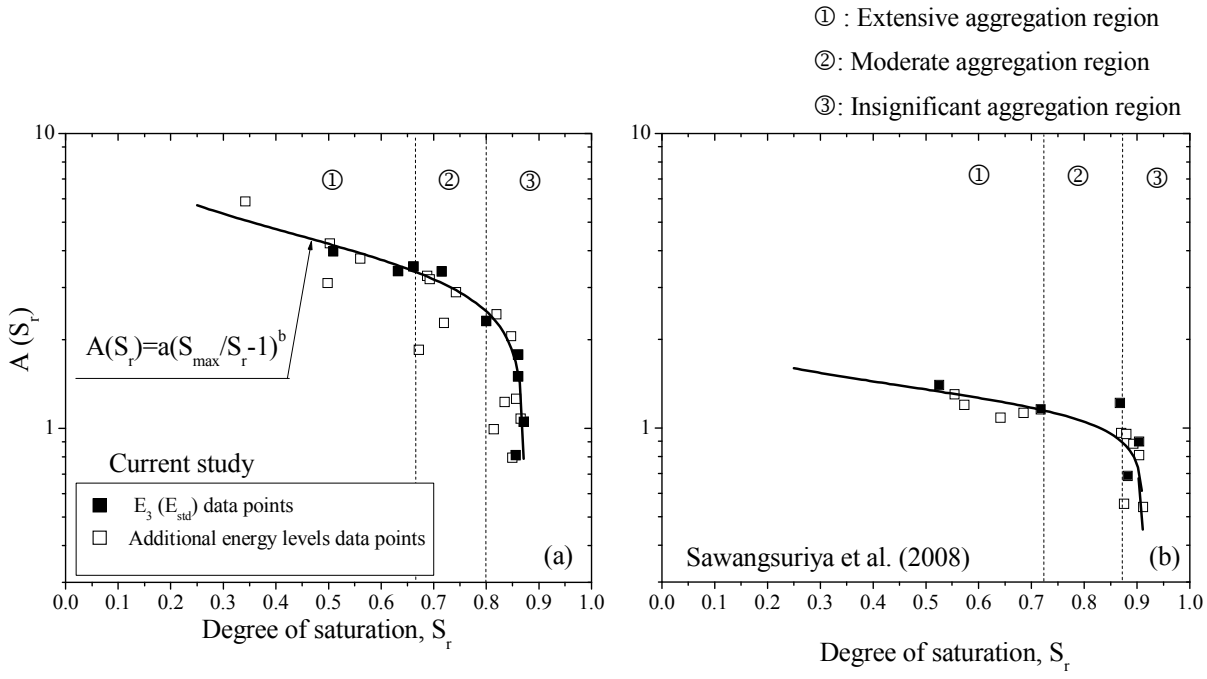

Figure 6.14 Parameter *A* for specimens of (a) silty sand and (b) clayey sand (Sawangsuriya et al., 2008) compacted at different energy levels.

Table 6.4 Empirical parameters based on laboratory observations

Parameters	Sandy silt soil (Current study)	Sandy clay soil (Sawangsuriya et al., 2008)
Stiffness coefficient n	0.2	0.2
Void ratio exponent x	1.7	1.9
p_r (kPa)	100	100
G_{sat} (kPa)	7	25
κ parameter	1.75	2.02
Confinement (kPa)	0	0
S_{max}	0.872	0.912
a	4.55	1.38
b	0.25	0.143

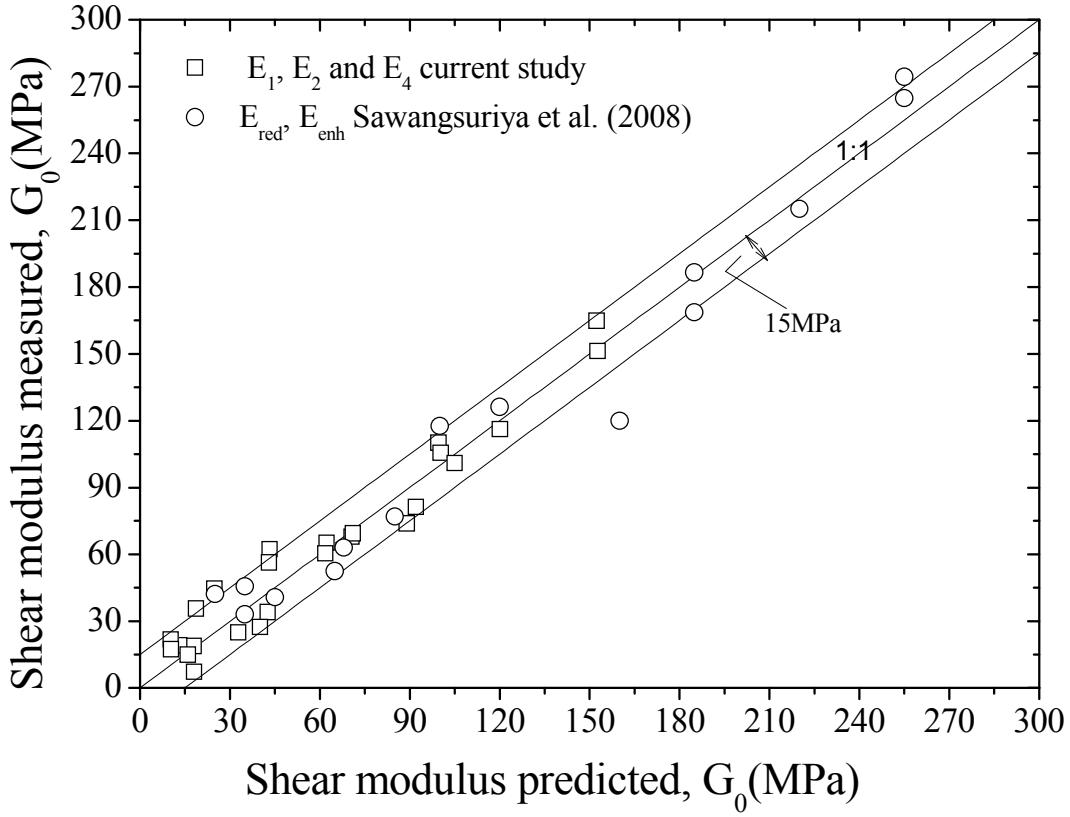

Figure 6.15 Predicted and measured small strain shear modulus for soils compacted with different conditions using Eq. (6.8).

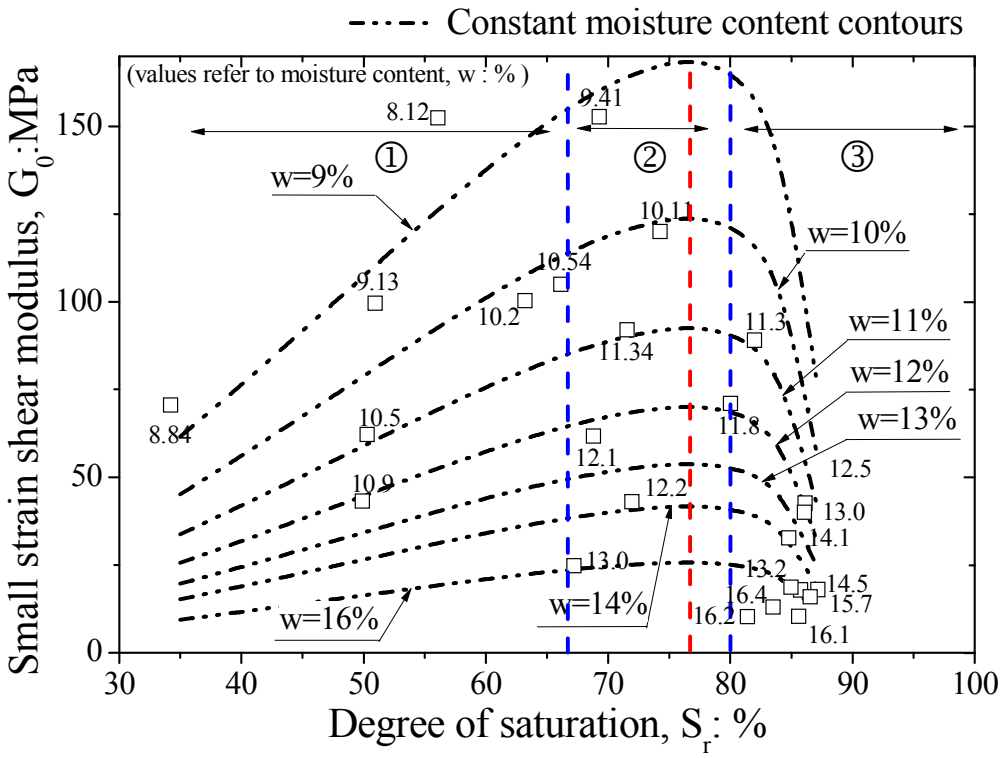

Figure 6.16 Variation of G_0 with S_r along water content contours.

6.5 SUMMARY

The empirical formulation for evaluating the current void ratio or degree of compaction based on shear wave propagation and suction was presented in this chapter. First, the aspects related to the propagation of shear wave on soils were introduced and considerations were made to its relative importance for evaluating the degree of compaction. Next, the underlying assumptions made in the formulation were thoroughly described and explained.

The shear wave velocity (V_s) was studied for additional compacted specimens where the influence of the void ratio and suction were investigated separately. The results showed that V_s varied linearly with the void ratio under approximately constant suction conditions, whereas it showed a non-linear variation with suction (resembling an inverse SWRC shape) at an approximately constant void ratio. A general V_s relationship developed for unsaturated soils was modified to incorporate the combined effect of changes in the void ratio or *f(e),* and suction or *f(s),* observed for different states of compaction. The predictions of the proposed relationship were compared with the test data reported in Chapter 4. There was good

agreement between the predictions and the actual trends, for both the as compacted and post compacted states, albeit some small inevitable discrepancies. The parametric study exposed the sensitivity of each parameter and also the interdependency between them, which may cause difficulties in establishing groups of parameters for other types of soil.

Finally, a new empirical relationship was derived to evaluate small strain shear modulus (G_0) for as compacted specimens prepared with different moisture contents and compaction energies. The most striking aspect of this new equation is that parameter A represents the soil fabric, which is usually taken as a constant, and it is now considered to vary with the degree of saturation.

CHAPTER SEVEN

7 . CONSTANT WATER CONTENT DIRECT SHEAR TESTS

7.1 GENERAL

In Chapter 6, the small strain behaviour of compacted soils was modelled using an empirical approach for estimating the degree of compaction through V_s and suction. However, during the service life of the fills, the strain range exceeds the very small strain domain significantly, for which V_s is indicative. To describe the mechanical behaviour of PLDC (Penrith Lakes Development Corporation) soil, a testing program consisting of constant water content direct shear (CWDS) tests was conducted rather than a constant suction condition, because failure would be expected to occur while maintaining this condition.

Specimens prepared by standard Proctor compaction were essentially tested under unsaturated condition. This chapter describes the results and modelling of the CWDS tests. While suction was not measured directly, a simple formulation based on the Hilf analysis of pore air/water pressure was derived to evaluate variations in suction during shearing. This formulation was compared with experimental data in past literature. The results of the CWDS tests on the as compacted specimens were described after. To investigate the effect of post-compaction change of suction in the fills, particularly important for the portion of the ground profile close to the ground surface likely to be subjected to climatic variations, a series of tests were also conducted for increasing levels of suction. Only drying paths were investigated, given the difficultly in producing specimens by wetting. The mechanical behaviour was analysed using commonly available constitutive frameworks. Finally, a summary of this chapter is presented.

7.2 EVALUATION OF SUCTION DURING CWDS TESTS

In recent years, a great deal of research has been devoted to the modification of traditional soil testing equipment to facilitate the determination of unsaturated shear strength parameters. A

simple approach is to use a direct shear box under constant water content, even though suction during shearing is likely to vary, and a conventional shear box does not have an independent system to measure suction. In the next subsections a simple method for evaluating the change in suction is proposed on the basis of volumetric changes. This relationship is validated using the direct shear data under which the suction was measured. The laboratory data revealed a promising agreement with the computed results, albeit a slight over estimate of suction at relatively large shear displacements.

7.2.1 Background

The modifications carried out when testing unsaturated soil in the direct shear apparatus are based on either active control, i.e., the suction is held constant throughout shearing, or passive control where the suction is measured independently under constant water content (CW) conditions (Table 7.1). The most common method for active suction control uses the axis translation technique (Gan et al., 1988; Escario and Saez, 1986; and de Campos and Carrillo, 1995), which imposes suction ($s = u_a - u_w$) by changing the air pressure u_a, while maintaining a relatively constant water pressure u_w in an air tight cell. While this type of active control is effective, the design of outer cells that can withstand high air pressures and maintain air tight conditions, can pose mechanical difficulties because when a prescribed value of suction needs to be applied and maintained during shearing, small displacement rates, sometimes as low as 1μm/min must be adopted, which is very time consuming. Furthermore, the laboratory conditions may not always be truly representative of those in the field, where the air pressure is atmospheric and the water pressure is negative. In contrast, the use of passive suction control techniques can benefit from higher rates of shearing and the transition from saturated to unsaturated states can be examined. Caruso and Tarantino (2004) and Tarantino and Tombolato (2005) adopted two high capacity tensiometers (HCT) up to 1000kPa, while Jotisankasa and Mairaing (2010) used a tensiometer (up 100kPa) to measure suction independently. The modifications to the direct shear apparatus using this technique are not very complex, which makes it attractive from a practical point of view. However, the suction for most fine grained soils exceeds 100kPa, limiting the choice of commercially available HCTs. In the absence of an independent system for measuring the matric suction, Oloo and Fredlund (1996), Vanapalli and Lane (2002) and Cokca et al. (2004) tested compacted specimens using a conventional direct shear box, and assumed that any changes in suction

during shearing would be small enough to be ignored. While the constant water content direct shear (CWDS) tests offer an interesting alternative for testing unsaturated soil, the lack of suction control during shearing poses the main practical problem.

Table 7.1. Summary of modifications to the direct shear apparatus used to test unsaturated soil.

Suction control by:	Type	Displacement rates	Suction range tested	Reference
Axis translation technique	Active Single or multistage	0.0102mm/min 0.0017mm/min	1-500kPa	Gan et al., 1988; Escario and Saez, 1986; de Campos and Carrillo, 1995
Hanging column	Active Single or multistage	0.006mm/min	0-10kPa	Likos et al (2010)
Trento HCT	Passive(CW tests) Single stage	0.005mm/min	0-100kPa	Caruso and Tarantino (2004)
	Passive(CW tests) Single stage	0.005mm/min	0-1000kPa	Tarantino and Tombolato (2005)
KU-tensiometer	Passive(CW tests) Single or multistage	0.1mm/min	0-100kPa	Jokintasa and Mairaing (2010)
-	Passive (CW tests)	1mm/min	100-1000kPa	Oloo and Fredlund (1996)
-	Passive(≈CW tests) Single stage	Not specified	100-5000kPa	Cokca et al (2004)
-	Passive(≈CW tests) Single stage	1.25mm/min	0-500kPa	Vanapalli and Lane (2002)

7.2.2 Pore air pressure evaluation

Under direct shear conditions, the vertical stress acting on the horizontal shear plane is applied by a dead load that is kept constant during shearing. This implies that the vertical displacement essentially represents the change in volume, either by compression or dilation. In CWDS testing, assuming the water and soil solids to be incompressible and that no grains are crushed during shearing, the change in volume is then the result of compression or dilation of voids, and the dissolution of air in the water phase ignoring any influence of vapour pressure and temperature fluctuations. The amount of air dissolution in the water phase is calculated using Henry's law, and the sum of the free air and dissolved air corresponds to the total volume of air. The initial conditions and final conditions (Figure 7.1), in terms of the total volume of air V_{ao} and V_{af}, respectively, can be expressed following the Hilf (1948) analysis,

$$V_{ao} = V_v - V_w + hV_w \tag{7.1}$$

$$V_{af} = V_v - V_w + hV_w - \Delta V \tag{7.2}$$

where V_v represents the volume of the voids, V_w the volume of the water in the voids and h is the solubility constant and ΔV represents the change in the volume from the initial and final conditions. Given that the air pressure is likely to change, the solubility constant is revaluated for a pressure changing environment in every calculation step considering constant temperature of 25^{o}C following Henry's Law. Note that the change in volume ΔV may be positive for shearing in compression or negative for shearing in dilation (Figure 7.1 b and c) and the volume units are computed for a parallelepiped idealised simple shear zone geometry. For undrained conditions, Boyle's law of pressure and volume equilibrium states that,

$$u_{ao}V_{ao} = u_{af}V_{af} \tag{7.3}$$

where, u_{ao} and u_{af} are the initial and final absolute pressures, respectively, with $u_{af} = u_{ao} + \Delta u_a$, (i.e. $u_{ao} = p_a = 100kPa$). Substituting Eqs. (7.1) and (7.2) into the Eq. (7.3) and rearranging for Δu_a, and then dividing by the initial volume (V_0), one can obtain:

$$\Delta u_a = \Delta u_w = \frac{u_{ao}\dfrac{\Delta V}{V_0}}{n_0 + (h-1)n_0 S_0 - \dfrac{\Delta V}{V_0}} \tag{7.4}$$

where, S_0 is the initial degree of saturation and n_0 is the initial porosity. Note that for undrained compression conditions, Hilf (1948) suggested that changes in air pressure could be related to equivalent changes in water pressure. While Eq. (7.4) resembles the expression proposed by Hilf (1948), the main differences lie with the adopted volume geometry and the manner in which the change in volume is interpreted considering of both compression and dilation, thus corresponding positive and negative air or water pressures and the fact that the air solubility is now taken as a function of the current air pressure in the system.

7.2.3 Evaluation of matric suction during shearing

In the direct shear test, the shear zone is localised and thin compared to the mass of the specimen (Jewell and Wroth, 1987). Figure 7.2 shows a diagram of a direct shear box test in which an idealised simple shear mode of deformation is assumed for the shear zone.

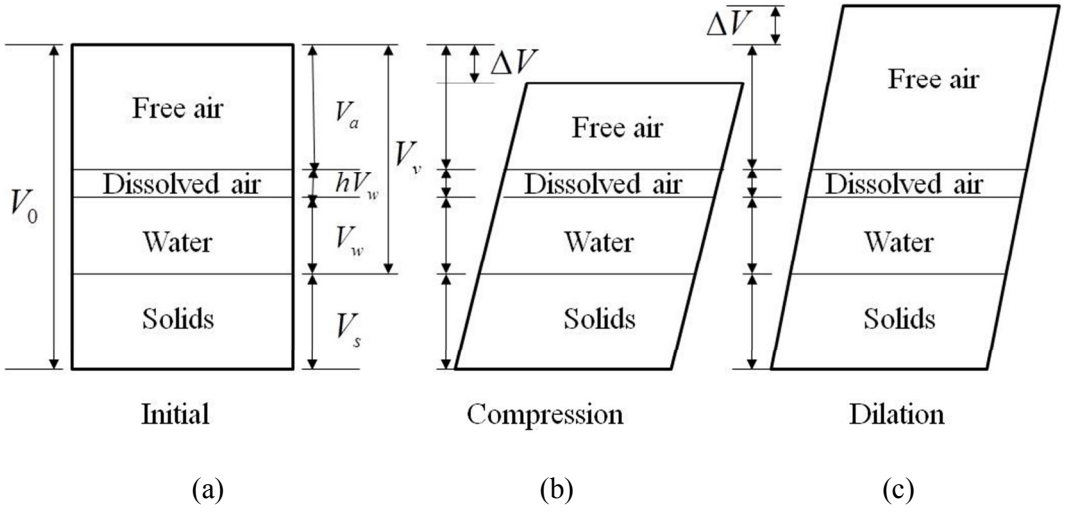

Figure 7.1 Initial and final volume conditions for compression and dilation cases of an idealised parallelepiped CWDS shear band.

The volumetric strain is obtained considering the principal strains (ε_1 and ε_3) that can be inferred from the Mohr circle of incremental strain (Figure 7.3, i.e. Bolton, 1986; Liu, 2006), thus,

$$\varepsilon_v = \varepsilon_1 + \varepsilon_3 = 2\varepsilon_y + \gamma_{yx}\tan(\delta) \tag{7.5}$$

In the above, the shear strain (γ_{yx}) on the horizontal plane can be computed by considering the thickness of the shear band (L), where the shear deformation approximates the simple shear condition (Liu, 2006). The angle of dilation (δ) is obtained by considering the rate of change of vertical displacement (Δy) with the horizontal shear displacement (Δx) or $\delta = \tan^{-1}(d\varepsilon_y / d\gamma_{yx}) = \tan^{-1}(dy/dx)$. Thus Eq. (7.5) can be rewritten by considering the vertical displacement (Δy) and the horizontal shear displacement (Δx) measured during the direct shear test as follows:

$$\varepsilon_v = 2\frac{\Delta y}{L} + \frac{\Delta x}{L}\left(-\frac{\Delta y}{\Delta x}\right) \tag{7.6}$$

Since shear deformation occurs in the central region of the sample, it is reasonable to assume that the ratio of the change in the volume by initial volume to be equivalent to the change in volumetric strain in the shear band (ε_v) as described in Eq.(7.7), hence,

$$\varepsilon_v = \frac{\Delta V}{V_0} \tag{7.7}$$

The change in air pressure associated with the volumetric variation that a specimen undergoes during direct shear, can now be determined by modifying Eq. (7.4) to account for the change of volumetric strain (ε_v), as follows:

$$\Delta u_a = \Delta u_w \approx \frac{u_{ao}\varepsilon_v}{n_0+(h-1)n_0 S_0-\varepsilon_v} \tag{7.8}$$

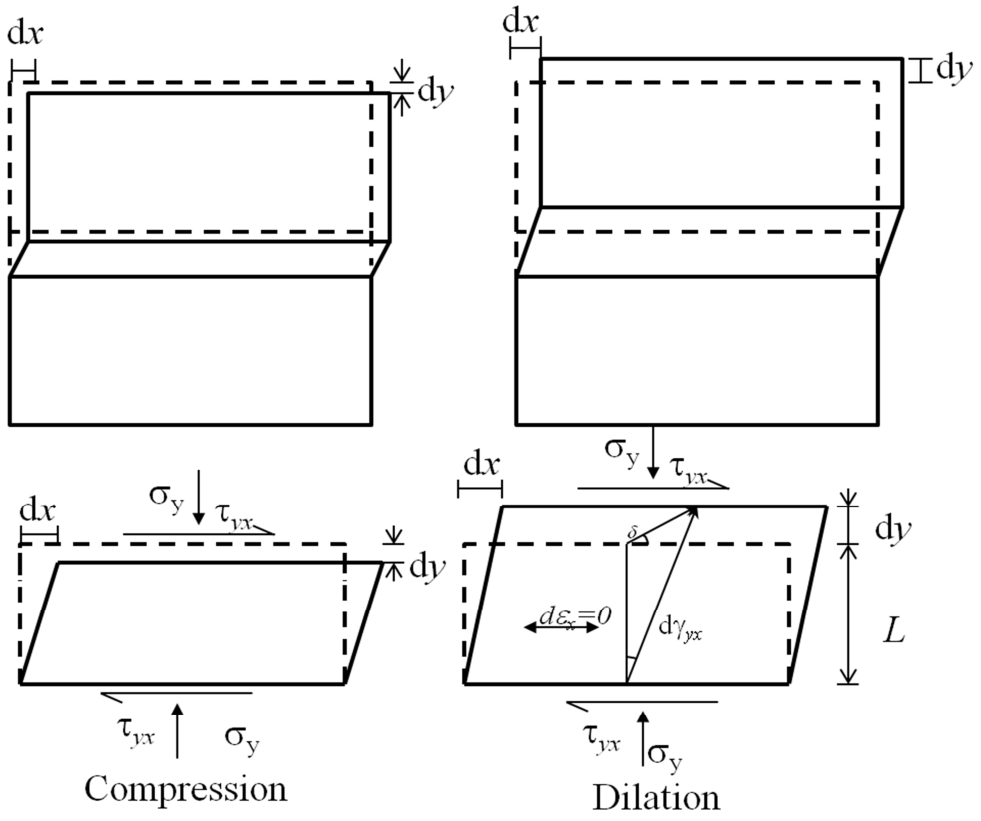

Figure 7.2 Diagram for the direct shear test for (top) idealised simple shear zone and (bottom) detail of the shear zone of specimens undergoing volumetric changes in compression and dilation.

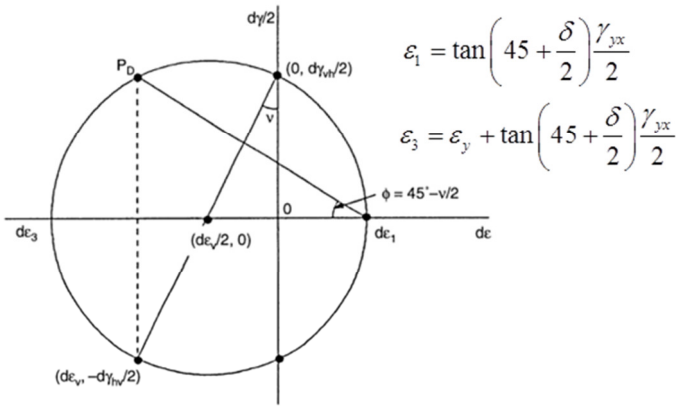

Figure 7.3 Incremental Mohr circle of strain for direct shear tests with an idealised shear zone simple shear deformation mode (modified after Liu, 2006).

It is important to note that in Eq. (7.8), the change in pore air or water pressure is evaluated by considering the initial values of porosity and degree of saturation as a starting reference, mainly because of the inevitable variation of these properties during shearing. In reality, during a direct shear test, the undrained condition for air phase may not be maintained. In fact, although the pore air pressure is likely to respond rapidly to changes in volume occurring at the shear plane it is also likely to dissipate due to the lack of effective measures to keep the system undrained for the air phase. Difficulties associated with maintaining the system undrained for water and air phases have also been recognised by Blight (1961) and Bishop et al. (1960). In a completely undrained system, the air phase transmits the pressure to water phase and thus the change in suction is zero (Hilf, 1948). However, during a direct shear box test the air pressure is likely to dissipate during shearing and therefore the change in suction can be set equal to the change in pore water pressure, which means that the net normal stress becomes the total normal stress. Notice that the interpretation described above has been adopted by Oloo and Fredlund (1996) for analysing the variation of suction during the compression stages of a direct shear box test. In this study, the concept is extended for interpreting suction changes occurring during shearing motivated by the variation of volume occurring in the shear band, owing to the uniqueness of the direct shear box geometry (Figure 10.2). Like this, during dilation there is increase in suction whereas in contraction it decreases. The cumulative magnitude of that change can be evaluated based on the Eq. (7.8) for different volumetric strains in relation to the initial condition. However, changes in suction during shearing are more likely to be related to the incremental change in volume and therefore to the water pressure, Eq. (7.9), thus;

$$ds \approx du_w \text{ or } s_f \approx du_w + s_i \tag{7.9}$$

where s_f is the current (final) suction and s_i represents the initial suction, measured at the compression stage of the direct shear test.

Note that in this approach, the effect of the difference in the contact angles when the material is undergoing mechanical wetting or drying, as a result of compression or dilation, is not considered. This is mainly because no microscopic evidence has been provided in past literature regarding this matter, although recent experimental evidence provided by Lourenco et al. (2012) has demonstrated the importance of contact angles during hydraulic wetting or

drying cycles. Nevertheless, the aim of Eq. (7.9) is only to give an approximation, and not intended to quantify the change in suction solely based on changes in the specimen's volume. This is because it still remains unclear how the surface curvature or contact angles on the water menisci and soil macrostructure change during direct shearing. It is also acknowledged that while the approach based on the pore air pressure change and its dissipation for inferring suction changes is simple and hence attractive for use in practice, the assumptions for undrained air phases even for a short period in the direct shear box apparatus require further experimental checking.

7.2.4 Model validation

Eq. (7.9) was evaluated using soil specimens tested in direct shear which exhibited the contractive behaviour of clayey silt (Caruso and Tarantino, 2004) and dilative behaviour of Omkoi silt (Jotisankasa and Mairaing 2010). The incremental interval adopted was 0.5mm and the thickness of the shear band was taken as 4mm and 7mm for the clayey silt and Omkoi silt, respectively. The thickness of the shear band differs because the adopted values take into account the mean particle size (Wood, 2002) and aspect ratio of the box (60×60×10 mm and ∅63×22 mm for the clayey silt and Omkoi silt, respectively; Wang and Gutierrez, 2010). Notice that for this particular prediction exercise the shear band thickness was adjusted by best fit to the experimental data. Figure 7.4 shows the results of two direct shear tests in terms of vertical displacement, pore air pressure, dilatancy, and matric suction. From Figure 7.4 (b) and (d) it can be observed that variations in the matric suction are intimately related to volumetric changes, i.e., peak dilatancy and corresponding peak matric suction occur almost at the same horizontal displacement. Figure 7.4 (c) represents the change of pore pressure with volumetric strain predicted by Eq. (7.8). While there was a positive increase in pore pressure for the specimens that contracted, there was a negative increase in pore pressure for those that dilated. This is consistent with the direct shear results of Zhan and Ng (2006) using the axis translation technique, in which shear contraction imposed water drainage, whereas shear dilatancy resulted in water extraction. The suction showed different patterns of behaviour in the clayey silt and omkoi silt (Figure 7.4d). A reduction in volume was accompanied by a decrease in suction in the clayey silt specimen, whereas an increase in volume was accompanied by an increase in suction in the Omkoi silt specimen. The predictions from Eq. (7.9) are represented in Figure 7.4d by the dashed lines. The predictions

agree well with the experimental results in the range of small horizontal displacements (i.e. up to 2.5mm), but overestimate the suction at larger displacements, particularly for clayey silt. This difference may be related to the interplay between inter-aggregate porosity (air voids) and intra-aggregate porosity (water filled voids) in the larger displacement range, where changes in the microstructure rather than the volumetric changes may regulate the suction behaviour. To further evaluate the validity of Eq. (7.9), the variation in suction of the complete data sets (i.e. different initial moisture content) induced by shearing of the Omkoi silt, was compared with the predictions. Overall, Eq. (7.9) was able to predict the variation in suction of the specimens compacted at different water contents (Figure 7.5) to an acceptable accuracy. For specimens with higher moisture contents (w > 25%), although the prediction captured the general trend in suction, the values showed small discrepancies that can be attributed to the air phase not being entirely interconnected (air entry value of around 20kPa). This means that the air pressure may have not been transmitted from void to void, thus the prediction would underestimate the change in suction.

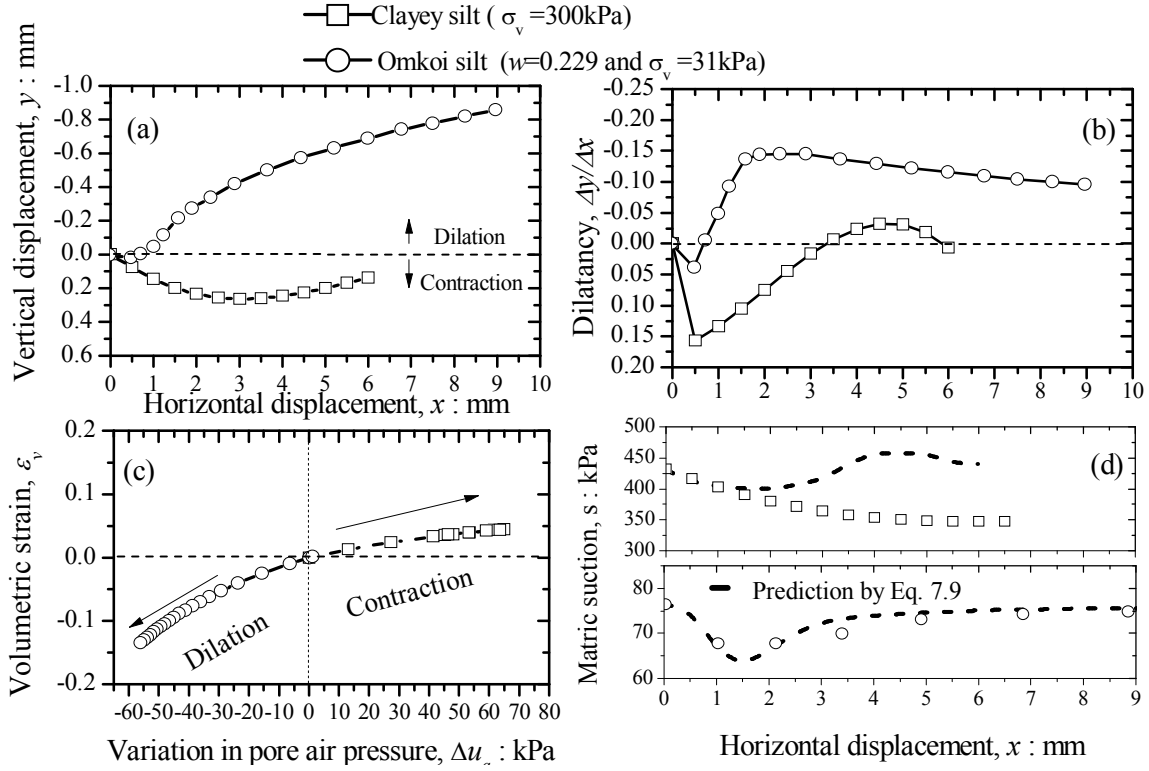

Figure 7.4. Shear tests results in terms of (a) vertical displacement, (b) dilatancy, (c) variation in pore air pressure (Eq.6) with volumetric strain relationship and (d) change in matric suction (Clayey silt data from Caruso and Tarantino, 2004 and Omkoi silt data from Jotisankasa and Mairaing, 2010)

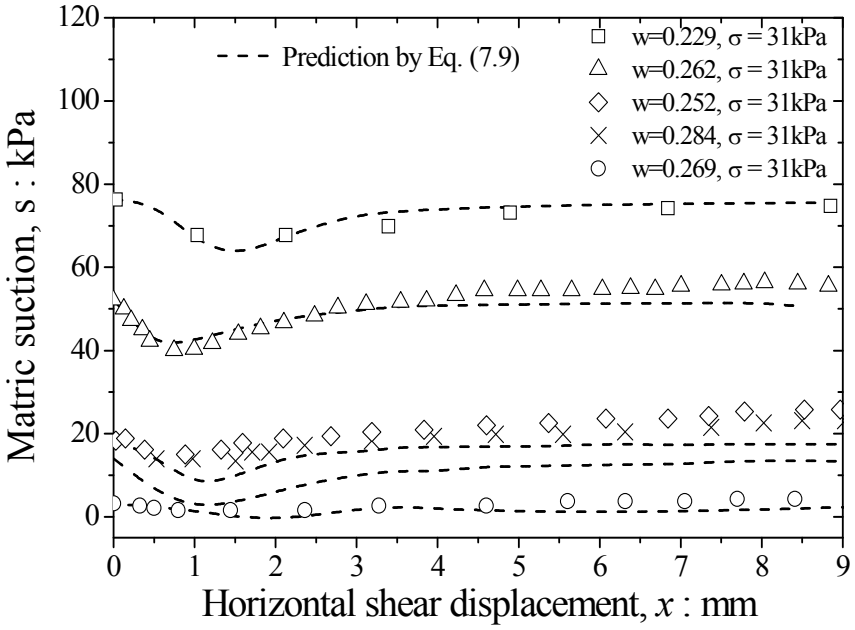

Figure 7.5. Variation in matric suction during direct shear for specimens tested at the same vertical stress (σv) and different moisture contents for Omkoi silt (data from Jotisankasa and Mairaing, 2010).

7.2.5 Limitations and shortcomings of the proposed approach

While an idealised simple shear mode of deformation has been amply observed and modelled for sands or sandy type materials in direct shear box tests (Jewell and Wroth, 1987; Liu, 2006; Shibuya et al., 1997), less research effort has been placed on clays or silts. Tchalenko(1970) and Morgenstern and Tchalenko (1969) reported the existence of a distinguished limited shear zone of deformation of kaolin specimens subjected to direct shear testing, although it may be argued whether simple shear was the governing mode of deformation. For that reason, while the present approach may be applied for sands and sand-silt mixtures, caution should be exercised when extending these concepts for clayey materials. In addition, this approach is limited to soils that are in the funicular stages of desaturation where both air and water phases are continuous.

7.2.6 CWDS test without an independent system for measuring suction

The direct application of the relationship presented in the previous subsections lies with the direct shear tests conducted using a conventional direct shear apparatus without using any independent instruments to measure suction. Although its application seems straightforward,

there are some aspects that should be considered before estimating the variation in suction caused by shearing. The first aspect is related to ensuring constant water conditions. To achieve this, some modifications to the conventional apparatus must be implemented so that no moisture is lost during the tests. This can be accomplished by adopting an anti-evaporation system similar to the one suggested by Caruso and Tarantino (2004) or Jotisankasa and Mairaing (2010). In this study a variation of the system adopted Caruso and Tarantino (2004) was selected (details are given earlier in section 4.2.3).

The second aspect is related to estimating the suction at the end of the compression stage. Despite the fact that the initial suction of the specimens can be easily determined using the filter paper method, suction at the end of the compression stage is more complex, mainly because the filter paper method is unable to simulate the same loading conditions. Ng and Pang (2000) pointed out the stress state dependency in SWCC. Without a direct measurement system such as an HCT, the suction at the end of compression stage may be estimated using the procedure outlined in Oloo and Fredlund (1996) based on the one dimensional compression Hilf analysis (Hilf, 1948), expressed as follows:

$$\Delta u_w = \Delta u_a = \frac{u_{ao}\Delta n}{(1-S_0)n_0 + hS_0 n_0 - \Delta n} \tag{7.10}$$

Oloo and Fredlund (1996) assumed that the change in pore air pressure drops to zero and the change in suction is equal to the variation of pore water pressure, and the net normal stress becomes the total normal stress. Thus, the suction at the end of compression can be computed using Eq. (7.10), and the difference in the height of the specimen from the settlement-time curve can be considered.

In summary, estimating the change in suction when using a conventional shear box apparatus involves the following steps:

1) Implement an anti-evaporation system in the conventional shear box apparatus,
2) Measure the as compacted or pre-compression suction,
3) Compute s_i based time-settlement curve using the approach proposed by Oloo and Fredlund (1996),
4) Select a strain rate slow enough to avoid pore water pressures arising during shearing in specimens with high degrees of saturation,

5) Monitor the vertical and horizontal displacements during shearing,
6) Compute the volumetric strain observed during the test using Eq. (7.6) and by selecting the appropriate shear band thickness,
7) Compute the cumulative change is suction based on the water pressure at every horizontal displacement increment, typically 0.5mm, in relation to initial condition,
8) Compute the change in suction at every 0.5mm increment and,
9) Compute the suction during shearing by adding every incremental change to the s_i value, representing suction at the end of the compression stage.

7.3 CWDS TESTS ON AS COMPACTED SPECIMENS

7.3.1 Compaction characteristics

The testing program consisted of CWDS tests conducted in specimens prepared by standard Proctor compaction tests. The details associated with the sample preparation were outlined in a previous section, for further details the reader is referred to 4.3.2. The tests were carried out in as compacted and post compacted conditions. A summary of the compaction characteristics adopted for specimens tested in an as compacted state is given in Table 7.2 and represented in Figure 7.6. The conceptual boundaries that translate the range of distinguishable aggregations, as defined in Chapter 5, for small strain stiffness behaviour are also represented.

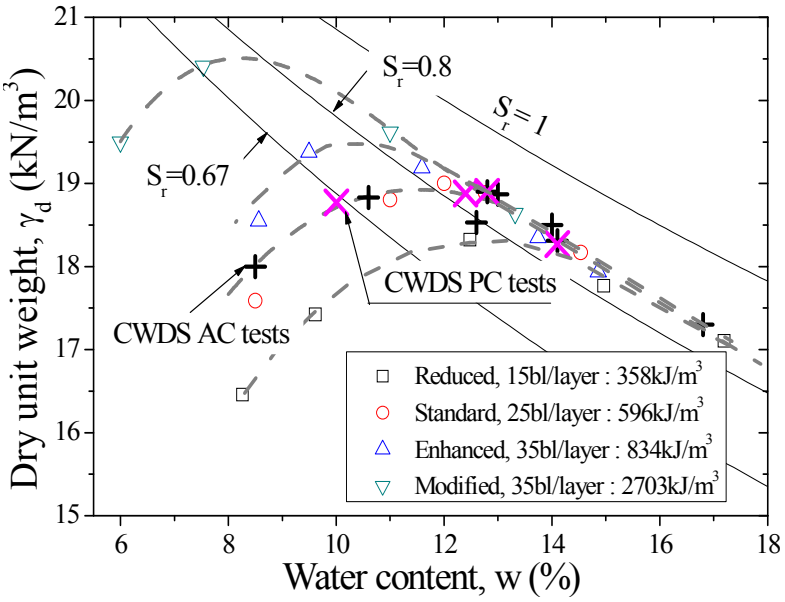

Figure 7.6 Compaction characteristics of CWDS test specimens.

Table 7.2 Summary of the testing program for the as compacted states test series with initial condition and at the end of the compression stage

Test ID		Energy level, E : kJ/m^3	Water content , w: %	Dry unit weight, γ_d : kN/m^3	Suction, s kpa	Void ratio e	Degree of Saturation S_r	Vertical stress, σ_v kPa
AC-8.5 (40)	Initial	596.0	8.5	18.0	608	0.48	0.471	38.4
	Final				605	0.47	0.481	
AC-8.5 (82)	Initial	596.0	8.5	18.0	608	0.48	0.471	79.55
	Final				603	0.46	0.489	
AC-8.5 (150)	Initial	596.0	8.5	18.0	608	0.48	0.471	146.7
	Final				587	0.39	0.57	
AC-10.6(40)	Initial	596.0	10.6	18.83	158	0.41	0.703	38.4
	Final				134	0.354	0.80	
AC-10.6(80)	Initial	596.0	10.6	18.83	158	0.41	0.703	79.55
	Final				130	0.349	0.818	
AC-10.6(150)	Initial	596.0	10.6	18.83	158	0.41	0.703	146.7
	Final				131.4	0.352	0.814	
AC-12.8 (40)	Initial	596.0	12.8	18.9	38	0.416	0.831	38.4
	Final				15.3	0.383	0.90	
AC-12.8 (80)	Initial	596.0	12.8	18.9	38	0.416	0.831	79.55
	Final				2.0	0.353	0.97	
AC-12.8(150)	Initial	596.0	12.8	18.9	38	0.416	0.831	146.7
	Final				0	0.341	1.0	
AC-14.1 (40)	Initial	596.0	14.11	18.31	23	0.461	0.825	38.4
	Final				0	0.423	0.89	
AC-14.1 (80)	Initial	596.0	14.11	18.31	23	0.461	0.825	79.55
	Final				0	0.409	0.92	
AC-14.1 (150)	Initial	596.0	14.11	18.31	23	0.461	0.825	146.7
	Final				0	0.354	1.0	
AC-16.8 (40)	Initial	596.0	16.8	17.3	7.0	0.546	0.854	38.4
	Final				0	0.51	0.889	
AC-16.8 (82)	Initial	596.0	16.8	17.3	7.8	0.546	0.854	79.55
	Final				0	0.53	0.885	
AC-16.8 (150)	Initial	596.0	16.8	17.3	6.5	0.546	0.854	146.7
	Final				0	0.508	0.891	
AC-12.6 (40)	Initial	358	12.6	18.53	43	0.444	0.77	38.4
	Final				9.1	0.363	0.93	
AC-12.6 (82)	Initial	358	12.6	18.53	43	0.444	0.77	79.55
	Final				9.6	0.363	0.93	
AC-12.6(150)	Initial	358	12.6	18.53	43	0.444	0.77	146.7
	Final				8.4	0.361	0.94	
AC-13.0 (40)	Initial	834	13.0	18.87	36	0.417	0.84	38.4
	Final				5.1	0.376	0.93	
AC-13.0 (80)	Initial	834	13.0	18.87	36	0.417	0.84	79.55
	Final				0	0.365	0.96	
AC-13.0(150)	Initial	834	13.0	18.87	36	0.417	0.84	146.7
	Final				0	0.39	1.0	
AC-14.0 (40)	Initial	834	14.0	18.5	25	0.446	0.847	38.4
	Final				0	0.384	0.96	
AC-14.0 (80)	Initial	834	14.0	18.5	25	0.446	0.847	79.55
	Final				0	0.40	0.98	
AC-14.0(150)	Initial	834	14.0	18.5	25	0.446	0.847	146.7
	Final				0	0.39	0.94	

Note that the AC designation refer to as compacted states. The water unit weight is γ_w=9.81 kN/m^3 and $e=\gamma_w G_s/\gamma_w - 1$ and $e_w = S_r e$

The equivalence to the specimens used for determination of V_s is made in terms of dry unit weight rather than compaction energy (see section 4.3.1). A summary of the initial, after equilibration, and at the end of compression characteristics of the specimens where the suction was varied using the axis translation technique with a pressure plate apparatus, are given in Table 7.3 and also represented in Figure 7.6. Further inspection of Table 7.2 reveals that some of the specimens reached near-saturation condition at the end of the compression stage, particularly those prepared to a water content located on the wet side of the compaction plane (S_r>0.8, Figure 7.6). Note that a small strain rate of 0.01mm/min was adopted, thus it is likely that the generation of positive pore water pressure induced by rapid shearing was avoided. Details of three specimens that were tested under saturation conditions are also included in Table 7.3. Although some tests were carried out in saturated and varying suction, more importance was placed on the as compacted conditions.

7.3.2 As compacted CWDS tests series

The results of the of the shear test in terms of shear stresses and vertical displacements for three different applied vertical stresses of 38.4, 82, and 150 kPa are represented in Figure 7.8, Figure 7.9, Figure 7.10, respectively. The variation in suction during the CWDS tests was estimated using the procedure outlined in section 7.2.6, for the specimens prepared at water contents of 0.085 and 0.105 (Figure 7.11). For the remaining specimens prepared at higher water content, the procedure lead to inaccurate estimations given that the air phase was likely occluded (Barden and Pavlakis, 1971). For these specimens, the suction was measured at the end of the test and was taken as the peak and ultimate suction.

The shear band for the volumetric strains was 5mm thick, and it was chosen on the basis of the change in density observed using CT-scan imaging of the specimens taken at the final stage of shearing, and by visual inspection of the specimens (Figure 7.7). Although by visual inspection the shear band appears to be 2mm thick, in the CT-scan image it appears to be around 5mm thick. While the displacement discontinuity is easily observed, differences in density are difficult to assess just by visual inspection, which is when CT-scan imaging proves to be a very useful tool that can capture differences in density indistinguishable to the naked eye. Although there is some interference due to the high density of the metal shear box

assembly, the change in density represented by the different shades of grey in the specimen mid- section is clear.

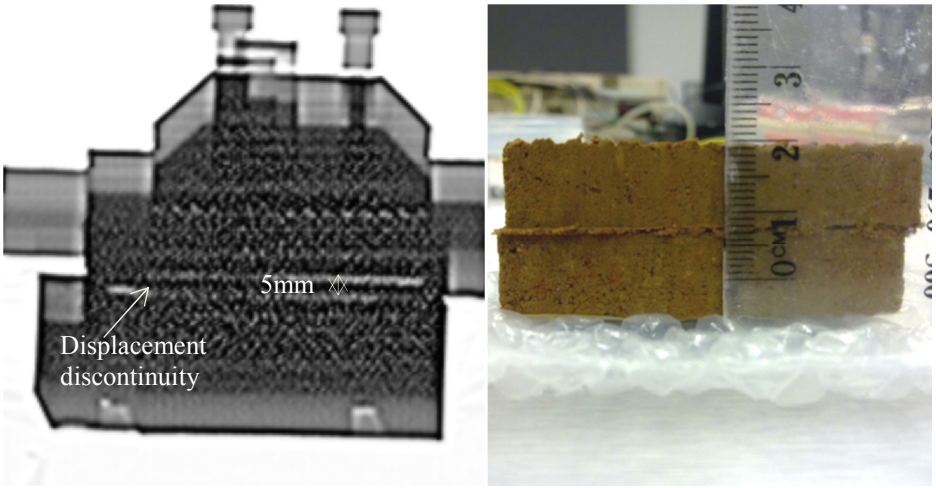

Figure 7.7 Shear band (a) Ct-scan image and (b) specimen photo.

Table 7.3 Summary of the testing program for the post compacted states test series with initial condition, at the end of the suction equilibration and compression stages.

Test ID		Energy level, E : kJ/m^3	Water content , w: %	Dry unit weight, γ_d : kN/m^3	Suction, s kpa	Void ratio *e*	Degree of saturation S_r	Applied Vertical stress, σ_v kPa
PC10.0(80)	Initial	596.0	10.0	18.77	153.5	0.410	0.657	79.55
	Equilibration		11.5	18.77	65.29	0.410	0.76	
PC10.0 (80)	Initial	596.0	10.0	18.77	155.9	0.410	0.657	79.55
	Equilibration		10.9	18.77	126.57	0.410	0.72	
PC10.0(80)	Initial	596.0	10.0	18.77	145.4	0.410	0.657	79.55
	Equilibration		9.16	18.75	282.7	0.413	0.599	
PC-14.1(80)	Initial	596.0	14.1	18.27	10.5	0.449	0.847	79.55
	Equilibration		13.2	18.26	38.49	0.450	0.792	
PC-14.1(80)	Initial	596.0	14.1	18.27	11.7	0.449	0.847	79.55
	Equilibration		12.5	18.26	53.19	0.450	0.75	
PC-14.1(80)	Initial	596.0	14.1	18.27	12.8	0.449	0.847	79.55
	Equilibration		10.94	18.26	151.5	0.450	0.656	
PC12.8(80)s42.8	Initial		12.8	18.9	42.5	0.401	0.86	
	Equilibration	596.0	12.8	18.9	42.5	0.401	0.86	79.55
PC12.8(80)	Initial		12.8	18.9	42.5	0.401	0.86	79.55
	Equilibration	596.0	12.2	18.85	47.41	0.405	0.81	
PC12.8(80)	Initial		12.8	18.9	42.5	0.401	0.86	79.55
	Equilibration	596.0	11.8	18.81	79.02	0.408	0.78	
SAT-12.5 (40)	Initial	596.0	12.4	18.88	55	0.403	0.83	38.4
SAT-12.5 (82)	Initial	596.0	12.4	18.88	55	0.403	0.83	79.55
SAT-12.5(150)	Initial	596.0	12.4	18.88	55	0.403	0.83	146.7

Note: PC and SAT designations refer to as post compacted and saturation states, respectively. The water unit weight is γ_w=9.81 kN/m^3 and $e=\gamma_w G_s/\gamma_w - 1$.

In general, all the specimens showed a peak followed by a decrease in shear stress before subsequently attaining a relatively constant value after 6.5 mm of horizontal displacement. Although strain softening was clearly evident in the specimen compacted at dry of OMC, the specimens compacted at OMC and wetter of OMC did not show a distinct post peak drop. It seems likely that this is the result of the difference between the degrees of particle aggregation as the moisture content increased. The displacement plots (Figure 7.8b, Figure 7.9b, Figure 7.10b) indicate that the specimens compacted dry of optimum had a more pronounced dilative behaviour, whereas the specimens compacted at and wet of OMC show a mainly contractive response.

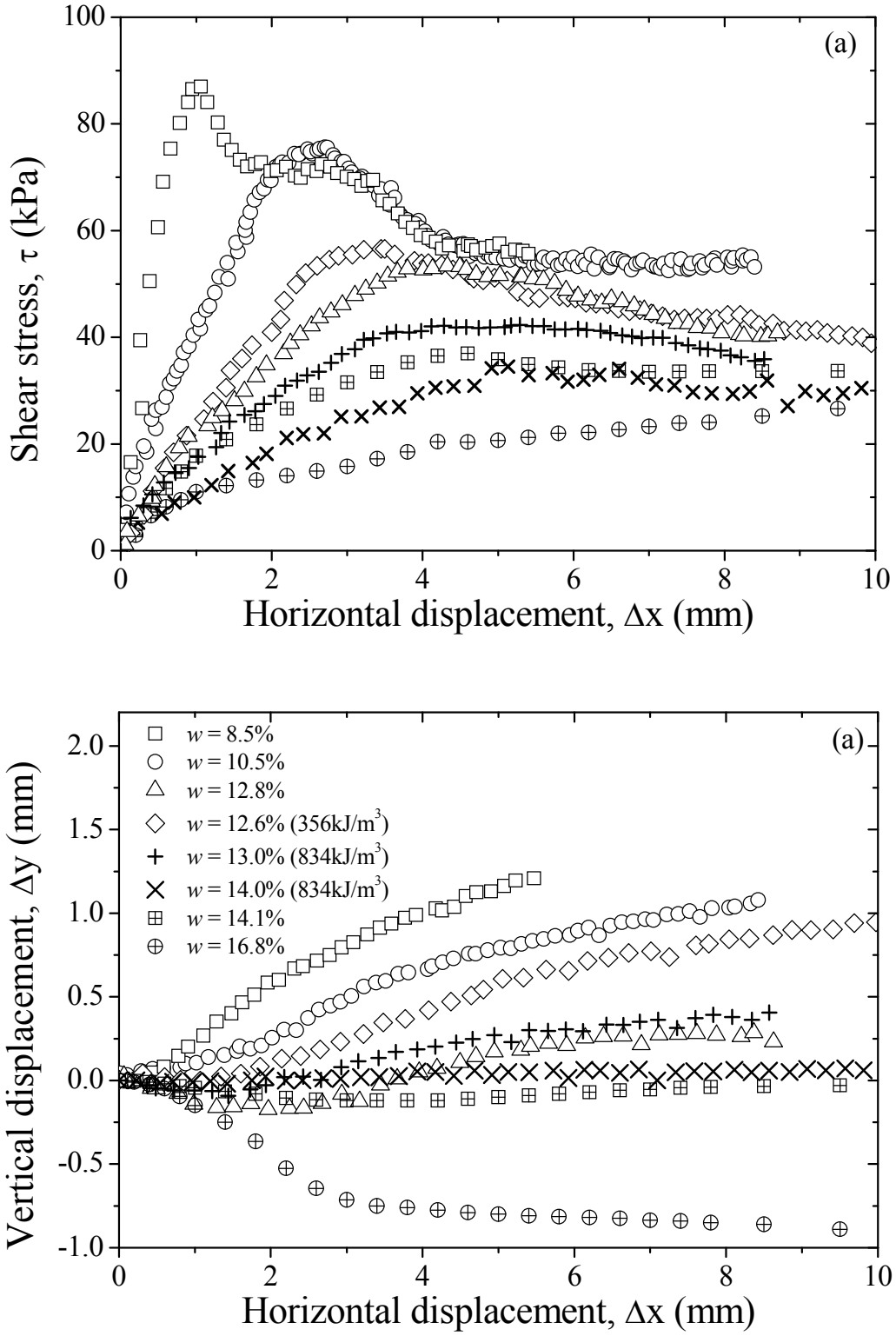

Figure 7.8 Shear tests on specimens compacted at various water contents (*w=8.5-16.8%*) and different energy levels (E=358, 596 and 834kJ/m^3) for a applied vertical stress of 38.5kpa in terms of (a) shear stress and (b) vertical displacement

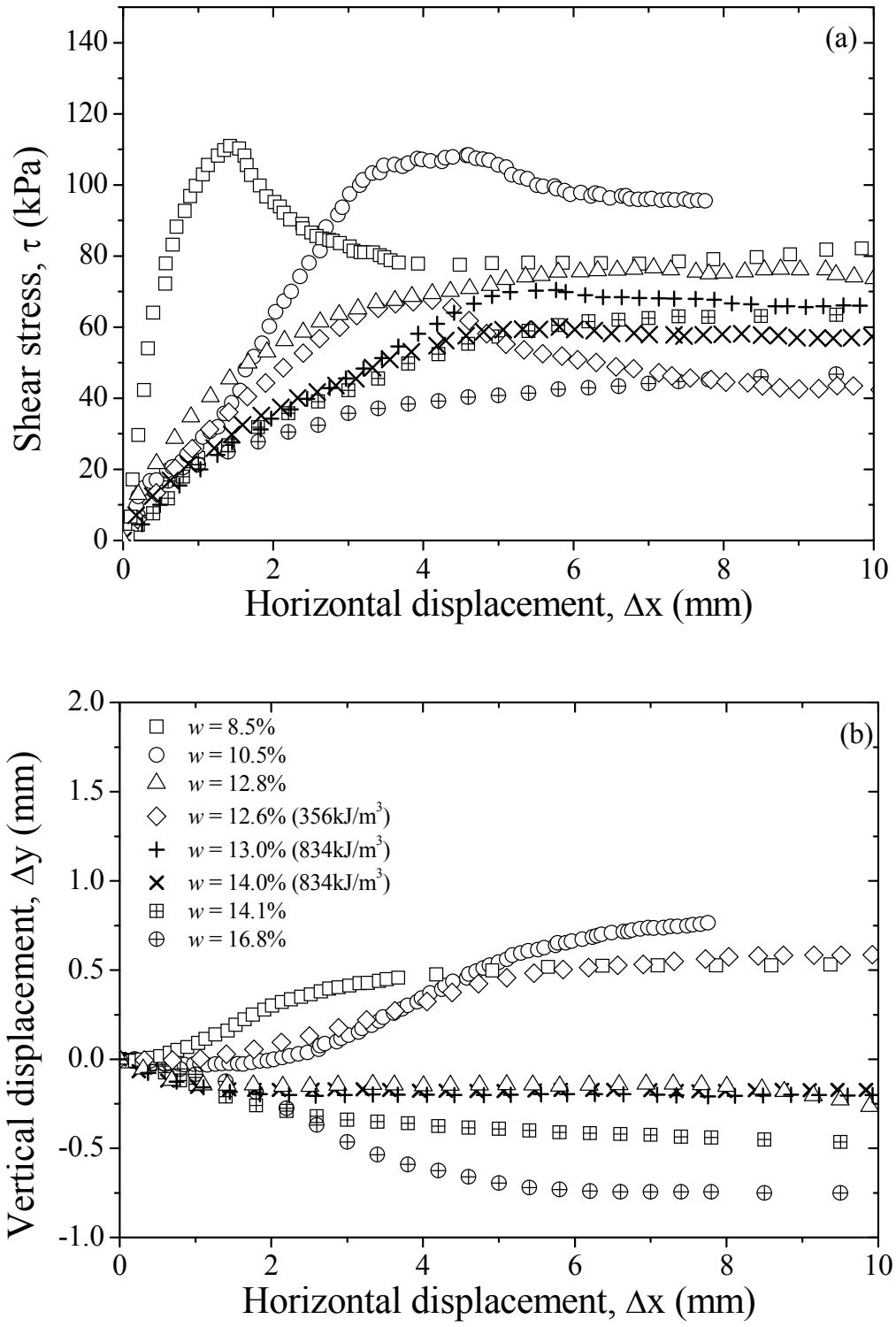

Figure 7.9 Shear tests on specimens compacted at various water contents (*w=8.5-16.8%*) and different energy levels (E=358, 596 and 834kJ/m^3) for a applied vertical stress of 79.55kpa in terms of (a) shear stress and (b) vertical displacement.

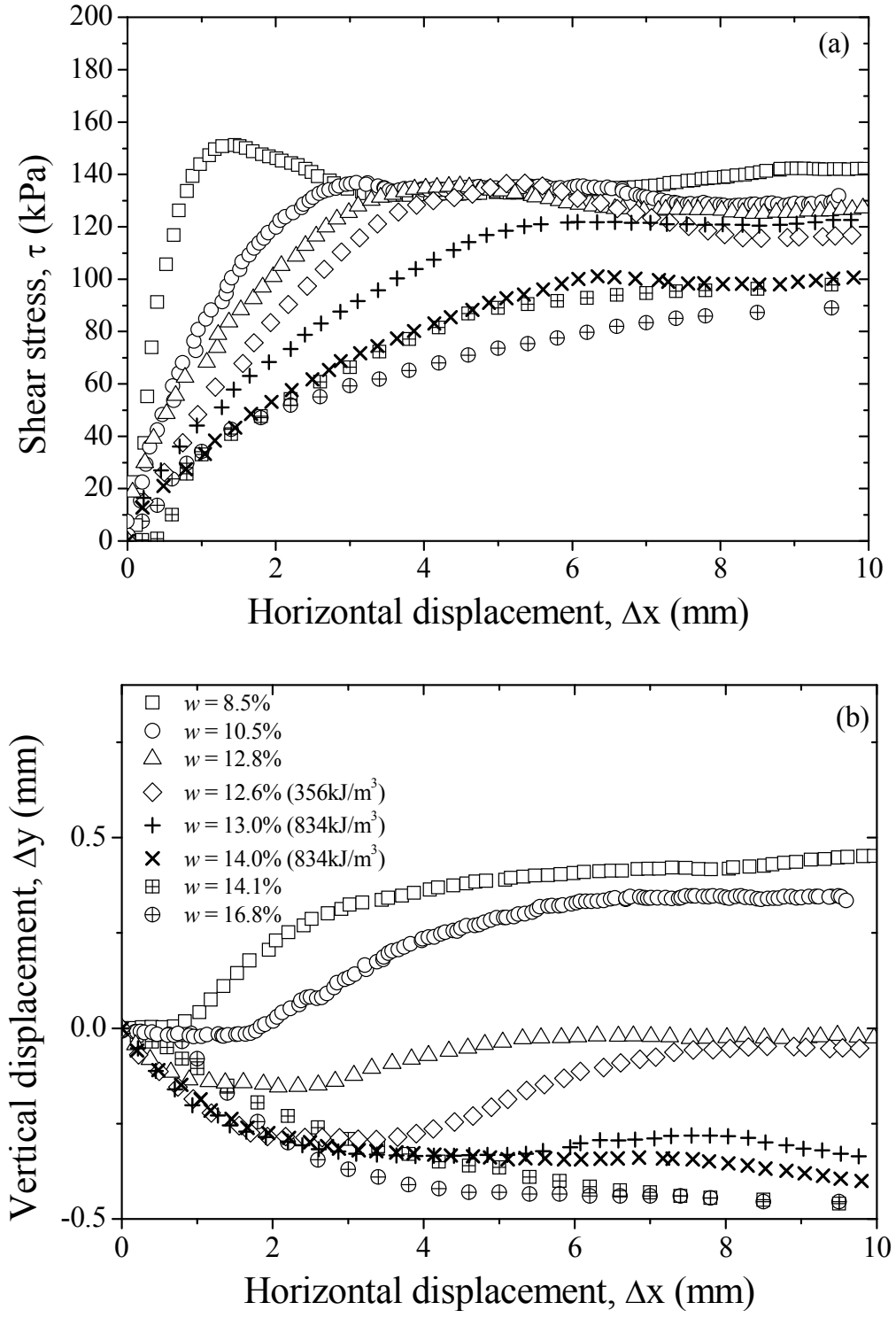

Figure 7.10 Shear tests on specimens compacted at various water contents (*w=8.5-16.8%*) and different energy levels (E=358, 596 and 834kJ/m^3) for a applied vertical stress of 147.5kpa in terms of (a) shear stress and (b) vertical displacement

The suction at peak failure was estimated using the procedure outlined in section 7.2.6 for specimens prepared at water contents of 0.085 and 0.105 (Figure 7.11). The peak suction of the remaining specimens was taken as the same as the final suction measured with filter

paper method that were conducted once the shearing test was over. This is mainly because in those specimens the initial compaction states were representative of optimum or wet of optimum water content, which means that the air phase was likely occluded and thus the procedure outlined in section 7.2.6 lead to inaccurate estimations.

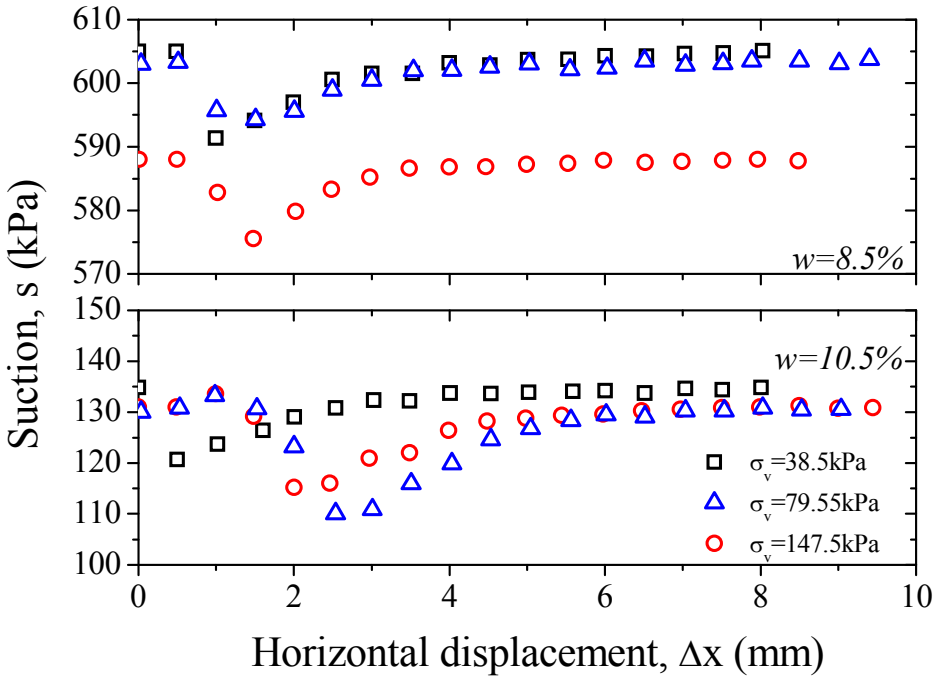

Figure 7.11 Variation of suction during shearing predicted using Eq. (7.9) on specimens compacted at water contents of *w=8.5%* and *w=10.5%* for a applied vertical stress of 38.5, 79.55 and 147.5kPa.

The changes in the specimen volume and associated suction occurring during shearing are likely to cause the stress state to move along the main wetting and drying curves, that is, for shearing induced wetting and drying volumetric changes, i.e. contraction and dilation, respectively. In Figure 7.12 the variation of degree of saturation (S_r) and suction (s) during a typical direct shear test is shown together with the water retention data and interpolated SWRC for increasing void ratio for the specimens prepared at water content of 0.85 and energy level of 596 kJ/m^3. The *s-Sr* after compression stage was computed based on the procedure described in section 7.2.6. The hydraulic paths during shearing computed based on the approach suggested are also represented in Figure 7.12 for the different applied stresses. Specimens that were subjected for higher applied stresses during compression, at the start of the shearing had lower degree of saturation and suction (square points in Figure 7.12). The shear stress and displacement plots of the specimens represented Figure 7.12a are given in

Figure 7.8b, Figure 7.9b, Figure 7.10b. Typically the specimens exhibit a limited contraction stage (up to horizontal displacements of 1.5-2mm) and thereafter the volumetric behaviour observed was mainly dilation. This change in volumetric regime can also be observed in the hydraulic paths Figure 7.12b, where there is a decrease in suction accompanied with small variation of S_r. Thereafter, the degree of saturation tends to decrease and this is accompanied by an increase in suction.

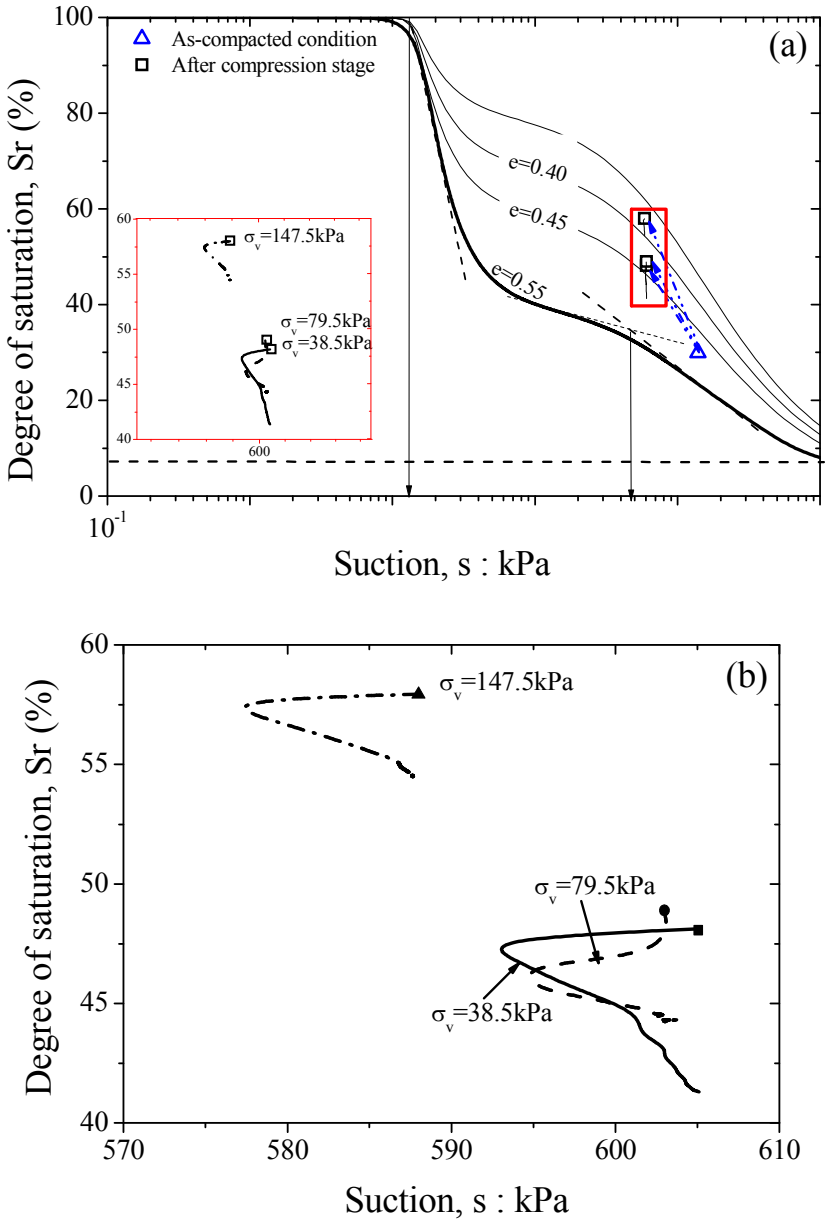

Figure 7.12 Representation of (a) *s-Sr* relationship during a direct shear test for specimens prepared at w=8.5% and (b) detail of the hydraulic paths (closed symbols represent initial conditions).

Figure 7.13 shows the peak failure envelopes for all specimens with various water content and energy levels. The peak envelopes were interpreted by considering the vertical stress at failure with cross section correction. In general it can be observed that the failure envelopes of those specimens prepared on the dry side and at optimum moisture content plotted higher in the shear stress-normal stress plane. In the tested specimens, the suction, dry unit weight, and fabric changed, and while the apparent cohesion seems to be governed mainly by suction (Vanapalli et al., 1996), the friction angle seems to be an indicator of the void ratio or fabric. Typically, the apparent cohesion varied from a maximum of 68kPa for specimens prepared at a water content of 0.085 and a minimum of 5kPa for specimens at 0.168, whereas friction angle had a maximum of 35° and minimum of 24° for specimens prepared at 0.125 and 0.168, respectively. This is better illustrated in Figure 7.14. In Figure 7.15 the peak and ultimate shear strength data is represented against the water content and degree of saturation. Both the peak and ultimate shear strength decreased with increasing water content, and the different levels of applied vertical stress showed a similar tendency. It is interesting to observe that when the shear strength data is represented in terms of the initial degree of saturation, the extent of aggregation regions defined along equal degrees of saturation lines for the small strain stiffness (see Figure 5.8 represented earlier) are also easily identified for the shear strength data. This seems to indicate that the fabric plays an equally important role in governing the shear strength behaviour for larger strain ranges.

The failure envelopes for the specimens prepared at same energy level but different water contents are represented in Figure 7.16a). The shear strength data was plotted in respecting to suction and grouped by the correspondent applied vertical stresses. Both peak and ultimate states are represented and the envelopes were interpolated using the procedure suggested by Vilar (2006). Both peak and ultimate shear strength increase with suction in a non-linear fashion and the rate of increase seems to gradually decrease with increasing suction. Moreover, the envelopes seem to suggest the existence of a critical suction value, after which suction increase is not very significant. For this particular study this value seems to be at suction of 100kPa, which corresponds to approximately 11.3% water content (slightly below OMC for standard compaction effort). It is interesting to note that the difference between the peak and ultimate shear strength envelopes increases with the applied vertical stress. This difference is probably due to the larger reduction in void ratio attained at the end of the compression stage for the specimens tested with higher vertical stresses. At the

beginning of the test, these specimens have denser particle arrangement and would likely experience a more pronounced softening behaviour that in turn causes larger differences between the peak and ultimate shear strength. In Figure 7.16b) the peak and ultimate shear strength is represented in terms of the level of compacted energy for specimens prepared at approximately the same water content of 0.128. The peak shear strength seems to decrease with increasing energy while ultimate shear strength is less affected. This difference may be attributed to the fact that initial soil structure is being erased during shearing (i.e. Toll, 1990). The differences in peak shear strength are then probably associated with the difference in soil structure that is likely to happen when the degree of saturation representing the line of optima is exceeded evidenced in the CT-scan images (Figure 4.39 and 4.40). While the specimens prepared at an energy level of 358kJ/m3 still exhibit the aggregated type of macrostructure evidenced in the CT-scan images, the specimens prepared at higher energy levels have progressively changed to a more matrix dominated macrostructure that is likely to develop a much lower shear strength. In addition, the specimens prepared at higher water content, for which the compaction end states are located on the wet side of the compaction plane, during compaction may have experienced larger pore water pressures that were quickly dissipated. This in conjunction with the change in structure may contribute to the deterioration of the soil strength; however, further confirmation of this hypothesis is desirable.

Similar trends were obtained for specimens prepared at a higher water content of 0.14, but the differences in the peak shear strength are smaller since in this range, the macrostructure of the soil is similar. Similarly to the behaviour observed for the small strain shear modulus, the peak shear strength decreases with increasing applied energy when the degree of saturation line defining the possible ultimate compaction state has been reached. Again, these results reinforce the idea that applying additional energy to the soil during compaction may not necessarily improve its shear strength. Given that the tested water content of 0.125 is actually close to the optimum water content for an energy level of 358 kJ/m^3, this seems to indicate that when the soil follows a mechanical wetting path through compaction, the shear strength is maximised for optimum conditions and subsequently deteriorates with additional applied energy, leading to the ultimate state of compaction. Nonetheless, while this behaviour has been well characterised for the small strain range (see earlier in Chapter 5), further CWDS testing would be recommended, particularly for lower energy levels, to ascertain the apparent soil behaviour reported here.

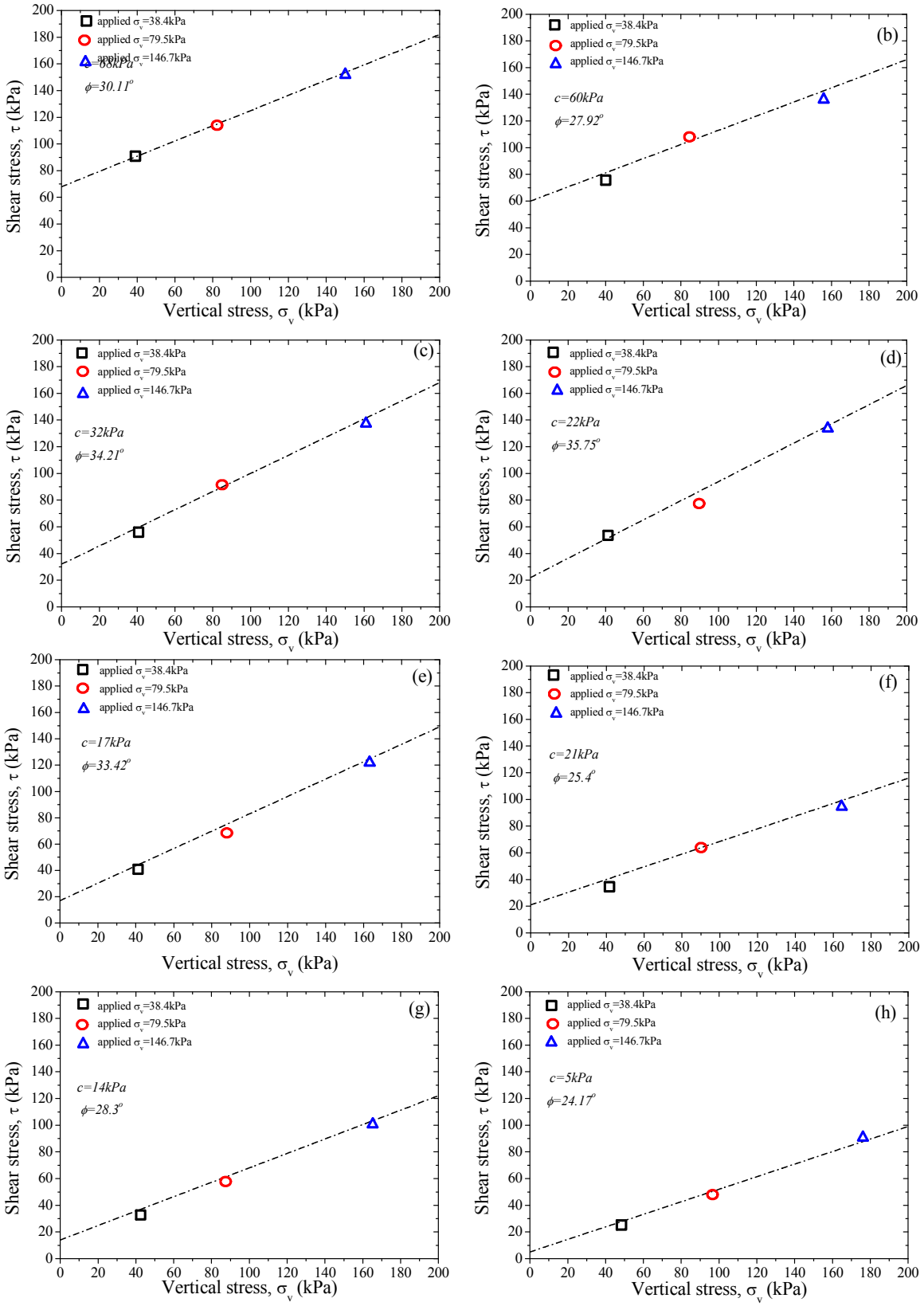

Figure 7.13 Peak failure envelopes for specimens prepared at water content and energy levels of (a) w=8.5%, E=596 kJ/m^3, (b) w=10.5%, E=596 kJ/m^3, (c) w=12.6%, E=358 kJ/m^3, (d) w=12.8%, E=596 kJ/m^3, (e) w=13.0%, E=834 kJ/m^3, (f) w=14.1%, E=596 kJ/m^3, (g) w=14.0%, E=834 kJ/m^3, (h) w=16.8%, E=596 kJ/m^3.

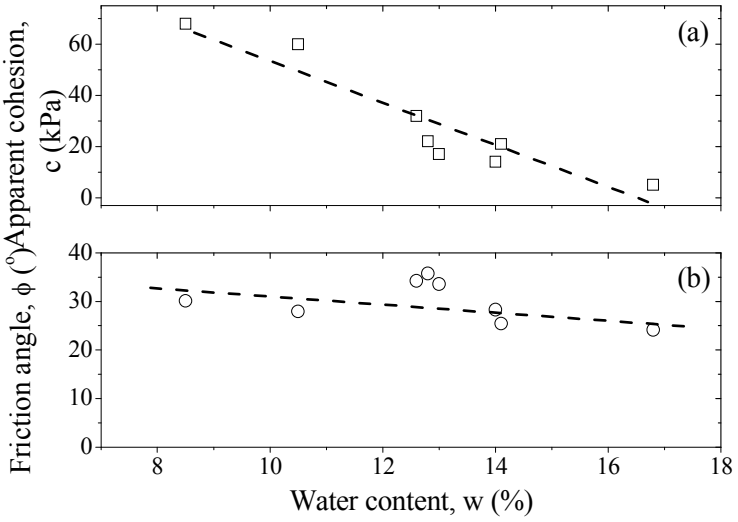

Figure 7.14 Peak failure envelopes (a) apparent cohesion and (b) friction angles with water content.

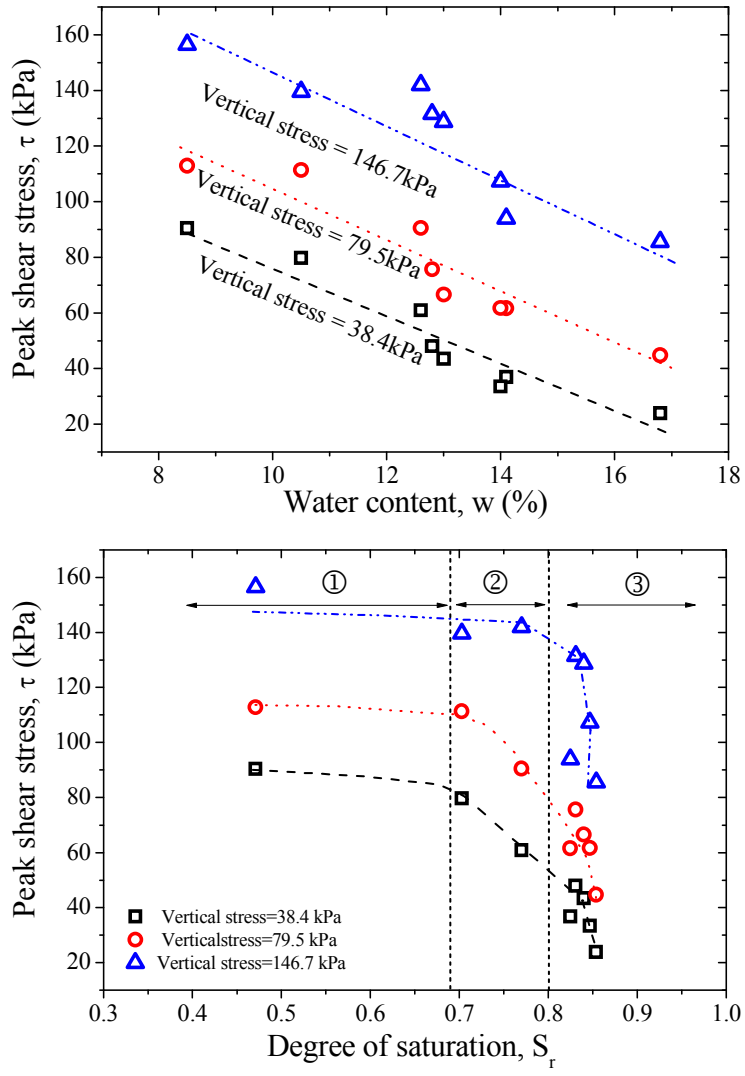

Figure 7.15 Peak shear stresses for different applied vertical stress in terms of (a) water content and (b) initial degree of saturation for specimens prepared at different water contents and energy levels.

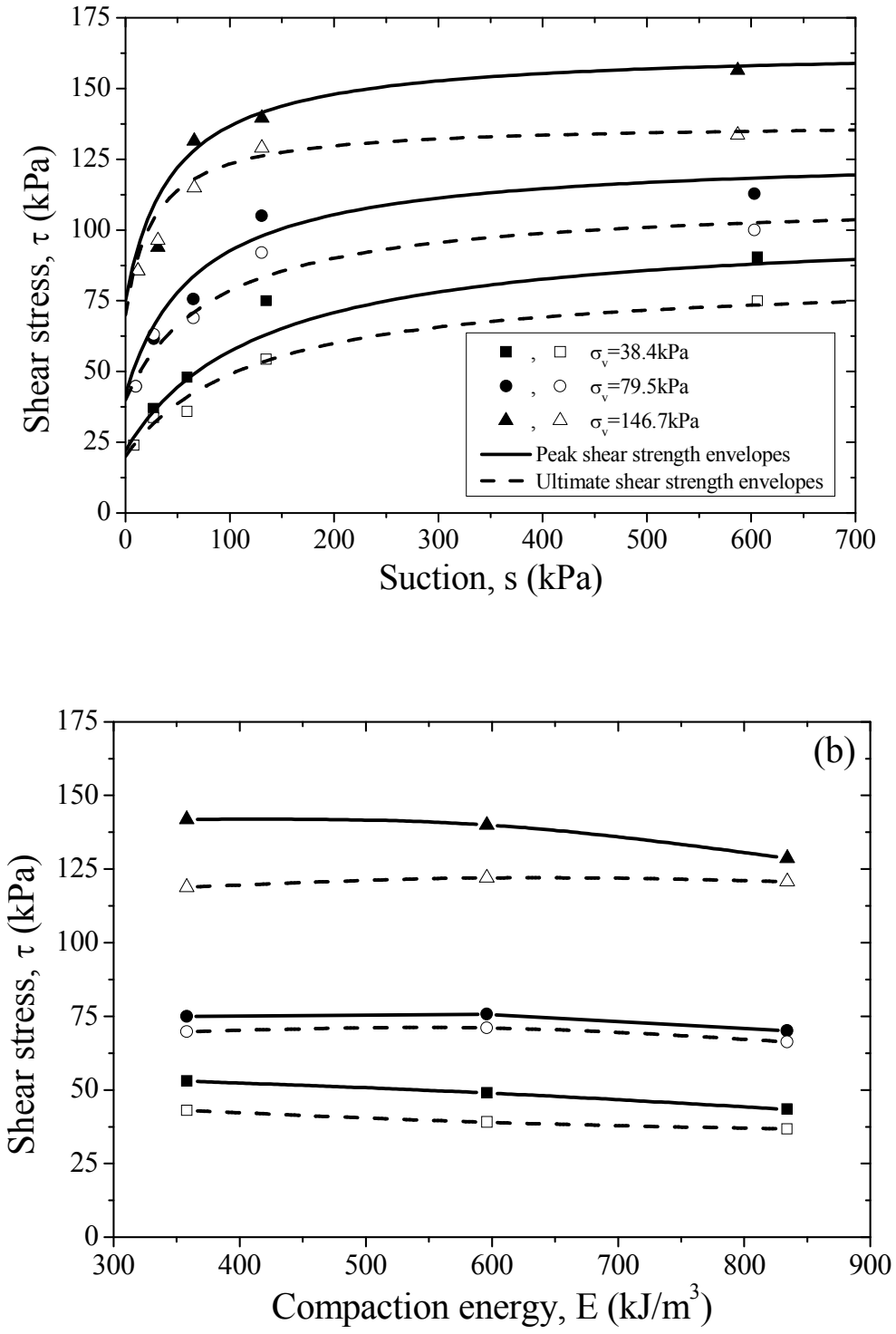

Figure 7.16 Failure envelopes for specimens prepared at (a) various water content and energy level of596kJ/m^3 and (b) at w=12.8-13% and E=358, 596 and 834kJ/m^3.

Considering a simple shear mode of deformation on the shear band, traditionally, the peak shear states have been interpreted in terms of the angle of shear resistance and dilatancy (i.e. Jewell and Wroth, 1987). The stress ratio ϕ_{ds} and dilatancy δ can be expressed as follows:

$$\phi_{ds} = \tan^{-1}(\tau / \sigma_v) \tag{7.11}$$

$$\delta = \tan^{-1}(-\delta y / \delta x) \tag{7.12}$$

where, δy and δx are the vertical and horizontal increments of displacement respectively. Taylor (1948) proposed an energy equation for the stress-displacement relationship for direct shear tests.

$$\tan(\phi_{ds}) = \tan(\phi_{ds})_r + \alpha \tan\delta \tag{7.13}$$

Furthermore, Kim et al. (2009) found that the relationship expressed by Eq. (7.13) is also valid for interpreting the peak states of a weathered granite soil with approximately the same density for different levels of suction, as follows,

$$\tan(\phi_{ds})_{\max} = \tan(\phi_{ds})_r + \alpha \tan\delta_f \tag{7.14}$$

where $(\phi_{ds})_{max}=tan(\tau_{max}/\sigma_v)$ is the maximum stress ratio, $(\phi_{ds})_r$ is the stress ratio at a residual state, α is the constant of proportionality, and δ_f is the angle of dilatancy at peak failure. Figure 7.17 shows the results of the shear tests interpreted in terms of the stress ratio and dilatancy, using a similar approach.

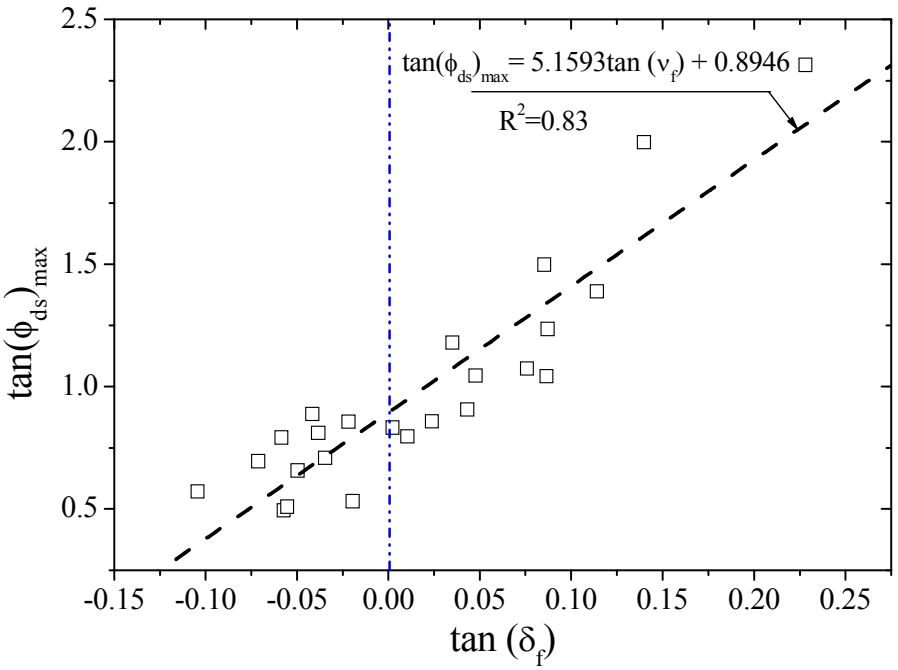

Figure 7.17 Variation of the maximum stress ratio with dilatancy.

While there is a clear trend between the peak shear stress ratio and dilatancy angle, the prediction of the peak stress ratios is quite poor, with a linear regression coefficient of 0.83.

This is likely related to the difference in the soil structure derived from compacting the soil at different water contents and energy levels. Nevertheless, Figure 7.17 clearly shows there is an apparent relationship between the maximum stress ratio and dilatancy which hints that the deformation mode in the shear band may be simple shear, as initially assumed.

7.3.2.1 Ultimate shear states

A summary of the ultimate shear tests data is given in Table 7.4. The results were modelled using two different approaches previously proposed to describe the critical state of as compacted specimens, namely, (a) using the average skeleton stress (Tarantino and Tombolato, 2005 and Tarantino, 2007) and (b) critical stress ratios (Toll, 1990; Toll and Ong, 2003). Both approaches make reference to the saturated states which were found to be relatively independent of the compaction characteristics.

Table 7.4 Summary of the shear test data at ultimate failure of as compacted specimens.

Water content, w (%)	Energy level, E (kJ/m^3)	Applied Vertical stress, σ_v (kPa)	Shear stress at failure, τ_u (kPa)	Suction at failure, s (kPa)	Vertical displacement Δy (mm)	Angle of friction, ϕ (^{o})	Apparent cohesion, c (kPa)
8.5	596	38.4 79.55 146.7	55.71 79.29 133.71	606.00 603.00 587.00	1.17 0.53 0.39	36.0	25.26
10.5	596	38.4 79.55 146.7	54.25 92.1 129.0	134.79 130.54 130.85	1.07 0.77 0.36	33.52	32.12
12.6	358	38.4 79.55 146.7	32.43 69.72 118.8	21.68 15.09 35.00	1.04 0.59 -0.04	38.34	3.86
12.8	596	38.4 79.55 146.7	35.87 59.85 128.49	59.00 65.05 66.08	0.32 -0.01 -0.05	40.21	3.02
13.0	834	38.4 79.55 146.7	36.72 66.28 120.7	28.00 44.00 40.00	0.41 -0.02 -0.44	37.91	5.85
14.1	596	38.4 79.55 146.7	33.66 63.1 96.34	27.68 27.75 31.87	-0.03 -0.45 -0.745	29.70	14.03
14.0	834	38.4 79.55 146.7	29.68 57.78 99	27.96 27.03 31.93	0.04 -0.16 -0.33	32.51	5.91
16.8	596	38.4 79.55 146.7	23.89 44.69 85.6	8.05 10.07 12.57	-0.041 -0.445 -0.445	30.15	1.5

In this study the saturated state parameters were established for a specimen prepared at an initial water content of 12.5%, and subsequently sheared under saturated conditions. The details of the shear strength failure envelope are given in section 7.3.3. Saturated tests were only conducted for these specimens, given the similar stress-strain behaviour between the saturated specimens and as compacted specimens that reached saturation conditions during compression and shearing, i.e. AC 12.8 (150), AC 13 (150), AC 14.1(40), AC 14.1(80), AC14.0 (80) represented in Figure 7.18. At a critical state, the shear strength of these specimens seemed relatively independent of the initial compaction characteristics, albeit there were small differences in the peak shear strength compared to specimens prepared at water contents of 0.128, 0.141 at energy level of 596kJ/m^3; and 0.13 and 0.14 at energy levels of 358 and 834kJ/m^3, respectively. All the specimens represented in Figure 7.18 showed a consistent ultimate stress ratio of 0.67.

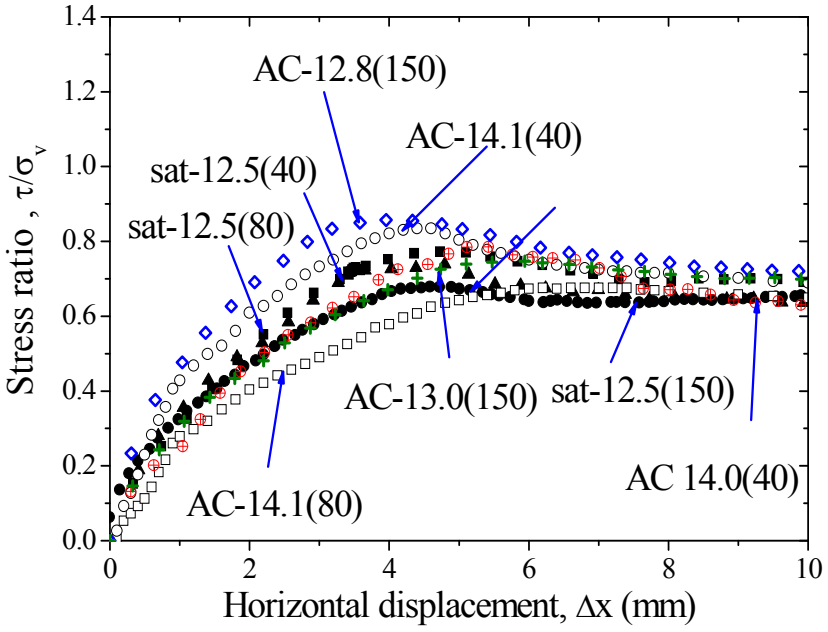

Figure 7.18 Stress ratio plotted against horizontal displacement for saturated drained tests (solid symbols) and constant water content test at high degrees of saturation (open symbols).

Average skeleton stress approach

This approach is based on the assumption that the water menisci have a negligible effect on the ultimate shear strength. The ultimate shear strength is modelled in terms of the average skeleton stress σ'_v, as expressed in Eq. (7.15) in terms of the total degree of saturation S_r and in terms of the degree of saturation of the macropores, or S_{rm}.

$$\sigma_v^{'} = \sigma_v + sS_r \tag{7.15}$$

The degree of saturation of the macropores is considered because this is the degree of saturation likely governing the mechanical behaviour. Similar observations towards the importance of macroporosity in governing the small strain stiffness behaviour are also described in Chapter 5. The shear strength τ, is given by considering the shear strength of saturated states at the same average skeleton stress τ_{sat}, as follows:

$$\tau = \tau_{sat}\left(\sigma_v + sS_{rm}\right) = \tau_{sat}\left(\sigma_v + s\frac{e_w - e_{wm}}{e - e_{wm}}\right) \tag{7.16}$$

where e_w and e are the water ratio ($e_w = e \times S_r$) and void ratio, respectively, and e_{wm} is the microstructural water ratio. The value of e_{wm} was found by the least squares method fitting of Eq. (7.16) of the ultimate shear strength data, and a value of 0.237 was obtained for e_{wm}. Figure 7.17 shows the comparison between the measured and predicted ultimate shear strength for all specimens, considering the average skeleton stress defined in terms of degree of saturation and degree of saturation of the macropores. The predictions considering the average skeleton stress in terms of the total degree of saturation are not accurate, particularly for the specimens prepared at a lower water content, and encircled in Figure 7.17, i.e. 0.105. In contrast, the predictions considering the degree of saturation of macropores are acceptable (see Figure 7.19). The main advantage of using this approach is related to the parameters, where just one additional parameter, besides the reference saturated conditions is required. Similar observations were reported by Tarantino and Tombolato (2005) for statically compacted specimens, despite the fact that the fabric considered was mainly representative of the dry side of optimum (Tarantino and De Col, 2009). It thus appears that the role of the average skeleton stress in governing the ultimate strength may to some extent reproduce a different fabric, given the close association of the degree of saturation with the degree of aggregation (Toll, 2000).

Critical stress ratios approach

This model was originally developed based on a critical state model for saturated soils with total stresses and suction considered separately to describe unsaturated conditions (Toll, 1990; Toll, 2000). The soil fabric was considered by including two individual stress ratios, where the change is governed by the degree of saturation.

This approach seems more appropriate given the strong interrelationship found between the small strain shear modulus and the degree of saturation, or the extent of aggregated macrostructure described in Chapter 5. Toll (2000) extended the general shear strength relationship proposed by Fredlund et al. (1978) expressed by,

$$\tau = c' + (\sigma - u_a)\tan\phi^a + (u_a - u_w)\tan\phi^b \tag{7.17}$$

for a critical state as follows:

$$\tau = \sigma_v \tan\phi^a + s\tan\phi^b \tag{7.18}$$

where, ϕ^a , ϕ^b, are the critical state friction angles in respect to the vertical stress, σ_v and suction, s. The critical state friction angles can be found using multiple linear regression techniques, as suggested by Toll (1990). The details of the multiple linear regression analysis are given in Appendix C. Figure 7.20 shows the smoothed functions obtained for both critical state friction angles, where the relative contribution of ϕ^b is very small in the lower degree of saturation compared with ϕ^a, with the angles varying between 0.006° and 3.4° and 50° and 39° (Sr < 0.8) for ϕ^b. and ϕ^a, respectively.

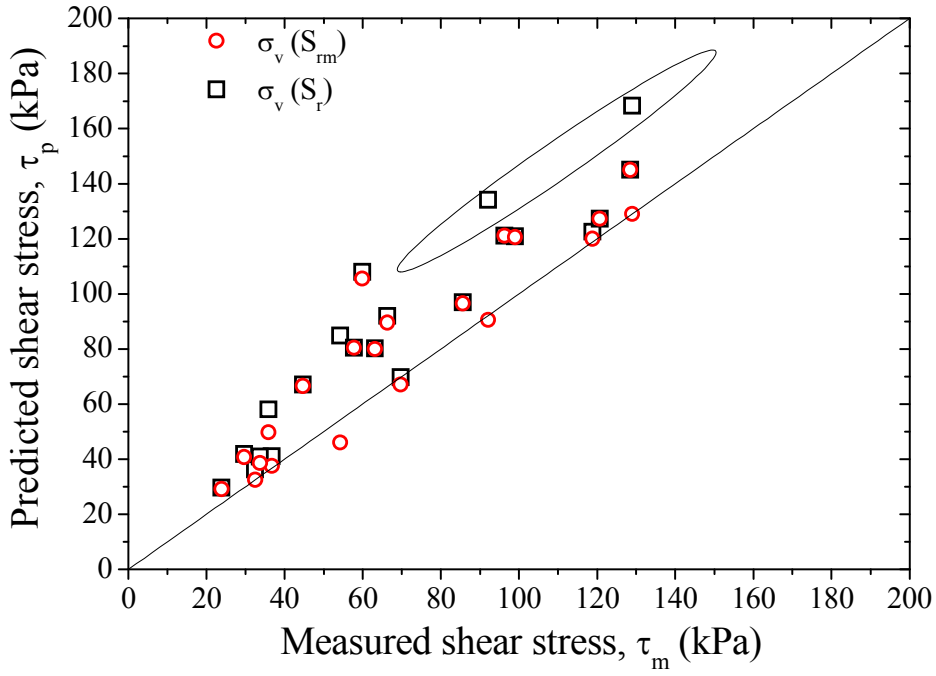

Figure 7.19 Prediction of the ultimate shear strength using the average skeleton approach in terms of degree of saturation (open symbols) and degree of saturation on macropores (solid symbols).

This means that in this range, suction has little effect on the shear strength, which in turn indicates that the water phase has shrunk back into the pores within the soil packets and no longer affects the particle contacts where shearing occurs. Toll (1990) reported similar

observations but for a slightly lower degree of saturation of 0.55, which was probably associated with the difference in the fabric of the soil. In addition, one may note that ϕ^a remains approximately around the same value for S_r<0.77, which might indicate that in this range, the suction holds the aggregations together, and the gradual decrease in ϕ^a in a higher degree of saturation is likely associated with a breakdown of the aggregations (Toll and Ong, 2003). Predicting the shear strength using ϕ^a and ϕ^b smoothed functions may prove difficult because the functions are rather irregular (Figure 7.20). To overcome this limitation, Toll and Ong (2003) suggested an alternative method for determining the critical friction angles ratio ϕ^b and ϕ^a functions. The functions adopted were the following:

$$\frac{\phi^b}{\phi'} = \left(\frac{S_r - S_{r2}}{S_{r1} - S_{r2}}\right)^{kb} \tag{7.19}$$

$$\frac{\phi^a}{\phi'} = \left(\frac{\phi^a}{\phi'}\right)_{\max} - \left[\left(\frac{\phi^a}{\phi'}\right)_{\max} - 1\right]\left(\frac{S_r - S_{r2}}{S_{r1} - S_{r2}}\right)^{ka} \tag{7.20}$$

where S_{r1} and S_{r2} are two reference degrees of saturation and ϕ' is the saturated friction angle. For degrees of saturation exceeding S_{r1}, ϕ^a/ϕ' and ϕ^b/ϕ' ratios are equal to ϕ' whereas for degree of saturation smaller than S_{r2}, $\phi^a/\phi' = (\phi^a/\phi')_{max}$ and $\phi^b/\phi'=0$. In this study the reference degree of saturation was taken as S_{r1}=1 (full saturation conditions) and S_{r2}=0.75, kb=2 and ka=1. Figure 7.21 shows the functions fitted using Eq. (7.19) and Eq. (7.20) where it can be seen they give a close fit to the experimental data.

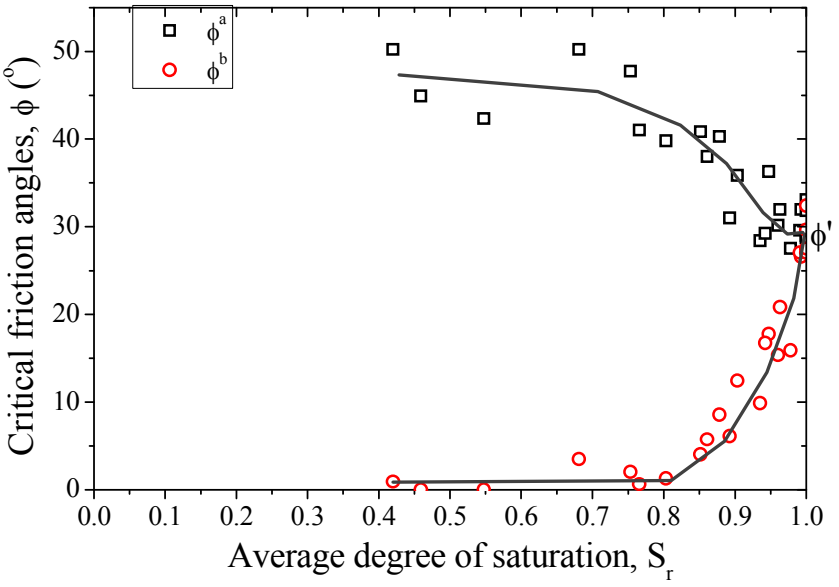

Figure 7.20 Critical friction angles with degree of saturation measured at critical state.

Figure 7.22 shows the comparison between the measured and predicted ultimate shear strength using the average skeleton approach while considering the degree of saturation of the macropores (Tarantino and Tombolato, 2005), and the critical friction angles approach (Toll, 1990; Toll, 2000; Toll and Ong, 2003). A prediction of the ultimate shear strength is favoured by using the critical friction angles approach, where the influence of fabric is associated with a change in the two different critical friction angles with degrees of saturation. Although both approaches are similar in terms of the number of parameters required, the critical friction angles approach seems superior in predicting the shear strength of soil prepared at a wide range of moisture contents, leading to different fabric. It is observed that the good fit of the predictions is satisfactory given that in this study a single set of parameters is used for modelling compaction states that differ in both water content and energy level.

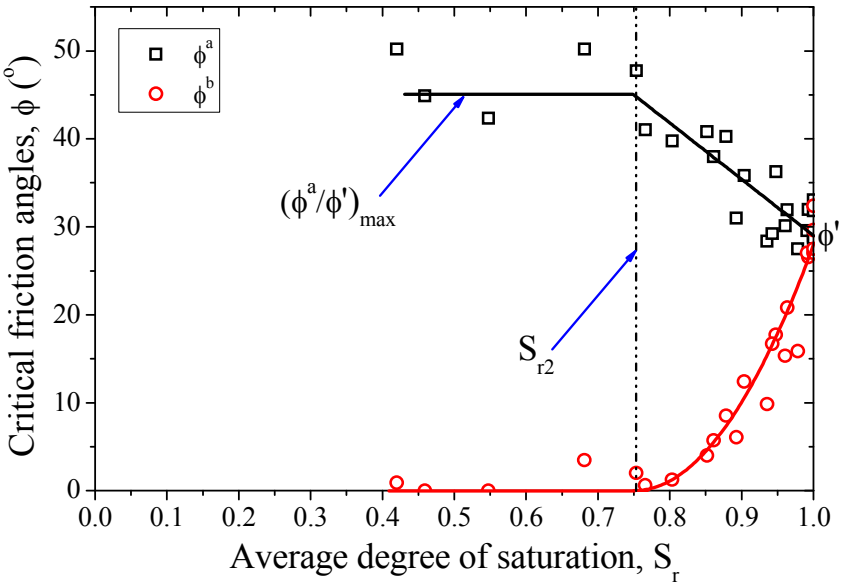

Figure 7.21 Critical friction angles with degree of saturation measured at critical state.

Ultimate void ratio

The ultimate void ratio e may be modelled using the Gallipoli et al. (2003) bonding variable $\xi=(1-S_r)f(s)$ concept, as follows,

$$e = e_s \cdot \left\{1 - a\left[1 - \exp(b\xi)\right]\right\} \tag{7.21}$$

where e_s represents the saturated void ratio at an equivalent average skeleton stress and a and b are fitting parameters. While this expression is adequate for modelling the ultimate void

ratio of the majority of the shear tests, it has some limitations for those that reached saturation conditions because unlike the ultimate shear strength, the final states of shearing in terms of the void ratio do not fall on the saturated *e-ln(σ_v)* envelope (Figure 7.26b).

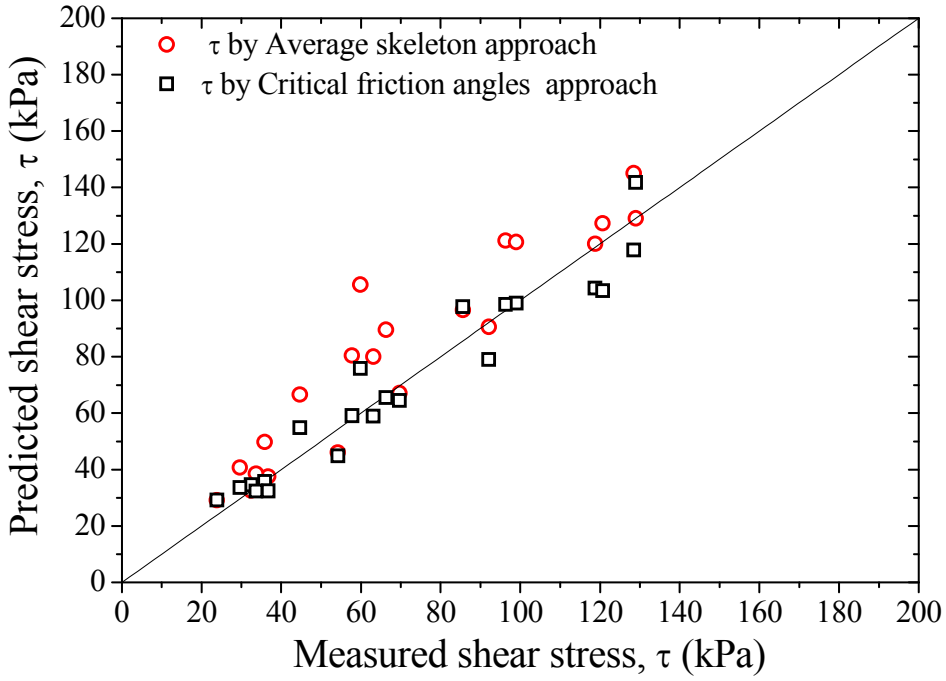

Figure 7.22 Prediction of the ultimate shear strength using the average skeleton approach and using the critical friction angles approach.

Thus, when ξ=0 for full saturation conditions the e/e_s ratio exceeds 1 (see Figure 7.24). Similar observations were also made by Tarantino and Tombolato (2005) for saturated water immersed and unsaturated air immersed kaolin specimens, although none of tested specimens reached full saturation conditions. This may be related to the fact that the initial fabric is not erased during shearing (Toll, 1990), and while the degree of saturation in the macropores reaches saturation conditions, the microspores are likely to remain under unsaturated conditions throughout the entire shearing stage, and thus account for less compressibility compared to the saturated states. The interpolated e/e_s-ξ curve and the parameters are also shown in Figure 7.24. To evaluate the bounding variable, a similar function of suction *f(s)* to that of Gallipoli et al. (2003) was used. The measured and predicted ultimate void ratios are plotted in Figure 7.24. The prediction may be considered satisfactory, given that the ultimate void ratio computed does not represent the variation of this variable on the shear band, it is merely an average value.

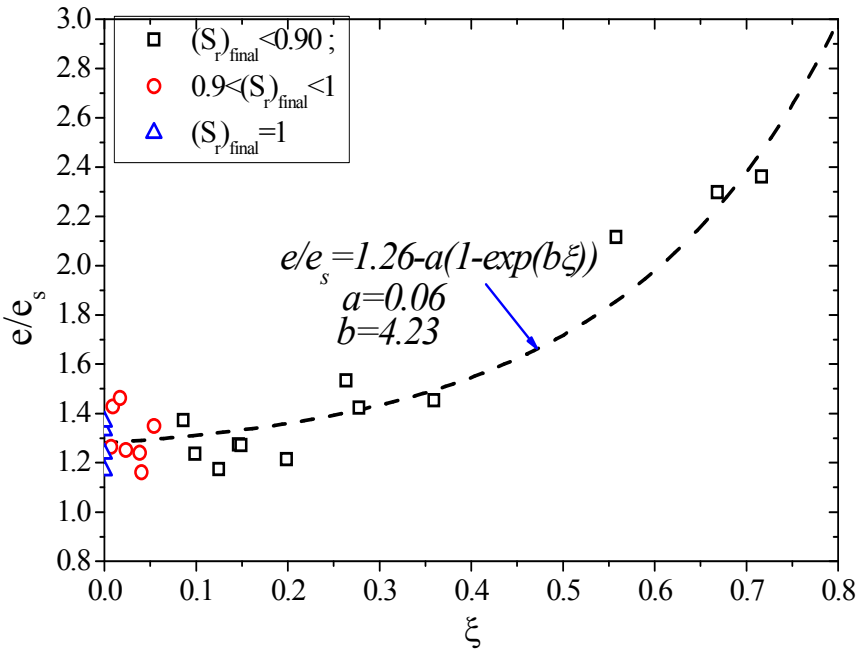

Figure 7.23 Relationship for e/e_s and bonding variable for ultimate state for all specimens.

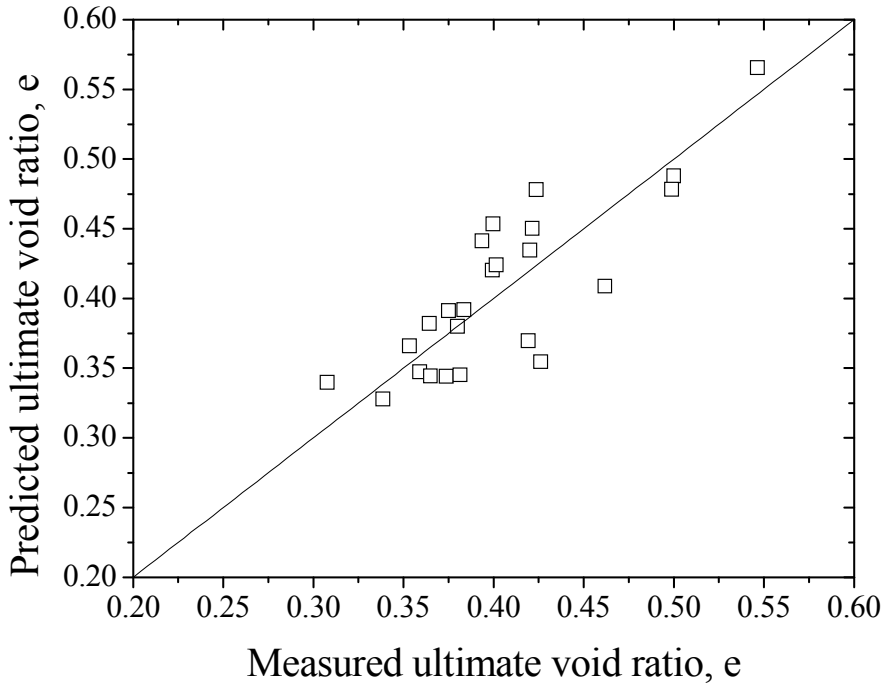

Figure 7.24 Measured and predicted ultimate void ratio using Gallipoli et al (2003) approach.

7.3.3 Post compaction series

To investigate the effect of the change in suction in a post compacted state, the selected specimens were tested for increasing values of suction. In the next sub-sections the results from the tests conducted under saturated and different values of suction will be shown.

7.3.3.1 Saturated states

A series of tests were conducted in saturated conditions so that the saturated parameters could be established. The specimens were prepared at a water content of 0.125 and an energy level of 596kN/m^3. The results from these tests are shown in Figure 7.25, and the peak and ultimate shear envelopes are represented in Figure 7.26. Although, the specimens exhibited predominantly strain hardening behaviour, there were small differences between the peak and ultimate shear strength. The ultimate shear strength of the compacted specimens appears to be independent of the compaction conditions, as both the data from the saturated tests and the as compacted shear tests that reached near saturation conditions, lie on the same curve.

7.3.3.2 Effect of suction and soil structure

Figure 7.28, Figure 7.27, and Figure 7.29, show the relationship between shear stress, vertical displacement, and horizontal displacement of specimens compacted at water content of 0.1, 0.123 and 0.141 and energy level of 596kJ/m^3, and subsequently subjected to varying suction (Table 7.3), the reference saturated state is also represented in Figure 7.28. The specimens were sheared under constant water content conditions, with an applied vertical stress of 79.55kPa. The increase of suction predominantly affects the peak shear stress, that is to say it increases with the increase of suction, whereas the ultimate shear stress seems less affected. These results are consistent with the triaxial constant water content tests conducted on compacted residual soil reported by Rahardjo et al. (2004) and Thu et al. (2006), albeit in these studies small differences were noted in the ultimate shear strength. It appears that an increase in suction contributes to a more pronounced strain softening behaviour. This in turn is likely associated with changes in the microstructure that the soil undergoes when it is subjected to wetting or drying (i.e. Koliji et al., 2006). During the drying process, the most dramatic changes in the soil structure are mainly concentrated at the macrostructure range, which means that the soil is becoming gradually more aggregated with increasing suction. In the first stages of shearing the behaviour is likely dominated by the frictional nature of the larger aggregations, which may be partially destroyed while shearing is underway, after which the shear strength is likely governed by the microporosity range. These results also expose the dangers of performing multi-stage tests for evaluating the shear strength of soil, as already discussed by Toll (2000).

The specimens sheared at initial lower suctions (i.e. 0, 12.8, 38.49, and 42.5 kPa) exhibited mainly contractive behaviour, whereas dilation was dominant in the specimens sheared at higher suctions (i.e. s>50kPa). All the data plots suggest that there is an increase in dilation with increasing suction. This is consistent with the results of unsaturated direct shear tests conducted on expansive clay, and reported by Zhan and Ng (2006).

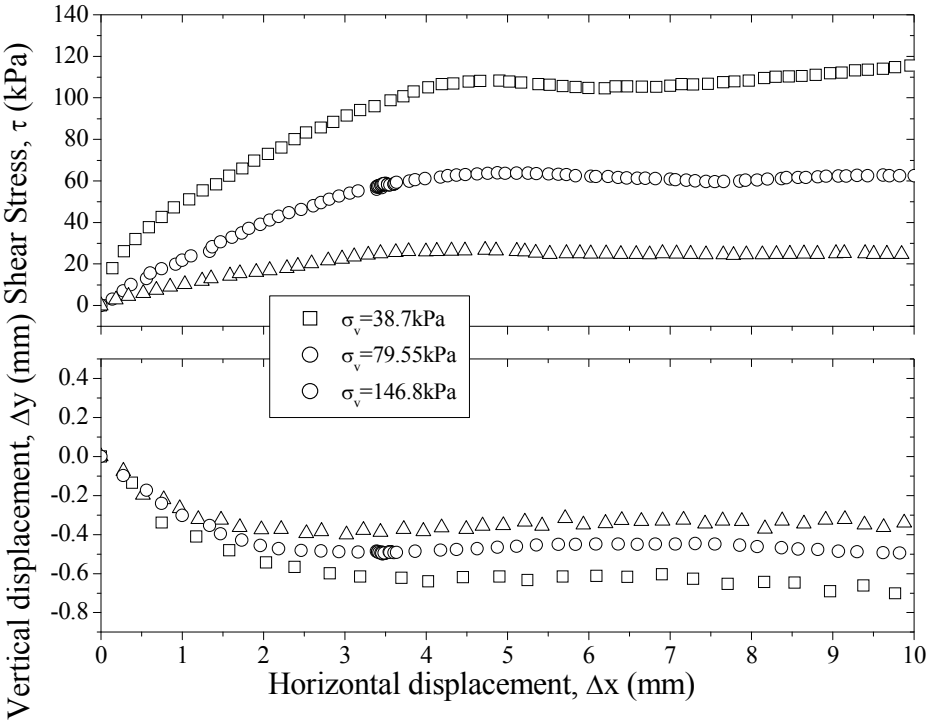

Figure 7.25 Shear tests on saturated specimens compacted at *w=12.5%* (top) shear stress and (bottom) vertical displacement

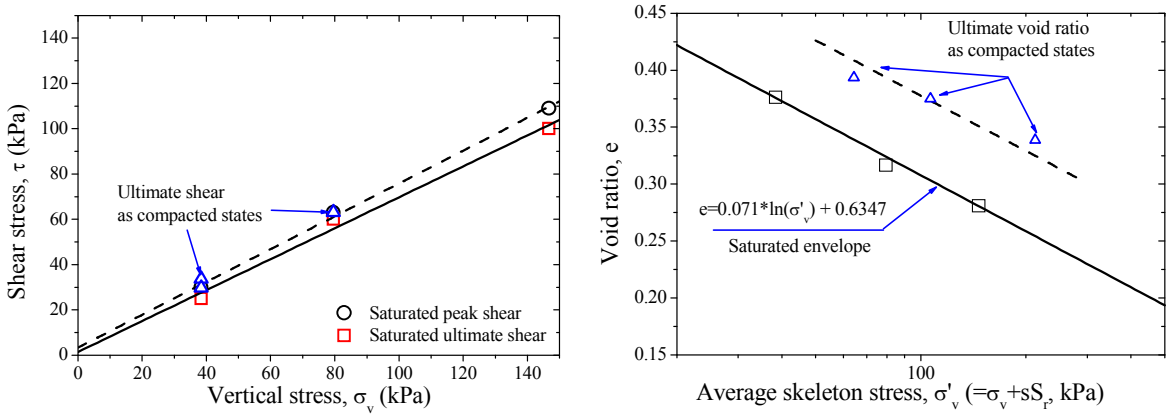

Figure 7.26 Shear tests on saturated specimens compacted at *w=12.5%* (a) failure envelopes and (b) ultimate void ratio.

The differences between the peak and ultimate shear strength can be described using the commonly adopted brittleness index or I_B, first introduced by Bishop (1967) and generalised I_{GB} by D'Elia et al. (1998), and can be expressed as follows,

$$I_B = \frac{\tau_p - \tau_r}{\tau_p} \tag{7.22}$$

where τ_p and τ_r represent the peak and ultimate shear strength. Figure 7.30a shows the brittleness index I_B, as defined in Eq. (7.22), plotted against suction. It is observed that the I_B increases with the logarithmic increase of suction, and while there is a close fit with a logarithmic relationship for the specimens initially compacted at a water content of 0.123, the specimens prepared at an initial water content of 0.10 and 0.14 seem to show a step wise increase. This difference is possibly related with different initial soil structure. Based on this relationship, since the ultimate shear strength seems reasonably unaffected by an increase in suction, the peak shear strength may be estimated for post compaction conditions. Note however, that the tested range was small leading to a change in water content of around 1-2%.

The peak and ultimate shear stress envelopes with respect to suction, interpolated using a hyperbolic model (Miao et al., 2001; Vilar, 2006), are represented in Figure 7.30b. In general, the shear stress exhibits a non-linear increase with suction for all the test specimens. The points belonging to the specimens with lower values of suction where the shear stress envelope seemed to follow close to the saturated line is worthy of note because the suction in these specimens did not exceed the air entry value, so the shear stress is governed by the saturated envelope. Also, the highest shear stresses were obtained for specimens compacted at 10.5% (dry of optimum). However, a previous study on statically compacted till (Vanapalli *et al.*, 1996), showed higher shear stress values on the wet side of OMC. This discrepancy might be attributed to the distinctly different soil structures (aggregation) produced by dynamic and static compaction procedures. It is interesting to note that the majority of the tested specimens seem to define a common ultimate shear stress envelope, despite the fact that their structure is likely different. These results seem to indicate that the suction acting on the inter-aggregation pores responsible for the different peak shear strength envelopes may not have such an important role in governing the shear strength when the soil reaches its ultimate state. In this range, the suction acting on the intra-aggregation pores is possibly governing the shear strength behaviour. Thus the existence of a common envelope would suggest that indeed the

soil structure at microporosity level of all specimens share some similarities. Nonetheless, further microscopic evidence would be advisable to ascertain this hypothesis.

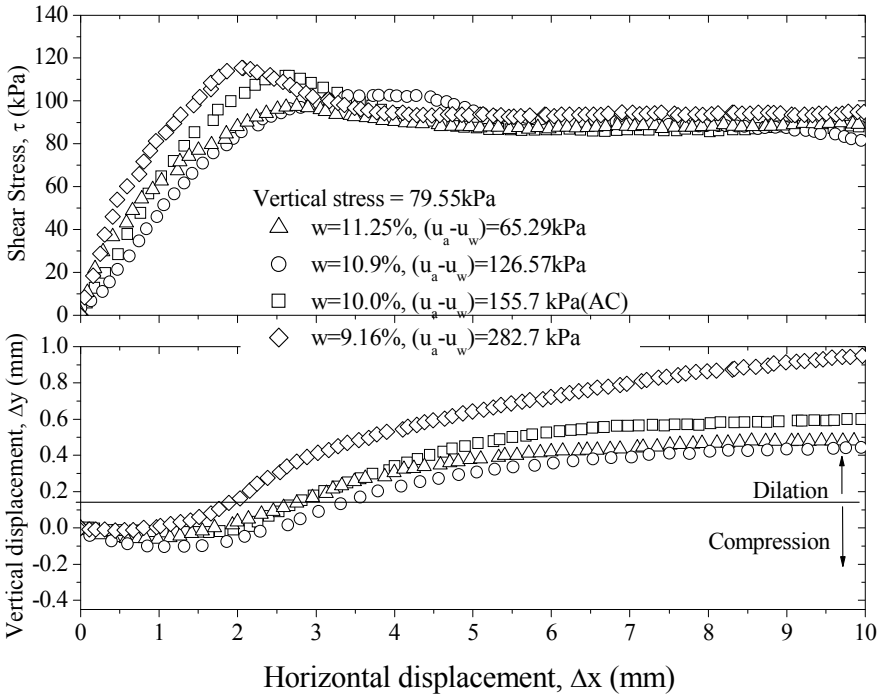

Figure 7.27 Shear tests on specimens compacted at *w=10.0%* but tested at different post compaction suction values (top) shear stress and (bottom) vertical displacement

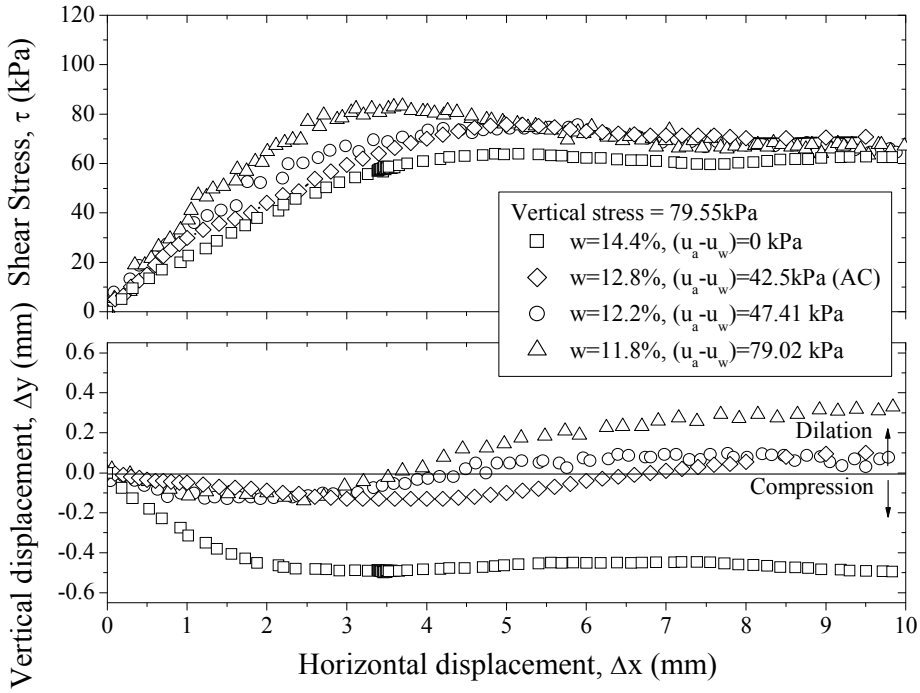

Figure 7.28 Shear tests on specimens compacted at *w=12.3%* but tested at different post compaction suction values (top) shear stress and (bottom) vertical displacement

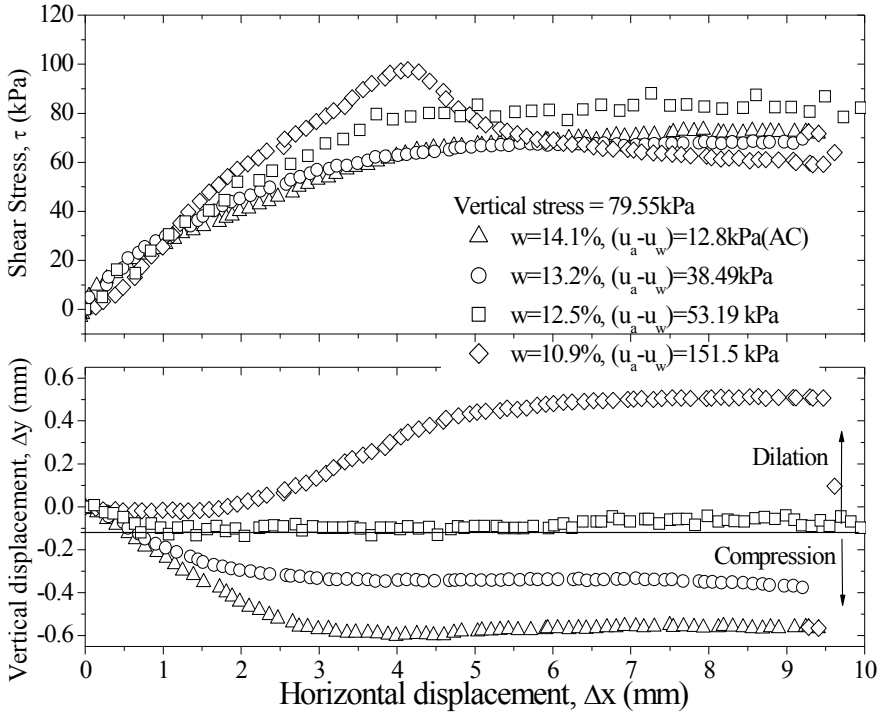

Figure 7.29 Shear tests on specimens compacted at w=14.1% but tested at different post compaction suction values (top) shear stress and (bottom) vertical displacement.

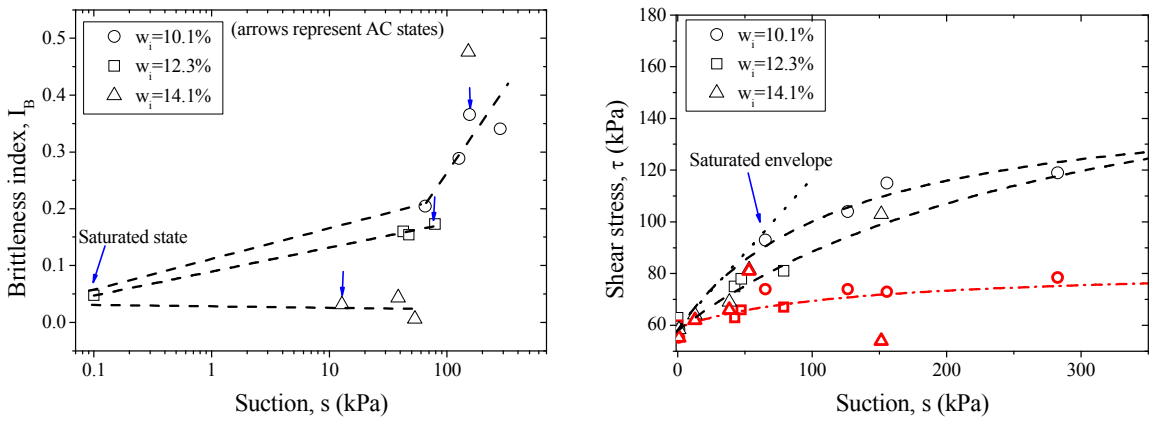

Figure 7.30 Variation of (a) the brittleness index and (b) shear stress with suction for specimens initially compacted at *w=12.3%* and subjected to different post compacted suction values.

7.4 SUMMARY

The limited test data for compacted specimens taken from Caruso and Tarantino (2004) and Jotisankasa and Mairaing (2010), enabled the variation in suction to be interpreted through

constant water content, direct shear (CWDS) testing. During shearing, the variation in suction could be corroborated with the volumetric changes of the specimens. A simple method for evaluating the variation in suction induced by CWDS was proposed based on the volumetric changes in the shear zone. For small horizontal displacements up to 2.5mm, the predictions of suction variation based on the proposed relationship were in acceptable agreement with the experimental data. However, the predictions overestimated the variation in suction at larger horizontal displacements (i.e. larger than 3mm) where the fabric seems to play a more important role in controlling suction during shearing. Small discrepancies between the predictions and experimental data were also found in the Omkoi silt specimens prepared at higher moisture content (with suction at or below the air entry value). This difference may be related to inadequate interconnection among the air voids. Since no particular upgrades were necessary for testing constant water conditions using a conventional shear box, provided that due care is taken to ensure undrained and air tight conditions, it is encouraging to use CWDS testing for determining the unsaturated shear strength parameters.

From a number of CWDS tests performed on as compacted specimens, it was noted that the difference in compaction history (water content and energy level) leads to the development of characteristic shear stress envelopes. Specimens compacted on the dry side of OMC exhibited the largest apparent cohesion, whereas the highest effective friction angle occurred in specimens compacted at near OMC. It is likely that the effective friction angle is associated with the structure of the soil or aggregation. The ultimate shear strength was modelled using both average skeleton stress and critical stress ratio approaches. It was found that the latter lead to more accurate predictions of ultimate shear strength. This difference was interpreted as the result of the difference in the initial fabric. While both approaches consider the effect of fabric through the degree of saturation, in the critical stress ratio approach this influence is defined explicitly in the degree of saturation functions. A similar association with fabric and degree of saturation was also considered in Chapter 6 for the small strain shear modulus. The ultimate void ratio was predicted using Galipolli et al. (2003) bonding variable concept, however, it was found that the ratio between the unsaturated and saturated void ratio at the same average skeleton exceeds 1 for the specimens that reached saturation during shearing. This was interpreted as the result of a lower compressibility of the specimens departing from the unsaturated states that despite having reached full saturation conditions

were likely maintaining unsaturated conditions in the intra-aggregate pores. The predictions were acceptable in comparison with experimental data.

The increase in post-compaction shear stress with respect to the suction was non-linear for every specimen, but conversely, it seems that the rate of increase in shear stress varies with the different initial compaction characteristics. It was also noted that while the peak shear strength envelopes among the three different initial compaction characteristics differed quite considerably, the ultimate shear strength was less affected.

CHAPTER EIGHT

8 . ANTICIPATED APPLICATIONS

8.1 GENERAL

This chapter describes two major applications of the present study. First, a site specific validation is outlined with special reference to PLDC site, where the site characteristics were described in Chapter 3. The predictions of field, dry unit weight are based on the theoretical and empirical developments outlined in Chapter 6, using the parameters calibrated in the laboratory. Design charts are also presented to facilitate the use of the proposed relationship. The ultimate bearing capacity is an important parameter in the design of shallow foundations where the expected range of field bearing capacity is obtained for the shear strength parameters determined in Chapter 7. Correlations with field shear wave velocity and elastic modulus that enable the estimation of load settlement relationships for unsaturated conditions are also described.

Secondly, the main aspects related to the use of the soil modulus to assess the quality of compaction based on the findings presented in Chapter 5 and 6 are discussed, and common end-product specifications are examined in light of these new findings. Finally, a summary of this chapter is presented.

8.2 EVALUATING THE COMPACTION AT THE PENRITH LAKES SITE

8.2.1 Field Validation

The study of the PLDC material was carried out in both laboratory and field conditions. From the laboratory experimental tests reported in Chapters 5 and 7, the small strain and “in service” strain behaviour of the material was appraised based on compacted specimens prepared at different water contents and energy levels. For field work, boreholes were conducted at selected locations, as shown in Chapter 3, and samples were collected at various depths to evaluate in-situ water contents which were shown in Chapter 4. To evaluate current

compaction conditions in terms of the dry unit weight of the fills, an empirical model incorporating the field measurements of V_s and suction, or the water content, was developed. While the performance of the empirical model was assessed for laboratory tests, these tests were conducted in laboratory controlled set-ups, which do not always represent field conditions, particularly in terms of material variability. For that reason, it is extremely important to validate the performance of the model against field measurements.

In the next sub-sections, the field results described in Chapter 3 and 4 are revisited and the predictions of the empirical model proposed in Chapter 6 are compared with the field in-situ bulk unit weights.

8.2.1.1 Normalising V_s for field assessments

In natural soil deposits the mean effective stress increases with increasing depth. Therefore, the measured V_s of deeper layers is expected to be larger than those in shallow layers, even when the density of the site is uniform. To assess the degree of compaction, or density, based on in-situ V_s, the effect of confinement (or overburden stress) should be considered. The issue of normalising V_s with depth or overburden pressure has been long recognised by many studies, originally conducted for SPT and CPT correlations (i.e. Tokimatsu and Uchida, 1990, Robertson and Wride, 1998; Kim and Park, 1999; Zhang et al., 2002; Zhang, 2010). This normalisation is intended to give a benchmark value of the shear wave velocity at a given depth, typically the depth equivalent to an overburden pressure equal to an atmospheric pressure of 100kPa (P_a), or in other words, $V_{s,n}=V_s$ for a depth where the in-situ vertical stress is 100kPa, for instance considering a bulk unit weight of 20kN/m^3, the reference correspondent depth is 5m. This aspect poses some difficulties if surface conditions are to be considered. In Eq. (8.1), V_s takes null values if the mean effective stress is zero. It seems more reasonable to modify Eq. (8.1) so that $V_{s,n}=V_s$ for the mid-point condition of a given seismic stratigraphy layer, as expressed in Eq. (8.2). The reference pressure at each layer mid-point becomes the benchmark instead, or in other words the $V_{s,n}=V_s$ in the mid-point of the layer (Figure 8.1).

Method 1:

$$V_{s,n} = V_s \left(\frac{P_a}{\sigma_m} \right)^n \tag{8.1}$$

where, $V_{s,n}$ is the normalised shear wave velocity, P_a is the reference stress (typically atmospheric pressure), n is the stiffness parameter taken as 0.25 and field mean effective stress or σ_m

Method 2:

$$V_{s,n} = V_s \left(\frac{P_a}{(P_a - \sigma_{mid}) + \sigma_m} \right)^n \tag{8.2}$$

where, σ_{mid} is field mean effective stress or σ_m at the mid layer, and it can be calculated as follows,

$$\sigma_m = \frac{(1 + 2K_0)\sigma_v}{3} \tag{8.3}$$

In the above, $\sigma_v (= \gamma_b z)$ is the vertical effective stress and K_0 is the earth pressure coefficient at rest, and n is the stress exponent taken as 0.25. The estimation of the coefficient of earth pressure at rest in an unsaturated soil is a somewhat complex topic (Fredlund et al., 2012). Although Fredlund et al. (2012) proposed a relationship for the unsaturated earth pressure at rest based on Poisson's ratio and the elastic modulus with respect to the change of suction and vertical stress, these parameters are not easily evaluated and depend on the stress history. At the PLDC site, the stress history of the soil is unknown, thus a simpler empirical relationship such as the one proposed by Jaky (1944) for granular materials that has been supported by previous experimental studies (i.e. Bishop, 1957; Broker and Ireland, 1965) is preferable, albeit some errors are likely to stem from this approximation. A value of K_0 of 0.436 was obtained considering the saturated drained friction angle (ϕ') of 34.3° which was determined in the saturated shear box tests (see Figure 7.25 described earlier in Chapter 7). To determine σ_v an average in situ bulk unit weight of 20.5kN/m^3 was considered based on the DHGD (Downhole Gamma Density) profiles previously examined (see earlier in Chapter 3).

Although widely used, method 1 is not suitable for this analysis because the mean effective stress term (σ_m) is explicitly defined in Eq. (6.6), therefore, the field V_s with no correction for confining stress should be used. The normalisation exercise proposed in method 2 is only useful to interpret the variation in V_s with depth within the different ranges or layers identified in the seismic stratigraphic profiles.

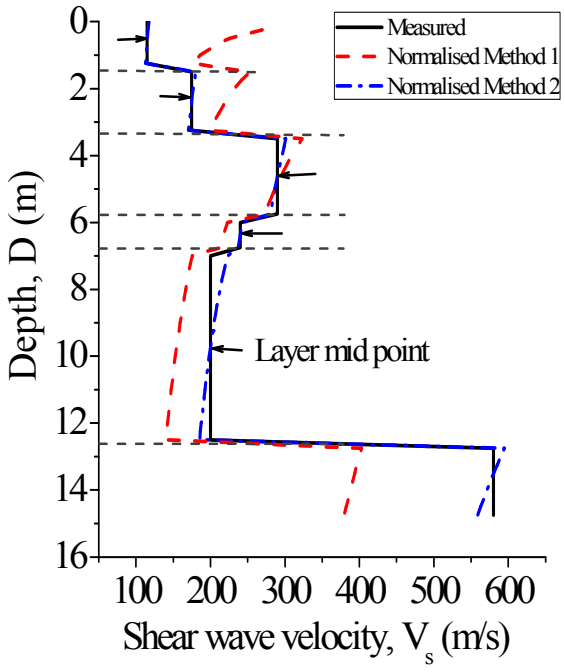

Figure 8.1 Shear wave velocity normalisation by method 1 and method 2 for borehole location 7.3; arrows indicate seismic stratigraphic layer midpoint (measured V_s data from Harutoonian, 2012).

8.2.1.2 Field bulk unit weight evaluation

To evaluate the field bulk unit weight, Eq. (6.6) was adopted using the same parameters obtained for the laboratory study given in Table 6.2 (post compaction states). The field suction was evaluated based on the experimental empirical relationship described in Figure 5.3. The field shear wave velocity data were obtained using HVSR (Horizontal-to-Vertical Spectral ratio) techniques. For further details the reader is referred to Harutoonian et al., 2012) and Harutoonian (2012). The performance of the prediction was compared in terms of the bulk unit weight which was monitored in selected boreholes using down-hole Gamma density (DHGD) tests. The model predicted the in-situ void ratio based on the measured V_s stratigraphy profiles and the measured or interpolated water content (w). For higher depths, exceeding the depths considered in field water content assessments, changes in the water content were noted. In this case, the values adopted were those obtained in the augured boreholes. The void ratio (e) obtained was then used to determine the bulk unit weight γ_b as follows,

$$\gamma_b = \frac{\gamma_w G_s}{1+e}(1+w) \tag{8.4}$$

where G_s=2.7 and γ_w=9.81kN/m^3. The predictions taking the reference soil calibration parameters and the field data for the selected boreholes considered in Chapter 3 are shown in Figure 8.2 - 8.4. Overall, the predictions matched well with the field DHGD bulk density despite the anticipated material variability described in Chapter 3. This seems to indicate that the reference material selected for this study was adequate. Although there were strong discrepancies, particularly in the top 2m for boreholes located at 7.3, 9.2 and 9.3,. in the borehole located at 7.2, there was good agreement after 0.5m depth. This suggests that the initial guess of 1.5m for the depth of influence H_s, based on the Thornthwaite moisture index (TMI) (Thornthwaite, 1948) may have been conservative, as the prediction of bulk density to a depth of 2m is poor. Other small discrepancies may be associated with some degree of material variability on site.

While there is almost no change in the V_s profile near the GWL (Figure 8.4), there is a significant change in the water content. The prediction tends to underestimate the measured bulk unit weight. Nonetheless, it seems sensible to judge the bulk unit density near the ground water level (GWL) to be the same as the one predicted slightly above the GWL. Below this point, V_s increases significantly up to values of 550m/s, confirming the presence of a larger stiffness layer which corresponds to the baseline of the filling operations (Golaszewski, 2012).

8.2.1.3 Quick reference w-γ_d -V_s charts

The graphical solution of Eq. (6.6), using the same parameters obtained for the laboratory study given in Table 6.2 (post compaction states) is shown in this section. These charts are useful for quick reference of the relationship along the compaction plane and also allows for a visual interpretation of Eq. (6.6). In Figure 8.6, the w-γ_d -V_s charts for different levels of field mean effective confining stress varying approximately from an equivalent depth of 2m (≈25kPa) up to 19.5m (≈250kPa) are plotted, the standard compaction energy compaction curve as well as the degree of saturation lines of 1, 0.8, and 0.67 are also represented. It is interesting to note that the equal V_s lines represented across the compaction are almost perpendicular to the degree of saturation lines. This is consistent with the experimental observations made in Chapter 5, which showed the close relationship between V_s and the degree of saturation.

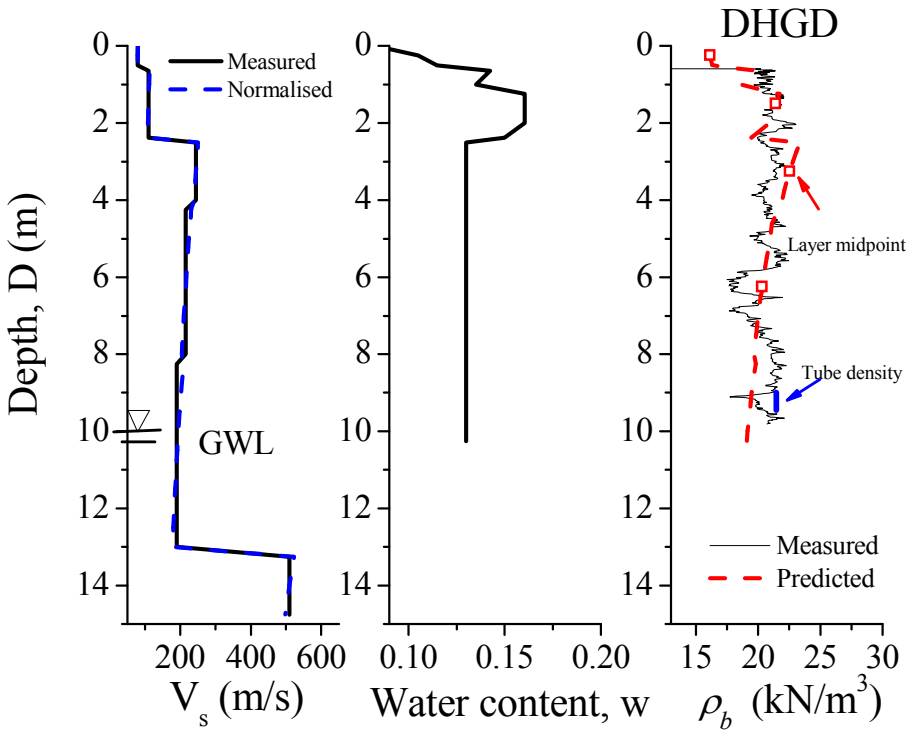

Figure 8.2 Comparison between the field measurements and model predictions for the borehole located at 7.2 (measured V_s data from Harutoonian, 2012).

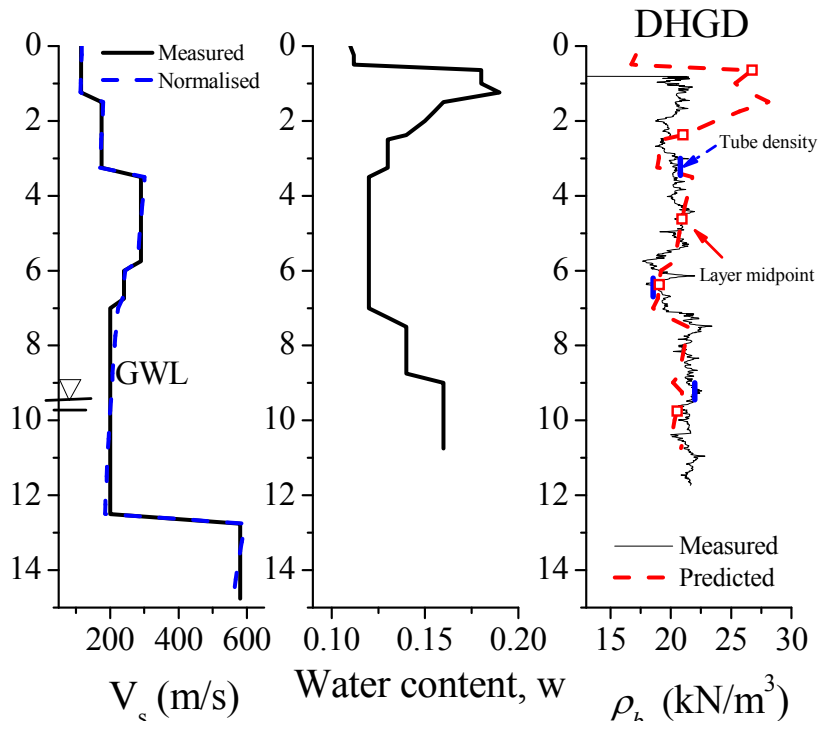

Figure 8.3 Comparison between the field measurements and model predictions for the borehole located at 7.3 (measured V_s data from Harutoonian, 2012).

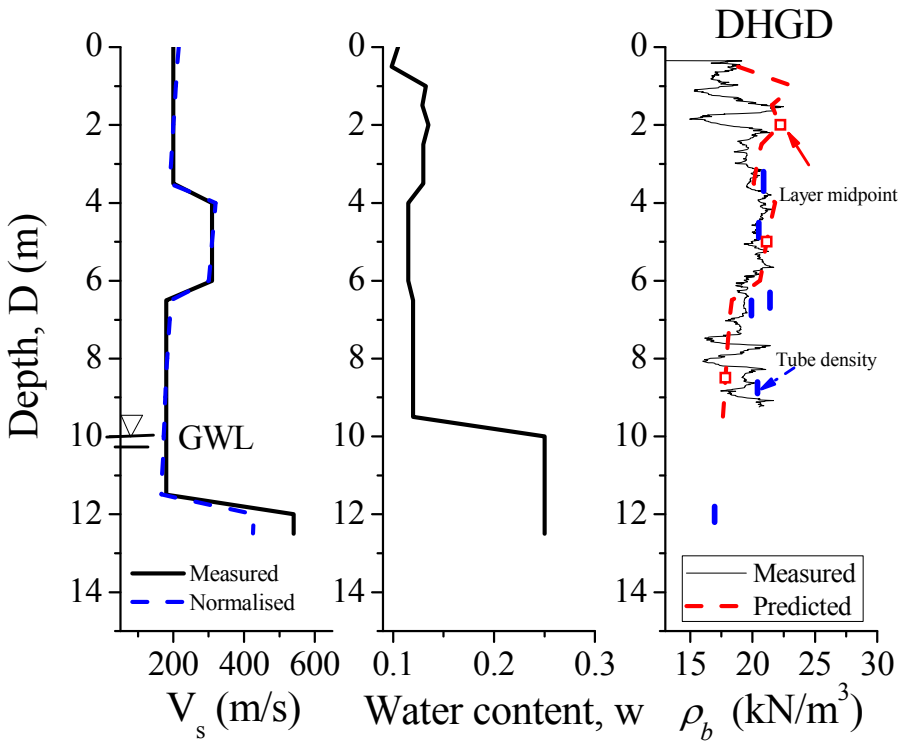

Figure 8.4 Comparison between the field measurements and model predictions for the borehole located at 9.2 (measured V_s data from Harutoonian, 2012).

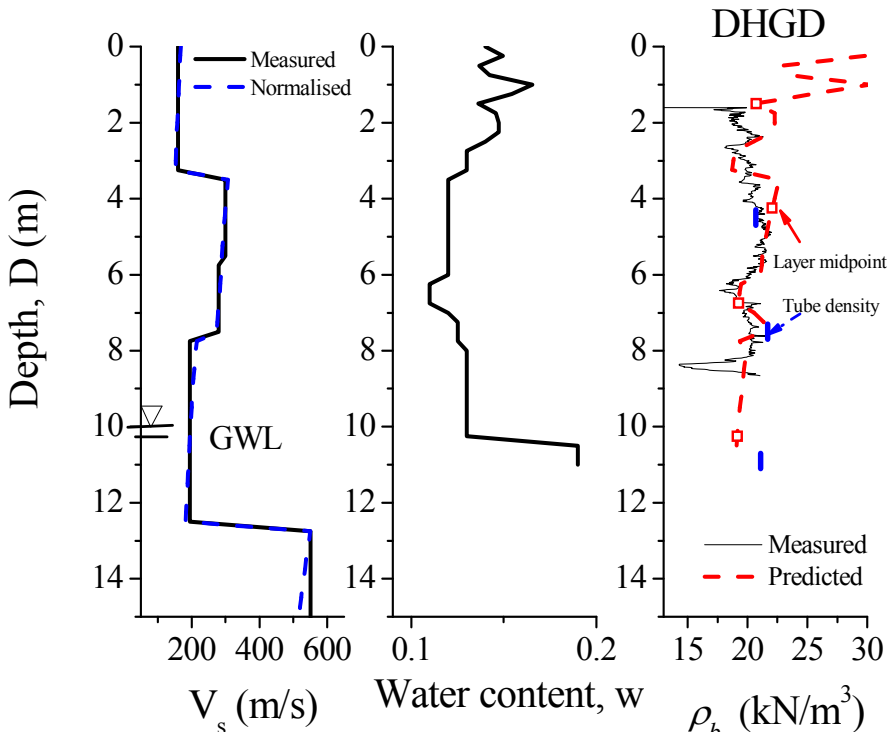

Figure 8.5 Comparison between the field measurements and model predictions for the borehole located at 9.3 (measured V_s data from Harutoonian, 2012).

The use of the quick reference chart is limited to the portion of the ground profile above the GWL, mainly because the calibration of the parameters is intended to reproduce "as compacted" conditions. Furthermore, below the water table, which is typically located between 10-12m deep, some degree of consolidation may have been occurring over time, given the significant overburden pressure resulting from the overlying materials. This aspect is not taken into account.

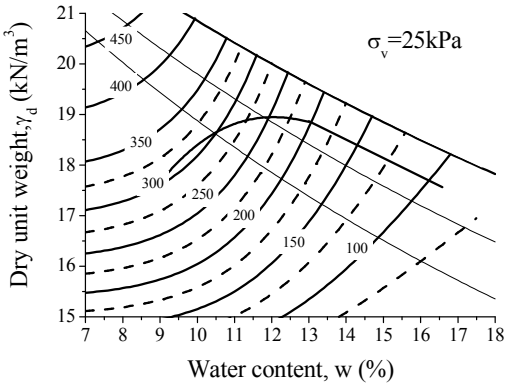

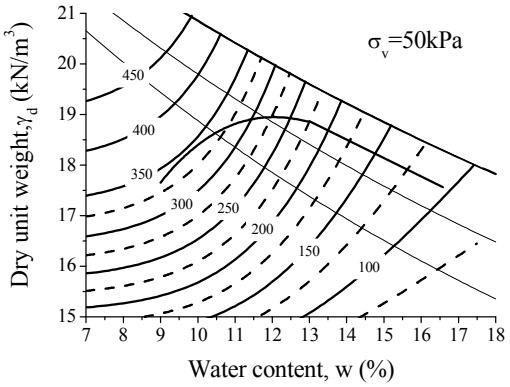

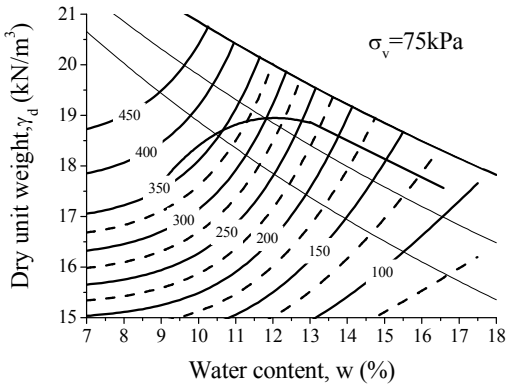

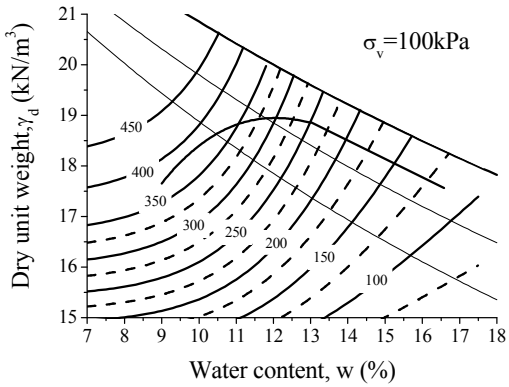

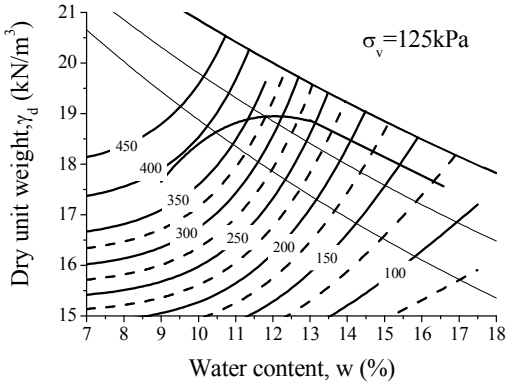

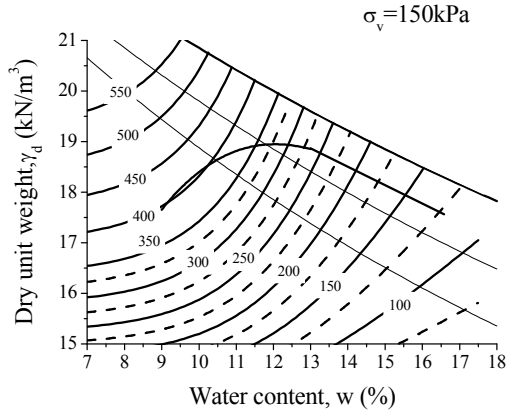

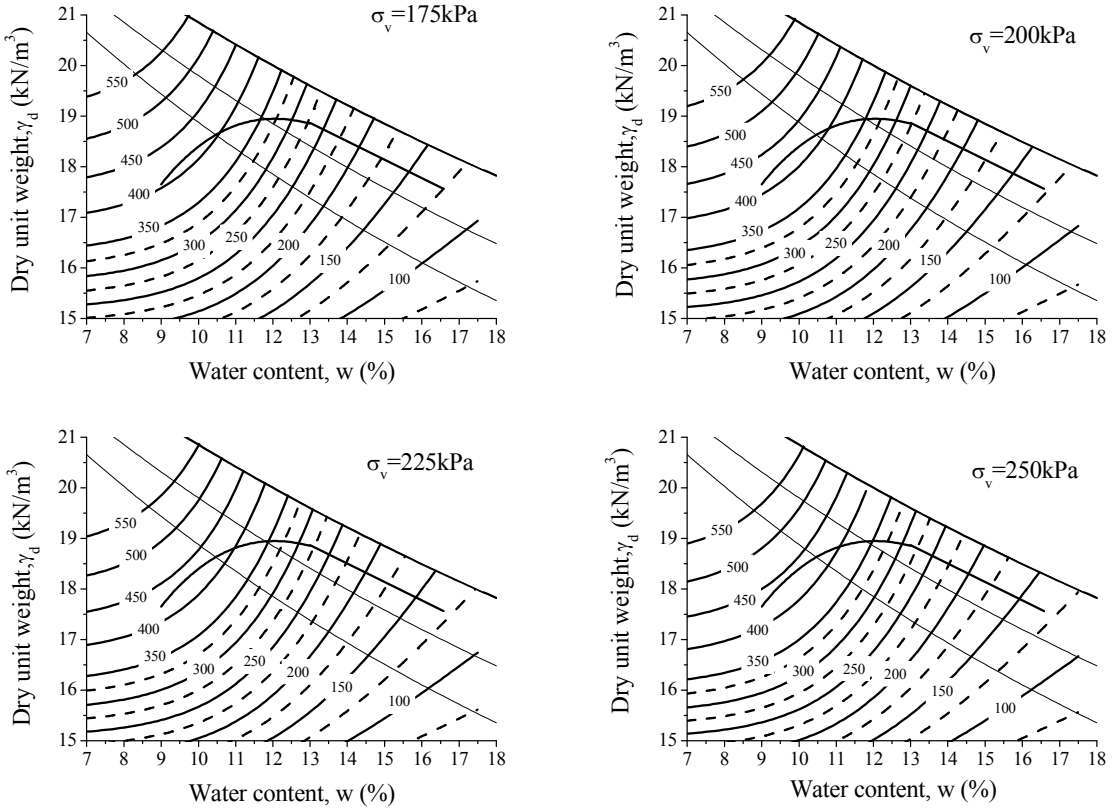

Figure 8.6 Quick reference w-γ_d -$V_{s,n}$ charts for different levels of vertical stress or confining pressure (bold and dash lines represent intervals of 50m/s and 25m/s of shear wave velocity, respectively).

The procedures for determining the dry unit weight based on the field measurements of V_s and water content using the charts are described step by step in the following paragraphs.

Step 1: Determine the mean vertical effective stress, σ_m at a given field depth using K_0=0.436 (Jaky's empirical equation) and an average bulk unit weight of 20.5 kN/m^3. For this example, let us consider a depth of approximately 7.75m which gives a σ_v *=158.88kPa* and this corresponds to a mean effective stress of approximately 100kPa using Eq. (8.3).

Step 2: Collect field data for V_s and water content (w); for this exercise we shall consider two cases. Case 1: *V_s=180m/s* and *w=12%* (CS9.2) and Case 2: *V_s=200m/s* and *w=14.0%* (CS7.3).

Step 3: Refer to the correct mean vertical stress chart (replotted in Figure 8.7) and determine the intersection for the water content in the horizontal axis and the desirable $V_{s,n}$

line obtained using Eq. (8.2) for Case 1: $V_{s,n}$=*186.27 m/s* and Case 2: $V_{s,n}$=*215.33 m/s* to find the corresponding dry unit weight on the y-axis.

The pair of field measurements considered in Case 1 would arrive at a dry unit weight of 16.2 kN/m^3, which is below a commonly adopted end product specification of a minimum of 95% of the maximum dry unit weight at the OMC (AS 3798 - 2007) taking the soil used in the study as a reference. This means that depending on the importance of the superstructure, additional soil improvement would be necessary. For case 2 we would arrive at a dry unit weight of 19.2 kN/m^3 which is above the reference soil minimum dry unit weight and hence the soil would not require any additional improvement. Notice that there may be physically unattainable conditions, relating to some degree of material variability, that may lead to pairs of water content and shear wave velocity for which the chart cannot be used in the manner explained previously.

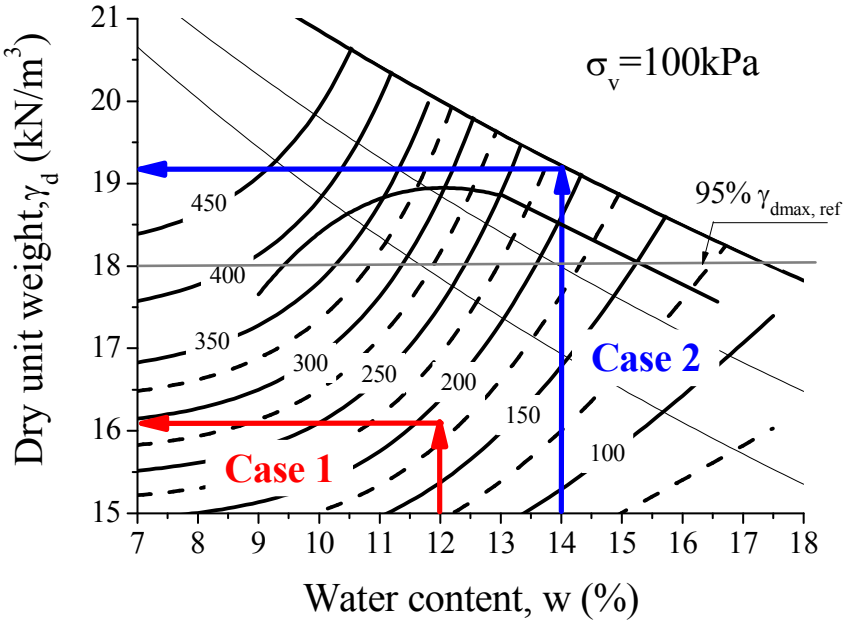

Figure 8.7 Illustration of the working flow of the w-γ_d -$V_{s,n}$ quick reference charts.

8.2.2 Estimation of unsaturated bearing capacity

The estimation of bearing capacity and settlement is currently used in engineering practice for the design of the foundations. Although the these parameters and their interpretation for

saturated conditions have been well established and widely used in practice (i.e. Poulos and Davis, 1974), less research has been focussed on investigating the effect of suction where the foundations lie on unsaturated ground. This aspect is particularly relevant in the PLDC site, given that a large portion of the landform is under unsaturated conditions.

As described earlier in Chapter 6, the unsaturated shear strength can be given through semi-empirical procedures while considering the saturated shear strength parameters, ϕ' and c' and current net stress $(\sigma - u_a)$ and suction $s = (u_a - u_w)$, and the degree of saturation S_r (Vanapalli et al., 1996), as follows:

$$\tau_{unsat} = c' + (\sigma - u_a)\tan\phi' + (u_a - u_w) S_r^{\kappa} \tan\phi' \tag{8.5}$$

where, c' is the effective saturated cohesion, ϕ' is the effective saturated friction angle, κ is a fitting parameter that is a function of the plasticity index (Vanapalli and Fredlund, 2000). Based on the shear strength concepts for unsaturated soil described in Eq. (8.5), Vanapalli and Mohamed (2007), and more recently Oh and Vanapalli (2011), extended the ultimate bearing capacity expression originally proposed by Terzaghi (1943), to account for the variation of suction as follows,

$$q_{ult(unsat)} = \left[c' + (u_a - u_w)_b \left(1 - S_r^{\psi} \tan\phi'\right) + (u_a - u_w)_{AVR} \tan\phi' \right] (N_c \xi_c) + 0.5 B \gamma_b N_\gamma \xi_\gamma \tag{8.6}$$

where, $q_{ult,unsat}$ is the ultimate bearing capacity, B is the width of the footing, L_f is the length of the footing, γ_b is the unit weight of the soil, N_c is a bearing capacity factor that follows from Terzaghi (1943), N_γ is a bearing capacity factor from Kumbhokjar (1993), $(u_a - u_w)_b$ is the air entry value, $(u_a - u_w)_{AVR}$ is the average value of measured suction and ξ_c and ξ_γ are the shape factors from Vesic (1973), as stated below:

$$\xi_c = 1 + \left(\frac{N_q}{N_c}\right)\left(\frac{B}{L_f}\right) \tag{8.7}$$

$$\xi_\gamma = 1 - 0.4\left(\frac{B}{L_f}\right) \tag{8.8}$$

The field average suction value $(u_a - u_w)_{AVR}$ may be estimated through the water content using the experimental relationship expressed in Figure 5.3 as follows,

$$w(s) = 18.5 - 1.56 \ln (u_a - u_w)_{AVR} \tag{8.9}$$

Close inspection of Eq. (8.6) reveals that the $q_{ult(unsat)}$ depends mainly on the current suction conditions owing to the effective cohesion and friction angles being relatively independent of the initial induced soil structure compacted at the ultimate state (see Figure 7.17 shown earlier in Chapter 7) and to the similarity of the macrostructure AEV (air entry value) for different initial conditions of compaction (see Table 4.2 shown earlier in Chapter 4). Similar quick reference charts may also be developed for estimating $q_{ult(unsat)}$ along the compaction plane. The parameters adopted for the graphical solution using Eq. (8.6), and represented in Figure 8.8, are listed in Table 8.1.

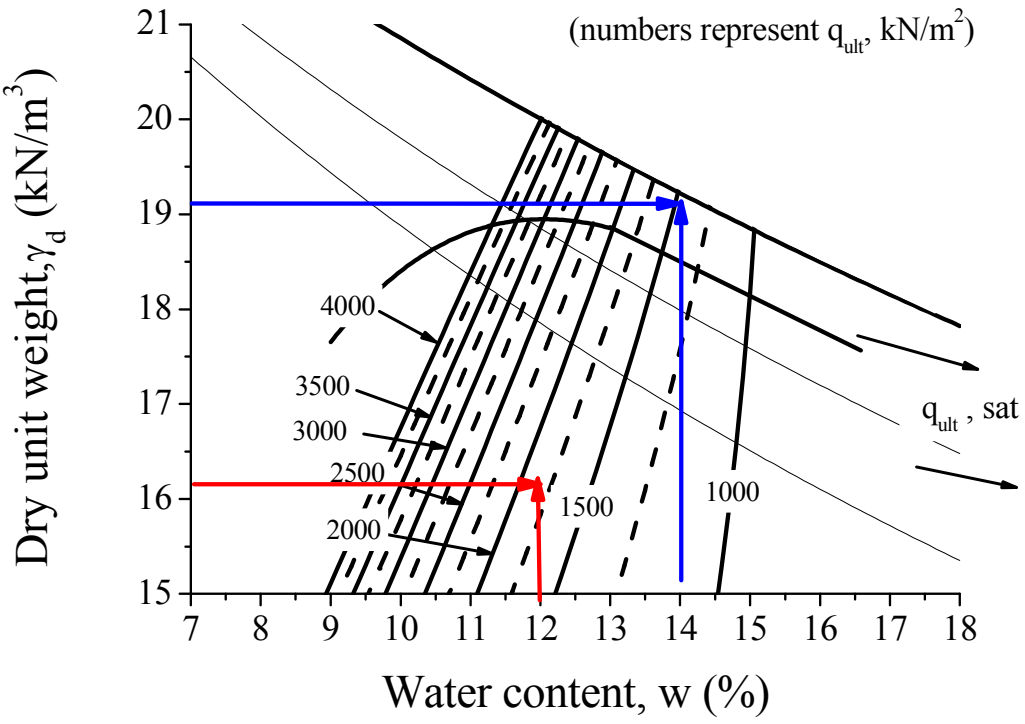

Figure 8.8 Graphical solution of Eq. (8.6) for the unsaturated ultimate bearing capacity (dash lines represent intervals of 250kN/m^2 of $q_{ult(unsat)}$).

Table 8.1. Summary of the bearing capacity parameters and shape factor used for calculating $q_{ult,unsat}$.

Parameter		Expression	Reference:
Mode of shear failure	General shear failure		
B(m) × L (m)	1×1		
c' (kPa)	1.40		Direct shear tests-Chapter 7
ϕ' (°)	35		Direct shear tests-Chapter 7
N_c	46.12	$N_c = \left(N_q - 1\right)\cot\phi'$	Terzaghi (1943)
N_q	33.3	$N_q = \exp(\pi \tan\phi')\tan^2\left(45 + \frac{\phi'}{2}\right)$	Terzaghi (1943)
N_γ	33.6		Kumbhokjar (1993)
$(u_a - u_w)_b$ (kPa)	1.5		SWRC – Chapter 4
ξ_c	1.722	$\xi_c = 1 + \left(\frac{N_q}{N_c}\right)\left(\frac{B}{L}\right)$	Vesic (1973)
ξ_γ	0.6	$\xi_\gamma = 1 - 0.4\left(\frac{B}{L}\right)$	Vesic (1973)
γ_b (kN/m^3)	20.5		In situ density tests, GHGD
ψ	1.8		Oh and Vanapalli (2011), Vanapalli and Fredlund (2000)

Note: *c'* and *ϕ'* selected correspond to the ultimate state parameters because for foundation design strength is considered for larger strains.

Despite the fact that Oh and Vanapalli (2011) reported an increase of bearing capacity by a factor 5 with few kPa variation of suction using Eq. (8.6), which may seem somewhat unrealistic, in fact, in this study Fig. 8.8 reports only an increase of around 4 times more when the soil moves from very wet compaction states to very dry, with suction varying quite considerably from the order of 5kPa to around 700kPa. This increase seems very reasonable considering that shear wave velocity increases 4-5 times more for approximately the same range (see i.e. Figure 8.7). While the domain of strain in which shear wave velocity and bearing capacity are measured is quite different, the differences may be expected to be of a similar order, which is the case. Nevertheless, because no field bearing capacity tests were performed to ascertain the prediction performance of Eq. (8.6) some degree of caution must be exercised while using Figure 8.8 and the ultimate bearing capacity values should be only taken as an indicator. Considering the linear elastic- perfectly plastic behaviour of soil (Figure 8.9), the different load settlement curves can be extrapolated by considering the in situ $V_{s,n}$ values. The method adopted follows Oh and Vanapalli (2011) in which the load settlement curve is composed of two lines, the L1 (elastic line) and L2 (plastic line), as represented in Figure 8.9. The line L1 defines the linear elastic range and its slope represents the modulus of

the sub-grade reaction $k_{is(unsat)}$ that can be estimated using in-situ $V_{s,n}$ and the elastic relationships as follows:

$$E_{unsat} = \frac{(1-\upsilon^2)I_w}{\Delta\delta / \Delta q} B = k_{is(unsat)}(1-\upsilon^2)I_w B_p \tag{8.10}$$

where, I_w is influence factor (0.79 for a circular plate and 0.88 for a square plate) and υ is the Poisson's ratio assumed as 0.33. Oh and Vanapalli (2011) proposed a empirical relationship to describe $k_{is(unsat)}$ as a function of $k_{is(sat)}$ for saturated conditions, degree of saturation, and suction. Given that for this study, $k_{is(sat)}$ is unknown, the estimation of $k_{is(unsat)}$ based on the elastic properties is preferable.

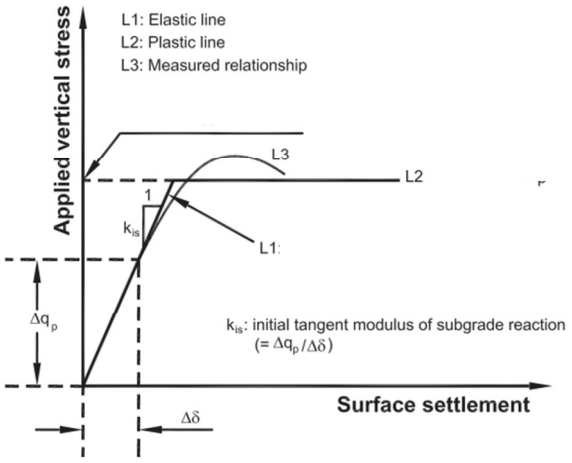

Figure 8.9 Schematic of measured and assumed applied vertical stresses versus surface settlement relationship in model footings (modified after Oh and Vanapalli, 2011).

Considering the elastic relationship between modulus of elasticity (E_{unsat}) and shear modulus (G_{unsat}) then,

$$E_{unsat} = 2G_{unsat}(1+\upsilon) = 2\left(\frac{\gamma}{g}V_{s,n}^2\right)(1+\upsilon) \tag{8.11}$$

Substituting Eq. (8.11) into (8.10) and rearranging for $k_{is(unsat)}$ gives:

$$k_{is(unsat)} = \frac{2G_{unsat}(1+\upsilon)}{(1-\upsilon^2)I_w B_p} = \frac{2}{(1-\upsilon)I_w B_p}\frac{\gamma}{g}V_{s,n}^2 \tag{8.12}$$

The load settlement line L1 describing the elastic range is expressed by:

$$\Delta q = k_{is(unsat)} \Delta \delta \tag{8.13}$$

In Eq. (8.13), $k_{is(unsat)}$ is proportional to the in-situ V_s value, and therefore, a similar chart to that of Figure 8.6 could be drawn for $k_{is(unsat)}$. Recalling Case 1 and Case 2 described earlier, the resultant load settlement relationship can be obtained by considering Eqs. (8.6), (8.12), and (8.13). For Case1: $V_{s,n}$=*186.27 m/s* and Case 2: $V_{s,n}$=*215.33 m/s* hence the slope $k_{is(unsat)}$ is slightly different and the $q_{ult(unsat)}$ shows some differences related to the in situ suction and dry unit weight (Figure 8.10). While in Case 1 the elastic domain is extended to nearly 6mm of settlement, in Case 2 it is substantially reduced to 1.8mm, despite having a smaller $V_{s,n}$. This shows the importance of the current conditions in terms of suction and dry unit weight on the ultimate bearing capacity. The use of this method may be preferable to FEM analysis because Oh and Vanapalli (2011) showed that a better agreement with the actual load settlement curves is obtained when it is compared with an FEM analysis for sandy soils.

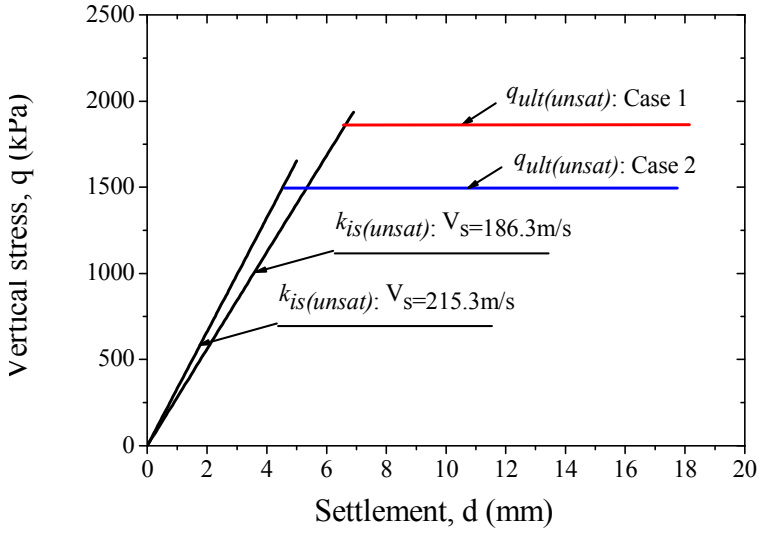

Figure 8.10 Load settlement elastic-perfectly plastic curves for case 1 and case 2.

8.3 SOIL MODULUS AND END-PRODUCT SPECIFICATIONS

Compaction has been widely used in most construction works such as road and railway embankments, dams, landfills, airfields, foundations, and hydraulic barriers. During construction the compaction characteristics are evaluated based on a minimum deviation interval from the pre-established laboratory key parameters (i.e. maximum dry unit weight, or MDD and optimum moisture content, or OMC). Although controlling the quality of compaction with those criteria, including different methods such as the sand cone, rubber balloon, and nuclear gauge, have been well established, problems related to poor compaction still occur (i.e. the differential settlements and increase in pavement roughness). This, in turn, often deems necessary the execution of costly and time consuming post-construction maintenance, because, the verification of compaction control can only cover a limited area (typically less than less than 1 % of the actual compacted area NCHRP 676, 2005).

In addition, field compaction using conventional rollers (i.e. with static and vibratory drums) may not provide uniform compaction due to differences in the hydration time and lift thickness. These variations can have substantial effects on the stress-strain behaviour of the compacted soil (Seed and Chan, 1956). Recently, intelligent compaction control (ICC) technologies have emerged to address this problem. Various manufacturers have equipped their compaction roller drums with an accelerometer based measuring systems (i.e. vibratory rollers), which are able to record how the soil responds (i.e. its stiffness or modulus) while it is being compacted (Anderegg, 2000) (Figure 8.11). The roller operator receives continuous feedback during operations which allows the fill to be compacted uniformly. Furthermore, the controlled area is equivalent to the entire compacted area.

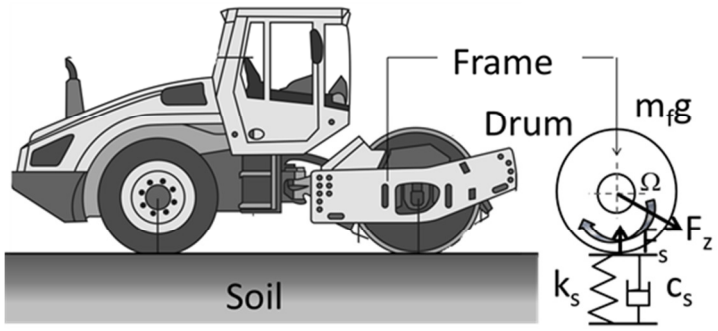

Figure 8.11 Illustration of a conceptual model of the interaction between soil and a vibratory roller (modified after Anderegg, 2000).

Preceding the placement of compacted fills, it is common to stipulate an end product specification, usually based on the standard Proctor compaction curve that aligns the strategic importance of the fill with the desired project objectives. An end product specification commonly adopted at most construction works consists of: (a) a minimum of 95% of the maximum dry unit weight at the OMC (AS 3798 - 2007), (b) an acceptable moisture deviation interval, typically 2% of the OMC or (c) less than the maximum acceptable value of air voids, e.g. 10% (Mokwa and Fridleifsson, 2007). Figure 8.12a, shows the compaction curves as per the above specifications. If the performance of the compacted soil is solely related to G_0, then it seems likely that compacting the soil between the S_r of 0.67 and 0.80 (i.e. in Region②-Figure 8.12b), may be preferable. In this range G_0 attains its maximum and changes in S_r (or applied energy under constant moisture content) do not cause substantial variations in G_0. However, if a minimum shear modulus is required, i.e. G_0 at OMC, compacting the soil slightly on the dry side may prove advantageous because the suction on the wet side decreases significantly and the desired shear modulus may not be achieved regardless of the level of energy applied. While compacting the soil on the dry side of OMC may be beneficial in terms of the magnitude of G_0, soil compacted under these conditions exhibits larger permeability and may become more susceptible to increased brittleness and long term shrink and swell problems associated with variations in the moisture compared to soil compacted on the wet side of OMC.

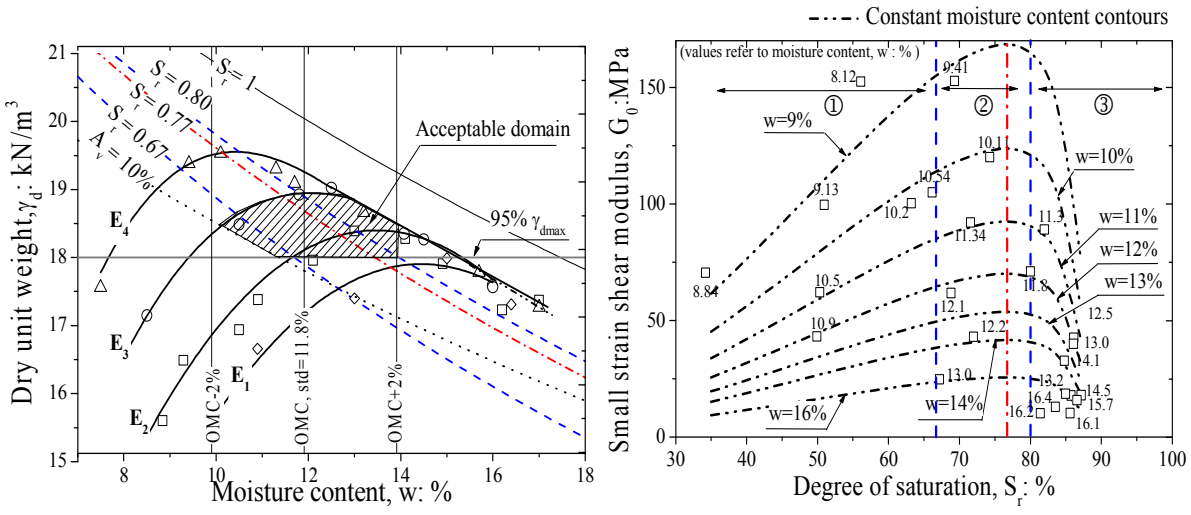

Figure 8.12 (a) Field compaction control criterion for silty sand (E3 represents standard Proctor) and (b) variation of G0 with degree of saturation (replotted from chapter 6).

8.4 SUMMARY

The site specific validation with special reference to PLDC site, using the empirical formulation described in Chapter 6 for evaluating the current void ratio or degree of compaction based on the shear wave velocity and suction, is presented in this chapter. First, the aspects related to the normalisation of shear wave velocity is introduced and a new normalisation method with V_s as the benchmark at the mid layer is discussed. This new method was used to estimate the variation with depth, of the field shear wave velocity, and establish V_s profiles for the borehole locations described in Chapter 3. The empirical formulation predictions is compared in terms of the bulk unit weight, and overall, the predictions match the observed field DHGD bulk unit weight well, but do show some discrepancies, particularly close to the ground surface and up to a depth of 2.5m. This suggests that an initial guess of 1.5 for the depth based on the TMI was conservative.

To facilitate the use of the proposed relationship, the empirical formulation is represented as a graphical solution in the w-γ_d plane. Quick reference charts based on w-γ_d -V_s were also developed for different levels of field mean effective stress that correspond to different field depths. The use of these charts enables an easy and straight forward method of estimating the dry unit weight based on the field shear velocity and water content.

The ultimate bearing capacity is an important parameter for the design of shallow foundations. The design of shallow foundations is mainly associated with larger ranges of shear strains (typically greater than 0.1%), exceeding the level of strains in which V_s is measured. Therefore, while the field ultimate bearing capacity is estimated using an expression proposed by Oh and Vanapalli (2011) that was developed for unsaturated conditions and the saturated shear strength parameters (Chapter 7), the modulus of the sub-grade reaction, which relates the applied load to its correspondent settlement in the elastic range, is computed based on the field $V_{s,n}$ by considering the elastic theory relationships between the shear modulus and elastic modulus. These two sets of parameters enable the approximate description of load settlement relationships for the PLDC site. Finally, the main aspects related with the use of the modulus of the soil to assess the quality of the compaction based on the findings presented in Chapters 5 and 6 seem to indicate that compacting the soil in Region② or between the S_r of 0.67 and 0.80 are optimal, which means that the range of the conventional end-product specifications becomes narrower.

CHAPTER NINE

9 . CONCLUSIONS AND RECOMMENDATIONS

9.1 GENERAL SUMMARY

Current conventional methods to determine field density are adequate during placement, but because of their localised nature and limited depth of investigation they are not suitable for assessing the compaction quality in post-construction stages. In this situation, classical destructive geotechnical surveys are used to evaluate the current fill conditions in terms of the degree of compaction, even though they often do not provide the level of information required because only certain locations are tested, and furthermore, they have tremendous implications in terms of cost and time. The use of non-destructive methodologies such as the shear wave velocity surveys, i.e. SASW or HVSR, offers a valuable alternative to efficiently control compaction over large areas during post-construction stages, as well as locating areas within the existing formations where the soil has not been sufficiently compacted. However, the direct application for assessing the current state of compacted fills (post-construction stages) is not straightforward because compacted soil is often under unsaturated conditions which mean that in-situ suction has an important role in controlling the shear strength. The study reported in this thesis has dealt with the implementation of a field methodology based on using the propagation of shear wave velocity and suction to evaluate the quality of compaction under partially saturated conditions. The methodology developed was first calibrated for a site specific soil in the laboratory and was then used to assess field conditions in Penrith taking the parameters of soil studied as reference for comparison. This enabled the evaluation of the current degree of compaction in relation to the reference soil which is of paramount importance for the future redevelopment of the site.

Chapter 3 introduced the Penrith Lakes field site, whereas Chapter 4 outlined the laboratory apparatus and field testing methods used to investigate the performance and feasibility of the methodology. In Chapter 5 the results used to characterise the unsaturated small strain behaviour of compacted soil were presented, and a new empirical formulation to evaluate the current void ratio or degree of compaction based on shear wave propagation and

suction was given in Chapter 6. Chapter 7 described the mechanical behaviour of PLDC soil through constant water content direct shear (CWDS) tests. Finally, in Chapter 8 a site specific validation with special reference to the soil studied and the PLDC site is presented.

9.2 WATER RETENTION CHARACTERISTICS

The water retention characteristics of the soil, typically defined by the Soil Water Retention Curve (SWRC), are one of the most fundamental aspects that need to be investigated when dealing with unsaturated conditions. The results of the water retention properties of selected specimens shown in Chapter 4 suggest that the compacted states influence the post compaction hydraulic behaviour of the soil. The SWRC of the specimens compacted at dry of optimum water content (OMC) possess steeper slopes than those on the wet of OMC. A strongly bimodal character was observed in all specimens, but predominately on those prepared at lower water contents, on the dry side of optimum moisture content. A strong void ratio and inherent dependency on the compacted fabric prevailed and shaped the SWRC response over the mid-suction range showing typically two air entry values that separated the macropore and micropores domain. Furthermore, the results of these tests also suggested that without knowing how compaction was carried out in terms of the water content and level of energy applied, evaluating the current condition in terms of the dry unit weight or void ratio of compacted ground likely to suffer severe changes in the hydraulic regimes caused by climatic fluctuations (i.e. temperature and rainfall) on the basis of its current *Sr*-*s* conditions, may prove a difficult task. This is mainly because the SWRCs are different for various compaction conditions and also the soil is likely to experience hysteretic behaviour on the drying and wetting branches of the SWRC. Based on these observations it was recognised that taking into account wetting and drying processes adds further intricacy to the problem, and its relatively small importance for the PLDC site has been the driving motivation behind one of the assumptions made while developing the empirical model.

9.3 COMPACTED SOIL MACROSTRUCTURE

Differences in compaction conditions (i.e. water content and energy level) are usually thought to produce essentially different soils, particularly in terms of its structure, which in turn often

results in distinct mechanical and hydraulic behaviour. The change in the macrostructure of compacted soil prepared at different water content and energy levels was examined using an X-ray CT-scan, and their results were shown in Chapter 4. This study demonstrated that an X-ray CT-scan can be used to investigate the compacted structure of soil in terms of its macroporosity. Even though the resolution of the images is approximately 1-2mm, the change in macroporosity between the specimens compacted at the dry and wet side of OMC is clear, given that they were tested in the "as compacted" condition, that is to say, without incurring any disturbance, as oppose to SEM (Scanning electron microscope) and MIP (mercury intrusion porosimetry) techniques. Evaluating variations in the structure of the soil based on its macroporosity was found to be adequate given that the compacted soil typically exhibits a bi-modal pore size distribution (see SWRC data) and changes in fabric occur mainly because of inter-particle bonding. The specimens compacted on the dry side of OMC had an aggregated structure dominated by a large amount of macropores whereas the aggregations were less distinguishable as the water content increased accompanied by a reduction in macroporosity. In those specimens compacted at the wet side of OMC, the macrostructure of the soil resembled a matrix where the grains of sand were easily individualised. One other interesting point revealed by this study was that the specimens compacted at a higher compaction effort show a typically matrix type of fabric where aggregations are not easily distinguishable, which indicates that the soil starts with a structure dominated by a large amount of macropores and during compaction at a constant water content, the macrostructure progresses into a matrix dominated structure with progressive occlusion of macroporosity. This seems to suggest that not only the initial water content, but also the energy level strongly controls the resulting compacted soil structure, or in other words, the structure evolves from an aggregation dominated in the lower water content range and energy levels, to a matrix dominated in the higher water content range and energy levels.

9.4 V_S BEHAVIOUR IN AS COMPACTED AND POST COMPACTED STATES

The results of the characterisation of the unsaturated small strain behaviour of compacted soil were presented in Chapter 5. Both the as compacted states and post compacted states were studied. While the shear wave velocity was measured using Bender elements, the suction was controlled and measured using an array of different techniques, including the axis translation technique, the filter paper method, and the tensiometer.

Several salient aspects were observed for the as compacted behaviour along the four different energy levels considered, and worth noting,

i) the existence of a unique water content-suction relationship for different energy levels, possibly associated with the continuously disturbed line (Croney, 1977; Brady, 1988),
ii) the V_s increases with the energy level on the low water content range, and
iii) a substantial decrease of V_s in the mid to large water content range, typically for degrees of saturation exceeding the line of optima.

Furthermore, a close relationship was found between V_s and the degree of saturation, which was in turn related to the type of fabric reflected in the macrostructure. This was surprising because the dry unit weight and water content were initially anticipated to be the governing variables. The effect of depth was investigated in a series of tests where the specimens were subjected to a constant water content isotopic compression. The V_s was found to increase with confining stresses, although the rate of increase was strongly associated with the initial water content. To evaluate the importance of field variations of water content, a series of specimens were subjected to cycles of wetting and drying. There was a marked hysteresis both on the V_s-suction plane and in the water retention data. The V_s-suction hysteresis amplitude differed for specimens compacted under different energy levels; higher amplitudes were found for specimens with lower initial dry unit weight or void ratio, albeit still small (maximum within 30m/s). It was also observed that subsequent cycles of drying caused reversible V_s values, whereas the wetting paths still show hysteresis which contributed to a successive increase in V_s. These results show that a great deal of understanding about the current state of compacted fills in post-construction stages, particularly near the ground surface exposed to seasonal climatic changes, can be achieved by simply conducting V_s. field surveys in different climatic seasons, i.e. the larger V_s. variations the poorer the conditions that may be expected.

The new empirical formulation for evaluating the current void ratio or degree of compaction based on shear wave propagation and suction was presented in Chapter 6. Particular considerations were given in respect to evaluating the depth of influence of that portion of the ground subjected to wetting and drying cycles and variations of suction over time. In addition, the results of supplementary tests showed that V_s varied linearly with the

void ratio under approximately constant suction conditions, whereas it showed a non-linear variation with suction (resembling a SWRC shape) at an approximately constant void ratio. Based on these observations, a general V_s relationship developed for unsaturated soils was modified to incorporate the combined effect of changes in the void ratio, or *f(e),* and suction, or *f(s),* observed for different states of compaction. The distinct features of this new relationship are related to the V_s linearity with the void ratio imposed by an upper and lower void ratio limits and the adoption of a function of suction that resembles the inverse of the SWCC. There was good agreement between the predictions and the actual trends, for both the as compacted and post compacted states, albeit with small discrepancies.

9.4.1 Small strain shear modulus behaviour for as compacted states

Recently, intelligent compaction control (ICC) technologies have emerged to address problems related to the lack uniform compaction associated with differences in hydration time and lift thickness, and to the limited area where compaction control is verified in conventional approaches to field density (typically less than less than 1 % of the actual compacted area NCHRP 676, 2005). While various manufacturers have equipped their compaction roller drums with accelerometer based measuring systems (i.e. vibratory rollers), which are able to record the response of the soil (i.e. its stiffness or modulus) while it is being compacted, research on the implications of assessing how a change of dry unit weight can affect the modulus of the soil has been very limited. Having this in mind, and given that the shear modulus can be directly related to V_s when the bulk unit weight is known, a new empirical relationship was derived to evaluate variations in the small strain shear modulus throughout the compaction plane (shown in Chapter 6). The most striking aspect of this new equation is that the parameter *A,* which is usually taken as a constant, is now considered to be a function of the degree of saturation that somehow translates the changes that occur in the fabric of the soil for different water contents and energy levels. This relationship is of great value since the small strain shear modulus can now be predicted across the whole compaction plane. In addition, it gives important insights into the changes of the modulus with an increasing degree of saturation, which in turn can be translated into ranges where compaction should be targeted to maximise the modulus (typically in region 2) in the context of common end-product specifications (shown in Chapter 8).

9.5 MECHANICAL BEHAVIOUR THROUGH CWDS TESTS

Given in-service strain is likely to exceed the small strain domain in which V_s is measured, Chapter 7 describes the mechanical behaviour of PLDC soil through constant water content direct shear (CWDS) tests. The tests were carried out on a conventional direct shear apparatus without an independent measurement of suction, and for that reason, a simple method for evaluating the variation in suction induced by CWDS based on the pore air pressure generation reflected in changes of pore water pressure associated with the volumetric changes in the shear zone was proposed. The predictions of suction variation based on the proposed relationship were in acceptable agreement with the experimental data provided by Caruso and Tarantino (2004) and Jotisankasa and Mairaing (2010). However, it seems that fabric rather than the volumetric changes play a more important role in controlling suction during shearing, particularly on the large displacement range. Also, discrepancies in the measured data and predictions were noted for specimens prepared and tested close to saturation, which may have been related to inadequate interconnection among the air voids.

The results from CWDS tests performed on as compacted specimens showed that the different compaction history leads to a development of characteristic shear stress envelopes. Specimens compacted on the dry side of OMC exhibited the largest apparent cohesion, whereas the highest effective friction angle occurred in specimens compacted at near OMC. It is likely that the effective friction angle is associated with the structure of the soil. The ultimate shear strength was modelled using both average skeleton stress and critical stress ratio approaches. It was found that the latter lead to more accurate predictions of ultimate shear strength. This difference was interpreted as the result of the difference in the initial fabric. While both approaches consider the effect of fabric through the degree of saturation in the critical stress ratio approach, this influence is defined explicitly in the degree of saturation functions. The ultimate void ratio was predicted using Galipolli et al. (2003) the bonding variable concept, however the ratio between the unsaturated and saturated void ratio at the same average skeleton exceeded unity for the specimens that reached saturation during shearing. This was interpreted as the result of lower compressibility of the specimens departing from the unsaturated states that despite being fully saturated were likely to maintain unsaturated conditions in the intra-aggregate pores. The increase in post-compaction shear stress with respect to the suction was non-linear, but it showed different rates of increase for

different initial compaction characteristics. It also observed that while the peak shear strength envelopes differed quite considerably among different initial compaction characteristics, the ultimate shear strength was less affected.

9.6 SITE CALIBRATION AND VALIDATION

The site specific validation with special reference to PLDC site was presented in Chapter 8. A new normalisation method of the shear wave velocity with the benchmark stress level lying at mid layer was introduced. This new method was applied to estimate the variation with depth of the field shear wave velocity and to establish $V_{s,n}$ profiles for the borehole locations described in Chapter 3. The empirical formulation predictions were compared in terms of bulk unit weight where the overall predictions matched the observed field DHGD bulk unit weight quite well, but showed some discrepancies close to the ground surface, to a depth of 2.5m. This suggested that the initial guess of 1.5 for the depth based on the TMI (Thornthwaite moisture index) was conservative.

In order to facilitate the use of the proposed relationship, the empirical formulation was represented as a graphical solution in the w-γ_d plane. Quick reference charts based on w-γ_d - $V_{s,n}$ were also developed for different levels of field mean effective stress that correspond to different field depths. These charts enable an easy and straight forward estimation of dry unit weight based on the field shear velocity and water content, and will of practical use for site investigations.

The ultimate bearing capacity is an important parameter for the design of shallow foundations. Since the foundation design is mainly associated with larger shear strains ranges (typically greater than 0.1%), exceeding the level of strains in which V_s is measured, the field bearing capacity is obtained by considering an expression proposed by Oh and Vanapalli (2011) and developed for unsaturated conditions and the modulus of sub-grade reaction is computed based on the field $V_{s,n}$. These two parameters enable the approximate description of load settlement relationships for the PLDC site.

9.7 RECOMMENDATIONS FOR FUTURE WORK

While the methodology proposed in this thesis has other potential applications related to the assessment of old embankment fills, the relationship was only calibrated for the reference soil used at the PLDC site, albeit there was some degree of material variability on site. The soil is typically a silty sand soil which developed relatively small suction values in its as compacted state. Although the suction-water content relationship observed in soil is likely to be present in other types of soil, the validity of the w-γ_d -V_s relationship should be assessed for use with other types of soil and the parameters should be calibrated on a case by case analysis. Further research should be also devoted to investigating whether a systematic grouping of the parameters is possible, based on common index properties such as the fine content or plasticity index.

Another important aspect is related to the seasonal climatic changes and its effect on V_s. In this study the depth of influence H_s was found to be small, and thus the influence of the cycles of wetting and drying was not taken into account. However, there may be locations in the central inland and the west coast of Australia with typically arid climates where the H_s may be too large to be neglected, i.e. larger than 4m depth for TMI smaller than -40 (Fityus and Buzzi, 2008). Therefore, further research should be spent on understanding the dynamics of the hydraulic hysteric behaviour and change in the soil structure and its implication on small strain stiffness in subsequent wetting and drying cycles.

Another aspect that would benefit from further investigation is coupling the macroscopic mechanical behaviour and changes in the fabric that occurs at microscopic level. The degree of saturation seems to represent the change in fabric across the compaction plane but because it is described by changes in the macroporosity, it should not be used as an absolute method to quantify the structure of compacted soil. Furthermore, it still remains unclear how the surface curvature or contact angles on the water menisci change when the material is undergoing mechanical wetting through compaction, or during post-compaction shearing. This area of study needs further research effort.

The technology transfer into engineering practice has been rather slow in the context of unsaturated soil mechanics. This may be related to the intricacies and costs associated with upgrading conventional soil mechanics apparatus for testing under unsaturated conditions.

Although there has been an increasingly amount of research effort put into developing relatively inexpensive modifications for conventional testing apparatus (i.e. direct shear), particularly for CW conditions, further study relating to the estimation the suction change during shearing, as well as, the effect of the specimen size and aspect ratio are desirable.

Finally, concerning the use of the soil modulus for controlling compaction, in this study only the small strain modulus behaviour was quantified. Although the relationship proposed in this study is likely valid for larger strain ranges, given the nature of the modulus degradation with increasing shear strain, further corrections are needed for field assessment of ICC compaction because the strains developed during vibratory roller compaction are expected to be larger and the modulus of the soil is expected to be smaller.

REFERENCES

Afifi, S. S. and Woods, R. D. (1971). Long-term pressure effects on the shear modulus of soils. J. Soil Mech. and Found. Div. Proc. ASCE 97(SM10): 1445-1460.

Ajaz, A. and Parry, R. H. G. (1975). Stress–strain behaviour of two compacted clays in tension and compression. Géotechnique 25(3): 495-512.

Alonso, E. E. (1998). Suction and moisture regimes in road bases and sub-grades. *Int. Symp. On Subdrainage in Roadway pavements and Subgrades*.

Alonso, E. E. (1998). Suction and moisture regimes in roadway bases and subgrades. *Int.Symp. on Subdrainage in roadway pavements and Subgrades*, Grenade.

Alonso, E. E., Josa, A. and Gens, A. (1990). A constitutive model for partially saturated soils. Géotechnique 40(3): 405-430.

Alramahi, B., Alshibli, K., Fratta, D. and Trautwein, S. (2007). A suction-control apparatus for the measurement of P and S-waves velocity in soils. Geotechnical Testing Journal 31(1): 1-12.

Alshibli, K. A., Alramahi, B. A. and Attia, A. M. (2006). Assessment of spatial distribution of porosity in synthetic quartz cores using microfocus computed tomography (μCT). Particulate Science and Techology 24(4): 369-380.

Anandarajah, A. and Kuganenthira, N. (1995). Some aspects of fabric anisotropy of soil. Géotechnique 45(1): 69-81.

Anderson, D. G. and Stokoe, K. H. I. (1978). Shear modulus: A time dependent soil property. Dynamic Geotechnical Testing. ASTM. STP 654**:** 66-90.

Anderson, D. G. and Wood, D. M. (1976). Time-dependent increase in shear modulus of clay. Journal of Geotechnical Engineering Division, ASCE 102(GT5): 525-537.

Arroyo, M., Wood, D. M. and Greening, P. D. (2003). Source near-field effects and pulse tests in soil samples. Geotechnique 53(3): 337-345.

Arulnathan, R., Boulanger, R. W. and Riemer, M. F. (1998). Analysis of Bender Element Tests. Geotechnical Testing Journal 21(2): 120–131.

ASTM (2003). Standard test method for measurement of soil potential (suction) using filter paper method. ASTM standard D 5298 Annual Book of Standards. West Conshohoken, PA., American Society of Testing Materials.

ASTM (2004). Standard guide for measuring matric potential in the vadose zone using tensiometers. ASTM Standard D3404-91. West Conshohoken, PA., American Society of Testing materials.

Atkinson, J. H. (2007). The mechanics of soils and foundations. London, Taylor & Francis.

Austroads (2004). Impact of Climate Change on Road Infrastructure. AP-R243. Sydney, Ausroads.

Bae, A., Stoffels, S. M., Antle, C. E. and Lee, S. W. (2008). Observed evidence of subgrade moisture influence on pavement longitudinal profile. Canadian Journal of Civil Engineering 35(10): 1050-1050.

Bagherieh, A. R., Khalili, N., Habibagahi, G. and Ghahramani, A. (2009). Drying response and effective stress in a double porosity aggregated soil. Engineering Geology 105(1): 44-50.

Baig, S., Picornell, M. and Nazarian, S. (1997). Low strain shear moduli of cemented sands. Journal of Geotechnical Engineering, ASCE 123: 540-545.

Barden, L. and Pavlakis, G. (1971). Air and Water Permeability of Compacted Unsaturated Cohesive Soil. Journal of Soil Science 22(3): 302-317.

Barden, L. and Sides, G. R. (1970). Engineering behavior and structure of compacted clay. Journal of the Soil Mechanics and Foundations Division 96(SM4): 1171-1197.

Biglari, M., d'Onofrio, A., Mancuso, C., Jafari, M. K., Shafiee, A. and Ashayeri, I. (2012). Small-strain stiffness of Zenoz kaolin in unsaturated conditions. Canadian Geotechnical Journal 49(3): 311-322.

Bishop, A. W. (1957). Some factors controlling the pore pressure set up during the construction of earth dams. Proceedings of the fourth international Conference on Soil Mechanics and Foundation Engineering London. 2: 294-300.

Bishop, A. W. (1959). The principle of effective stress. Teknisk Ukeblad 106(39): 859-863.

Bishop, A. W. (1967). Progressive failure - with special reference to the mechanism causing it. *Proceedings of the Geotechnical Conference*, Oslo.

Blatz, J. A., Cui, Y. and Oldecop, L. (2008). Vapour Equilibrium and Osmotic Technique for Suction Control. Geotechnical and Geological Engineering 26(6): 661-673.

Blatz, J. A. and Graham, J. (2003). Elastic-plastic modelling of unsaturated soil using results from a new triaxial test with controlled suction. Geotechnique 53(1): 113-122.

Bolton, M. D. (1986). The strength and dilatancy of sands. Géotechnique 36(1): 65-78.

Bolzon, G., Schrefler, B. and Zienkiewicz, O. C. (1996). Elastoplastic soil constitutive laws generalised to partially saturated states. Geotechnique 46(2): 279-289.

Bonal, J., Donohue, S. and McNally, C. (2012). Wavelet analysis of bender element signals. Géotechnique 62(3): 243-252.

Boso, M., Tarantino, A. and Mongiovı, L. (2005). A direct shear box improved with the osmotic technique. Proceedings of advanced experimental unsaturated soil mechanics. Trento: 85-91.

Bosscher, P. J. and Nelson, D. L. (1987). Resonant column testing of frozen Ottawa sand. Geotechnical testing Journal 10(3): 123-134.

Brady, K. C. (1988). Soil suction and the critical state. Géotechnique 38(1): 117-120.

Brignoli, E. G. M., Gotti, M. and Stokoe, K. H. (1996). Measurement of Shear Waves in Laboratory Specimens by Means of Piezoelectric Transducers. Geotechnical Testing Journal 19(4): 384-397.

Broker, E. W. and Ireland, H. O. (1965). Earth pressure at rest related to stress history. Canadian Geotechnical Journal 2(1): 1-15.

Bulut, R. and Wray, W. K. (2005). Free energy of water-suction in filter papers. Geotechnical Testing Journal 28(4): 355-364.

Burger, C. A. and Shackelford, C. D. (2001). Soil-water characteristic curves and dual porosity of sand-diatomaceous earth mixtures. Journal of Geotechnical and Geoenvironmental Engineering 127(9): 790-800.

Caruso, M. and Tarantino, A. (2004). A shearbox for testing unsaturated soils at medium to high degrees of saturation. Géotechnique 54(4): 281-284.

Casagrande, A. and Hirschfeld, A. M. (1960). Stress-deformation and strength characteristics of a clay compacted to a constant dry unit weight. Research Conference on Shear Strength of cohesive soils: 359 - 417.

Casini, F., Vaunat, J., Romero, E. and Desideri, A. (2012). Consequences on water retention properties of double-porosity features in a compacted silt. Acta Geotechnica 7(2): 139-150.

Cha, M. S. and Cho, G. C. (2007). Shear strength estimation of sandy soils using shear wave velocity. Geotechnical Testing Journal 30(6): 484-495.

Cho, G. C. and Santamarina, J. C. (2001). Unsaturated particulate materials—particle level studies. Journal of Geotechnical and Geoenvironmental Engineering 127(1): 84–96.

Claria Jr, J. J. and Rinaldi, V. A. (2007). Shear wave velocity of a compacted clayey silt. Geotechnical Testing Journal 30(5): 399-408.

Clayton, C. R. I. (2011). Stiffness at small strain: research and practice. Geotechnique 61(1): 5-37.

Clough, G. W., Sitar, N., Bachus, R. C. and Rad, N. S. (1981). Cemented sands under static loading. Journal of the Geotechnical Engineering Division, ASCE 107: 799-817.

Cokca, E., Erol, O. and Armangil, F. (2004). Effects of compaction moisture content on the shear strength of an unsaturated clay. Geotechnical and Geological Engineering 22(2): 285-297.

Colmenares, M. J. E. (2002). Suction and volume changes of compacted sand bentonite mixtures. London, UK, University of London. Imperial College. PhD thesis.

Coppola, A. (2000). Unimodal and bimodal descriptions of hydraulic properties for aggregated soils. Soil Sci. Soc. Am. J. 64(4): 1252-1262.

Cuccovillo, T. and Coop, M. R. (1997). Yielding and pre-failure deformation of structure sands. Geotechnique 47(3): 491-508.

Cui, Y. J. and Delage, P. (1996). Yielding and plastic behaviour of an unsaturated compacted silt. Geotechnique 46(2): 291-311.

Cuisinier, O. and Laloui, L. (2004). Fabric evolution during hydromechanical loading of a compacted silt. International Journal for Numerical and Analytical Methods in Geomechanics 28(6): 483-499.

D'Elia, B., Picarelli, L., Leroueil, S. and Vaunat , J. (1998). Geotechnical characterisation of slope movements in structurally complex clay soils and stiff jointed clays. Rivista Italiana di Geotecnica 3: 5-32.

D'Onza, F., Gallipoli, D., et al. (2011). Benchmark of constitutive models for unsaturated soils. Géotechnique 61(4): 283-302.

Da Fonseca, A. V., Ferreira, C. and Fahey, M. (2009). A framework interpreting bender element tests, combining time-domain and frequency-domain methods. Geotechnical Testing Journal 32(Compendex): 91-107.

de Campos, T. M. P. and Carrillo, C. W. (1995). Direct shear testing on an unsaturated soil from Rio de Janeiro. *1st International Conference on Unsaturated Soils*, A.A. Balkema, .

Delage, P., Audiguier, M., Cui, Y. J. and Howat, M. D. (1996). Microstructure of a Compacted Silt. Canadian Geotechnical Journal 33: 150–158.

Delage, P. and Graham, J. (1995). Mechanical behaviour of unsaturated soils. 1st International Conference on Unsaturated Soils Paris, Balkema, Rotterdam. 3: 1223-1256.

Diamond, S. (1970). Pore size distribution in clays. Clays and Clay Minerals 18: 7-23.

Dyvik, R. and Madshus, C. (1985). Laboratory Measurements of G_{max} using Bender elements. Proc. of Advances in the Art of Testing Soils Under Cyclic Conditions. Detroit, MI, Engl, ASCE: 186-196.

Escario, V. and Saez, J. (1986). The shear strength of partly saturated soils. Géotechnique 36(3): 453-456.

Fam, M., Santamarina, J. C. and Dusseault, M. (1998). Wave-based monitoring processes in granular salt. Journal of Enviromental and Engineering Geophysics 3: 15-26.

Fernandez, A. L. and Santamarina, J. C. (2001). Effect of cementation on the small-strain parameters of sands. Canadian Geotechical Journal 38(1): 191-199.

Fisher, R. A. (1926). On the capillary forces in an ideal soil; correction of formulae given by W. B. Haines. The Journal of Agricultural Science 16: 492-505.

Fityus, S. and Buzzi, O. (2008). On the use of the Thornwaite Moisture index to infer depths of seasonal moisture change. Australian Geomechanics 43(4): 69-76.

Fredlund, D., Morgenstern, N. and Widger, A. (1978). Shear strength of unsaturated soils. Canadian Geotechical Journal 15: 313-321.

Fredlund, D. and Xing, A. (1994). Equations for soil water characteristic curve. Canadian Geotechnical Journal 31(3): 521-532.

Fredlund, D. G. (1987). The stress state for expansive soils *Procedings of 6th Int. Conf. on Expansive soils*, Keynote address.

Fredlund, D. G. (2006). Unsaturated Soil Mechanics in Engineering Practice. Journal of Geotechnical and Geoenvironmental Engineering 132(3): 286.

Fredlund, D. G. and Rahardjo, H. (1993). Soil Mechanics for Unsaturated soils, John Wiley and Sons Inc.

Fredlund, D. G., Rahardjo, H. and Fredlund, M. D. (2012). Unsaturated soil mechanics in engineering practice. Hoboken, N.J, John Wiley & Sons.

Fredlund, D. G., Xing, A., Fredlund, M. D. and Barbour, S. L. (1996). The relationship of the unsaturated soil shear strength to the soil-water characteristic curve. Canadian Geotechnical Journal 33(3): 440-448.

Fredlund, M. D., Wilson, G. W. and Fredlund, D. G. (2002). Use of the grain-size distribution for estimation of the soil-water characteristic curve. CANADIAN GEOTECHNICAL JOURNAL 39(5): 1103-1103.

Gallipoli, D., Gens, A., Sharma, R. and Vaunat, J. (2003). An elasto-plastic model for unsaturated soil incorporating the effects of suction and degree of saturation on mechanical behaviour. Géotechnique 53(1): 123-135.

Gallipoli, D., Wheeler, S. J. and Karstunen, M. (2003). Modelling the variation of degree of saturation in a deformable unsaturated soil. Géotechnique 53(1): 105-112.

Gan, J. K. M., Fredlund, D. G. and Rahardjo, H. (1988). Determination of the shear strength parameters of an unsaturated soil using the direct shear testing. Canadian Geotechnical Journal 25(3): 500-510

Golaszewski, R. (2012). Bedrock depth at areas 7 and 9. Personal communication.

Gomes Correia, A. (1996). Prediction of subgrade moisture conditions for purposes of pavement design. Flexible Pavements Correia, G. Rotterdam, Balkema**:** 99-104.

Hardin, B. O. and Black, W. L. (1966). Sand stiffness under various triaxial stresses. J. Soil Mech. and Found. Div. Proc. ASCE 92(SM2): 27-42.

Hardin, B. O. and Richart, F. E. (1963). Elastic waves velocities in granular soils. J. Soil Mech. and Found. Div. Proc. ASCE 89(SM1): 33-65.

Harutoonian, P. (2012). Geotechnical Characterization of Compacted Ground by Passive Ambient Noise HVSR Techniques. Engineering. Penrith, University of Western Sydney. PhD Thesis.

Harutoonian, P., Leo, C. J., et al. (2012). Microtremor measurements of rolling compacted ground. Soil Dynamics and Earthquake Engineering 41(Journal Article): 23-31.

Hilf, J. W. (1948). Estimating Construction Pore Pressures in Rolled Earth Dams. Proc. 2nd Int. Con& Soil Mech. Found. Eng. . Rotterdam, The Netherlands. 3: 234-240.

Hogentogler, C. A. (1936). Essentials of Soil Compaction. Proceedings Highway Research Bd., Natl. Research Council: 309 - 316.

Huang, G. and Zhang, R. (2005). Evaluation of soil water retention curve with the pore–solid fractal model. Geoderma 127(1): 52-61.

Inci, G., Yesiller, N. and Kagawa, T. (2003). Experimental investigation of dynamic response of compacted clayey soils. Geotechnical Testing Journal 26(2): 125-141.

Indraratna, B., Dilema, E. and Nutalaya, P. (1990). Design of granular filters for a lateritic residual soil. Dam Engineering 1(3): 201-220.

Iwasaki, T., Tatsuoka, F. and Takagi, Y. (1978). Shear moduli of sands under cyclic torsional shear loading. Soil and Foundations 18(1): 39-56.

Jaky, J. (1944). The coefficient of earth pressure at rest. In Hungarian "A nyugalmi nyomas tenyezoje". J. Soc. Hung. Eng. Arch. (Magyar Mernok es Epitesz-Egylet Kozlonye): 355–358.

Jardine, R. J. and Shibuya, S. (2005). TC29 workshop: Laboratory tests. Report. Proceedings of the 16th International Conference on Soil Mechanics and Geotechnical Engineering. Osaka. 5: 3275-3276.

Jewell, R. A. and Wroth, C. P. (1987). Direct shear tests on reinforced sand. Géotechnique 37(1): 53-68.

Jiang, G.-L., Tatsuoka, F., Koseki, J. and Flora, A. (1997). Inherent and stress-state-induced anisotropy in very small strain stiffness of a sandy gravel. Géotechnique 47(3): 509-521.

Jotisankasa, A. and Mairaing, W. (2010). Suction-Monitored Direct Shear Testing of Residual Soils from Landslide-Prone Areas. Journal of Geotechnical and Geoenvironmental Engineering 136(3): 533.

Jovicic, V. and Coop, M. (1998). The influence of plastic strains during compression on the inherent anisotropy of G_{max}. Pre-failure deformation behaviour of geomaterials. Jardine, R. J., Davies, M. C. R., Hight, D. W., Smith, A. K. C. and Stallebrass, S. E., ICE**:** 395-397.

Jovicic, V. and Coop, M. R. (1997). Stiffness of coarse-grained soils at small strains. Géotechnique 47(3): 545-561.

Jovicic, V., Coop, M. R. and Simic, M. (1996). Objective criteria for determining G_{max} from bender element. Geotechnique 46(2): 357-362.

Kalender, W. A. (2005). Computed tomography: fundamentals, system technology, image quality, applications. Erlangen, Germany, Publicis Corporate Publishing.

Kemmer, G. and Keller, S. (2010). Nonlinear least-squares data fitting in Excel spreadsheets. Nature protocols 5(2): 267-281.

Kenai, S., Bahar, R. and Benazzoug, M. (2006). Experimental analysis of the effect of some compaction methods on mechanical properties and durability of cement stabilized soil. Journal of Materials Science 41(21): 6956-6964.

Ketcham, R. A. and Carlson, W. D. (2001). Acquisition, optimization and interpretation of X-ray computed tomographic imagery: applications to the geosciences. COMPUTERS & GEOSCIENCES 27(4): 381-400.

Khalili, N., Geiser, F. and Blight, G. E. (2004). Effective stress in unsaturated soils: Review with new evidence. International Journal of Geomechanics 4(2): 115-126.

Kim, D. S. and Park, H. C. (1999). Evaluation of ground densification using sasw and resonant column tests. Cananadian Geotechnical Journal 36(2): 291–299.

Kohler, R. and Hofstetter, G. (2008). A cap model for partially saturated soils. International Journal of Numerical Analytical Methods in Geomechanics 32: 981-1004.

Kokusho, T. (1987). In situ dynamic soil properties and their evaluation. *Proceedings of 8th Asian regional Conference on Soil Mechanics and Foundation Engineering*, Kyoto, Japan.

Koliji, A., Laloui, L., Cusinier, O. and Vulliet, L. (2006). Suction Induced Effects on the Fabric of a Structured Soil. Transport in Porous Media 64(2): 261-278.

Koliji, A., Vulliet, L. and Laloui, L. (2010). Structural characterization of unsaturated aggregated soil. CANADIAN GEOTECHNICAL JOURNAL 47(3): 297-297.

Kumbhojkar, A. S. (1993). Numerical evaluation of Terzaghi's Ng. Journal of Geotechnical Engineering 119(3): 598-607.

Lade, P. V. and Overton, D. D. (1989). Cementation effects in frictional materials. Journal of Geotechnical Engineering, ASCE 115: 1373-1387.

Lambe, W. (1958). Compacted clays: Engineering Behaviour. Journal of soil mechanics and Foundations division (Transactions) 125(Part I): 718-.

Lambe, W. (1958). Compacted clays: structure. Journal of soil mechanics and Foundations division (Transactions) 125(Part I): 682-.

Leong, E. C., Cahyadi, J. and Rahardjo, H. (2009). Measuring shear and compression wave velocities of soil using bender-extender elements. Canadian Geotechnical Journal 46(7): 792-812.

Leong, E. C., He, L. and Rahardjo, H. (2002). Factors affecting the filter paper method for total and matric suction measurements. Geotechnical Testing Journal 25(3): 322-333.

Leong, E. C. and Rahardjo, H. (1997). Review of soil-water characteristic curve equations. Journal of Geotechnical and Geoenvironmental Engineering 123(12): 1106-1117.

Leong, E. C., Yeo, S. H. and Rahardjo, H. (2005). Measuring Shear Wave Velocity Using Bender Elements. Geotechnical Testing Journal 28(5): 1-11.

Leroueil, S. and Hight, D. W. (2003). Behaviour and properties of natural soils and rocks. Singapore, A.A. Balkema.

Li, X., Zhang, L. M. and Li, J. H. (2009). Development of a Modified Axis Translation Technique for Measuring SWCCs for Gravel Soils at Very Low Suctions. Geotechnical Testing Journal 32(6): 478-488.

Liu, S. H. (2006). Simulating a direct shear box test by DEM. Canadian Geotechnical Journal 43(2): 155-155.

Lo Presti, D. C. F. (1995). Measurement of the shear deformation of geomaterials in laboratory : General report. Pre-failure Deformation of Geomaterials. Shibuya, M. M., Balkema. 2: 1067-1088.

Loret, B. and Khalili, N. (2002). An effective stress elastic-plastic model for unsaturated porous media. Mechanics of Materials 34: 97-116.

Lourenco, S. D. N., Gallipoli, D., Augarde, C. E., Toll, D. G., Fisher, P. C. and Congreve, A. (2012). Formation and evolution of water menisci in unsaturated granular media. Géotechnique 62(3): 193-199.

Mancuso, C., Vassallo, R. and d'Onofrio, A. (2002). Small strain behaviour of a silty sand in controlled suction resonant column-torsional shear tests. Canadian Geotechnical Journal 39: 22-32.

Marcuson, W. F. and Wahls, H. E. (1972). Time Effects on Dynamic Shear Modulus of Clays. J. Soil Mech. and Found. Div. Proc. ASCE 98(12): 1359-1373.

Marinho, A. M. and Stuermer, M. M. (2000). The influence of compaction energy on the SWCC of a residual soil. Proc. of the sessions of Geo-Denver. Denver: 125-141.

Marinho, F. A. M. (1994). Shrinkage behaviour of some plastic soils. London, UK, Imperical College. PhD thesis.

Marinho, F. A. M., Chandler, R. J. and Crilly, M. S. (1996). Stiffness Measurements on an Unsaturated High plasticity clay using Bender Elements. 1st International Conference on Unsaturated soils Paris, France. 1: 1179-1200.

Mendes, J. (2011). Assessment of the impact of climate change on an instrumented embankment: an unsaturated soil mechanics approach. Doctoral thesis. Durham, Durham University.

Miao, L. C., Yin, Z. Z. and Liu, S. Y. (2001). Empirical function representing the shear strength of unsaturated soils. GEOTECHNICAL TESTING JOURNAL 24(2): 220-223.

Miller, C. J., Yesiller, N., Yaldo, K. and Merayyan, S. (2002). Impact of soil type and compaction conditions on soil water characteristic. Journal of Geotechnical and Geoenvironmental Engineering 128(9): 733-742.

Mitchell, J. K. and Soga, K. (2005). Fundamentals of soil behavior. Chichester, Wiley.

Mokwa, R. L. and Fridleifsson, S. (2007). Earthwork compaction evaluation using soil air voids. Canadian Geotechnical Journal 44(2): 151-159.

Monroy, R. (2005). The influence of load and suction changes on the volumetric behaviour of compacted London clay. London, UK, Imperial College. PhD thesis.

Morgenstern, N. R. and Tchalenko, J. S. (1969). Microscopic Structures in Kaolin Subjected to Direct Shear. Géotechnique 19(3): 426-427.

Moyle, R. (2007). Geotechnical investigation and monitoring report : Dynamic compaction on prototype trial compaction area 9, Coffey Geotechnics, Pty Ltd ;. GEOTLCOV20023BL-DB: 125.

Ng, C. and Menzies, B. (2007). Advanced unsaturated soil mechanics and engineering, Taylor & Francis.

Ng, C. W., Leung, E. H. Y. and Lau, C. K. (2004). Inherent anisotropic stiffness of weathered geomaterial and its influence on ground deformations around deep excavations. CANADIAN GEOTECHNICAL JOURNAL 41(1): 12-12.

Ng, C. W. W. and Pang, Y. W. (2000). Influence of stress state on soil-water characteristics and slope stability. Journal of Geotechnical and Geoenvironmental Engineering 126(2): 157-166.

Ng, C. W. W. and Xu, J. (2012). Effects of current suction ratio and recent suction history on small-strain behaviour of an unsaturated soil. Canadian Geotechnical Journal 49(2): 226-243.

Ng, C. W. W., Xu, J. and Yung, S. Y. (2009). Effects of wetting-drying and stress ratio on anisotropic stiffness of an unsaturated soil at very small strains. Canadian Geotechnical Journal 46(9): 1062-1076.

Ng, C. W. W. and Yung, S. Y. (2008). Determination of the anisotropic shear stiffness of an unsaturated decomposed soil. Géotechnique 58(1): 23-35.

Ng, C. W. W. and Zhan, T. L. (2006). Shear strength characteristics of an unsaturated expansive clay. Canadian Geotechnical Journal 43(7): 751-751.

Nyunt, T. T., Leong, E. C. and Rahardjo, H. (2011). Strength and Small-Strain Stiffness Characteristics of Unsaturated Sand. GEOTECHNICAL TESTING JOURNAL 34(5): 551-561.

Oh, W. T. and Vanapalli, S. K. (2011). Modelling the applied vertical stress and settlement relationship of shallow foundations in saturated and unsaturated sands. Canadian Geotechnical Journal 48: 425–438.

Oliveira, O. M. and Fernando, A. M. (2006). Study of Equilibration time in the Pressure Plate. Proceedings of the Forth International Conference of Unsaturated Soils. ASCE - Geotechnical Special Publication, n. Carefree - Arizona, ASCE. 2: 1864-1874.

Oliveira, O. M. and Marinho, F. A. M. (2007). Estudo de Barreiras Capilares por Meio de Simulação de Chuva em Coluna de Solo. VI Simpósio Brasileiro de Solos Não Saturados. Salvador-Bahia. 1: 291-297 (in Portuguese).

Oloo, S. Y. and Fredlund, D. G. (1996). A method for determination of ϕ_b for statically compacted soils. Canadian Geotechnical Journal 33(2): 272-280.

Olson, R. E. (1963). Effective stress theory of Soil compaction. Journal of soil mechanics and Foundations division (Transactions) SM2.

Olson, R. E. and Langfelder, L. J. (1965). Pore pressure in unsaturated soils. Journal of Soil Mechanics and Foundations Division 91(SM4): 127-150.

Pennington, D. S., Nash, D. F. T. and Lings, M. L. (1997). Anisotropy of G0 shear stiffness in Gault Clay. Géotechnique 47(3): 391-398.

Pennington, D. S., Nash, D. F. T. and Lings, M. L. (2001). Horizontally Mounted Bender Elements for Measuring Anistropic Shear Moduli in Triaxial Clay Specimens. Geotechnical Testing Journal 24(2): 133-144.

Perera, Y. Y., Zapata, C. E., Houston, W. N. and Houston, S. L. (2004). Moisture equilibria beneath highway pavements. Transportation Research Board 83rd Annual Meeting. Board, T. R. Washington, D.C.

Pham, H. Q., Fredlund, D. G. and Barbour, S. L. (2005). A study of hysteresis models for soil-water characteristic curves. Canadian Geotechnical Journal 42(6): 1548-1568.

Poulos, H. G. and Davis, E. H. (1974). Elastic solutions for soil and rock mechanics. New York, John Wiley and Sons.

Pournaghiazar, M., Russell, A. R. and Khalili, N. (2011). Development of a new calibration chamber for conducting cone penetration tests in unsaturated soils. Canadian Geotechnical Journal 48(2): 314-321.

Power, K. C., Vanapalli, S. K. and Garga, V. K. (2008). A Revised Contact Filter Paper Method. Geotechnical Testing Journal 31(6): 461-469.

Proctor, R. R. (1933). Fundamental Principles of Soil Compaction. Engineering News Record 111(9): 245-248.

Puech, P. A., Boussel, L., Belfkih, S., Lemaitre, L., Douek, P. and Beuscart, R. (2007). DicomWorks: Software for Reviewing DICOM Studies and Promoting Low-cost Teleradiology. Journal of Digital Imaging 20(2): 122-130.

Puppala, A. J., Manosuthkij, T., Nazarian, S. and Hoyos, L. R. (2011). Threshold moisture content and matric suction potentials in expansive clays prior to initiation of cracking in pavements. Canadian Geotechical Journal 48(4): 519-531.

Qian, X., Gray, D. H. and Woods, R. D. (1993). Voids and Granulometry: Effects on Shear Modulus of Unsaturated Sands. Journal of Geotechnical Engineering 119(2): 295.

Rahardjo, H., Ong, B. H. and Leong, E. C. (2004). Shear strength of a compacted residual soil from consolidated drained and constant water content triaxial tests. Canadian Geotechical Journal 41(3): 421-436.

Rampello, S., Silvestri, F. and Viggiani, G. (1995). The dependence of G0 on the stress state and history. *1st Int. Symp. on Prefailure Deformation of Geomaterials*, Sapporo, Japan.

Rampello, S., Viggiani, G. M. B. and Amorosi, A. (1997). Small-strain stiffness of reconstituted clay compressed along constant triaxial effective stress ratio paths. Géotechnique 47(3): 475-489.

Richart, F. E., Hall, J. R. and Woods, R. D. (1970). Vibration of Soil and Foundations, . Prentice-Hall.

Rio, J. F. M. E. (2006). Advances in Laboratory Geophysics using Bender Elements. PhD thesis. London, University College of London.

Robertson, P. K. and Wride, C. E. (1998). Evaluating cyclic liquefaction potential using the cone penetration test. CANADIAN GEOTECHNICAL JOURNAL 35(3): 442-459.

Romero, E., Della Vecchia, G. and Jommi, C. (2011). An insight into the water retention properties of compacted clayey soils. Géotechnique 61(4): 313-328.

Romero, E., Gens, A. and Lloret, A. (1999). Water permeability, water retention and microstructure of unsaturated compacted Boom clay. Engineering Geology 54(1-2): 117-127.

Romero, E. and Simms, P. H. (2008). Microstructure Investigation in Unsaturated Soils: A Review with Special Attention to Contribution of Mercury Intrusion Porosimetry and Environmental Scanning Electron Microscopy. Geotechnical and Geological Engineering 26(6): 705-727.

Russam, K. and Coleman, J. D. (1961). The Effect of Climatic Factors on Subgrade Moisture Conditions. Géotechnique 11(1): 22-28.

Russell, A. R. (2010). Water retention characteristics of soils with double porosity. EUROPEAN JOURNAL OF SOIL SCIENCE 61(3): 412-424.

Russell, A. R. and Buzzi, O. (2012). A fractal basis for soil-water characteristics curves with hydraulic hysteresis. Géotechnique 62(3): 269-274.

Russell, A. R. and Khalili, N. (2006). Cavity expansion and the cone penetration test in unsaturated sands. Proc. 4th Int. Conf. Unsat. Soils. Carefree, Arizona.

Sanchez-Salinero, I., Roesset, J. M. and Stokoe, K. H. (1986). Analytical studies of body wave propagation and attenuation. GR- 85-15. Austin, University of Texas.

Santamarina, J. C. and Cascante, G. (1996). Stress anisotropy and wave propagation: a micromechanical view. Canadian Geotechical Journal 33(5): 770-782.

Santamarina , J. C., Klein, K. and Fam, M. (2001). Soils and waves: Particulate materials behaviour characterization and process monitoring, John Wiley and Sons.

Santamarina , J. C., Rinaldi, V. A., Fratta, D., Klein, K. A., Wang, Y., Cho, G. C. and Cascante, G. (2005). A survey of elastic and electromagnetic properties of Near-surface soils. Near Surface Geophysics. Near-Surface Geophysics. E. D Butler, S.**:** 71-87.

Sawangsuriya, A., Edil, T. B. and Bosscher, P. J. (2008). Modulus-suction-moisture relationship for compacted soils. Canadian Geotechnical Journal 45(7): 973-983.

Sawangsuriya, A. E., T. B., Bosscher P. J. (2009). Modulus-Suction-Moisture Relationship for Compacted Soils in Postcompaction State. Journal of Geotechnical and Geoenvironmental Engineering 135(10): 1390-1403.

Seed, B. and Chan, C. K. (1959). Compacted clays: Structure and strength characteristics. Journal of soil mechanics and Foundations division Transactions 126(Part I): 1344-1380.

Seed, B. and Chan, C. K. (1959). Compacted clays: Structure and strength characteristics. Journal of soil mechanics and Foundations division Transactions 126(I): 1344.

Sheng, D., Fredlund, D. G. and Gens, A. (2008). A new modelling approach for unsaturated soils using independent stress variables. Canadian Geotechical Journal 45: 511-534.

Shibuya, S., Hwang, S. C. and Mitachi, T. (1997). Elastic shear modulus of soft clays from shear wave velocity measurement. Géotechnique 47(3): 593-601.

Shibuya, S., Mitachi, T. and Tamate, S. (1997). Interpretation of direct shear box testing of sands as quasi-simple shear. Géotechnique 47(4): 769-790.

Shibuya, S. and Tanaka, H. (1996). Estimate of elastic shear modulus in holocene soil deposits. Soil and Foundations 36(4): 45-55.

Sivakumar, V. and Doran, I. G. (2000). Yielding characteristics of unsaturated compacted soils. Mechanics of Cohesive-Frictional Materials 5(4): 291-303.

Skempton, A. W. (1953). The colloidal activity of clays. Proceedings of the 3rd ICSMFE. Zurich. 1: 57-61.

Sridharan, A. and Sivapullaiah, P. V. (2005). Mini Compaction Test Apparatus for Fine Grained Soils. Geotechnical Testing Journal 28(3): 1-6.

Standards Australia (1996). Residential slabs and footings - Construction. Australian Standard AS 2870-1996. Sydney, Standards Australia.

Standards Australia (1998). Method for testing soils for engineering purposes - Soil strength and consolidation tests - Determination of shear strength of a soil - Direct shear test using a shear box. Australian Standard AS 1289.6.2.2—1998. Sydney, Standards Australia.

Standards Australia (2002). Methods of testing soils for engineering purposes - Soil classification tests - Determination of the cone liquid limit of a soil. Australian Standard AS 1289.3.9.1-2002. Sydney, Standards Australia.

Standards Australia (2003). Method for testing soils for engineering purposes - Soil compaction and density tests - Determination of the dry density/moisture content relation of a soil using modified compactive effort. Australian Standard AS 1289.5.2.1-2003. Sydney, Standards Australia.

Standards Australia (2003). Method for testing soils for engineering purposes - Soil compaction and density tests - Determination of the dry density/moisture content relation of a soil using standard compactive effort. Australian Standard AS 1289.5.1.1 - 2003. Sydney, Standards Australia.

Standards Australia (2007). Guidelines on earthworks for commercial and residential developments. Australian Standard AS 3798. Sydney.

Standards Australia (2009). Methods of testing soils for engineering purposes - Soil classification tests - Determination of the plastic limit of a soil - Standard method. Australian Standard AS 1289.3.2.1-2009. Sydney, Standards Australia.

Stokoe, K. H. I., Lee, J. N. K. and Lee, S. H. H. (1991). Characterization of soil calibration chambers with seismic waves. *1st Int. Symp. on Calibration Chamber Testing*.

Stokoe, K. H. I. and Richart, F. E. (1973). In situ and laboratory shear wave velocities. *Proceedings on the 8th International Conference on Soil Mechanics and Foundation Engineering*, Moscow, USSR.

Sun, D. A., Sheng, D. C., Cui, H. B. and Sloan, S. W. (2007). A density-dependent elastoplastic hydro-mechanical model for unsaturated compacted soils. International Journal for Numerical and Analytical Methods in Geomechanics 31(11): 1257-1279.

Tang, A. M., Vu, M. N. and Cui, Y. J. (2011). Effects of the maximum soil aggregates size and cyclic wetting-drying on the stiffness of a lime-treated clayey soil. Géotechnique 61(5): 421-429.

Tarantino, A. and De Col, E. (2008). Compaction behaviour of clay. Géotechnique 58(3): 199-213.

Tarantino, A. and Tombolato, S. (2005). Coupling of hydraulic and mechanical behaviour in unsaturated compacted clay. Géotechnique 55(4): 307-317.

Taylor, D. W. (1948). Fundamentals of Soil Mechanics.

Tchalenko, J. S. (1970). Similarities between Shear Zones of Different Magnitudes. GSA Bulletin 81(6): 1625.

Terzaghi, K. (1943). Theoretical soil mechanics. New York, John Wiley and Sons.

Thadkamalla, G. B. G., K. P.; (1995). Characterization of subgrade soils at simulated field moisture. Transportation Research Record. 1481.

Thornthwaite, C. W. (1948). An Approach Toward a Rational Classification of Climate. Soil Science 66(1): 77.

Thu, T. M., Rahardjo, H. and Leong, E. C. (2006). Shear strength and pore-water pressure characteristics during constant water content triaxial tests. Journal of Geotechnical and Geoenvironmental Engineering 132(3): 411-419.

Thu, T. M., Rahardjo, H. and Leong, E. C. (2007). Elastoplastic model for unsaturated soil wih incorporation of the soil-water characteristic curve. Canadian Geotechical Journal 44: 62-77.

Tokimatsu, K. and Uchida, A. (1990). Constitutive relation for sand under cyclic loading based on elasto-plasticity theory. Soils and Foundations 30(2): 33-42.

Toll, D. G. (1990). A framework for unsaturated soil behaviour. Géotechnique 40(1): 31-44.

Toll, D. G. (2000). The influence of fabric on the shear behavior of unsaturated soils. Advances in Unsaturated Geotechnics:Procedings of the sessions of Geo-Denver. Shackelford, C. D. H., S.L., Chang, N.Y. Denver, Geo Institute: ASCE: 222-234.

Toll, D. G. and Ong, B. H. (2003). Critical-state parameters for an unsaturated residual sandy clay. Geotechnique 53(1): 93-103.

Toshiba Corp. (1994). CT Scanner Asteion. Technical Note No. MPDCT0005EAA. Division, T. M. S. Tokyo, Japan.

Troncoso, J. H. and Garcés, E. (2000). Ageing effects in the shear modulus of soils. Soil Dynamics and Earthquake Engineering 19(8): 595-601.

Turnbull, W. J. and Foster, C. R. (1956). Stabilization of Materials by Compaction. Journal of the Soil Mechanics and Foundations Division 82(SM2: 934): 1-23.

Uzan, J. (1998). Characterization of clayey subgrade materials for mechanistic design of flexible pavements. Transportation Research Record 1629(189-196).

van Genutchen (1980). A close form equation for predicting the water permeability of unsaturated soils. Journal of Soil science 44: 892-898

Vanapalli, S. K. and Fredlund, D. G. (2000). Comparison of different procedures to predict the shear strength of unsaturated soils uses the soil-water characteristic curve. Geo-Denver 2000. American Society of Civil Engineers, S. P., ASCE. 99: 195-209.

Vanapalli, S. K., Fredlund, D. G. and Pufahl, D. E. (1996). The Relationship Between the Soil-Water Characteristic Curve and the Unsaturated Shear Strength of a Compacted Glacial Till. Geotechnical Testing Journal 19,(3): 259-268.

Vanapalli, S. K. and Lane, J. (2002). A simple technique for determining the shear strength of unsaturated soils using the conventional direct shear apparatus. Second Canadian specialty conference on computer applications in geotechnique. Winnipeg: 245-253.

Vanapalli, S. K. and Mohamed, F. M. O. (2007). Bearing capacity of model footings in unsaturated soils. Experimental unsaturated soil mechanics. Berlin Heidelberg, Germany, Springer-Verlag**:** 483–493.

Vaunat , J., Merchán, V., Romero, E. and Pineda, J. (2007). Residual strength of clays at high suctions. *Proc. of the 2nd International Conference on Mechanics of Unsaturated Soils: Theoretical and Numerical Unsaturated Soil Mechanics Series*, Weimar, Germany, Springer.

Vesic, A. B. (1973). Analysis of ultimate loads of shallow foundations. Journal of the Soil Mechanics and Foundations Division (ASCE) 99(1): 45–73.

Viggiani, G. and Atkinson, J. H. (1995). Interpretation of bender element tests. Geotechnique 45(1): 149–154.

Vilar, O. M. (2006). A simplified procedure to estimate the shear strength envelope of unsaturated soils. Canadian Geotechnical Journal 43(10): 1088-1088.

Vinale, F., D'Onofrio, A., Mancuso, C., Santucci de Magistris, F. and Tatsuoka, F. (1999). The pre-failure behaviour of soils as construction materials, Torino, Italy, shers.

Vinale, F., D'Onofrio, A., Mancuso, C., Santucci de Magistris, F. and Tatsuoka, F. (2001). The pre-failure behaviour of soils as construction materials. Torino, Italy: 955-1007.

Wang, J. and Gutierrez, M. (2010). Discrete element simulations of direct shear specimen scale effects. Géotechnique 60(5): 395-409.

Wang, Y. and Ng, C. W. (2005). Effects of stress paths on the small-strain stiffness of completely decomposed granite. Canadian Geotechical Journal 42(4): 1200-1200.

Wheeler, S. J., Sharma, R. J. and Buisson, M. S. R. (2003). Coupling of hydraulic hysteresis and stress-strain behaviour in unsaturated soils. Geotechnique 53(1): 41-54.

Wheeler, S. J. and Sivakumar, V. (2000). Influence of compaction procedure on the mechanical behaviour of an unsaturated compacted clay. Part 2: Shearing and constitutive modelling. Geotechnique 50(4): 369-376.

Wood, D. M. (2002). Some observations of volumetric instabilities in soils. International Journal of Solids and Structures 39(13): 3429-3449.

Wu, S., Gray, D. H. and Richart, F. E. J. (1984). Capillary effects on dynamic modulus of sands and silts Journal of Geotechnical Engineering 110(9): 1188-1203.

Yimsiri, S. and Soga, K. (2011). Cross-anisotropic elastic parameters of two natural stiff clays. Géotechnique 61(9): 809-814.

Youn, J., Choo, Y. and Kim, D. (2008). Measurement of small-strain shear modulus Gmax of dry and saturated sands by bender element, resonant column, and torsional shear tests. Canadian Geotechnical Journal 45(10): 1426-1426.

Zhan, T. L. and Ng, C. W. W. (2006). Shear strength characteristics of an unsaturated expansive clay. Canadian Geotechnical Journal 43(7): 751-751.

Zhang, G., Robertson, P. K. and Brachman, R. W. I. (2002). Estimating liquefaction-induced ground settlements from CPT for level ground. CANADIAN GEOTECHNICAL JOURNAL 39(5): 1168-1180.

Zhang, L. (2010). A simple method for evaluating liquefaction potential from shear wave velocity. Frontiers of Architecture and Civil Engineering in China 4(2): 178-195.

Zhang, L. M. and Chen, Q. (2005). Predicting bimodal soil-water characteristic curves. Journal of Geotechnical and Geoenvironmental Engineering 131(5): 666-670.

Zhou, A. N., Sheng, D. and Carter, J. P. (2012). Modelling the effect of initial density on soil-water characteristic curves. Géotechnique 62(8): 669-680.

APPENDIX A . BODY WAVES IN A INFINITE CONTINUUM

A.1 GENERAL

Consider an element in an infinite, linear, elastic, isotropic and homogenous continuum subjected to a perturbation such that a stress gradient develops between the parallel faces (Figure A.1).

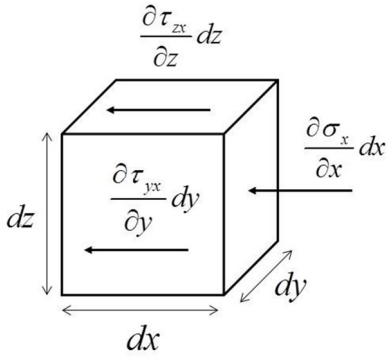

Figure A.1. Stresses acting on an element during wave propagation with perturbation travelling in the x-direction.

Equilibrium requires that the forces acting on the element must equal Newton's inertial force ($F=ma$). By considering the sum of the forces in the x-direction, the equilibrium equation becomes (with dx, dy, dz cancelling on both sides of the equation):

$$\rho \frac{\partial^2 u_x}{\partial t^2} = \frac{\partial \sigma_x}{\partial x} + \frac{\partial \tau_{yx}}{\partial y} + \frac{\partial \tau_{zx}}{\partial z} \tag{A.1}$$

where ρ is the mass density of the medium and $\partial^2 u_x/\partial t^2$ is acceleration in the x-direction. The stress terms can be expressed in terms of strains while considering the following constitutive equations:

$$\sigma_x = M \varepsilon_v - 2G(\varepsilon_x + \varepsilon_y) \tag{A.2}$$

$$\tau_{yx} = G \gamma_{yx} \tag{A.3}$$

where, M is the constraint modulus (σ_x/ε_x for $\varepsilon_y=\varepsilon_z=0$) and G is the shear modulus. Note that Eq. (A.2) and (A.3) can also be expressed for the y and z directions in a similar way.

Substituting Eq. (A.2)and (A.3)into Eq. (A.1) we can obtain:

$$\rho \frac{\partial^2 u_x}{\partial t^2} = M \frac{\partial \varepsilon_v}{\partial x} + G\left(-2\frac{\partial \varepsilon_y}{\partial x} - 2\frac{\partial \varepsilon_z}{\partial x} + \frac{\partial \gamma_{yx}}{\partial y} + \frac{\partial \gamma_{zx}}{\partial z} \right) \tag{A.4}$$

Replacing strains in terms of deformation (i.e. $\varepsilon_x = \partial u_x / \partial x$) and rearranging:

$$\rho \frac{\partial^2 u_x}{\partial t^2} = (M - G)\left(\frac{\partial^2 u_x}{\partial x^2} + \frac{\partial^2 u_y}{\partial x \partial y} + \frac{\partial^2 u_z}{\partial x \partial z} \right) + G\left(\frac{\partial^2 u_x}{\partial x^2} + \frac{\partial^2 u_x}{\partial y^2} + \frac{\partial^2 u_x}{\partial z^2} \right) \tag{A.5}$$

The displacement field that satisfies this equation describes a variation in time and space, also known as the wave equation, and predicts two types of body waves (i.e. different propagations), compression waves and shear waves. The wave equation relates the temporal variation of a particle motion to its spatial variation. An exponential relation for the particle motion u is a solution to the wave equation:

$$u = Ae^{i(\omega t \pm \kappa x)} \tag{A.6}$$

where, A is the maximum amplitude of the motion, $\omega = 2\pi/T$ is the temporal angular frequency, $\kappa = 2\pi/\lambda$ is the spatial frequency or wave number, T is the period, λ is the wavelength, t is the time and $i = \sqrt{-1}$ denotes an imaginary number.

A.2 COMPRESSION WAVES

The first mode of propagation corresponds to dilation without rotation. Consider a wave propagating in the x-direction, with the particle motion in the x-direction or u_x with $u_y = u_z = 0$. For a plane wave u_x that does not vary across the wave front (i.e. y-z direction) Eq.(A.5) can be simplified to:

$$\frac{\partial^2 u_x}{\partial t^2} = \frac{M}{\rho} \frac{\partial^2 u_x}{\partial x^2} \tag{A.7}$$

When compression waves, widely known as primary waves or simply P-waves, propagate in an isotropic medium, the motion of a point is parallel to the direction of the propagation (Figure A.2). P-waves can be transmitted through both fluids and solids. If the particle motion expressed in Eq. (A.6) is substituted in the wave equation for the P-wave, then the result is $\omega/\kappa = \sqrt{(M/\rho)}$, and this ratio also corresponds to the distance travelled by the wave in one cycle (i.e. the phase velocity of the wave $\omega/\kappa = \lambda/T$), thus the velocity of the P-wave is,

$$V_P = \sqrt{\frac{M}{\rho}} \tag{A.8}$$

A.3 SHEAR WAVES

The second mode of propagation corresponds to a wave travelling in the *x*-direction but with particle motion on the *y*-direction, thus Eq. (A.5) can be re-written in a similar way in terms of u_y as follows,

$$\rho \frac{\partial^2 u_y}{\partial t^2} = (M - G)\left(\frac{\partial^2 u_x}{\partial x \partial y} + \frac{\partial^2 u_y}{\partial y^2} + \frac{\partial^2 u_z}{\partial y \partial z} \right) + G\left(\frac{\partial^2 u_y}{\partial x^2} + \frac{\partial^2 u_y}{\partial y^2} + \frac{\partial^2 u_y}{\partial z^2} \right) \tag{A.9}$$

If the particle motion is only for the *y*-direction, this means that $u_x = u_z = 0$ and because the u_y of a plane wave travelling in the *x*-direction does not change across the wave front, then the previous equation can be simplified to:

$$\frac{\partial^2 u_y}{\partial t^2} = \frac{G}{\rho} \frac{\partial^2 u_y}{\partial x^2} \tag{A.10}$$

The shear waves, widely known as secondary waves, or simply S-waves, propagate perpendicularly to the direction of propagation, and shear distortion is applied (Figure A.2). S-waves can only be transmitted through mediums with shear stiffness (i.e. solids with G>0), as fluid (liquid and gas) do not support shear stresses. In a similar manner, if the particle motion is substituted in Eq. (A.10) then the velocity of the S-wave can be expressed as,

$$V_S = \sqrt{\frac{G}{\rho}} \tag{A.11}$$

The shear wave can be decomposed into two normal polarisation components, that is, with propagation in the *x*-direction and particle motion either in the *y*-direction or *z*-direction. The directions of polarisation that are usually adopted in the ground are the vertically polarised or SV wave, and the horizontally polarised or SH wave.

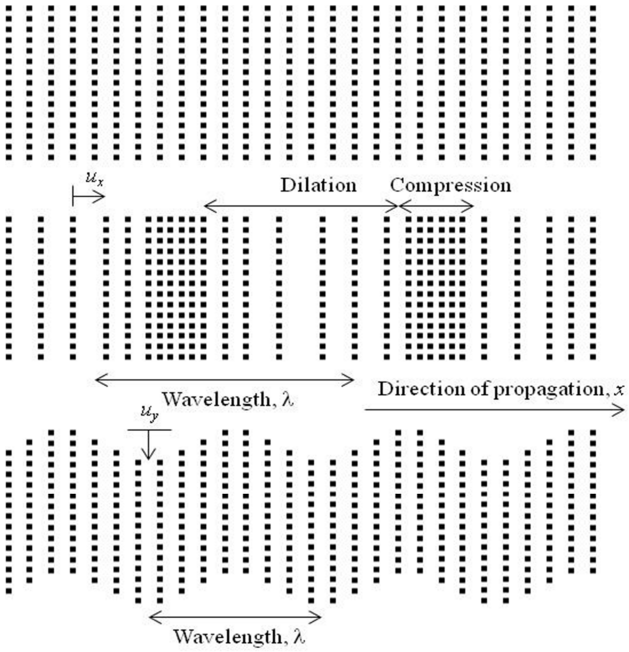

Figure A.2. Particle motion in a continuum during wave propagation (top) before the propagation, (middle) and (bottom) positions for P-wave and S-wave propagation, respectively.

APPENDIX B . PENRITH LAKES AERIAL PHOTOGRAPH

Figure B.1. Aerial Photograph of the Penrith Lakes scheme (courtesy of Penrith Lakes Development Corporation, 2009).

APPENDIX C . ASPECTS RELATED TO SHEAR WAVE PROPAGATION AND STIFFNESS OF SOIL AT SMALL STRAINS

C.1 CURRENT STATE

The current state of soil specimens in the small strain range is defined by the normal stress or mean effective stress (confining pressure) applied in the direction of wave propagation and particle motion, in addition to the void ratio (or density of the soil) and suction, as outlined in Chapter 2. Under saturated or dry conditions, the shear wave velocity for particulate materials can then be given by Hardin and Richart (1963) cited Richart et al. (1970), Stokoe et al. (1991); Santamarina and Cascante (1996),

$$V_s = \theta \left(\frac{\sigma'_m}{1kPa} \right)^{\beta} \tag{C.1}$$

where, θ and β are empirical parameters, σ'_m is the mean effective stress, and 1kPa is used for dimensionality. The empirical parameter β reflects the nature of the grain contacts, for instance, β=1/6 for Hertzian contacts, β=1/4 for plastic spherical contact (angular or rough particles), $\beta \approx 0.2$ to 0.25 for sands (the looser the sand the higher the β) and $\beta \approx 0.27$ to 0.3 for kaolin (Cho and Santamarina, 2001). In an analogous manner, a general empirical expression has also been derived for the small strain shear modulus proposed by Mitchell and Soga (2005), and can be expressed by:

$$G_0 = A f(e) \left(p' \right)^n \tag{C.2}$$

where A is a parameter associated with the structure of the soil, $f(e)$ is a function of the void ratio, p' is the mean effective stress, and n is a fitting parameter associated with the state of stress. Similar expressions have also been proposed for soils ranging from sand (Hardin and Black, 1966, Iwasaki et al., 1978; Lo Presti, 1995; Cuccovillo and Coop, 1997; Jovicic and Coop, 1997) to remoulded, undisturbed, and reconstituted clays (Marcuson and Wahls, 1972; Shibuya and Tanaka, 1996;Shibuya et al., 1997; Rampello et al., 1997). The main differences between the several relationships resides in the void ratio functions $f(e)$, and the magnitude of the empirical parameters adopted.

C.2 ANISOTROPY

The anisotropy of soils in the small strain range is generally associated with stress induced anisotropy and inherent structural anisotropy (Anandarajah and Kuganenthira, 1995; Jiang et al., 1997; Jovicic and Coop, 1998; Yimsiri and Soga, 2011). While the stress induced anisotropy is related to the current stress, the inherent anisotropy results from the structure or fabric of the soil. To ascertain the effect of stress induced anisotropy, the specimens are usually subjected to anisotropic states of stress obtained by increasing the vertical stress while maintaining the average principal stress constant. In the preceding sections of the thesis, the tests were carried out under isotropic loading conditions, and therefore, the main concern in terms of anisotropy is mainly related to the inherent component. Pennington et al. (1997), Jovicic and Coop (1998) and more recently Pennington et al. (2001), Ng et al. (2004); Wang and Ng (2005), Ng and Yung (2008) and Ng et al. (2009) investigated anisotropy in triaxial specimens using vertical and horizontal mounted bender elements to study wave propagation in different orientations and with different planes of polarisation (Figure C.1).

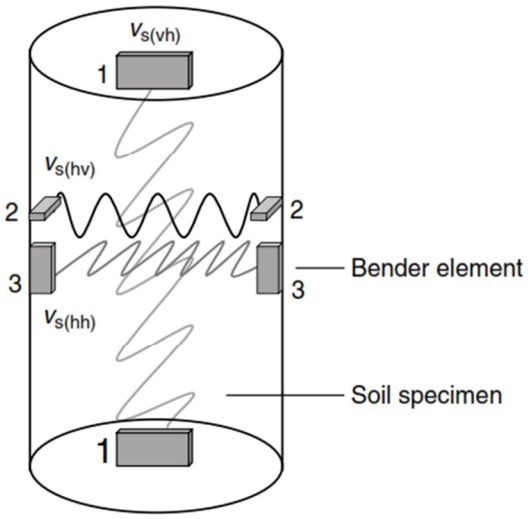

Figure C.1. Schematic diagram showing the vertical and horizontal position used to investigate the inherent anisotropy of soil (Ng and Yung, 2008).

The effect of inherent anisotropy is particularly important when compacted soil is of interest, mainly because of the fabric anisotropy induced by compaction and the anisotropy induced by suction. Ng and Yung (2008) conducted a series of tests on compacted and completely decomposed tuff (CDT) specimens, targeting the optimum water content compaction state and

different post-compaction suction and net stress states. Measurements of the shear wave velocity under full saturation indicated the presence of inherent fabric anisotropy which was found to be linked to the net stress applied, that is, the higher the net mean stress the greater the anisotropy. Also the degree of small strain stiffness anisotropy increases with increasing suction before reaching the air entry value. The degree of anisotropy with increasing net mean stress was relatively independent of suction, although there was an inherent anisotropy among the two main bender elements orientations of about 0.2 (i.e. vertical or *vh* and horizontal or *hv*), where the difference was consistent for specimens subjected to the same isotropic loading and suction paths.

In this study, the influence of inherent anisotropy on the shear wave propagation was not addressed because every specimen was prepared using the same method (compaction process), so any induced anisotropy is likely to affect all specimens in a similar manner. Nevertheless, to understand the effect of any inherent anisotropy on the shear wave propagation induced by compaction, a series of tests where vertical and horizontal propagation were monitored, were conducted in a specimen compacted at optimum moisture content and standard compaction energy. Typically the specimens were compacted in three layers (see AS1289.5.1.1 –2003) and for that reason were measured across the three layers (Figure C.2).

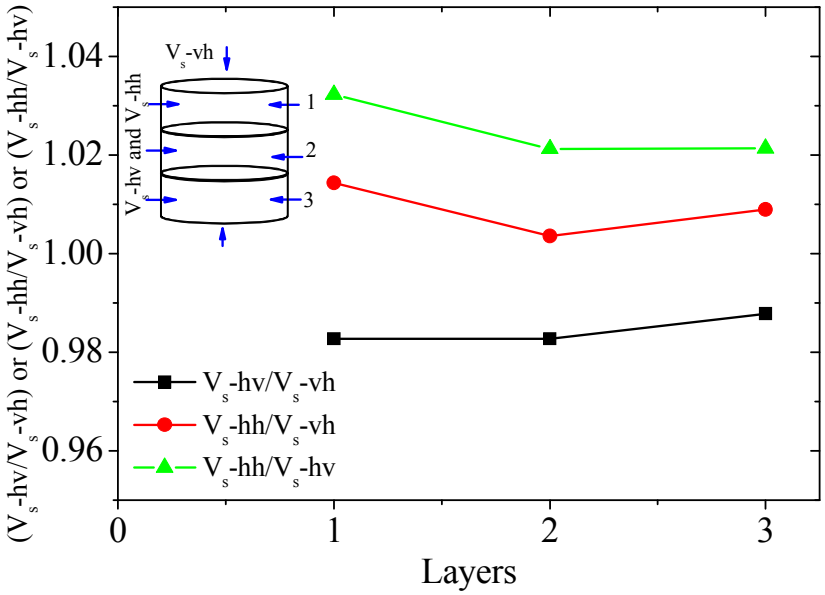

Figure C.2. Unconfined inherent anisotropy for a silty sand specimen compacted at optimum moisture content with standard compaction energy (w=12%, E= 596kJ/m^3).

The results indicate there is an inherent fabric anisotropy in the compacted specimen where typically, the difference between the three planes of wave propagation is not substantial, usually within 2-3%, and the highest velocity was found for the V_s-*hh*, which is consistent with the findings by Ng and Yung (2008).

C.3 AGEING

The influence of the stress history and age on the shear wave or small strain modulus has been investigated by several different studies (Afifi and Woods, 1971; Marcuson and Wahls, 1972; Stokoe and Richart, 1973; Anderson and Wood, 1976; Anderson and Stokoe, 1978, Kokusho, 1987, Shibuya et al., 1997; Troncoso and Garcés, 2000). The effects of ageing are important for predicting how the dynamic properties of soil structures evolve. Two different ranges of ageing effects have usually been identified, an initial phase due to primary consolidation associated with a strengthening of the particle bonding, and a second phase with long term effects associated with thixotropic changes in the structure of clay soils. For this reason the magnitude of ageing is strongly dependent on the type of soil and stress condition (i.e. confining pressure). For instance, the ageing increment coefficient (N_G) for normally consolidated clays ranges from 5-20%, varies between 3-10% for over consolidated clays, and reduces to 1 to 3% (Figure C.3) in sands. The soil that makes up most of the fills used in Penrith Lakes consists predominantly of sand so ageing is not considered.

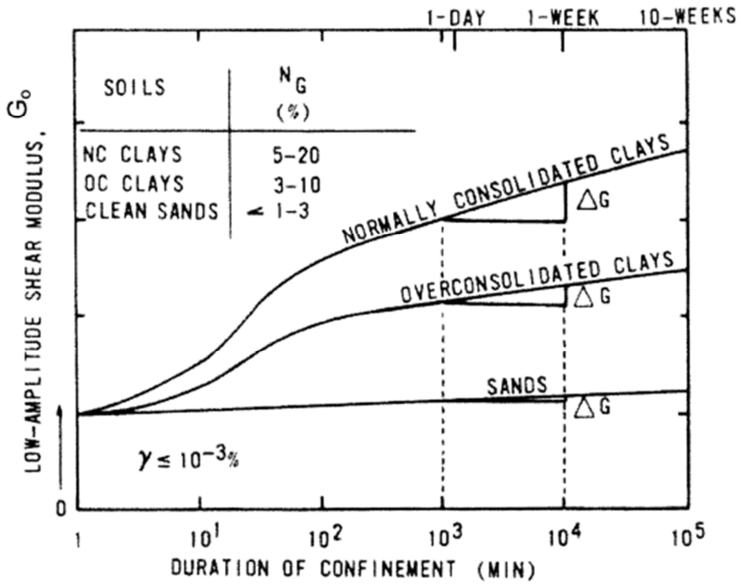

Figure C.3. Variation of small strain shear modulus with time, reflecting the effect of ageing (Andersen and Stokoe, 1978).

C.4 CEMENTATION

Cementation is usually caused by either natural (i.e. precipitation of salts, alumina, silicates, iron oxides) or artificial (i.e. lime, cement, fly ash) soil stabilisation processes and can have a strong influence in the small strain behaviour (Clough et al., 1981; Lade and Overton, 1989; Baig et al., 1997; Fernandez and Santamarina, 2001,Tang et al., 2011). The wave velocity or small strain shear modulus of cemented sandy soils increases with an increase of the cementing agent present, and also with the confining pressure. In addition, the load deformation behaviour of loose cemented specimens is brittle at low confining stresses and becomes ductile as confinement increases (Santamarina et al., 2001). The influence of cementation on the shear velocity is not considered because there was no natural bonding agent in the materials used in the fills, and the content of salts is negligible. Thus, the effect of cementation is likewise not taken into consideration.

C.5 TEMPERATURE

The temperature and time dependent variation of the shear wave velocity has been reported by Fam et al. (1998) and Bosscher and Nelson (1987). Fam et al (1998) studied the evolution of velocity with time for a granular salt subjected to a temperature step, which reflects heating and cooling cycles. The rate of increase in the velocity was directly related to the temperature applied, that is, higher rates of increase for higher temperatures. In contrast, Bosscher and Nelson (1987) found that frozen sands yield higher small strain shear modulus than non-frozen sands, and when the temperature approaches the melting point of ice, the small strain shear modulus depends mainly on the confining pressure, the degree of ice saturation, and density. Likewise in this analysis, the effect of temperature was not taken into account.

C.6 DEPTH OF THE CHANGE IN MOISTURE H_S

Climatic factors have been long recognised by studies on changes in the moisture content of subgrade soils beneath pavements (Russam and Coleman, 1961; Thadkamalla, 1995; Gomes Correia, 1996; Uzan, 1998; Perera et al., 2004; Bae et al., 2008 and more recently Puppala et al., 2011). In fact, it is thought that the moisture in subgrades eventually reaches equilibrium after construction and then remains constant. This equilibrium can be represented by soil suction that can be correlated to the average value of the Thornthwaite moisture index (TMI)

(Thornthwaite, 1948). Furthermore, in fills exposed to climatic changes (i.e. protective coverage is absent) the TMI is related to the depth where moisture experiences larger changes as a result of dry and wet seasons.

In Figure C.4 the average value of TMI contours are represented for Australia, where a value of 60 can be obtained for the location at Penrith Lakes. The depth where the moisture changes or H_s can be estimated using Table C.1 and thus for Penrith Lakes, classified as wet and coastal, the H_s can be taken as 1.5m.

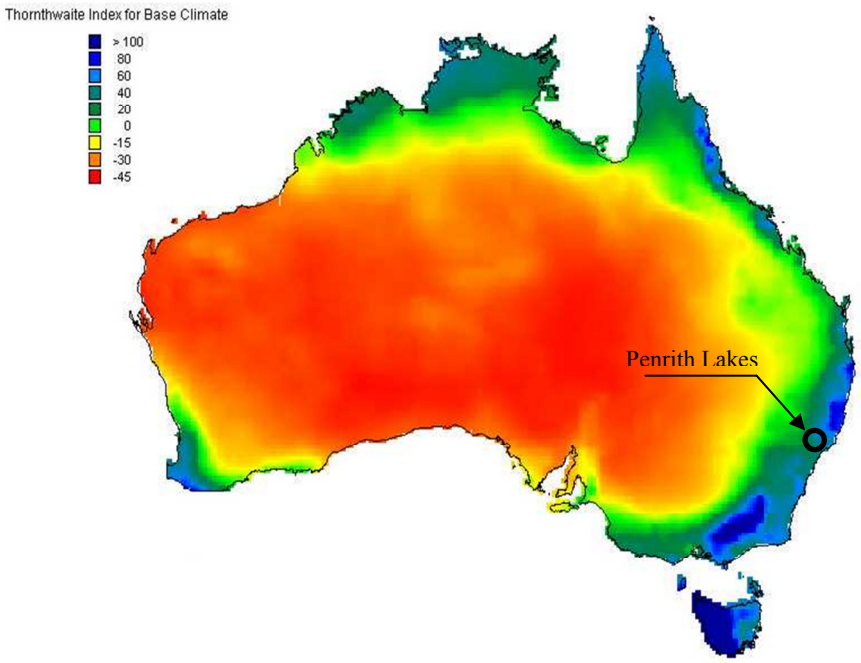

Figure C.4. Distribution contours of TMI in Australia for base climate (2000) (Austroads, 2004)

Table C.1. Correlation between TMI and Hs (later revised by Fityus and Buzzi, 2008)

TMI	Classification	Depth of moisture change, H_s (m)
>40	Wet coastal	1.5
10 to 40	Wet temperate	15.-1.8
-5 to 10	Temperate	1.8-2.3
-25 to -5	Dry Temperate	2.3-3.0
-40 to -25	Semi-arid	3.0-4.0
<-40	Arid	>4.0

C.7 MOISTURE CHANGE IN TIME BELOW THE ACTIVE ZONE

Oliveira and Marinho (2007) showed that while conducting infiltration tests on compacted residual soil columns subjected to artificial rain at an intensity of 30mm/h for 2h periods, there were larger differences in the suction and water content of the top portion of the columns, in fact for a 1.25m horizon there was hardly any change in moisture and suction. Furthermore, Mendes (2011) recently conducted long term measurements of moisture and suction in a compacted embankment and found that the upper layers experience large changes compared to deeper layers.

REFERENCES

Afifi, S. S. and Woods, R. D. (1971). Long-term pressure effects on the shear modulus of soils. *J. Soil Mech. and Found. Div. Proc. ASCE* 97(SM10), 1445-1460.

Anandarajah, A. and Kuganenthira, N. (1995). Some aspects of fabric anisotropy of soil. *Géotechnique* 45(1), 69-81.

Anderson, D. G. and Stokoe, K. H. I. (1978). Shear modulus: A time dependent soil property. Dynamic Geotechnical Testing. ASTM. STP 654**:** 66-90.

Anderson, D. G. and Wood, D. M. (1976). Time-dependent increase in shear modulus of clay. *Journal of Geotechnical Engineering Division, ASCE* 102(GT5), 525-537.

Austroads (2004). Impact of Climate Change on Road Infrastructure. AP-R243. Sydney, Ausroads.

Bae, A., Stoffels, S. M., Antle, C. E. and Lee, S. W. (2008). Observed evidence of subgrade moisture influence on pavement longitudinal profile. *Canadian Journal of Civil Engineering* 35(10), 1050-1050.

Baig, S., Picornell, M. and Nazarian, S. (1997). Low strain shear moduli of cemented sands. *Journal of Geotechnical Engineering, ASCE* 123, 540-545.

Bosscher, P. J. and Nelson, D. L. (1987). Resonant column testing of frozen Ottawa sand. *Geotechnical testing Journal* 10(3), 123-134.

Cho, G. C. and Santamarina, J. C. (2001). Unsaturated particulate materials—particle level studies. *Journal of Geotechnical and Geoenvironmental Engineering* 127(1), 84–96.

Clough, G. W., Sitar, N., Bachus, R. C. and Rad, N. S. (1981). Cemented sands under static loading. *Journal of the Geotechnical Engineering Division, ASCE* 107, 799-817.

Cuccovillo, T. and Coop, M. R. (1997). Yielding and pre-failure deformation of structure sands. *Geotechnique* 47(3), 491-508.

Fam, M., Santamarina, J. C. and Dusseault, M. (1998). Wave-based monitoring processes in granular salt. *Journal of Enviromental and Engineering Geophysics* 3, 15-26.

Fernandez, A. L. and Santamarina, J. C. (2001). Effect of cementation on the small-strain parameters of sands. *Canadian Geotechical Journal* 38(1), 191-199.

Fityus, S. and Buzzi, O. (2008). On the use of the Thornwaite Moisture index to infer depths of seasonal moisture change. *Australian Geomechanics* 43(4), 69-76.

Gomes Correia, A. (1996). Prediction of subgrade moisture conditions for purposes of pavement design. Flexible Pavements G. Correia. Rotterdam, Balkema**:** 99-104.

Hardin, B. O. and Black, W. L. (1966). Sand stiffness under various triaxial stresses. *J. Soil Mech. and Found. Div. Proc. ASCE* 92(SM2), 27-42.

Hardin, B. O. and Richart, F. E. (1963). Elastic waves velocities in granular soils. *J. Soil Mech. and Found. Div. Proc. ASCE* 89(SM1), 33-65.

Iwasaki, T., Tatsuoka, F. and Takagi, Y. (1978). Shear moduli of sands under cyclic torsional shear loading. *Soil and Foundations* 18(1), 39-56.

Jiang, G.-L., Tatsuoka, F., Koseki, J. and Flora, A. (1997). Inherent and stress-state-induced anisotropy in very small strain stiffness of a sandy gravel. *Géotechnique* 47(3), 509-521.

Jovicic, V. and Coop, M. (1998). The influence of plastic strains during compression on the inherent anisotropy of G_{max}. Pre-failure deformation behaviour of geomaterials. R. J. Jardine, M. C. R. Davies, D. W. Hight, A. K. C. Smith and S. E. Stallebrass, ICE**:** 395-397.

Jovicic, V. and Coop, M. R. (1997). Stiffness of coarse-grained soils at small strains. *Géotechnique* 47(3), 545-561.

Kokusho, T. (1987). In situ dynamic soil properties and their evaluation. Proceedings of 8th Asian regional Conference on Soil Mechanics and Foundation Engineering, Kyoto, Japan.

Lade, P. V. and Overton, D. D. (1989). Cementation effects in frictional materials. *Journal of Geotechnical Engineering, ASCE* 115, 1373-1387.

Lo Presti, D. C. F. (1995). Measurement of the shear deformation of geomaterials in laboratory : General report. Pre-failure Deformation of Geomaterials. M. M. Shibuya, Balkema. 2**:** 1067-1088.

Marcuson, W. F. and Wahls, H. E. (1972). Time Effects on Dynamic Shear Modulus of Clays. *J. Soil Mech. and Found. Div. Proc. ASCE* 98(12), 1359-1373.

Mendes, J. (2011). Assessment of the impact of climate change on an instrumented embankment: an unsaturated soil mechanics approach. Doctoral thesis. Durham, Durham University.

Mitchell, J. K. and Soga, K. (2005). *Fundamentals of soil behavior*. Chichester, Wiley.

Ng, C. W., Leung, E. H. Y. and Lau, C. K. (2004). Inherent anisotropic stiffness of weathered geomaterial and its influence on ground deformations around deep excavations. *CANADIAN GEOTECHNICAL JOURNAL* 41(1), 12-12.

Ng, C. W. W., Xu, J. and Yung, S. Y. (2009). Effects of wetting-drying and stress ratio on anisotropic stiffness of an unsaturated soil at very small strains. *Canadian Geotechnical Journal* 46(9), 1062-1076.

Ng, C. W. W. and Yung, S. Y. (2008). Determination of the anisotropic shear stiffness of an unsaturated decomposed soil. *Géotechnique* 58(1), 23-35.

Oliveira, O. M. and Marinho, F. A. M. (2007). Estudo de Barreiras Capilares por Meio de Simulação de Chuva em Coluna de Solo. VI Simpósio Brasileiro de Solos Não Saturados. Salvador-Bahia. 1**:** 291-297 (in Portuguese).

Pennington, D. S., Nash, D. F. T. and Lings, M. L. (1997). Anisotropy of G0 shear stiffness in Gault Clay. *Géotechnique* 47(3), 391-398.

Pennington, D. S., Nash, D. F. T. and Lings, M. L. (2001). Horizontally Mounted Bender Elements for Measuring Anistropic Shear Moduli in Triaxial Clay Specimens. *Geotechnical Testing Journal*

24(2), 133-144.

Perera, Y. Y., Zapata, C. E., Houston, W. N. and Houston, S. L. (2004). Moisture equilibria beneath highway pavements. Transportation Research Board 83rd Annual Meeting. T. R. Board. Washington, D.C.

Puppala, A. J., Manosuthkij, T., Nazarian, S. and Hoyos, L. R. (2011). Threshold moisture content and matric suction potentials in expansive clays prior to initiation of cracking in pavements. *Canadian Geotechical Journal* 48(4), 519-531.

Rampello, S., Viggiani, G. M. B. and Amorosi, A. (1997). Small-strain stiffness of reconstituted clay compressed along constant triaxial effective stress ratio paths. *Géotechnique* 47(3), 475-489.

Richart, F. E., Hall, J. R. and Woods, R. D. (1969). *Vibration of Soil and Foundations,* . Prentice-Hall.

Russam, K. and Coleman, J. D. (1961). The Effect of Climatic Factors on Subgrade Moisture Conditions. *Géotechnique* 11(1), 22-28.

Santamarina, J. C. and Cascante, G. (1996). Stress anisotropy and wave propagation: a micromechanical view. *Canadian Geotechical Journal* 33(5), 770-782.

Santamarina , J. C., Klein, K. and Fam, M. (2001). *Soils and waves: Particulate materials behaviour characterization and process monitoring*, John Wiley and Sons.

Shibuya, S., Hwang, S. C. and Mitachi, T. (1997). Elastic shear modulus of soft clays from shear wave velocity measurement. *Géotechnique* 47(3), 593-601.

Shibuya, S. and Tanaka, H. (1996). Estimate of elastic shear modulus in holocene soil deposits. *Soil and Foundations* 36(4), 45-55.

Standards Australia (1996). Residential slabs and footings - Construction. Australian Standard AS 2870-1996. Sydney, Standards Australia.

Standards Australia (2003). Method for testing soils for engineering purposes - Soil compaction and density tests - Determination of the dry density/moisture content relation of a soil using standard compactive effort. Australian Standard AS 1289.5.1.1 - 2003. Sydney, Standards Australia.

Stokoe, K. H. I., Lee, J. N. K. and Lee, S. H. H. (1991). Characterization of soil calibration chambers with seismic waves. 1st Int. Symp. on Calibration Chamber Testing.

Stokoe, K. H. I. and Richart, F. E. (1973). In situ and laboratory shear wave velocities. Proceedings on the 8th International Conference on Soil Mechanics and Foundation Engineering, Moscow, USSR.

Tang, A. M., Vu, M. N. and Cui, Y. J. (2011). Effects of the maximum soil aggregates size and cyclic wetting-drying on the stiffness of a lime-treated clayey soil. *Géotechnique* 61(5), 421-429.

Thadkamalla, G. B. G., K. P.; (1995). Characterization of subgrade soils at simulated field moisture. *Transportation Research Record. 1481*.

Thornthwaite, C. W. (1948). An Approach Toward a Rational Classification of Climate. *Soil Science* 66(1), 77.

Troncoso, J. H. and Garcés, E. (2000). Ageing effects in the shear modulus of soils. *Soil Dynamics and Earthquake Engineering* 19(8), 595-601.

Uzan, J. (1998). Characterization of clayey subgrade materials for mechanistic design of flexible pavements. *Transportation Research Record 1629*(189-196).

Wang, Y. and Ng, C. W. (2005). Effects of stress paths on the small-strain stiffness of completely decomposed granite. *Canadian Geotechical Journal* 42(4), 1200-1200.

Yimsiri, S. and Soga, K. (2011). Cross-anisotropic elastic parameters of two natural stiff clays. *Géotechnique* 61(9), 809-814.

APPENDIX D . CT-SCAN RAW IMAGES

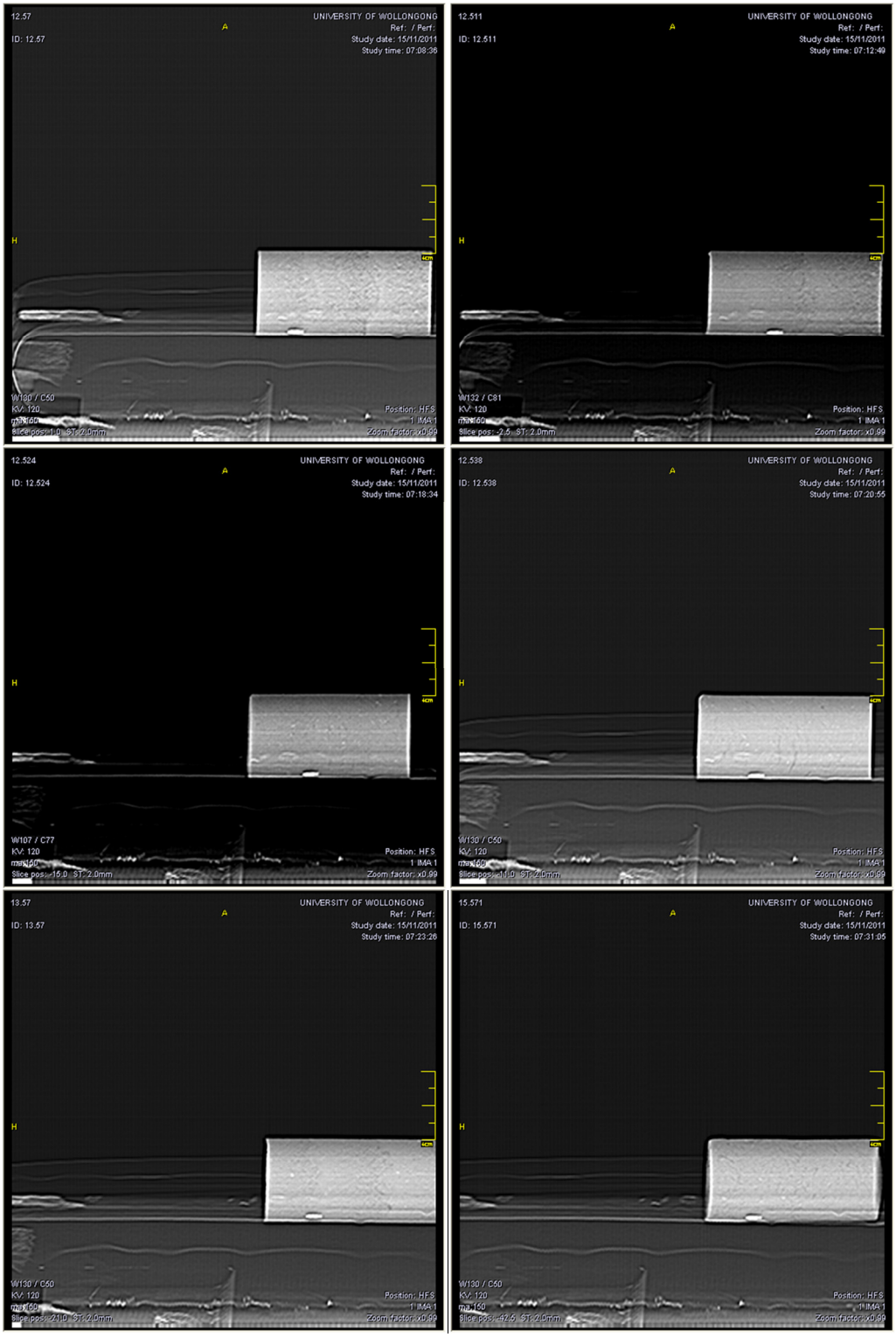

Figure D.1. X-ray CT-Scan images: global aspect of the compacted specimens (specimens ID is code represents the water content followed by the number of blows per layer)

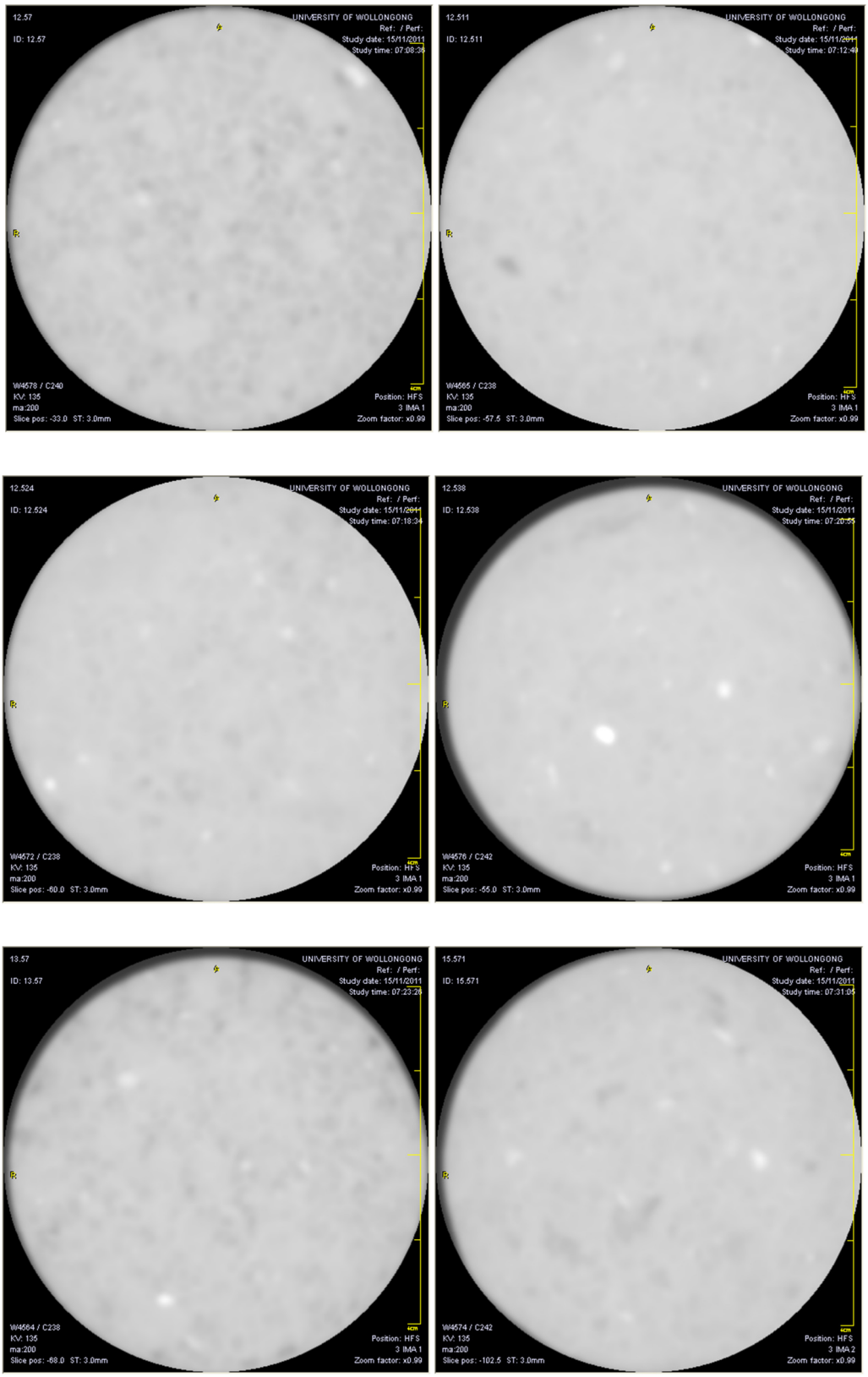

Figure D.2. X-Ray CT-scan raw images of the compacted for specimens obtained with voltage of 135kV, intensity of 200mA and field of view of 50mm.

APPENDIX E . FIELD MOISTURE CONTENT: AREA 7 AND 9

E.1 AREA 7

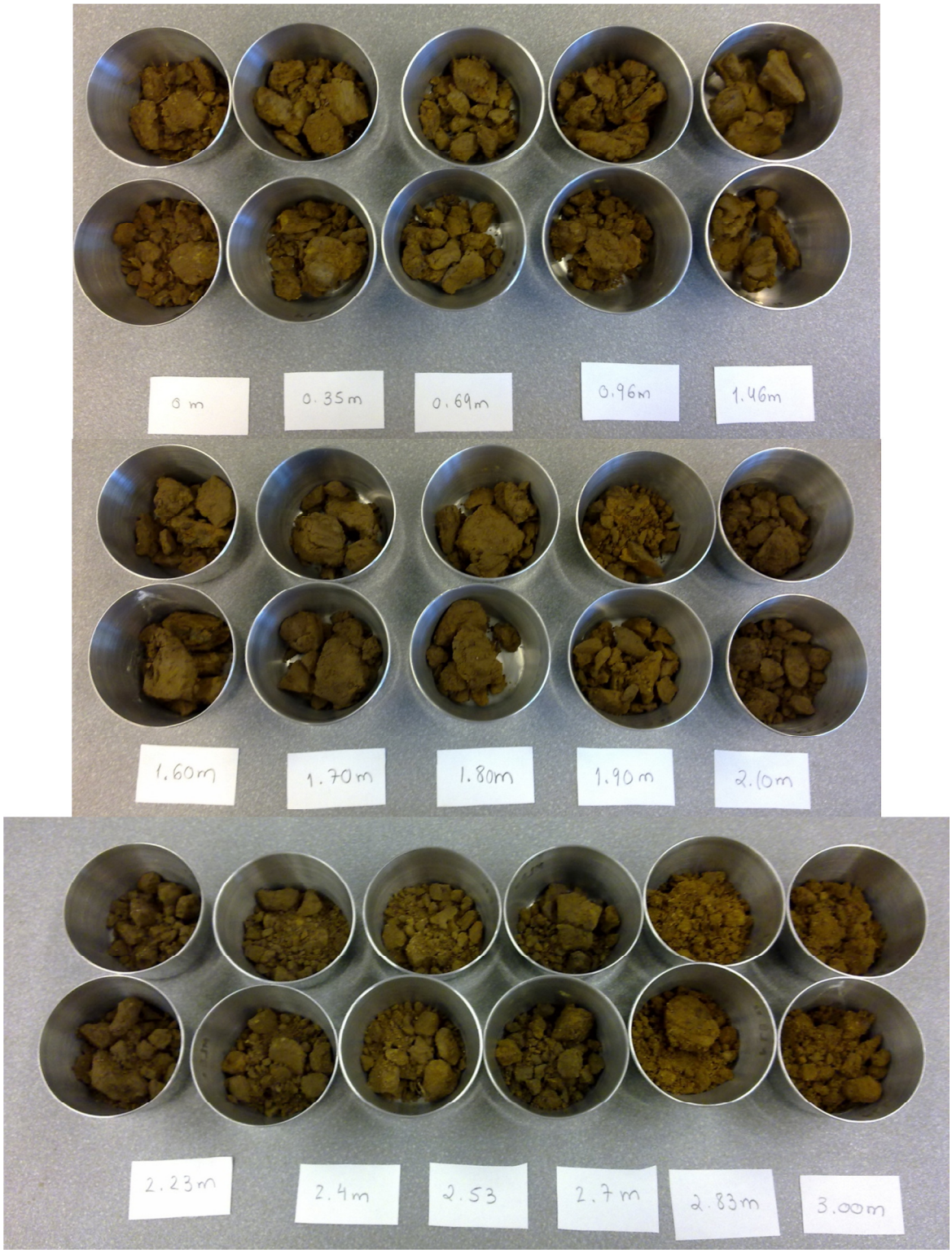

Figure E.1. Area 7 – Location 1: CS7.2.

Figure E.2. Area 7 – Location 2: CS 7.3.

E.2 AREA 9

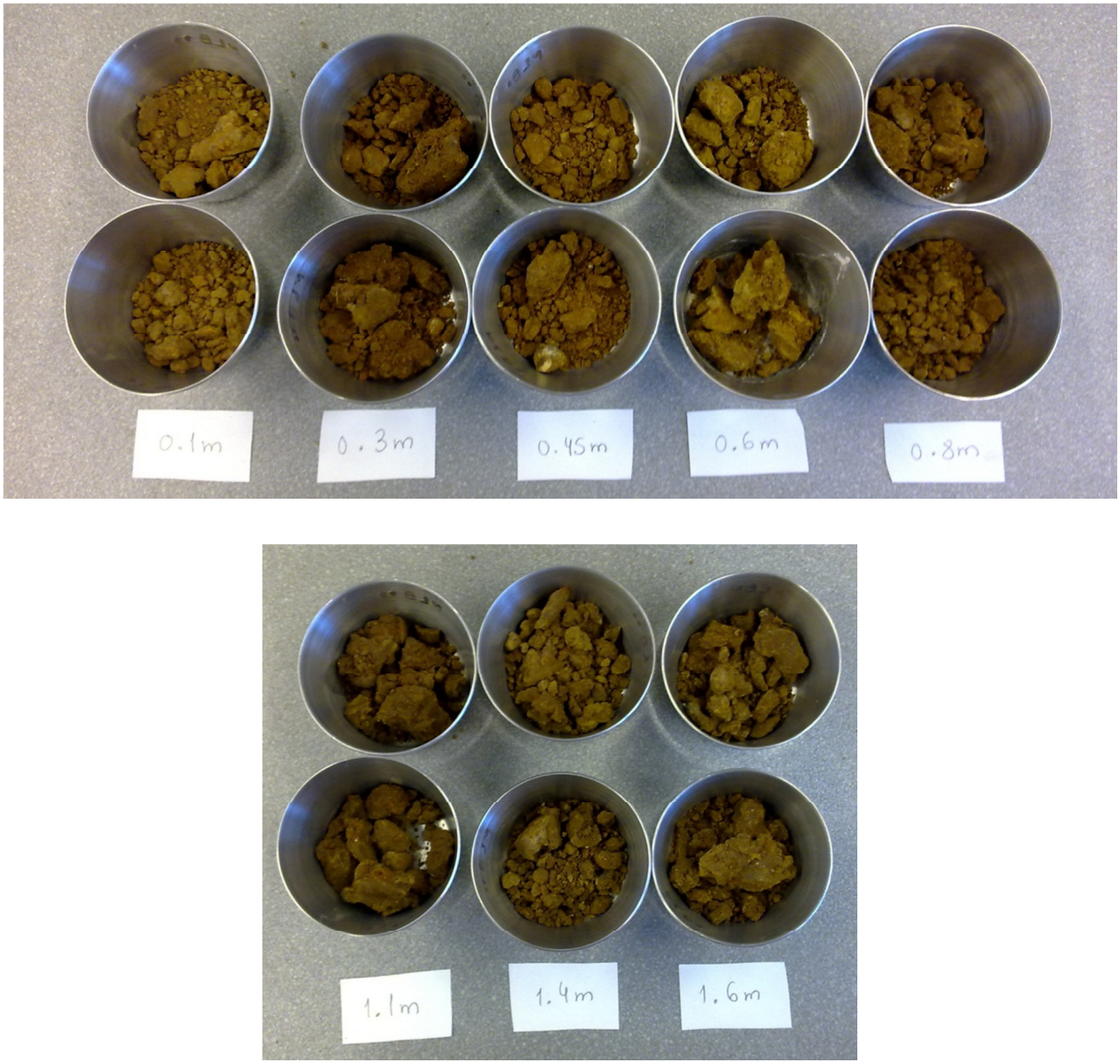

Figure E.3. Area 9 – Location 1 :CS9.2

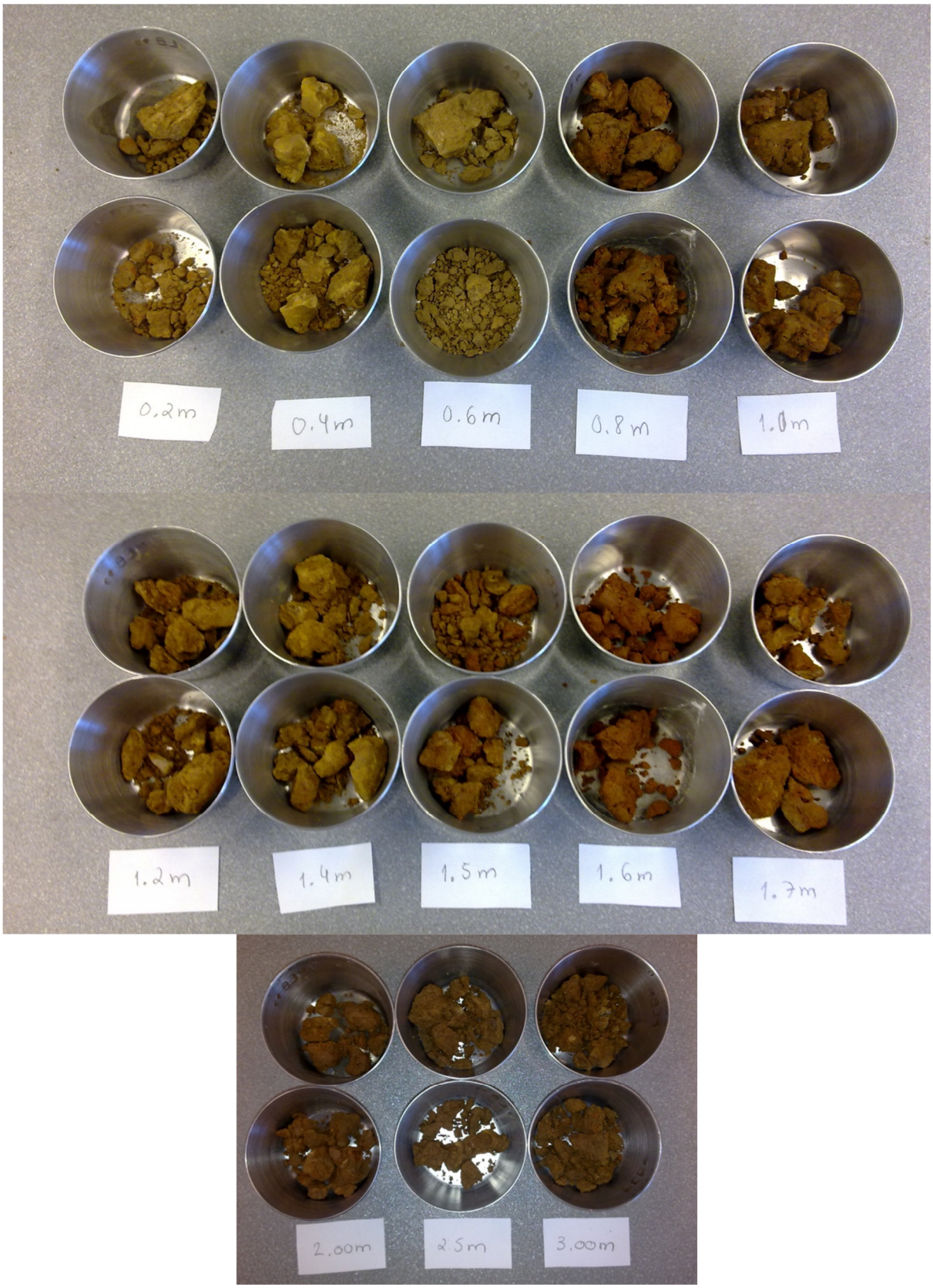

Figure E.4. Area 9 – Location 2:CS9.3

APPENDIX F . FITTING PROCEDURES USING MICROSOFT EXCEL

F.1 LEAST SQUARE FITTING METHOD WITH SOLVER

The least square fitting method is a very common method for fitting experimental data to non-linear functions. This is particularly important when dealing with empirical relationships where different parameters often represent different conditions or types of materials.

Consider the problem of fitting the experimental water retention data in Figure F.1 with the Zhang and Chen (2005) model:

$$S_{re} = p_M \frac{1}{\left[1+\left(\alpha_M s\right)^{n_M}\right]^{m_M}} + p_m \frac{1}{\left[1+\left(\alpha_m s\right)^{n_m}\right]^{m_m}} \tag{F.1}$$

where S_{re} is the effective degree of saturation, s is suction and α_M , α_m, m_M , m_m n_M and n_m are the fitting parameters to be found by the least square method. Given that the degree of uncertainty is similar for all the unknown parameters, the unweighted least square method is appropriate. The experimental values may be listed in a Microsoft Excel spread sheet (Table F.1) and the vertical deviation of the i^{th} point from the smooth curve is,

$$vertical\ deviation = y_{i-observed} - y_{i-calculated} \tag{F.2}$$

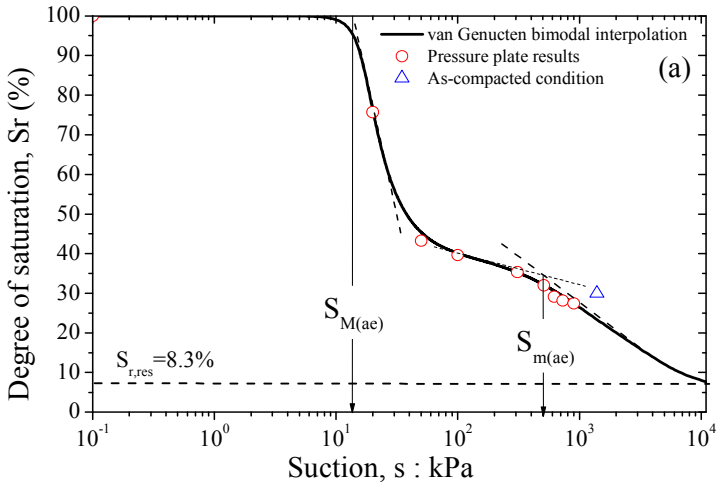

Figure F.1 Water retention data for a specimen prepared with an energy level of E = 529.5 kJ/m3at water content of 7.21% (replotted from Chapter 4).

According to the least square criterion, the square sum of the *n*-points deviations should be minimal. For every i^{th} point the square difference between the measured y_i and the calculated y_{i-m} values can be computed (Table F.1) by:

$$(y_i - y_{i-m}) = \sum_{i=1}^{n} \left[y_i - \left(p_M \frac{1}{[1 + (\alpha_M s)^{n_M}]^{m_M}} + p_m \frac{1}{[1 + (\alpha_m s)^{n_m}]^{m_m}} \right) \right]^2 \quad \text{(F.3)}$$

Table F.1 Summary of the measured and calculated values

x	y_i	y_{i-m}	$(y_i-y_{i-m})^2$
0.1	100.000	99.840	0.026
20	75.708	66.576	83.394
50	43.256	53.563	106.234
100	39.655	44.998	28.553
310	35.301	33.645	2.743
510	32.017	29.576	5.956
620	29.128	28.116	1.024
730	28.138	26.950	1.413
900	27.465	25.525	3.767

To perform the least square method in a Microsoft Excel spreadsheet we need to choose “data analysis” in the Data tab and then select the option for Solver (Figure A.1). The target cell represents the sum of the square differences, and the changing cells represent the parameters α, m, and n. Once the appropriate cells in the spreadsheet are selected, by clicking “solve” the solver tool looks up in matter of seconds the best combination of the selected parameters, and updates their values in spreadsheet.

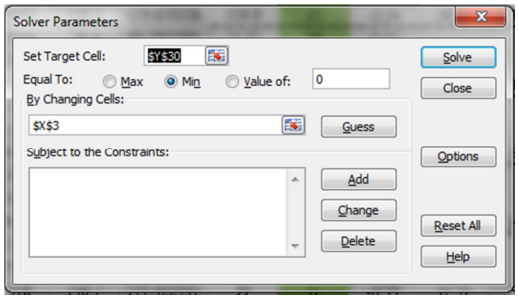

Figure F.2 Screenshot of the Microsoft Excel solver plugin.

F.2 MULTIPLE REGRESSION ANALYSIS

This technique was used to investigate the critical state friction angles with respect to the vertical stress and suction, and to analyse the separate contribution made by the two variables. The procedure adopted followed the method suggested by Toll (1990) using Microsoft Excel. In the next section the procedure using Microsoft Excel is described.

A multiple regression analysis consists of finding the best set of parameters, such that the model predicts the experimental values of the dependent variables as accurately as possible. It is also a good tool to evaluate whether the model with a given set of dependent variables is good enough to fit a given set of experimental data.

Taking the critical states friction angles as an example we have,

$$\tau = \sigma_v \tan\left(\phi^a\right)_c + s \tan\left(\phi^b\right)_c \tag{F.4}$$

where the independent variables initially assumed are the applied vertical stress σ_v and suction s, whereas the shear strength or τ is the dependent variable. For a multiple linear regression analysis we can rewrite Eq. (2.14) as follows,

$$y = b_0 + b_1 x_1 + b_2 x_2 \tag{F.5}$$

where b_0, b_1 and b_2 are the fitting coefficients and x_1 and x_2 represent the independent variables. The fitting coefficients can be found by solving the following set of equations:

$$\sum y = n b_0 + b_1 \sum x_1 + b_2 \sum x_2 \tag{F.6}$$

$$\sum y x_1 = b_0 \sum x_1 + b_1 \sum x_1^{\,2} + b_2 \sum x_1 x_2 \tag{F.7}$$

$$\sum y x_2 = b_0 \sum x_2 + b_1 \sum x_1 x_2 + b_2 \sum x_2^{\,2} \tag{F.8}$$

where *n* represents the number of observations for which the coefficients are sought. To determine the critical state friction angles, the test results were grouped in set of five, and to create a bias to the origin since b_0 coefficient is null in Eq. (2.14), an additional five null results were considered to be represented in Table F.3 (Toll, 1990). The critical friction angles are thought to be a function of the degree of saturation, thus the results are grouped in an ascending order of the degree of saturation (Table 7.3).

To perform multiple regression in a Microsoft Excel spreadsheet we need to choose "data analysis" in the Data tab and then select the option for regression (Figure A.2). After selecting the dependent and independent variables ranges in the spreadsheet, a number of options related to the statistical output of the regression are available. For this analysis, a confidence interval of 95% was adopted and a residual option was selected to evaluate the goodness of the model.

Table F.2 Summary of the shear results grouped in an ascending order of the degree of saturation

	$x_1=\sigma_v$	$x_2=s$	S_r	y
AC-8.5 (40)	38.4	606	0.42000224	55.71
AC-8.5 (82)	79.55	603	0.45895344	79.29
AC-8.5 (150)	146.7	587	0.547482	133.71
AC-10.6(40)	38.4	134.79	0.68119815	54.25
AC-10.6(80)	79.55	130.54	0.75328088	92.1
AC-10.6(150)	146.7	130.85	0.76588328	129
AC-12.6 (40)	38.4	21.68	0.80302465	32.43
AC-12.6 (82)	79.55	15.09	0.85179605	69.72
AC-12.8 (40)	38.4	59	0.86090014	35.87
AC-13.0 (40)	38.4	28	0.87816222	36.72
AC-16.8 (40)	38.4	8	0.8927325	23.89
AC-14.1 (40)	38.4	27	0.90327606	33.66
AC-12.6(150)	146.7	35	0.94772937	118.8
AC-16.8 (82)	79.55	10	0.93532135	44.69
AC-16.8 (150)	146.7	12	0.94253494	85.6
AC-13.0 (80)	79.55	44	0.96346807	66.28
AC-14.0 (40)	38.4	27	0.96045877	29.68
AC-12.8 (80)	79.55	65	0.97817776	59.85
AC-14.1 (80)	79.55	27	0.99276522	63.1
AC-14.0(150)	146.7	31	0.99104959	99
AC-14.0 (80)	79.55	27	1	57.78
AC-12.8(150)	146.7	66	1	128.49
AC-13.0(150)	146.7	40	1	120.7
AC-14.1 (150)	146.7	31	1	96.34

If there is any particular correlation between the residuals and any of the independent variables x_1 or x_2, i.e. the residuals increase as the variable increases, this means that the model is inadequate. Figure F.4 shows the residual plots for the first ten points, and it can be

observed that the residuals are random, and thus the proposed interdependency considered in Eq. (2.14) is adequate.

Further confirmation can be obtained by examining the ANOVA (Analysis of Variance) regression output (Table F.4). For further details regarding an analysis of the significance of the statistical output measures, the reader can refer to Affifi and Azen (1979). The values for the correlation coefficients should also be checked; typically a minimum of R2 of 0.98 was considered to be a good fit. The regression coefficients obtained for b1 and b2 are 0.91 and 0.01, respectively and b0 or intercept is 4.21 even though there was a heavy origin biased regression. The procedure is then repeated for the following five points, dropping one every time and gradually advancing through the complete set of results (Toll, 1990).

Table F.3 Multiple regression analysis first ten points.

	$x_1=\sigma_v$	$x_2=s$	y
AC-8.5 (40)	38.4	606	55.71
AC-8.5 (82)	79.55	603	79.29
AC-8.5 (150)	146.7	587	133.71
AC-10.6(40)	38.4	134.79	54.25
AC-10.6(80)	79.55	130.54	92.1
6	0	0	0
7	0	0	0
8	0	0	0
9	0	0	0
10	0	0	0

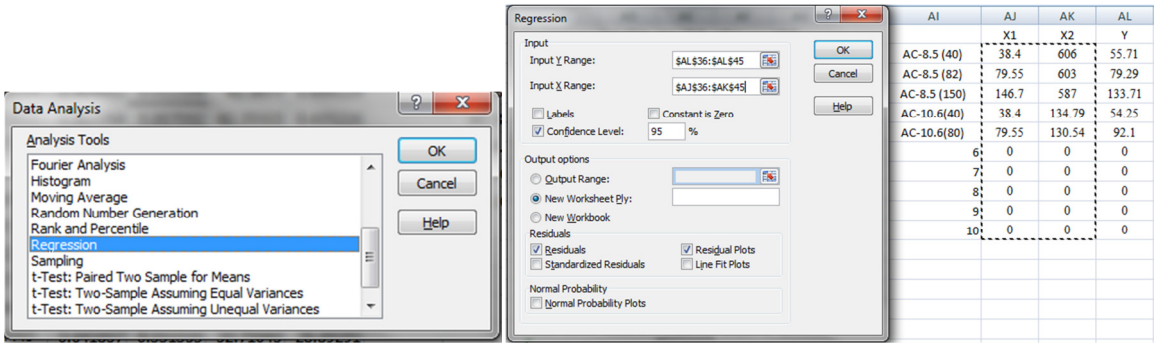

(a) (b)

Figure F.3 Microsoft Excel screenshot of the (a) data analysis menu and (b) regression menu.

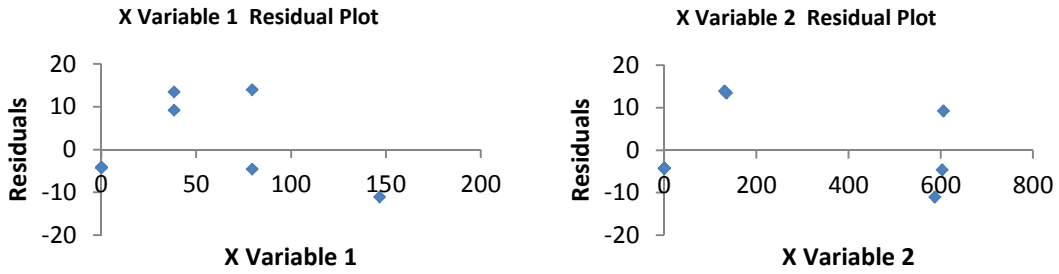

Figure F.4 Residuals plots for the first ten points.

Table F.4 ANOVA regression output for the first ten points.

ANOVA

	df	*SS*	*MS*	*F*	*Significance F*
Regression	2.00	20773.68	10386.84	104.89	6×10^{-6}
Residual	7.00	693.18	99.03		
Total	9.00	21466.86			

	Coefficients	*Standard Error*	*t Stat*	*P-value*	*Lower 95%*	*Upper 95%*	*Lower 95.0%*	*Upper 95.0%*
Intercept	4.21	4.13	1.02	0.34	-5.56	13.98	-5.56	13.98
X1	0.91	0.10	8.95	0.00	0.67	1.15	0.67	1.15
X2	0.01	0.02	0.66	0.53	-0.03	0.06	-0.03	0.06

Table F.5 shows the results of the calculations with the values of the critical friction angles obtained for each iteration; the values of the intercept and the correlation coefficient are also listed. The maximum intercept is 4.223 and the minimum correlation coefficient obtained is 0.984, which indicates a very good fit. The friction angles in Figure F.4 are plotted against the average degree of saturation. Although there seems to be a clear relationship between the critical friction angles and degree of saturation at this stage, only a general trend can be interpreted, as outlined by Toll (1990). In the following stages, the smoothed curves drawn in stage 1 are compared with the data points to refine the best fit parameters, while the data points are compared separately with each of the smoothed functions. Assuming that ϕ^b is correct, we can then recalculate the ϕ^a values using the data points, and repeat the procedure

to recalculate ϕ^b by assuming that ϕ^a is correct. The results of stages 2 and 3 are shown in Figure F.6.

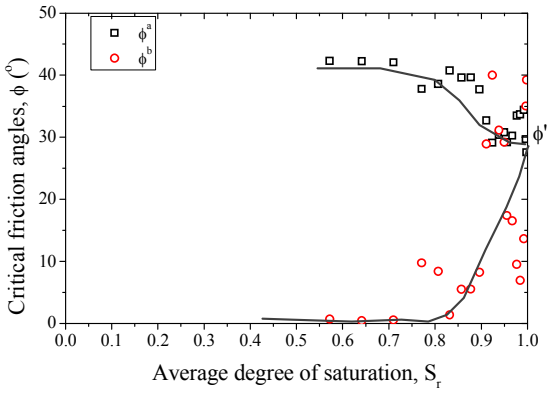

Figure F.5 Variation of the critical friction angles obtained in the multiple linear regression analysis stage 1.

Table F.5 Summary of the multiple regression analysis of the complete data set.

No. iterations	Average S_r	Intercept=b_0	tanϕ^a	tanϕ^b	R^2	ϕ^a	ϕ^b
1	0.572	4.213	0.909	0.012	0.984	42.308	0.694
2	0.641	2.192	0.908	0.008	0.990	42.253	0.435
3	0.710	1.887	0.902	0.010	0.989	42.056	0.559
4	0.771	0.849	0.774	0.172	0.996	37.773	9.758
5	0.807	1.343	0.797	0.148	0.996	38.567	8.404
6	0.832	0.360	0.861	0.024	1.000	40.750	1.382
7	0.857	-0.681	0.827	0.096	0.992	39.603	5.499
8	0.877	-0.649	0.828	0.097	0.992	39.650	5.533
9	0.897	-0.568	0.772	0.144	0.998	37.700	8.223
10	0.911	-2.096	0.642	0.552	0.992	32.710	28.893
11	0.924	-2.070	0.556	0.838	0.992	29.105	39.990
12	0.938	-1.593	0.586	0.603	0.991	30.390	31.124
13	0.950	-1.875	0.595	0.558	0.990	30.788	29.197
14	0.956	-0.005	0.559	0.313	0.995	29.204	17.382
15	0.967	0.551	0.583	0.297	0.992	30.260	16.535
16	0.977	0.542	0.661	0.167	0.996	33.475	9.503
17	0.984	0.547	0.666	0.122	0.998	33.698	6.940
18	0.992	-0.819	0.684	0.242	0.992	34.402	13.622
19	0.997	-0.581	0.569	0.700	0.997	29.672	35.010
20	0.998	-0.487	0.522	0.816	0.996	27.587	39.251

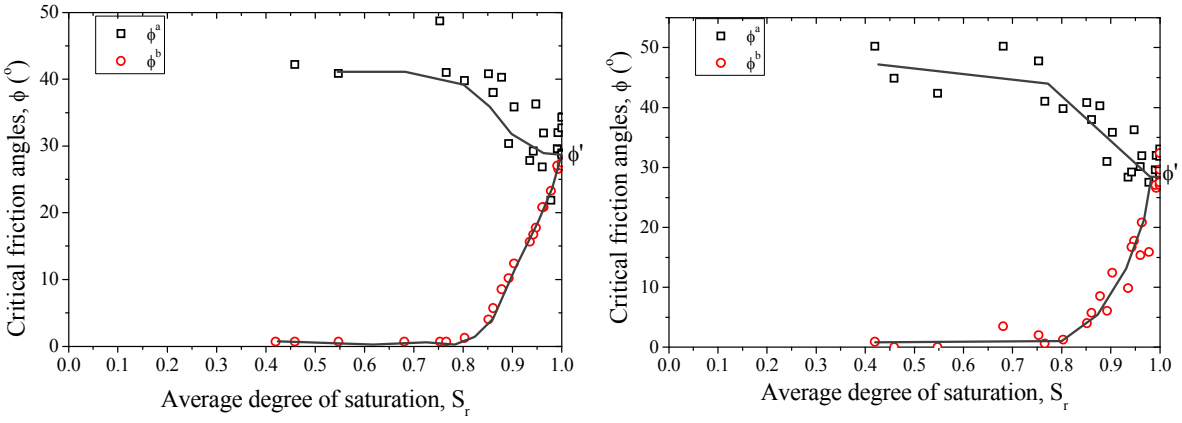

Figure F.6 Variation of the critical friction angles obtained in the multiple linear regression analysis stages 2 and 3.

APPENDIX G . SHEAR WAVE TIME SERIES

G.1 GENERAL

For ease of reading throughout the thesis, some of the shear wave time series plots that are fundamental to determine the time of travel were not included in the previous chapters. Those are included here.

G.2 AS COMPACTED SERIES

The shear wave velocities computed for the specimens prepared at different water content and energy levels and tested in as compacted condition, represented in Chapter 5, are shown in Figure G.1.

G.3 POST-COMPACTED SERIES

The shear wave velocities computed for the specimens prepared at different water content and energy levels and tested in post-compacted condition for increasing confining pressure and the wetting-drying cycles, represented in Chapter 5, are shown in Figure G.2 and Figure G.3, respectively.

G.4 DRYING PROCESS AND COMPACTION ENERGY

The shear wave velocities computed for the drying process and for the increase in void ratio at constant suction represented in Chapter 4 are shown in Figure G.4.

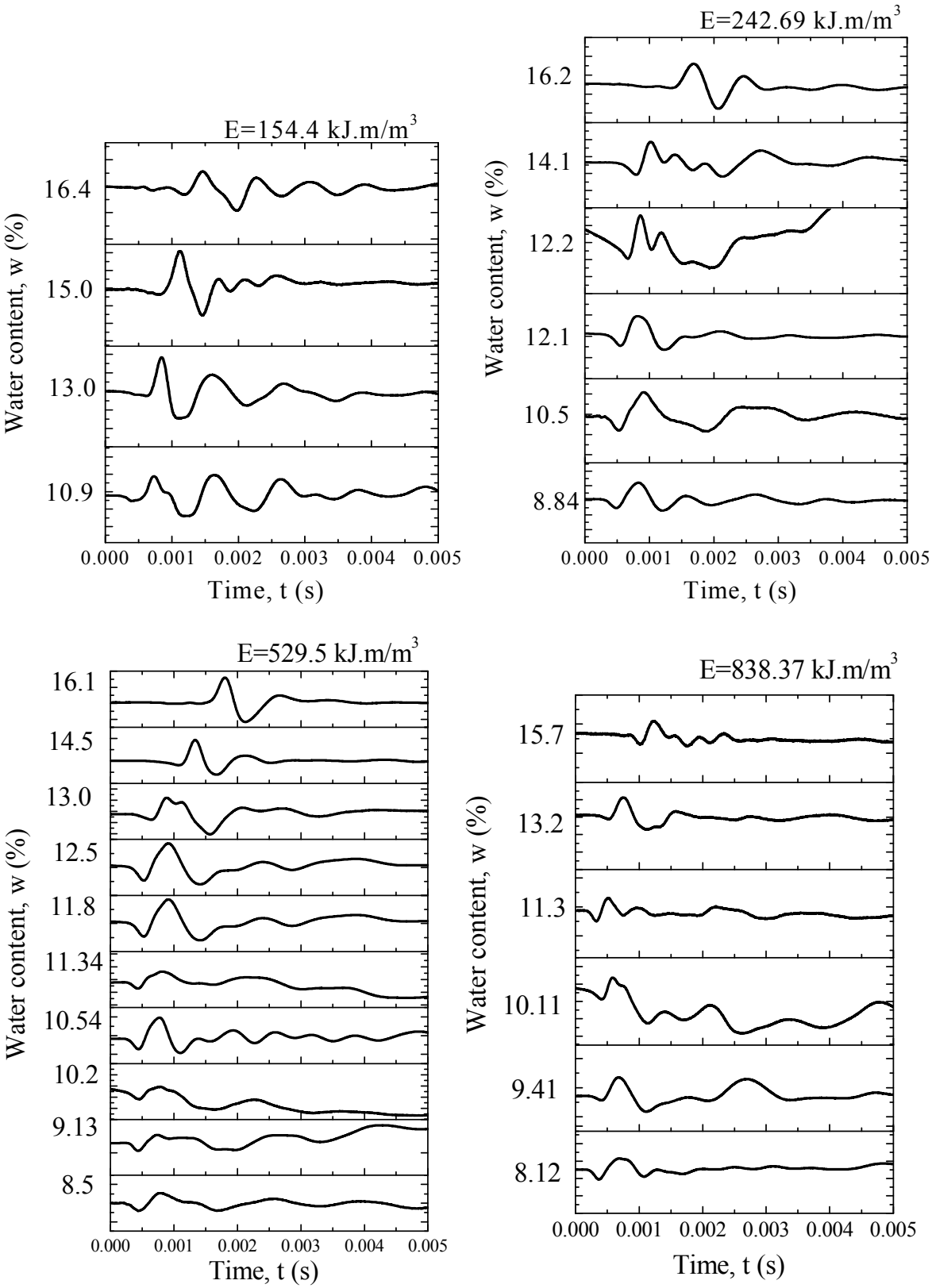

Figure G.1 Traces of shear waves for specimens compacted under different moisture contents at a compaction energy of E_1 = 154.5 kN.m/m^3, E_2 = 242.7 kN.m/m^3, E_3 = 529.5 kN.m/m^3, E_4 = 838.4 kN.m/m^3.

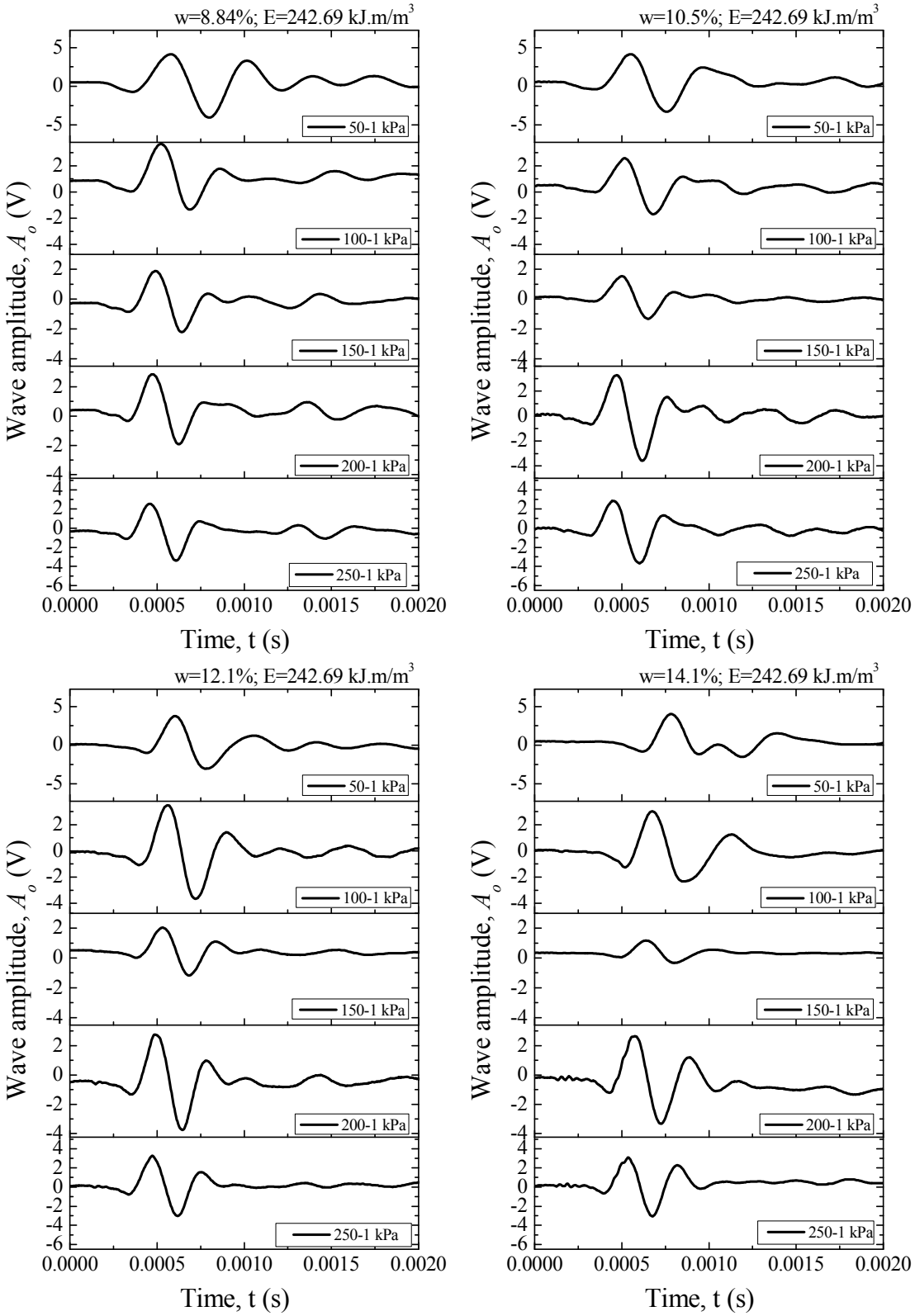
w=8.84%; E=242.69 kJ.m/m3
w=10.5%; E=242.69 kJ.m/m3
w=12.1%; E=242.69 kJ.m/m3
w=14.1%; E=242.69 kJ.m/m3
Wave amplitude, A_o (V)
Time, t (s)
50-1 kPa
100-1 kPa
150-1 kPa
200-1 kPa
250-1 kPa
0.0000
0.0005
0.0010
0.0015
0.0020

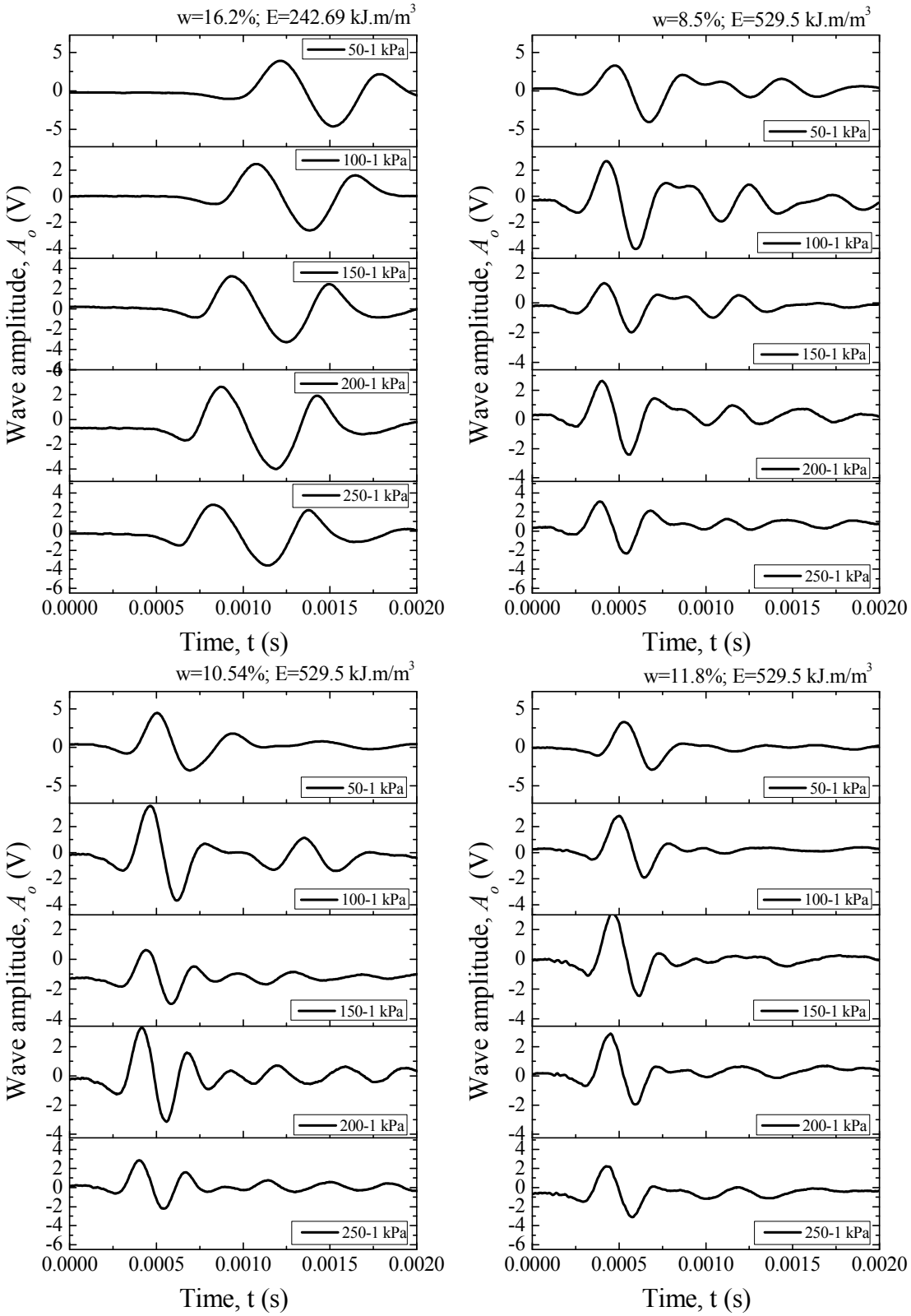
w=16.2%; E=242.69 kJ.m/m3
w=8.5%; E=529.5 kJ.m/m3
w=10.54%; E=529.5 kJ.m/m3
w=11.8%; E=529.5 kJ.m/m3
50-1 kPa
100-1 kPa
150-1 kPa
200-1 kPa
250-1 kPa
Wave amplitude, A_o (V)
Time, t (s)
0.0000
0.0005
0.0010
0.0015
0.0020

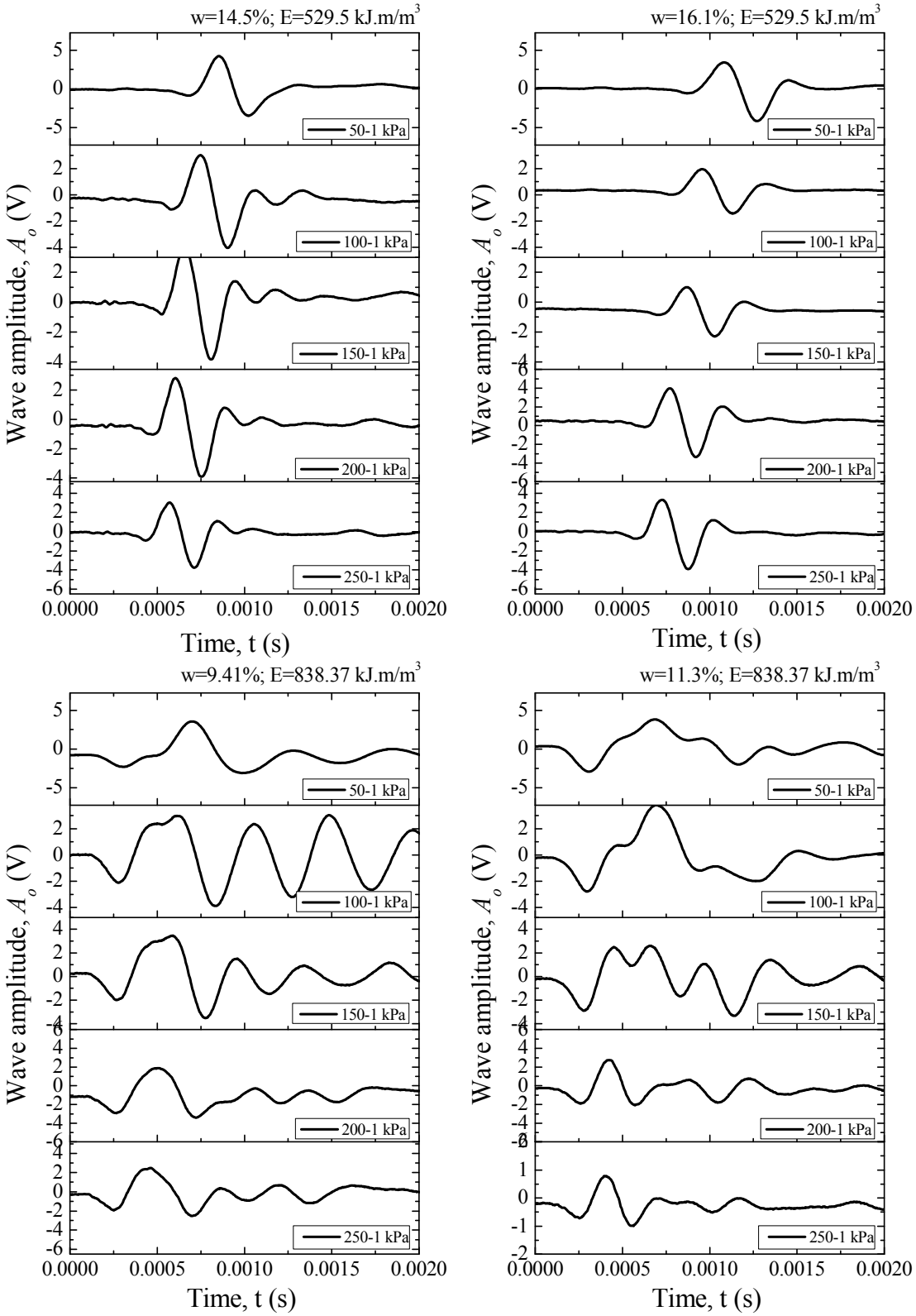
w=14.5%; E=529.5 kJ.m/m3
w=16.1%; E=529.5 kJ.m/m3
w=9.41%; E=838.37 kJ.m/m3
w=11.3%; E=838.37 kJ.m/m3
Wave amplitude, A_o (V)
Time, t (s)
50-1 kPa
100-1 kPa
150-1 kPa
200-1 kPa
250-1 kPa

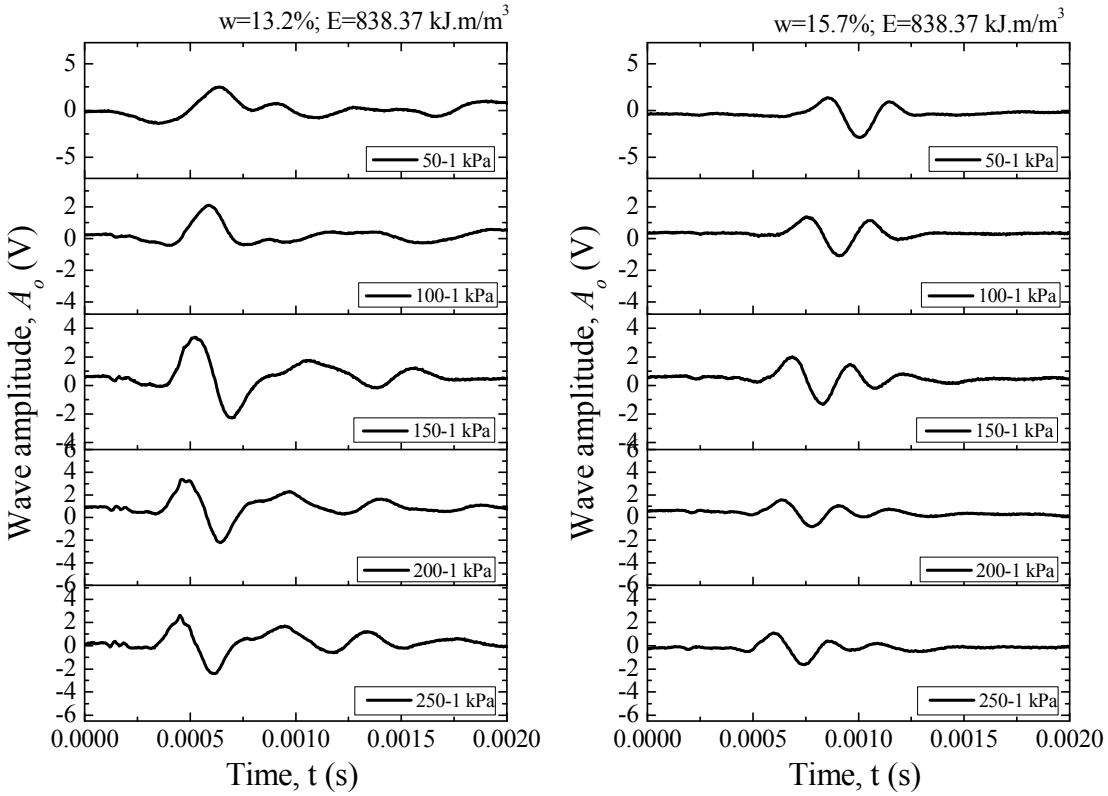

Figure G.2 Traces of the shear wave with increasing confining pressure (50-250kPa) measured in specimens prepared at different water content and energy levels.

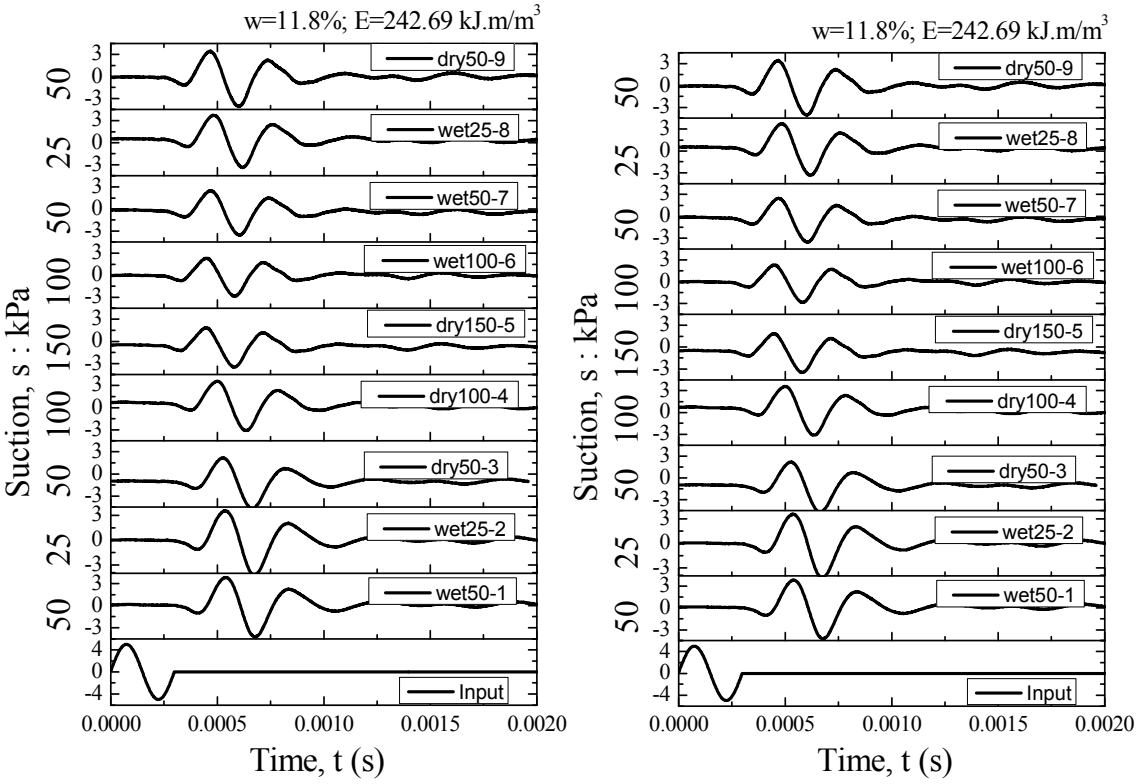

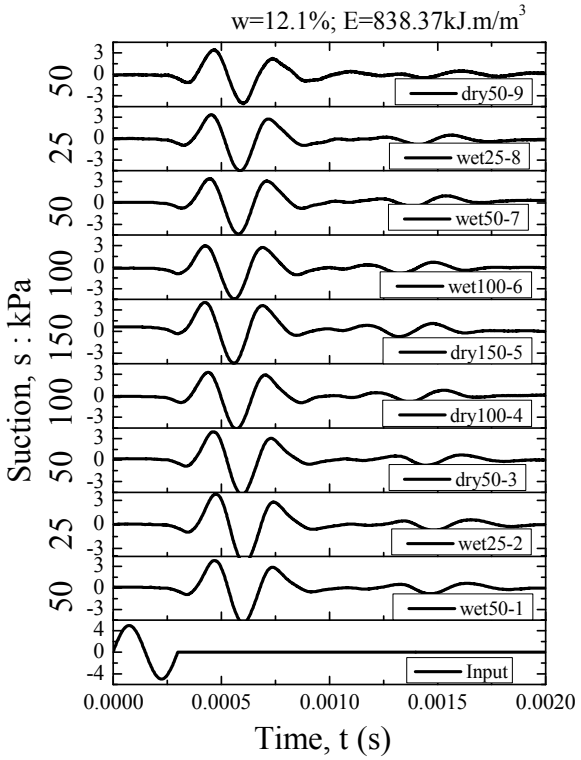

Figure G.3.Shear wave time series of the specimens subjected to post-compaction wetting and drying cycles.

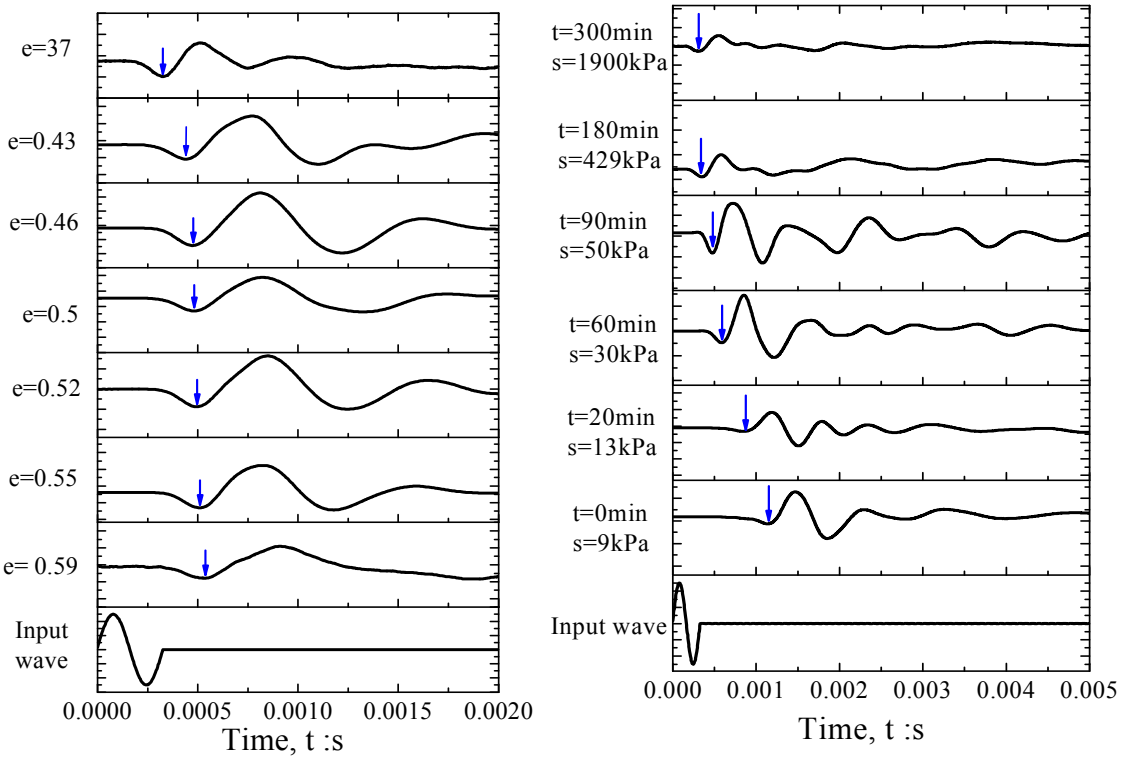

Figure G.4.Shear wave time series with (left) void ratio of specimens compacted at 10.5% with different compaction efforts and (right) drying process of specimen compacted at 15.8% with equivalent standard compaction effort